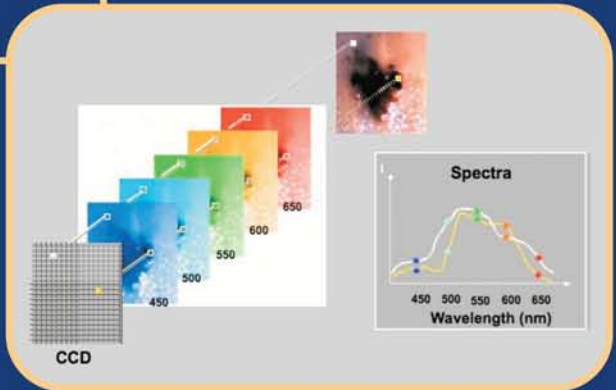
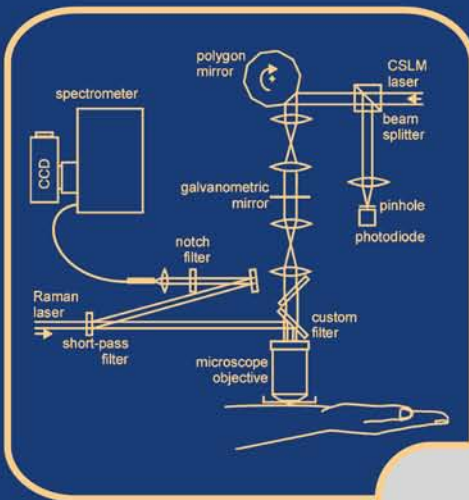


BIOENGINEERING OF THE SKIN

Skin Imaging and Analysis

Second Edition



Edited by

Klaus-P. Wilhelm
Peter Elsner

Enzo Berardesca
Howard I. Maibach

DERMATOLOGY: CLINICAL & BASIC SCIENCE SERIES/31

DERMATOLOGY: CLINICAL & BASIC SCIENCE SERIES

BIOENGINEERING OF THE SKIN

DERMATOLOGY
CLINICAL & BASIC SCIENCE SERIES

Series Editor

Howard I. Maibach, M.D.

University of California at San Francisco School of Medicine
San Francisco, California, U.S.A.

1. Health Risk Assessment: Dermal and Inhalation Exposure and Absorption of Toxicants, *edited by Rhoda G. M. Wang, James B. Knaack, and Howard I. Maibach*
2. Pigmentation and Pigmentary Disorders, *edited by Norman Levine and Howard I. Maibach*
3. Hand Eczema, *edited by Torkil Menné and Howard I. Maibach*
4. Protective Gloves for Occupational Use, *edited by Gunh A. Mellstrom, Jan E. Wahlberg, and Howard I. Maibach*
5. Bioengineering of the Skin (Five Volume Set), *edited by Howard I. Maibach*
6. Bioengineering of the Skin: Water and the Stratum Corneum, Volume I, *edited by Peter Elsner, Enzo Berardesca, and Howard I. Maibach*
7. Bioengineering of the Skin: Cutaneous Blood Flow and Erythema, Volume II, *edited by Enzo Berardesca, Peter Elsner, and Howard I. Maibach*
8. Skin Cancer: Mechanisms and Human Relevance, *edited by Hasan Mukhtar*
9. Bioengineering of the Skin: Methods and Instrumentation, Volume III, *edited by Enzo Berardesca, Peter Elsner, Klaus-P. Wilhelm, and Howard I. Maibach*
10. Dermatologic Research Techniques, *edited by Howard I. Maibach*
11. The Irritant Contact Dermatitis Syndrome, *edited by Pieter van der Valk, Pieter Coenrads, and Howard I. Maibach*
12. Human Papillomavirus Infections in Dermatovenereology, *edited by Gerd Gross and Geo von Krogh*
13. Bioengineering of the Skin: Skin Surface, Imaging, and Analysis, Volume IV, *edited by Klaus-P. Wilhelm, Peter Elsner, Enzo Berardesca, and Howard I. Maibach*
14. Contact Urticaria Syndrome, *edited by Smita Amin, Howard I. Maibach, and Arto Lahti*
15. Skin Reactions to Drugs, *edited by Kirsti Kauppinen, Kristiina Alanko, Matti Hannuksela, and Howard I. Maibach*
16. Dry Skin and Moisturizers: Chemistry and Function, *edited by Marie Lodén and Howard I. Maibach*
17. Dermatologic Botany, *edited by Javier Avalos and Howard I. Maibach*
18. Hand Eczema, Second Edition, *edited by Torkil Menné and Howard I. Maibach*

19. Pesticide Dermatoses, *edited by Homero Penagos, Michael O'Malley, and Howard I. Maibach*
20. Bioengineering of the Skin: Skin Biomechanics, Volume V, *edited by Peter Elsner, Enzo Berardesca, Klaus-P. Wilhelm, and Howard I. Maibach*
21. Nickel and the Skin: Absorption, Immunology, Epidemiology, and Metallurgy, *edited by Jurij J. Hostýnek and Howard I. Maibach*
22. The Epidermis in Wound Healing, *edited by David T. Rovee and Howard I. Maibach*
23. Bioengineering of the Skin: Water and the Stratum Corneum, Second Edition, *edited by Joachim W. Fluhr, Peter Elsner, Enzo Berardesca, and Howard I. Maibach*
24. Protective Gloves for Occupational Use, Second Edition, *edited by Anders Boman, Tuula Estlander, Jan E. Wahlberg, and Howard I. Maibach*
25. Latex Intolerance: Basic Science, Epidemiology, and Clinical Management, *edited by Mahbub M. U. Chowdhry and Howard I. Maibach*
26. Cutaneous T-Cell Lymphoma: Mycosis Fungoides and Sezary Syndrome, *edited by Herschel S. Zackheim*
27. Dry Skin and Moisturizers: Chemistry and Function, Second Edition, *edited by Marie Lodén and Howard I. Maibach*
28. Ethnic Skin and Hair, *edited by Enzo Berardesca, Jean-Luc Lévêque, and Howard Maibach*
29. Sensitive Skin Syndrome, *edited by Enzo Berardesca, Joachim W. Fluhr, and Howard I. Maibach*
30. Copper and the Skin, *edited by Jurij J. Hostýnek, and Howard I. Maibach*
31. Bioengineering of the Skin: Skin Imaging and Analysis, Second Edition, *edited by Klaus-P. Wilhelm, Peter Elsner, Enzo Berardesca, and Howard I. Maibach*

DERMATOLOGY: CLINICAL & BASIC SCIENCE SERIES

BIOENGINEERING OF THE SKIN

Skin Imaging and Analysis

Second Edition

Edited by

Klaus-P. Wilhelm

*University of Lübeck
Lübeck, Germany*

*proDERM Institute for Applied Dermatological Research
Schenefeld/Hamburg, Germany*

Peter Elsner

*University of Jena
Jena, Germany*

Enzo Berardesca

*San Gallicano Dermatological Institute
Rome, Italy*

Howard I. Maibach

*University of California at San Francisco School of Medicine
San Francisco, California, U.S.A.*

informa

healthcare

New York London

Informa Healthcare USA, Inc.
270 Madison Avenue
New York, NY 10016

© 2007 by Informa Healthcare USA, Inc.
Informa Healthcare is an Informa business

No claim to original U.S. Government works
Printed in the United States of America on acid-free paper
10 9 8 7 6 5 4 3 2 1

International Standard Book Number-10: 0-8493-3817-4 (Hardcover)
International Standard Book Number-13: 978-0-8493-3817-5 (Hardcover)

This book contains information obtained from authentic and highly regarded sources. Reprinted material is quoted with permission, and sources are indicated. A wide variety of references are listed. Reasonable efforts have been made to publish reliable data and information, but the author and the publisher cannot assume responsibility for the validity of all materials or for the consequences of their use.

No part of this book may be reprinted, reproduced, transmitted, or utilized in any form by any electronic, mechanical, or other means, now known or hereafter invented, including photocopying, microfilming, and recording, or in any information storage or retrieval system, without written permission from the publishers.

For permission to photocopy or use material electronically from this work, please access www.copyright.com (<http://www.copyright.com/>) or contact the Copyright Clearance Center, Inc. (CCC) 222 Rosewood Drive, Danvers, MA 01923, 978-750-8400. CCC is a not-for-profit organization that provides licenses and registration for a variety of users. For organizations that have been granted a photocopy license by the CCC, a separate system of payment has been arranged.

Trademark Notice: Product or corporate names may be trademarks or registered trademarks, and are used only for identification and explanation without intent to infringe.

Library of Congress Cataloging-in-Publication Data

Bioengineering of the skin : skin imaging and analysis / edited by Klaus-P. Wilhelm ...
[et al.]. -- 2nd ed.

p. ; cm. -- (Dermatology : clinical & basic science ; 31)

Includes bibliographical references and index.

ISBN-13: 978-0-8493-3817-5 (hardcover : alk. paper)

ISBN-10: 0-8493-3817-4 (hardcover : alk. paper)

1. Epidermis--Imaging. I. Wilhelm, Klaus-Peter. II. Series: Dermatology (Informa Healthcare) ; 31.

[DNLN: 1. Epidermis--anatomy & histology. 2. Biomedical Engineering. 3.

Diagnostic Imaging--methods. 4. Skin Diseases--diagnosis. WR 101 B616 2006]

RL105.B54 2006
616.5'0754--dc22

2006046574

Visit the Informa Web site at
www.informa.com

and the Informa Healthcare Web site at
www.informahealthcare.com

Preface to the Second Edition

In the eight years since publication of the first edition, enormous progress has been made in the field of skin imaging and analysis. Because of the broad array of new methods now available to the research scientist—and more and more to the clinically-oriented dermatologist—we were able to widen the scope of this book from the skin surface to the entire skin. This is also reflected in the change of the volume title, *Bioengineering of the Skin: Skin Imaging and Analysis*.

Hence, this second edition is a major revision of the first edition, with more than 30 new chapters added.

Those chapters that were already included in the first edition were revised to reflect up-to-date knowledge. In order to comply with space and cost requirements, those chapters dealing with “older methodology,” which might still have their right and value for many research and/or clinical objectives, but with little change and development from the time of publication of the first edition could not be included in this volume.

In a time of ever-increasing speed, budget constraints, and double and triple obligations, we extend our sincerest thanks to our valued contributors—the eminent experts in the field of skin imaging and analysis: without the enthusiasm and commitment to write contributions in their “leisure time,” this book would not have been possible.

We acknowledge the skillful secretarial assistance of Anna-Karin Jenzen and Anet Carstensen and thank Barbara Ellen Norwitz, Kari Budyk, Sandra Beberman, and Dana Bigelow at Informa Healthcare, U.S.A., Inc./CRC Press for committing to this volume and for accelerating the editorial process. We hope that this new and completely revised edition will remain the reference book in the rapidly developing field of skin imaging and analysis and that the format will continue to provide a perfect introduction to the novice and be the valued reference and stimulation for the expert.

*Klaus-P. Wilhelm
Peter Elsner
Enzo Berardesca
Howard I. Maibach*

Preface to the First Edition

The fourth volume of our series on *Bioengineering of the Skin* is devoted to the methods for skin surface imaging and analysis. Although the skin as the outermost organ is at least partially visible at the first instant, its fine lines and furrows are not fully appreciated and quantified by the naked eye.

By continuous research and development of modern instrumentation, analysis and visualization of minute structures of the skin surface are now possible. The progress in this area has greatly influenced the cosmetic chemist and the basic researcher alike, which is reflected in this book.

This volume maintains the general outline of the series by focusing on the instrumentation and the techniques available to image and analyze the skin surface with special regard to *what* these instruments do measure and *why* and *when* to use them in skin research and product testing.

We thank our contributors; without their enthusiasm and commitment, this work would not have been possible.

We acknowledge the skillful secretarial assistance of Helga Schuhbauer and Paul Petralia, and thank Cindy R. Carelli, and Debbie Didier at CRC Press for accelerating the editorial process.

We hope that this book will be a perfect introduction to novice researchers and a valued reference for the expert.

Klaus-P. Wilhelm
Peter Elsner
Enzo Berardesca
Howard I. Maibach

Contents

Preface to the Second Edition iii
Preface to the First Edition v
Contributors xvii

1. Anatomy of the Skin Surface **1**
Claudia El Gammal, Stephan El Gammal, and Albert M. Kligman
Introduction 1
What Defines How the Skin Surface Appears to
Our Eyes? 1
References 13

2. Multimodal Imaging—What Can We Expect? **17**
Michael Vogt and Helmut Ermert
Introduction 17
Skin-Imaging Techniques 18
Multimodal Skin Imaging 20
Summary and Conclusions 27
References 28

**3. Comparative Studies of Scanning Electron Microscopy
and Transmission Electron Microscopy** **31**
Masaaki Ito, Fumiko Sakamoto, and Ken Hashimoto
Introduction 31
Normal Human Skin 32
Pathological Skin 40
References 48

**4. Multimodal Imaging of Skin Structures: Imagining
Imaging of the Skin** **51**
*Roger Wepf, Tobias Richter, Stefan S. Biel, Holger Schlüter,
Frank Fischer, Klaus-Peter Wittern, and Heinrich Hohenberg*
Introduction 51
General Strategy: An “Information-Transfer Chain” 52

One Biopsy for Multimodal Imaging—the Principle	55
Lipids—Often Ignored in Biology, Essential for the Skin Barrier	57
Application: Reviewing Barrier Morphology and Dynamics	58
A New Barrier in Epidermis at the Live-Death Transition	63
Multimodal Imaging of the Barriers—More Than One Barrier in Skin	64
Future Perspective	65
References	68
5. Image Analysis of D-Squames, Sebutapes and of Cyanoacrylate Follicular Biopsies	71
<i>Alessandra Pagnoni, Iqbal Sadiq, Tracy Stoudemayer, and Albert M. Kligman</i>	
Introduction	71
Cyanoacrylate Follicular Biopsy	71
Sebutape	74
D-Squames	76
References	79
6. High-Resolution Ultrasound	83
<i>Michael Vogt and Helmut Ermert</i>	
Introduction	83
Ultrasound Biomicroscopy of Skin	83
HFUS Scanner	88
Results	92
Summary and Discussion	95
References	96
7. Magnetic Resonance Imaging of Human Skin In Vivo	99
<i>Bernard Querleux, Luc Darrasse, and Jacques Bittoun</i>	
Introduction	99
Review of Magnetic Resonance Imaging of the Skin	99
Progress in MR Skin Imaging: Spatial Resolution and Water Behavior in Skin Layers	103
Perspectives of MR Skin Imaging: Local Microscopy in Clinical Body Scanners	105
Summary	106
References	108

8. High-Resolution In Vivo Multiphoton Tomography of Skin 111

Karsten König

- Introduction 111
- State-of-the-Art Skin Imaging Technologies 112
- Principle of Multiphoton Tomography 113
- The Multiphoton Tomograph DermaInspect 116
- Multiphoton Sectioning of Human Skin 117
- In Vivo Fluorescence Lifetime Imaging 119
- Early Detection of Melanoma 121
- In Situ Drug Screening 122
- Laser Safety Aspects 123
- Outlook 124
- References 124

9. Optical Coherence Tomography 127

Julia Welzel

- Introduction 127
- Technique 127
- OCT Studies in Dermatology 128
- Potential of the Technique 133
- Conclusion 134
- References 134

10. Fringe Projection for In Vivo Topometry 137

Sören Jaspers

- Introduction 137
- Technical Background 137
- In Vivo Topometry 140
- PRIMOS Systems 142
- Parameters 143
- Conclusion 146
- References 147

11. Confocal Microscopy of Skin In Vitro and Ex Vivo 149

Stefan S. Biel, Roger Wepf, and Sonja Wessel

- Introduction 149
- Applications of Confocal Microscopy:
 - Reflectance Imaging 154
- Applications of Confocal Microscopy:
 - Fluorescence Imaging 157

- Further Prospects of Confocal Microscopy 161
 Confocal Microscopy in the Context of Other
 Microscopic Techniques 162
 References 163
- 12. Histometry of the Skin by Means of In Vivo
 Confocal Microscopy 165**
Kirsten Sauermann and Sören Jaspers
 Introduction 165
 Vertical Parameters Measured with
 the Micronscrew 165
 Distance from Papilla to Capillary 171
 Horizontal Parameters Using Image Analysis 173
 Object Density Parameters 173
 References 174
- 13. Two-Photon Microscopy and Confocal Laser
 Scanning Microscopy of In Vivo Skin 177**
Gerald W. Lucassen and Rob F. M. Hendriks
 Introduction 177
 Confocal Laser Scanning Microscopy 177
 Two-Photon Fluorescence Microscopy 178
 Combined TPFM and CLSM 179
 Results 180
 Discussion and Conclusion 188
 References 189
- 14. Stereoimaging for Skin Contour Measurement 191**
Chilhwan Oh, Min Gi Kim, and Jong Sub Moon
 Introduction 191
 Methodological Principles 192
 Clinical Applications 197
 References 207
- 15. Development of a Digital Imaging System for Objective
 Measurement of Hyperpigmented Spots on the Face 209**
*Kukizo Miyamoto, Hirotsugu Takiwaki, Seiji Arase, and
 Greg G. Hillebrand*
 Introduction 209
 Material and Methods 209
 Results 214

Discussion and Conclusions 217
 References 219

16. Skin Documentation with Multimodal Imaging or Integrated Imaging Approaches 221

Nikiforos Kollias

Introduction 221
 The Interaction of Light with the Skin 222
 Macroimaging of the Skin 228
 Integrated Imaging: Mode—Wavelength 229
 Polarized Light Imaging of Skin 231
 Fluorescence Imaging of the Skin with Excitation in the
 Ultraviolet-A Radiation or the Blue 238
 Wavelength Integration 244
 Suggested Reading 246

17. Combined Raman Spectroscopy and Confocal Microscopy 247

Peter J. Caspers, Gerwin J. Puppels, and Gerald W. Lucassen

Introduction 247
 Raman Spectroscopy 247
 Confocal Scanning Laser Microscopy 250
 Combined Raman and CSLM 250
 Results 253
 Discussion and Conclusions 257
 References 258

18. Morphometry in Clinical Dermatology 259

Friedrich A. Bahmer

Introduction 259
 Morphometry: Principles and Applications in 2-D 260
 Stereology: From 2-D to 3-D 267
 Conclusions 268
 References 269

19. Measurement of Human Hair Growth 271

Dominique Van Neste

Introduction 271
 Basics About Hair Structure and Function 271
 Hair Photography and Imaging 272
 Conclusion 283
 References 285

20. Atopic Dermatitis and Other Skin Diseases 289
Marie Lodén
 Introduction 289
 Dry Skin in Atopic Patients 289
 Psoriatic Plaques 291
 The Ichtyoses 292
 Plaques of Morphea 293
 Melanoma 293
 Microcomedones 294
 Conclusions 295
 References 295

21. Differentiation Between Benign and Malignant Skin Tumors by Image Analysis, Neural Networks, and Other Methods of Machine Learning 297
Michael Binder, Harald Kittler, Hubert Pehamberger, and Stephan Dreiseitl
 Introduction 297
 Data Acquisition and Preprocessing 298
 Image Segmentation 298
 Feature Extraction 299
 Feature Selection 299
 Value of Clinical Information 299
 Model Building 300
 Logistic Regression 300
 Artificial Neural Networks 300
 Support Vector Machines 301
 Applying Computer Diagnosis on Melanoma and Pigmented Skin Lesions 301
 Conclusion 302
 References 303

22. Early Detection of Melanoma by Image Analysis 305
Stefania Seidenari, Giovanni Pellacani, and Costantino Grana
 The “A” of the ABCD Rule: Asymmetry Assessment 307
 The “B” of the ABCD Rule: Border Evaluation 308
 The “C” of the ABCD Rule: Colors 309
 The “D” of the ABCD Rule: Differential Structures 309
 Comparison Between Human and Computer Assessment 310
 References 311

23. Visualization of Skin pH 313
Martin J. Behne
 Introduction 313
 Established Technique 314
 Alternative Approaches 314
 Imaging Approaches 315
 The Microscopic Approach 315
 Fluorescence Lifetime Imaging Microscopy 316
 Appendix: Web Resources to Orient the Reader 320
 References 321

24. Visualization of Skin Oxygenation 325
*Markus Stücker, Paul Hartmann, Dietrich W. Lübbbers,
 David Harrison, and Peter Altmeyer*
 Heterogeneity of Skin Oxygenation 325
 Oxygen Uptake from the Atmosphere 325
 Measuring Transcutaneous Oxygen Flux 326
 Imaging of $tcpO_2$ and $tcJO_2$ 326
 Measuring Procedure 327
 Examples for Visualization of Skin Oxygenation 328
 Conclusion 329
 References 330

25. Capacitance Imaging of the Skin Surface 331
Jean-Luc Lévêque
 Introduction 331
 Technical Aspects of the Method 331
 Skin Images 332
 Relationship Between SkinChip and Corneometer
 Parameters 333
 Skin Surface Hydration Mapping 333
 Skin Microrelief 335
 Conclusion 336
 References 337

**26. Applications of Reflectance Confocal Microscopy
 in Clinical Dermatology 339**
*Cristiane Benvenuto-Andrade, Anna Liza C. Agero, Yogesh G. Patel,
 Milind Rajadhyaksha, Allan Halpern, Salvador Gonzalez, and
 Susanne Astner*
 Imaging Parameters for Reflectance-Mode Scanning
 Laser Confocal Microscopy 339

Confocal Microscopy of Normal Skin 339
 Reflectance Confocal Microscopy Findings of Inflammatory
 Skin Conditions 341
 Reflectance Confocal Microscopy Findings of Nonmelanocytic
 Skin Lesions 344
 Reflectance Confocal Microscopy of Melanocytic
 Skin Lesions 346
 Reflectance Confocal Microscopy as an Adjuvant for
 Mohs Micrographic Surgery 349
 Further Developments and Applications of RCM 349
 References 350

27. Sonography of the Skin in Health and Disease 353

*Stephan El Gammal, Claudia El Gammal, Peter Altmeyer,
 Michael Vogt, and Helmut Ermert*
 Introduction 353
 Methods and Patients 356
 Results 358
 Discussion 371
 References 373

28. Noninvasive Imaging in the Evaluation of Cellulite 377

Theresa Callaghan and Klaus-P. Wilhelm
 Introduction 377
 Evaluating the Condition—Clinical Considerations 378
 Conclusions 386
 References 387

29. Effects of Detergents 391

Minehiro Okuda and Keiichi Kawai
 What Is Detergent? 391
 Effects of Detergents on the Skin 394
 References 401

**30. Monitoring Skin Hydration by Near-Infrared Spectroscopy
 and Multispectral Imaging 403**

Shuliang L. Zhang
 Introduction 403
 Instrumentation 405
 Clinical Design and Evaluation Methods 406
 Hydration Images and Data Analysis 408
 Results and Discussion 408

Conclusion 414
 References 415

31. Assessment of Anticellulite Efficacy 417

Claudia Rona and Enzo Berardesca

Introduction 417
 Cellulitic Skin Features 417
 Cellulite Stages 418
 Pathogenesis 418
 Noninvasive Techniques to Evaluate Cellulite 419
 Conclusions 422
 References 422

32. Digital Imaging as an Effective Means of Recording and Measuring the Visual Signs of Skin Aging 423

Paul J. Matts, Kukizo Miyamoto, and Greg G. Hillebrand

Introduction 423
 First Principles: Understanding the Interaction of Light with Aging Skin 424
 Changes in the Expression and Presentation of Melanin, Hemoglobin, Collagen, and in Surface Topography with Age 425
 The Effect of Chromophore and Topography Changes in Aging Skin Upon Perception of Age, Health, and Beauty 428
 The Core Principle of Effective Digital Imaging—Reproducibility 429
 The Practical Use of Imaging of Aging Skin 433
 State-of-the-Art Color Analysis of Aging Skin—The Emerging Science of Chromophore Mapping 435
 Conclusion 443
 References 443

33. Evaluation of Comedogenic Activity by Skin Fluorescence Imaging Analysis (Skin Analyzing Fluorescence Imaging Recorder) 447

Andreas Herpens, Silke Schagen, Stefan Scheede, and Boris Kristof

Introduction 447
 Origins of Fluorescence Signals from Sebaceous Follicles 448
 The Skin Analyzing Fluorescence Imaging Recorder and Fluorescence Imaging System 450

Biological Qualification of the SAFIR Fluorescence
 Imaging System 454
 Conclusion 457
 References 458

**34. Quantifying Skin Ashing Using
 Cross-Polarized Imaging 459**

Robert Velthuizen, Helene Santanastasio, and Srinivasan Krishnan
 Introduction 459
 Visual Grading Scale 459
 Digital Image Analysis 461
 Results 463
 Discussion and Conclusions 466
 References 467

**35. Imaging of Pore Size and Sebum Secretion by Sebumtape
 During Treatment for Skin Oiliness 469**

Enzo Berardesca, Claudia Rona, M. B. Finkey, and Yohin Appa
 Introduction 469
 Materials and Methods 469
 Results 471
 Discussion 472
 Conclusions 473
 References 473

**36. Utilization of a High-Resolution Digital Imaging System
 for the Objective and Quantitative Assessment of
 Hyperpigmented Spots on the Face 475**

*Kukizo Miyamoto, Hirotsugu Takiwaki, Greg G. Hillebrand
 and Seiji Arase*
 Introduction 475
 Materials and Methods 476
 Results 477
 Discussion and Conclusions 479
 References 482

Index 483

Contributors

Anna Liza C. Agero Dermatology Service, Memorial Sloan-Kettering Cancer Center, New York, New York, U.S.A.

Peter Altmeyer Department of Dermatology, Ruhr-University, and Dermatological Clinic of the Ruhr-University, St. Josef Hospital, Bochum, Germany

Yohin Appa Neutrogena Corporation, Los Angeles, California, U.S.A.

Seiji Arase Department of Dermatology, School of Medicine, The University of Tokushima, Kuramoto-cho, Tokushima, Japan

Susanne Astner Department of Dermatology, Venerology and Allergology, Charité University Medicine Berlin, Charitéplatz, Berlin, Germany

Friedrich A. Bahmer Department of Dermatology, Central Hospital, Bremen, Germany

Martin J. Behne Department of Dermatology and Venerology, University of Medical Center Hamburg-Eppendorf, University of Hamburg, Germany

Cristiane Benvenuto-Andrade Dermatology Service, Memorial Sloan-Kettering Cancer Center, New York, New York, U.S.A.

Enzo Berardesca San Gallicano Dermatological Institute, Rome, Italy

Stefan S. Biel Beiersdorf AG, Research Microscopy, Hamburg, Germany

Michael Binder Division of General Dermatology, Department of Dermatology, Medical University of Vienna, Währingergürtel, Vienna, Austria

Jacques Bittoun U2R2M UMR8081-CNRS-Université Paris-Sud, CIERM-hospital Bicetre, Le Kremlin-Bicetre, France

Theresa Callaghan proDERM Institute for Applied Dermatological Research, Kiebitzweg, Hamburg, Germany

Peter J. Caspers Department of General Surgery, Center for Optical Diagnostics and Therapy, Erasmus MC, and River Diagnostics B.V., Rotterdam, The Netherlands

Luc Darrasse U2R2M UMR8081-CNRS-Université Paris-Sud, Orsay, France

Stephan Dreiseitl Department of Software Engineering, Upper Austria University of Applied Sciences, Upper Austria, Austria

Claudia El Gammal Department of Dermatology, Medical Care Center, Jung-Stilling Hospital, Siegen, Germany

Stephan El Gammal Dermatological Clinic, Hospital Bethesda, Freudenberg, Germany

Helmut Ermert Institute of High Frequency Engineering, Ruhr-University Bochum, Bochum, Germany

M. B. Finkey Neutrogena Corporation, Los Angeles, California, U.S.A.

Frank Fischer Beiersdorf AG, Advanced Development Deo/AP, Hamburg, Germany

Salvador Gonzalez Dermatology Service, Memorial Sloan-Kettering Cancer Center, New York, New York, U.S.A.

Costantino Grana Department of Computer Engineering, University of Modena and Reggio Emilia, Italy

Allan Halpern Dermatology Service, Memorial Sloan-Kettering Cancer Center, New York, New York, U.S.A.

David Harrison Regional Medical Physics Department, Durham Unit, University Hospital of North Durham, U.K.

Paul Hartmann Roche Diagnostics GmbH, Graz, Austria

Ken Hashimoto Department of Dermatology, Wayne State University School of Medicine, Detroit, Michigan, U.S.A.

Rob F. M. Hendriks Philips Research (WA11), Eindhoven, and Lumileds, Best, The Netherlands

Andreas Herpens Department of Bioengineering, Beiersdorf AG Research, Hamburg, Germany

Greg G. Hillebrand Procter & Gamble Company, Higashinada-Ku, Kobe, Japan, and Procter & Gamble Company, Cincinnati, Ohio, U.S.A.

Heinrich Hohenberg Beiersdorf AG, Advanced Development Deo/AP,
Hamburg, Germany

Masaaki Ito Department of Dermatology, Niigata University School of
Medicine, Niigata, Japan

Sören Jaspers Research and Development, Biophysics, Beiersdorf AG,
Hamburg, Germany

Keiichi Kawai Kawai Medical Laboratory for Cutaneous Health, Shimogyo-ku,
Kyoto, Japan

Min Gi Kim Department of Electronics and Information Engineering, Korea
University, Yeonkigun, Choognam, South Korea

Harald Kittler Division of General Dermatology, Department of Dermatology,
Medical University of Vienna, Wahringergurtel, Vienna, Austria

Albert M. Kligman Department of Dermatology, University of Pennsylvania,
Philadelphia, Pennsylvania, U.S.A.

Nikiforos Kollias Methods and Models, Johnson and Johnson Consumer and
Personal Products Worldwide Co., Skillman, New Jersey, U.S.A.

Karsten König Fraunhofer Institute of Biomedical Technology (IBMT),
St. Ingbert, and Faculty of Mechatronics and Physics, Saarland University,
Saarbrücken, Germany

Srinivasan Krishnan Unilever Research and Development, Trumbull,
Connecticut, U.S.A.

Boris Kristof Department of Bioengineering, Beiersdorf AG Research,
Hamburg, Germany

Jean-Luc Lévêque L'Oréal Recherche, Centre Charles Zviak, Clichy, France

Marie Lodén ACO HUD AB, Research & Development, Upplands Väsby,
Sweden

Gerald W. Lucassen Care & Health Applications, Philips Research,
Eindhoven, The Netherlands

Dietrich W. Lübbers Max Planck Institut für Molekulare Physiologie,
Dortmund, Germany

Paul J. Matts Procter & Gamble, Rusham Park Technical Centre, Egham,
Surrey, U.K.

Kukizo Miyamoto Department of Dermatology, School of Medicine, The University of Tokushima, Kuramoto-cho, Tokushima, and Research and Development, Personal Beauty Care, Tokushima, and Procter & Gamble Company, Higashinada-Ku, Kobe, Japan, and Procter & Gamble Company, Cincinnati, Ohio, U.S.A.

Jong Sub Moon Department of Electronics and Information Engineering, Korea University, Yeonkigun, Choognam, South Korea

Chilhwan Oh Department of Electronics and Information Engineering, Korea University, Yeonkigun, Choognam, South Korea

Minehiro Okuda Kao Corporation, Safety and Microbial Control Research Center, Tochigi, Japan

Alessandra Pagnoni Pagnoni Consulting, LLC, Yardley, Pennsylvania, U.S.A.

Yogesh G. Patel Dermatology Service, Memorial Sloan-Kettering Cancer Center, New York, New York, U.S.A.

Hubert Pehamberger Division of General Dermatology, Department of Dermatology, Medical University of Vienna, Währingergurtel, Vienna, Austria

Giovanni Pellacani Department of Dermatology, University of Modena and Reggio Emilia, Italy

Gerwin J. Puppels Department of General Surgery, Center for Optical Diagnostics and Therapy, Erasmus MC, and River Diagnostics B.V., Rotterdam, The Netherlands

Bernard Querleux L'Oréal Recherche, Aulnay-sous-bois, France

Milind Rajadhyaksha Dermatology Service, Memorial Sloan-Kettering Cancer Center, New York, New York, U.S.A.

Tobias Richter Beiersdorf AG, Advanced Development Deo/AP, Hamburg, Germany

Claudia Rona Department of Dermatology, University of Pavia, Pavia, Italy

Iqbal Sadiq S.K.I.N. Incorporated, Conshohocken, Pennsylvania, U.S.A.

Fumiko Sakamoto Department of Dermatology, Niigata University School of Medicine, Niigata, Japan

Helene Santanastasio Unilever Research and Development, Trumbull, Connecticut, U.S.A.

Kirsten Sauermann Research and Development, Biophysics, Beiersdorf AG, Hamburg, Germany

Silke Schagen Department of Bioengineering, Beiersdorf AG Research, Hamburg, Germany

Stefan Scheede Department of Bioengineering, Beiersdorf AG Research, Hamburg, Germany

Holger Schlüter Beiersdorf AG, Advanced Development Deo/AP, Hamburg, Germany

Stefania Seidenari Department of Dermatology, University of Modena and Reggio Emilia, Italy

Tracy Stoudemayer S.K.I.N. Incorporated, Conshohocken, Pennsylvania, U.S.A.

Markus Stücker Department of Dermatology, Ruhr-University Bochum, St. Josef Hospital, Bochum, Germany

Hirotsugu Takiwaki Department of Dermatology, School of Medicine, The University of Tokushima, Kuramoto-cho, Tokushima, Japan

Dominique van Neste Skinterface, Tournai, Belgium

Robert Velthuisen Unilever Research and Development, Trumbull, Connecticut, U.S.A.

Michael Vogt Institute of High Frequency Engineering, Ruhr-University Bochum, Bochum, Germany

Julia Welzel Department of Dermatology, General Hospital Augsburg, Augsburg, Germany

Roger Wepf Beiersdorf AG, Research Microscopy, Hamburg, Germany

Sonja Wessel Beiersdorf AG, Research Microscopy, Hamburg, Germany

Klaus-P. Wilhelm University of Lübeck, Lübeck, and proDERM Institute for Applied Dermatological Research, Schenefeld/Hamburg, Germany

Klaus-Peter Wittern Beiersdorf AG, Advanced Development Deo/AP, Hamburg, Germany

Shuliang L. Zhang Unilever Research and Development, Trumbull Measurement Science, Trumbull, Connecticut, U.S.A.

Claudia El Gammal

*Department of Dermatology, Medical Care Center, Jung-Stilling Hospital,
Siegen, Germany*

Stephan El Gammal

Dermatological Clinic, Hospital Bethesda, Freudenberg, Germany

Albert M. Kligman

*Department of Dermatology, University of Pennsylvania,
Philadelphia, Pennsylvania, U.S.A.*

INTRODUCTION

Human perception is based on visualization of surfaces. Because we cannot look inside, we define objects through their interfaces. This, of course, holds true for human skin. The interface, which meets our eyes, is the stratum corneum, the dead outer layer of the epidermis, composed of flattened horny cells, which are constantly being shed. Still, the physical state of the stratum corneum often reflects changes that have occurred below in the viable tissue. For example, in the epidermis, either thickening (acanthosis) or thinning (atrophy) results in characteristic changes of the glyphic patterns. Inflammation is typically followed by scaling in patterns, which often enable us to diagnose the underlying disorder. Examples are endless, including dermal and epidermal pigmentation, respectively reflecting brown or blue coloration, and numerous forms of hyperkeratosis, follicular and nonfollicular, resulting in a rough, dry, cracked surface. Pathologic events in the dermis can cause soft or firm swellings of the surface. It is important to realize that clinical diagnosis frequently depends on how we perceive the surface. Knowledge about the stratum corneum in health and disease is thus crucial to dermatologic practitioners.

WHAT DEFINES HOW THE SKIN SURFACE APPEARS TO OUR EYES?

Texture of the Surface

The first consideration is texture, a common term that is not easy to define physically. What we see depends greatly on the distance from the object or on magnification. Deep wrinkles of the cheek due to actinic damage can be perceived from a distance. The wrinkled surface of a single corneocyte is visible only by scanning electron microscopy at magnifications from 1000 \times to 5000 \times (Fig. 1).

Corneocytes

The corneocytes are the smallest cellular elements making up the surface. These penta- or hexagonal, very flat, keratinized cells of about 30 to 40 μm diameter overlap at their edges, sometimes randomly and sometimes forming columns. This is the reason that with epiluminescence microscopy their boundaries can hardly be seen.

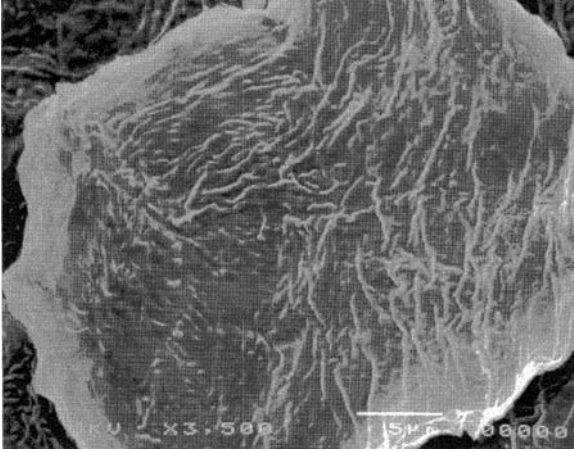


FIGURE 1 Single corneocyte within the upper stratum corneum layers in normal skin. Scanning electron microscopy (SEM) 3500 \times .

Soaking in sodium hydroxide, however, makes them swell, and a remarkably orderly geometrical arrangement becomes apparent. This polygonal outline of individual corneocytes has been designated as tertiary lines. The furrows on the corneocyte surface are termed quaternary lines (1,2). By stripping with Scotch Tape[®] or adhesive discs, the corneocytes can be studied in greater detail (3–5). In 1939, Wolf (3) was able to demonstrate in unstained adhesive tape specimens examined microscopically that the corneocyte surface had furrows. Serial tape stripping with staining reveals the shape, the overlapping edges, and the nuclear remnants of these cells (Fig. 2). Viewing the specimens by phase-contrast microscopy gives an idea of their inner contents, namely the fibrous cytoskeleton.

When the surface is smooth, monolayers of corneocytes come off by stripping. In scaling conditions, thick clusters of corneocytes stick to the tape. In hyperkeratotic inflammation disorders, notably psoriasis, parakeratotic (nucleated)

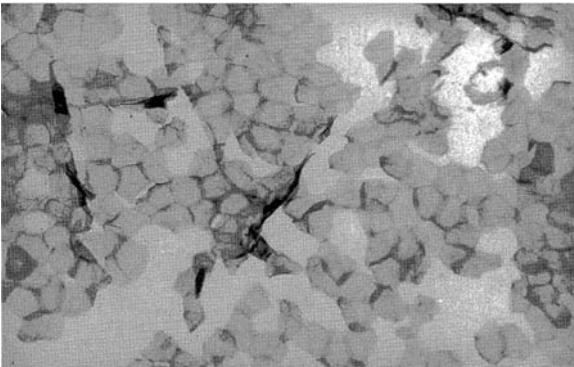


FIGURE 2 Corneocytes from the volar forearm in healthy skin, obtained by tape stripping, stained with rhodamine B/methylene blue, 400 \times .

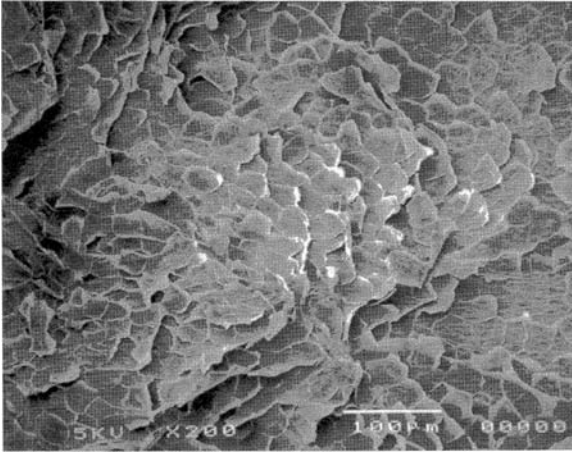


FIGURE 3 Cyanoacrylate surface biopsy: scanning electron microscopy of the undersurface of corneocytes from dry, scaly skin, 200 \times .

cells are often present. Scanning electron microscopy is another powerful way to study the corneocyte surface (6,7). In Figure 3, the undersurface of corneocytes from dry, scaly skin can be seen on stratum corneum sheets obtained by a cyanoacrylate surface biopsy.

After a long period of neglect, the stratum corneum has been extensively investigated in the last decade, which has led to a much better understanding of the morphologic and chemical structure of corneocytes. Consequently, a good deal is known about the molecular composition of the keratin filaments, of filaggrin, the cornified envelope, as well as the intercellular lipid membrane bilayers. The chromosomal localization of many genes coding keratin proteins is also becoming known (8–13).

Still, the alterations of corneocytes and intercellular lipid layers causing different forms of scaling are poorly understood. Lit microscopically, the single corneocytes appear fairly uniform and often show little change in different scaling disorders. Inflammation of the epidermis with increased cell turnover leads to a decrease in their diameter (14) and eventually to parakeratotic cells, which are always markedly smaller than normal corneocytes. When the viable epidermis is irregularly disturbed as in chronic actinically damaged skin, there occurs a great variation in size, shape, and staining properties of corneocytes compared to healthy skin of young persons. On the other hand, one has to be struck by the relatively minor changes in morphology of corneocytes obtained from ichthyotic states and even seborrheic keratoses.

Corneocytes are remarkably resistant to a variety of tissue-altering chemicals, viz, application of keratolytic substances like salicylic acid or urea. This is made use of in the detergent scrub method (15), where corneocytes are obtained by scrubbing the surface in a detergent solution (Triton[®] X 100, 0.1%). Indefinite storage in this solution causes no change in size, shape, or staining properties—not even an increase in diameter. Concentrated alkaline solutions of sodium hydroxide are necessary to make corneocytes swell, with eventual rupture and dissolution of the contents. Likewise, after application of a 20% salicylic acid solution in ethanol

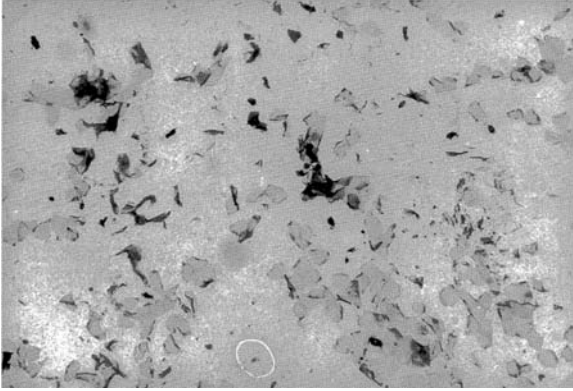


FIGURE 4 Corneocytes from the volar forearm after application of a 20% salicylic acid solution in ethanol for 60 minutes. Obtained by tape stripping, stained with rhodamine B/methylene blue, 165 \times .

on the volar forearm for 60 minutes, we found many torn and folded corneocytes as well as disintegrated cells on tape stripping (Fig. 4). Strong soap solutions will also swell corneocytes on samples obtained by stripping.

The Microrelief (Glyphic Pattern)

Human skin is traversed by many fine grooves that intersect to form irregular geometric patterns called glyphics that are characteristic for different regions. On the palms and soles, the furrows alternate with ridges to form the well-known dermatoglyphics used in fingerprinting for multiple purposes in criminology, for example. Dermatoglyphics have been useful in studying chromosomal aberrations and skin disorders such as Darier's disease, psoriasis, and others (16–18). Dermatoglyphics form loops, whorls, and arches on the fingertips. They are irregularly criss-crossed by straight or slightly curved, deeper lines, which are especially numerous on the palms. In the above-mentioned genetically determined diseases, certain patterns, e.g., ulnar deviation of the lines or arches, occur in a statistically significant higher number than in the normal population.

By contrast, the glyphic lines of glabrous skin are furrows that cross each other to form squares, rectangles, triangles, and trapezoids. While dermatoglyphics can be studied by means of ink fingerprints, investigation of the glyphics of glabrous skin greatly makes use of casts composed of silicon material (1,19–22). The most widely used material is Silflo[®] (Flexico Ltd., U.K.), which, after mixing with a catalyst, is applied as a fluid and polymerizes within a few minutes. After removal from the skin, a flexible, rubber-like sheet is obtained with a negative imprint of the glyphic lines. Glyphics can be visualized by means of a stereomicroscope or by scanning electron microscopy on a positive araldite cast after gold-coating. Tape stripping and cyanoacrylate surface biopsies (see below) can also be used to study glyphics.

It is customary to classify surface lines according to their depth and direction. Primary lines are parallel and always longer, broader, and deeper than secondary lines (1,23). The latter form diagonals with the primary lines, dividing the surface into triangles, rhomboids, and trapezoids. As mentioned above, the tertiary lines

define the boundaries of corneocytes. Quaternary lines are the surface markings on individual corneocytes.

The geometry of the glyphs varies considerably according to region and is influenced by age and skin diseases (1,3,23). Several forms can be distinguished. In the rhomboid pattern, the primary lines intersect at an angle of less than 90° forming rhomboids. In some places, secondary lines divide these rhomboids into triangles. This pattern can be found on the inner aspects of the extremities. On the volar forearm, the conversion of the rhomboids into squares during pronation is particularly impressive. Other regions show prominent squares (e.g., lateral upper leg).

The star-shaped pattern is characterized by lines radiating from a central point, fading toward the periphery (abdomen, dorsal, and ventral upper leg, pretibial). Triangles of primary and secondary lines are found mainly on the buttocks. A pattern with primary and secondary lines forming rectangles is seen on the forehead and the lateral aspect of the upper arms. There, the diagonal lines are largely missing. Over hinge joints such as the knees or elbows, long, deep, parallel primary lines predominate. Often, a fine cobblestone appearance is visible between these lines (Fig. 5), comprising from 30 to 60 corneocytes each. Regions where there are no glyphic lines are the scalp and the tip of the nose. In elderly people, the number of lines is reduced and the patterns are blurred and disordered. The remaining lines show increased depth (24–26).

Glyphic patterns are peculiar to the human surface. What purpose do they serve? Several hypotheses have been offered. To us, the most likely seems the theory of Schellander and Headington that "the creases and indentations found in the resting skin act as prefolds which determine the exact points of flexion and extension when the stratum corneum is deformed" (23). In short, they are pleats that allow deformations compensating for stresses, which could result in cracks. Over joints, where the skin is subject to tension during movement, the glyphic lines are much deeper and oriented perpendicular to the direction of maximal skin extension (e.g., elbow, knee, and dorsum of fingers; Fig. 6A and B). The cobblestone appearance found in these regions provides an additional reserve for stretching. Skin regions with multidirectional tension show a star-like pattern.

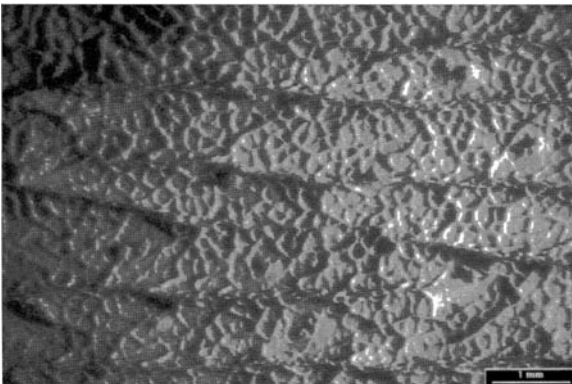


FIGURE 5 Silicon replica from the knee of a 10-year-old boy.

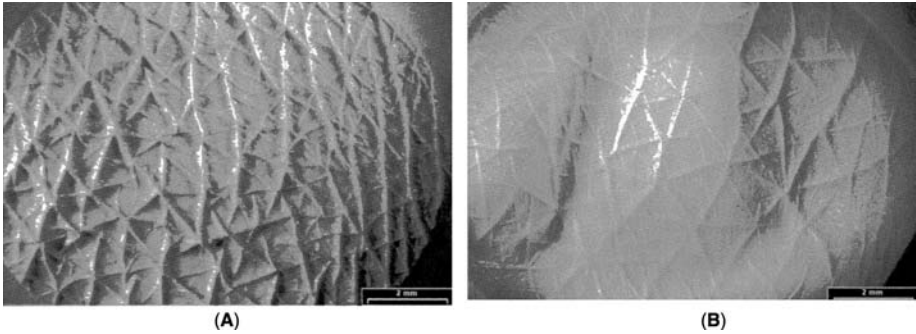


FIGURE 6 Silicon replica from the dorsum of the hand (base of the third finger) of a 30-year-old woman. (A) Extension and (B) flexion.

Comparison of newborn and adult skin shows that the specific patterns described above are genetically determined and present from birth. With growth of the body, the distances between the lines enlarge proportionally and their depth markedly increases under the influence of mechanical forces (Figs. 6A and B, 7A and B).

The network of glyphic lines considerably increases the surface of the skin. It remains doubtful, however, whether this has any biological function, as respiration through the skin is negligible in man. Finally, the lines might play a role in draining sweat or sebum, which easily spread in these channels. It is interesting in this regard that sebum is excreted precisely at the intersections of furrows.

What exactly determines the glyphic pattern of the surface remains speculative. Several studies have demonstrated that it persists throughout the stratum corneum and the upper epidermis, shown by means of repeated tape stripping and ammonium hydroxide blistering (27). After removal of the entire epidermis, either *in vivo* or *in vitro* by incubation of biopsies in sodium bromide, the primary lines remain visible on the surface of the papillary dermis. They separate groups of about 20 to 50 dermal papillae (1,28). After injuries that destroy the dermal papillae and lead to scar formation, the glyphic pattern of the surface is no longer present.

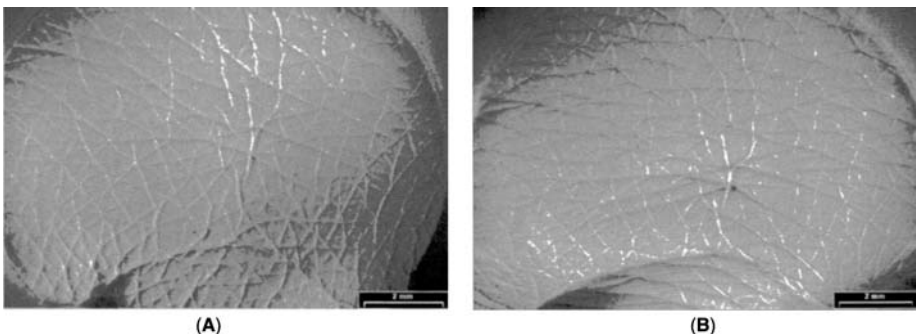


FIGURE 7 Silicon replica from the dorsum of the hand (base of the third finger) of a three-month-old child. (A) Extension and (B) flexion.

These observations suggest that the genetic disposition determining the glyphic lines is realized in the uppermost dermis.

Wrinkles

In contrast to the genetically determined glyphic lines, wrinkles are acquired after adult life, reflecting deterioration of the dermal matrix. Loss of elasticity is a consistent feature that underlies wrinkle formation. Their development in the elderly is the result of both intrinsic and extrinsic aging (photoaging), with the latter playing the greater role (29–31). The predominating histological correlate is severe elastosis, an overgrowth of abnormal elastic fibers. Facial wrinkles are mainly a result of chronic actinic damage. Ultraviolet (UV)B and UVA, as well as infrared radiation, seem to play a role. There is loss of collagen and clumping of degraded elastic fibers into amorphous masses. Sudden weight reduction with loss of subcutaneous tissue causes flabby, folded skin, e.g., on the lower abdomen or the buttocks. Wrinkles appear in the direction of skin tension. As they develop, the primary and secondary glyphic lines are reduced or completely wiped out. Figure 8 shows the lateral lower leg from a 67-year-old woman. Long parallel ridges have evolved under the influence of gravity and local stresses. Fine scaling is apparent. The picture was obtained using reflected UVA photography; UVA, especially of the shorter wavelengths, is reflected much more from the skin surface and the horny layer than visible light. It dramatically reveals surface structures. In this case, not surprisingly, the histology revealed fairly marked actinic elastosis. The lower legs, especially in women, receive a good deal of UV exposure during the lifetime.

Scaling

Scales are corneocyte aggregations that break from the skin surface like ice blocks from an arctic glacier. There are many varieties of scaling. Examples of this spectrum are the large, thick, and irregular flakes in psoriasis, which come off quite easily, the thick adherent scales of ichthyosis vulgaris, or the tiny scales in pityriasis versicolor, resembling fine dust. Probably the most common form of scaling is seen in ordinary dry skin (xerosis vulgaris, winter xerosis), which is especially prevalent on the lower legs.

Scaling can mask the glyphic patterns; these become visible again after a few tape strippings. Fine scales often originate in the lines. Figure 9 shows the development of scaling on the lateral lower leg, induced by a 5% sodium lauryl sulfate patch applied for 24 hours. The picture was taken seven days after the removal of the patch. Fine cracks form within the primary glyphic lines, which have reappeared.

Objective measurement of the degree of scaling has proved very difficult. For practical reasons, clinical grading systems are most widely used despite their subjectivity and poor reproducibility (32–34). The appearance and feel of scaly, dry skin is strongly influenced by ambient conditions. Low temperatures and humidities result in rapid worsening; by contrast, wetness immediately masks scaling. Attempts have been made to measure xerosis using indirect methods such as electrical conductance, on the assumption that the desquamating portion of the stratum corneum lacks water (35–38). However, here too, changes in humidity yield false values. Another approach has been to obtain silicon replicas from scaly skin and determine so-called roughness parameters of the surface using laser-profilometry (19,20,22). The results have been disappointing. Apart from the

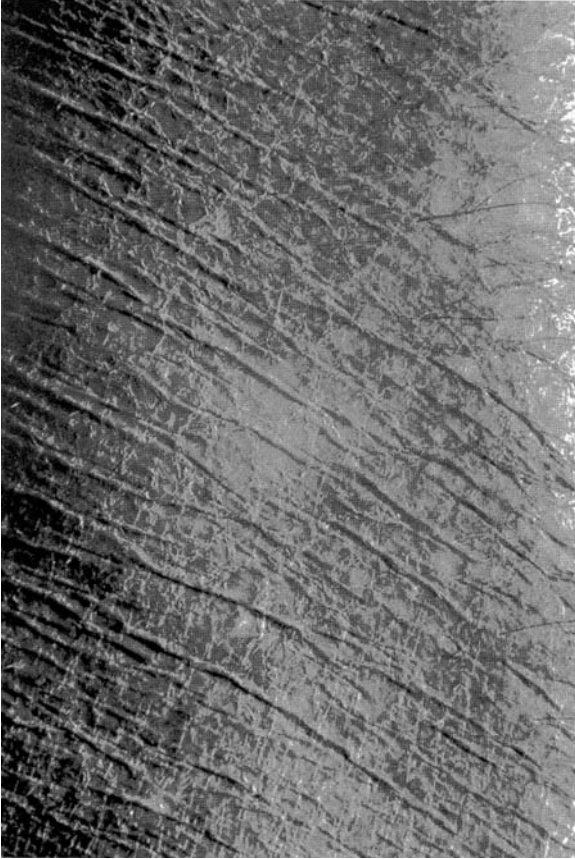


FIGURE 8 Reflected ultraviolet A photography: lateral lower leg of a 67-year-old woman.

problem that scales tend to stick to the silicon material, scaling cannot solely be defined by an increase in roughness of the surface. A wrinkled surface without scaling, e.g., on the lower leg in the elderly, may show greater variations in depth than when covered with large scales, which mask the wrinkles.

In our experience, scales can be best assessed after removal from the surface. They can be collected on adhesive tape, "sticky slides," or cyanoacrylate surface biopsies (4,26,32). Recently, a device has become available which makes it simple and convenient to sample the surface. The D-Squame[®] is a clear, adhesive-coated disc of 1 in. diameter (39,40). When pressed on the skin and then gently pulled off with forceps, scales and the superficial layers of the stratum corneum adhere to the disc. It is important to defat the skin prior to application because lipids prevent scales from sticking to the tape. We use an ether/acetone solution for 30 seconds in a glass well. This is a very effective way to reveal scaling; the skin surface becomes white and rough.

For evaluation, D-Squame discs are placed in a white light box and illuminated from two sides. Scales scatter and reflect light, appearing white against a

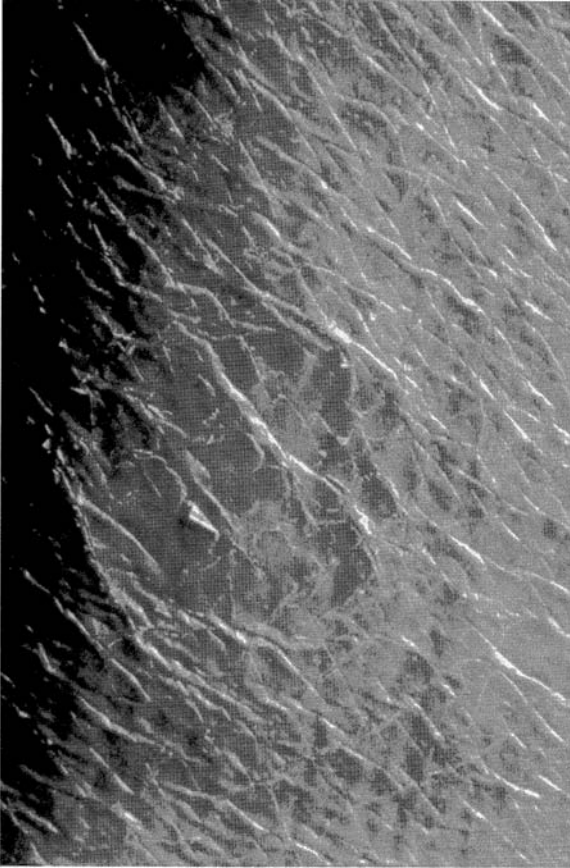


FIGURE 9 Lateral lower leg: scaling seven days after the application of a 5% sodium lauryl sulfate patch for 24 hours.

black background. In Figure 10A and B, the difference between dry and nondry skin of the lower legs of young women is shown. In xerosis, large white scales are present. The D-Squame disc from nondry skin is characterized by a more uniform coating and occasional tiny scales.

To objectively quantify scaling, we developed an image analysis program for D-Squame discs, on the basis of the assumption that the whiteness of the scales is to some extent proportional to their thickness. To eliminate systematic errors due to inuniform illumination, first a pixel-wise calibration of the black filing card and a white card is performed (Fig. 11). For each D-Squame, the pixel distribution of the grey levels [ranging from 0 (black) to 255 (white)] is determined by the image analysis program and a so-called scaling index (SI) is calculated as follows:

$$SI = \frac{1}{w \times h} \sum_{x=1, y=1}^{x=w, y=h} \frac{D(x, y) - B(x, y) - [W(x, y) - B(x, y)] \times T\%}{W(x, y) - B(x, y) - [W(x, y) - B(x, y)] \times T\%}$$

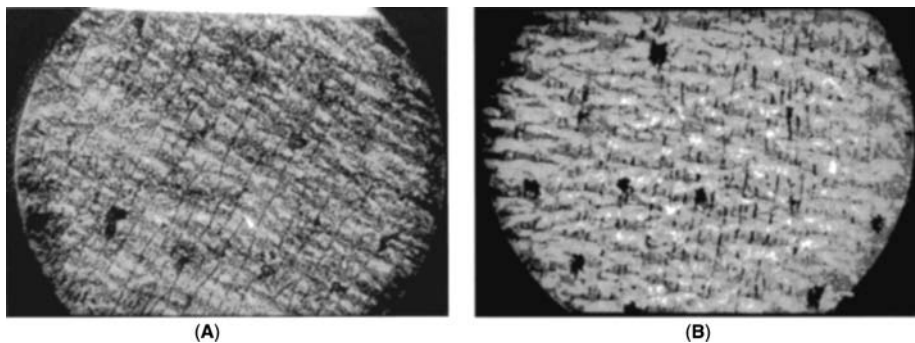


FIGURE 10 D-Squame[®] discs from the lateral lower leg, against a black background, lighting from two sides: (A) Normal skin from a 26-year-old woman, (B) dry skin from a 44-year-old woman.

where D is the D-Square image, $T\%$ is the trigger level, W is the white calibration image, w is the image width, B is the black calibration image, and h is the image height.

We set a trigger level at 10%, i.e., the grey levels below 10% are not considered in order to exclude regions of the D-Squame that are not covered by corneocytes (e.g., “black holes” of hair follicles or areas where no scales stuck to the adhesive). The SI ranges from 0 to 1 according to the average thickness of scales on the specimen. The percent area showing grey levels higher than 10% (total area covered) gives information about the adherence properties of the scales. In disorders where the scales stick tightly to the skin surface, e.g., in psoriasis, it is much lower than, for instance, in xerosis vulgaris.

To see the distribution of scale-thicknesses, we arbitrarily classify them into five grey-level classes. The thinnest, darkest scales belong to class 1, the thickest and whitest to class 5. Figure 12 shows the results from the evaluation of dry versus nondry skin. Both D-Squame discs are fairly evenly covered with scales amounting to about 93% of the surface (total area covered). However, the SI of

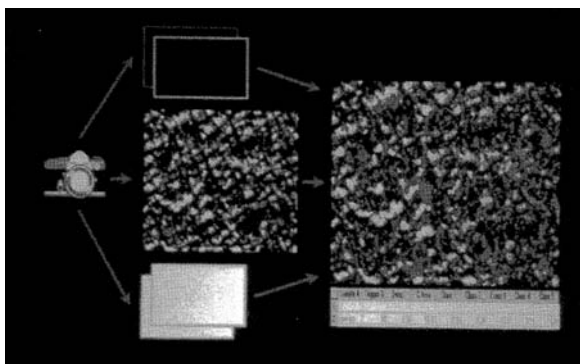


FIGURE 11 Schematic representation of image analysis of D-Squame discs: to eliminate uneven illumination, a pixel-wise calibration according to a black and white reference card is performed. A trigger level of 10% (lowest grey values) excludes areas that are not covered by corneocytes.

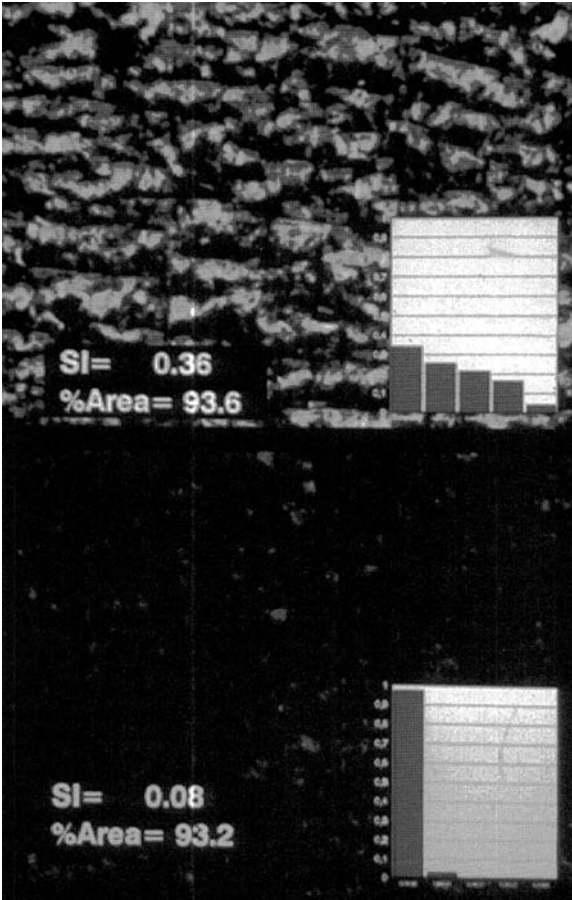


FIGURE 12 Scaling index, percent area covered, and grey-level class distribution in a D-Squame[®] of dry (*above*) and normal (*below*) skin.

the dry sample is 0.36, the one of the nondry sample 0.08. In very dry skin, scales of all thickness groups are found. In nondry skin, almost all scales belong to group 1 with the lowest grey levels. Few belong to group 2. Thicker scales of groups from 3 to 5 are not found at all.

This image analytical method is a valuable tool to assess xerosis vulgaris, or xerosis induced by soaps, irradiation, tape stripping, etc. The method has been successfully used on a variety of clinical studies, especially evaluating the efficacy of moisturizers. Disorders of keratinization with very thick scales are less suitable for this method of study. In black skin, scales adherent on the disc often appear dark because corneocytes contain undegraded melanosomes, limiting the usefulness of the method in this group.

Skin Appendages

Hair follicle openings are located at the intersection of primary and secondary lines. Groups of mostly three follicles originate in neighboring crossings, with a

principal terminal hair in the middle, surrounded by smaller vellus hairs (41). This pattern is found throughout the entire body with variations in the distance between follicle groups. As the pilosebaceous units extend down into the subcutaneous fat, they act as anchoring structures when a dermal edema occurs. In a weal, follicle openings are therefore often visible as indentations. On the other hand, contraction of the arrector pili muscles leads to cutis anserina (goose flesh) with prominent follicles. Hair follicle openings are markedly larger than sweat gland orifices, which are found preferably in the middle of the triangles and rhomboids formed by the glyphics (42).

For investigation of hair follicles (with the exception of the scalp), cyanoacrylate surface biopsies are advantageous (26,42,43). A drop of cyanoacrylate (e.g., Krazy Glue[®]) is applied on a transparent plastic slide and pressed onto the skin. After a few minutes, the slide is carefully pulled off. A sheet of the outermost horny layer is separated to which vellus hairs are attached. The density and size of the openings of follicles can be determined. In silicon replica casts, only the follicular orifices can be studied.

The density of follicles has received little attention in the literature. On the head, it is much higher than in other body regions, e.g., the leg with about 50/cm² (44). In the face, the density of follicles decreases from centofacial (alae nasi and nose: 1200/cm²; to lateral preauricular: 460/cm²) (42). There is little inter-individual variation. On the scalp, a decline in follicular density with aging has been observed. This is particularly marked in androgenetic alopecia (45).

Skin Color

Skin color is influenced by a variety of factors, including blood flow, scaling, and skin surface lipids. However, the various shades of pigmentation which separate racial groupings are mainly due to the content and distribution of melanin. Different ambient lighting conditions influence the appearance of skin color considerably. It is therefore good practice in dermatology to estimate color under standard illumination conditions, for example, indirect sunlight. Color can be measured more precisely using the Minolta CR[®] 200 colorimeter (46,47). This instrument uses a xenon arc lamp (cold light) and six silicon photocells—three to measure the source illumination and three for reflected light. Different filters select value pairs for blue (450 nm), green (550 nm), and red (600 nm). Minolta colorimetry is especially appropriate in dermatology because it perceives skin color like the human eye. It has a stable light source controlled by the measuring unit, and a small (8 mm) measuring field. The three measured values are integrated into a color, which is described by three dimensions: lightness, L; redness, a (green–red axis); and blueness, b (blue–yellow axis).

We used Minolta colorimetry to determine whether persons can be classified into skin types I–IV according to the lightness (L) of their skin. We examined the skin color of sun-exposed regions (forehead, dorsum of the hand) and sun-protected regions (buttocks) in 382 subjects (46). They were sorted into phototypes according to Fitzpatrick's classification on the basis of answers to a questionnaire. Although a tendency to darker skin could be observed in skin types III and IV, overlapping within the groups was surprisingly high. However, after exposure to UVB, both the intensity of the tan and the time required for tanning was specific for each skin type. To determine reliably the skin type and predict the risk for sunburn by instrumental methods, a standard dose of UVB is required.

Erythema is mainly due to accumulation of blood in the dermal vascular plexus. Pigmentation of the skin influences the visibility of erythema, the most impressive example being black skin, in which no red hues can be perceived. Bode in 1934 (48) speculated that pigmentation has a grey filter effect. This holds also for measurements with the colorimeter: the a-values (redness) are only comparable in skin with about the same melanin content.

Physiological Properties of the Surface

Although this chapter deals mainly with morphology of the surface, it should be mentioned that physiological properties indirectly influence how the skin is perceived by our sight, touch, and smell. Important factors, for example, are the elasticity of the skin, influenced mainly by dermal factors, and the pliability of the stratum corneum, for which the intercellular lipid membrane bilayers are essential. Then, there is sweat production, which softens the horny layer. Sebum production on the face adds lubricity, but can also make the skin look and feel greasy. The temperature of the skin surface may also contribute to the appearance of skin. Within the last years, numerous, mostly noninvasive techniques have been developed for assessment of these physiological properties.

REFERENCES

1. Leveque JL, Corcuff P. The surface of the skin—the microrelief. In: Frosch PJ, Kligman AM, eds. *Noninvasive Methods for the Quantification of Skin Functions*. Springer, 1993:3.
2. Tring FC, Lyndon BN. Surface microtopography of normal human skin. *Arch Dermatol* 1974; 109:223.
3. Wolf J. Die innere Struktur der zellen des stratum desquamans der menschlichen epidermis. *Z Mikros Anat Forsch* 1939; 46:170–202.
4. Goldschmidt H, Kligman AM. Exfoliative cytology of the human horny layer. *Arch Dermatol* 1967; 96:572–576.
5. Marks R. Clinical methods for measuring scaling and desquamation. *Bioeng Skin* 1987; 3:319–333.
6. Ryan RL, Hing SAO, Theiler RF. A replica technique for the evaluation of human skin by scanning electron microscopy. *J Cutan Pathol* 1983; 10:262.
7. Mihara M. Scanning electron microscopy of skin surface and the internal structure of corneocyte in normal human skin. An application of the osmium-dimethyl sulfoxide-osmium method. *Arch Dermatol Res* 1988; 280:293.
8. Harding CR, Scott IR. Histidine rich proteins (filaggrins). Structural and functional heterogeneity during epidermal differentiation. *J Mol Biol* 1987; 170:9:651.
9. Lessin SR, Heubner K, Isobe M, et al. Chromosomal mapping of human keratin genes: evidence of non-linkage. *J Invest Dermatol* 1988; 91:572.
10. Lynley AM, Dale BA. The characterisation of human epidermal filaggrin, a histidine-rich keratin filament-aggregating protein. *Biochim Biophys Acta* 1983; 744:28.
11. Mehrel T, Hohl D, Rothnagel JA, et al. Identification of a major keratinocyte cell envelope protein, loricrin. *Am J Anat* 1971; 130:93.
12. Elias PM. Epidermal lipids, barrier function, and desquamation. *J Invest Dermatol* 1983; 80:44s.
13. Schwartzendruber DC, Wertz PW, Kitko DJ, et al. Molecular models of the intercellular lipid lamellae in mammalian stratum corneum. *J Invest Dermatol* 1989; 92:251.
14. Grove GL. Exfoliative cytological procedures as a nonintrusive method for dermatogerontological studies. *J Invest Dermatol* 1979; 73:67.
15. McGinley KJ, Marples RR, Plewig G. A method for visualizing and quantitating the desquamating portion of the human stratum corneum. *J Invest Dermatol* 1969; 53:107.

16. Cummins H. Dermatoglyphics: a brief review. In: Montagna W, Lobitz WC, Jr., eds. *The Epidermis*. New York: Academic Press, 1964:375.
17. Verbov J. Clinical significance and genetics of epidermal ridges-a review of dermatoglyphics. *Invest Dermatol* 1970; 45:261.
18. Montagna W. *The Structure and Function of the Skin*. New York, London: Academic Press, 1962, Chapter 1.
19. Cook Th. Profilometry of skin-a useful tool for the substantiation of cosmetic efficacy. *J Soc Cosmet Chem* 1980; 31:339.
20. Hoppe U, Lunderstädt R, Sauermann G. Quantitative analysis of the skin's surface by digital signal processing. In: Frosch PJ, Kligman AM, eds. *Noninvasive Methods for the Quantification of Skin Functions*. Springer Verlag, 1993:25.
21. Grove GL, Lavker RM, Hälzle E, Kligman AM. Use of nonintrusive tests to monitor age-associated changes in human skin. *J Soc Cosmet Chem* 1981; 32:15.
22. Leveque JL. Physical methods to measure the efficacy of cosmetics in humans. *Cosm Toilet* 1985; 99:43.
23. Schellander FA, Headington JT. The stratum corneum-some structural and functional correlates. *Br J Dermatol* 1974; 91:507.
24. Corcuff P, de Lacharrière O, Lévèque JL. Extension-induced changes in the microrelief of the human volar forearm: variations with age. *J Gerontol* 1991; 46:M223.
25. Corcuff P, Lévèque JL, Grove GL, Kligman AM. The impact of aging on the microrelief of peri-orbital and leg skin. *J Soc Cosm Chem* 1987; 82:145.
26. Piérard-Franchimont C, Piérard GE. Assessment of aging and actinic damages by cyanoacrylate skin surface strippings. *Am J Dermatopathol* 1987; 9:500.
27. Hatzis J, Tosca A, Varelzidis A, Stratigos J. Skin surface marking on the prickle cell layer. *Br J Dermatol* 1987; 116:497.
28. Montagna W. *The Structure and Function of the Skin*. New York, London: Academic Press, 1962, Chapter 2.
29. Gilchrest BA. Skin aging and photoaging: an overview. *J Am Acad Dermatol* 1989; 21:610.
30. Lavker RM, Zheng P, Dong G. Aged skin: a study by light, transmission, and scanning electron microscopy. *J Invest Dermatol* 1987; 88:S44.
31. Montagna W, Carlisle K. Structural changes in aging skin. *Br J Dermatol* 1990; 122(suppl 35):61.
32. Kligman AM, Lavker RM, Grove GL, Stoudemayer TJ. Some aspects of dry skin and its treatment. In: Kligman AM, Leyden JJ, eds. *Safety and Efficacy of Topical Drugs and Cosmetics*. New York: Grune & Stratton, 1982:221.
33. Kligman AM. Regression method for assessing the efficacy of moisturizers. *Cosm Toilet* 1987; 93:27.
34. Boisits EK, Nole GE, Cheney MC. The refined regression method. *J Cut Aging Cosm Dermatol* 1980; 1:155-163.
35. Batt MD, Fairhurst E. Hydration of the stratum corneum. *Int J Cosm Sci* 1986; 8:253.
36. Blichmann CW, Serup J. Hydration studies on scaly hand eczema. *Cont Derm* 1987; 16:155.
37. Blichmann CW, Serup J. Assessment of skin moisture. Measurement of electrical conductance, capacitance, and transepidermal water loss. *Acta Derm Venereol (Stockh)* 1988; 68:284.
38. Neste van D. Comparative study of normal and rough human skin hydration in vivo: evaluation with four different instruments. *J Dermatol Sci* 1991; 2(2):119.
39. Schatz H, Kligman AM, Manning S, Stoudemayer T. Quantification of dry (xerotic) skin by image analysis of scales removed by adhesive discs (D-Squames[®]). *J Soc Cosm Chem* 1993; 44:53.
40. Serup J, Winther A, Blichmann CA. Simple method for the study of scale pattern and effects of a moisturizer-qualitative and quantitative evaluation by D-Squame[®] tape compared with parameters of epidermal hydration. *Clin Exp Dermatol* 1989; 14:277.
41. Montagna W. *The Structure and Function of the Skin*. New York, London: Academic Press, 1962, Chapter 4.

42. Pagnoni A, Kligman AM, el Gammal S, Stoudemayer T. Determination of density of follicles on various regions of the face by cyanoacrylate biopsy: correlation with sebum output. *Br J Dermatol* 1994; 131:862.
43. Mills OH, Kligman AM. The follicular biopsy. *Dermatologica* 1983; 167:57.
44. Szabo G. The regional frequency and distribution of hair follicles in human skin. In: Montagna W, Ellis WA, eds. *The Biology of Hair Growth*. New York: Academic Press, 1958:3.
45. Giacometti L. The anatomy of the human scalp. In: Montagna W, ed. *Advances in the Biology of Skin, Volume VI, Ageing*. Oxford: Pergamon Press, 1965:97.
46. el Gammal S, Hoffmann K, Steiert P, et al. Objective assessment of human skin reaction to sun and UVB. In: Frosch PJ, Kligman AM, eds. *Noninvasive Methods for the Quantification of Skin Functions*. Springer, 1993:133.
47. Wilhelm KP, Maibach HI. Skin color reflectance measurements for objective quantification of erythema in human beings. *J Am Acad Dermatol* 1989; 21:1306.
48. Bode HG. Über spektralphotometrische untersuchungen an menschlicher haut unter besonderer berücksichtigung der erythem- und pigmentmessung. *Strahlenther* 1934; 51:81.

Multimodal Imaging— What Can We Expect?

Michael Vogt and Helmut Ermert

*Institute of High Frequency Engineering, Ruhr-University Bochum,
Bochum, Germany*

INTRODUCTION

Noninvasive imaging techniques are of great value in all fields of medical diagnostics. Because the skin is directly accessible, the established and most common method in dermatology for the identification of suspicious skin lesions and evaluation of skin diseases is the direct inspection by the dermatologist. However, different techniques such as high-frequency ultrasound (HFUS), optical coherence tomography (OCT), high-resolution magnetic resonance imaging (HR-MRI), confocal laser scanning microscopy, and others are available for noninvasive imaging of skin over depth to support the diagnostics. Imaging systems make use of different kinds of rays, waves, and physical phenomena (light, ultrasound, electromagnetic waves, nuclear magnetic resonance, etc.) to image tissue structures. Video-dermatoscopy (VD) and epiluminescence microscopy (ELM) are technical instruments to improve conventional dermatoscopy by optically obtaining information from the skin surface and uppermost skin layers.

The general aim of medical imaging is to collect spatially distributed information of a medical object with respect to its morphology, function, and histology for diagnostic purposes. In dermatology, morphology is the most interesting information requiring high-resolution imaging capabilities. Functional information such as transflux activity, thermoregulation, and perfusion, as well as histological information of tissue such as malignancy, inflammation, or skin aging effects are of increasing interest. Functional and histological imaging approaches can be understood as quantitative modalities, as they are based on a quantitative analysis of image data and signals, in addition to morphological information.

In this contribution, multimodal skin imaging and analysis concepts and their potential are discussed. The main motivation of multimodality is to increase the completeness and the accuracy of information by combining nonredundant information from different modalities. Because each imaging modality has its limitations, multimodality concepts can have a significant benefit to skin imaging with respect to morphology and to functional imaging based on image fusion methods. Below, an overview of different skin-imaging modalities with emphasis on a project of the Ruhr Center of Excellence for Medical Engineering (KMR), Bochum, Germany (1) in cooperation with associated partners is given. Results of comparative studies of different skin-imaging modalities are reported. Finally, results of image and sensor fusion approaches, which combine surface oriented optical imaging modalities with tomographic modalities such as ultrasound, are presented to give an idea of what can be expected from multimodal skin imaging.

SKIN-IMAGING TECHNIQUES

Imaging modalities with major relevance to skin imaging include various modifications of electromagnetic wave imaging [optical, infrared (IR), Terra-Hertz (THz), nuclear magnetic resonance, and electrical impedance], acoustical wave imaging (HFUS, acoustical microscopy, and air-coupled ultrasound), and mechanical wave and thermal wave imaging.

Usually, tomographic images, i.e., two-dimensional (2-D) cross-sectional images, are acquired with medical imaging systems. Depending on the spatial orientation of the cross sections, these images depict information about tissue over depth or any other direction. Three-dimensional (3-D) tissue volumes are usually imaged by acquiring a “stack” of consecutive 2-D images, which are parallel to each other. The advantage of medical imaging systems is that they facilitate non-invasively obtaining information which is conventionally only accessible by invasion into the body, for example, by analyzing histological sections of excised tissue. Beside the ability to image tissue which is not directly visible, another conceptual benefit is that a different kind of information is obtained. For these reasons, imaging techniques support the dermatologist in making diagnoses of skin diseases and lesions. High-resolution microscopic imaging techniques are required because the interesting skin structures are very small.

Optical Skin Surface Imaging

The visual inspection by the dermatologist is the most common method to evaluate skin lesions and diseases. In conventional dermatoscopy, magnifying glasses are used to improve the visibility. However, the diagnostic output significantly depends on the individual experience of the physician. The information that is obtained under the described conditions is limited to the skin surface. Nevertheless, dermatoscopy is the standard method for skin-tumor detection. In VD, modern digital image acquisition techniques are used for quantitative and automated image analysis and long-term observations of the progression of skin tumors. In ELM, a glass plate is placed on the skin surface, a contact fluid is inserted between the plate and the skin, and the surface images are digitized like in VD. With this method, the penetration of light into the uppermost skin layers is improved, and the images contain more information. The advantage of VD and ELM is that the skin is imaged under standardized and reproducible conditions concerning illumination and calibrated imaging of colors. Images can be stored in a patient database and analyzed with modern digital image processing methods. This makes follow-up examinations and documentation of suspicious skin lesions straightforward. Some typical images acquired with the microDERMTM system (Visomed AG, Bochum, Germany) (2) are presented below. Acquired images are automatically analyzed with relevance to the ABCD-rule of dermatology. Imaged lesions are segmented on the basis of features such as shape, color, and size used as input features for a neural network classifier for the discrimination of benign and malignant lesions. In a multicenter study, skin lesions were imaged, and excised lesions were classified based on histopathological findings. The neural network was trained with this database (3).

High-Frequency Ultrasound Imaging

The techniques discussed above suffer from the limitation that only superficial skin information is obtained. HFUS-based sonography is a tomographic imaging

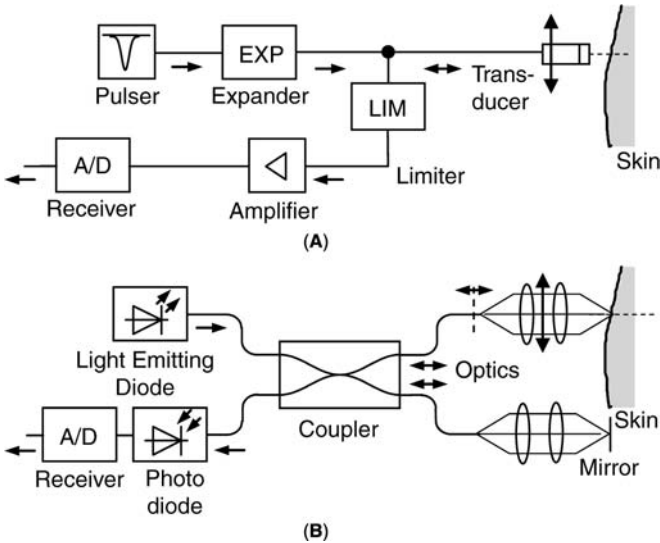


FIGURE 1 (A) HFUS imaging system and (B) block diagram of an OCT imaging system.

technique, which enables noninvasive acquisition of cross-sectional images over depth. In Figure 1A, the concept of HFUS imaging systems is illustrated. Pulse-echo measurements are performed by exciting an ultrasound transducer with a pulsed signal generated by a pulser. Ultrasound waves, which are backscattered and reflected at acoustic inhomogeneities inside the skin and propagate back to the transducer, are converted into an electrical echo signal. The signal is amplified and digitized, and images are generated in a grayscale proportional to the signal's amplitude over time-of-flight, the latter being proportional to the axial coordinate along the sound propagation direction. HFUS in the 20 MHz frequency range is already a well-established modality for imaging of the complete skin and subcutaneous fat (4–6). However, the spatial resolution of HFUS imaging systems can be improved by utilizing broadband ultrasound at higher frequencies. Limitations are caused by the fact that the attenuation of ultrasound waves significantly increases with increased frequencies. For this reason, a compromise between the opposing demands for good spatial resolution and high penetration depth has to be found (7–11). HFUS images presented in this chapter were acquired with a new 20 and 100 MHz range HFUS scanner developed in the framework of the Ruhr Center of Excellence for Medical Engineering (KMR), Bochum, Germany (1) in cooperation with a partner from industry (taberna pro medicum GmbH, Lüneburg, Germany) (12).

Optical Coherence Tomography

The concept of OCT, which is a relatively new modality, is similar to ultrasound imaging, but light in the near-IR spectrum is applied instead of ultrasound waves. In Figure 1B, a block diagram of an OCT imaging system is shown. While pulse-echo measurements are performed in sonography, OCT is based on

interferometry (13,14). Near-IR light from a light-emitting diode is split and coupled into a reference arm and a measurement arm, whereby the latter includes the skin. The light, which is reflected at a mirror in the reference arm and backscattered at optical inhomogeneities inside the skin from the measurement arm, is superimposed at a photodiode (PD) and detected. Because the light source is broadband and low coherent, a measurement signal at the PD output is only obtained if the optical path lengths in both the arms are equal. A scanning over depth is achieved by changing one of the optical path lengths, what can be achieved by moving the mirror or the lens system. The OCT images presented below were acquired with a SkinDex 300TM scanner (Isis optronics GmbH, Mannheim, Germany) (15–17).

High-Resolution Magnetic Resonance Imaging

In MRI, the phenomenon of nuclear magnetic resonance is applied to obtain information about tissues noninvasively. The patient is exposed to a strong static magnetic field with a magnetic inductance on the order of 1 to 3 T. Electromagnetic waves at the water proton's resonance frequency (Larmor frequency) are emitted into the body to cause a precession of the magnetic moment that is linked to the protons. As a result, electromagnetic waves are emitted, thus making an evaluation of proton densities and relaxation times of tissue possible. The problem in applying MRI for skin imaging is to detect the emitted electromagnetic waves with a sufficiently high signal to noise ratio, which is challenging because of the very small image volume elements (voxels). With specially designed receive coils, conventional clinical MRI imaging systems can be utilized for high-resolution skin imaging (18).

MULTIMODAL SKIN IMAGING

Depth information about skin lesions is included in VD and ELM images only to a very limited extent. On the other hand, HFUS, OCT, and HR-MRI enable noninvasive imaging of skin structures with high resolution over depth. Images that are obtained with these techniques can be combined in a multimodal approach to take advantage of the different kinds of information. Because each imaging modality has its limitations, multimodal imaging increases the completeness. We have made VD, ELM, HFUS, and OCT imaging systems available at the Bioengineering Lab of the Dermatological University Hospital of the Ruhr-University Bochum, Germany. The goal is to combine these modalities to assist the early diagnosis of skin cancer and therapy planning.

Multimodal Imaging Concept

Multimodality includes both the utilization of different physical phenomena for imaging as well as different signal and image processing concepts for the assessment of tissue parameters concerning morphology, function, and histology. From the methodological point of view, *morphology* is imaged by measuring backscattering, reflection, or transmission of rays and waves. For *functional* imaging, parameters like blood perfusion, flow velocities, etc. are assessed with signal processing concepts for Doppler measurements and others. *Histological* information is noninvasively obtained by quantitatively analyzing waves and rays after they have interacted with the tissue. In the context of medical tissue characterization (TC),

image data is analyzed quantitatively with respect to features of medical image objects such as shape and texture. *Image fusion* is the representation of images which are acquired with different modalities, in the same coordinate system, i.e., in the same spatial arrangement. Established digital image processing methods can be applied for this purpose. Imaged structures are spatially aligned to each other by utilization of nonrigid or rigid registration methods, depending on whether object deformations should be accounted for or not.

Hybrid Imaging Concept

The concept of *hybrid* imaging utilizes interaction of different kinds of fields and waves to image further tissue properties. Examples include photo-acoustic, thermo-acoustic, acousto-mechanic, and acousto-optic imaging approaches. Recently, *elastography*, which is a relatively new modality for the imaging and analysis of mechanical properties of tissue, has gained a lot of attraction in medical imaging. The concept of elastography is to apply static or dynamic mechanical excitation (compression, vibration) to the tissue and to assess the resulting displacements inside the tissue with conventional imaging systems such as MRI and sonography. The mechanical strain is calculated from estimated displacements and depicts qualitatively differences between “soft” and “hard” tissues. Ongoing research in elastography is largely directed toward quantitative reconstructions of mechanical tissue parameters.

Examples and Results

In this chapter, some examples and results from our work on the combination of different skin imaging modalities are presented. In Figure 2, the scanners that were included in the studies are shown. Skin lesions are imaged with separate VD/ELM, HFUS, and OCT imaging systems in the clinical bioengineering lab. Furthermore, we have conducted a study to compare HR-MRI with HFUS (18). An experimental prototype system for skin elastography with HFUS was implemented and evaluated in a preliminary study (19–21).

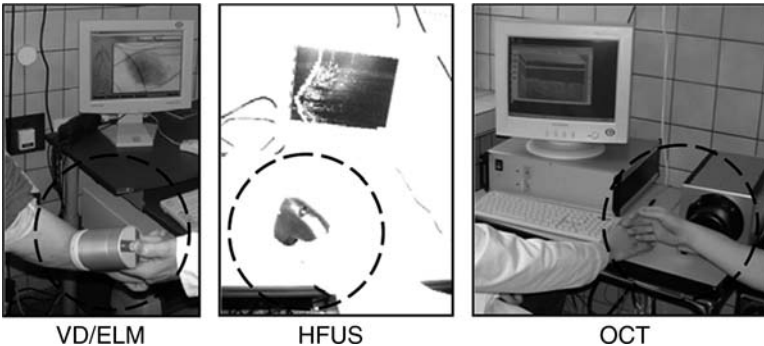


FIGURE 2 Skin imaging systems: VD/ELM, HFUS, and OCT. *Abbreviations:* VD, video-dermatoscopy; ELM, epiluminescence microscopy; HFUS, high-frequency ultrasound; OCT, optical coherence tomography.

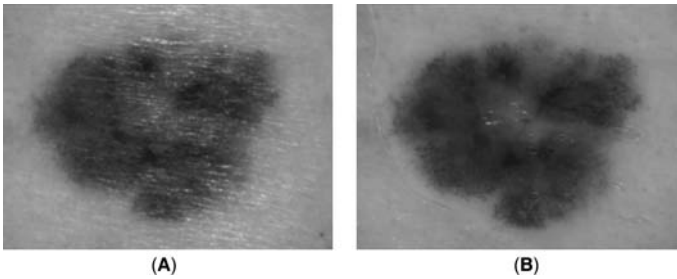


FIGURE 3 Optical surface skin imaging (benign lesion): (A) video-dermatoscopy; (B) epiluminescence microscopy.

Video-Dermatoscopy and Epiluminescence Microscopy

Digital image acquisition techniques are, nowadays, available for skin surface imaging. In Figure 3A, a clinical VD image of a benign lesion is shown. Parameters like the shape, size, and pigmentation are valuable information to support experienced dermatologists in the classification of skin lesions. However, the image contains only the information from the skin surface, and strong reflections of light partly disturb the visibility of the lesion. In the ELM image in Figure 3B, more details of the lesion's pigmentation and structure are visible, and the disturbing light reflections are avoided.

High-Frequency Ultrasound

In dermatology, HFUS in the 20 MHz range is the standard technique for ultrasound skin imaging. The example in Figure 4 shows that the complete skin can be imaged with 20 MHz range sonography. The spatial resolution is insufficient to resolve the relative thin epidermis at the forearm, while the corium appears as a hyperechoic band. In the subcutaneous fat, only small reflections and back-scattering are found, whereas the muscle fibers cause strong reflections (Fig. 4A).

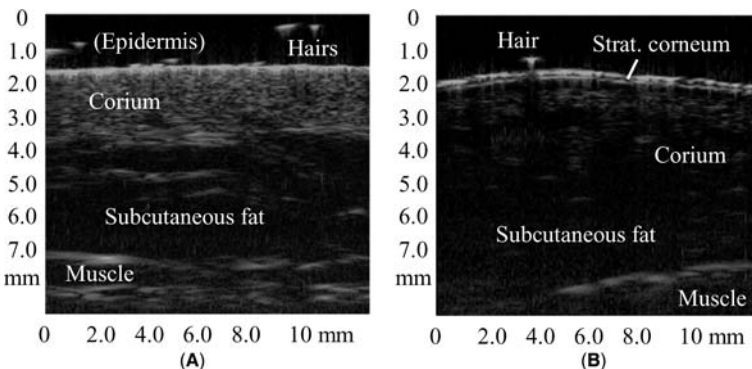


FIGURE 4 High-frequency ultrasound (20 MHz range) skin imaging: (A) healthy skin at the forearm; (B) healthy skin at the back of the hand.

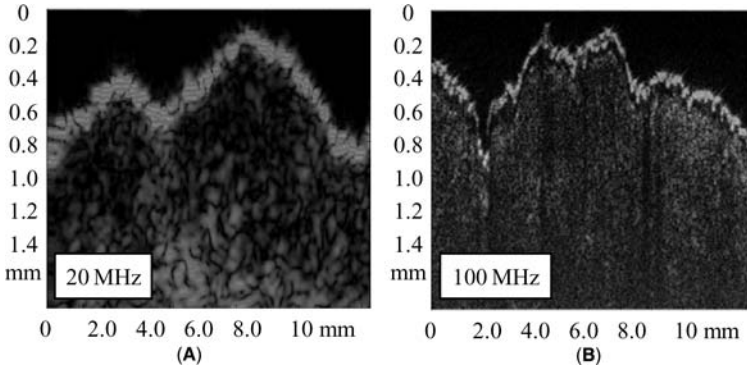


FIGURE 5 High-frequency ultrasound skin imaging (basalioma): (A) 20 MHz range ultrasound; (B) 100 MHz range ultrasound.

The ultrasound image in Figure 4B was acquired at a hand, where the backscatter from the corium is relatively low. The 20 MHz range HFUS images cover a maximum axial and lateral field of view (FOV) of 8.2 and 12.4 mm, respectively.

It was already stated above that the spatial resolution can be improved by utilizing broadband ultrasound at higher frequencies. In the new HFUS imaging system which we have implemented, a second ultrasound applicator for the 100 MHz range is available for high-resolution imaging, with a maximum axial and lateral FOV of 1.6 and 12.4 mm. In Figure 5, 20 and 100 MHz range ultrasound images of a basalioma, which cover the same FOV, are shown. The spatial resolution is significantly improved with the higher frequencies. In the 100 MHz range ultrasound image, the epidermis can be identified. In Figure 6, ultrasound images of a squamous cell carcinoma (SCC) at the cheek of a patient are shown as another example. Again, the relatively thick epidermis is visible as a low-echoic band beneath the skin surface in the 100 MHz range ultrasound image, while it cannot be resolved with 20 MHz range ultrasound because of the worse spatial resolution.

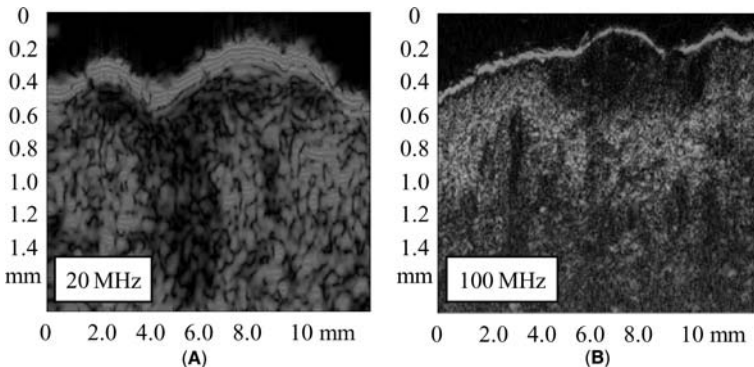


FIGURE 6 High-frequency ultrasound skin imaging (squamous cell carcinoma): (A) 20 MHz range ultrasound; (B) 100 MHz range ultrasound.

The SCC appears as hypoechoic band below the dermis. The minimum axial and lateral resolutions of the implemented system are 39 and 210 μm , respectively, with the 20 MHz range ultrasound transducer. In the 100 MHz frequency range, improved minimum axial and lateral resolutions of 10 and 84 μm are achieved.

We have implemented a 20 MHz range HFUS elastography system for the assessment of mechanical skin properties. A vacuum chamber is placed on top of the skin and frames of ultrasound echo signals are acquired, while the skin surface is vertically sucked into the chamber. The resulting displacements of skin structures are estimated by analyzing acquired signals and strain images are reconstructed. We were able to show that the resistance of the skin against the applied suction is predominantly due to the dermis, where only small strains were measured, while large strains were found in the subcutaneous fat. A significant change of elastic properties was found in burned skin because of the destruction of collagen fibers. Strain images of a nevus have shown that the mechanical properties of the nevus are significantly different from those of the surrounding dermis. This was concluded from the fact that large strains were found inside the nevus, while strains were small in the surrounding dermis (19–21).

Optical Coherence Tomography

Images which are obtained with OCT are very similar to ultrasound images, but information about optical instead of acoustical backscattering is obtained. The OCT image of healthy skin in Figure 7 shows skin structures with a very high resolution, but the penetration depth is limited to about 500 μm . OCT enables the imaging of the epidermis and upper corium with a maximum axial and lateral FOV of the OCT system of 1.0 mm \times 1.0 mm. Analyzing reference images of a glass plate surface and wire phantom, minimum axial and lateral resolutions of 5.8 and 4.1 μm , respectively, were measured (22).

The refraction index (RI) of skin depends significantly on the water content. In the OCT system, light is focused with optical lenses in the measurement arm, and focusing changes with varying RI of skin. If the focal point is determined for different lens configurations by analyzing acquired image data, the RI can be quantitatively reconstructed. In Figure 8A, a backscatter image of healthy skin is shown. The same image information with superimposed RI data is shown in Figure 8B.

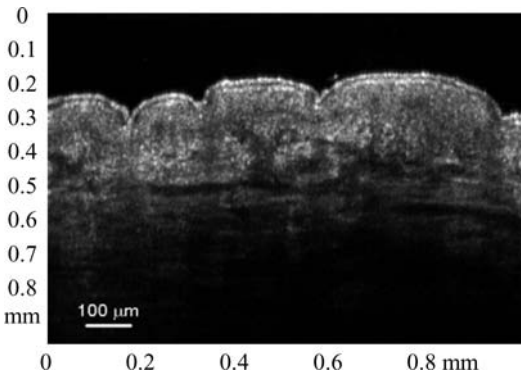


FIGURE 7 Optical coherence tomography skin imaging (healthy skin): backscatter image.

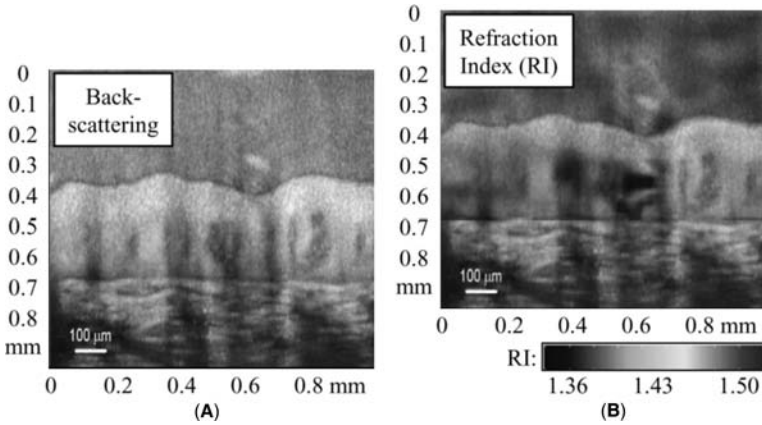


FIGURE 8 Optical coherence tomography skin imaging (healthy skin): (A) backscatter image; (B) RI image. *Abbreviation:* RI, refraction index.

High-Resolution Magnetic Resonance Imaging

An example of the comparative study between HR-MRI and 100 MHz range HFUS is shown in Figure 9. A special receive coil was designed, and HR-MRI images of skin were acquired in a conventional clinical MRI-tomograph with a magnetic inductance of 1.5 T (18). In the HR-MRI image of healthy skin in Figure 9A, the layered skin can clearly be identified. Imaging is performed with an in-plane resolution of 40 and 80 μm, respectively, and a slice thickness of 800 μm. The corresponding skin structures can be seen in the HFUS image in Figure 9B.

Image Fusion

In Figure 10, an example for the fusion of ELM and HFUS images is shown. A 3D volume of a melanocytic nevus was imaged with 100 MHz HFUS, and the skin

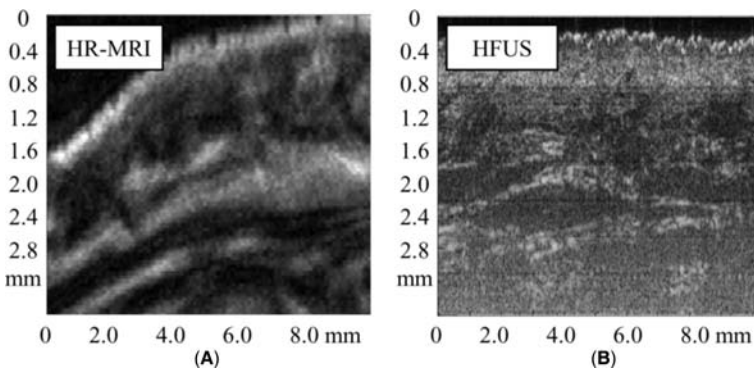


FIGURE 9 Multimodal skin imaging (healthy skin): (A) HR-MRI image; (B) 100 MHz range HFUS image. *Abbreviations:* HR-MRI, high-resolution magnetic resonance imaging; HFUS, high-frequency ultrasound.

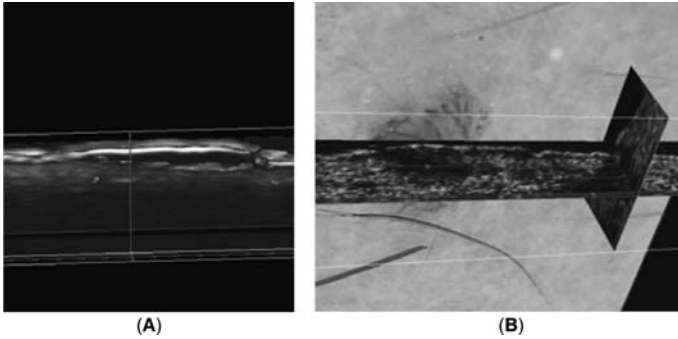


FIGURE 10 Image fusion (melanocytic nevus): (A) 100 MHz range high-frequency ultrasound image with segmented skin surface and nevus area; (B) registered high-frequency ultrasound and epiluminescence microscopy image data in the same coordinate system.

surface and nevus area were segmented in the individual ultrasound images (Fig. 10A). Segmentation of the surface was done automatically by applying threshold segmentation. HFUS images were spatially aligned to the acquired ELM surface image by applying a nonrigid registration with manually selected landmarks. HFUS and ELM image data after registration are shown in the same coordinate

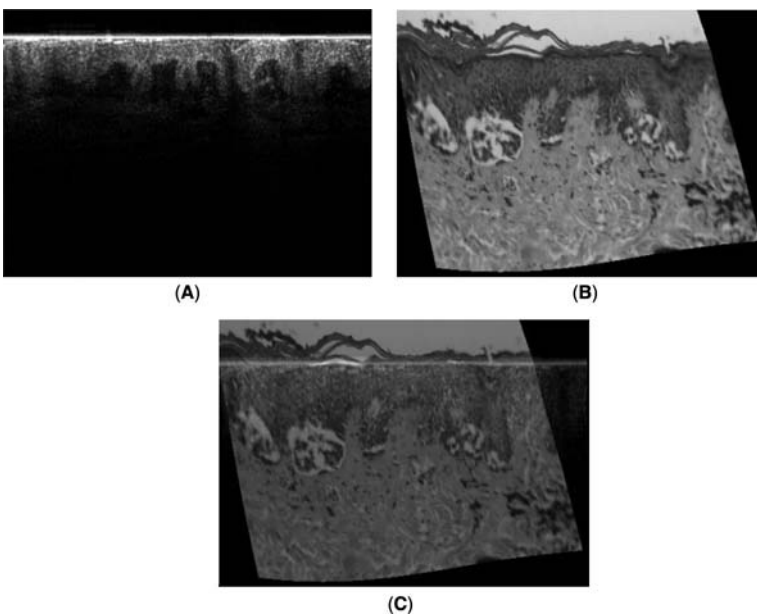


FIGURE 11 Image fusion (basalioma): (A) optical coherence tomography image; (B) histology; (C) fusion and superposition of registered optical coherence tomography and histology images.

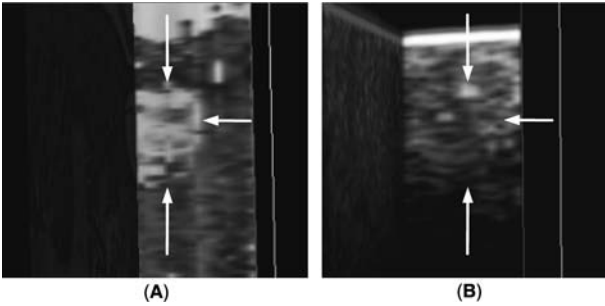


FIGURE 12 Image fusion (nevus): (A) histology; (B) optical coherence tomography image.

system in Figure 10B. The example demonstrates the advantage of applying HFUS for tomographic imaging supplemented to optical skin surface imaging. While the pigmentation of the lesion is visible in the ELM image, its depth is only accessible in the HFUS image data. The fusion of images allows relating the structures and features found in individual images to each other spatially (23).

In Figure 11, an example of the fusion of noninvasive tomographic images with histological sections is shown. A basalioma was imaged with OCT first (Fig. 11A), and histological cross sections of excised tissue were postoperatively prepared. Histology images were electronically acquired with a digital camera connected to a light-microscope (Fig. 11B). Again, images were registered with manually selected landmarks, and fused images were represented in one single coordinate system (Fig. 11C). This example illustrates that the fusion of tomographic images with histological sections offers a means to evaluate the noninvasive imaging technique regarding image content and the correct depiction of the skin structures.

In Figure 12, an example of the fusion of OCT images with 3D histological image data is shown. The fused images show that the dimension and size of the nevus are appropriately depicted with OCT.

SUMMARY AND CONCLUSIONS

Physical concepts of noninvasive modalities with relevance to skin imaging were discussed above. VD and ELM image skin surface structures optically, while HFUS, OCT, and HR-MRI enable cross-sectional imaging by utilizing ultrasound waves, light in the near-IR spectrum and the phenomenon of nuclear magnetic resonance. The concept of multimodal imaging was motivated and examples for image fusion were presented.

The advantage of multimodality is that information of different kinds is obtained with different modalities. Acquired HFUS and OCT images contain morphological information, but the tissue parameters, which determine the image amplitude, are different. While the backscattering and reflection at *acoustical* inhomogeneities is imaged with HFUS, *optical* properties are relevant in OCT. HFUS elastography and RI imaging with OCT deliver additional information about skin. The preliminary results of strain imaging in a nevus discussed above suggest that the mechanical properties of skin are a promising feature for further TC. HFUS in the 20 MHz range enables qualitative and high-resolution imaging of

mechanical properties of skin. Further studies have to be conducted to evaluate the potential of the method in clinical applications.

HR-MRI makes use of nuclear magnetic resonance, i.e., completely different physical phenomena. Each imaging modality has its specific advantages and limitations. With HFUS in the 20 MHz range, the complete skin and the subcutaneous fat can be imaged. Utilizing broadband ultrasound at higher frequencies in the 100 MHz range allows high-resolution imaging of the epidermis and upper dermis. The advantage of OCT in comparison to HFUS is the better and more isotropic spatial resolution, but the penetration depth and the FOV are much smaller. OCT is very well suited for high-resolution imaging of the uppermost skin layers. In vivo MRI of skin is so far not yet established in dermatology, although studies have shown that HR-MRI of skin can be implemented with standard clinical tomographs and specially designed receive coils. However, MRI systems are usually not available and are too expensive for dermatological diagnostics, the acquisition time is on the order of several minutes, and the resolution is significantly worse than with HFUS and OCT.

It was shown that improved morphological information is obtained and depth information is included by image fusion. Further studies have to be conducted to evaluate the potential of multimodal skin imaging and image fusion for the classification of skin lesions. From the conceptual point of view, a higher "hit-rate" is expected to be obtained for automated, computerized skin lesion characterization, as well as for conventional diagnostics by the dermatologist.

ACKNOWLEDGMENT

The presented work is a project of the Ruhr Center of Excellence for Medical Engineering (KMR), Bochum, Germany, which is supported by the Federal Ministry of Education and Research, Germany, Grant No. 13N8079. The contribution of our project partners Rüdiger Scharenberg, Sven Scharenberg, and Bodo Paul (Taberna pro medicum GmbH, Lüneburg, Germany), Alexander Knüttel (Isis optronics GmbH, Mannheim, Germany) as well as Dr. med. Klaus Hoffmann, Georg Moussa, Dr. med. Michael Sand and Prof. Dr. med. Peter Altmeyer (Dermatological University Hospital, Bochum, Germany) is greatly appreciated.

REFERENCES

1. www.kmr-bochum.de
2. www.visiomed.de
3. Husemann R, Tölg S, von Seelen W, et al. Computerised diagnosis of skin cancer using neural networks. In: Altmeyer P, Hoffmann K, Stücker M, eds. *Skin Cancer and UV Radiation*. Berlin, Heidelberg, New York: Springer, 1997:1023–1051.
4. Payne PA. Application of ultrasound in dermatology. *Bioeng Skin* 1985; 1:293–320.
5. Altmeyer P, el-Gammal S, Hoffmann K. *Ultrasound in Dermatology*. Berlin, Heidelberg, New York: Springer, 1992.
6. Hoffmann K, Schatz H, el-Gammal S, Altmeyer P. B-scan sonography in dermatological routine diagnostics. In: Ermert H, Harjes HP, eds. *Acoustical Imaging*. 19. New York: Plenum Press, 1992.
7. Ermert H, Vogt M, Passmann C, et al. High frequency ultrasound (50–150 MHz) in dermatology. In: Altmeyer P, Hoffmann K, Stücker M, eds. *Skin Cancer and UV Radiation*. Berlin, Heidelberg, New York: Springer, 1997:1023–1051.
8. Ermert H, Vogt M. High frequency ultrasonic imaging and its applications in skin. *Proc Int Soc Optical Eng (SPIE)* 1999:44–55.

9. Vogt M, Kaspar K, Altmeyer P, Hoffmann K, El Gammal S. High frequency ultrasound for high-resolution skin imaging. *Frequenz* 2001; 55(1–2):12–20.
10. Foster FS, Pavlin CJ, Harasiewicz KA, Christopher DA, Turnbull DH. Advances in ultrasound biomicroscopy. *Ultrasound Med Biol* 2000; 26(1):1–27.
11. Foster FS, Pavlin CJ, Lockwood GR, et al. Principles and applications of ultrasound backscatter microscopy. *IEEE Trans Ultrason Ferroelectrics Frequency Control* 1993; 40(5):608–617.
12. www.tpm-online.de
13. Huang D, Swanson EA, Lin CP, et al. Optical coherence tomography. *Science* 1991; 254:1178–1181.
14. Pagnoni A, Knuettel A, Welker P, et al. Optical coherence tomography in dermatology. *Skin Res Technol* 1999; 5:83–87.
15. Knüttel A, Koch S, Schork R, Böcker D. Tissue characterization with optical coherence tomography (OCT). *SPIE* 1996; 2676:54–64.
16. Knüttel A, Breit M, Böcker D. Tissue characterization with optical coherence tomography. *SPIE* 1997; 2981:7–18.
17. www.isis-optronics.de
18. Liffers A, Vogt M, Ermert H. In vivo biomicroscopy of the skin with high-resolution magnetic resonance imaging and high frequency ultrasound. *Biomedizinische Technik* 2003; 48(5):130–134.
19. Vogt M, Scharenberg S, Scharenberg R, Hoffmann K, Altmeyer P, Ermert H. In vivo evaluation and imaging of skin elasticity applying high frequency (22 MHz) ultrasound. *Proc IEEE Ultrason Symp* 2002:1819–1822.
20. Vogt M, Ermert H. Development and evaluation of a high-frequency ultrasound based system for in vivo strain imaging of the skin. *IEEE Trans Ultrason Ferroelectrics Frequency Control* 2005; 52(3):375–385.
21. Vogt M, Ermert H. Strain imaging of skin utilizing high frequency ultrasound. *IEEE Trans Ultrason Ferroelectrics Frequency Control* 2005; 52(3).
22. Vogt M, Knüttel A, Hoffmann K, Altmeyer P, Ermert H. Comparison of high frequency ultrasound and optical coherence tomography as modalities for high resolution and non invasive skin imaging. *Biomedizinische Technik* 2003; 48(5):116–121.
23. Vogt M, Scharenberg S, Scharenberg R, et al. Multimodal imaging of the skin with high frequency ultrasound, optical coherence tomography and epiluminescence microscopy. *Biomedizinische Technik* 2004; 49(Ergänzungsband 2):854–855.

Comparative Studies of Scanning Electron Microscopy and Transmission Electron Microscopy

Masaaki Ito and Fumiko Sakamoto

*Department of Dermatology, Niigata University School of Medicine,
Niigata, Japan*

Ken Hashimoto

*Department of Dermatology, Wayne State University School of Medicine,
Detroit, Michigan, U.S.A.*

INTRODUCTION

Scanning electron microscopy (SEM) allows us to observe three-dimensional (3D) architectures of biological materials in high resolution down to a few nanometers, while transmission electron microscopy (TEM) visualizes two-dimensional (2D) and sectional surface of the materials in higher resolution, and details of cell membranes and cellular organelles can be resolved. Usually in histopathology, TEM surveys are often employed following light microscopic examinations and are essential parts of pathological diagnosis in many skin diseases such as amyloidosis and epidermolysis bullosa. Recently, molecular biology has rapidly advanced and immunohistochemistry with antibodies to various components of skin tissues is quite frequently performed and must be important for the diagnosis of skin disorders; in such cases, however, the TEM findings are sure to be fundamental. On the other hand, although SEM offers us fine 3D figures of the pathological skin materials, the diagnostic utilities of SEM have been less explored than those of light microscopy (LM), immunohistochemistry, and TEM, except for hair abnormalities (1). The SEM images of the skin surface, i.e., epidermal horny cells, can easily be obtained by several methods, such as tape stripping and replication, and have been shown in several skin conditions including normal skin (2–4), psoriasis (3–5), ichthyosis vulgaris (3), ichthyosiform erythroderma (3), eczemas (5), and others. However, these SEM surveys have shown only the fact that villous projections are present on the undersurface of the horny cells and varied in size among different anatomical sites (2) and keratinization disorders (3–5). In the normal skin, those projections are known to be well developed at volar sites, but poorly developed at body sites (2). SEM surveys (4,6) of biopsied skin materials have confirmed that the projections on the undersurface of a horny cell fit the pores or depressions on the uppersurface of the next horny cell, indicating that epidermal horny cells form many tiny concave–convex interdigitations between them, probably to gain a stability to resist shearing forces applied to the skin in daily life. At body sites, horny cells form columnar stacks (2), each of which is derived from a linearly arranged stream of epidermal keratinocytes originating from the matrix basal layer and differentiating to spinous and granular layers. TEM examinations (2,6) have shown that each horny cell in a columnar stack is overlapping upon one another

at the cell edges, with horny cells in neighboring stacks. The overlapping parts of the horny cell borders become pressed thin; these horny cells are shown to be hexagonal in shape (2,6). At volar sites, however, horny cells have been known to lack either such a column formation or a hexagonal cell shape (2).

In this chapter, these previously documented data are discussed, and further to investigate more details of 2D and 3D findings of the epidermis, the TEM findings and SEM findings of several normal skin materials from different anatomical sites, including face, leg, palm, and sole, and pathological skin materials of nevus sebaceous and X-linked ichthyosis will be shown. Each material was cut into two or three pieces. One piece was fixed in 1.5% glutaraldehyde (GA) in 0.1 M cacodylate buffer (CB) (pH 7.4) for 20 minutes and stained in 0.5% tannic acid (TA) in 1.5% GA in CB (pH 7.2) for 30 minutes, and in 1% TA in 2% GA in CB (pH 7.0) for one hour. After postfixation in 1% osmium tetroxide in CB (pH 7.4) and rinsing in CB, this piece was dehydrated in graded concentrations of alcohol, immersed in isoamylacetate, dried up in a critical point drying apparatus with CO₂, and observed in a SEM (JSM-840) following gold coating in an ion sputter (JFC-1100). Another piece was cut into smaller pieces, double-fixed in 5% GA and in 1% osmium tetroxide in CB (pH 7.4b), dehydrated in graded concentrations of alcohol and acetone, and embedded in EponTM. For observation by LM, 1- μ m thick sections of the embedded specimens were made with a diamond knife in an ultramicrotome (MT-5000) and stained in a toluidine blue solution. Ultrathin sections of the specimens were similarly made, double stained with 1% uranylacetate and Reynolds' lead citrate (7) solutions, and observed in a TEM (JEM-1010B). A remaining piece was fixed in 10% formalin solution and routinely processed for LM observation with hematoxylin–eosin staining.

NORMAL HUMAN SKIN

Body Sites

Normal human skin materials from face, leg, and back showed basically similar SEM and TEM findings. At a low magnification by SEM (Fig. 1), sulci or grooves ran in various directions on the skin surface and the elevated areas surrounded by the demarcating sulci showed a triangular shape. Hairs grew out at the crossroads of some sulci, where the sulci became relatively deeper. These sulci and elevations of the skin surface as seen by SEM were pronounced by actual degrees due to tissue shrinkage after fixation and dehydration processes. In relatively dirt-free areas, the skin surface was observed to be covered by orderly arranged horny cells with a hexagonal cell shape (Fig. 2). When several superficial cell layers of the horny layer were artificially cut and removed with a knife just after biopsy, much clear cell surface became visible. On the upper surface of these deep horny cells, small pores or tiny furrows were evenly distributed (Fig. 3). When a half-peeled horny cell was seen, small villous projections or chains of villi forming ridges were observed on its undersurface and shown to correspond well to the pores or furrows of the upper surface of the next horny cell (Fig. 4). If in normal human body skin, the most superficial horny cells show a smooth cell surface without pores and villi (4,6), the present observation suggests that these cell surface structures of epidermal horny cells may decrease in degree and finally disappear during the movement of the cells through the horny layer.

TEM showed that the epidermal keratinocytes produced lamellar bodies in the spinous-through-granular layers and keratohyaline granules in the granular

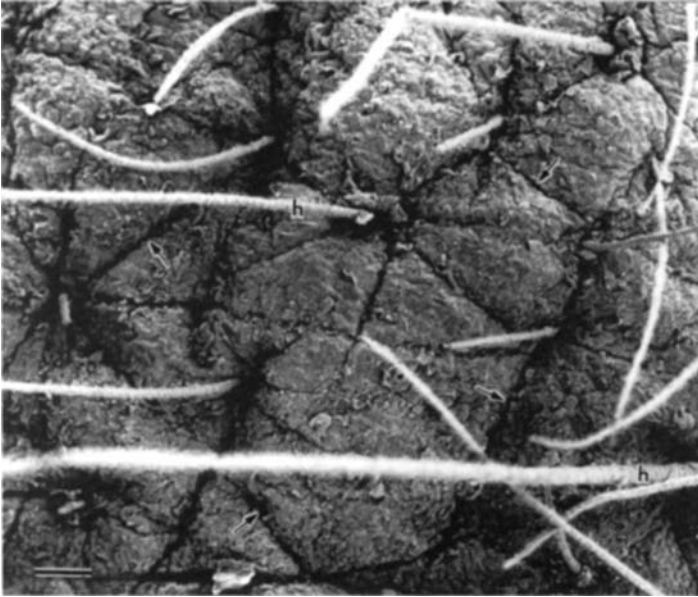


FIGURE 1 Scanning electron microscopy of the normal skin surface of the cheek of a five-year-old Japanese male. *Arrow*—sulcus. Bar = 100 μm . *Abbreviation*: h, hair.

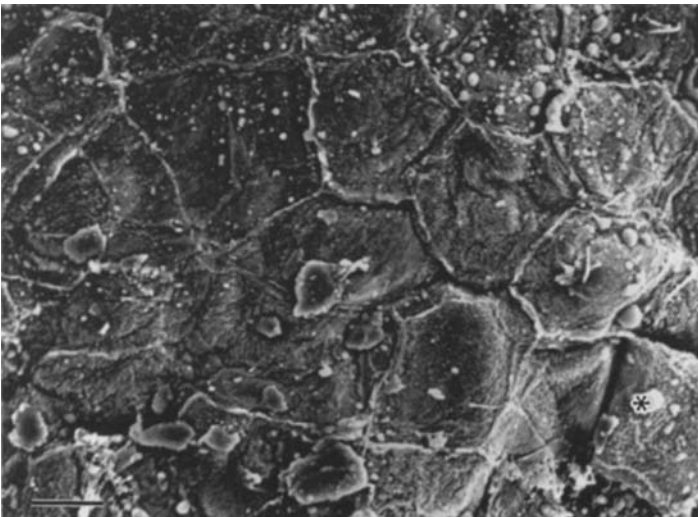


FIGURE 2 Scanning electron microscopy of a high magnification of the same case as used in Figure 1. Each hexagonal scale represents individual horny cell. The area indicated by the *asterisk* is enlarged in Figure 4. Bar = 10 μm .

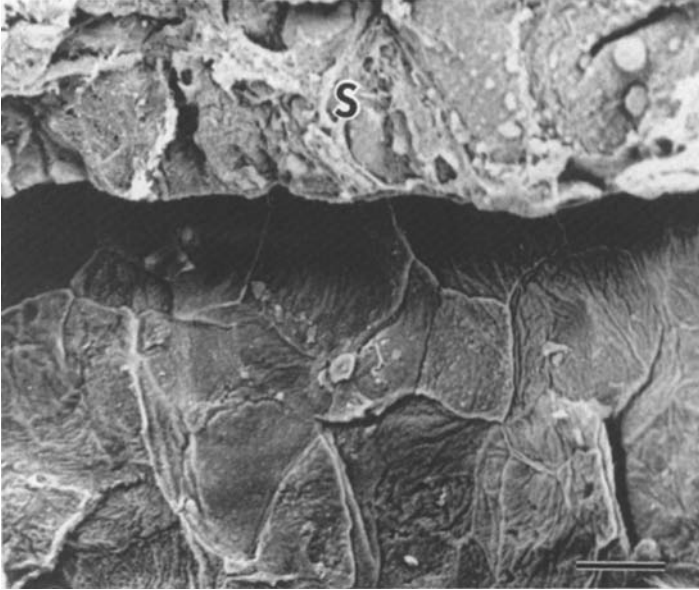


FIGURE 3 Freshly exposed horny cells seen after the desquamation of a sheet of superficial horny layer (S). The same case is used in Figure 1. Bar = 10 μ m.

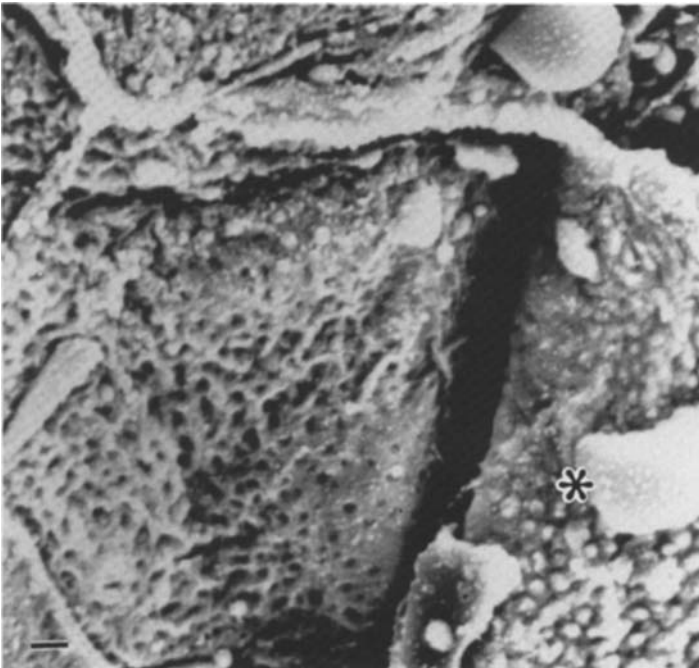


FIGURE 4 Close-up view of the horny cells shown in Figure 2. A half-peeled horny cell (*asterisk*) reveals numerous villous projections on the undersurface and corresponding pores in the underlying horny cell are seen. Bar = 1 μ m.

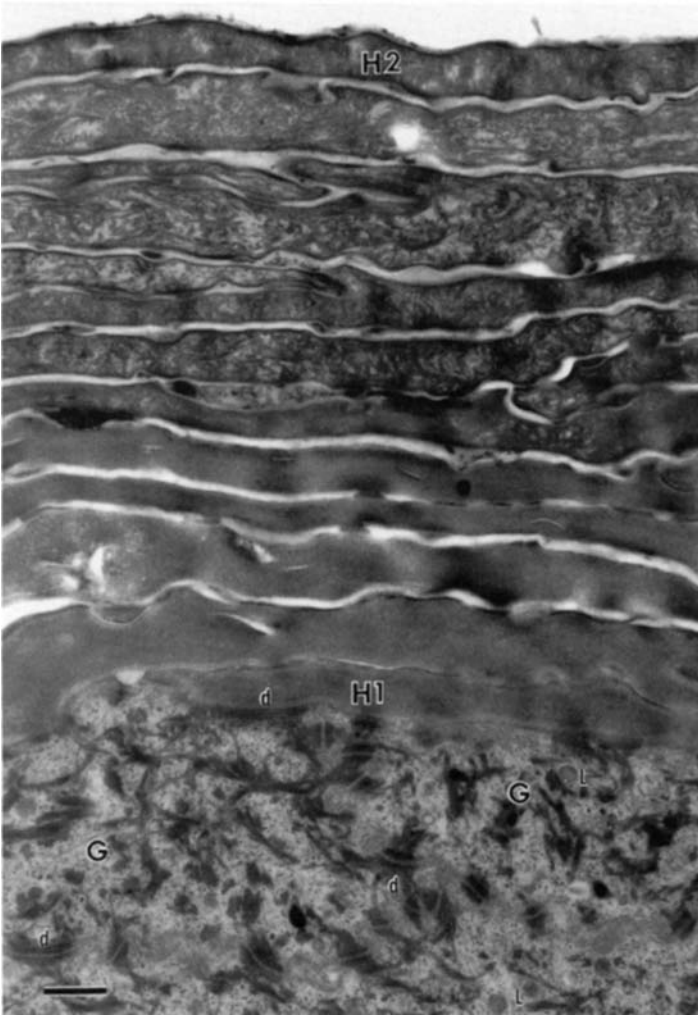


FIGURE 5 Transmission electron microscopy of the horny layer in the normal epidermis of the back skin of a 22-year-old Japanese female. Note that compactness or density of horny cells decreases from H1 to H2. Uranyl acetate–lead citrate staining. Bar = 0.5 μm . *Abbreviations:* d, desmosome; G, granular cell just before keratinization; H1, the deepest horny cell just after keratinization; H2, superficial horny cell; L, lamellar body.

layer, and finally keratinized in the horny layer, forming a flat cell with a compact keratin pattern in the cytoplasm and losing almost all cell organelles (Fig. 5). The upper granular cells and a few layers of deep horny cells compactly adhered to each other with desmosomes and an intercellular substance derived from the cytoplasmic lamellar bodies (8). This intercellular substance is known to be an intercellular lamellar structure (9) composed of ceramides (10) and to play an important role in permeability barrier function of the epidermis (11). On the other hand, the compact keratin pattern of the deeper horny cells is induced by aggregation of keratin filaments caused by filaggrin, which has been produced by

degradation of profilaggrin, a macromolecular protein, in keratohyaline granules in the granular cells (12).

Although the adhesion line of the granular cells and the lower horny cells was smooth or slightly wavy in vertically cut skin sections, several cells in the mid-horny layer revealed some sharp elevations and indentations of their cell membrane (Fig. 5). The cell surface indentations and invaginations of horny cells observed by SEM above seemed to be formed just after the horny cells had lost such a close cell adhesion. The loss of cell adhesions may be either achieved by ceramidases (13) digesting ceramides of the intercellular lamellar structure or by proteases (14) degrading desmosome structures. These enzymes are also derived from cytoplasmic lamellar bodies (13,14). Then, the horny cells in the mid-to-superficial horny layer became relatively thicker in cell thickness and lost the compact keratin pattern, leaving loosely running keratin filaments in the cytoplasm, and a marginal band (15) along the inside of the cell membrane was visualized (Figs. 5 and 6). The loss of aggregation of keratin filaments is known to be caused by further digestion of filaggrin to smaller molecules such as amino acids (16); the small molecules are believed to play a role in water-holding property of the horny cells (16), as natural moisturizing factors. The most superficial horny cells, which had been seen by SEM as a natural skin surface structure, showed a wavy line of their cell membrane but fewer indentations than deeper horny cells (Fig. 5). However, a convincing difference in the degree of the cell membrane indentations between the superficial and

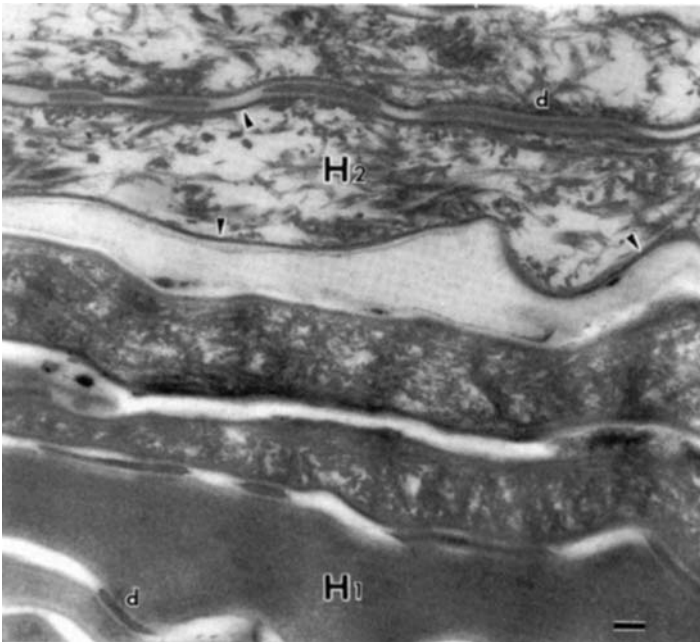


FIGURE 6 Transmission electron microscopy of a higher magnification of Figure 5. *Arrowhead*—marginal band. Uranyl acetate–lead citrate staining. Bar = 0.1 μm . *Abbreviations:* d, desmosome; H1, deep horny cell with compact cytoplasm filled with keratin filaments; H2, more superficial horny cell with loose cytoplasm containing sparsely running keratin filaments.

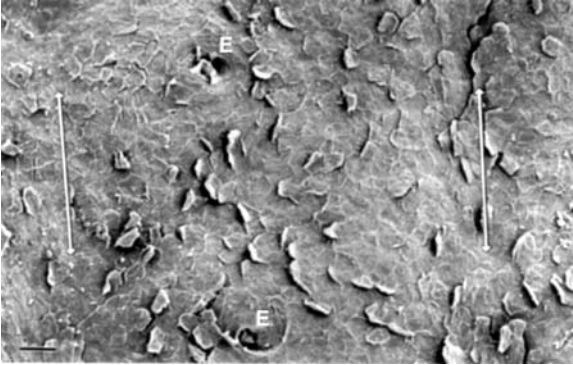


FIGURE 7 Scanning electron microscopy of the normal plantar skin surface of a 24-year-old Japanese female. *Arrow*—shallow and gentle sulcus. *Bar* = 50 μm . *Abbreviation*: E, eccrine pore.

deep horny cells as corresponding counterparts of SEM images could not be demonstrated by TEM (Fig. 5). There might be a difference in the degree of tissue shrinkage during specimen preparation between TEM and SEM.

Volar Sites

At palmar and plantar sites, the skin surface seen at a low magnification by SEM (Fig. 7) showed very shallow and gentle sulci and slightly elevated areas surrounded by the sulci. Eccrine pores were regularly distributed on slightly elevated ridges, usually at the center of each ridge (Fig. 7). At higher magnifications, the surface horny cells showed polygonal or irregular, but not hexagonal, cell shapes and distinctive formation of small pores or furrows on the cell surface (Figs. 8 and 9); these depressions were much deeper than those at body sites observed above. Similarly, a half-peeled horny cell reveals sharply protruded villous projections or ridges on its undersurface (Fig. 9), indicating firmer interdigitations between the underlying horny cells, which received these villi and ridges with pores and furrows. Occasionally, membrane-like structures, on which many filaments with a similar thickness were fixed, were seen (Figs. 8 and 10). These filaments ran in various directions parallel to the skin surface plane and partly formed a network image (Fig. 10). The membrane-like structures were irregularly shaped but looked uniform in thickness and incompletely covered one or few horny cells, masking the cell surface indentations of the horny cells (Figs. 8 and 10).

By TEM, the thickness of the horny layer as well as the cell number of the overlapping horny cells was much greater in the volar epidermis than in the epidermis at body sites. Epidermal keratinocytes formed 10 cell layers of compact horny cells, and the horny cells in the mid-through-superficial horny layer still showed a relatively compact cell feature filled with abundant keratin filaments; the mid-through-superficial horny cells revealed marked indentations of their cell membranes even at the most superficial horny cells (Figs. 11 and 12). Although the most superficial horny cells at body sites seemed to peel off intact and completely (Fig. 6), at volar sites they did not always show such complete desquamation; some broken horny cells occasionally remained on the skin surface, still keeping a firm cell-to-cell adhesion with the underlying horny cell (Fig. 11). This indicated that the horny cells might be broken away by cell damage as well as peeled off

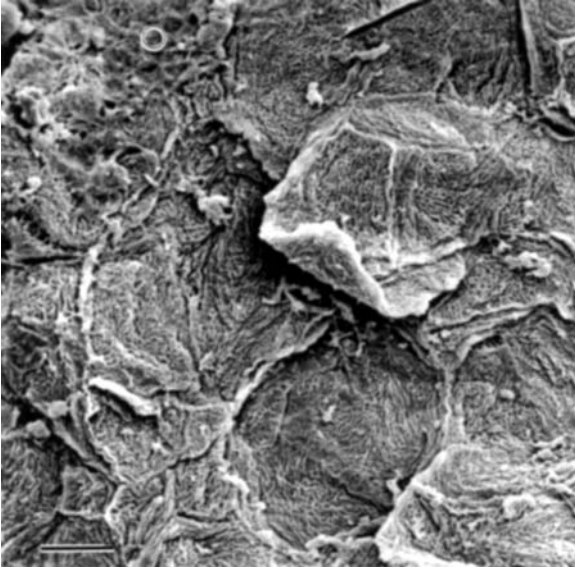


FIGURE 8 Scanning electron microscopy of a higher magnification of Figure 7. The area indicated by the circle is enlarged in Figure 10. Bar = 10 μm .

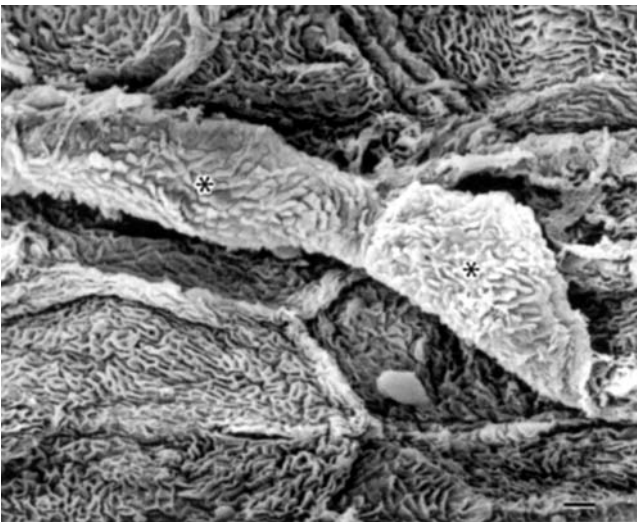


FIGURE 9 Close-up view of the horny cells of the same case as used in Figure 7. Sharp villi or ridges on the undersurface of the half-peeled horny cells (*asterisks*) apparently interdigitated with pores or furrows of the underlying horny cells. Bar = 2 μm .

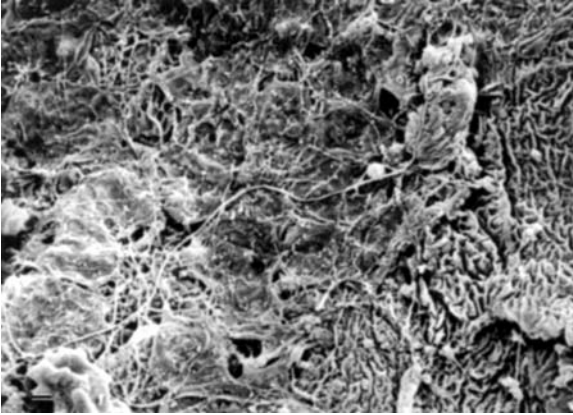


FIGURE 10 Enlargement of a membrane-like structure and many filaments on the surface of the normal plantar skin. The same case as used in Figure 7. Bar = 1 μ m.

by intact separation (Fig. 12) at volar sites. The remnants of the broken horny cells seemed to correspond to membrane-like structures with filaments as seen by SEM (Fig. 10). The filaments should represent keratin filaments of bundles released from the broken horny cells. Because volar sites are subject to constant pressures or frictions from the environment, firm cell-to-cell adhesion and deeper indentations between overlapping horny cells may be needed, and this feature is kept up to the surface of the skin. Although it is still unclear whether or not the difference in keratin compositions in the suprabasal keratinocytes between the volar epidermis (K1 and K9) and body site epidermis (K1 and K10) (17) is related to the maintenance of the compact feature of keratin filaments in the superficial horny cells, the increased amount of filaggrin indicated by well-developed keratohyaline granules in the volar epidermis may result in delay of the filaggrin digestion,



FIGURE 11 Transmission electron microscopy of the epidermal horny layer of the normal plantar skin of a 58-year-old Japanese female. A broken horny cell at the most superficial layer is still attached to the underlying horny cell. Uranyl acetate-lead citrate staining. Bar = 1 μ m. *Abbreviation:* bH, broken horny cell.

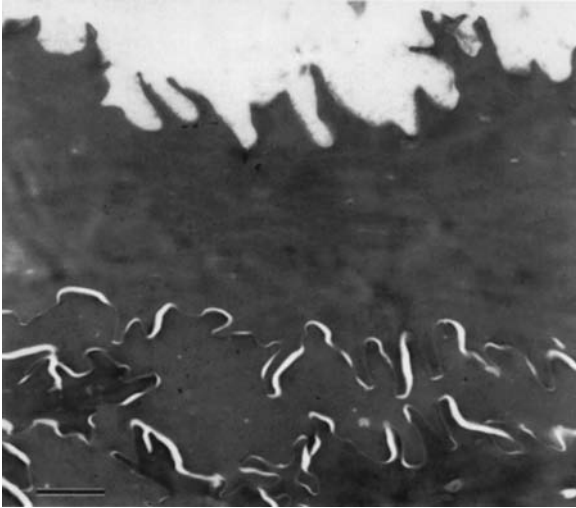


FIGURE 12 Transmission electron microscopy of the epidermal horny layer of the normal plantar skin of a 23-year-old Japanese female. The most superficial horny cell is cleanly separated with intact cell membrane. Uranyl acetate–lead citrate staining. Bar = 1 μ m.

namely keeping the aggregated condition of keratin filaments in a longer time. However, a depressed activity of proteases reacting for filaggrin digestion is also a possible mechanism to explain the cytological feature of the volar horny cells, as discussed above.

When the cell organization of epidermis is discussed, we must consider it based on the stem cell concept (18,19); the epidermal basal cells divide and proliferate not randomly, but regularly following a rule of order of cell division. Namely, stem cells, which are slowly cycling and located in the basal layer, produce some transient amplifying cells, which are still located around the stem cells in the basal layer and undergo further cell division producing daughter cells (18). The daughter cells differentiate through the spinous and granular cell layers and keratinize, forming the horny cell layer. The stem cells may be located at the tips of deep rete ridges in the volar epidermis (18,19), whereas at body sites they may be present in the basal cell layer adjacent to the tips of the dermal papillae (19). Moreover, in the body sites, especially in the hairy skin, the hair bulge stem cells (20) can supply epidermal keratinocytes under activation of c-Myc (21,22). Based on the locations of stem cells and transient amplifying cells, the arrangement of the differentiating and keratinizing cells and further morphology of surface skin structures may be determined; however, it is still unsettled how the columnar stacks of keratinocytes are formed at body sites and not at volar sites.

PATHOLOGICAL SKIN

Nevus Sebaceous

Nevus sebaceous is a common hamartomatous skin disorder, usually found at birth, and shows gradual proliferation of the epithelial components through the

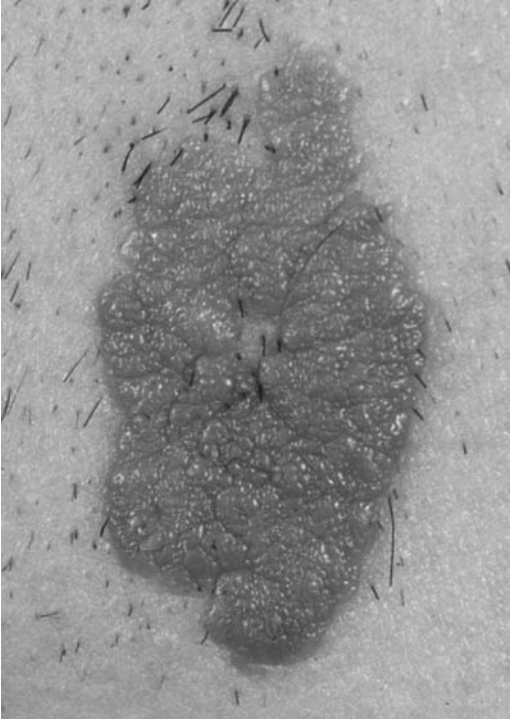


FIGURE 13 (See color insert) Clinical feature of nevus sebaceous. The right temporal area of a 16-year-old Japanese male patient. Hair on the skin surrounding the lesion has been cut away.

lifetime, sometimes giving rise to generation of various epithelial tumors (23). Around puberty, the lesion usually shows a well-demarcated, yellow-to-brown-colored elevation with a granular or verrucous surface (Fig. 13). Histologically, the investigated cases showed that the lesions were constituted with the anomalously proliferated epidermal and sebaceous components (Fig. 14). By SEM, the surface of the lesion was occupied by closely distributed hemispheric-shaped convolutions with diameters of a few hundred micrometers (Fig. 15); these convolutions were thought to correspond to the papillomatous protrusions of the affected epidermis as indicated by bi-headed arrows in Figure 14. In some cases of nevus sebaceous, their SEM features displayed polygonal, not spherical, shapes of the surface convolutions, with relatively flat tops, as a whole showing a stone pavement-like appearance (not shown). At a higher magnification, the surface of each convolution revealed desquamation of various sizes of peels of horny cells (Fig. 16).

X-Linked Ichthyosis

X-linked ichthyosis is an inherited keratinization disorder characterized by rough-surfaced skin over the entire body and especially by rhagadiform hyperkeratotic lesions on extremities. Within the brown-colored fish scale-like areas surrounded by the large conspicuous rhagades, many minor or shallow rhagades-like linear divisions are seen (Fig. 17). By LM, the specimen obtained from a leg lesion showed the hypergranulosis and hyperkeratosis of the epidermis. The compact

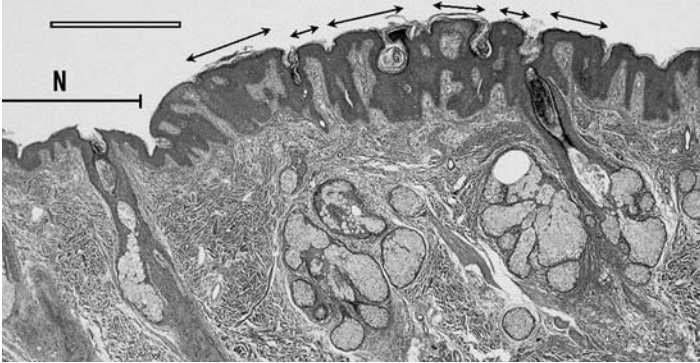


FIGURE 14 Light microscopy finding of nevus sebaceous. The same case as used in Figure 13. The epidermis shows anomalous and papillomatous proliferation. The protrusions of the epidermis indicated by bi-headed arrows may correspond to the surface convolutions shown in Figure 15. Bar = 500 μm . *Abbreviation:* N, a normal part of the skin adjacent to the nevus sebaceous lesion.

horny layer was entirely flat and accompanied by occasional valley-like crevices of horny layer invaginated in various degrees into the lower epidermal layer (Fig. 18). By SEM, deep straight sulci were observed to run on the skin surface and the surface areas surrounded by the sulci produced plateau-like images (Fig. 19). In addition to the deep sulci, shallow sulci were often seen on the plateau areas, often showing a curved linear depression (Fig 19). The deep sulci, plateaus, and shallow sulci seemed to correspond to the clinically observed large rhagades, fish scale-like areas and minor or shallow rhagades (Fig. 17), respectively. These shallow sulci were covered with horny cells with a concave surface on the sidewalls and even

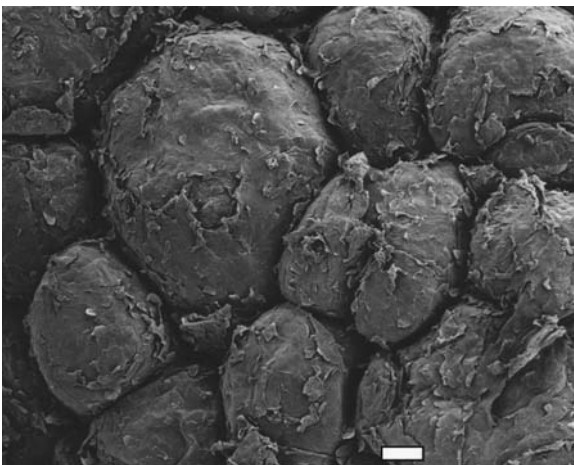


FIGURE 15 Scanning electron microscopy finding of the skin surface of nevus sebaceous. The same case as used in Figure 13. The skin surface is occupied of hemispheric-shaped convolutions with diameters of a few hundred micrometers. Bar = 100 μm .

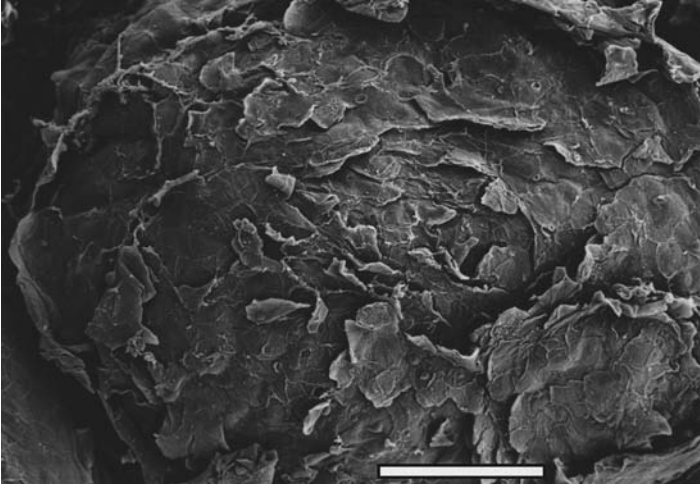


FIGURE 16 An enlarged feature of a convolution in the skin surface of nevus sebaceous. The same case as used in Figure 13. Various sizes of peels of horny cells are seen. Bar = 100 μ m.



FIGURE 17 (See color insert) Clinical feature of X-linked ichthyosis. The calf of a 42-year-old Japanese male patient.

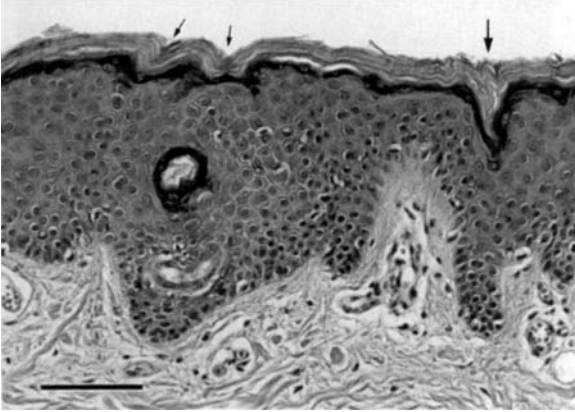


FIGURE 18 Light microscopy finding of the epidermis in X-linked ichthyosis. The leg lesion of an eight-year-old Japanese male patient. *Large arrow*—valley-like or wedge-shaped crevice of the horny layer; this corresponds to a deep rhagade. *Small arrows*—minor or shallow rhagades, Hematoxylin–eosin staining. Bar = 100 μm .

at the bottom of the sulci. These were neither sharp rhagades nor fissures in the bottom (Figs. 19 and 20). At shoulder edges of the shallow sulci, almost perpendicularly layered horny cells were packed and exhibited their laminated edges, sometimes resembling overlapping petals of a flower (Figs. 19 and 20). These sulci seemed to correspond to valley-like invaginations of the horny layer observed by LM above (Fig. 18). The skin surface of the plateaus was covered by flat and relatively hexagonal-shaped horny cells; however, the uppersurface of the horny cells revealed marked pore of furrow-like depressions (Fig. 21) and half-peeled cells showed villous projections at their undersurface.

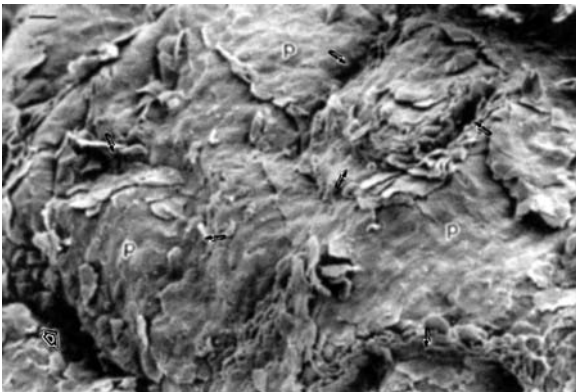


FIGURE 19 Scanning electron microscopy of the skin surface in X-linked ichthyosis. The leg lesion of a seven-year-old Japanese male patient. *Thin arrows*—curved shallow sulci with shoulder edges showing a flower-petals-like appearance; *thick arrow*—deep sulcus. The area indicated by the *asterisk* is enlarged in Figure 20. Bar = 20 μm . *Abbreviation:* p, plateau of the skin surface.

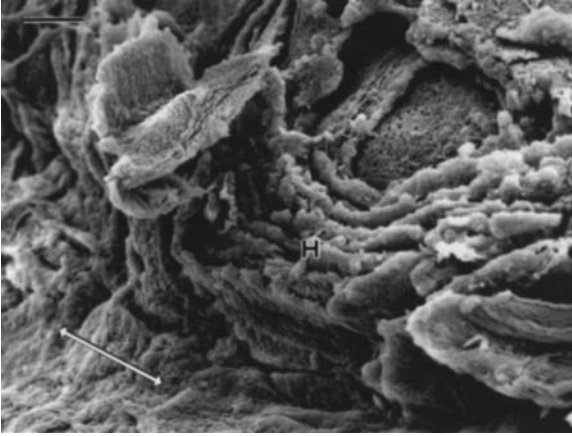


FIGURE 20 A shallow sulcus on the skin surface in X-linked ichthyosis. The same case as used in Figure 19. *Arrows*—bottom of the sulcus, (**H**) a stack of laminated horny cells standing perpendicular to the skin surface at the shoulder edge of a shallow sulcus. Bar = 5 μ m.

By TEM, thin lamellar horny cells had compact cytoplasm and overlapped through the entire horny layer. These horny cells interdigitated through villous projections, which often possessed desmosomes (Figs. 22 and 23). Corresponding to the SEM picture of shallow sulci (Fig. 20), at the shoulders of valley-like portions of the horny layer, the broken edges of the overlapping horny cells were seen as if these cells had been sheared with a sharp knife (Figs. 22 and 23). The cut surface of these “cut” horny cells seemed to correspond to the “flower petals” at the shoulders of shallow sulci seen by SEM (Figs. 19 and 20). The granular cells before keratinization produced well-developed keratohyaline granules and many lamellar bodies in the cytoplasm (Fig. 24).

In X-linked ichthyosis, steroid sulfatase deficiency has been found (24,25) and known to cause the keratinization disorder. The enzyme deficiency results from the critical point mutations of the steroid sulfatase gene (26), which is located

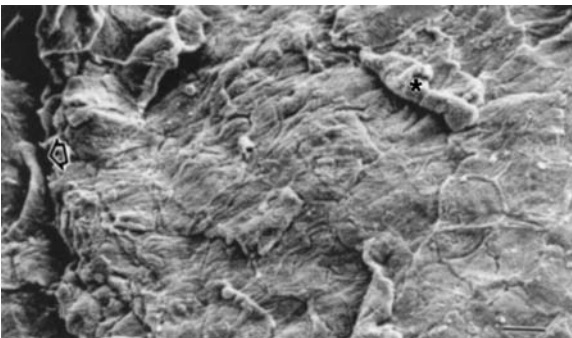


FIGURE 21 Enlargement of a plateau area of the skin surface in X-linked ichthyosis. The same case used in Figure 19. *Arrow*—deep sulcus; *asterisk*—half-peeled horny cell. Bar = 10 μ m.

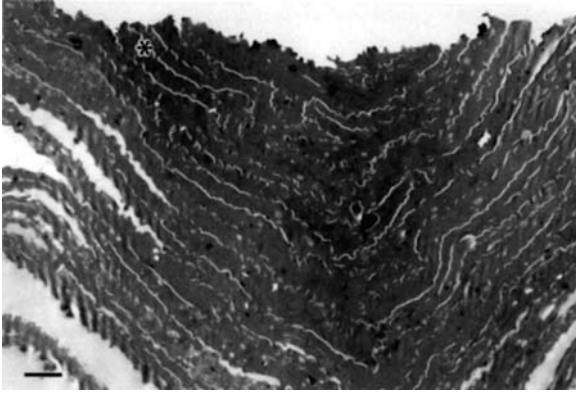


FIGURE 22 Transmission electron microscopy of a crevice of the epidermal horny layer in X-linked ichthyosis. The same case as used in Figure 19. The area indicated by the *asterisk* is enlarged in Figure 23. Uranyl acetate–lead citrate staining. Bar = 2 μm .

on the distal short arm of X chromosome (27). This enzyme digests cholesterol sulfate, which has been produced by cholesterol sulfotransferase in the basal-through-spinous cell layers and distributed over the outer surface of the cell membrane of the granular cells and deep horny cells, as a component in the intercellular lipid layer; as the cholesterol sulfate is lipophilic and amphiphilic and diffuses

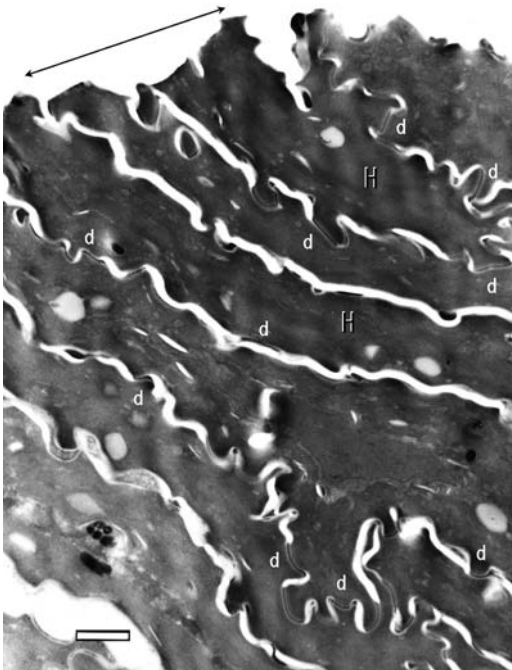


FIGURE 23 Transmission electron microscopy of the flower petals of horny cells seen by scanning electron microscopy. The edges of the horny cells are sharply sheared in a linear plane (*arrow*). The horny cells maintain compact cytoplasm in X-linked ichthyosis in contrast to loosening up of cytoplasm in the normal skin (Figs. 5 and 6). Many desmosome structures (**d**) still remain in the superficial horny layer. The same case as used in Figure 19. Uranyl acetate–lead citrate staining. Bar = 0.5 μm .

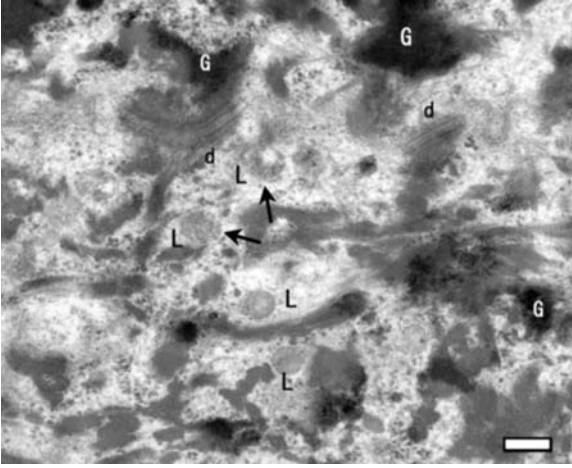


FIGURE 24 Transmission electron microscopy of the granular cell layer in X-linked ichthyosis. The same case as used in Figure 19. The arrows indicate lamellar bodies (L), in which inner lamellar structures are visible; (d), desmosome; and (G) keratohyaline granules in the granular cells. Uranyl acetate–lead citrate staining. Bar = 0.2 μm .

across the cell membrane, it may work as a partition (14) surrounding the internal hydrophobic cytoplasm containing keratin, filaggrin, and so on. The cholesterol sulfate is subsequently digested to cholesterol by steroid sulfatase in the mid-horny layer; the metabolism from cholesterol to cholesterol sulfate again through cholesterol is called “epidermal cholesterol sulfate cycle” (28). The deficiency of the steroid sulfatase results in excess of cholesterol sulfate in the intercellular spaces in the deep horny layer and/or persistence of cholesterol sulfate in the mid-through-superficial horny layer. The excess of cholesterol sulfate may cause an abnormality in permeability barrier function in X-linked ichthyosis (29). While, cholesterol sulfate is an inhibitor for serine proteases, which mediate desquamation of horny cells by degrading their desmosome structures (30); therefore, in X-linked ichthyosis, the desmosome structures are not digested and still remain in the superficial horny layer (Fig. 23), keeping the firm connection of horny cells each other. These findings may explain the mechanism of retention hyperkeratosis (31) in X-linked ichthyosis. Although steroid sulfatase (14) as well as other hydrolases, proteases and ceramidases are derived from lamellar bodies of keratinocytes, the TEM features of the lamellar bodies looked normal in X-linked ichthyosis (Fig. 24); the lack of a single component such as steroid sulfatase may not influence the production and ultrastructure of lamellar bodies. Another characteristic TEM feature of the superficial horny cells in X-linked ichthyosis was the compactness of the cytoplasm containing aggregated keratin filaments; this must be due to the remaining of still active filaggrin as described in the section “Volar Sites.” However, the superficial horny cells in X-linked ichthyosis showed significantly more compact cytoplasm and thinner cell thickness (Fig. 22) than those (Fig. 11) in the normal volar superficial horny cells. It is still unclear why filaggrin is not degraded in X-linked ichthyosis; there seems to be a possibility that the persistent cholesterol sulfate may also prevent the degradation of filaggrin.

Anyhow, such firm adhesion and compactness of horny cells must produce flat horny layers as seen in LM and the many plateaus of the skin surface as shown by SEM. The deep and shallow sulci on the surface are thought to be formed to absorb surplus skin areas created concomitant to keratinization. Many rigid flat areas (plateaus) are much larger than the elevated dome-shaped areas in the normal skin and probably formed at the skin surface by the plateau-forming kinetics of the entire horny layer. Such a flat board-like character of the horny layer may cause decrease in number of sulci and if sulci are ever formed, their depth is exaggerated (Fig. 18). The clinical "rhagadiform" appearance of the skin is not by cleavage or severance (rhagades) in the horny layer, but by sulci formed by plication of the horny layer.

REFERENCES

1. Ito M, Hashimoto K. Hair abnormalities. In: Johannessen JV, Hashimoto K, eds. *Electron Microscopy in Human Medicine*. Vol. 11(a). The Skin. New York: McGraw-Hill Inc., 1985:Chap. 8.
2. David NM, Eisen AZ. Structure and organization of mammalian stratum corneum. *Ultrastr Res* 1971; 35:247.
3. Dawber RPR, Marks R, Swift JA. Scanning electron microscopy of the stratum corneum. *Br J Dermatol* 1972; 86:272.
4. Mishima Y, Matsunaka M, Nagao S. Subcellular changes in keratin and granular cells of keratin-stripped and psoriatic epidermis revealed by scanning and transmission electron microscopy. *Acta Dermatovener (Stockholm)* 1973; (suppl 73):83.
5. Marks R, Barton S, King CS, Nicholls S. Formation of the horny layer in psoriasis; primarily defective or secondarily affected. *Acta Dermatovener (Stockholm)* 1973; 87:77.
6. Hashimoto K, Kanzaki T. Surface ultrastructure of human skin. *Acta Dermatovener (Stockholm)* 1975; 55:413.
7. Reynolds ES. The use of lead citrate at high pH as an electron-opaque stain in electron microscopy. *J Cell Biol* 1963; 17:208.
8. Landmann L. The epidermal permeability barrier. *Anat Embryol* 1988; 178:1.
9. Swartzendruber DC, Wertz PW, Kitko DJ, Madison KC, Downing DT. Molecular models of the intercellular lipid lamellae in mammalian stratum corneum. *J Invest Dermatol* 1989; 92:251.
10. Freinkel RK, Traczyk TN. Lipid composition and acid hydrolase content of lamellar granules of fetal rat epidermis. *J Invest Dermatol* 1985; 85:295.
11. Imokawa G, Akasaki S, Minematsu Y, Kawai M. Importance of intercellular lipids in water-retention properties of the stratum corneum: induction and recovery study of surfactant dry skin. *Arch Dermatol Res* 1989; 281:45.
12. Dale BA, Resing KA, Presland RB. Keratohyalin granule proteins. In: Leigh I, Lane B, Watt F, eds. *The Keratinocyte Handbook*. Cambridge: Cambridge University Press, 1994:323.
13. Yada Y, Higuchi K, Imokawa G. Purification and biochemical characterization of membrane-bound epidermal ceramidases from guinea pig skin. *J Biol Chem* 1995; 270:12,677.
14. Elias PM, Crumrine D, Rassner U, et al. Basis for abnormal desquamation and permeability barrier dysfunction in RXLI. *J Invest Dermatol* 2004; 122:314.
15. Hashimoto K. The marginal band; a demonstration of the thickened cellular envelope of the human nail cell with the aid of lanthanum staining. *Arch Dermatol* 1971; 103:387.
16. Katagiri C, Sato J, Nomura J, Denda M. Changes in environmental humidity affect the water-holding property of the stratum corneum and its free amino acid content, and the expression of filaggrin in the epidermis of hairless mice. *J Dermatol Sci* 2003; 31:29.
17. Moll R, Franke WW, Schiller DL, Geiger B, Krepler R. The catalog of human cyto-keratins: patterns of expression in normal epithelia, tumors, and cultured cells. *Cell* 1982; 31:11.
18. Lavker RM, Sun TT. Epidermal stem cell. *J Invest Dermatol* 1983; 81:121s.

19. Jones PH, Harper S, Watt FM. Stem cell patterning and fate in human epidermis. *Cell* 1995; 80:83.
20. Cotsarelis G, Sun TT, Lavker RM. Label-retaining cells reside in the bulge area of pilosebaceous unit: implications for follicular stem cells, hair cycle, and skin carcinogenesis. *Cell* 1990; 61:1329.
21. Arnold I, Watt FM. c-Myc activation in transgenic mouse epidermis results in mobilization of stem cells and differentiation of their progeny. *Curr Biol* 2001; 11:55.
22. Waikel RL, Kawachi Y, Waikel PA, Wang XJ, Roop DR. Deregulated expression of c-Myc depletes epidermal stem cells. *Nat Genet* 2001; 28:165.
23. Mehregan AH, Pinkus H. Life history of organoid nevi, special reference to nevus sebaceous of Jadassohn. *Arch Dermatol* 1965; 91:574.
24. Shapiro LJ. Steroid sulfatase deficiency and X-linked ichthyosis. In: Stanbury JB, Wyngaarden JB, Fredrickson DS, Goldstein JL, Brown MS, eds. *The Metabolic Basis of Inherited Disease*. 5th ed. New York: McGraw-Hill Inc., 1983:1027.
25. Serizawa S, Nagai T, Ito M, Sato Y. Cholesterol sulfate levels in the hair and nails of patients with recessive X-linked ichthyosis. *Clin Exp Dermatol* 1990; 15:13.
26. Ghosh D. Mutations in X-linked ichthyosis disrupt the active site structure of estrone/DHEA sulfatase. *Biochim Biophys Acta* 2004; 1739:1.
27. Hernandez-Martin A, Gonzalez-Sarmiento R, De Unamuno P. X-linked ichthyosis: an update. *Br J Dermatol* 1999; 141:617.
28. Epstein EH, Williams ML, Elias PM. The epidermal cholesterol sulfate cycle. *J Am Acad Dermatol* 1984; 10:866.
29. Zettersten E, Man M, Sato J. Recessive X-linked ichthyosis: role of cholesterol-sulfate accumulation in the barrier abnormality. *J Invest Dermatol* 1998; 111:784.
30. Ekholm IE, Brattsand M, Egelrud T. Stratum corneum tryptic enzyme in normal epidermis: a missing link in the desquamation process. *J Invest Dermatol* 2000; 114:56.
31. Lever WF, Schumburg-Lever G. *Histopathology of the Skin*. 7th ed. Philadelphia: J.B. Lippincott Co, 1990:66.

Multimodal Imaging of Skin Structures: Imagining Imaging of the Skin

Roger Wepf

Beiersdorf AG, Research Microscopy, Hamburg, Germany

Tobias Richter

Beiersdorf AG, Advanced Development Deo/AP, Hamburg, Germany

Stefan S. Biel

Beiersdorf AG, Research Microscopy, Hamburg, Germany

**Holger Schlüter, Frank Fischer, Klaus-Peter Wittern, and
Heinrich Hohenberg**

Beiersdorf AG, Advanced Development Deo/AP, Hamburg, Germany

INTRODUCTION

Qualitative evaluation of the cellular complexity and structural integrity of skin biopsies has been used by scientists for decades to gain insight into the structure and function of this complex and important organ. The well-accepted correlation between the tissue structure and function conveys important lessons for the development of experimental models for the study of normal and—in the framework of experimental scenarios—specifically altered or treated skin.

To translate the findings from basic cellular research into application, biopsy-based models need the absolute preservation of three-dimensional (3-D)-organization and the multicellular complexity of skin and at the same time to accommodate systematic experimental intervention.

Implementation of physiologically relevant models has enabled researchers to study the intrinsic cell regulation pathways and has also provided compelling evidence for the role of certain skin compartments in directing cellular function in dysfunction. The reason why the 3-D tissue comes more and more into the focus of system biology is that there is a big difference between a flat layer of cells and a complex, 3-D tissue. But until recently, many scientists have glossed over this fact.

In addition, the recent elucidation of the complete genomes of several organisms, including that of humans, has heightened our awareness that most interactions in cells and tissues take place not simply on the level of single macromolecules, but within the framework of extended higher-order structures. On top of this high structural complexity, there is a complex feedback context of organelles and cells, e.g., the differentiated layered cell groups resembling the epidermis in human skin, which functions in a highly coordinated manner. How essential this context information is becomes even clearer if we investigate the highly efficient skin barrier itself. This most efficient barrier structure in nature is formed after the cells go through apoptosis. Its formation is completely controlled by self-assembly—meaning all the essential molecules have been delivered at the live-death transition zone. In this chapter, we give a brief overview of how such complex structure and its transition can be studied with the use of state-of-the-art microscopy approaches.

The structure researcher's dream—in order to study such a complex morphological context in its native functional state—is an imaging tool that allows viewing *in vivo* from a millimeter (mm) scale and continuously zooming up to a few nanometer (nm) at different skin layers. Due to physical limitation of the excitation wavelength, such a device will never exist because it would have to cover wavelengths from subnanometer (electrons) to hundreds of nanometers (photons and ultrasound). Thus, the structure-researcher faces a methodological problem if he/she wants to study a tissue like the skin on a large resolution and information level scale.

This problem has been partially solved by establishing preparation techniques which allow investigating the same skin biopsy with different imaging techniques and hence circumvent the physical limitation by using a multimodal imaging strategy.

Here we would like to describe and show what kind of knowledge and coherent context information such a multimodal imaging approach offers to the dermatological community and in part allow the dream of a structural analyst to become true. Due to the complexity of the different imaging and preparation techniques, we only show the major route and refer to literature for more details or as a starting point for further reading.

GENERAL STRATEGY: AN “INFORMATION-TRANSFER CHAIN”

The challenge we have to face is that we deal with a biological, dynamic, and hydrated specimen that needs constant environmental parameters to avoid changes of the morphological context during manipulation, preparation, and imaging. Therefore the gap between basic histology and high-resolution electron microscopy (EM), which is the method of choice to understand and analyze the nano-organization of life-like biological material in context (1), can be only closed by a dedicated and careful preparation. Our goal is to use the information obtained by EM analysis for the investigation and description of the biological nanomolecular organization on the basis of intact cells and tissues at a defined differentiation state and still explore these structures in their natural context, e.g., in the epidermis.

This can only be reached by cryoimmobilization and cryoprocessing techniques that vitrify the cellular water (2,3), simultaneously rapidly arresting all physiological processes and preventing artifact-induced changes during specimen processing. Routing techniques to put this goal into practice are given in Figure 1, which briefly shows the “information-transfer chain” for investigation of human skin biopsies: (i) a life-like and environmental sampling of biomaterial, e.g., micro-biopsies; (ii) freezing this material in milliseconds, thus trapping dynamic cellular processes and functional hydrated states [in the case of complex material this is only possible by high-pressure freezing (HPF)]; (iii) preserving the native molecular arrangement of biomaterial by cryopreparation and cryotransfer techniques; (iv) serial sectioning of freeze-substituted and low temperature embedded material; (v) direct or tomographic imaging in the light or electron microscope at high resolution; (vi) section alignment and structure rendering for digital processing; (vii) 3-D reconstruction; and (viii) 3-D model analysis, interpretation, and simulation. For more details on critical steps in the “information-transfer chain,” refer to Figure 1.

Structure Preservation and Information

Figure 2 shows the gain on structural context after HPF of human skin biopsies (Fig. 2C) compared to standard rapid freezing techniques routinely used for light microscopy (LM) such as plunge freezing in liquid nitrogen (Fig. 2A and B) or freezing on solid carbon dioxide. Figure 2B shows a liquid nitrogen frozen biopsy cross section

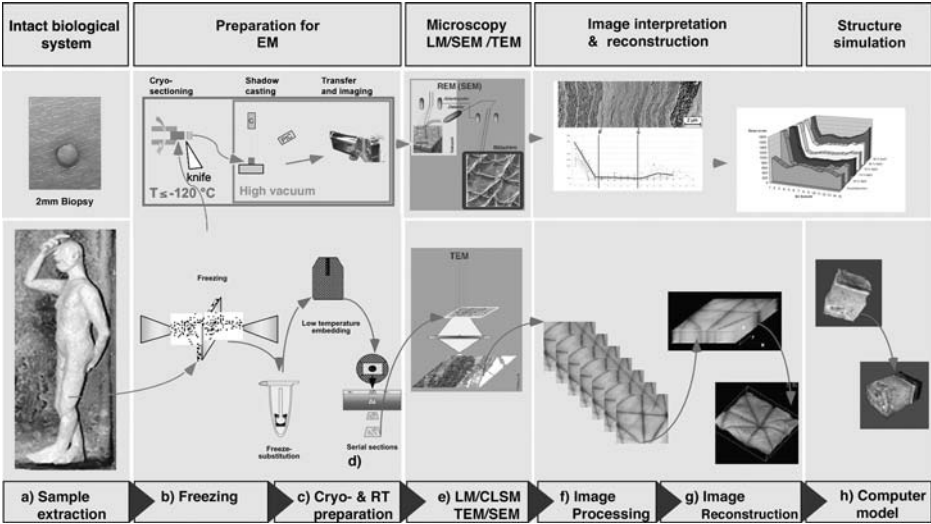


FIGURE 1 (See color insert) Flow process chart and schema of the “information-transfer-chain” for microscopical investigation of human skin biopsies: (A) life-like and environmental sampling of biomaterial, e.g., microbiopsies, (B) freezing this material in milliseconds, thus trapping dynamic cellular processes and functional hydrated states; in the case of complex material this is only possible by high pressure freezing, (C) preserving the native molecular arrangement of biomaterial by cryopreparation and cryotransfer techniques, (D) serial sectioning of freeze-substituted and low temperature embedded material, (E) direct or tomographic imaging in the light or electron microscope at high resolution, (F) section alignment and structure rendering for digital processing, (G) 3-D-reconstruction, and (H) 3-D-model analysis, interpretation, and simulation. *Abbreviations:* EM, electron microscopy; LM, light microscopy; SEM, scanning electron microscope; TEM, transmission electron microscopy.

imaged using a cryo-scanning electron microscope (SEM), after the water has been removed by a freeze-drying process. Holes are revealed in the tissue where water has segregated from the biological tissue in order to form ice crystals during the freezing process. These holes are surrounded by compressed biological matrix and therefore resemble an artificial organization of the biological tissue with huge delocalization of biomolecules. Due to the “grace of the low resolution power,” even in confocal light microscopy (CLSM) images, one is not directly aware of the structural changes induced by freezing except if one considers that this skin cryosection was stained with a lipophilic stain (nile red—Fig. 2). Nile red should only stain lipid-containing areas between the corneocytes in the stratum corneum (SC) as shown in detail in Figure 3 and should not be spread in the intercellular space nor in the cytoplasm in viable cell layers of the epidermis as extensively as shown in Figure 2A. Nevertheless, it allows a wonderful description of the corneocyte stacking in the SC.

Due to the better time resolution, better epitope preservation, and better structure preservation of biopolymers by cryofixation, images with a very high information density can be generated with more precise localization and identification of specific molecules by immunocytochemical labeling inside an intact nanomorphology for light microscopic (Fig. 2D and E) as well as for EM investigations (Figs. 2C, 3, and 4). Figure 2C shows a high-pressure frozen and freeze-fractured skin biopsy and therefore reveals the compactness and the complexity of the outermost layers of human epidermis in its frozen-hydrated native state. Note that there are neither holes nor areas without fine structural details;

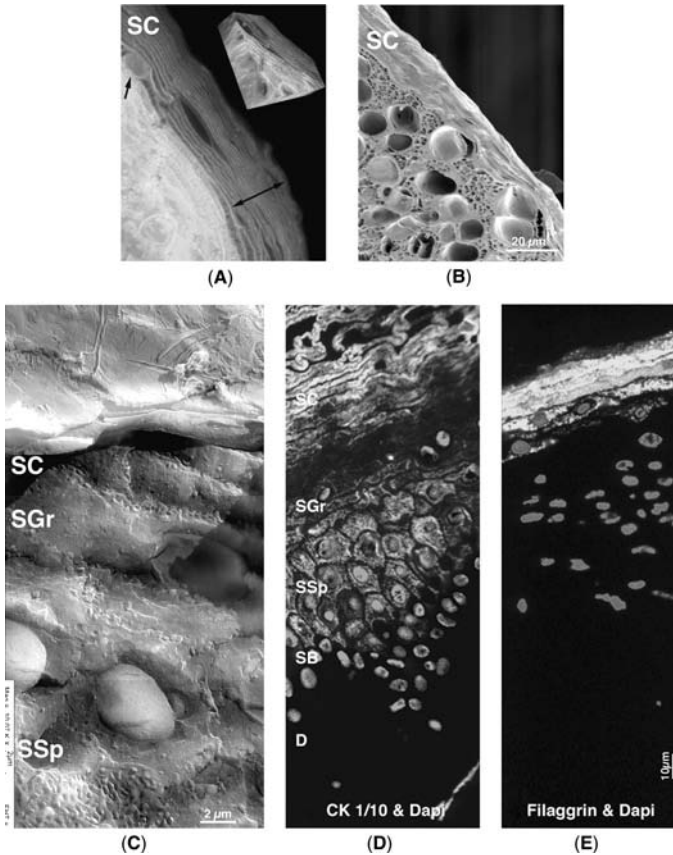


FIGURE 2 (See color insert) Structure preservation and information depth on human skin biopsies viewed fully hydrated with a cryo-SEM or after freeze-substitution and immunohistochemical staining for immunofluorescence light microscopy. Liquid nitrogen frozen biopsy cross-section imaged (A) with a CLSM after Nile red staining or (B) with a cryo-scanning electron microscope (SEM). High-pressure frozen human skin biopsies imaged (C) with a cryo-SEM at -120°C or (D–E) after freeze-substitution, thin sectioning, labelling against different antigens (cytokeratin 1/10, Filaggrin) and DNA (Dapi) and imaged with a light microscope. Due to the better time resolution, better epitope preservation, and better structure preservation of biopolymers by cryofixation, images with a very high information density can be generated with a more precise localization and identification of specific—SC, SGr, and SSp. *Abbreviations:* SEM, scanning electron microscope; SC, stratum corneum; SGr, stratum granulosum; SSp, stratum spinosum; CLSM, confocal laser scanning microscopy; DNA, deoxyribonucleic acid.

it thus reflects the native nanobioorganization of the tissue at the time-point of tissue extraction and immobilization. This cellular complexity can only be further investigated either with the help of high-resolution SEM imaging by morphological identification of macromolecular complexes or by freeze-substitution and identification of single antigens with the help of antibodies. The second approach may also be taken after the tissue had been first investigated in a cryo-SEM or immediately after HPF and is described in more detail in Figure 4 and in the chapter 11 CLSM by Biel et al. in this book.

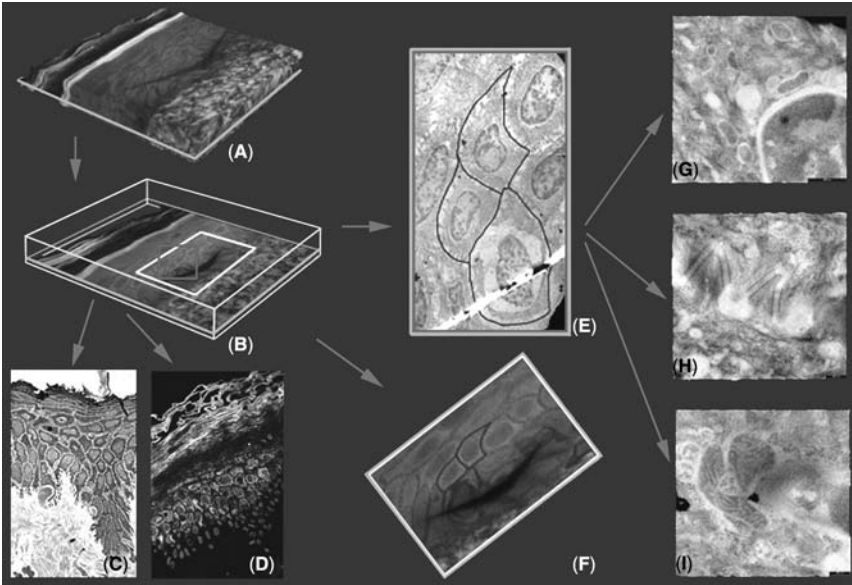


FIGURE 3 (See color insert) Schema for the imaging strategy of high pressure frozen, freeze-substituted and embedded skin biopsies: one sample for multimodal imaging. After embedding and preparation of a plain block-face through the skin sample in the polymer matrix, the specimen can first be examined by CLSM in 3D (A, B, and F) prior to further preparations. Selected sections of defined planes in the embedded biopsy can be depicted and either stained for histological or immunological investigations (C and D) or areas of interest (A and B green layer lines) can be selected and prepared for transmission electron microscopy examination (E, G–I). Such prepared samples turned out to be optimal, for histological investigations (C and D) as well as for investigating complex 3-D tissue structures with confocal light microscopy (A, B, and F) and for describing ultrastructure and constituents of the same, identical cells with electron microscopy (E, G–I).

ONE BIOPSY FOR MULTIMODAL IMAGING—THE PRINCIPLE

Detailed structural investigation of skin biopsies requires the coupling of optimal structural preparation of arrested frozen samples with preserved detailed information, gained by HPF, with image collection at the light and electron microscopic level. HPF provides the best structural preservation (4); it is, however, used routinely only for EM investigations, while for LM, chemical fixation or simplified cryofixation protocols (e.g., Fig. 2A and B) have been established. These invasive fixation protocols have the drawback of introducing unpredictable fixation artifacts. Therefore, comparative histopathological (i.e., light microscopic) and ultrastructural (i.e., electron microscopic) results are usually obtained from in-parallel prepared samples that have not been prepared identically and never by examining exactly the same features in exactly the same sample. To overcome the handicap of handling data derived from differently prepared samples and to introduce the superior structural preservation of HPF into LM investigations, we developed a new freeze-substitution protocol (5) suitable for LM and EM investigations (Fig. 4).

The well-established freeze-substitution technique was modified to allow the investigation of resin-embedded cryoimmobilized tissue by LM and/or confocal

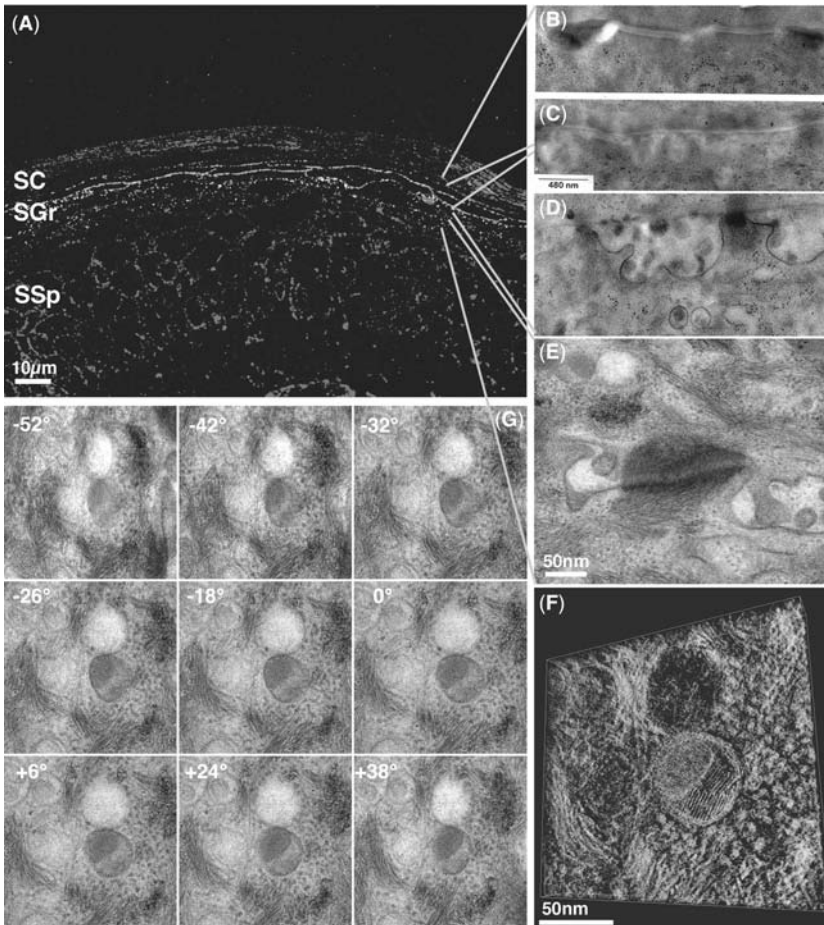


FIGURE 4 (See color insert) Lipids in human skin imaged after high pressure freezing and freeze-substitution. (A) Antibodies were used against a ceramide (red) and its glucosylated (green) precursor on semithin sections (200 nm) to show that the various lipid species can be specifically localized after cryopreparation. The antibodies were detected with a fluorescence-labelled secondary antibody and visualized with the help of a CLSM (B–E). To study the organization of the lipids at the molecular level, sections were taken for electron microscopy. (B) An area out of the SC with desmosomes and lamellar lipids in the intercellular space, (C,D) an area at the last layer of the SGr with vesicular structures in the intercellular space. (E) An area in the SGr with a lipid vesicle highlighted in green corresponding to one dotted green vesicle as revealed in (A). The same vesicle was tilted in the TEM from -60° to $+60^\circ$ and some images from the TEM tomogram are shown in the gallery (G). Under different tilting angles, it becomes obvious that the vesicles contain several (here three) entities of lipid stacks arranged within an organelle membrane. (F) A reconstruction of the lamellar body—SC, SGr, SSp. *Abbreviations:* SC, stratum corneum; SGr, stratum granulosum; SSp, stratum spinosum; CLSM, confocal laser scanning microscopy; TEM, transmission electron microscopy.

laser scanning microscopy (CLSM) prior to EM examination. This is facilitated by the addition of specific fluorescent dyes during the first freeze-substitution exchange step. Selective binding properties of various dyes to different cellular structures allow a direct histological description of the tissue at the light microscope

level (5). After embedding and preparation of a plain block-face through the skin sample in the polymer matrix, the specimen can first be examined by CLSM (Fig. 4A, B, and F) or sections may be taken (Fig. 4C and D) for histological or immunological investigations. For areas of interest, the depth in the resin block is determined with the help of the CLSM (Fig. 4A and B green layer lines), followed by removal of the tissue lying above with an ultramicrotome. Then, the tissue can be cut into a series of ultrathin sections and examined by transmission electron microscopy (TEM) for determination of the subcellular and nanostructural organization in two (Fig. 4E and G–I) and three dimension. Such prepared samples turned out to be optimal, for histological investigations (Fig. 4C and D) as well as for investigating complex 3-D tissue structures with CLSM (Fig. 4A, B, and E) and for describing ultrastructure and constituents of the same, identical cells with EM (Fig. 4F–I).

This approach allows cells throughout the whole tissue block to be depicted by CLSM (white and red box in Fig. 4B) and subsequently selectively prepared by targeted sectioning for follow-up investigation of the identical structure by TEM (Fig. 4E and F).

Finally, this approach also solves the problem of finding an area of interest for EM investigation within a complex tissue context known as the “searching for a needle in a haystack” problem. The major advantage of such an approach is that the cellular complexity stored in a single section becomes manageable by transferring these into digital info packages so called “data sections” at different resolution levels. This may be one way of overcoming the “complexity dilemma” in structure research for life science.

LIPIDS—OFTEN IGNORED IN BIOLOGY, ESSENTIAL FOR THE SKIN BARRIER

Major components for the permeability properties of the skin barrier are lipids arranged between the cornified corneocytes in the SC (6). The extensive diversity of these lipids is rarely appreciated in ultrastructural investigation due to the lack of lipid arrangement preservation by the various preparation techniques used. This is also drastically improved by the use of HPF combined with freeze-substitution (7,8). Preservation of the lipid within its natural context is only one part of the story; because the spacing of lipid lamellae is in the range of 3 to 5 nm, it becomes essential to view these lamellae in exactly the same plane of lipid orientation in TEM (parallel electron beam to lipid sheet) to reveal significant contrast of the layered structure. This can only be reached with modern EM techniques such as TEM tomography (Fig. 3) (9).

In Figure 3A, antibodies were used against a ceramide (red) and its glucosylated (green) precursor (10,11) on ultrathin (200 nm) sections of a high-pressure frozen and freeze-substituted human skin sample to show that the various lipid species can be specifically localized after cryopreparation. The antibodies were detected with a fluorescence-labelled secondary antibody and visualized with the help of a CLSM equipped with a spectrometer for a better separation of the signal, revealing the single entities of lipid vesicles as dotted green structures in the stratum granulosum (SGr), at its best resolution power. EM is essential to further study the organization of such lipid vesicles, also called lamellar bodies (12) or other lipid arrangements (Fig. 3B–F). For example, imaging the intercellular space in the transition zone between the SGr to the SC allows visualizing the extrusion of

lamellar lipids (Fig. 3C and D) into the intercellular space as well as the rearrangement of lipids in this space (Fig. 3C and B). To reveal the molecular arrangement of the lipids in a dotted green vesicle as revealed in Figure 3A, it is essential to tilt the ultrathin section (100 nm) in the TEM and view the preserved and embedded structure under various tilting angles (Fig. 3E). Under different tilting angles, it becomes obvious that the vesicles contain several (here three) entities of lipid stacks arranged within an organelle membrane. By continuously tilting the specimen in 1° steps with the help of modern TEM specimen stages, it is possible to acquire a tomographic tilt series, which, with the help of 3-D visualization software, allows to reconstruct the 3-D objects in the 100 nm ultrathin section. Such a reconstruction of the lamellar bodies in Figure 3E is shown in Figure 3F and highlights the three different “lamellar bodies” surrounded by one organelle lipid bilayer embedded in a dense cytoplasm matrix enriched with filaments, ribosomes, and multivesicular bodies.

Figures 3 and 4 clearly show the benefit of a better structure preservation and a multimodal imaging strategy helping to address questions of skin tissue organization at the macromolecular level toward a better understanding of the nano-bioorganization of biological matter.

APPLICATION: REVIEWING BARRIER MORPHOLOGY AND DYNAMICS

Stratum Corneum Morphology and Cohesion

In the “brick and mortar” model (13,14), the penetration barrier of the skin is generally associated with lateral variations of lamellar lipid arrangements within the “mortar” phase. This model reduces the skin barrier mainly to a lipid barrier in a protein environment and explains the enormously reduced water exchange rates by a prolonged penetration pathway through the different lamellar lipid phases. However, this model does not explain the strong cohesive resistance of the only 5 to 10 μm thick depth but highly sealing outermost layer of the human body against mechanical stress.

The improved structure preservation by HPF of human skin biopsies combined with cryoprocessing for TEM and cryo-SEM have revealed a much more complex structural organization of the SC and hence different views of the penetration pathway (Fig. 5). In TEM cross-section images of freeze-substituted SC from the forearm (Fig. 5A), it becomes obvious how densely packed the corneocytes are. The single corneocyte is held in position not only by corneodesmosomes (*arrows*) but also by hook-like structures (*arrowheads*) at the edge of each corneocyte (7). Some corneocytes have even stronger interdigitating structures (*asterisk*), often correlating with the mechanical use of a body skin area. The hook-like structures are not single structural entities but extended 3-D clamp-like rims (Fig. 5B–D, *arrowheads*), which are arranged along a corneocyte edge by the next underlying corneocyte in the area of overlap (Fig. 5E). Figure 5E shows overlaps in the SEM images as shadow contrast from removed corneocytes in the SEM surface representation of turned-over freeze-fractured SC with an average overlap area up to 15% to 20% (Fig. 6 corneocyte overlap area). This overlap area becomes even more pronounced in “in vivo” investigation of human epidermis by multiphoton laser scanning microscopy [multiphoton laserscanning microscope (MPLSM)—see chapter 8 by König et al. and chapter 13 by Lucassen et al.] of the SC (Fig. 6A–D).

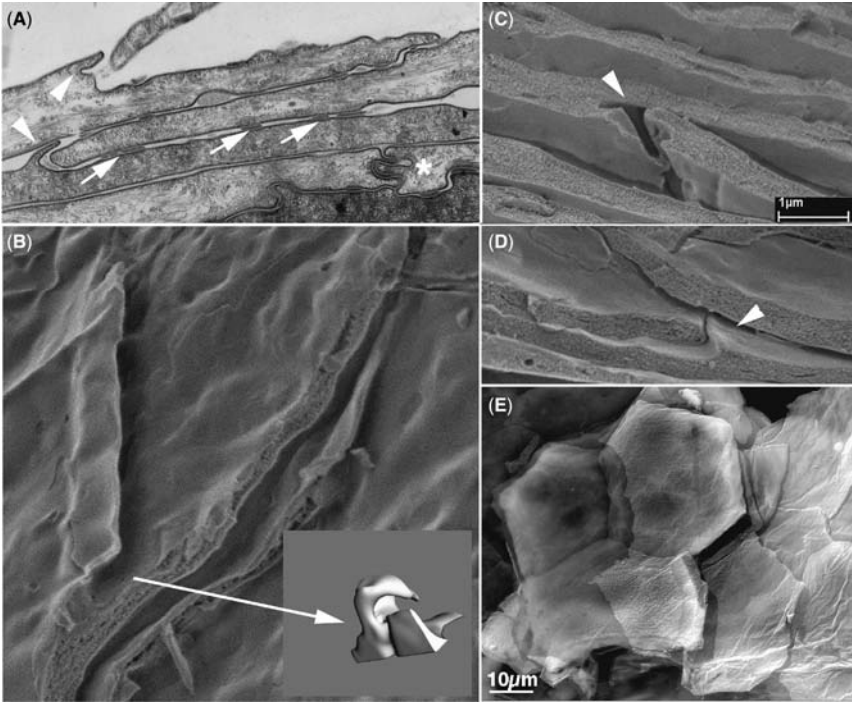


FIGURE 5 Stratum corneum morphology after high-pressure freezing and freeze-substitution and sectioning for RT TEM or freeze-fractured and imaged frozen-hydrated in a cryo-SEM. (A) TEM cross-section image of freeze-substituted SC; it becomes obvious how densely packed the corneocytes in the SC are. The single corneocyte is held in position not only by corneodesmosomes (arrows) but also by hook-like structures (arrowheads) at the edge of each corneocyte. Some corneocytes have even stronger interdigitating structures (asterisk). (B–E) Cryo-SEM images of freeze-fractured SC. The hook-like structures are extended 3D clamp-like rims (B–D arrowheads), which are arranged along a corneocyte edge by the next underlying corneocyte in the area of overlap best seen in turned-over freeze-fractured corneocytes (E). *Abbreviations:* RT TEM, room temperature scanning electron microscopy; SEM, scanning electron microscopy.

Figure 6A shows an autofluorescence image of the SC from a forearm (male 39 years old) and Figures 6B and C show 3-D representations of the outermost layer of the SC of normal and atopic skin biopsies, with a regular overlap area in normal and an irregular overlap area in atopic skin. This overlap area was calculated from CLSM SC images of normal and atopic skin biopsies (Fig. 6D) and reveals an area of overlap of $21\% \pm 3\%$ for normal and $17\% \pm 5\%$ for atopic skin, respectively.

The extra interdigitating “corneocyte-cell-extensions” are found mainly on the apical side, forming a special rim around the entire corneocyte surface as have been described by atomic force microscopy investigations (Fig. 1A and Fig. 6F, arrowheads) (15). This “hook-like” rim reinforces the lateral stability of the entire SC by the hexagonal to pentagonal geometrical organization of the corneocyte packaging in the SC for each SC layer and between the layers (Figs. 5E, 6A and F).

Desmosomes and desmosomal structures, or corneodesmosomes, were also found to be much better preserved after cryoprocessing, exposing the typical

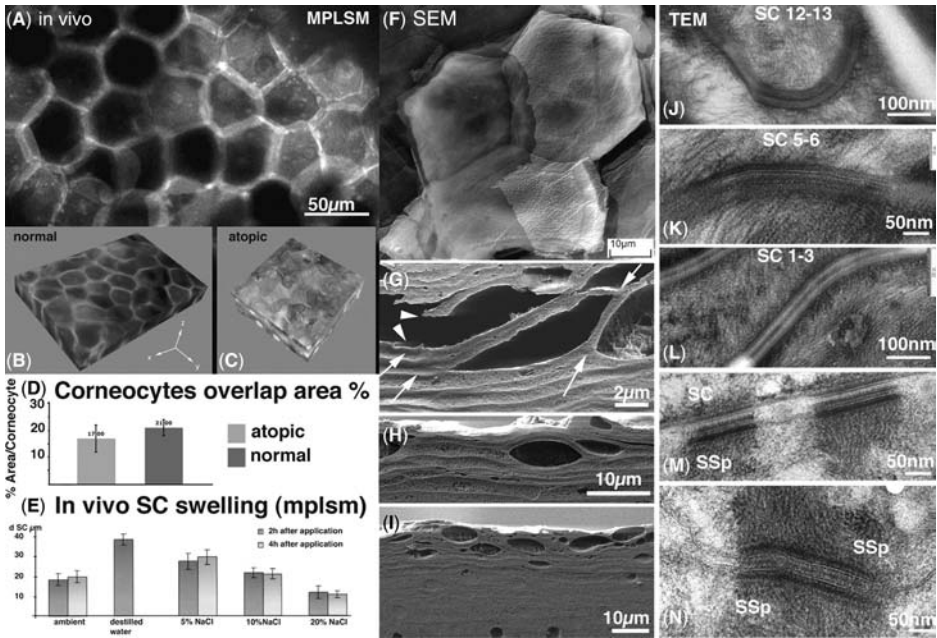


FIGURE 6 (See color insert) Multimodal imaging of the SC from in vivo to frozen-hydrated or with molecular resolution. **(A)** MPLSM autofluorescence imaging of the SC from a forearm (male, 39 years old) in vivo. **(B and C)** The outermost layer of the SC of normal and atopic skin biopsies imaged by CLSM and reconstructed to 3D models. **(D)** Calculating the overlap area of corneocytes reveals an area of overlap of $21\% \pm 3\%$ for normal and $17\% \pm 5\%$ for atopic skin, respectively. **(F–I)** Cryo-SEM images of SC stressed by hyperhydration. Upon hyperhydration of the SC with distilled water for **(H and I)** two hours or **(G)** 12 hours, the SC exposes large water inclusions between the single corneocyte layers. Corneodesmosomes between adjacent corneocytes are disrupted by the water inclusion and the hook-like structures outwear longer (arrows). These structures are disrupted if the tension increases (arrowheads). **(K–O)** TEM images of desmosomes and corneodesmosomes were also found to be much better preserved after cryoprocessing, exposing the typical “five-layer-like” morphology throughout the whole viable cell layers, as well as throughout the SC (numbers represent the SC layer starting by counting 1 as the first layer after the live-death transition). *Abbreviations:* MPLSM, multiphoton laser scanning microscope; SEM, scanning electron microscope; SC, stratum corneum; SSp, stratum spinosum; TEM, transmission electron microscopy; CLSM, confocal laser scanning microscopy.

“five-layer like” morphology throughout the whole viable cell layers as well as throughout the SC (Figs. 4E, 6K–O). Whereas the plug of the desmosomes with the interacting keratin filaments is fully established in the stratum spinosum (Fig. 6O) and the SGr (Figs. 4E and 6N), this plug shows less density and less intermediate filaments linking to the corneodesmosomes in the SC (Fig. 6K–M).

Whether either the corneodesmosomes or the hook-like rims are the major cohesion-strengthening element cannot be deduced by a static description of these structure. Therefore, the SC was stressed (e.g., by hyper-hydration), to see which of the contacts are loosened first. Upon hyperhydration of the SC with distilled water for 2 to 12 hours, the SC exposes large water inclusions between the single corneocyte layers (Fig. 6G–I). These water inclusions (15,16) disrupt the corneodesmosomes between the adjacent corneocytes and resist longest at the hook-like structures (arrows). These structures are only disrupted if the tension increases

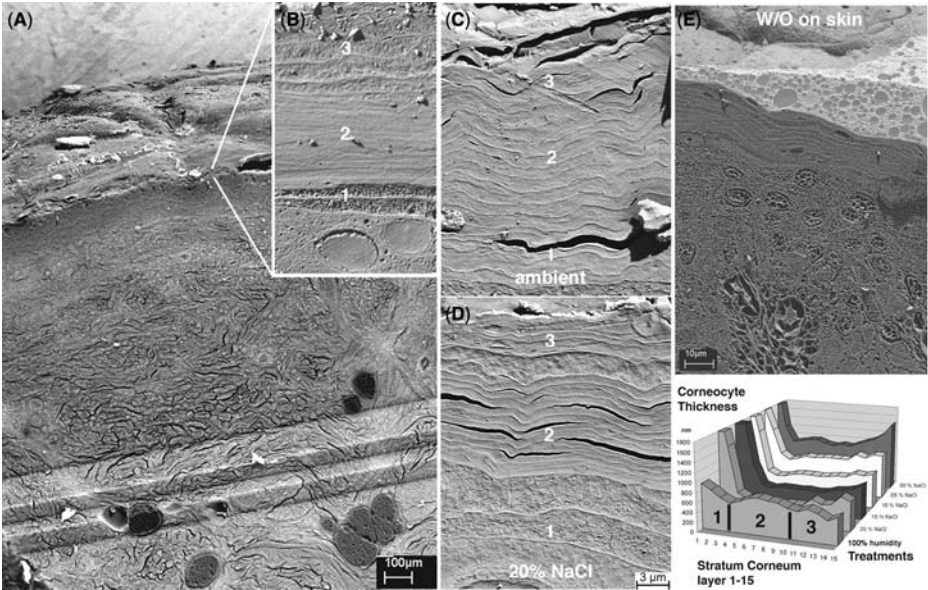


FIGURE 7 (See color insert) Hydration changes of the stratum corneum (SC) investigated in a cryo-SEM. (A) To study different frozen-hydrated stratum corneum (SC) states, large cross-section planes through the epidermis had been prepared by cryosectioning to obtain large plane block-faces of skin biopsies. (B–D) Thickness variation within the SC of various SC hydration experiments: (B) after hydration in a 100% humidity environment, (C) a fresh-taken biopsy (ambient condition), (D) after 12-hour treatment with a 20% NaCl solution, and (E) after applying a w/o emulsion on skin. These frozen-hydrated cross sections allow us to identify three different structural zones within the SC, with different cell thickness and thickness dynamics (zone 1–3 in F). (F) Following topical treatment are shown from rear to front: distilled water (0% NaCl); 5% NaCl; 10% NaCl; 15% NaCl; 20% NaCl, and humidity chamber (100% humidity). *Abbreviations:* w/o, water-in-oil; SEM, scanning electron microscopy; SC, stratum corneum.

and finally also the hook-like structures can be dismantled (arrowheads). Careful investigation of these hook-like rims show extended corneodesmosomal structures within the whole clamp (Fig. 7C), which seem to be the last docking point of a corneocyte in the process of desquamation (Fig. 5A).

Stratum Corneum Dynamics upon Hydration

Structure research by EM is sometimes hampered by the fact that biological structures are not static but typically have to adapt mechanically and biochemically to fulfill their specific functions, and hence normally show simultaneously dynamic changes and intrinsic biological variation in their morphology. Whenever measuring morphological parameters, one has to find out whether the results are representative or just extreme cases. Normally, this cannot be accomplished by the interpretation of individual experiments or images but rather requires a series of similar experiments. Therefore individual experiments and images should not be over-interpreted but requires rather a series of similar experiments to distinguish between systemic effects and intrinsic biological variations by acquiring sufficient data for statistic analysis.

To study the dynamic changes of the skin barrier upon various hydration effects and product interactions, we have established an investigation concept which allows researchers to distinguish between intrinsic variations and variations upon treatments (15), based on immobilizing the hydrated state by rapid freezing and investigating the frozen-hydrated sample in a cryo-SEM.

In Figure 7, we provide examples of different frozen-hydrated SC states prepared in such a way that large cross-section planes through the epidermis (Fig. 7A) become accessible for imaging and statistical data collection. Figure 7B–D reveals the thickness and thickness variation within the SC, cell by cell, of various SC hydration experiments. These frozen-hydrated cross sections allow the identification of three different structural zones within the SC (15). The smallest mean corneocyte thickness is found in the middle zone, which also exhibits the smallest variation in standard deviation (Zone 2). Whereas, a high variation in corneocyte thickness is found in the outermost zone (Zone 3) because it has direct contact with and is influenced by the environment. The innermost zone is characterized by relatively thick corneocytes with a loose organization of the cytoplasm (Zone 1). Upon

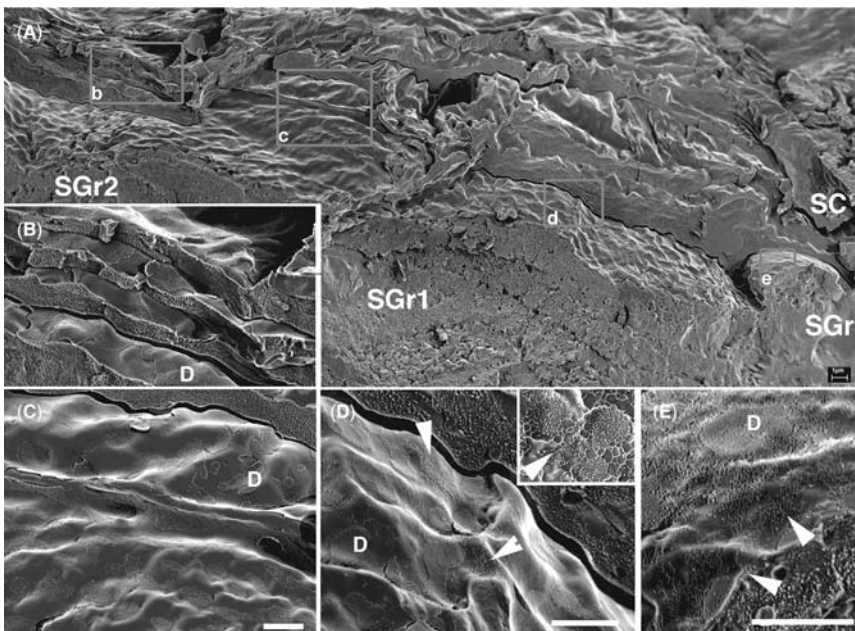


FIGURE 8 Localization of a new barrier in epidermis at the live-death transition zone (SGr-SC). (A) Cryo-SEM overview image of frozen-hydrated and freeze-fractured human epidermis. Large fracture steps throughout the different layers become accessible for further high-resolution investigations. Interestingly, (D) desmosomal/corneodesmosomal structures are found throughout the whole SC (B and C). Representative images of areas in small boxes are given in (B–E). Additional junctional structures in the membrane planes become only accessible in membrane areas belonging to the SGr (D and E). These additional structures are ribbon-like chains of transmembrane elements linked in a complex way between desmosomal structures of the keratinocyte (see also inset in D). These structures found only on the apical membrane of SGr keratinocytes (D) attach the SGr layer to the basal-most membrane of the SC. *Abbreviations:* SC, stratum corneum, SGr, stratum granulosum.

changes of the hydration level from ambient (Fig. 8C) to a treatment with water (Fig. 8B) or 20% of NaCl (Fig. 8D), it becomes obvious that the outermost and the innermost zones are affected most and the central zone remains the most compact structure over all treatments. Upon hydration, the outermost and innermost layers start to swell (Fig. 8B and Fig. 8 graphic); in contrast upon dehydration by high osmotic pressure (20% NaCl), the outermost zone shrinks and the innermost zone remains fully hydrated. Statistical data are given for various SC thickness measurements (y -axis nm) in the graphic plot of Figure 8 for following topical treatment: distilled water (0% NaCl), 5% NaCl, 10% NaCl, 15% NaCl, 20% NaCl, and humidity chamber (100% humidity). This kind of representation reflects the three-zone organization of the SC and shows the thickness variations upon the different treatments for each cell layer (x -axis 1–15) and for each zone (1–3). It becomes obvious that the central zone (Zone 2) is, in all treatments, the most compact and stable part of the skin barrier. The finding that, upon hydration, a central part of the SC remains most compact supports the idea that only the corneocytes in these layers act as a tight scaffold for the lipid organization and hence for the skin barrier formation and full functionality.

A NEW BARRIER IN EPIDERMIS AT THE LIVE-DEATH TRANSITION

During reinvestigation of the skin barrier and its behavior, it became apparent from work on knock-out mice mutants (17), skin models (18), and structural investigations (19) that additional barriers to the lipid–corneocyte barrier must exist in the upper epidermis. Multimodal imaging of the live-death transition in skin proved that real complex tight junction (TJ) structures are also present in normal adult epidermis (19) and not only in embryonic and prenatal skin (20). It could be shown that the lateral membranes of the cells of the SGr are connected by an extended subapical complex system integrating desmosomes and TJ structures identified as sites of close membrane–membrane contact and as regions of membrane-to-membrane apposition by TEM and LM (19).

The location of this additional barrier, which is still not completely understood functionally, can be best documented by cryo-SEM investigations on frozen-hydrated and freeze-fractured human epidermis (Fig. 7, a overview of the fractured SC and SGr). Interestingly, desmosomal/corneodesmosomal structures (D) are found throughout the whole SC (Fig. 7B–C). Additional junctional structures in the membrane planes become only accessible in membranes areas belonging to the SGr (Fig. 8D and E—see also the boxes in Fig. 8A on the right side). These additional structures are ribbon-like chains of transmembrane elements linked in a complex way between desmosomal structures of the keratinocyte (see also inset in Fig. 8D). These structures, found only on the apical membrane of SGr keratinocytes (Fig. 8D), attach the SGr layer to the basal-most membrane of the SC. They form an extended system integrating desmosomes with intramembranous ridge configurations that appear as strands, circles, lariats, or complex meshworks showing numerous continuities with the desmosomes (Fig. 8D–E). In some regions, this system interconnecting desmosomes with curvilinear ridge structures occupies the major part of the plasma membrane. Sometimes, these structures are also found on the contact side between neighboring keratinocytes in the outermost SGr layer. The large variety of complexity of these structures formed at the first layer of the SGr, finally reaching the highest degree of complexity at the last layer of the SGr and disappearing after the live-death transition in the

first layer of the SC, supports the idea of a specialized and dedicated additional barrier structures in adult human epidermis.

The molecular organizations and possible functional contributions of this system positioned at the border between the living portion of the epidermis and the corneal layer is still an open field of research. These additional structures form functional units, but their barrier function, in particular in relation to the formation of a stable association between the two layers or of a barrier to the paracellular flow of molecules and particles, still needs to be explored.

MULTIMODAL IMAGING OF THE BARRIERS—MORE THAN ONE BARRIER IN SKIN

By combining new dedicated preparation techniques and imaging techniques in more than a correlative and coordinated way, one can not only produce synergies on the experimental side but also improve the view and hence the imagination and models of a structure under investigation. The base or an essential prerequisite is a common structure preservation quality close to the native structure, so that data from different imaging approaches can be directly compared and merged. This leads to far more than comparing data from the same structure and deducing common features; it is the “sine qua non” for a multimodal integrating structure modelling and virtual modelling strategy for computer models based on real data.

Correlative or Multimodal Imaging Approach for Skin Research

Modern preparation and imaging techniques allowing the closure of the bridge from in vivo structure arrangement to the nanomorphology of biological tissue as has been demonstrated in this chapter, e.g., for the skin barrier structure. On one side, this fulfills the dream of having a zoom-imaging tool throughout the different resolution levels for investigation of biological samples and on the other side reduces workload in processing statistically relevant amount of samples to compensate for the biological intrinsic variations, starting from in vivo by preselection of areas of interest with a MPLSM and recording the structures prior to taking a biopsy for further investigations at higher resolution. With the help of CLSM investigation of samples prepared as described above, it is possible to visualize a broad range of characteristic structures within the selected biopsy at optimal structure preservation. 3-D information from MPLSM and CLSM can be used for the reconstruction of continuous structures within single cells as well as for the visualization of the whole tissue sample (3-D histology) and brought into register with histological and immunological images from single selected section of the embedded material. Alternatively after CLSM examination, (scanning) transmission electron microscopy [(S) TEM] of targeted ultrathin sections can be used to find answers to ultrastructural questions on structures preselected by 3-D LM. Thus, a clear-cut TEM description of these structures eliminates the risk of (over-) interpreting light microscopic staining pattern by precisely defining the stained structures, e.g., membranes. Zooming from the sample overview into ultrastructural details within a multimodal dataset is a prerequisite for a holistic structural analysis. This allows for the first time closure of the gap between histology and ultramorphology in two dimensions and even in three dimensions. Identifying macromolecular arrangements in their histological context and precisely describing exactly the same structures at high resolution becomes possible

and is the only way to cope with biological structural variance. With TEM tomography becoming a routine technique, 3-D analysis of biological details can be pushed from LM level to a level allowing the nanobiomorphology (e.g., Figure 4, lamellar lipids in vesicles) in 3-D to be described.

If the hydration state of a tissue is of interest, alternatively processing the sample in its frozen-hydrated state is the method of choice allowing, for instance, the study of the effect of emulsion on the hydration level of the SC (Fig. 7E). With the adequate cryopreparation equipment, it is possible to get statistical data together with high-resolution images of the same sample (SC of human skin).

The results of such work on frozen-hydrated skin samples proved on one side the high intrinsic variation within biological samples, but also showed a way to acquire enough data for statistically relevant data handling and to cope with the high variations of biological samples.

Learnings from a Multimodal Approach to the Skin Barrier

As discussed in Chapters 2 and 3, the aim of merging information at different information levels, is to get a holistic model and hence a better understanding of a biological system under investigation. Detailed information may be used at any time to dig further into the context-driven properties, starting from a simple model. This simple model can be a virtual model e.g., on a web page or in silico allowing, the operator the enhancement of details such as molecular information and 3-D features of important elements or the simulation of dynamic changes and biological functions. The advantage of such an approach is that at each resolution level it is based on real scientific data. Such an attempt is given in a simplified manner in Figure 9 A and B, which allows in an easy way of presenting the new information gained about our skin barrier.

The improved structure preservation and preserving the hydrated state revealed

1. a tighter packaging of corneocytes in the SC (A),
2. additional clamp-like and interdigitating structures with a defined overlap, which explain the enhanced cohesion properties of the SC (A),
3. the amount of corneodesmosomes that remain stable (400–600/corneocyte) until desquamation,
4. that corneocytes swell only in thickness and not in lateral dimension (B),
5. that single corneocytes can swell up to 100% in thickness (B)
6. that the swelling potential of corneocytes is different throughout the SC (B),
7. that the SC is organized in three zones of hydration activity (A,B),
8. that the most stable SC zone is the central zone, ideally dedicated as scaffold for a stable lipid barrier organization (B),
9. that lipid layers and corneodesmosomes are not essential for the SC cohesion,
10. an additional molecular barrier structure that exists at the live-death transition zone formed by desmosomes and TJs (A), and
11. that lamellar bodies are multilipid bodies containing vesicles organized in discs or stacks (A).

FUTURE PERSPECTIVE

Classical histology describes the organization of a tissue, e.g., position, size, and overview of its cellular units in a more or less descriptive way. It does not allow

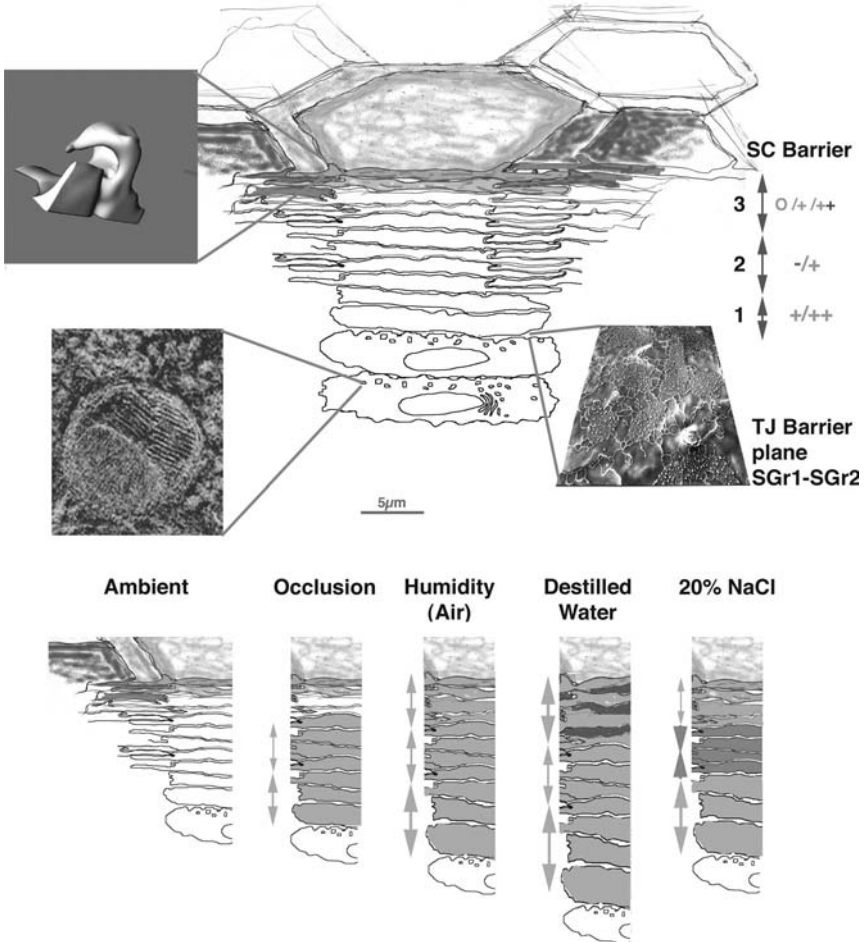


FIGURE 9 (See color insert) New findings by multimodal imaging of human skin biopsies to review the organization of the stratum corneum toward a structural based holistic model. Based on close to native prepared structure data, a simplified representative scale model is shown in Figure 9 allowing us to summarize in an easy way the new information gained about our skin barrier: (i) a tighter packaging of corneocytes in the stratum corneum is shown, (ii) additional clamp-like (see inset hook) and interdigitating structures with a defined overlap, which explain the enhanced cohesion properties of the stratum corneum are drawn, (iii) corneocytes swell only in thickness and not in lateral dimension (green—increase in thickness; red—decrease in thickness) and single corneocytes can swell up to 100% in thickness (ambient vs. distilled water), (iv) the swelling potential of corneocytes is different throughout the stratum corneum—see zone 1–3 and the different thickness of double arrows represent the swelling potential in the corresponding layer, (v) the stratum corneum is organized in three zones of hydration activity, the most stable stratum corneum zone is the central zone, ideally dedicated as scaffold for a stable lipid barrier organization, (vi) lipid layers and corneodesmosomes are not essential for the stratum corneum cohesion, (vii) an additional molecular barrier structure exists at the live-death transition zone formed by desmosomes and tight junctions (see inset “TJ barrier plane”), and (viii) lamellar bodies are multilipid bodies containing vesicles organized in discs or stacks (see inset LB).

the description of functional or dynamic interactions of different cells or cellular components acting as parts of the transcellular information network reflecting proliferation, differentiation, apoptosis, and special synthesis. The reasons for this limitation are the applied methods and imaging techniques such as optical coherence technique (OCT), LM, etc.

The big advantage of histology is the ability to get a fast and easy interpretable overview of a tissue or changes toward abnormality of the tissue (histopathology). The instrumentation and methodology used with their “grace of low resolution power”—low resolution in time and space—mirror the limited and low knowledge at the functional or molecular level. It may partially be compensated by immunohistochemical histopathology.

To make use of the advantages of histology and to integrate the ultrastructural details, it is essential to enhance the quality of histological description to the same level as ultrastructural investigations, for example, using a unique cryoimmobilization technique such as HPF as the base of any further investigation by dedicated cryopreparation and imaging techniques. The aim must always be to preserve the life-like material until imaging.

This procedure allows us to permanently control and judge the quality of preservation at the ultrastructural level and make use of the higher organization quality also at the histological level. On one side, this allows us to compare it with the old histological results from standard techniques and allows us to get histological descriptions of controlled life-like material. On the other side, it becomes possible to use the low-resolution map and continuously zoom-in to the details of interest at a macromolecular and molecular level. Therefore, it enables us to study functional units and still keep the overview in mind.

This offers the following possibilities:

1. To build up a universal model based on the cellular and subcellular component and their information network from real data
2. To learn from the structural organization about its information network; this information network is usually hidden and overlays the structural complexity and can only be addressed on the base of a native functional state
3. The prerequisite to build up a standardized database and become the base for any virtual model for skin simulations. A database is only reliable if the stored data fulfills certain common criteria (e.g., structure preservation)
4. To become a pool and organization platform to integrate biophysical, biochemical, and molecular biological findings at one “virtual side”

Since a tissue itself is a complex database of information driven by cells organizing themselves in location, size, place, time, and differentiation state and with a defined genetic background, such a system will become predictable *in silico*. The self-regulating and organizing system of cells, programmed as agents in a computer, leads to an integrating larger unit with additional functions and information (21). Such a model is far more than the sum of the single entities. If we feed data with too low resolution or modified by the investigation techniques (artifacts), simulations will produce false hypotheses or misleading models.

One of the ideas for the future is—if the basic unit of skin can be described as an unified database—simulation and modelling of skin state, virtual experimenting becomes possible. This will allow us to combine the *in vivo* data with *in silico* data and enhance our knowledge of skin for beyond the real world, leading not only to synergistic findings and allowing researchers to stimulate experiments which may

not be possible ethically in the real world, to reduce animal experimentation, and to reduce expensive experiments. In addition, a unified structure database at high quality also demystifies misleading concepts and models in our imaginations.

ACKNOWLEDGMENTS

We thank K. Dunckelmann, S. Wessel, G. Vielhaber, K. Kawaschinski, S. Pfeiffer, T. Mehm, F. Pflücker, V. Schreiner, J. P. Vietzke, and H. Wenck for support and excellent work on the skin barrier structure. Special thanks go to U. Hintze for his enthusiastic support over several years.

REFERENCES

1. McIntosh JR. Electron microscopy of cells: a new beginning for a new century. *J Cell Biol* 2001; 153(6):F25–F32.
2. Echlin P. *Low-Temperature Microscopy and Analysis*. New York and London: Plenum Press, 1992:59–99.
3. Hohenberg H, Tobler M, Müller M. High-pressure freezing of tissue obtained by fine-needle biopsy. *J Microsc* 1996; 183:133–139.
4. Hohenberg H, Mannweiler K, Müller M. High-pressure freezing of cell suspensions in cellulose capillary tubes. *J Microsc* 1994; 175: 34–43.
5. Biel SS, Kawaschinski K, Wittern KP, Hintze U, Wepf R. From tissue to (sub-) cellular fine structure: closing the gap between micro- and ultrastructural imaging. *J Microsc* 2003; 212:91–99.
6. Wertz PW. Lipids and barrier function of the skin. *Acta Derm Venereol Suppl (Stockh)* 2000; 208:7–11.
7. Pfeiffer S, Vielhaber G, Vietzke JP, Wittern KP, Hintze U, Wepf R. High-pressure freezing provides new information on human epidermis: simultaneous protein antigen and lamellar lipid structure preservation. Study on human epidermis by cryoimmobilization. *J Invest Dermatol* 2000; 114:1031–1038.
8. Norlen L, Al-Amoudi A, Dubochet J. A cryotransmission electron microscopy study of skin barrier formation. *J Invest Dermatol* 2003; 120:555–560.
9. Biel SS, Wilke K, Wepf R. From Milli- to nanometer scale—no compromise in correlative microscopy. *Imag Microsc* 2005; 7:26–29.
10. Vielhaber G, Pfeiffer S, Brade L, et al. Localization of ceramide and glucosylceramide in human epidermis by immunogold electron microscopy. *J Invest Dermatol* 2001; 117: 1126–1136.
11. Futerman AH, Hannun YA. The complex life of simple sphingolipids. *EMBO reports* 2004; 5(8):777–782.
12. Landmann L. Epidermal permeability barrier: transformation of lamellar granule-disks into intercellular sheets by a membrane-fusion process, a freeze-fracture study. *J Invest Dermatol* 1986; 87:202–209.
13. Elias PM, Friends DS. The permeability barrier in mammalian epidermis. *J Cell Biol* 1975; 20:1–19.
14. Michaelis AS, Chandrasekaran SK, Shaw JE. Drug permeation through human skin: theory and in vitro experimental measurement. *Am Inst Chem Eng J* 1975; 21:985–996.
15. Richter T, Peuckert C, Sattler M, et al. Dead but highly dynamic—the stratum corneum is divided into three hydration zones. *Skin Pharmacol Physiol* 2004; 17:246–257.
16. Warner RR, Stone KJ, Boissy YL. Hydration disrupts human stratum corneum ultrastructure. *J Invest Dermatol* 2003; 120:275–284.
17. Furuse MHM, Furuse K, Yoshida Y, et al. Claudin-based tight junctions are crucial for the mammalian epidermal barrier: a lesson from claudin-1-deficient mice. *J Cell Biol* 2002; 156:1099–1111.
18. Brandner JM, Kief S, Grund C, et al. Organization and formation of the tight junction system in human epidermis and cultured keratinocytes. *Eur J Cell Biol* 2002; 81:253–263.

19. Schluter H, Wepf R, Moll I, Franke WW. Sealing the live part of the skin: the integrated meshwork of desmosomes, tight junctions and curvilinear ridge structures in the cells of the uppermost granular layer of the human epidermis. *Eur J Cell Biol* 2004; 83: 655–665.
20. Tunggal JA, Helfrich I, Schmitz A, et al. E-cadherin is essential for in vivo epidermal barrier function by regulating tight junctions. *EMBO J* 2005 Epub; 23; 24(6):1146–1156.
21. Grabe N, Neuber K. A multicellular system biology model predicts epidermal morphology kinetics and Ca^{2+} flow. *Bioinformatics* 2005; 21(17):3541–3547.

5

Image Analysis of D-Squames, Sebutapes and of Cyanoacrylate Follicular Biopsies

Alessandra Pagnoni

Pagnoni Consulting, LLC, Yardley, Pennsylvania, U.S.A.

Iqbal Sadiq and Tracy Stoudemayer

S.K.I.N. Incorporated, Conshohocken, Pennsylvania, U.S.A.

Albert M. Kligman

Department of Dermatology, University of Pennsylvania, Philadelphia, Pennsylvania, U.S.A.

INTRODUCTION

Many skin characteristics can be sampled noninvasively and evaluated *ex vivo*. D-Squame[®], Sebutape[®], and cyanoacrylate follicular biopsies (CFBs) are just some examples of sampling techniques frequently employed in clinical testing. D-Squames are used to quantify skin dryness, Sebutapes to determine sebum output, and follicular biopsies are used to evaluate microcomedones. The simplicity and safety of the techniques have rendered these methods very popular.

Widely accepted image analysis software is not yet commercially available because individual companies often build their own systems. This chapter will describe the methods most frequently reported in the literature.

CYANOACRYLATE FOLLICULAR BIOPSY

CFB was originally introduced by Marks and Dawber in 1971 as a “skin surface biopsy” to study primarily the stratum corneum (1). Subsequently, in 1992, Holmes et al. used this technique in acne patients to visualize the horny follicular impactions also known as microcomedones (2). The cyanoacrylate method was later elaborated by Mills and Kligman, who designated the procedure as “follicular biopsy” (3). They stressed the advantages of the method to study the content of facial sebaceous follicles, namely size and distribution of microcomedones, lipids, microorganisms, Demodex mites, and trichostasis folliculorum (3).

Since then, investigators have continued to use CFB to examine (i) corneocytes (4), (ii) skin surface glyphics (5), and (iii) microcomedones (6–14). An obvious development of CFB was its use to evaluate the comedogenic potential of cosmetics and the comedolytic efficacy of acne drugs (6–9,11–15).

Sample Collection

A drop of cyanoacrylate glue (Krazy Glue[®], Borden Inc., HPPG Columbus, Ohio, U.S.A.) is applied to the skin, prepared with one Scotch Tape[®] stripping. A plastic slide is pressed over the droplet to spread it evenly into a thin film. The polymer hardens in a few minutes and the slide is then gently lifted from the surface.

The samples can be conveniently scanned under a dissecting microscope for visual evaluation or to be saved onto a computer system.

Image Analysis

Initially microcomedones were evaluated for size and density visually under a stereomicroscope. In 1992, Groh et al. described a computerized image analysis program using polarized light to illuminate and contrast horny casts extracted by follicular biopsies (9). They used this procedure to evaluate the comedogenicity of a variety of skin-care products. Although they found a linear correlation between image analysis data and stereomicroscope scores, artifacts were common. These included holes in the glue where follicular contents were not extracted and dry skin flakes or clumps of materials falsely identified as microcomedones (9). Thus, the computerized values could both overestimate and underestimate the density of microcomedones. We later described an image analysis method to quantify microcomedones (10) and the area of follicular orifices (12) more precisely. Almost at the same time, Pierard-Franchimont and coworkers developed a method to size horny casts by analyzing follicular biopsies after these were stained with a toluidine blue basic fuchsin solution (16).

It should be mentioned that, in general, follicular biopsies are difficult to evaluate by image analysis. In fact, two types of errors usually occur: (i) any three-dimensional material such as hairs and scales may be erroneously identified as horny casts by the automatic analyzer and (ii) each cone-shaped microcomedone sits on the slide with a different spatial orientation, changing the dimensions seen by the analyzer. It is reported that the staining of samples has greatly improved the discrimination of casts against the stratum corneum background (16); however, from our experience, artifacts may still occur in samples with a lot of scales.

We improved the accuracy of this type of image analysis by *manually selecting* microcomedones and follicular orifices. The slides were viewed under a stereomicroscope at 10X to 15X to count and size horny casts, and under a light microscope with a 4X objective to measure follicular orifices. We transferred images to an image analyzer (analySIS[®], Soft-Imaging Software GmbH, Munster, Germany) through a black-and-white video camera (CCD-72, DAGE-MTI[®], Michigan City, Indiana, U.S.A.). A "sharpen" filter was used for edge enhancement (sharper image). The images were then scanned over defined areas allowing microcomedones and orifices to be separated into groups according to size. We designated microcomedones having a width of between 0.016 and 0.042 mm² as small. Microcomedones exceeding 0.042 mm² were designated as large (Fig. 1). Follicular orifices were classified into three groups according to area: (i) 0.003 to 0.016 mm², (ii) 0.016 to 0.042 mm², and (iii) greater than 0.042 mm².

Applications

Follicular Map of the Skin

We have used image analysis to study the density of vellus follicles and microcomedones on various sites of the face (forehead, nose, cheek, and chin) of healthy Caucasian women (10). The literature gives estimates of 400 to 900/cm² follicles

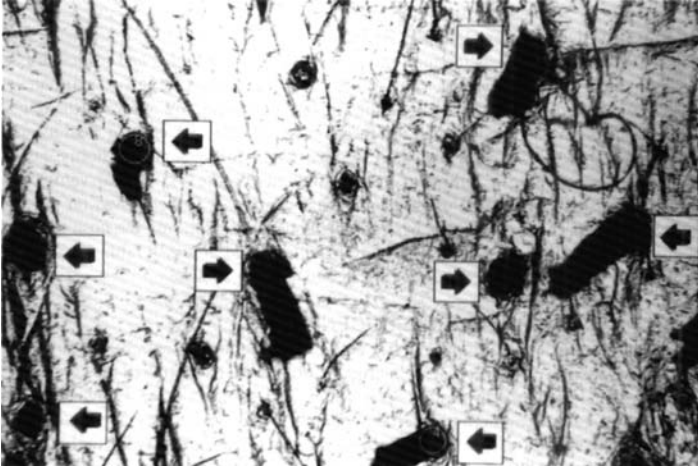


FIGURE 1 Image analysis of microcomedones. Circles are made to match the base of microcomedones (arrow). The base size is an indication of the size of the microcomedone.

on histological studies of facial biopsies. We found that the density of both the follicles and the horny casts decreased laterally on the face (Table 1).

Comedolysis and Comedogenesis

The follicular biopsy is often used to investigate the potential of substances to induce a reduction or an increase in microcomedones (11–15). We have applied this method to study the comedolytic effect of topical tretinoin in a short-term test (12). Twelve Caucasian women with numerous microcomedones applied 0.01% tretinoin cream (Retin-A[®], Ortho Pharmaceutical Corporation, Raritan, New Jersey, U.S.A.) to the forehead twice daily for three weeks. Follicular biopsies were taken at baseline and end of applications from symmetrical sites. Image analysis was used to quantify (i) number and size of casts and (ii) number and areas of follicular orifices. After three weeks, the density of microcomedones decreased by 37% ($p = 0.067$), from a mean of 18.4 to 11.6/cm². Also, the number of orifices larger than 0.003 mm² decreased by 38% ($p < 0.01$) from a mean of 218 to 134/cm² after

TABLE 1 Follicular Distribution on the Face^a (number/cm²)

Site	Number of follicles	Microcomedones ^b
Mid-forehead	966	12
Lateral forehead	455	3
Naso-labial cheek	838	20
Mid-cheek	643	10
Lateral cheek	610	4
Preauricular area	466	2
Chin	688	12
Tip nose	1112	24
Ala-nose	1220	23

^aAverage of 12 subjects.

^bMicrocomedones larger than 0.016 mm².

treatment, indicating a reduction in the size of orifices. The good correlation between these two values substantiates the idea that microcomedones distend the orifices and their removal should be reflected in diminished size of the orifices. This strong comedolytic effect is in accordance with other tretinoin studies on the face using CFB (8,11,13).

Pierard-Franchimont et al., in a six-week split-face treatment, used image analysis to calculate the sum of the sizes of the 30 largest microcomedones for each patient and product (0.1% adapalene vs. 0.05% tretinoin). They took follicular biopsies every two weeks from symmetrical sites of the forehead. At the end of the study, they found a 50% reduction in comedo volume in 48% of the adapalene samples and in 84% of the tretinoin samples (13).

SEBUTAPE

The measurement of sebum production is important in order to understand the pathophysiology of disorders related to seborrhea and their response to therapy. Through the years, investigators have used various techniques to collect and measure follicular sebum output, such as cigarette paper (17–19), bentonite clay (20), optical densitometry (21–23), and Sebutape (24). Currently, two types of techniques are popular for estimating sebum output: (i) optical densitometry by Lipometre[®] (L'Oreal, France) (23) or by Sebumeter[®] (Courage and Khazaka electronic, Germany) (25), which gives an immediate reading in $\mu\text{g}/\text{cm}^2$; and (ii) adhesive tapes such as Sebutape (CuDerm Corporation, Dallas, Texas, U.S.A.), which are left on the skin for up to a few hours.

Earlier investigations on sebum output have been instrumental in understanding the dynamic of sebum output. For example, during sequential collections of sebum using cigarette papers, much higher amounts of lipids were observed at the beginning than in later samples. This suggested that the initial high level was due to a follicular reservoir while the “true excretory rate” was reflected in the later samples (17). This important finding has since been confirmed by others (19,20,26). Using Sebutape, we also found that five serial one-hour collections yielded a steady output in oily subjects after the first one-hour sample, while in subjects with nonoily skin, the output did not change significantly.

Sample Collection

Sebutape is a rectangular white adhesive tape containing microcavities to trap the sebum. Its surface is hydrophobic. As sebum issues from the follicles, it is trapped into the cavities and the white background turns transparent showing “sebum spots.”

To prepare the site, the skin is first cleansed so that most of the sebum is removed: a mild detergent can be used, followed by water and then patted dry. Sebutapes are fixed to the skin for approximately one hour, time sufficient to differentiate persons with oily and nonoily skin. In fact, collection on the forehead of less than one hour may not reveal droplets in nonoily people, while with longer times the spots fuse in very oily subjects (24).

Sebutapes are placed on a black card where the transparent sebum spots are visualized as black. The Sebutape can also be placed on a transparent plastic sheet or a glass slide. Additionally, lipids can be extracted and analyzed by thin layer chromatography (TLC) (24,27).

The condition of storage of the samples is critical for reliable image analysis (28). We found that placing the tape on a plastic transparent sheet over the black card optimizes the contrast between the white background of the tape and the dark sebum spots. Also, Sebutapes should be preferably analyzed within a short time after removal (e.g., 30 minutes). If not, larger sebum spots diffuse outward, increasing considerably in size and often fusing together. This reduces the density of spots and increases the area covered by sebum. These changes can occur in one day at room temperature or in the first week in the freezer (28).

Image Analysis

On the black storage card, the sebum spots appear black against the white tape. To achieve a uniform lighting, we illuminate the sample from two opposite sides inside a white box. The image is captured through a black-and-white video camera (CCD-72, DAGE-MTI, Michigan city, Indiana, U.S.A.) connected to a stereomicroscope (OPMI-1FC[®], ZEISS, Germany). The image is then examined by an image analyzer (analySIS, Soft-Imaging Software GmbH, Munster, Germany). An edge detection filter is applied to sharpen the picture. Sebum spots are subsequently detected using a gray levels threshold. If illumination is uneven, a shading correction can be performed that will automatically redistribute the gray levels. The most important values in the analysis are the percentage of area covered by sebum spots and the density of spots. The percentage of area correlates directly with the sebum output and is the most meaningful parameter. Density reflects the number of active sebaceous follicles (Fig. 2) (29). However, due to a frequent fusion of adjacent spots in very oily persons, the number of spots/cm² (active follicles) is actually underestimated. A third value that could be useful is the size of individual spots, but its interpretation could be difficult.

Applications

Activity of Sebaceous Follicles

It has been shown that sebum output decreases from the mid-to-lateral regions of the face (Table 2) (10). This should be considered when sampling facial sebum and it is in accordance with the perception of oiliness in the so-called "T-zone."

Sebum output has also been found to vary from follicle to follicle on the forehead (30), with some follicles being quiescent (29). The high sebum output of acne prone subjects has been attributed to the presence of a few highly active sebaceous follicles. On the other hand, the seborrhea of acne-free individuals mainly reflects a greater number of moderately active follicles (31). A monthly rhythm has also been described (32), and a higher sebum output has been found in summer (33). Changes also occur during the menstrual cycle, with highest output in the week prior to the menstruation in oily women (34).

Sebosuppression

Sebutape has been used to evaluate the capacity of a drug to reduce sebum output. High and mid-potency corticosteroids (clobetasol propionate and budesonide, respectively) have been shown to significantly decrease sebum output after four weeks of daily applications to the forehead (35). Pierard and Pierard-Franchimont, also, evaluated sebum suppression of an erythromycin-zinc formulation using

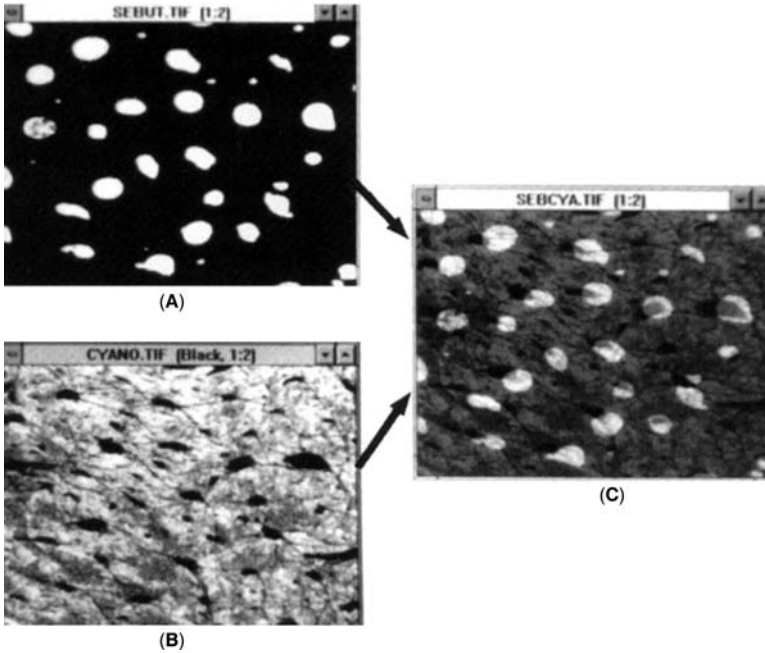


FIGURE 2 Relationship between sebum spots and sebaceous follicles. The number of spots on the Sebutape is theoretically an indication of the number of active sebaceous follicles. From the overlap of a Sebutape and a cyanoacrylate follicular biopsy (C), we can see how each round sebum spot on the Sebutape (A), comes from one sebaceous follicle detected in the cyanoacrylate follicular biopsy (B).

four sequential one-hour Sebutape collections. Decreased output was detected mainly from the most active sebaceous follicles (36).

D-SQUAMES

Various pathological and physiological conditions can increase skin dryness and scaliness (or desquamation). Excessive scaliness can also be induced experimentally

TABLE 2 Regional Sebum Output

Site	Percentage of area covered by sebum
Mid-forehead	9.94
Lateral forehead	5.35
Nasolabial cheek	8.75
Mid-cheek	3.8
Lateral cheek	2.47
Preauricular area	2.41
Chin	8.87
Nose	10.15

(e.g., irritating chemicals or ultraviolet light exposure). When partially loose corneocytes aggregate together in scales, these become whitish and visible to the naked eye. The degree of scaliness can be quantified *ex vivo* by means of commercially available sticky discs. D-Squames (CuDerm Corporation, Dallas, Texas, U.S.A.) are standardized, clear, plastic discs of 22 or 14 mm in diameter, coated on one side with a medical grade adhesive (synthetic polyacrylate ester). The size of the disc used will depend on the site or lesion to be tested, but for wider areas, the larger size should be preferred. The adhesive is strong enough to remove loose corneocytes and scales from the superficial stratum corneum.

Sample Collection

Any skin site can be tested, including the face, as long as the area is relatively flat to allow homogeneous sampling. The skin should be free from moisturizers and other topicals to allow the adhesive disc to adhere to the scales. A defatting procedure employing 1 mL solution of ether : acetone (1:1) in a glass cup for one minute and removed by absorption on a cotton pad has been reported in the literature (37,38). Because pressure changes the amount of scales removed, the D-Squame should be applied under standard pressure and time (e.g., for 30 seconds, using a calibrated plunger). The disc is then gently removed with forceps and placed on a standard black card for image analysis.

Image Analysis

The use of image analysis to quantify D-Squames was first described by Schatz et al. (38). The calculation of the desquamation index (DI) was based on categorizing the whiteness of scales (gray levels of individual pixels) into five classes. The DI, ranging from 0 to 100, integrated the percentage of area covered by scales and the percentage of pixels in each whiteness (thickness) group. We improved this method by analyzing the samples using a continuum of 255 gray levels and by calibrating the lighting condition on the black-and-white background of the storage card (37). More recently, Wilhelm et al. used the DI and/or scaliness index (SI) algorithms in a public domain image analysis software for routine analysis of large number of samples (39).

The system we currently use is the one originally published by our group (37). The samples are placed inside a white box and are evenly illuminated by fiber-optic cables at two opposite sides. The D-Squame picture is captured through a black-and-white video camera (DAGE-MTI CCD-72, Michigan city, Indiana, U.S.A.) connected to a stereomicroscope (OPMI-1FC, ZEISS, Germany). The camera is connected to an IP-8/AT Matrox frame grabber board. We analyze the images using the analySIS program (Soft-Imaging Software GmbH, Munster, Germany). The illumination is standardized by first conducting a pixel-wise calibration of the black and of the white portions of the storage card. The analysis produces an SI based on the pixel distribution of gray levels from 0 (black) to 255 (white). SI is calculated on the assumption that the whiteness of the scales is proportional to their thickness. SI can range from 0 to 1 (dryer) and it is calculated as follows:

$$SI = \frac{1}{w \times h} \sum_{x=1, y=1}^{x=w, y=h} \frac{D(x, y) - B(x, y) - [W(x, y) - B(x, y)] \times T\%}{W(x, y) - B(x, y) - [W(x, y) - B(x, y)] \times T\%}$$

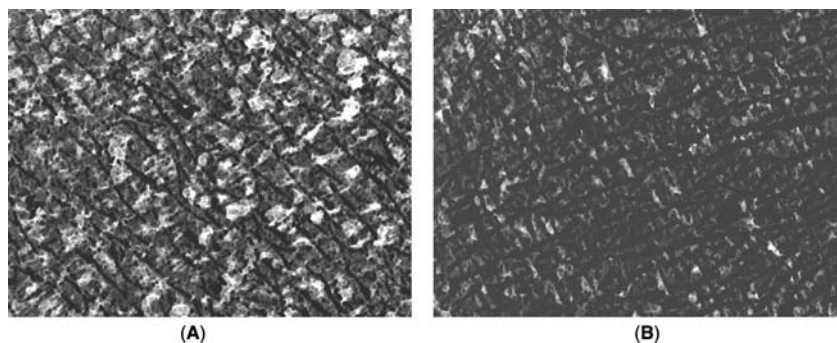


FIGURE 3 A two-week treatment regimen on dry legs shows reduction of scales. (A) Before treatment, the analysis showed scaliness index (SI) = 0.355, percentage of area = 94.5; (B) after treatment, the analysis was SI = 0.238, percentage of area = 83.7.

where D is the D-Squame image, W the white calibration image, B the black calibration image, $T\%$ the trigger level, w the image width, h the image height.

Applications

Efficacy of Moisturizers

D-Squame is typically used to study the efficacy of moisturizers. Samples are collected before treatment and at definite time points during and after treatment. A regression design is also used to determine the duration of efficacy after treatment is stopped.

An example of moisturization efficacy is shown in Figure 3. Dry legs were treated with a moisturizer for two weeks. D-Squame sampling was made at baseline (pretreatment) and after treatment. The results showed a dramatic decrease in desquamation. It is noteworthy that, with moisturization, there is not only a decrease in scale thickness (less white), but there is also a decrease in skin surface (area) covered by scales.

In another study (Table 3), 10 subjects with dry legs were treated with a moisturizer for four weeks. D-Squame sampling was made at baseline and at one, two, and seven days after treatment (regression). Significant decrease in desquamation was observed at all time points posttreatment, and the regression study showed good moisturization till seven days after the end of treatment.

TABLE 3 Moisturization Efficacy (Average Scaliness Index of Sites Using the Treatment)

	Scaliness index (SD)	Differences from baseline
Baseline	0.326 (0.10)	—
Post-treatment (4 wk)	0.124 (0.04)	$p = 0.0001$
Regression day 2	0.150 (0.04)	$p = 0.0001$
Regression day 7	0.173 (0.06)	$p = 0.0005$

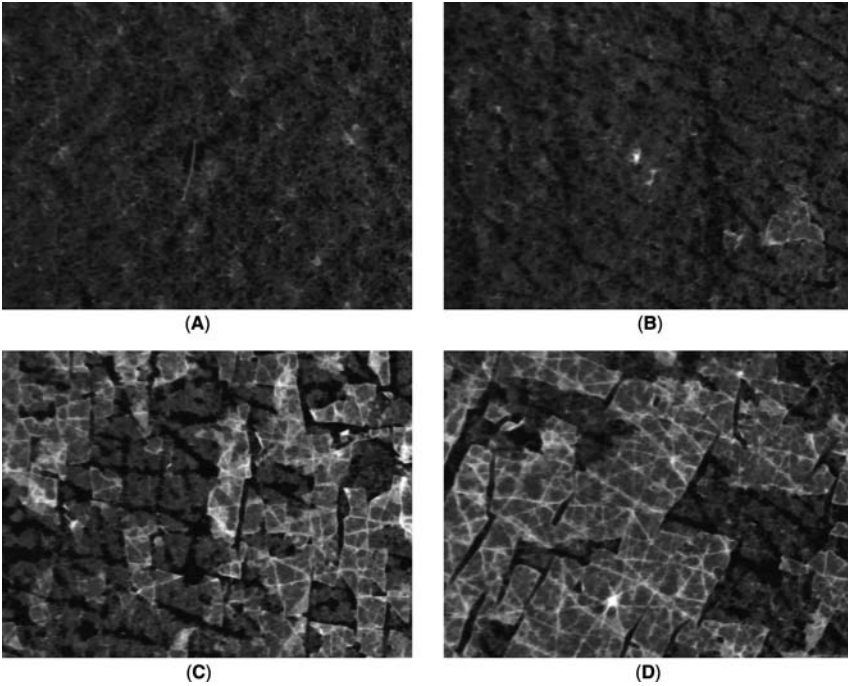


FIGURE 4 Fourteen days after SLS treatment (24-hour patches), desquamation increased proportionally to the concentration of sodium lauryl sulfate (SLS). (A) Normal skin; (B) SLS 0.125%; (C) SLS 0.25%; and (D) SLS 0.5%.

Experimental Irritation

Skin irritation, either by irritants or by physical stimuli (e.g., ultraviolet), may produce increased skin dryness detectable by D-Squame. Sodium lauryl sulfate (SLS), for example, induces a dose-dependent desquamation after the inflammatory phase.

SLS applied at different concentrations (0.125%, 0.25%, and 0.5%) for 24 hours under Hilltop chambers showed a dose-dependent increase in scaliness two weeks after the SLS insult (Fig. 4). This suggests that the scaliness is likely proportional to the intensity of prior irritation.

REFERENCES

1. Marks R, Dawber RPR. Skin surface biopsy: an improved technique for the examination of the horny layer. *Br J Derm* 1971; 84:117.
2. Holmes RL, Williams M, Cunliffe WJ. Pilo-sebaceous duct obstruction and acne. *Br J Derm* 1972; 87:327.
3. Mills OH, Kligman AM. The follicular biopsy. *Dermatologica* 1983; 167:57.
4. King CS, Barton SP, Nicholls S, et al. The change in properties of the stratum corneum as a function of depth. *Br J Derm* 1979; 100:165.
5. Lavker RM, Kwong F, Kligman AM. Changes in skin surface patterns with age. *J Gerontol* 1980; 35(3):348.

6. Mills OH, Kligman AM. A human model for assessing comedogenic substances. *Arch Derm* 1982; 118:903.
7. Mills OH, Kligman AM. A human model for assaying comedolytic substances. *Br J Derm* 1982; 107:543.
8. Lavker RM, Leyden JJ, Thorne EG. An ultrastructural study of the effects of topical tretinoin on microcomedones. *Clin Ther* 1992; 14(6):773.
9. Groh DG, Mills OH, Kligman AM. Quantitative assessment of cyanoacrylate follicular biopsies by image analysis. *J Soc Cosmet Chem* 1992; 43:101.
10. Pagnoni A, Kligman AM, el Gammal S, et al. Determination of density of follicles on various regions of the face by cyanoacrylate biopsy: correlation with sebum output. *Br J Derm* 1994; 131:862.
11. Mills OH, Kligman AM. Assay of comedolytic activity in acne patients. *Acta Dermatovenere* 1983; 63:68.
12. Pagnoni A, Stoudemayer T, Kligman AM. A new assay for comedolytic activity in humans. *J Invest Derm* 1994; 102:608.
13. Pierard-Franchimont C, Henry F, Fraiture AL, et al. Split-face clinical and bio-instrumental comparison of 0.1% adapalene and 0.05% tretinoin in facial acne. *Dermatol* 1999; 198:218.
14. Letawe C, Boone M, Pierard GE. Digital image analysis of the effect of topically applied linoleic acid on acne microcomedones. *Clin Exp Dermatol* 1998; 23:56.
15. Knaggs H, Santanastasio H, Bowman J, et al. A multi-sample design for assessing the comedolytic activity of topical products. *Int J Cosmet Sci* 2004; 26:239.
16. Pierard GE, Pierard-Franchimont C, Goffin V. Digital image analysis of microcomedones. *Dermatology* 1995; 190:99.
17. Miescher G, Schonberg A. Untersuchungen Uber die funktion der talgdrusen. *Bull Schweiz Akad Medizin Wissensch* 1944; 1:101.
18. Strauss JS, Pochi PE. The quantitative gravimetric determination of sebum production. *J Invest Derm* 1961; 36:293.
19. Kligman AM, Shelley WB. An investigation of the biology of the human sebaceous gland. *J Invest Derm* 1958; 30:94.
20. Downing DT, Stranieri AM, Strauss JS. The effect of accumulated lipids on measurements of sebum secretion in human skin. *J Invest Derm* 1982; 79:226.
21. Schaefer H, Kuhn-Bussius M. Methodik zur quantitativen Bestimmung der Menschlichen Talgsekretion. *Archiv Klinische Experim Derm* 1970; 238:429.
22. Agache P, Blanc V, Barrand C, et al. Sebum levels during the first year of life. *Br J Derm* 1980; 103:643.
23. Saint Leger D, Berreti C, Duboz C, et al. The lipometre: an easy tool for rapid quantitation of skin surface lipids (SSL) in man. *Arch Derm Res* 1979; 265:79.
24. Kligman AM, Miller DL, McGinley KJ. Sebutape: a device for visualizing and measuring human sebaceous secretion. *J Soc Cosmet Chem* 1986; 37:369.
25. Pierard-Franchimont C, Martalo O, Richard A, et al. Sebum rheology evaluated by two methods in vivo. Split-face study of the effect of a cosmetic formulation. *Eur J Dermatol* 1999; 9:455.
26. Cunliffe WJ, Shuster S. The rate of sebum excretion in man. *Br J Derm* 1969; 81:697.
27. Nordstrom KM, Schmus HG, McGinley KJ, et al. Measurement of sebum output using a lipid absorbent tape. *J Invest Derm* 1986; 87:260.
28. Pagnoni A, Kligman AM, el Gammal S, et al. An improved procedure for quantitative analysis of sebum production using Sebutape[®]. *J Soc Cosmet Chem* 1994; 45:221.
29. Pierard GE. Rate and topography of follicular sebum excretion. *Dermatologica* 1987; 175:280.
30. Pierard GE. Follicule to follicule heterogeneity of sebum excretion. *Dermatologica* 1986; 173:61.
31. Pierard GE, Pierard-Franchimont C, Le T. Seborrhoea in acne-prone and acne-free patients. *Dermatologica* 1987; 175:5.
32. Pierard GE. Is there a rhythm in the secretion rate of sebaceous follicles? *J Appl Cosmetol* 1987; 5:37.

33. Pierard-Franchimont C, Pierard GE, Kligman AM. Seasonal modulation of sebum excretion. *Dermatologica* 1990; 181:21.
34. Pierard-Franchimont C, Pierard GE, Kligman AM. Rhythm of sebum excretion during the menstrual cycle. *Dermatologica* 1990; 182:211.
35. Leveque JL, Pierard-Franchimont C, de Rigal J, et al. Effect of topical corticosteroids on human sebum production assessed by two different methods. *Arch Dermatol Res* 1991; 283:372.
36. Pierard GE, Pierard-Franchimont C. Effect of a topical erythromycin-zinc formulation on sebum delivery. Evaluation by combined photometric-multi-step samplings with Sebutape[®]. *Clin Experim Derm* 1993; 18:410.
37. el Gammal C, Pagnoni A, Kligman AM, et al. A model to assess the efficacy of moisturizers—the quantification of soap-induced xerosis by image analysis of adhesive-coated discs (D-Squames). *Clin Exp Dermatol* 1996; 21:338.
38. Schatz H, Kligman AM, Manning S, et al. Quantification of dry (xerotic) skin by image analysis of scales removed by adhesive discs (D-Squames[®]). *J Soc Cosmet Chem* 1993; 44:53.
39. Wilhelm KP, Kaspar K, Schumann F, et al. Development and validation of a semiautomatic image analysis system for measuring skin desquamation with D-Squames[®]. *Skin Res Technol* 2002; 8:98.

Michael Vogt and Helmut Ermert

Institute of High Frequency Engineering, Ruhr-University Bochum, Bochum, Germany

INTRODUCTION

Optical inspection of skin is the most common method used in dermatology to identify suspicious skin lesions and to evaluate the success of therapies and evolution of skin diseases. In conventional dermatoscopy and video dermatoscopy, investigations are supported by technical instruments. However, the information that is obtained under these conditions, is limited to the skin surface and uppermost skin layers, but it still is the “gold standard” for skin tumor classification. Medical imaging systems make use of different kinds of rays, waves, and physical phenomena (light, X rays, electromagnetic waves, nuclear magnetic resonance, ultrasound, etc.) to noninvasively obtain information about tissue for diagnostic. With these modalities, organs and tissue can be examined which are otherwise invisible. There is also the conceptual benefit that different kind of information about tissue is obtained. Unlike in many other medical disciplines, the development and utilization of noninvasive imaging techniques has only slowly advanced in dermatology. A major reason for this is that the skin is directly accessible to the physician and that the relatively small skin structures require microscopic, high-resolution imaging techniques that are challenging to be designed and implemented. Sonography, i.e., ultrasound imaging, has many potential benefits compared to modalities such as optical coherence tomography, high-resolution magnetic resonance imaging and confocal laser scanning microscopy. It is easy to apply and inexpensive, and dermatologists have already gained a lot of experience in the field of skin sonography.

In this contribution, the technical concepts of ultrasound skin imaging systems are discussed. It will be demonstrated that the utilization of high frequency and broadband ultrasound enables high resolution and microscopic imaging. System parameters and designs of high-frequency ultrasound (HFUS) scanners are analyzed and presented. The echo signal processing concepts, which are utilized to generate morphological ultrasound images, are discussed in order to improve the understanding of the characteristics and content of ultrasound skin images. Phantom images and in vivo skin images are presented to show the potential and limitations of high-resolution ultrasound skin imaging.

ULTRASOUND BIOMICROSCOPY OF SKIN

Sonography is a *tomographic* imaging technique, i.e., one or several cross-sectional images of tissue are acquired utilizing ultrasound waves. Individual two-dimensional (2D) images depict tissue structures along the body’s surface (lateral coordinate) and over depth (axial coordinate). Ultrasound imaging is a noninvasive modality and gives access to information that is normally obtained by

histological cuts of excised tissue. For this reason and like in other medical fields, sonography is suited to support the dermatologists in making diagnoses of skin diseases and lesions.

In the beginning, ultrasound examinations of skin were performed by acquiring echo signals along one single sound beam. The resulting "A-scans" (A: amplitude) delivered only information about skin structures along a one-dimensional (1D) spatial coordinate. Later, a significant improvement was achieved by mechanically scanning the ultrasound transducer and reconstructing 2D "B-mode images" (B: brightness). Nowadays, 20 MHz range ultrasound B-mode scanners are routinely used in dermatological diagnosis. Ultrasound images enable the measurement of tumor and inflammatory processes thickness, and many studies on normal and pathological skin have been conducted (1–12). The aim of technical developments in the past was the improvement of spatial resolution and imaging capabilities of HFUS imaging systems by utilizing higher ultrasound frequencies (13–25).

The goal of the work that is presented in this contribution was the application of HFUS in the 20 and 100 MHz range for high resolution in vivo skin imaging in the clinical environment. The challenge is to account for the attenuation of ultrasound waves in tissue, which becomes more prominent with increasing frequency, and to find a compromise between the opposite demands for good spatial resolution and high penetration depth (26–28). A new HFUS skin imaging system is presented below, that was designed based on experiences gained with a prototype system built at the Institute of High Frequency Engineering of the Ruhr-University Bochum, Germany (22–32).

Ultrasound Imaging Concept

Medical ultrasound scanners usually perform pulse-echo measurements with ultrasound waves in the frequency range above 1 MHz to image tissue and organs. The imaging principle is shown in Figure 1. An ultrasound transducer is excited with a *pulsed* electrical signal that is converted into ultrasound waves, i.e., the transducer is an electro-acoustic converter. Because ultrasound waves in the relevant frequency range are strongly attenuated in air, a hydrous acoustic sound propagation medium has to be inserted between the transducer and the tissue. Ultrasound waves are coupled into the tissue and propagate in axial direction z . Waves, which are scattered or reflected at acoustic inhomogeneities, partially propagate back toward the transducer, and are converted into an electrical echo signal. 2D ultrasound images are generated by acquiring and digitizing echo signals at consecutive lateral transducer positions x_i , with $i = 1, 2, \dots, N$ along the lateral coordinate x over time-of-flight (TOF). A pencil-beam-like sound field characteristic, i.e., a narrow "sound beam," is generated with the help of *focused* ultrasound transducers to be able to spatially assign echo signals to tissue structures. For imaging, the amplitude of backscattered and reflected ultrasound waves is gray-scale coded over TOF at each lateral transducer position. Under the assumption of a constant and known speed of sound (SOS) $c \approx 1600$ m/sec inside the tissue, the TOF t is directly linked with the axial coordinate z :

$$z = \frac{c}{2} \cdot t \approx 800 \mu\text{m} \cdot \left(\frac{t}{\mu\text{sec}} \right) \quad (1)$$

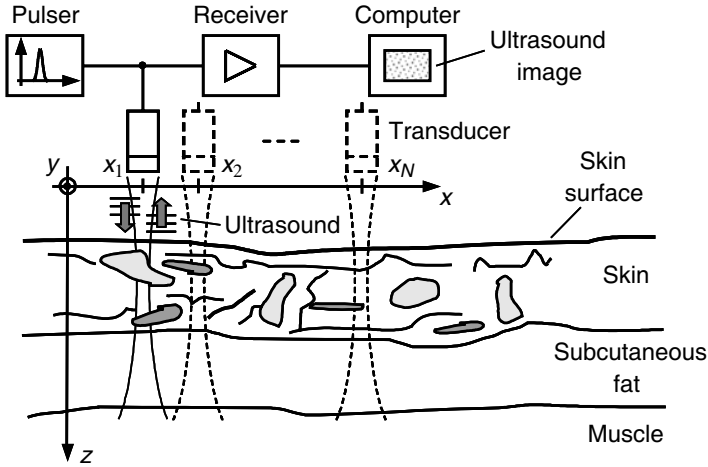


FIGURE 1 Ultrasound skin imaging concept (*schematic*): pulse-echo measurement with focused pencil-beam; lateral, axial, and elevational directions x , z , and y , lateral transducer positions x_i , and two-dimensional imaging plane (x,z).

With the above described scanning scheme, a 2D tomographic cross-sectional image of insonified tissue is obtained. A three-dimensional tissue volume can be imaged by acquiring consecutive 2D images along the elevational direction y (Fig. 1).

Ultrasound wave propagation in tissue is undistorted as long as the acoustic impedance of the sound propagation medium does not change. Water, which is usually used as sound propagation medium between the transducer and the skin in HFUS imaging systems, is a homogeneous medium as long as air bubbles inside the water are negligible. Consequently, no reflection or backscattering of ultrasound waves occurs inside the water path. At the border between the water and the skin surface, the acoustic impedance changes significantly. For this reason, ultrasound waves are strongly reflected, and a strong echo signal occurs. The waves, which propagate inside the skin, are also backscattered or reflected at acoustic inhomogeneities. Significant changes of the acoustic impedance are, for example, given at the border between the epidermis and dermis, at collagen fibers and hair follicles inside the dermis, at the boundary between the dermis and the subcutaneous fat and at the muscle fibers. *Backscattering* describes the phenomenon that acoustic waves, which propagate toward an acoustic inhomogeneity with a spatial extent that is *small* against the wavelength, are *diffusely* propagated in all directions. *Reflection* at the other hand denotes the *directed* backward propagation of ultrasound waves, which occurs at planar boundaries between the two media with different acoustic impedances that are *large* against the wavelength. Because the backscattering in tissue is typically very weak, *multiple* scattering of ultrasound waves is usually negligible.

The above-described conditions illustrate that ultrasound images depict the *morphology* of insonified skin and tissue. Echo signal amplitudes show a rather qualitative dependency of the acoustic properties of tissue, while axial and lateral distances are quantitatively accessible in ultrasound images as long as the assumptions for the SOS inside the tissue are sufficiently accurate.

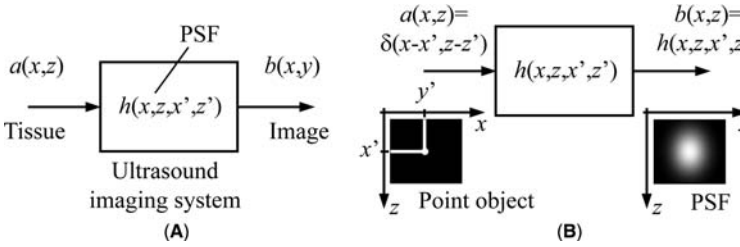


FIGURE 2 System theoretic model: **(A)** object function $a(x,z)$, image function $b(x,z)$, PSF $h(x,z,x',z')$ **(B)** PSF: system's response for point object. *Abbreviation:* PSF, point spread function.

High Frequency and Broadband Ultrasound for High-Resolution Imaging

The quality and diagnostic value of medical images depend on many parameters of the imaging system such as spatial resolution, dynamic range, measurement sensitivity, temporal resolution, maximum field of view, and others. Limitations are particularly caused by the system's bandwidth limitations, noise, and processing time. For conventional sonography in fields such as internal medicine, ultrasound in the range from 1 to about 13 MHz is utilized. It is shown below that larger ultrasound frequencies have to be applied for high-resolution skin imaging.

Generally, imaging systems can be described as a "black box" in a system theoretical model (Fig. 2A). The object function $a(x,z)$, which describes the imaged tissue, is the system's input. The output, which is the generated image, is described by the image function $b(x,z)$. Presumed the system is *linear*, $b(x,z)$ can be described by the 2D *convolution* of $a(x,z)$, with the system's *point spread function* (PSF) $h(x,z,x',z')$:

$$b(x,z) = a(x,z) \cdot h(x,z,x',z') = \int_{z'} \int_{x'} a(x',z') \cdot h(x,z,x',z') dx' dz' \quad (2)$$

Consequently, the PSF $h(x,z,x',z')$ is an important measure to characterize the system's imaging properties. It is the system's response for an infinitesimal small point object $a(x,z) = \delta(x-x', z-z')$ at a coordinate (x',z') at the input (Fig. 2B). Because the transducer's sound field characteristics changes over depth z (Fig. 3), ultrasound systems are *space variant*, i.e., the PSF depends on the axial location z' of the point object. In practice, the ultrasound system's PSF can be measured by scanning a point-like object, for example, a thin metal wire, at different depths or by analyzing echo signals that are acquired at speckle phantoms. The system is completely described by the PSF as long as *nonlinear* distortions do not occur. Below, the spatial extent of the PSF is quantified as a measure of the system's *spatial resolution*.

It was already explained above that TOF measurements are performed with focused sound beams. The system's ability to measure the TOF improves with shorter ultrasound pulses. Consequently, the system's bandwidth B is the parameter that determines the axial resolution δ_z in axial direction z . On the other hand, the spatial resolution in the perpendicular (lateral and elevational) directions depends on the focusing and consequently on the transducer's aperture size and

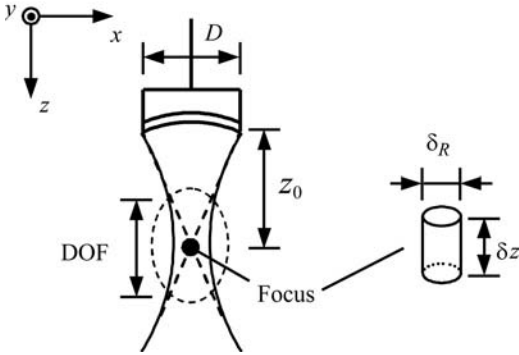


FIGURE 3 Spherically focused single element transducer: Aperture diameter D , focus length z_0 ; “resolution cell”: Axial and radial resolution δ_z and δ_R , respectively. *Abbreviation:* DOF, depth of field.

center frequency f_0 . Because typically ultrasound transducers with a rotational symmetric sound beam are utilized in HFUS skin imaging systems, a spatial resolution δ_R in the *radial* direction $R = (x^2 + y^2)^{1/2}$ perpendicularly to the axial sound propagation direction z can be specified (Fig. 3). The ultrasound transducer is a bandpass system and usually the element inside the system that specifies and limits the bandwidth and center frequency. With high frequency and broadband ultrasound, the system’s spatial resolution reaches a microscopic scale that is required for skin imaging (22,25–28).

Ultrasound Images Properties

The bandpass characteristic of ultrasound transducers significantly determines the properties of acquired ultrasound images. The echo signal for a single point object is a bandpass signal, which can be described as a sinusoidal carrier signal at the center frequency f_0 , with a Gaussian envelope whose pulse width is inversely proportional to the bandwidth B (28). Based on this model, the following axial and radial resolution δ_z and δ_R , respectively, are obtained (Fig. 3) (26–28):

$$\delta_z = \frac{2 \cdot c \cdot \ln 2}{\pi \cdot B} = 0.441 \cdot \frac{c}{B} \approx 706 \mu\text{m} \cdot \frac{1}{(B/\text{MHz})}, \tag{3}$$

$$\delta_R = \frac{c}{f_0} \cdot F \approx 1600 \mu\text{m} \cdot \frac{F}{(f_0/\text{MHz})}$$

The “f-number” F in Eq. (3) describes the transducer’s focused sound field characteristic. For spherically focused transducers, F depends on the transducer diameter D and focus length z_0 (Fig. 3):

$$F = \frac{z_0}{D} \tag{4}$$

An axial resolution δ_z in the range from 70 to 10 μm can be obtained with bandwidths in the range from 10 to 70 MHz. Radial resolution δ_R in the range from 320 to 20 μm are expected to be found with center frequencies in the range from 10 to 80 MHz and typical f-numbers F in the range from one to two. However, the frequency dependent attenuation of ultrasound waves in tissue causes a decay of both parameters with increasing depth. Consequently, the spatial resolution is degraded in large depths (25,28,31).

The object function $a(x,z)$ in Eq. (2) describes the tissue properties that are relevant for imaging, i.e., the acoustic backscatter in the case of ultrasound imaging. The spatial resolutions of the rotational symmetric sound beam in Eq. (3) define a *resolution cell*, which is a cylinder with diameter δ_R and height δ_z (Fig. 3). The spatial extension of imaged acoustic inhomogeneities relative to the resolution cell very strongly determines the system's response and ultrasound image properties. If many acoustic scatterers fit into the cell, the superposition of coherent bandpass signals, which are backscattered at the individual scatterers, results in a characteristic texture of the generated B-mode image. The statistical image amplitude variations, which are visible under these conditions, are denoted as *speckle* pattern, whereby the mean speckle size is proportional to the axial and radial resolution δ_z and δ_R . Tissue structures can only be identified in ultrasound images if their spatial extent is large against the resolution cell size.

Another crucial parameter of ultrasound imaging systems is the *dynamic range*, which is the maximum variation of echo signal amplitudes that can be detected and imaged. The larger the system's dynamic is, the larger the axial imaging depth range is because the tissue attenuation causes a decay of echo signal amplitudes over depth.

HFUS SCANNER

In this section, the design of a new HFUS skin imaging system is presented and discussed. Based on the experience, which was collected with a prototype system at the Institute of High-Frequency Engineering of the Ruhr-University Bochum, Germany (22–28), a new clinical scanner was developed in cooperation with partners from industry (taberna pro medicum GmbH, Lüneburg, Germany) in the framework of the Ruhr-Center of Excellence for Medical Engineering (KMR), Bochum, Germany (30–33).

System Design

In Figure 4A, a block diagram of the implemented system is shown. Two applicators with different transducers are available for imaging. A conventional 20 MHz range transducer is used for imaging the complete skin and subcutaneous fat.

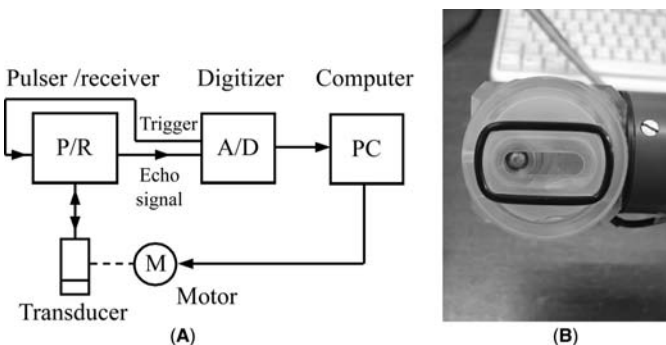


FIGURE 4 Implemented 20 to 100 MHz range high-frequency ultrasound skin imaging system: (A) block diagram; (B) applicator with 100 MHz range transducer.

High-resolution imaging of the uppermost skin layers and the dermis is performed with another transducer, which emits ultrasound in the 100 MHz frequency range. In low frequency sonography, images are usually acquired with ultrasound transducer arrays, i.e., the lateral scanning is performed electronically. In the HFUS range, transducer arrays are currently only available for frequencies up to about 30 MHz, but they still suffer from many technological limitations. For this reason, spherically focused single element transducers are utilized in the implemented HFUS imaging system, and mechanical lateral scans are performed. Starting at the near field directly beneath the transducer aperture, the ultrasound beam converges toward the focus region and diverges in the far field (Fig. 3). For imaging, the transducer focus is axially positioned at the center of the region of interest, and echo signals from inside the transducer's depth of field (DOF) are acquired. In Figure 4B, the applicator, which is used for 100 MHz range ultrasound skin imaging, is shown. The applicator has a slot at the bottom side, which is placed at the top of the skin, and water serves as sound propagation medium between the transducer and the skin. An adjusting screw allows the user to manually move the transducer up and down for axial adjustment of the focus position relative to the skin.

The transducer is excited with a broadband pulsed signal, which is generated by a pulser/receiver (Fig. 4A). Reflected and backscattered waves are converted into an electrical echo signal by the same transducer, and the echo signal is amplified by a low noise small signal amplifier inside the pulser/receiver. The signal is sampled and quantized by an analog to digital (A/D) converter in a digitizer unit. For the 20 MHz range transducer, the signal is acquired with a 100 MHz sampling frequency. Because the echo signals that are obtained with the 100 MHz range transducer are more broadband, they are digitized with a higher sampling frequency of 500 MHz. The dynamic range of acquired ultrasound images especially depends on the eight-bit amplitude resolution of the A/D converter used in this setup.

Mechanical scans are performed in lateral direction by moving the transducer with a direct current motor. The pulse generator is triggered at equidistant lateral transducer positions and the echo signals are sampled starting after a fixed and predefined time delay, which determines the axial position of the image region relative to the transducer. All components of the system are controlled by a personal computer that is also utilized for echo signal processing as well as for image generation and visualization.

Echo Signal Processing and Image Generation

In the implemented HFUS imaging system, the radio frequency (RF) echo signals, i.e., the signals that are directly available at the transducer, are digitized. A typical RF echo signal $S_E(t)$, which was acquired at a constant lateral transducer position, is shown in Figure 5A. As was already explained above, the system's response is a bandpass signal, i.e., a carrier signal, which is amplitude modulated by the signal's envelope. For 2-D morphological B-mode imaging, the signal *amplitude* is gray-scale coded over TOF at consecutive lateral transducer positions. If the *alternating* RF echo signal was evaluated for imaging directly, the B-mode image amplitude would alternate as well, and the tissue morphology would be inappropriately depicted. For this reason, the echo signal envelope has to be detected by means of digital signal processing. In the implemented system, first the analytical echo signal $S_{E+}(t)$ of an acquired RF echo signal $S_E(t)$ is calculated at each lateral

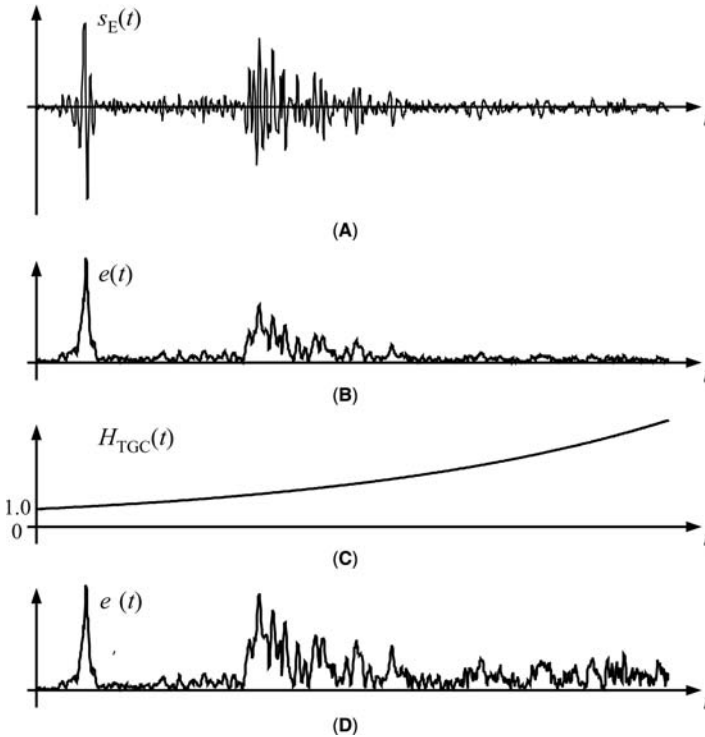
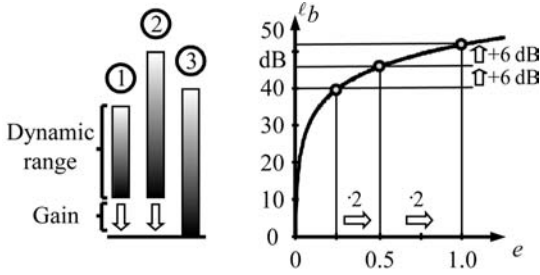


FIGURE 5 (A) Acquired radio frequency echo signal $s_E(t)$ for a single lateral transducer position (100 MHz range ultrasound); (B) echo signal envelope $e(t)$; (C) TGC curve $H_{TGC}(t)$ for a mean attenuation coefficient $\bar{\alpha} = 5$ dB/mm; (D) echo signal envelope $e'(t)$ behind TGC amplifier. *Abbreviation:* TGC, time gain control.

transducer position by the Hilbert transform. The signal envelope $e(t)$ (Fig. 5B), which is the magnitude of the analytical signal $S_{E+}(t)$, contains information about the strength of backscattered and reflected ultrasound waves along the axial coordinate z .

The dynamic range of echo signals from skin is very large. For this reason, a logarithmic amplitude transformation is applied to the echo signal envelope $e(t)$, and the resulting logarithmic image amplitude ${}^l b(z)$ is utilized for imaging to enable the visualization of tissue with very high and low backscattering and reflectivity. In other words, the echo signal envelope is logarithmically mapped to a linear gray scale (Fig. 6). The transformation curve is fixed, except for two degrees of freedom, the *dynamic range* and the *gain*, which are both adjustable by the user. With the help of these two parameters, the contrast and amplitude amplification of the displayed image can be adjusted according to the physicians' needs. The examples in Figure 6 show that the dynamic range determines the ratio of maximum and minimum echo signal amplitude, whereas the gain determines the amplification. Here, like in other technical fields, the advantage of logarithmic measures is exploited. A repeated



- ① 25 dB dynamic range / -10 dB gain
- ② 40 dB dynamic range / -10 dB gain
- ③ 40 dB dynamic range / 0 dB gain

FIGURE 6 Logarithmic image amplitude transformation: Echo signal envelope e , logarithmic image amplitude ${}^l b$.

scaling of the echo signal envelope by a given multiplication factor gives a repeated summation of a constant summand. The logarithmic image amplitude ${}^l b(z)$ increases by 6 dB for any doubling of the envelope signal $e(t)$ (Fig. 6).

Because ultrasound waves are scattered in all directions in tissue and consequently only a small part of the transmitted ultrasound energy is backscattered toward the transducer, waves are attenuated with propagation in tissue. Furthermore, because axial distances along the sound beam are directly linked with the TOF, Eq. (1), a time varying amplification can be applied to account for the tissue attenuation. In sonography, this amplification is implemented in a *time gain control* (TGC) unit, sometimes also denoted as *depth gain control*. Because the attenuation of ultrasound waves in tissue is frequency-dependent, the TGC can only partly compensate for the attenuation. An exponential decay of ultrasound waves over depth is assumed, and the following TGC transfer functions, $H_{TGC}(z)$ and $H_{TGC}(t)$ over the axial coordinate z and TOF t , respectively, are utilized:

$$H_{TGC}(z) = 10^{2 \cdot \bar{\alpha} \cdot z / 20 \text{ dB}} = e^{2 \cdot \bar{\alpha} \cdot z / 8.69 \text{ dB}}, \quad H_{TGC}(t) = 10^{\bar{\alpha} \cdot c \cdot t / 20 \text{ dB}} \tag{5}$$

In Figure 5C and D, $H_{TGC}(t)$, and the echo signal envelope $e'(t)$ behind the TGC amplifier unit are shown for a mean attenuation coefficient $\bar{\alpha} = 5 \text{ dB/mm}$, which was utilized for all below presented 100 MHz range in vivo ultrasound images of skin:

$$e'(t) = e(t) \cdot H_{TGC}(t) \tag{6}$$

System Performance Measurement and Analysis

It was already explained above that the ultrasound system’s spatial resolution depends on the spectral characteristics. Reference measurements on well-defined technical objects were performed to quantitatively assess the PSF and system’s performance. Echoes from a glass plate surface at the transducer focus (Fig. 7A) and a thin wire with a diameter smaller than the wavelength were acquired and analyzed. The spectral characteristics were analyzed by calculating the Fast Fourier Transform of digitized glass plate surface echo signals.

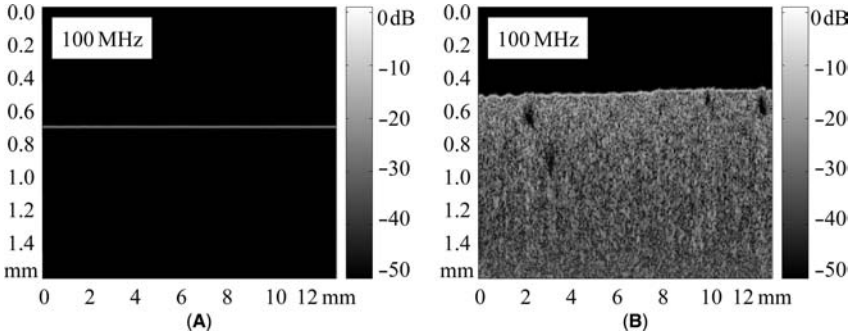


FIGURE 7 Reference measurements (100 MHz range ultrasound): **(A)** glass plate surface at transducer focus; **(B)** speckle phantom, silica gel particles in agar (mean attenuation coefficient $\bar{\alpha} = 10 \text{ dB/mm}$).

Further measurements were performed on speckle phantoms consisting of agar, whose ultrasound properties are close to those of tissue. Silica gel particles with a mean diameter of $15 \mu\text{m}$ were added to obtain a homogeneous backscattering (Fig. 7B). A high scatterer concentration was chosen to obtain “fully developed” speckle. Under these conditions, the speckle characteristics can be statistically analyzed by calculating and analyzing the auto-covariance function $C_{bb}(x,z)$ of acquired B-mode images $b(x,z)$ (34):

$$c_{bb}(x,z) = \int_{z'} \int_{x'} (b(x',z') - \bar{b}) \cdot (b(x+x',z') - \bar{b}) dx' dz', \text{ with:} \quad (7)$$

$$\bar{b} = \int_{z'} \int_{x'} b(x',z') dx' dz'$$

RESULTS

In this chapter, results of measurements that were performed to evaluate the imaging properties of the implemented HFUS skin imaging system are presented. Measurements on phantoms were performed for a quantitative analysis, and acquired in vivo images are shown to assess the potential of high-resolution ultrasound in clinical applications.

Imaging Properties and Image Generation

The imaging properties of the implemented HFUS imaging system were evaluated by phantom measurements. In Table 1 the results of this evaluation are summarized. The echo signal spectrum that was obtained from a glass plate surface at the transducer focus shows relevant contents in the frequency range from 5 to 25 MHz for the nominal 20 MHz range transducer no. 1 (-6 dB cut-off frequencies). For the nominal 100 MHz frequency range transducer no. 2, the spectrum ranges from 24 to 97 MHz. A significant downshift in frequency is caused by the frequency and temperature dependent attenuation of the water, which is used as sound propagation medium (31). The measured axial and radial resolutions δ_z

TABLE 1 Transducer Specifications and Imaging Properties

	Transducer no. 1	Transducer no. 2
Echo signal spectrum	5–25 MHz	24–97 MHz
Axial resolution δ_z	39 μm	9.9 μm
Radial resolution δ_r	210 μm	84 μm
DOF	3.8 mm	1.1 mm
Focus length z_0	15 mm	4.3 mm

Abbreviation: DOF, depth of field.

and δ_R (–6 dB resolutions) are given in Table 1. They are very close to the resolutions, which is to be expected based on the theoretical considerations in Eq. (3), with the measured center frequencies f_0 and bandwidths B .

The resolutions were measured by analyzing echoes from a glass plate surface and wire phantom at the transducer focus. Outside the focus region, the system’s response is downshifted in frequency, and the spatial resolution is worse because of the depth dependent and diffracted sound beam characteristic (32). Consequently, δ_z and δ_R in Table 1 are the best achievable resolutions under optimal conditions. Inside the skin, the resolution degrades with increasing depth because of the frequency dependent attenuation of tissue and the focused sound field characteristics. The DOF in Table 1, which was measured by analyzing echoes from a glass plate surface at different depths z , quantifies the typically utilizable axial imaging range.

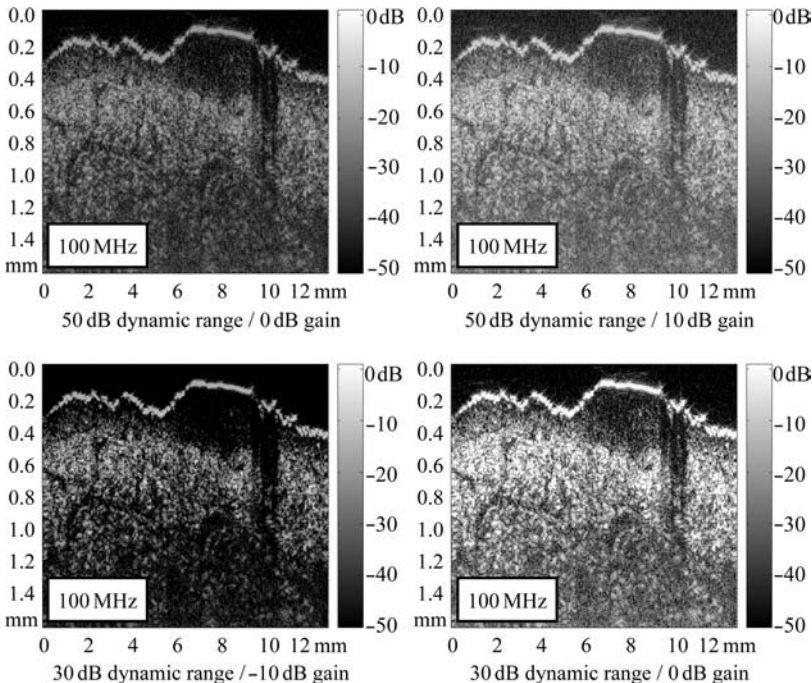


FIGURE 8 In vivo ultrasound B-mode images (100 MHz range) for different dynamic range and gain settings: nevus at the back of a patient.

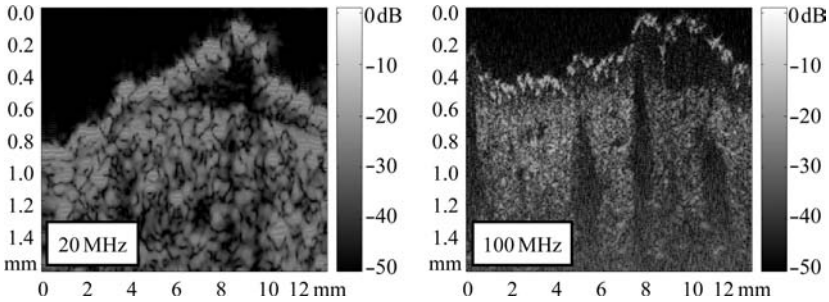


FIGURE 9 In vivo B-mode images of nevus at the back: 20 MHz range (*left*) and 100 MHz range (*right*) ultrasound.

In Figure 8, in vivo B-mode images of a nevus are shown. Echo signals were acquired with the 100 MHz range transducer. The images were obtained with different dynamic range and gain settings in the context of the above-discussed logarithmic gray-scale mapping (Fig. 6). At the top, the boundary between the water path and the skin surface is visible as a strongly reflecting border. Beneath, the hyperechoic dermis is imaged, whereby the backscattering is caused by the collagen fiber network. The imaged nevus appears as a hypoechoic structure closely beneath the skin surface.

The B-mode images in Figure 8 illustrate the effect of changing the dynamic range and gain. The higher the dynamic range, the larger the visible maximum image amplitude variations become. Consequently, the dynamic range must be large if different tissue structures with high and low backscattering should be visualized in one single image. A low dynamic range can be utilized to emphasize either strongly or weakly backscattering structures. The gain, which is the second adjustable parameter, is used to shift the image amplitude relative to the logarithmic gray-scale display. With increasing gain, more and more tissue structures with low backscattering become visible, while large backscattering structures increasingly overdrive the image display. If the gain is set too large, the system's noise becomes visible. A low gain is utilized to image tissue structures with high backscattering. In practice, both parameters, dynamic range and gain, have to be set appropriately to image the tissue structures, which are relevant for the diagnostic question.

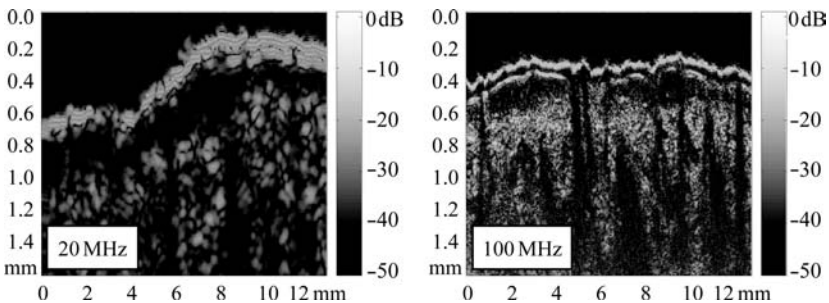


FIGURE 10 In vivo B-mode images of squamous cell carcinoma of the cheek: 20 MHz range (*left*) and 100 MHz range (*right*).

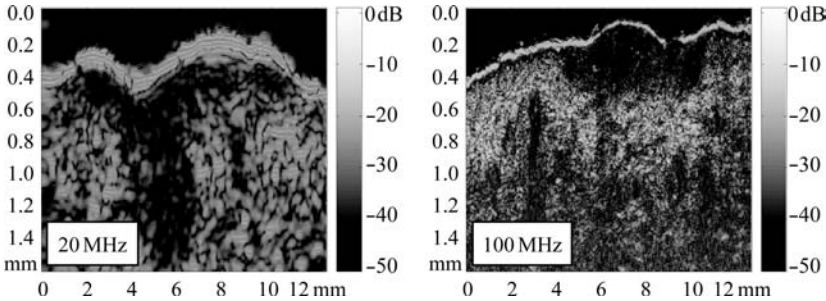


FIGURE 11 In vivo B-mode images of squamous cell carcinoma at the shoulder: 20 MHz range (left) and 100 MHz range (right) ultrasound.

In Vivo Images

In vivo images were acquired with both applicators at the same locations to enable a comparison between the standard 20 MHz range sonography and the new implemented high resolution 100 MHz range imaging system. As a first example, in Figure 9 a nevus is shown, which was imaged at the back of a patient. Both the B-mode images have the same axial and lateral dimensions of 1.6 and 12.4 mm, respectively. Consequently, the spatial scaling in the two coordinates is different, and the image is stretched along the axial coordinate. The images confirm that the spatial resolution is significantly better with the 100 MHz range ultrasound compared to the standard 20 MHz range technique. Much more details are visible and imaged skin structures are much better distinguishable from each other. The example shows that the skin entry echo from the border between the water path and the skin as well as the imaged nevus are much better demarcated. Furthermore, much more details in the highly backscattering dermis are visible, whereby hair follicles appear as hypoechoic vertical structures. Thus, the potential to assess the depth and structure of imaged nevi improves significantly with the new high-resolution ultrasound imaging technique.

In Figure 10, in vivo B-mode images of a squamous cell carcinoma (SCC) at the cheek of a patient are shown. In the 100 MHz range image, the relatively thick epidermis is visible as a low echoic band beneath the skin surface, while it cannot be resolved in the 20 MHz range image because of the worse spatial resolution. The SCC appears as hypoechoic band below the dermis. Another SCC that was imaged at a patient's shoulder is shown in Figure 11. Again, the image quality is significantly improved with increased ultrasound frequencies.

SUMMARY AND DISCUSSION

In this chapter, the concept of ultrasound imaging systems was discussed. It was motivated and explained that high frequency and broadband ultrasound can be utilized for high-resolution imaging of tissues. HFUS in the range up to 100 MHz range fulfills the requirements concerning spatial resolution for microscopic skin imaging. The design of a new HFUS skin imaging system was presented. Spherically focused single element transducers are used in this system and a broadband electronics was developed to appropriately drive the transducers. Two separate applicators support sonography in the well-established standard 20 MHz range as well as in the

100 MHz range with high resolution. In the implemented system, the RF echo signals are digitized, and images are generated by digitally processing the acquired signals. The echo signal envelope is calculated utilizing the Hilbert transform and gray-scale coded B-mode images are generated applying a TGC and logarithmic amplitude transformation. The performance of the system was evaluated using a glass plate surface, wire phantom and tissue-like phantom. Quantitative evaluations show that significantly improved minimum axial and radial resolutions of 9.9 and 84 μm , respectively, are achieved in the 100 MHz range compared to the poorer resolution of 39 and 210 μm , respectively, with 20 MHz HFUS. Clinical in vivo images were acquired with both applicators at the same locations and compared to each other. It was shown that the new 100 MHz range ultrasound skin imaging modality enables a very high-resolution imaging of the uppermost skin layers and upper dermis in clinical applications. Consequently, the diagnostic value and the potential to analyze skin tumors and to assess their depth are clearly improved. Generally, much more details in the fine structure of skin lesions and layered skin anatomy are visible.

ACKNOWLEDGMENT

The presented work is a project of the Ruhr Center of Excellence for Medical Engineering (KMR) Bochum, Germany, which is supported by the Federal Ministry of Education and Research, Germany, Grant No. 13N8079. The contribution of our project partners Rüdiger Scharenberg, Sven Scharenberg, and Bodo Paul (taberna pro medicum GmbH, Lüneburg, Germany) as well as Dr. med. Klaus Hoffmann, Georg Moussa, Dr. med. Michael Sand, and Prof. Dr. med. Peter Altmeyer (Dermatological University Hospital, Bochum, Germany) is greatly appreciated.

REFERENCES

1. Payne PA. Application of ultrasound in dermatology. *Bioengin Skin* 1985; 1:293–320.
2. Querleux B, Leveque JL, de-Rigal J. In vivo cross-sectional ultrasonic imaging of human skin. *Dermatologica* 1988; 177:332–337.
3. Breitbart EW, Müller CE, Hicks R, Vieluf D. New developments in ultrasound diagnostic in dermatology. *Akt Dermatol* 1989; 15:57–61.
4. Murakami S, Miki Y. Human skin histology using high-resolution echography. *J Ultrasound Med* 1989; 17:77–82.
5. Altmeyer P, el-Gammal S, Hoffmann K. *Ultrasound in dermatology*. Berlin, Heidelberg, New York: Springer, 1992.
6. Berson M, Vaillant L, Patat F, Pourcelot L. High-resolution, real-time ultrasonic scanner. *Ultrasound Med Biol* 1992; 18(5):471–478.
7. Bamber JC, Harland CC, Gusterson BA, Mortimer PS. Correlation between histology and high resolution echographic images of small skin tumors. *Acoust Imaging* 1992; 19:369–374.
8. Hoffmann K, Schatz H, el-Gammal S, Altmeyer P. B-scan sonography in dermatological routine diagnostics. In: Ermert H, Harjes HP, eds. *Acoustical Imaging*. 19. New York: Plenum Press, 1992.
9. Fornage BD, Mc Gavran MH, Duciv M, Waldron CA. Imaging of the skin with 20-MHz US. *Radiology* 1993; 189:69–76.
10. Hoffmann K, Stücker M, Dirschka T, et al. 20 MHz B-scan sonography for visualization and skin thickness measurement of human skin. *J Eur Acad Dermatol* 1994; 3:302–313.
11. Gniadecka M. Effects of ageing on dermal echoenicity. *Skin Res Technol* 2001; 7:204–207.
12. Dyson M, Moodley S, Verjee L, Verling W, Weinmann J, Wilson P. Wound healing assessment using 20 MHz ultrasound and photography. *Skin Res Technol* 2003; 9:116–121.

13. Yano T, Fukukita H, Ueno S, Fukumoto A. 40 MHz ultrasound diagnostic system for dermatologic examination. *Proc IEEE Ultrason Symp* 1987:875–878.
14. Foster FS, Pavlin CJ, Lockwood GR, et al. Principles and applications of ultrasound backscatter microscopy. *IEEE Trans Ultrason Ferroelectr Frequency Control* 1993; 40(5):608–617.
15. Turnbull DH, Starkoski BG, Harasiewicz KA, et al. A 40–100 MHz ultrasound backscatter microscope for skin imaging. *Ultrasound Med Biol* 1995; 21(1):79–88.
16. Lockwood GR, Turnbull DH, Christopher DA, Foster FS. Beyond 30 MHz. *IEEE Eng Med Biol* 1996; 15(6):60–71.
17. Knapik DA, Starkoski B, Pavlin CJ, Foster FS. A realtime 200 MHz ultrasound B-scan imager. *Proc IEEE Ultrason Symp* 1997:1457–1460.
18. Foster FS, Pavlin CJ, Harasiewicz KA, Christopher DA, Turnbull DH. Advances in ultrasound biomicroscopy. *Ultrasound Med Biol* 2000; 26(1):1–27.
19. Knapik DA, Starkoski B, Pavlin CJ, Foster FS. A 100–200 MHz ultrasound biomicroscope. *IEEE Trans Ultrason Ferroelectr Frequency Control* 2000; 47(6):1540–1549.
20. Chen WH, Gottlieb EJ, Cannata JM, Chen YF, Shung KK. Development of sector scanning ultrasonic backscatter microscope. *Proc IEEE Ultrason Symp* 2000:1681–1684.
21. Erickson S, Kruse D, Ferrara K. A hand-held, high frequency ultrasound scanner. *Proc IEEE Ultrason Symp* 2001:1465–1468.
22. Hoess A, Ermert H, el-Gammal S, Altmeyer P. A 50 MHz ultrasonic imaging system for dermatologic application. *Proc IEEE Ultrason Symp* 1989:849–852; *Proc IEEE Ultrason Symp* 2001:1465–1468.
23. Passmann C, Ermert H, Auer T, Kaspar K, el-Gammal S, Altmeyer P. In vivo ultrasound biomicroscopy. *Proc IEEE Ultrason Symp* 1989:1015–1018.
24. Passmann C, Ermert H, el-Gammal S, Altmeyer P. 150 MHz adaptive ultrasound imaging of the eye and skin. *Acoust Imaging* 1995; 22:495–500.
25. Passmann C, Ermert H. A 100-MHz ultrasound imaging system for dermatologic and ophthalmologic diagnostics. *IEEE Trans Ultrason Ferroelectr Frequency Control* 1996; 43(4):545–552.
26. Ermert H, Vogt M, Passmann C, et al. High frequency ultrasound (50–150 MHz) in dermatology. In: Altmeyer P, Hoffmann K, Stücker M, eds. *Skin Cancer and UV Radiation*. Berlin, Heidelberg, New York: Springer, 1997:1023–1051.
27. Ermert H, Vogt M. High frequency ultrasonic imaging and its applications in skin. *Proc Int Soc Opt Eng* 1999:44–55.
28. Vogt M, Kaspar K, Altmeyer P, Hoffmann K, El Gammal S. High frequency ultrasound for high resolution skin imaging. *Frequenz* 2001; 55(1–2):12–20.
29. El Gammal S, El Gammal C, Kaspar K, et al. Sonography of the skin at 100 MHz enables in vivo visualization of stratum corneum and viable epidermis in palmar skin and psoriatic plaques. *J Invest Dermatol* 1999; 5:821–829.
30. Vogt M, Paul B, Scharenberg S, Scharenberg R, Ermert H. Development of a high frequency ultrasound skin imaging system: optimization utilizing time domain reflectometry and network analysis. *Proc IEEE Ultrason Symp* 2003:744–747.
31. Vogt M, Paul B, Scharenberg S, Scharenberg R, Ermert H. Analysis and measurement of spectral characteristics and spatial resolution of high frequency ultrasound imaging systems. *Proc IEEE Ultrason Symp* 2004:2137–2140.
32. Vogt M, Paul B, Scharenberg S, Scharenberg R, Ermert H. In vivo ultrasound biomicroscopy of skin with 20 MHz and 100 MHz range ultrasound: Inverse echo signal filtering optimization. *Proc IEEE Ultrason Symp* 2005:508–511.
33. <http://www.kmr-bochum.de>.
34. Wagner RF, Smith SW, Sandrik JM, Lopez H. Statistics of speckle in ultrasound B-scans. *IEEE Trans Sonics Ultrason* 1983; 30(3):156–163.

Magnetic Resonance Imaging of Human Skin In Vivo

Bernard Querleux

L'Oréal Recherche, Aulnay-sous-bois, France

Luc Darrasse

U2R2M UMR8081-CNRS-Université Paris-Sud, Orsay, France

Jacques Bittoun

U2R2M UMR8081-CNRS-Université Paris-Sud, CIERM-hospital Bicetre, Le Kremlin-Bicetre, France

INTRODUCTION

Since the first cross-sectional images of the human skin in vivo by high-frequency ultrasound were published in the early 1980s, numerous imaging techniques have been proposed for improving our knowledge of the morphology and physiology of the different skin layers in vivo. Ultrasound imaging at 20 to 25 MHz is nowadays the most widespread method (1–3), whereas ultra high-resolution ultrasound scanners operating in the 100 to 150 MHz range are still prototypes (4,5). Optical techniques, such as confocal microscopy, have provided new insight into the microscopic level of the outermost part of the skin (6–9); more recently, optical coherence tomography, with a 1 to 10 μm resolution range, seems very promising (10–12). The next key step in skin imaging is just starting: the combination of microscopic images coupled with localized spectroscopy as proposed with confocal Raman microscopy (13,14) or multiphoton microscopy (15,16).

In addition to the imaging methods listed above, magnetic resonance (MR) imaging is one of the molecular imaging techniques capable of combining high-spatial resolution imaging, albeit not at microscopic level, with some biochemical information through MR spectroscopy or physiological information through the measurement of physicochemical MR parameters.

This chapter will be divided into three parts. The first part presents a review of the most significant results obtained in earlier MR skin studies. The second part focuses on recent results on water mobility in the skin layers and age-related effects. Finally, a highly efficient technological solution based on cryogenic detectors enabling skin studies in new clinical body scanners is discussed in the third section. This could be the key to the widespread use of MR imaging for studying healthy and diseased skin in vivo in the near future.

REVIEW OF MAGNETIC RESONANCE IMAGING OF THE SKIN

Magnetic Resonance Skin Imaging

Although MR imaging is rapidly developing in clinical diagnosis, its use in the study of the skin is still limited, not least of all because high-spatial resolution of



FIGURE 1 In vivo cross-sectional magnetic resonance imaging of the skin on the dorsal side of the calf. The epidermis corresponds to the bright outer layer, and the dermis to a hyposignal structure where cutaneous appendages are well recognized: hair follicles as structures in continuity with the living epidermis and hypodermal inclusions. Within the subcutaneous adipose tissue, fine hypointense structures correspond to fibrous septae dividing adipose tissue into lobules.

about 0.1 mm still poses a difficult challenge. With a sub-millimeter resolution accessible with clinical MR scanners in the early 1990s, images of healthy skin structure gave sparse information (17,18) and only large skin lesions were studied (19–24). These constraints and limitations explain why MR imaging of the skin is still limited to a few MR research centers. In our collaborative research, we initially designed a specific surface gradient coil in the antero-posterior direction, which can be connected to a clinical body scanner. Combined with a dedicated surface radiofrequency coil, this specific add-on module allowed us to achieve a resolution of 30 to 80 μm in the direction perpendicular to the skin surface (25).

In such images, the epidermis appears as a thin, bright outer layer, and the dermis as a hypointense inner layer. The hypodermis appears in hypersignal, whereas its fibrous septae are detected as thin, hypointense structures. Within the dermis on the dorsal side of the thigh (Fig. 1), hair follicles are clearly differentiated as inclusions in continuity with the epidermis, whereas hypodermal indentations allow us to describe precisely the topography of the dermo-hypodermal junction,

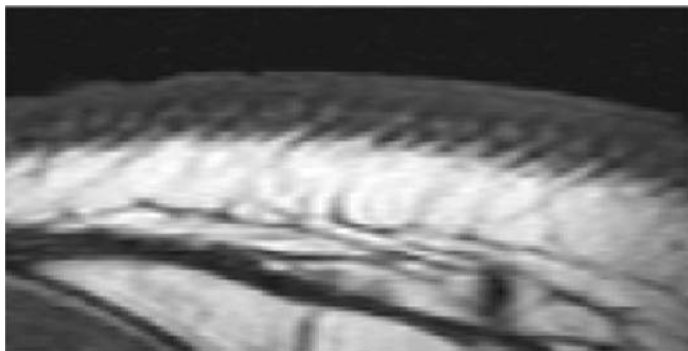


FIGURE 2 In vivo cross-sectional magnetic resonance imaging of the skin on the temple. White spots within the dermis correspond to the sebaceous glands, which are specifically enlarged on the temple.

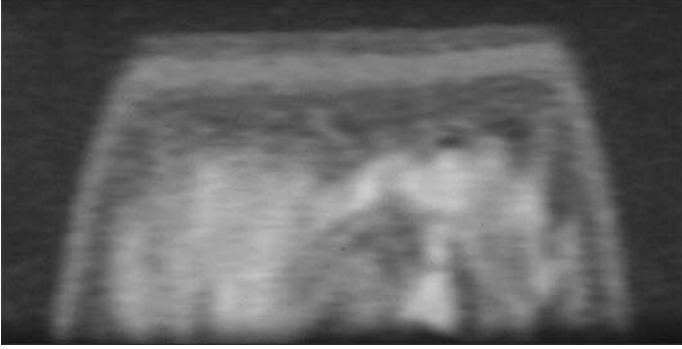


FIGURE 3 Magnetic resonance image of the pulp of the finger. The first layer corresponds to a 200- μm thick stratum corneum. A thickened living epidermis is also visible. Finally, the dermis appears as a homogeneous layer.

which has proved to be far more pronounced in women with cellulite than in women without cellulite (26). On the temple (Fig. 2), white spots within the dermis probably correspond to the sebaceous glands, which are particularly large and numerous at this skin site.

Skin in the palmo-plantar regions is characterized by a thickened stratum corneum, a thickened epidermis, while the dermis appears as a very homogenous layer (Fig. 3).

In diseased skin, we studied unilateral lymphedema in 21 patients (27). Alterations of the skin and hypodermis were easily detected, such as an increase in skin thickness and thickened fibrous septae in the hypodermis in the diseased leg compared to the healthy contralateral one (Fig. 4). Another study concerned very painful lesions such as glomus tumors. These are difficult to detect and localize by palpation, as they are often localized under the nail. We have confirmed the interest of MR imaging for an optimizing pre-operative strategy (28). Other preliminary results on acne with accurate, three-dimensional delineation of the papule

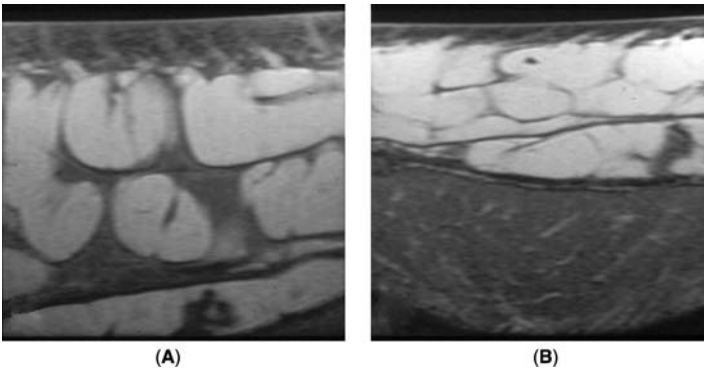


FIGURE 4 Magnetic resonance images in unilateral lymphedema disease. (A) Diseased leg; (B) healthy contralateral leg. Important alterations are detected in the skin and hypodermis: an approximate increase of 300% in the thickness of the skin and the presence of very thick, fibrous septae separating hypertrophic fat lobules.

volume were obtained (29). In psoriasis, it was reported that the thickened bright layer detected on MR images was clearly correlated to the epidermal hyperplasia measured at the bottom of the elongated epidermal ridges and differentiated from the inflammatory process in the outer dermis (29).

Biochemical Characterization of the Skin by Quantitative Magnetic Resonance Imaging

Compared to most imaging techniques, MR imaging has a major advantage in that the measured signal depends on numerous intrinsic parameters of the examined tissues, such as relaxation times, proton density, and perfusion and diffusion coefficients. Most of these parameters describe interactions between protons and their close environment and provide additional information on the physiology of biological tissues, in general, and of the skin, in our case.

Taking advantage of this capacity, it has been shown by comparison with other soft tissues, for instance, that short T_2 in the dermis (<25 msec) could be related to its high content of collagen fibers (30).

In healthy skin, it was demonstrated that intrinsic skin aging induces no statistically significant difference in relaxation times in the epidermis or dermis, but causes a significant increase in the free water content in the outer part of the aged dermis compared to that of young subjects (Table 1) (31).

Aging is marked by a decrease in both dermal collagen content and dermal collagen density and a reduction in the amount of glycosaminoglycans. A reduced macromolecular content would result in a decrease in the fraction of water corresponding to the hydration layer of collagen. All these modifications account for the higher proton density in the aged outer dermis and confirm previous results obtained by ultrasound imaging, namely that the major effects of skin aging take place in the outer part of the dermis (32).

Proton density was also used in order to localize and quantify water in the thick stratum corneum in palmo-plantar regions (33,34). Calculated hydration profiles in depth of the skin allow us to delineate two different structures in the stratum corneum: an outer layer where hydration can be modified by external mechanisms such as a dehydration process by repeated soaping and short-term hydration after a bath or application of a moisturizer, and an inner layer where hydration is unaltered.

In diseased skin, only a limited number of studies have been published including some additional quantitative measurements of MR parameters. However, applications to pre-operative staging, post-operative follow-up, and for assessing the efficacy of new dermatological products have already been demonstrated.

TABLE 1 Proton Density ($m \pm SD$) of the Different Skin Layers According to Age

Free water content ^a	Young subjects	Elderly subjects	
Epidermis	0.90±0.08	0.96±0.11	N.S.
Outer dermis ^b	0.48±0.10	0.58±0.11	$p < 0.05$
Inner dermis	0.40±0.11	0.47±0.08	N.S.

^aFree water content was normalized to an external reference imitating magnetic resonance skin parameters comprising a 5% agar gel spiked with a 0.06 mM solution of $MnCl_2$.

^bThe outer dermis corresponds to a subepidermal layer, 200 μm in thickness. Cutaneous appendages within the inner dermis were excluded after image processing.

Abbreviation: N.S., not significant.

PROGRESS IN MR SKIN IMAGING: SPATIAL RESOLUTION AND WATER BEHAVIOR IN SKIN LAYERS

Progress in High Spatial Resolution Imaging

Recent studies presented images of the skin at a 50- μm resolution in depth, which confirmed the morphological description of the skin structure previously reported (35,36). In our group, we aimed to improve the resolution in depth of the skin because of the layered structure of the skin. By using a pixel size of 19 μm , we strongly believe that the thin gray layer below the epidermis corresponds to the papillary dermis (Fig. 5). As such an image requires a 15-minute acquisition time, this resolution is not available for studies in many volunteers, in whom in-depth resolution was limited to 35 μm —a trade-off for improving living epidermis characterization within a reasonable acquisition time.

If MR imaging at microscopic level is hardly feasible, a new system called the Garfield magnet was recently introduced that provides one-dimensional (1-D) MR profiles of human skin in vivo at a resolution of 5.5 μm (37). Although an in-plane resolution of about 6 mm would eventually decrease the effective axial resolution, acquired profiles differentiated, for the first time, the thin stratum corneum from the living epidermis on the forearm in vivo.

Progress in Water Behavior Analysis

MR signal is particularly interesting for studying the microstructure of the skin and for improving our knowledge of water behavior in skin. For instance, additional analysis in skin layers was achieved with the magnetization transfer (MT) technique, which provides a new type of contrast based on interactions between bulk water protons and macromolecular protons. Hydration of the skin triggered different MT activity in the stratum corneum, giving a new insight into exogenous water molecules interacting with the stratum corneum (36).

With a 1-D profile analysis of the skin at a resolution of 5.5 μm , water mobility in the stratum corneum and epidermis was reported through a self-diffusion coefficient, which probes the movement of water molecules within the intricate tissue environment. An increased self-diffusion coefficient after moisturizing the skin

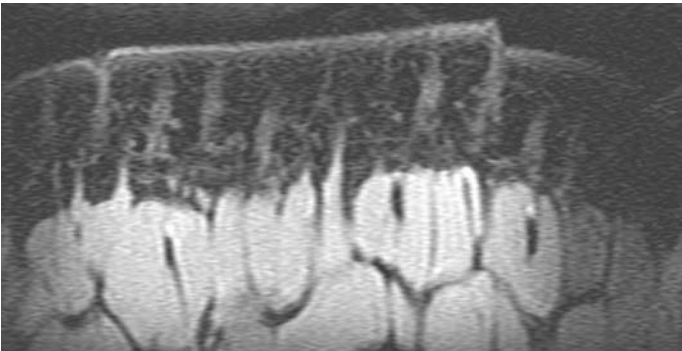


FIGURE 5 Ultra high-resolution magnetic resonance image of the calf. By using an in-depth resolution of 20 μm , beneath the outer, bright, thin layer corresponding to the epidermis, the papillary dermis, as a thin gray level, is well differentiated from the reticular dermis.

was reported and could lead to a breakthrough in our understanding of the water status in the stratum corneum (37).

Our group also recently conducted a preliminary study on two-dimensional diffusion-weighted MR imaging to explore water behavior in the living epidermis and dermis. Age-related effects were evaluated by comparing two groups of healthy volunteers: 10 young women (25 ± 3 years) and 10 elderly women (65 ± 3 years). In the epidermis, the apparent diffusion coefficient (ADC) was measured by following the 2 pixels ($70 \mu\text{m}$) with the highest values in the epidermis obtained from the mean intensity profile in depth. In the outer part of the dermis, the ADC value was calculated from three rectangular regions of interest, approximately $105 \mu\text{m}$ in thickness, placed below the living epidermis. Finally, the ADC value in the inner dermis was calculated from mean intensity values measured in a series of at least 10 isolated pixels to avoid hypodermal inclusions.

Mean values and standard deviations of the ADC in the skin in young and elderly subjects are presented in Figure 6 .

The ADC values in the direction perpendicular to the skin surface in the epidermis and the outer dermis are quite similar, whereas the ADC value in the inner dermis is significantly lower. While the epidermis and outer dermis are rather isotropic tissues, the inner dermis is much more anisotropic, the direction for collagen fibers being parallel to the skin surface. Modifications in collagen structures in the inner dermis and measurements in the perpendicular direction to the collagen fibers could explain the lower values recorded in the inner dermis.

As regards age-related effects, our results confirm alterations in the outer part of the dermis with a statistically significant increase in the mean ADC value in elderly subjects ($n = 15$) compared to young subjects ($n = 15$). This increase corroborates the findings of our previous study as well as knowledge of the skin-aging process (33). The most striking result is the potential to differentiate by MR imaging any increase in water mobility in the aged epidermis compared to the young epidermis. MR diffusion appears to be a sensitive marker of tissue water state. The improved resolution of $35 \mu\text{m}$ cannot explain the latest results in the epidermis, as we checked that T_1 , T_2 , and proton density did not differ in the young epidermis from that recorded in the aged epidermis. The measurement of water diffusion in the living epidermis should prove very interesting to expand our knowledge of the skin barrier function mechanisms in both healthy and diseased skin.

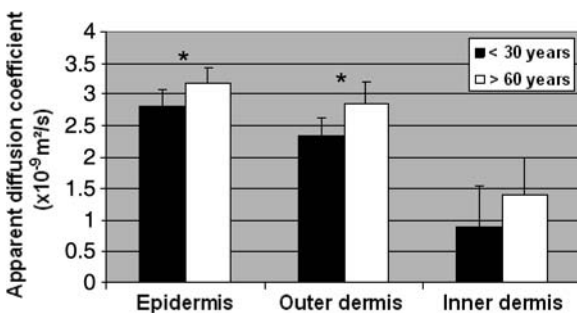


FIGURE 6 Apparent diffusion coefficients measured in skin layers. Increased apparent diffusion coefficient values in the aged epidermis and aged dermis characterize age-related effects. Asterisk indicates statistically significant.

PERSPECTIVES OF MR SKIN IMAGING: LOCAL MICROSCOPY IN CLINICAL BODY SCANNERS

Introduction

With a spatial resolution of about 0.3 mm, former clinical scanners were generally too limited to offer images of sufficient interest in skin studies. Since the end of the 1990s, most new clinical systems have been equipped with powerful gradient systems, achieving peak gradient amplitudes above 20 mT/m. Such gradients can be used to obtain MR pixels of 0.1 mm. Currently, gradient intensity on most MR imaging systems can reach and even exceed 50 mT/m. We consider that these new features on recent clinical MR scanners could be the focal point in the more widespread use of MR imaging of the human skin.

However, there is still an important obstacle to overcome, as the sensitivity of MR imaging substantially depends on the image voxel size. It is beyond the scope of this chapter to describe the physics of the MR imaging signal in detail, but as reported in relation (1), the signal-to-noise ratio (SNR) in the image, which qualitatively corresponds to the quality of the image, depends on the sensitivity of the detecting coil, the voxel size, and the total acquisition time:

$$SNR \propto S_{rf} d_x d_y d_z \sqrt{T_{scan}} \quad (1)$$

where S_{rf} corresponds to the sensitivity factor of the receiving detector, d_x , d_y , d_z to the pixel dimensions, and the T_{scan} to the total image acquisition time.

Relation (1) shows that, if we reduce the voxel size two-fold in all three dimensions, the SNR of the new image will decrease by a factor of 8. To obtain a similar SNR, the acquisition time should increase by a factor of 64, transforming each minute of acquisition time into one hour. Alternatively, one solution would be to improve the sensitivity of the receiving detector by a factor of 8. This can be achieved by designing cryogenic MR detectors, as described in the next paragraph.

A Promising Solution: New, Highly Sensitive Superconducting Detectors

The use of small-surface copper coils was the first step in increasing the sensitivity of MR skin imaging (17,25). Indeed, decreasing the coil dimension gives an improved coupling between the coil and the detected magnetization and leads to a proportionally increased signal. Superconductivity can drastically reduce noise, which, in the case of MR imaging with small coils, is mainly related to the thermal fluctuation of electrical charges inside the windings material. For this reason, superconducting detectors have recently been established as a new and highly efficient approach to high-spatial MR imaging (38,39), essentially for in vivo skin studies (40,41).

A small cryogenic detector (Fig. 7) comprising a high-temperature, superconducting (HTS) coil with an outer diameter of 14.6 mm has been developed. The detector is cooled down to the temperature of liquid nitrogen in a specific cryostat so that the distance between the skin in contact with the surface of the cryostat and the cooled detector is limited to 1 mm (40).

Depending on the body site, the SNR of the HTS coil is improved by a factor of 4 to 9 compared to a similar room temperature copper coil.

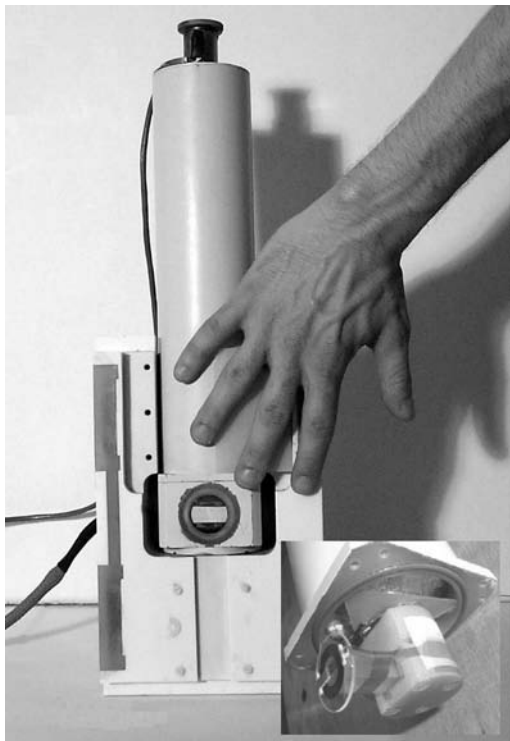


FIGURE 7 View of the cryogenic module connected to a 1.5T clinical magnetic resonance scanner.

Figure 8 presents a microscopic MR image of the skin on the calf of a healthy volunteer. Compared to Figures 1 and 2, the increased sensitivity reveals, for the first time, fine ramifications within the dermis, the interpretation of which is still under discussion. Figure 9 presents the exact delineation of a 500- μm thick basal cell carcinoma on the calf and adjacent normal skin.

Conclusion

Cryogenic probes connected to new clinical body scanners can achieve spatial resolution below 100 μm in each spatial direction within acquisition times of a few minutes, without the need for ultra-high static magnetic fields. We are confident that numerous clinical research centers could take advantage of such a solution to conduct advanced investigations in ophthalmology, joint diseases, superficial vessel diseases, and in healthy and diseased skin.

SUMMARY

New MR clinical systems nowadays allow skin images to be obtained at a sufficient spatial resolution. Even if MR spatial resolution is typically limited to 50 μm in depth of the skin, physico-chemical parameters are related to molecular interactions, justifying the classification of MR imaging as a molecular imaging technique. The still limited literature has already published new descriptions of

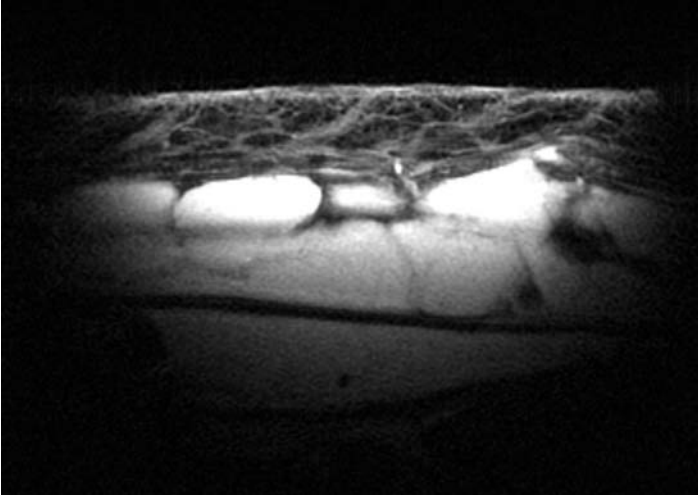


FIGURE 8 Magnetic resonance microimaging of the skin achieved on a clinical 1.5T system equipped with a dedicated high-temperature, superconducting coil detector. Owing to the increased sensitivity, fine ramifications within the dermis are revealed for the first time.

water behavior in the various skin layers, differentiating between water protons in the mobile and restricted pools, or by assessing quantitative measurements of water mobility. Some studies have already demonstrated the potential of MR imaging in healthy and diseased skin characterization and in the follow-up of pharmaceutical and cosmetic products.

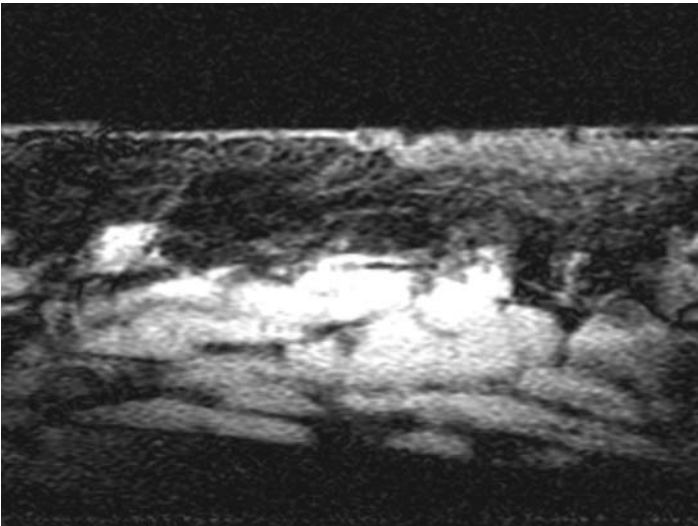


FIGURE 9 Magnetic resonance microimaging of a basal cell carcinoma on the calf obtained under the same conditions. An in-depth voxel size of $19\ \mu\text{m}$ allows accurate detection of the thin lesion.

If cryogenic skin probes could become commercially available in the near future, radiologists who already use dedicated MR detectors for the head and spine, for instance, should become familiar with the skin-specific instruments. This will herald a new era dedicated to clinical MR imaging: local microscopy in clinical scanners.

REFERENCES

1. Querleux B, Lévêque JL, de Rigal J. In vivo cross sectional ultrasonic imaging of human skin. *Dermatologica* 1988; 177:332–337.
2. Hoffmann K, Dirschka T, Stücker M, El-Gammal S, Altmeyer P. Assessment of actinic skin damage by 20-MHz sonography. *Photodermatol Photoimmunol Photomed* 1994; 10:97–101.
3. Turnbull D, Starkoski B, Harasiewicz K, et al. A 40–100 MHz B-scan ultrasound backscatter microscope for skin imaging. *Ultrasound Med Biol* 1995; 21:79–88.
4. El-Gammal S, El-Gammal C, Kaspar K, et al. Sonography of the skin at 100 MHz enables in vivo visualization of stratum corneum and viable epidermis in palmar skin and psoriatic plaques. *J Invest Dermatol* 1999; 113:821–829.
5. Baldeweck T, Cornillon C, Querleux B. In vivo characterization of wrinkles with high frequency ultrasound imaging, World Congress of Dermatology, satellite meeting on Skin in Health and Disease, Paris, 2002.
6. Corcuff P, Gonnord G, Pierard GE, Lévêque JL. In vivo confocal microscopy of human skin: a new design for cosmetology and dermatology. *Scanning* 1996; 18:351–355.
7. Rajadhyaksha M, Gonzalez S, Zavislan JM, Anderson RR, Webb RH. In vivo confocal scanning laser microscopy of human skin II: advances in instrumentation and comparison with histology. *J Invest Dermatol* 1999; 113:293–303.
8. Sauermann K, Clemann S, Jaspers S, et al. Age related changes of human skin investigated with histometric measurements by confocal laser scanning microscopy in vivo. *Skin Res Technol* 2002; 8:52–56.
9. Rajadhyaksha M, Gonzalez S, Zavislan JM. Detectability of contrast agents for confocal reflectance imaging of skin and microcirculation. *J Biomed Opt* 2004; 9:323–331.
10. Welzel J. Optical coherence tomography in dermatology: a review. *Skin Res Technol* 2001; 7:1–9.
11. Knüttel A, Bonev S, Knaak W. New method for evaluation of in vivo scattering and refractive index properties obtained with optical coherence tomography. *J Biomed Opt* 2004; 9:265–273.
12. Pierce MC, Strasswimmer J, Park BH, Cense B, de Boer JF. Advances in optical coherence tomography imaging for dermatology. *J Invest Dermatol* 2004; 123:458–463.
13. Caspers PJ, Lucassen GW, Carter EA, Bruining HA, Puppels GJ. In vivo confocal Raman microspectroscopy of the skin: noninvasive determination of molecular concentration profiles. *J Invest Dermatol* 2001; 116:434–442.
14. Chrit L, Hadjur C, Morel S, et al. In vivo chemical investigation of Human skin using a confocal Raman optic microprobe. *J Biomed Opt* 2005; 10(4):44007.
15. König K, Riemann I. High-resolution multiphoton tomography of human skin with sub-cellular spatial resolution and picosecond time resolution. *J Biomed Opt* 2003; 8:432–439.
16. Hanson KM, Clegg RM. Two-photon fluorescence imaging and reactive oxygen species detection within the epidermis. *Meth Mol Biol* 2005; 289:413–422.
17. Hyde JS, Jesmanowicz A, Kneeland JB. Surface coil for MR imaging of the skin. *Magn Reson Med* 1987; 5:456–461.
18. Querleux B, Yassine MM, Darrasse L, Saint-Jalmes H, Sauzade M, Lévêque JL. Magnetic resonance imaging of the skin: a comparison with the ultrasonic technique. *Bioeng Skin* 1988; 4:1–14.
19. Zemtsov A, Lorig R, Bergfield WF, Bailin PL, Ng TC. Magnetic resonance imaging of cutaneous melanocytic lesions. *J Dermatol Surg Oncol* 1989; 15:854–858.
20. Zemtsov A, Lorig R, Ng TC, et al. Magnetic resonance imaging of cutaneous neoplasms: clinicopathologic correlation. *J Dermatol Surg Oncol* 1991; 17:416–422.

21. Schwaighofer BW, Fruehwald FX, Pohl Markl H, Neuhold A, Wicke L, Landrum WL. MRI evaluation of pigmented skin tumors. Preliminary study. *Invest Radiol* 1989; 24:289–293.
22. Takahashi M, Kohda H. Diagnostic utility of magnetic resonance imaging in malignant melanoma. *J Am Acad Dermatol* 1992; 27:51–54.
23. Maurer J, Knollmann FD, Schlums D. Role of high-resolution magnetic resonance imaging for differentiating melanin-containing skin tumors. *Invest Radiol* 1995; 30:638.
24. Maurer J, Schlums D, Knollmann FD. Failure of gadopentetate dimeglumine-enhanced, high-resolution magnetic resonance imaging to differentiate among melanin-containing skin tumors. *Acad Radiol* 1996; 3:186–191.
25. Bittoun J, Saint-Jalmes H, Querleux B, et al. In vivo high-resolution MR imaging of the skin in a whole-body system at 1.5T. *Radiology* 1990; 176:457–460.
26. Querleux B, Jolivet O, Cornillon C, Bittoun J. Anatomy and physiology of subcutaneous adipose tissue by in vivo MR imaging and spectroscopy: relationships with sex and presence of cellulite. *Skin Res Technol* 2002; 8:118–124.
27. Idy-Peretti I, Bittoun J, Alliot FA, Richard S, Querleux B, Cluzan RV. Lymphedematous skin and subcutis: in vivo high resolution magnetic resonance imaging evaluation. *J Invest Dermatol* 1998; 110:101–106.
28. Goettmann S, Drapé JL, Idy-Peretti I, et al. Magnetic resonance imaging: a new tool in the diagnosis of tumours of the nail apparatus. *Br J Dermatol* 1994; 130:701–710.
29. Querleux B, Rizova E, Volkenstein P, Ghautier B, Revuz J, Bittoun J. In vivo characterization of skin lesions by high resolution magnetic resonance imaging. *J Invest Dermatol* 1997; 108:672.
30. Richard S, Querleux B, Bittoun J, et al. In vivo proton relaxation times analysis of the skin layers by magnetic resonance imaging. *J Invest Dermatol* 1991; 97:120–125.
31. Richard S, Querleux B, Bittoun J, et al. Characterization of the skin in vivo by high resolution magnetic resonance imaging: water behavior and age-related effects. *J Invest Dermatol* 1993; 100:705–709.
32. de Rigal J, Escoffier C, Querleux B, Faivre B, Agache P, Lévêque JL. Assessment of aging of the human skin by in vivo ultrasonic imaging. *J Invest Dermatol* 1989; 93:621–625.
33. Querleux B, Richard S, Bittoun J, et al. In vivo hydration profile in skin layers by high-resolution magnetic resonance imaging. *Skin Pharmacol* 1994; 7:210–216.
34. Salter DC, Hodgson RJ, Hall LD, Carpenter TA, Ablett S. Moisturization processes in living human skin studied by magnetic resonance imaging microscopy. *Int J Cosmet Sci* 1993; 15:219–226.
35. Mirrashed F, Sharp JC. In vivo morphological characterisation of skin by MRI micro-imaging methods. *Skin Res Technol* 2004; 10:149–160.
36. Mirrashed F, Sharp JC. In vivo quantitative analysis of the effect of hydration (immersion and Vaseline treatment) in skin layers using high-resolution MRI and magnetization transfer contrast. *Skin Res Technol* 2004; 10:14–22.
37. McDonald PJ, Akhmerov A, Backhouse LJ, Pitts S. Magnetic resonance profiling of human skin in vivo using GARField magnets. *J Pharm Sci* 2005; 94:1850–1860.
38. Hall AS, Alford NM, Button TW, Gilderdale DJ, Gehring KA, Young IR. Use of high temperature superconductor in a receiver coil for magnetic resonance imaging. *Magn Reson Med* 1991; 20:340–343.
39. Darrasse L, Ginefri JC. Perspectives with cryogenic RF probes in biomedical MRI. *Biochimie* 2003; 85:915–937.
40. Ginefri JC, Darrasse L, Crozat P. High-temperature superconducting surface coil for in vivo microimaging of the human skin. *Magn Reson Med* 2001; 45:376–382.
41. Liffers A, Vogt M, Ermert H. In vivo biomicroscopy of the skin with high-resolution magnetic resonance imaging and high frequency ultrasound. *Biomed Tech* 2003; 48: 130–134.

High-Resolution In Vivo Multiphoton Tomography of Skin

Karsten König

Fraunhofer Institute of Biomedical Technology (IBMT), St. Ingbert, and Faculty of Mechatronics and Physics, Saarland University, Saarbrücken, Germany

INTRODUCTION

In contrast to the standard technique of histopathology of mechanically-removed, sliced, and stained biopsies, noninvasive three-dimensional (3D) high-resolution imaging has the advantages of (i) providing a painless method without tissue removal, (ii) access to fast (immediate) information, (iii) the examination under natural physiological in vivo conditions, and (iv) the possibility of long-term studies on the same tissue area. Long-term studies are of particular interest for in vivo drug screening and the monitoring of therapeutic effects.

Nonoptical techniques such as X-ray, NMR, and ultrasound have been used to obtain 3D images from the human body. However, their resolution was found not to be sufficient to visualize cellular structures in tissues, in particular in skin.

By contrast, optical radiation can provide 3D skin images with cellular resolution. High-resolution optical methods with the capability of 3D optical sectioning include confocal microscopy (1) and optical coherence tomography (OCT). Confocal microscopy offers imaging with subcellular resolution based on fluorescence or backscattered light. However, standard one-photon confocal fluorescence microscopy is based on the application of exogenous fluorophores. There are limitations regarding (i) regulations to apply fluorescent probes to humans, (ii) fluorophore delivery and diffusion kinetics, (iii) the low-light penetration depth of the excitation light, and (iv) the use of spatial filters (pinholes). The information obtained by the backscattered signal is limited because changes in the intratissue refractive index only are detected. Functional imaging is not possible.

By contrast, multiphoton tomography as a novel multidimensional imaging technology with subcellular resolution has the advantage of exciting endogenous fluorophores and the extracellular matrix component collagen. Staining is not required. It is also not based on confocal detection and, therefore, does not require pinholes. Multiphoton tomography is performed with near-infrared (NIR) femto-second laser pulses. It enables functional imaging of deep-tissue cells and cellular compartments. In particular, the mitochondrial-reduced coenzyme NAD(P) H can be detected. NAD(P) H maps provide information on the intracellular redox state and modifications of the cellular metabolism.

Multiphoton tomography enables a detailed look into the skin. Even intratissue intracellular single mitochondria can be imaged. Melanocytes and macrophages can be detected as well the intracellular network of elastin fibres and collagen bundles. Pharmaceutical and cosmetical components can be traced and their spatially resolved diffusion kinetics determined. Noninvasive optical biopsies with subcellular resolution become reality.

STATE-OF-THE-ART SKIN IMAGING TECHNOLOGIES

Skin diagnostics is often based on visualization with the naked eye or with a magnifying glass. Also, ultraviolet (UV) light sources such as the Wood lamp are employed to gain information due to superficial fluorescence.

Dermatoscopy is based on the application of CCD cameras and image processing software. Typically, white light LEDs are used as light sources. The camera captures the backscattered light. In order to reduce the influence of direct reflected light (Fresnel reflection) from the surface, crossed polarizers can be employed. Light reflected from the skin surface is polarized when using polarized incident light in contrast to scattered nonpolarized light. However, the signal from deep-tissue areas and the resolution of the two-dimensional (2D) image are poor.

There is also no high-resolution 3D imaging possible when using incident lamp light at different wavelengths. Although red and NIR radiation has a higher light penetration depth compared to UV and blue light, 3D imaging of turbid media such as skin requires confocal setups.

Confocal laser scanning microscopes are based on highly focused laser radiation, typically in the blue/green spectral region, as well as on a confocal detection unit, which consists of a pinhole in front of the photodetector [photomultiplier (PMT)]. The pinhole is required to suppress out-of-focus photons. Confocal microscopes have been used to perform optical skin sectioning mainly in the reflection mode (2–4), which does not require skin staining. The confocal laser scanning system VivaScope[®] (Lucid Inc.) for skin imaging is on the market. It employs a NIR cw 16 mW laser diode at 830 nm and a resonance scanner combined with numerical aperture (NA) 0.9 focusing optics. Cellular membranes, nuclei, and melanosomes can be imaged. The resolution is about 5 μm .

OCT is also based on backscattered light. A light source with low coherence length (e.g., superluminescent diodes or ultrashort lasers) is required. The signal is based on the interference of reference light with the backscattered light from phase transitions within the skin. Sweat glands and other relatively large features can be visualized but not single cells. The quality of the current OCT images is poor compared to the microscope images of the dermatopathologist monitoring the 7 μm thick histological sections on a cellular level.

Figure 1 shows state-of-the-art images from a nevus of a 37-year-old volunteer obtained with dermatoscopy, ultrasound, OCT, and confocal reflection microscopy. In particular, a typical 2D image obtained with the color CCD camera and the white LED light source of the commercial dermoscope FotoFinder[®] is shown. The ultrasound image was obtained from a standard clinical 20 MHz system. The OCT system based on a SLD was designed by the ISIS Optronics GmbH for skin imaging. Confocal images were obtained with the system VivaScope. As demonstrated, images with subcellular resolution can only be obtained with the confocal reflection system.

Clinical confocal fluorescence microscopy is possible with systems provided by the companies Optiscan/Pentax. However, the use of this system with a typical excitation wavelength of 488 nm requires the application of the exogenous, clinically proven fluorophore FITC.

The alternative to the use of exogenous fluorescent probes is the detection of the autofluorescence (5). Endogenous fluorophores such as flavins and NAD(P)H coenzymes, metal-free porphyrins, collagen, and elastin show a weak autofluorescence. Interestingly, only the reduced form of the pyridine coenzymes NADH and

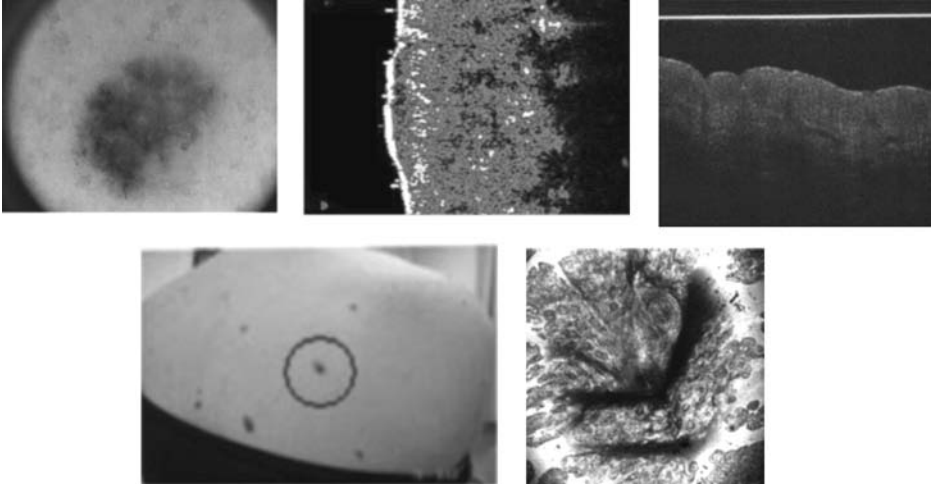


FIGURE 1 (See color insert) State-of-the-art images from a human nevus. The images present back-scattered white light using the dermatoscope FotoFinder[®], ultrasound signals from a 20 MHz source, optical coherence signals using a superluminescent near infrared diode, and an optical skin section based on backscattered 830 nm photons detected by the confocal system VivaScope.[®]

NADPH fluoresce in contrast to the oxidized version NAD and NADP. These coenzymes act, therefore, as sensitive bioindicators of the intracellular redox status and as indicators of the cellular metabolism. This allows functional imaging. The fluorescence detection is a technique of high sensitivity because fluorescence photons occur at a different wavelength than the excitation photons and single fluorescence photons can be counted (single photon counting).

However, conventional (one-photon) autofluorescence excitation with UV and blue/green radiation has the disadvantages of low light penetration depth, out-of-focus photodamage, and out-of-focus photobleaching. In addition, multiple scattering reduces the information obtained in the confocal detection mode due to those scattered out-of-focus photons, which are still able to transmit through the pinhole. Furthermore, the photon collection efficiency is relatively low due to the spatial filtering by the pinhole. So far, in vivo confocal autofluorescence images were obtained at depths down to 85 μm using excitation wavelengths at 365 and 488 nm (5).

These disadvantages can be overcome by multiphoton fluorophore excitation using nonconfocal multiphoton microscopy based on NIR femtosecond laser pulses and high NA objectives (6). NIR radiation in the range of 700 to 1200 nm is used because the one-photon absorption and scattering coefficients of skin are low in this spectral range and the light penetration depth high compared to UV/visible radiation.

PRINCIPLE OF MULTIPHOTON TOMOGRAPHY

The low absorption coefficient is the reason that transient NIR intensities even as high as GW/cm^2 can be applied without thermal damage to tissues and

fluorophores. This was proven by 24-hour NIR laser exposure of hamster embryos which survived in contrast to visible laser light.

Such high light intensities are required to realize the process of multiphoton absorption, which was predicted by Maria Goepfert-Meyer in her Ph.D. thesis in 1931. In the case of two-photon absorption, two NIR photons are absorbed simultaneously. Each photon provides half of the energy, which is normally required to excite the molecule into a higher electronic state from which fluorescence may occur. In three-photon absorption, three photons are absorbed. The high-NA objective is used to realize the high intensity within a tiny focal volume (Fig. 2). Only in this subfemtoliter volume occurs absorption and fluorescence excitation.

Using fast galvoscaner and a piezodriven objective, the position of the multiphoton excitation volume can be changed in all three directions with minimum steps in the submicron range. This enables deep tissue optical sectioning with sub-cellular resolution. Two-photon and three-photon excited fluorescence can be detected. By means of pinhole-free detectors in the de-scanned mode (fluorescence not transmitted through the scanners), fluorescence imaging at high photon collection efficiency can be realized. For this feature, image processing has to be performed with signals as function of the pixel clock, line sync, and frame sync of the x/y-scanner and of the voltage of the piezosystem (z-position).

Blue/green emitting fluorophores such as NAD(P) H, which normally require UV excitation, can be imaged even in the dermis. It was predicted that diffraction-limited image resolution with a resolution in the range of submicrometers

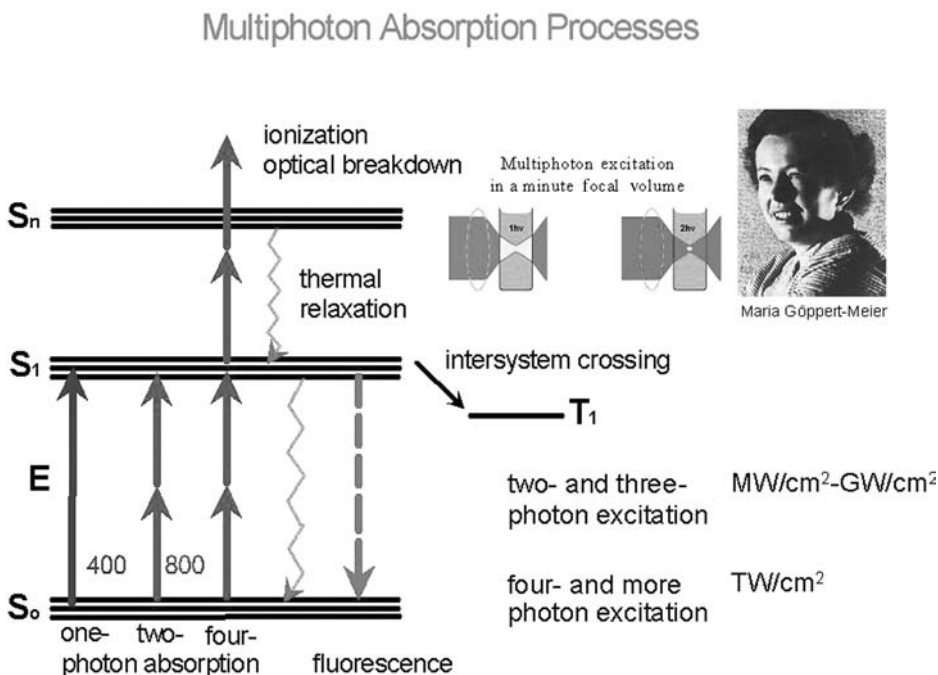


FIGURE 2 (See color insert) Principle of multiphoton processes. Fluorescence in the blue, green, yellow, and red spectral range can be excited via a two-photon absorption process.

Fluorophore	Emission (nm)	τ (ns)	
NAD(P)H	460	0.3	→
NAD(P)H-protein	440	2.0-2.3	
Flavines	530	5.2	
Elastin	420-460	0.3/2	→ SHG
Collagen	420-460	0.3/2	
	$\lambda/2$ (360 - 480)	0	
Melanin	440, 520, 575	0.1/1.9/8	
PPIX	635, 710	10-12	

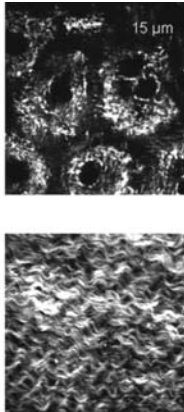


FIGURE 3 Multiphoton tomography enables the deep-tissue imaging of a variety of fluorescent bio-molecules. The emission peaks and fluorescence lifetimes are listed. The upper image shows the reduced coenzyme NAD(P)H in the mitochondria of deep-tissue cells. The nonfluorescent nuclei appear as black spheres/ellipsoids. Collagen can be detected by second harmonic generation at half the incident laser wavelength (*lower image*).

in the lateral direction and 1 to 2 μm in the axial resolution can be maintained for skin tissue of thickness up to 500 μm (7).

Using a two-photon femtosecond laser scanning microscope, Masters et al. (8) detected the autofluorescence of human skin in depth down to 200 μm . Optical sectioning of animal and human skin by NIR femtosecond laser autofluorescence microscopy has been reported, e.g., by So and Kim (9), Masters et al. (10), Hendriks and Lucassen (11), König et al. (12–15), and Peuckert et al. (16). Interestingly, the pigment melanin shows a luminescence when excited with NIR femtosecond laser pulses (17). Figure 3 lists a variety of important endogenous skin fluorophores that can be excited with NIR femtosecond lasers.

Microscopes are not suitable for imaging of human skin. Here we report on a novel femtosecond laser-scanning device called *DermaInspect* for high-resolution multiphoton tomography of normal human skin. These tomographs are in clinical use to detect dermatological disorders and are employed for in situ drug screening (18,19).

The system *DermaInspect*[®] enables imaging of endogenous and exogenous fluorophores with submicron resolution by the detection of the fluorescence intensity as well as of the fluorescence decay kinetics with a resolution of about 200 psec. This additional feature allows the calculation of the mean fluorescence lifetime per pixel and the construction of a fluorescence lifetime image (FLIM). The fluorescence lifetime t is a characteristic parameter of the fluorescent molecule and its microenvironment. For example, the fluorescence lifetime of flavomononucleotide is 5.2 nsec and of protoporphyrin IX from 10 to 12 nsec. Free NAD(P)H has a lifetime in the picosecond range whereas a NADH-protein complex has a typical value of 2.2 nsec (Fig. 3). The sensitive detection of even single fluorescence photons with the system *DermaInspect* is possible due to the technique of time-correlated single photon counting (TCSPC) and fast PMTs.

Besides the monitoring of endogenous and exogenous (dyes, pharmaceutical, and cosmetic products) fluorophores, the biomolecule collagen can be selectively imaged by a process called second harmonic generation (SHG).

SHG occurs in certain nonsymmetric molecules such as collagen when excited with intense ultrashort laser pulses. It results in the formation of light at a wavelength at exactly half the excitation wavelength. That means, e.g., blue light at 410 nm is emitted from collagen when exposed to 820 nm femtosecond laser pulses. The SHG signal from collagen can be selectively detected by means of spectral filters as well as by TCSPC.

THE MULTIPHOTON TOMOGRAPH DERMAINSPECT

A photograph and a scheme of the CE-certified *in vivo* laser imaging system DermaInspect (JenLab GmbH, Jena, Germany) (20) is depicted in Figure 4. The system with a total dimension of $75 \times 120 \times 140 \text{ cm}^3$ is mounted on a transportable workstation. It is considered as class 1M device according to the new European laser safety regulations and consists of the following three major modules.

1. Compact, turn-key, solid-state, mode-locked 80 MHz titanium:sapphire laser (MaiTai, Spectra Physics or Chameleon, Coherent) with a typical tuning range from 730 to 960 nm, a maximum laser output of about 1.5 W and an output pulse width of about 75 fsec.
2. Scanning module including fast x,y galvoscaner, a motorized beam attenuator, a laser safety shutter, a trigger module for the TCSPC unit, and piezodriven 40 times focusing optics with NA 1.3, two PMTs or PMT arrays in combination with a polychromator, as well as an interface with an $0.17 \mu\text{m}$ thick glass window. Filters in front of the detector avoid the detection of scattered laser light and isolate the fluorescence signal from the SHG signal.
3. Control module with power supplies, scan controller, and image-processing hardware. The software includes features such as on-line control of laser



FIGURE 4 Photograph of the multiphoton imaging tool DermaInspect 110[®] for four-dimensional autofluorescence and second harmonic generation imaging with intracellular spatial resolution (around $1 \mu\text{m}$) and 250 psec temporal resolution.

power and step-motor driven fine power adjustment according to tissue depth, piezodriven modification of the intratissue z-position of the laser focus with an accuracy of less than 100 nm, scanning of region of interests, line scan as well as single-point-illumination. For FLIM measurements, a PC with TCSPC board and an additional image processing system is required.

So far, DermalInspect is the only multiphoton imaging system worldwide for in vivo diagnostics in clinics.

Test Measurements

Test measurements on biopsies and tissue phantoms have been performed to determine the spatial and temporal resolution of the system, the image quality, and the type of information obtained from multiphoton excited autofluorescence of skin tissues with dermatological disorders.

Biopsies were obtained from patients with a variety of diseases including psoriasis, nevi, melanoma, and dermatomycosis. For transportation and safe measurement, the samples were introduced into sterile biopsy chambers (MiniCeM-biopsy[®], JenLab GmbH) consisting of silicon gaskets with 4 mm holes and 0.17 μm thick glass windows on both sides for imaging with high-NA objectives (Fig. 2). Isotonic NaCl solution was used to avoid drying. The measurements occurred within one hour after excision.

Tissue phantoms for microscopy based on sterile microchambers with 0.17 μm thick glass windows filled with 1% low-melting-agarose, Intralipid[®] 10 scattering particles and fluorescent microspheres of different sizes and of different fluorescence spectra have been used to characterize the spatial and temporal resolution of the system.

The tissue phantoms have been used for proper beam alignment and to test the imaging system by the determination of point-spread-functions (PSF) in dependence on intratissue depth of the excitation volume and the fluorescence wavelength as well as to probe the temporal resolution. A lateral PSF width from 0.4 to 0.6 μm and an axial PSF from 1.2 to 2.0 μm during optical sectioning between 0 and 100 μm depth in spite of scattering material (0–1%) and a temporal resolution of about 250 psec was determined.

MULTIPHOTON SECTIONING OF HUMAN SKIN

For 3D measurements, the accurate location of the skin surface stratum corneum (SC) has to be determined. Typically, that alignment was performed during fast scanning (one second per frame of $512 \times 512 = 262144$ pixels), modification of the z-position, and by the simultaneous detection of the intense autofluorescence of corresponds to a low pulse energy of 25 pJ. When the boundary glass/water/skin surface was determined, the value of the z-position of the objective was defined as zero.

In order to obtain high-contrast images (high signal-to-noise ratio) of intratissue optical sections, the scan speed was reduced down to eight seconds per frame, which corresponds to a mean beam dwell time per pixel of 30 μsec . The z-position was varied in steps of 1, 5, or 10 μm to a deeper position. For in-depth imaging the incident laser power was increased. When imaging at a tissue depth of 100 μm at 750 nm laser excitation, typically the incident mean laser power was chosen to be 20 mW.

Interestingly, high-resolution images could be obtained through the whole epidermis and even within dermal structures. As depicted in Figure 5, intratissue cell by cell can be clearly monitored with the system *DermaInspect*. Not only the morphology of each epidermal cell can be imaged, but also intracellular structures can be clearly seen. The exact position of the nonfluorescent nucleus can be imaged, cell divisions monitored, and even single fluorescent intratissue mitochondria visualized when using the optical zoom of the system.

Optical sectioning of the dermis provides the possibility to monitor single elastin fibers and collagen structures. Typically we monitor down to a depth of $200\ \mu\text{m}$ which corresponds to the working distance of the focusing optics.

The SC with its fluorescent component keratin exhibits an intense autofluorescence when excited within the tuning range of the laser. The excitation spectra vary between different locations within this cornified tissue layer. The cell borders of the hexagonal-shaped corneocytes with a mean cell diameter of $36 \pm 15\ \mu\text{m}$ induce often the strongest fluorescence of the tissue. Note that the fluorescence pattern on the skin surface is interrupted by nonfluorescent areas with a thickness of up to $100\ \mu\text{m}$ due to epidermal ridges. However, the fluorescent borders (corneocytes) of these incisions

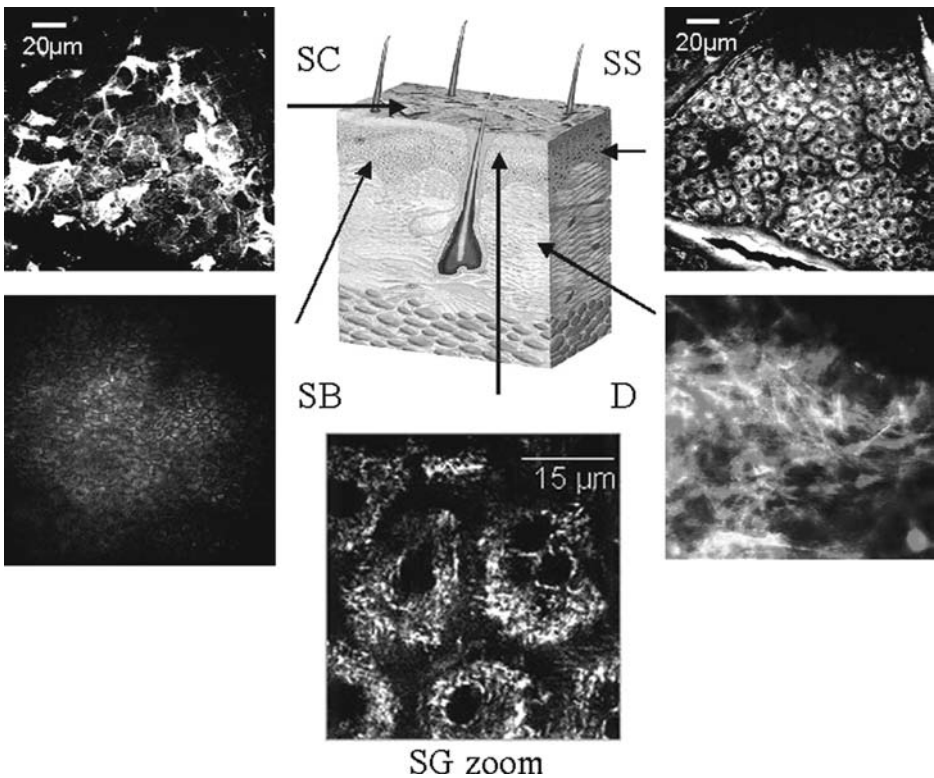


FIGURE 5 (See color insert) High-resolution in vivo multiphoton autofluorescence/SHG images of different skin layers. The major fluorophores are keratin in the stratum corneum, NAD(P)H in the stratum granulosum and stratum spinosum, melanin in the stratum basale, and elastin in the dermis. Collagen (red false color) can be detected by SHG. Abbreviations: SHG, second harmonic generation; SC, stratum corneum; SS, stratum spinosum.

were responsible for highly luminescent areas down to 50 μm and more. Hairs appeared also as highly fluorescent structures. The typical SC thickness in the lower forearm was found to be 10 to 15 μm (female volunteers aged 30–40) and 15 to 20 μm (male persons aged around 40).

The transition to the stratum granulosum can be detected by the occurrence of living cells with a different cell shape, a fluorescent cytoplasm, and nonfluorescent nuclei. In general, the autofluorescence of this tissue layer appeared of low contrast and more diffuse due to the coexistence of living and dead fluorescent cells. A typical thickness of about 10 μm for this tissue layer was found.

Within the stratum spinosum (SS), the single cells and cellular compartments can be clearly seen by strong fluorescent granula in the cytoplasm and the borders of the large round nonfluorescent nuclei. The cell diameter decreases with increasing tissue depth and was found to be in the upper part of this layer $26 \pm 3 \mu\text{m}$ and in the deepest cell layer $16 \pm 4 \mu\text{m}$. Also, the ratio between the volume of the cytoplasm to the volume of the nuclei decreases. Sometimes cells with two nuclei can be found.

The single innermost cell layer of the epidermis, the stratum basale, can be determined by cuboidal cells with higher fluorescence intensity than living cells in the upper layers. Very likely are these cells the basal cells, which differentiate and migrate towards the skin surface. Within these cells, strong fluorescent granula in the upper part of the perinuclear region have been detected. The basal cells have the lowest diameter of the epidermal cells with $9 \pm 1 \mu\text{m}$ as well as the lowest cytoplasm volume/nuclei volume ratio. During optical sectioning, the basal cells occur as a cluster of circular shape around the tip of a papilla.

The transition between epidermis and corium (cutis) is determined by the papillae distribution. Typically this junction can be found in a depth of 55 to 70 μm and 70 to 100 μm in 40-year-old females and males, respectively. Connective tissue, in particular single fluorescent long elastin fibers with a thickness of less than 1 μm , can be clearly visualized by autofluorescence. Collagen structures also exhibit an autofluorescence; however, the SHG signal is stronger when using laser wavelength larger than 800 nm.

IN VIVO FLUORESCENCE LIFETIME IMAGING

In addition to the imaging of autofluorescence intensity, fluorescence decay kinetics per pixel can be measured with the DermaInspect. In this case, the arrival time of the fluorescence photon on the detector is measured with respect to the femtosecond excitation pulse. Typically, 128 time channels are used covering 50 psec per channel. Working with typical photon count numbers of 50,000 per second, fast time-correlated fluorescence measurements with a few microsecond beam dwell time per pixel and less than 25-second scan times per frame, respectively, can be realized. Fluorescence decay curves from each pixel are obtained. Using special fitting procedures, mono- and biexponential curves with the parameters amplitudes A_1 and A_2 (%) and fluorescence lifetime t_1 , t_2 (nsec) as well as a mean fluorescence lifetime t can be calculated. A false-color FLIM are obtained by depicting the spatial distribution of t . From these large amounts of data two major fluorescence lifetime components in all skin layers have been determined. The shorter one has a time within the response time of the detector and is likely to the SHG signal in the UV and blue spectral range and a small amount of scattered light, which was able to transmit the filters. The long component is due to

autofluorescence. Its lifetime has been calculated and depicted as false-color FLIM. Typically the fluorescence lifetime of an intratissue cell was found to be on the order of 1.8 to 2.4 nsec. Figure 6 demonstrates two optical sections out of a stack of 3D *t*-maps. One image shows the autofluorescence lifetime image of the SS. The histogram of the fluorescence lifetime distribution (right upper corner of the image) shows a maximum at about 2 nsec. The lifetime image is dominated by green and blue pixels due to the chosen false color table where green corresponds from 1.7 to 2.3 nsec. A particular decay curve of an intratissue mitochondrion is shown in the lower part. Deconvolution resulted in the calculation of a long-lived component with a mean fluorescence lifetime of 2.1 nsec which corresponds to NAD(P)H-protein complexes.

In contrast, the lower image taken in 80 μm tissue depth within upper dermis show maxima of about 1.8 nsec and less than 100 psec. The single fluorescence decay curve exhibits a major component in the less than 100 psec region due to the generation of SHG of collagen.

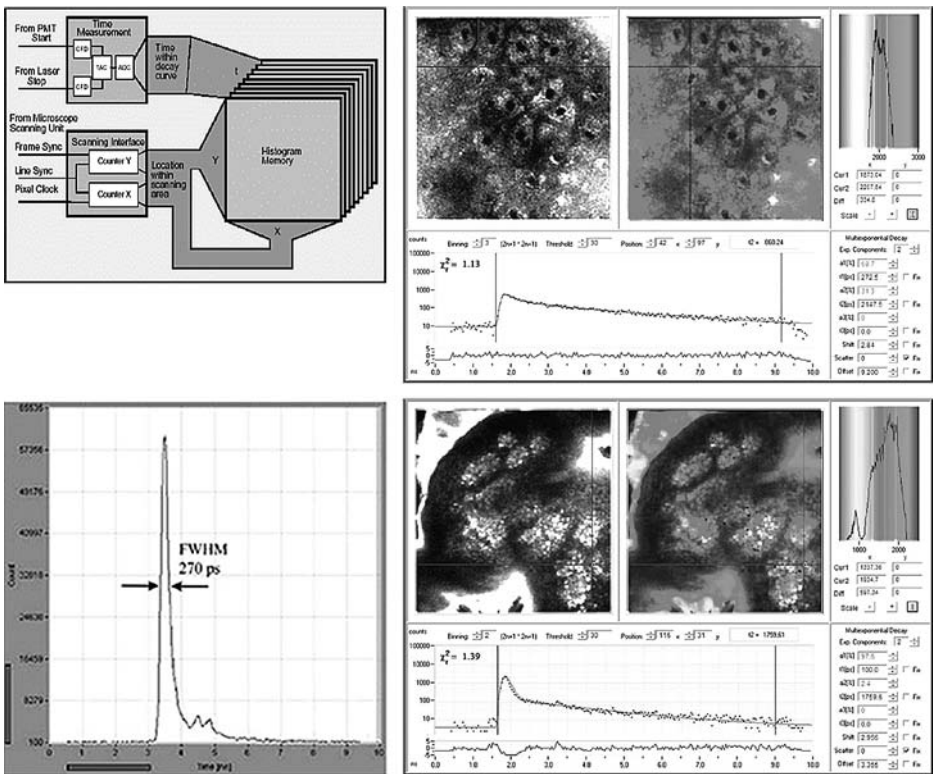


FIGURE 6 (See color insert) In vivo luminescence lifetime images of the stratum spinosum (right upper part) and the dermis (right lower part). The lifetime in the dermis is determined by the immediate second harmonic generation signal. The left part shows the principle of time-correlated single photon counting where the histogram reflects the arrival times of the photons. The temporal resolution of the system is also depicted.

These *in vivo* studies on normal human skin demonstrate the capability of four-dimensional autofluorescence imaging in deep tissue with subcellular resolution in the range of 1 μm and picosecond temporal resolution. TCS-SPS enables the measurements of intratissue fluorescence decay kinetics and the calculation of mean fluorescence lifetimes. In addition, it supports the detection of SHG in the tissue depth by the detection of a short luminescence component limited by the temporal resolution of the detector. The process of SHG occurs immediately in contrast to fluorescence with its typical lifetime in the nanosecond range.

FLIM imaging provides information on the type of fluorophore and is in particular useful when discriminating between pharmaceutical/cosmetical agents and endogenous fluorophores.

EARLY DETECTION OF MELANOMA

We monitored a variety of dermatological disorders such as psoriasis, trichophytosis, and skin allergies. However, of major interest is the detection of cancer cells, in particular within pigmented areas.

So far, about 250 patients with Caucasian skin and suspicious nevi were scanned with the *in vivo* system *DermaInspect* at the Department of Dermatology at the University of Jena.

We found that NIR femtosecond laser pulses can be used to image the intense fluorescence of melanin. Pigmented and nonpigmented areas can be clearly differentiated. In the case of a melanocytic compound nevi the autofluorescence intensity was significantly increased.

In part, cells involved in inflammatory processes have been detected. These monocytes and granulocytes were found to be larger than the surrounding corneocytes and showed a kidney-shaped nucleus.

The multiphoton images of melanoma areas show significant differences in the tissue architecture as well as in the cell morphologies of the epidermal layers compared to normal skin. Often, the upper epidermal layers were interrupted with

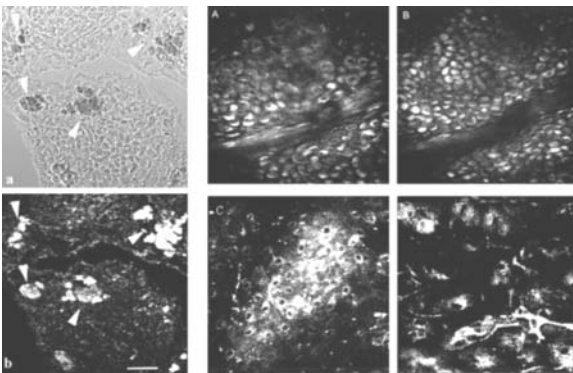


FIGURE 7 Multiphoton autofluorescence images depicting melanin. The left images of a cryosection demonstrate the strong luminescence from the pigment melanin. The right upper two images represent multiphoton sections from normal nevi, whereas the lower images demonstrate *in vivo* optical sections of patients with malignant melanoma. Note the appearance of dendritic cells.

bright luminescent smaller cells, large intercellular spaces, and the occurrence of luminescent melanocytes (Fig. 7).

Our multiphoton data were confirmed by histological analysis after taking biopsies.

However, further studies on a larger number of patients are required to draw final conclusions regarding the use of multiphoton tomography as a novel method in early melanoma diagnostics.

IN SITU DRUG SCREENING

An interesting application field of multiphoton tomographs is *in vivo*, *in situ* drug screening. The diffusion behavior of topical applied cosmetic and pharmaceutical compounds, their intratissue accumulation, and interaction with the skin cells can be studied. Figure 8 demonstrates two examples. In the first case, aqueous solutions with different ionic strength due to specific NaCl concentration were applied for several hours to the forearms of volunteers. Although the solution did not show any autofluorescence, the effect of swelling and shrinking in different skin layers could be clearly visualized. In addition, modifications of the cellular autofluorescence have been monitored.

In another example, the effect of a specific novel cream for cosmetics has been tested. Active compounds of the formula exhibited fluorescence. Due to this signal, the penetration behaviour of the cream could be visualized. In dependence on the

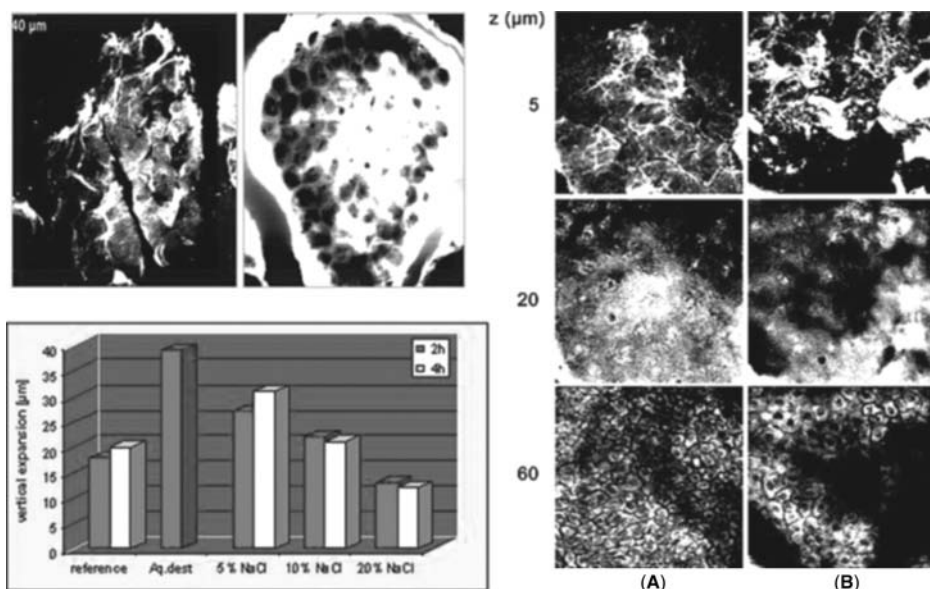


FIGURE 8 Multiphoton tomography for pharmaceutical and cosmetic research. The left part demonstrates the effect of aqueous solutions of different ionic strength. Swelling and shrinking effects can be monitored *in vivo* over a long time period. The right part shows examples of *in situ* drug screening. (A) Normal skin at different tissue depths was compared with (B) skin after cream administration.

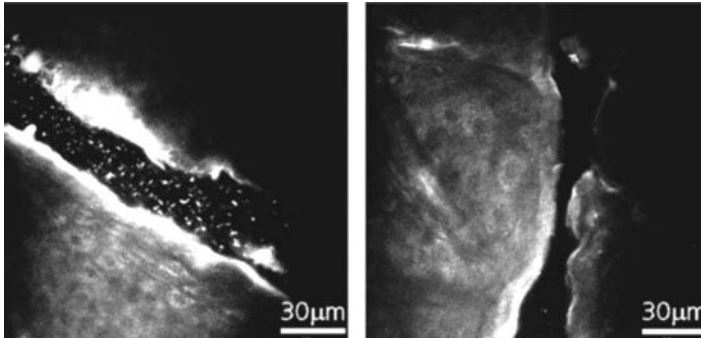


FIGURE 9 Multiphoton sectioning was performed to study the function of the drug barrier *stratum corneum* in the case of the topical administration of fluorescent nanobeads. The beads were not able to enter the deeper epidermis but accumulate in the epidermal ridges.

administration time, the effect of the cream on the extracellular matrix components elastin and collagen has been monitored (19).

LASER SAFETY ASPECTS

NIR femtosecond laser pulses have been employed for vital cell microscopy since 1990. In a study of the University of Wisconsin, hamster embryos have been exposed for 24 hours to the laser sources of scanning microscopes. Only the group of NIR femtosecond laser irradiated embryos survived and developed normally after reimplantation into the mother animal (21).

Nevertheless, in dependence on intensity, wavelength, and pulse length, NIR femtosecond laser pulses can induce damaging effects. A slow two-photon destructive photochemical effect has been determined in cell cloning assays using Chinese hamster ovary cells. When enhancing the transient light intensity to TW/cm^2 , optical breakdown and plasma formation may occur. In this case, laser-scanned cells will be destroyed immediately (22).

Therefore, the mean laser power at the target should not exceed certain values. The DermaInspect system has a motor-driven feedback system, which adjusts the beam power in dependence on the position of the intratissue multiphoton excitation volume. Typically, the mean incident power is about 2 mW when imaging the superficial skin layers, which corresponds to a low laser pulse energy of 25 pJ only, and up to 30 mW when imaging in a tissue depth of 100 μm . Typically the beam dwell time is on the order of 10 μsec per pixel. Considering an in situ pulse width of 250 fsec, the total exposure time per pixel is nanoseconds only.

DNA damage studies on the influence of NIR femtosecond laser pulses of the DermaInspect system compared to UVA exposure of standard light sources have been performed. Shortly after exposure, the exposed skin was examined immunohistochemically and assayed for structural DNA modifications, in particular, for the formation of cyclobutane pyridine dimers (CNP). The studies showed that a typical multiphoton measurement is neither able to induce erythema nor to produce a significant amount of CNP compared to UV exposed skin (data submitted for publication).

Therefore, NIR femtosecond laser imaging can be considered as safe diagnostic tool when respecting certain laser power limitations. There is also no danger to destructive eye exposure due to the short 200 μm working distance of the NA 1.3 focusing optics of the system *DermaInspect*. According to the European safety regulations, the system was, therefore, certified by the authorities as class 1M device.

OUTLOOK

Multiphoton imaging provides deep skin images of superior spatial resolution compared to ultrasound, X ray, MRT, OCT, and light reflection. It also enables sensitive imaging of mitochondrial coenzymes, melanin clusters, and single elastin fibers and collagen structures.

The *DermaInspect* laser system is the first multiphoton imaging system in clinical use. It provides in vivo images from inside the intact skin never seen before with a lateral resolution comparable with the conventional 2-D microscope of the dermatopathologist. In contrast to the 7 μm thick, stained, fixed histological sections of a mechanically removed biopsy, multiphoton imaging enables immediate 3-D optical in vivo biopsies under native physiological conditions without destructive procedures and staining. For the first time, fluorescent coenzymes and melanin clusters can be monitored in deep skin tissue with intracellular resolution. In addition to the detection of spatially resolved fluorescence intensities, fluorescence lifetime imaging and collagen detection by SHG monitoring can be performed. These additional features provide completely new parameters for optical diagnostics.

Multiphoton tomography has the potential to provide novel noninvasive high-resolution diagnostic tools for the early diagnosis of skin cancer and other dermatological disorders, the long-term monitoring of therapeutical effects on a cellular level, and the in situ intratissue screening of pharmaceutical and cosmetrical agents.

ACKNOWLEDGMENTS

The author wish to thank Dr. I. Riemann (Fraunhofer IBMT), Dr. F. Stracke (IBMT), A. Ehlers (IBMT), E. Dimitrov (FSU Jena), Dr. M. Kaatz (FSU), Dr. J. Fluhr (FSU), Prof. P. Elsner (FSU), and R. Bueckle (JenLab GmbH) for their helpful contributions to realize first in vivo multiphoton studies.

In part, financial support was obtained by the European Commission (MED-PHOT) and by the German Ministry of Education and Research (BMBT, Grant No. 01EZ0331).

REFERENCES

1. Pawley JB, ed. Handbook of Biological Confocal Microscopy. New York and London: Plenum Press, 1995.
2. Rajadhyaksha M, Gonzalez S, Zavislan JM, Anderson RR, Webb RH. In vivo confocal laser scanning laser microscopy of human skin II: advances in instrumentation and comparison with histology. *J Invest Dermatol* 1999; 113:293–303.
3. Rajadhyaksha M, Rox Anderson R, Webb RH. Video-rate confocal scanning laser microscope for imaging human tissues in vivo. *Appl Opt* 1999; 38:2105–2115.

4. Peuckert C, Riemann I, Wollina U, König K. Remission microscopy with NIR femtosecond laser pulses for 3D in vivo imaging of human skin. *Cell Mol Biol* 2000; 46 (abstract 117).
5. Masters BR. Three-dimensional confocal microscopy of human skin in vivo: autofluorescence of human skin. *Bioimages* 1996; 4:13–19.
6. Denk W, Strickler JH, Webb WW. Two-photon laser scanning microscopy. *Science* 1990; 248:73–76.
7. Deng X, Gan X, Gu M. Multiphoton fluorescence microscopic imaging through double-layer turbid tissue media. *J Appl Phys* 2002; 91:4659–4665.
8. Masters BR, So PTC, Gratton E. Multiphoton excitation fluorescence microscopy and spectroscopy of in vivo human skin. *Biophys J* 1997; 72:2405–2412.
9. So PTC, Kim H. Two-photon deep tissue ex vivo imaging of mouse dermal and subcutaneous structures. *Opt Express* 1998; 3:339–350.
10. Masters BR, So PTC, Gratton E. Multiphoton excitation microscopy of in vivo human skin. *Ann NY Acad Sci* 1998; 838:58–67.
11. Hendriks RFM, Lucassen GW. Two photon fluorescence microscopy of in vivo human skin. *SPIE* 1999; 4164.
12. König K. Multiphoton Microscopy in Life Sciences. *J Microsc* 2000; 200:83–104.
13. König K. Laser tweezers and multiphoton microscopes in life sciences. *Histochem Cell Biol* 2000; 114:79–92.
14. König K, Peuckert C, Riemann I, Wollina U. Non-invasive 3D optical biopsy of human skin with NIR-femtosecond laser pulses for diagnosis of dermatological disorders. *Cell Mol Biol* 2000; 46 (abstract 117).
15. König K, Wollina U, Riemann I, et al. Optical tomography of human skin with subcellular spatial and picosecond time resolution using near infrared femtosecond laser pulses. *SPIE* 2002; 4620:90–201.
16. Peuckert C, Riemann I, König K. Two photon induced autofluorescence of in vivo human skin with femtosecond laser pulses—a novel imaging tool of high spatial, spectral and temporal resolution. *Cell Mol Biol* 2000; 46 (abstract 179).
17. Teuchner K, Freyer W, Leupold D, et al. Femtosecond two-photon excited fluorescence of melanin. *Photochem Photobiol* 1999; 70:146–151.
18. König K, Riemann I. High-resolution multiphoton tomography of human skin with subcellular spatial resolution and picosecond time resolution. *J Biomed Opt* 2003; 8:450–459.
19. König K, Ehlers A, Stracke F, Riemann I. In vivo drug screening in human skin using femtosecond laser multiphoton tomography. *Skin Pharmacol Physiol*. In press.
20. www.jenlab.de.
21. Squirrel JM, Wokosin DL, White JG, Bavister BD. Long-term two-photon fluorescence imaging of mammalian embryos without compromising vitality. *Nature Biotech* 1999; 17:763–767.
22. König K. Cellular response to laser radiation in fluorescence microscopes. In: Periasamy A, ed. *Methods in Cellular Imaging*. Oxford University Press, 2001:236–251.

Julia Welzel

Department of Dermatology, General Hospital Augsburg, Augsburg, Germany

INTRODUCTION

Histological examination of biopsies is still the gold standard of morphological investigation of the skin. Despite its invasive character, histology has several disadvantages. The biopsy technique causes artifacts of the tissue, i.e., squeezing, shrinkage, collapse of vessels, and dehydration. The preparation of the probe is time consuming and expensive. It represents a snapshot of the reality and is never repeatable at the same site. Hence, there is a demand for a noninvasive high-resolution imaging technique to improve diagnosis and control of therapeutic efficacy. In addition, an *in vivo* method bears the potential to give a new insight into dynamic processes, which will never be detectable by histology.

In the last decade, advances in light sources and optical fibers resulted in the development of optical imaging technologies for high-resolution visualization of the tissue. An interferometric method, the so-called optical coherence tomography (OCT), has been established as a diagnostic method in several medical fields (1–4). In the cross-sectional OCT images, the axial and lateral resolution of less than 10 μm allows the detection of tissue layers and single cells.

TECHNIQUE

The principle of OCT is based on Michelson interferometry. A light beam is divided into a reference and a probe beam by a beam splitter. The reference beam is reflected by a mirror and the probe beam is backscattered by the tissue. Both beams are recombined again and interfere only if they match within the coherence length. For OCT, broad-band light sources with a short coherence length are used. Assumed that the path length of the reference beam is defined, the interference modulation provides information on the optical properties of the tissue sample. Thus, the coherence length determines the axial resolution. By lateral scanning, two-dimensional images can be composed of the single signals. The lateral resolution is mainly determined by the focusing of the lens system and by the step width. The penetration depth of the signal in the tissue is limited by several factors. The power of the light source as well as the wavelength is important. Light propagation is influenced by the medium. Soft tissue has a refractive index of about 1.33 similar to water (5). Coupling of the probe beam to the skin using water or gel reduces the light reflection of the surface by index matching. The propagation of light inside the tissue is influenced by both scattering and absorption, whereas the latter is much lower in the near infrared. Therefore, the slope of the exponential light attenuation is proportional to the scattering coefficient [μ_s], which is the probability of a photon being backscattered per centimeter tissue depth. Light sources in the near infrared, the so-called diagnostic window, are preferred because both absorption by hemoglobin, melanin, and water and scattering are relatively low in this

range (6,7). For OCT, compact superluminescent diodes or femtosecond-pulsed solid-state lasers are used. Regarding the impact of scattering on the image information, the size and distribution of particles as well as the refractive index of scattering centers such as cell aggregates are of higher importance than the pigmentation. Therefore, edema leads to a decrease of the signal attenuation coefficient.

In the OCT systems, the light is coupled into optical fibers. Different techniques of moving the reference arm are established. The length can be varied by moving mirror systems as well as by fiber stretching. Another technique is the so-called no-motion OCT, in which the reference arm has a static position, and the interference modulation is detected by a spectrometer (spectral radar OCT). In a more confocal OCT realization, the lateral resolution is increased by strong focusing lens systems. To obtain information on deeper areas of the tissue, which are out of focus, the lenses must be moved in z-direction during depth scanning. An alternative is a larger spot size with a less-focused beam, which remains sufficiently sharp over the entire imaging depth at the expense of resolution. The axial resolution depends on the light source. New developments of superluminescent diodes and lasers enable a high-resolution OCT, with a resolution down to 1 μm (8,9). Another approach to broad-band light is combining two sources with adjacent wavelength, resulting in an ultrashort coherence length (10).

In conventional OCT, the spatial variation of the backscattered photons is the main source of contrast. Nevertheless, the probe signal is influenced by several other physical properties of the tissue. The refractive index can be determined in different depth of the tissue, providing information on the water content (5,11,12,12). The light is changed in amplitude, phase, and polarization. This additional information might be of diagnostic value and can be extracted comparable with a tissue staining for increasing the contrast. Like in ultrasound, Doppler-OCT flow measurements can be performed by measuring the Doppler shift of light scattered from blood (13–16). Polarization-sensitive OCT has the ability to visualize the skin birefringence, which is mainly dependent on the collagen orientation (17–23). OCT elastography is an imaging of microscopic deformation, strain, and stiffness of tissue (24). With all these techniques, the contrast between normal and diseased skin can be enhanced.

OCT STUDIES IN DERMATOLOGY

Compared to other tissues such as the eye or mucous membranes, the skin is difficult to image with OCT because it is a strong scattering medium. Therefore, the imaging depth is more limited. On the other side, the skin surface is easy to reach by applicators of the system.

Healthy Skin

Dependent on the location, the visible appearance of normal skin in OCT is variable. In general, the reflection of light at the skin surface leads to a strong entrance signal. The degree of backscattering at the surface is dependent on the refractive index mismatch of the medium above the skin (normally air) compared to the skin. The entrance signal can be lowered by the application of gel or creams onto the surface for index matching. At ridged skin, the entrance signal is split into two lines when using high-resolution OCT (Fig. 1). This thin superficial layer

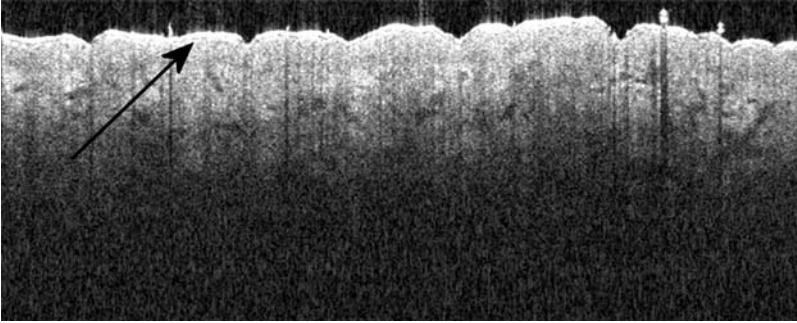


FIGURE 1 High-resolution optical coherence tomography image of healthy forearm skin. The entrance signal is split into two lines (*arrow*) corresponding to the thin stratum corneum, 2 mm \times 0.8 mm. (Optical coherence tomography system provided by Thorlabs HL AG.)

corresponds to the stratum corneum, which has a thickness of about 10 μm . The next more or less flat layer is the viable epidermis. The scattering inside the epidermis is low and homogenous. In the papillary dermis, the signal intensity increases again. Therefore, it is mostly possible to determine the border between epidermis and dermis (25–27). The reticular dermis shows a strong scattering with several lower reflecting structures. Hair follicles and glands can be distinguished by the characteristic shape, whereas blood and lymphatic vessels are signal-free longish or round cavities. The signal intensity in deeper parts of the dermis decreases due to a limited penetration depth of the light caused by multiple scattering and absorption. In palmoplantar skin, the stratum corneum is much thicker and constitutes a thick wavy homogenous layer at the surface with some spiral sweat gland ducts inside (Fig. 2) (28). The border between the epidermis and dermis is less demarcated because it is more toothed. The dermis is less signal intense compared to other regions of the body (29–33).

Inflammatory Skin Diseases

Inflammation of the skin results in specific morphologic changes known from histology. The stratum corneum shows a hyper- and parakeratosis. The epidermis is thickened due to spongiosis and proliferation. An edema and inflammatory cellular infiltrates are typical changes in the dermis. Systematic studies of inflammatory skin diseases have demonstrated that these changes are visible and could be quantified and monitored over time using OCT. Experimentally induced irritant contact dermatitis after application of sodium lauryl sulphate showed a thickening of the entrance signal and the epidermis, as well as a dilation of vessels in the upper dermis and a decrease in light scattering due to edema (32). In blistering diseases, the location of the cleft can be determined. In psoriasis, a severe parakeratosis leads to a multilayered entrance signal. Pustules are seen as cavities within the epidermis, filled with inhomogenous material (34). Wound healing can be observed in a non-invasive way using OCT (35). The occlusion of the defect by blood crusts and the regeneration of the epithelium are detectable. The granulation tissue and the scar formation lead to characteristic changes of the signal attenuation coefficient in the upper dermis with a lowering in the first phases of wound healing and an increase at the end (Fig. 3).

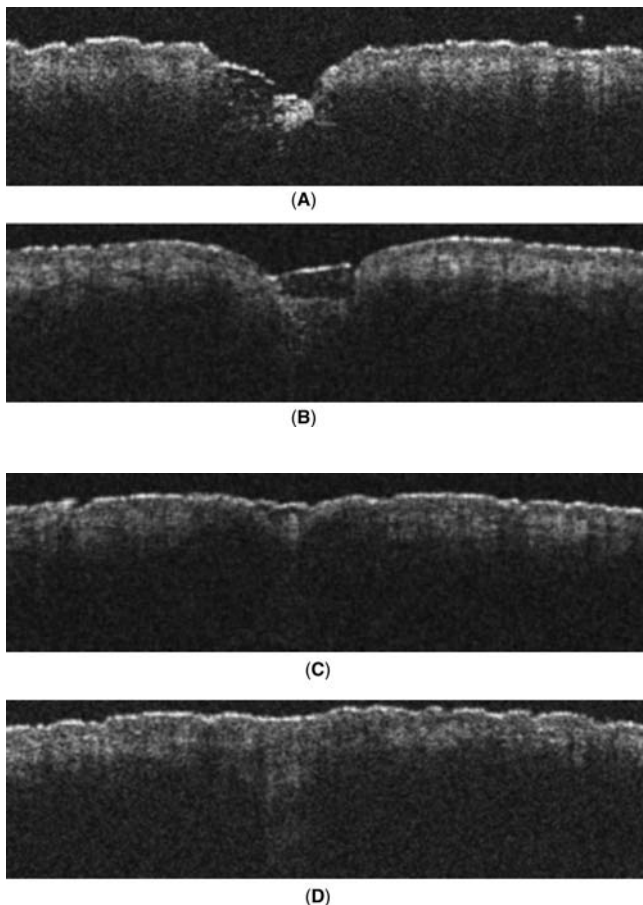


FIGURE 2 Optical coherence tomography of wound healing of an incision. The fresh cut (A) is covered with a crust after four days (B). After 13 days, the scattering in the upper dermis is lower due to granulation tissue (C). After 26 days, the surface is closed (D). The scattering in the upper dermis is increased due to fibrosis and scar formation; 6 mm × 1.7 mm.

Skin Tumors

Superficial parts of epithelial, mesenchymal, and melanocytic skin tumors are visible in the OCT images (33).

In epithelial tumors such as basal cell carcinoma, the origin of the tumor from the epidermis is evident because the tumor aggregates have contact with the epithelium and have a similar appearance regarding signal density and distribution. The tumor can be distinguished from the surrounding stroma (36). Typically, enlarged blood vessels are seen in the upper dermis, lying above the tumor aggregates (Fig. 4).

Mesenchymal tumors such as fibrous histiocytoma appear as deep irregularities of the collagen distribution below an elevated, but unaffected epidermis.

Melanocytic lesions are represented as strong scattering areas with a cloudy appearance in the OCT image. Larger nests of nevus cells are distinguishable.

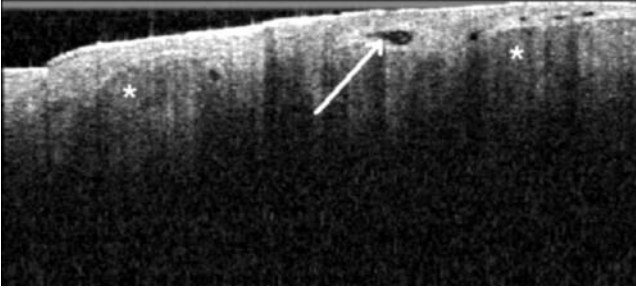


FIGURE 3 High-resolution optical coherence tomography of a basal cell carcinoma at the back. The tumor cell aggregates are marked by stars; the dilated vessels by an arrow; 2 mm \times 0.9 mm.

Morphologic changes of the epidermis, such as acanthosis and enlargement of the rete ridges can be detected. In malignant melanoma, the signal distribution is less homogenous compared to benign nevi. The signal attenuation coefficient [μ] is significantly increased in the melanoma compared to the adjacent healthy skin (own unpublished data). Some strong reflecting pigmented globules of atypical melanocytes or melanophages induced a signal shadow below (Fig. 5). Like in melanocytic nevi, changes of the epidermis, such as ulceration, crusts, and atrophy are visible. In most cases, the demarcation between epidermis and dermis is less clear due to the tumor infiltrates in the junctional zone. The contrast between melanocytes and keratinocytes is too bad to see a pagetoid spread of melanoma cells inside the epidermis. Therefore, a clear-cut differential diagnosis between benign and malignant melanocytic lesions is not possible using OCT at its present resolution.

In general, systematic studies on skin tumors using OCT are still lacking.

Treatment Effects

Additionally to the assessment of morphologic changes, OCT enables an exact determination of the thickness of layers. Therefore, this imaging method is a valuable tool to monitor the course of diseases and to quantify treatment effects.

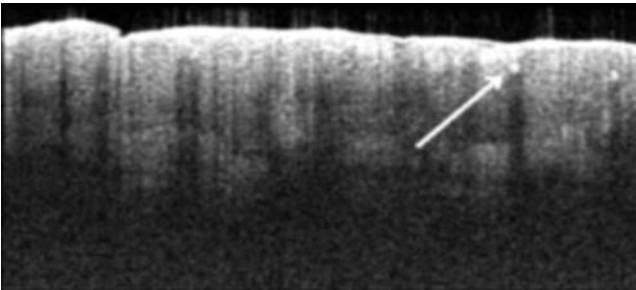


FIGURE 4 High-resolution optical coherence tomography of a malignant melanoma at the back. Some signal rich cells showed a signal shadow below (*arrow*). The scattering inside the tumor is very irregular; 2 mm \times 0.9 mm.

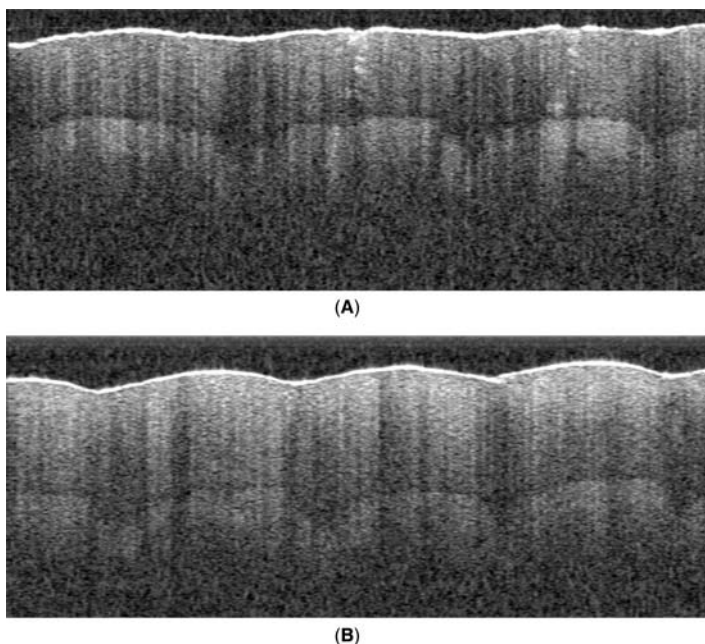


FIGURE 5 (A) High-resolution optical coherence tomography image of healthy skin at the fingertip. The first thick wavy layer is the stratum corneum with some spiral sweat gland ducts. (B) After two hours of wearing gloves, the stratum corneum shows a swelling. The scattering of upper parts of the horny layer is increased; 2 mm \times 0.8 mm.

A treatment of the skin surface with various agents (glycerol, paraffin oil, 10% urea in petrolatum, petrolatum, and ultrasonic gel) is followed by a decrease of the reflectivity of the skin surface, accompanied by a smaller entrance peak in the averaged A-scan (32). The penetration depth of the light signal is increased due to a lower light attenuation and scattering at the surface. This unspecific effect is attributed to refractive index matching and is greatest for paraffin oil. In an animal model, it could be demonstrated that application and injection of glycerol prior to OCT measurements also increase the penetration depth of the signal by reduction of random scattering, thereby making the skin less turbid for visible wavelengths (37,38).

In psoriasis, OCT studies have shown that the severely thickened epidermis nearly turned to normal after four weeks of therapy without reaching the values of the adjacent healthy skin (34). Ultraviolet irradiation leads to visible changes of the epidermis, such as parakeratosis and thickening, accompanied by alterations of the scattering coefficient due to erythema and pigmentation (39,40). An increase of the water content of the stratum corneum by occlusion, prolonged water contact, or application of moisturizers is followed by a marked swelling, which can be quantified easily at the fingertips using OCT (Fig. 2). Moreover, the effect of consecutive tape stripping on the thickness of the stratum corneum can be quantified in the OCT images (32).

Skin atrophy is an important side effect of corticosteroid therapy. The decrease of dermal thickness can be monitored using high-frequency ultrasound.

The thickness of the epidermis is only measurable using OCT due to the higher resolution of this method. A systematic OCT study on steroid atrophy has shown that the epidermal atrophy starts already within the first days of therapy and is more pronounced than the change of dermal thickness. The degree of epidermal thinning correlates to the potency of the corticosteroids, but is observed even in the new-generation steroids with increased benefit-risk ratio (41).

POTENTIAL OF THE TECHNIQUE

Biomedical optics is a rapidly developing area of research from which OCT profits. Recent advances in photonic and laser technology stimulate the field of noninvasive imaging.

There are some conventional OCT scanners for dermatological purposes, which are already available on a commercial basis (SkinDex 300[®], ISIS optronics GmbH, Mannheim, Germany; Imalux Niris[®] Imaging System, IMALUX, Cleveland, Ohio, U.S.A.). Experimental OCT devices are built by several research institutes and can be modified for dermatologic questions (i.e., spectral high-resolution OCT, Thorlabs HL AG, Lübeck, Germany). In most cases, the instruments are compact and easy to handle (Fig. 6).

Future developments focus on broad-band light sources with an ultrashort coherence length to increase the resolution. Alternatively, femtosecond-pulsed lasers are used for high-resolution OCT (42,43). At the human eye, this OCT technique already provides excellent images *in vivo*. By combining different optical methods such as epiluminescence microscopy, OCT, and confocal microscopy within one system, the diagnostic value of the single methods may be improved significantly. Contrast agents or staining methods for tissue differentiation are still under investigation.



FIGURE 6 Prototype of a spectral radar no-motion optical coherence tomography (OCT) built by the medical laser center Lübeck GmbH/Thorlabs HL AG, Germany. The compact device has a small handheld applicator connected by optical fibers.

CONCLUSION

OCT is a noninvasive imaging method with a resolution between high-frequency ultrasound and confocal microscopy. It is an ideal tool for imaging superficial layers of the skin *in vivo*. In the cross-sectional images, a determination of the thickness of the stratum corneum and the epidermis is easily possible. Therefore, OCT is a useful method for monitoring of inflammatory skin diseases and wound healing as well as for the quantification of treatment effects such as steroid atrophy. For tumor diagnosis, OCT provides information on the architecture of a lesion. Systematic studies on the sensitivity and specificity for differential diagnosis are still lacking. However, the resolution and contrast are still not high enough to differentiate between benign and malignant tissue on a cellular level. On the other side, the increasing importance of nonsurgical therapeutic modalities of skin cancer requires a noninvasive method for control of healing to replace biopsies.

Furthermore, OCT as a dynamic, noninvasive method might provide new insight into physiologic or pathophysiologic processes that are dependent on the integrity of tissue.

The field of high-resolution optical imaging methods is rapidly developing. Therefore, recent advances of OCT technology as well as the aforementioned functional techniques for tissue characterization might lead to new applications in dermatology in the near future.

REFERENCES

1. Huang D, Swanson EA, Lin CP, et al. Optical coherence tomography. *Science* 1991; 254:1178.
2. Schmitt JM. Optical coherence tomography (OCT): a review. *IEEE* 1999; 5:1205.
3. Fercher AF, Drexler W, Hitzinger CK, Lasser T. Optical coherence tomography—principles and applications. *Rep Prog Phys* 2003; 66:239.
4. Tearney GJ, Brezinski ME, Bouma BE, et al. *In vivo* endoscopic optical biopsy with optical coherence tomography. *Science* 1997; 276:2037.
5. Tearney GT, Brezinski ME, Souther JF, et al. Determination of the refractive index of highly scattering human tissue by optical coherence tomography. *Opt Lett* 1995; 20:2258.
6. Sainter AW, King TA, Dickinson MR. Effect of target biological tissue and choice of light source on penetration depth and resolution in optical coherence tomography. *J Biomed Opt* 2004; 9:193.
7. Troy TL, Thennadil SN. Optical properties of human skin in the near infrared wavelength range of 1000–2200 nm. *J Biomed Opt* 2001; 6:167.
8. Fujimoto JG. Optical coherence tomography for ultrahigh resolution *in vivo* imaging. *Nat Biotechnol* 2003; 21:1361.
9. Drexler W. Ultrahigh-resolution optical coherence tomography. *J Biomed Opt* 2004; 9:47.
10. Unterhuber A, Povazay B, Bizheva K, et al. Advances in broad bandwidth light sources for ultrahigh resolution optical coherence tomography. *Phys Med Biol* 2004; 49:1235.
11. Knüttel A, Boehlau-Godau M. Spatially confined and temporally resolved refractive index and scattering evaluation in human skin performed with optical coherence tomography. *J Biomed Opt* 2000; 5:83.
12. Knüttel A, Bonev S, Knaak W. New method for evaluation of *in vivo* scattering and refractive index properties obtained with optical coherence tomography. *J Biomed Opt* 2004; 9:265.
13. Park BH, Pierce MC, Cense B, de Boer JF. Real-time multi-functional optical coherence tomography. *Opt Express* 2003; 11:782.

14. Yang VXD, Pekar J, Lo SSW, et al. Optical coherence and Doppler tomography for monitoring tissue changes induced by laser thermal therapy—an in vivo feasibility study. *Rev Sci Instrum* 2003; 74:437.
15. Kehlet Barton J, Izatt JA, Kulkarni MD, et al. Three-dimensional reconstruction of blood vessels from in vivo color Doppler optical coherence tomography images. *Dermatology* 1999; 198:355.
16. Tang SJ, Gordon ML, Yang VX, et al. In vivo Doppler optical coherence tomography of mucocutaneous telangiectases in hereditary hemorrhagic telangiectasia. *Gastrointest Endosc* 2003; 58:591.
17. Pierce MC, Strasswimmer J, Hyle Park B, et al. Advances in optical coherence tomography imaging for dermatology. *J Invest Dermatol* 2004; 123:458.
18. Strasswimmer J, Pierce MC, Park BH, et al. Polarization-sensitive optical coherence tomography of invasive basal cell carcinoma. *J Biomed Opt* 2004; 9:292.
19. Pierce MC, Strasswimmer H, Hyle Park B, et al. Birefringence measurements in human skin using polarization-sensitive optical coherence tomography. *J Biomed Opt* 2004; 9:287.
20. Pircher M, Goetzinger E, Leitgeb R, Hitzenberger CK. Three dimensional polarization sensitive OCT of human skin in vivo. *Opt Express* 2004; 12:3236.
21. de Boer JF, Srinivas SM, Malekafzali A, et al. Imaging thermally damaged tissue by polarization sensitive optical coherence tomography. *Opt Express* 1998; 3:212.
22. Srinivas SM, de Boer JF, Park BH, et al. Determination of burn depth by polarization-sensitive optical coherence tomography. *J Biomed Opt* 2004; 9:207.
23. Applegate BE, Yang C, Rollins AM, Izatt JA. Polarization-resolved second-harmonic generation optical coherence tomography in collagen. *Opt Lett* 2004; 29:2252.
24. Schmitt JM. OCT elastography: imaging microscopic deformation and strain of tissue. *Opt Express* 1998; 3:199.
25. Weissman J, Hancewicz T, Kaplan P. Optical coherence tomography of skin for measurement of epidermal thickness by shapelet-based image analysis. *Opt Express* 2004; 12:5760.
26. Gambichler T, Boms S, Stücker M, et al. Comparison of histometric data obtained by optical coherence tomography and routine histology. *J Biomed Opt* 2005; 10:44,008.
27. Neerken S, Lucassen GW, Bisschop BA, et al. Characterization of age-related effects in human skin: a comparative study that applies confocal laser scanning microscopy and optical coherence tomography. *J Biomed Opt* 2004; 9:274.
28. Fruhstorfer H, Abel U, Garthen CD, Krüttel A. Thickness of the stratum corneum of the volar fingertips. *Clin Anat* 2000; 13:429.
29. Welzel J, Lankenau E, Bimgruber R, Engelhardt R. Optical coherence tomography of the human skin. *J Am Acad Dermatol* 1997; 37:958.
30. Pagnoni A, Knüttel A, Welker P, et al. Optical coherence tomography in dermatology. *Skin Res Technol* 1999; 5:83.
31. Gladova ND, Petrova GA, Nikulin NK, et al. In vivo optical coherence tomography imaging of human skin: norm and pathology. *Skin Res Technol* 2000; 6:6.
32. Welzel J, Reinhardt C, Lankenau E, et al. Changes in function and morphology of normal human skin: evaluation using optical coherence tomography. *Br J Dermatol* 2004; 150:220.
33. Welzel J. Optical coherence tomography in dermatology: a review. *Skin Res Technol* 2001; 7:1.
34. Welzel J, Bruhns M, Wolff HH. Optical coherence tomography in contact dermatitis and psoriasis. *Arch Dermatol Res* 2003; 295:50.
35. Yeh AT, Kao B, Jung WG, et al. Imaging wound healing using optical coherence tomography and multiphoton microscopy in an in vitro skin equivalent tissue model. *J Biomed Opt* 2004; 9:248.
36. Bechara FG, Gambichler T, Stücker M, et al. Histomorphologic correlation with routine histology and optical coherence tomography. *Skin Res Technol* 2004; 10:169.
37. Vargas G, Chan EK, Barton JK, et al. Use of an agent to reduce scattering in skin. *Lasers Surg Med* 1999; 24:133.

38. Vargas G, Readinger A, Dozier SS, Welsh AJ. Morphological changes in blood vessels produced by hyperosmotic agents and measured by optical coherence tomography. *Photochem Photobiol* 2003; 77:541.
39. Gambichler T, Künzlberger B, Paech V, et al. UVA1 and UVB irradiated skin investigated by optical coherence tomography in vivo: a preliminary study. *Clin Exp Dermatol* 2005; 30:79.
40. Gambichler T, Boms S, Stücker M, et al. Skin alterations following ultraviolet radiation investigated by optical coherence tomography. *Arch Dermatol Res* 2005; 297:218.
41. Cossmann M, Welzel J. Evaluation of the atrophogenic potential of different corticosteroids using OCT, 20 MHz ultrasound and profilometry. *Br J Dermatol*. In Press.
42. Bizheva K, Povazay B, Hermann B, et al. Compact, broad-bandwidth fiber laser for sub-2-microm axial resolution optical coherence tomography in the 1300-nm wavelength region. *Opt Lett* 2003; 28:707.
43. Nishizawa N, Chen Y, Hsiung P, et al. Real-time, ultrahigh resolution optical coherence tomography with an all-fiber, femtosecond fiber laser continuum at 1.5 microm. *Opt Lett* 2004; 29:2,846.

Sören Jaspers

*Research and Development, Biophysics, Beiersdorf AG,
Hamburg, Germany*

INTRODUCTION

The quantitative determination of the skin's surface topology, both skin roughness and macrostructures such as wrinkles or cellulite, is one of the most important and probably most frequently performed investigations in the field of cosmetics, and increasingly in dermatological research as well. A still very common method of evaluating skin roughness involves the use of silicon replica as used in dentistry. But especially when we focus on macrostructures, making these imprints is either quite challenging and sometimes error-prone (for example, when investigating wrinkles), or actually nearly impracticable (for example, when investigating cellulite or face and body contours).

The introduction of active image triangulation in conjunction with phase-shift techniques in skin topometry allows for fast, noninvasive measurement of the skin's surface in vivo. These systems facilitate a wide range of possibilities in the field of cosmetic and dermatological research.

TECHNICAL BACKGROUND

At present, the phaseshifting rapid in vivo measurement of skin (PRIMOS[®]) system (1) (GF Messtechnik GmbH, D-14513 Teltow, Germany) is in all probability one of the most widespread in vivo systems for determining skin topology. This chapter will thus concentrate primarily on the technical background of, and the possibilities offered by the various PRIMOS devices, which are currently available. Other instruments which are based on similar principles include, for example, the fast optical in vivo topometry skin (FOITS[®]) system (2) (Breuckmann GmbH, D-88709 Meersburg, Germany), or the SkinBio technologies skin profile solution (3) (SkinBio[®] Technologies, D-50705 Cologne, Germany).

The main attribute of in vivo topometry systems like PRIMOS is the projection of a regular sinusoidal intensity pattern with a sophisticated digital projection device onto the surface of the skin at a certain angle of incidence. Height information for the structured surface is coded in the distorted intensity pattern, which is recorded by means of an appropriate video technique.

Principle of Active Image Triangulation

The system's measuring head consists of a digital micromirror device (DMD[™]) from Texas Instruments, used as the projection unit, and a charge-coupled device (CCD) camera used as a recording unit. Figure 1 (1) shows the angle at which the optical axis of the projector lens intersects the optical axis of the camera lens. Angle α between the axes is designated as the system's triangulation angle.

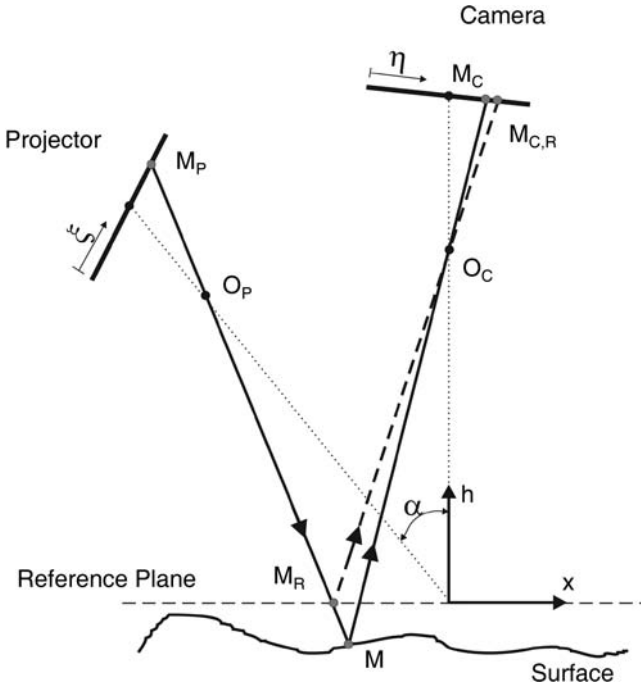


FIGURE 1 Principle of active image triangulation.

Intensity encoded point M at coordinate ξ_M of the projection plane is projected via center O_P onto the surface under investigation for active image triangulation. Its image M on the surface is recorded via center O_C at coordinate η_M in the camera plane (Fig. 1, *solid line*). Coordinates h and x of point M are, in this case, a function of coordinates ξ_M and η_M and of vector P , describing the parameters of the triangulation system. These parameters specify the location of the projection centers O_P and O_C in the coordinate system (h, x) , triangulation angle α , and the arrangement of the projector and camera plane in relation to the projection centers.

Because of the limited dynamic range of the projector in conjunction with the unknown, spatially varying surface properties such as background intensity and reflection characteristics, it is not possible to encode each point of the surface unequivocally with only one projected intensity pattern. This leads to a matching problem typical in triangulation systems, which can be solved by using temporal phase-shift algorithms.

Temporal Phase-Shift Algorithm

Recording an intensity encoded point M projected onto a flat reference plane during calibration (Fig. 1, *dashed line*), and onto a structured surface such as the human skin during the actual investigation (Fig. 1, *solid line*), a shift in coordinate η can be observed in the plane of the camera's CCD chip resulting from the structure of the surface. Thus, when a spatially sinusoidal intensity pattern is projected onto

the reference plane, and afterwards onto the structured surface, phase changes can be observed in the camera plane. These phase changes contain the desired height information.

The recorded intensity distribution on the camera plane of the projected sinusoidal pattern on the reference plane can be expressed as:

$$I_R(\eta) = a(\eta) + b(\eta) \cos(2\pi \cdot n + \Phi_R(\eta)) \quad (1)$$

where $a(\eta)$ is the background intensity, and $b(\eta)$ is the fringe contrast. $\Phi_R(\eta)$ is the phase map reduced to the 0 to 2π range, and n is an integer. The intensity distribution observed on the structured surface is the same as that which would have been observed on the reference plane modified by object reflectivity $r(\eta)$, and by a changed phase map $\Phi(\eta)$.

$$I(\eta) = r(\eta) \cdot [a(\eta) + b(\eta) \cos(2\pi \cdot n + \Phi(\eta))] \quad (2)$$

A temporal phase-shift algorithm is applied to calculate the phase map $\Phi(\eta)$. During measurement, the projected sinusoidal intensity pattern is shifted M times with a phase increment of $2\pi/M$.

Each pattern, I_1, I_2, \dots, I_M , is recorded in the camera plane. The following is obtained for the phase map of the measured surface from these intensity maps (4):

$$\tan(\Phi(\eta)) = \frac{\sum_{k=1}^M I_k \cdot \sin(2\pi k/M)}{\sum_{k=1}^M I_k \cdot \cos(2\pi k/M)} \quad (3)$$

The phase map of reference plane $\Phi_R(\eta)$ is obtained in the system calibration process by the same method. The phase changes caused by the topography of the surface are expressed as:

$$\Delta\Phi(\eta) = \Phi_R(\eta) - \Phi(\eta) \quad (4)$$

The transformation from phase map $\Delta\Phi(\eta)$ to desired height map $h(x)$ is in principle straightforward, and is specified by the system's triangulation relations. In actual practice, the inner and outer parameters of the triangulation system represent a great degree of freedom. Each parameter can be quantified with certain tolerance only. This would lead to unacceptable uncertainty in resulting height map $h(x)$. Furthermore, unavoidable distortions resulting from the lenses have to be considered in the transformation.

For this reason, calibration pieces are used, and a three-step calibration algorithm has been implemented, which determines the best approximation in the least square sense for the system's phase to height transformation function.

Digital Micromirror Device

The accuracy of an active image triangulation system depends directly on the features of the projected intensity pattern. Digital spatial light modulators make it possible to project an artificial fringe pattern with the required spatial extension.

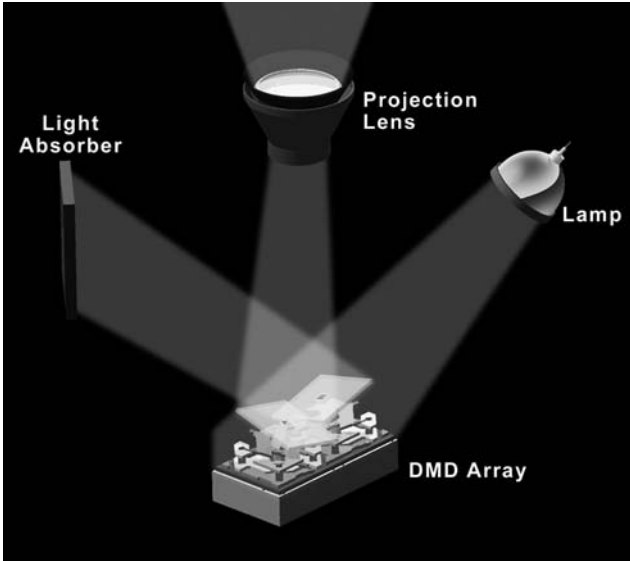


FIGURE 2 Principle of digital micromirror device.

Aiming at high accuracy on the one hand, and trying to avoid phase discontinuities on the other hand, the wavelength of the projected fringe pattern can be easily adjusted to the topographical characteristics of the measured skin area. Because short measurement time is required, the projection unit's response time must be sufficiently short when switching from one intensity pattern to another. Because of the demanding requirements mentioned above, a DMD manufactured by Texas Instruments is used as a digital spatial light modulator, i.e., as a projection unit. Figure 2 illustrates the principle of digital image projection using a DMD.

The DMD consists of an array of 1024×768 square $16 \times 16 \mu\text{m}^2$ mirrors. Pixel spacing is about $17 \mu\text{m}$ measured from center to center. Each mirror covers one cell of a complementary metal oxide semiconductor (CMOS) static random access memory (RAM) (Fig. 3). Depending on the data in the underlying memory cell, each mirror can be tilted by means of electrostatic forces either $+10^\circ$ (on) or -10° (off). In the on position, light arriving from the projector's light source is reflected through a projection lens on the surface, whereas mirrors set to the off position reflect the light to an absorber. Pulse width modulation determines for how long each mirror remains tilted in either direction, and thus determines the intensity of the corresponding pixel on the surface. The DMD has a switching time of less than $20 \mu\text{sec}$. The projector is able to display high resolution eight-bit gray scale (256 shades) intensity patterns at a frequency of 180 Hz.

IN VIVO TOPOMETRY

As discussed in detail in the previous paragraph, the main feature of fringe projection systems such as PRIMOS is the projection of a regular sinusoidal intensity pattern onto the surface of the skin at a certain angle of incidence. This allows

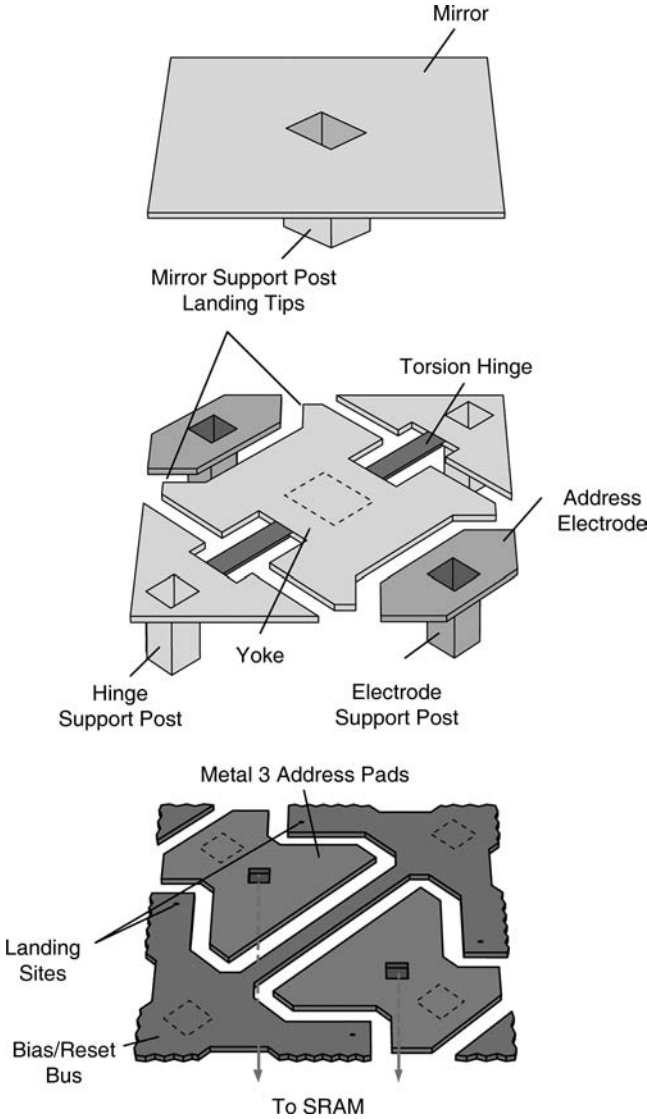


FIGURE 3 Layout of one single digital micromirror device element.

us to measure an entire area without having any contact with the skin. This principle is illustrated in Figure 4. A pattern of parallel stripes in a reference plane, as depicted in Figure 4A, is projected onto a wrinkle structure (Fig. 4B), and the height information of the structured surface is coded in the distorted intensity pattern (Fig. 4C), which is recorded by means of CCD video technology.

As mentioned above, it is necessary to record several of these images while the fringe pattern is moving through defined phase shifts to obtain reliable height information for the entire surface.

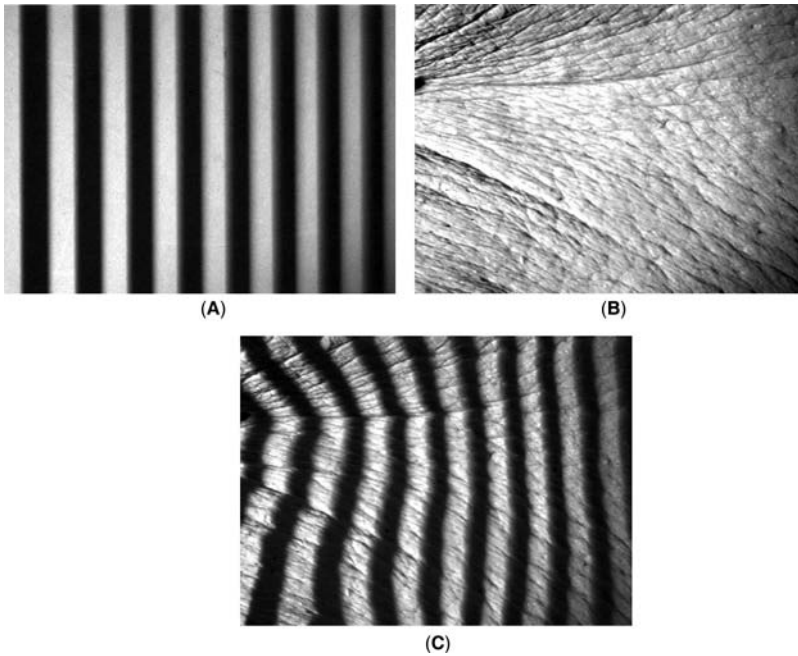


FIGURE 4 Example of the distortion of originally parallel stripes due to the wrinkle structure. (A) Originally parallel stripes; (B) wrinkle structure; (C) distortion.

PRIMOS SYSTEMS

Various PRIMOS systems are currently available from the market. The most reliable device at the moment consists of a digitally controlled DMD, with a resolution of 1024×768 pixels, and a high-resolution digital CCD camera, with a working resolution of 1000×620 pixels. Most wrinkle measurement systems include fields of view measuring approximately 18×13 to 40×30 mm, with a vertical resolution of about $2 \mu\text{m}$. Four to eight phase shifts are typically executed during any given measurement, depending upon desired quality. This results in measuring periods from 68 to 136 msec.

During the course of working with the different PRIMOS systems, it becomes apparent that handling these systems necessitates a certain amount of accuracy and training. Some aspects turned out to be of particular importance: if the volunteers maintain a relaxed posture, body movement is reduced considerably, which is of course especially important for measurements targeted at resolution in the micrometer range. Furthermore, it prevents deformations of the structure of interest. It is self-evident that a vibration-free stand with a highly reproducible positioning construction and numerous degrees of freedom is absolutely necessary for this kind of investigation. Figure 5 shows a typical arrangement for measuring wrinkles in the corner of the eye.

Exact reidentification of the previously measured sites is fundamental in order to achieve best possible results. The PRIMOS system features a video overlay function, which is quite helpful, once the operator has had sufficient practice.



FIGURE 5 Arrangement for facial studies.

Furthermore, immediate checking of data quality is advisable as well. Artifacts resulting from movement, defocusing, improper brightness, or other problems can be detected in time, and the measurement can be repeated.

A further fundamental aspect concerns the depth of focus of the optical components. Quite recently, the most common focusing tool involved the use of projected central crosshairs which have to be aligned to a cross mark on the computer screen (Fig. 6A). We examined the amplitude of measured topologies with this tool and found that a huge amount of data was outside of the system's depth of focus range of about ± 1 mm (Fig. 6B). We therefore developed a new focusing aid, which was implemented by the manufacturer. Now the operator not only has to align the crosshairs, but rather has four small projected marks in the corners of the image as well. Using this technique, significant improvement was achieved in adhering to the depth of focus range (Fig. 6D).

PARAMETERS

ISO Standards

The measurement of surface roughness is defined by a series of international standards. These standards cover the characteristics of the measuring equipment, and specify the mathematical definitions of the many parameters used today.

The current basis for the use of ISO parameters in profilometry is ISO 4287: *Geometrical Product Specifications—Surface texture: Profile method—Terms, definitions, and surface texture parameters* dated 1997.

According to ISO specifications, a surface is defined as the peripheral skin of a body, which separates it from the surrounding medium. This surface incorporates structural deviations from a reference line, which are classified as form,

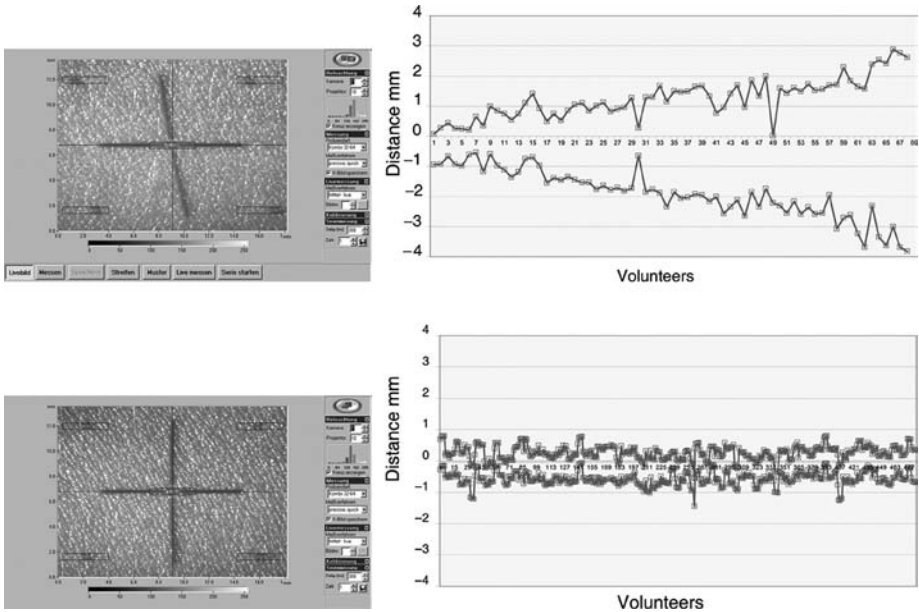


FIGURE 6 Reduction of the number of out of focus images due to the use of the special focusing aid.

waviness, and surface roughness. To separate the three elements, we use filters. Either roughness or waviness filters can be selected for most measuring instruments. If a roughness filter is selected, waviness elements are removed leaving the roughness profile for evaluation. If a waviness filter is selected, roughness elements are removed leaving the waviness profile for evaluation. There is no fixed setpoint at which roughness becomes waviness or vice versa, as this depends on the size and nature of the application.

All of the ISO parameters have been developed for mechanically processed surfaces, for which they are thus particularly suitable. For this reason, some of the rules and procedures for the assessment of surface texture listed in ISO 4288 are not entirely reasonable or even applicable for modern optical topometry systems.

Selection of Roughness Profile Parameters

Of the entire range of parameters set forth in the Deutsches Institut für Normung e. V., the German Institute for Standardization (DIN) specifications, those appropriate for evaluation of surface features and their changes due to treatment or healing have to be selected (5). Monti et al. (6) report a statistically significant difference between uninvolved and involved psoriatic skin for R_a but not for R_z DIN. Other authors report an increase in amplitude parameters and a decrease in the number of peaks in dry atopic skin (7). Accordingly, spacing parameter S_m should increase. Our own experiments show significant decreases in amplitude parameters in cases of hydration, and increases associated with skin ageing (1,5,8,9).

Murahata et al. (10) attempted to correlate subjective evaluations of the skin surface with surface parameters for roughness measured over a length of 7.5 mm

on positive replicas. "Plumpness" was used as a parameter for hydration, and scales and cracks for damage to the stratum corneum during visual assessment. On the other hand, R_z DIN and R_a were used as roughness parameters during assessments conducted with measuring instruments. Both roughness parameters were found to correlate significantly with plumpness, but not with scaliness and number of cracks.

Surface Parameters

As mentioned before, all of the parameters described above have been developed for use with mechanical sensors. However, modern devices for topometry not only provide profile information, but rather surface area information as well. Therefore, on behalf of the European Union, a workgroup has begun transforming and upgrading the well-known parameters into the third dimension (11). Their handbook, "Development of Methods for the Characterization of Roughness in Three Dimensions," provides the basis for a unified approach to three-dimensional (3-D) surface finish assessment. It covers a range of issues related to 3-D microtopography with an emphasis on standardization and interpretation. Many meaningful parameters such as S_a , S_q , S_c , S_z , etc. are defined and discussed.

The most common parameters are S_a and S_q :

$$S_a = \frac{1}{NM} \sum_{x=0}^{N-1} \sum_{y=0}^{M-1} |Z_{x,y}| \quad (5)$$

$$S_q = \sqrt{\frac{1}{NM} \sum_{x=0}^{N-1} \sum_{y=0}^{M-1} Z_{x,y}^2} \quad (6)$$

These 3-D parameters are extrapolations of the two-dimensional parameters normalized in the ISO 4287 standard. They are defined as the sum of z deviations in N rows and M lines. Thus, each single pixel of the measured surface (in most systems more than 600,000) is taken into account. These parameters are thus very meaningful and representative, depending on the particular task at hand.

Volume Parameters

Another approach, especially for assessing crows-feet, is the calculation of wrinkle volume. Unfortunately, this is not a standard parameter in today's data analysis software. Hopefully, standard algorithms will be available in the future for automatically detecting and analyzing wrinkles, for example, resulting from edge detection procedures in combination with suitable filter algorithms for separating roughness and wrinkle structures. We have developed software algorithms with these features, which have proven to be very meaningful. Interactive determination of the volume parameter is still somewhat time-consuming but the results are very sensitive, and at the same time very descriptive.

Studies

Optical topometry has proven its worth for studies in the field of cosmetic and dermatological research in recent years. The standard systems are commonly used for

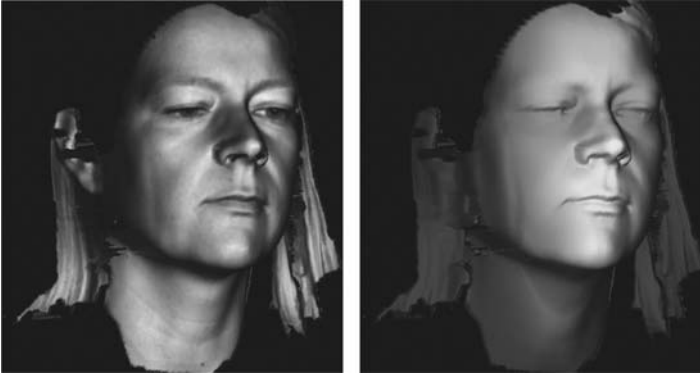


FIGURE 7 (See color insert) Large field measurement of the entire face.

substantiating smoothing claims and antiwrinkle claims. Friedman et al. demonstrated the capability of documenting and quantifying the wrinkle structure following multiple treatment sessions with a 1064 nm QS Nd:YAG laser (12). They found correlations with clinical and subjective assessments, and state that optical topometry provides objective verification and technical understanding of nonablative laser technology. Roques et al. used PRIMOS to measure and evaluate scar surfaces with good definition and reproducibility (13).

Additional types of studies have become possible as a result of modified systems using larger fields of view. In our studies, objective and quantitative assessments of cellulite and body wrinkles—for example at the décolleté—have turned out to be very valuable and reliable.

The PRIMOS body system represents a special setup which allows for the investigation of larger body sites such as the entire face (Fig. 7A), and also specifies the color texture of the measured area (Fig. 7B). With the help of this instrument, objective studies are possible involving, for example, the contours of the face.

CONCLUSION

Optical topometry with fringe projection systems offers a wide range of improved and new approaches in the field of cosmetic and dermatological research. The flexibility of these systems facilitates conventional studies on the inner forearm as well as, for example, studies of the facial area. As a result, a multitude of test designs have become less complicated, or even possible for the first time. But as always when using complex biophysical methods, we have to keep in mind that skilled operators who are capable of performing accurate measurements are absolutely essential for the acquisition of meaningful results. In the future, the development of new parameters and improvement of quality control mechanisms, speed and resolution will continue. Due to the fact that optical systems for topometrical measurements are becoming more and more widespread, further improvements can be expected in the future.

REFERENCES

1. Jaspers S, Hopermann H, Sauer mann G, Hoppe U, Lunderstädt R, Ennen J. Rapid in-vivo measurement of the topography of human skin by active image triangulation using a digital micromirror device. *Skin Res Technol* 1999; 5:195–207.
2. Rohr M, Brandt M, Schrader A. Skin surface—claim support by FOITS. *SÖFW J* 2000; 126(8):2–11.
3. www.skinbiotec.com, 31.08.2005.
4. Bruning JH, Herriott DR, Gallagher JE. Digital wavefront measuring interferometer for testing optical surfaces and lenses. *Appl Opt* 1974; 13:2693–2703.
5. Schreiner V, Sauer mann G, Hoppe U. Characterization of the skin surface by ISO parameters for microtopography. In: Wilhelm KP, Elsner P, Berardesca E, Maibach HI, eds. *Bioengineering of the Skin: Skin Surface Imaging and Analysis*. 4. CRC press, 1996.
6. Monti M, Bozzetti M, Motta S, Barbareschi M. Usefulness of surface topography analysis in psoriatic skin. *Acta Dermato-Venereol* 1989; 69:81.
7. Linde YW, Bengtsson A, Loden M. Dry skin in atopic dermatitis II. A surface profilometry study. *Acta Dermato-Venereol* 1989; 69:315.
8. Schreiner V, Hoppe U, Sauer mann G, Wenghöfer C. Microtopography of human skin—a validated method of analysis of analogous and Fourier transformed signals. *Allergologie* 1993; 16:165.
9. Hoppe U, Sauer mann G. Quantitative analysis of skin's surface by means of digital signal processing. *J Soc Cosmet Chem* 1985; 36:105.
10. Murahata RI, Crowe DM, Roheim JR. Evaluation of hydration state and surface defects in the stratum corneum: comparison of computer analysis and visual appraisal of positive replicas of human skin. *J Soc Cosmet Chem* 1984; 35:327.
11. Stout K, Blunt L. *Development of Methods for the Characterisation of Roughness in Three Dimensions*. Penton Press, London, 1998.
12. Friedman PM, Skover GR, Payonk GK, Arielle NB, Geronemus RG. 3D In-vivo optical skin imaging for topographical quantitative assessment of non-ablative laser technology. *Dermato Surg* 2002; 28(3):199–204.
13. Roques C, Teot L, Frasson N, Meaume S. PRIMOS: an optical system that produces three-dimensional measurements of skin surfaces. *J Wound Care* 2003; 12(9):362–364.

Confocal Microscopy of Skin In Vitro and Ex Vivo

Stefan S. Biel, Roger Wepf, and Sonja Wessel

*Beiersdorf AG, Research Microscopy,
Hamburg, Germany*

INTRODUCTION

Confocal laser scanning microscopy (CLSM) is a modern light microscopy technique that enables high-resolution three-dimensional imaging of biological and technical samples. The concept of a confocal microscope was first patented by Marvin Minsky in 1957; the first laser-scanning microscope was built in the early 1970s by Davidovits and Egger. In the mid- 1980s, the commercialization of confocal laser scanning microscopes started, and during the last 15 years, instruments were improved especially regarding velocity and resolution, mainly due to faster computers and more effective optics and electronics. A detailed synopsis of the basics of confocal imaging as well as of various optical and technical aspects of microscope setups and image analysis is given by Pawley (1) or Diaspro (2).

In cell biology, a rapidly growing number of applications rely on microscopy-based imaging techniques. These applications include a wide variety of time-dependent studies, as well as morphological investigations of a wide spectrum of tissues and primary or permanent cell culture systems. In addition, the introduction of new fluorescent proteins is rapidly expanding the number of original research reports. Other applications include resonance energy transfer, stem cell research, photobleaching studies, fluorescence lifetime imaging (FLIM), multiphoton microscopy, total internal reflection, DNA hybridization, membrane and ion probes, bioluminescent proteins, and epitope tagging. Good overviews of these cell biological applications are given by Matsumoto (3) and Hibbs (4).

In skin research, confocal techniques are commonly used for in vivo investigation of surfaces, tissue structure, or cell cultures as well as for ex vivo histological studies (Table 1). Besides fundamental dermatopathology or diagnostic problems, cosmetic issues are also addressed, e.g., superficial effects of cosmetic treatment on skin folds or penetration pathways for active ingredients. In the following, we want to provide an insight into the manifold possibilities of confocal microscopy on skin samples using both remission and fluorescence CLSM.

Principles of Confocal Imaging

Looking at the number of different imaging modes in confocal microscopy, two basic operating modes can be differentiated: reflectance CLSM and fluorescence CLSM (Table 1). In reflectance mode, the detection wavelength is identical with the excitation wavelength. Here, light from reflection and scattering events is recorded, but not fluorescence signal because the wavelength of fluorescence is always longer than the excitation wavelength. In this imaging mode, the image contrast derives mainly from refractive index changes, and the highest signal

TABLE 1 Basic Information on Confocal and Light Microscopy Techniques

Imaging technique	Light source/spectral properties	Resolution		Signal is based on	Feasible sample types		
		(Lateral)	(z)		Solid body/surface	Section	Stain/label necessary
Light microscopy	Arc-discharge lamp: UV to near-IR	350 nm	^a -	Reflection/remission Transmitted light	+	-	+
Confocal laser scanning microscopy	Laser: UV to IR (continuous wave)	200 nm	400 nm	Fluorescence	-	(+)	-
				Reflection/remission	(+)	+	(+)
Multiphoton microscopy	Laser: IR (pulsed)	1 μ m 300 nm	2-3 μ m 400 nm	Fluorescence	+	+	-
				Raman spectroscopy	+	+	(+)
				Reflection/remission	+	+	+
				Fluorescence	+	-	+
				Spectroscopy (e.g., FLIM)	+	-	+
				Second harmonic generation	+	-	+

Note: This table provides a rough survey of different confocal imaging techniques in comparison to plain light microscopy. Besides some technical data on the illumination light source and the achievable resolution of each technique, also the possible operating modes of the detection system are listed as well as the corresponding sample types that can be examined in the respective operating mode.

^aResolution in z is determined by sample thickness.

Abbreviations: UV, ultraviolet; IR, infrared; FLIM, fluorescence lifetime imaging.

intensity usually originates from the transition between air and the sample surface. Thus, this mode is ideal for visualizing the topography of surfaces. Moreover, by using an immersion medium different from air (immersion oil, glycerin, or water), structures lying under the sample surface can also be observed. Because the reflectance mode does not require staining of the sample, this mode can easily be used also for *in vivo* imaging of skin surfaces and pathology (see Chapter 12).

In fluorescence mode, the detection wavelength is longer than the excitation wavelength because fluorescence emission always displays a red shift characteristic for the respective fluorophore. This fluorescence is emitted either by skin autofluorophores, e.g., lipofuscin or NAD(P)H, or by fluorescent dyes that have been introduced into the sample following a specific staining protocol. The specificity of these staining techniques ranges from the general depiction of skin structure up to the highly specific staining of single target molecules in skin cells (Table 2). Using a combination of fluorescent dyes with different emission characteristics, different target structures can also be simultaneously stained and visualized in parallel.

Compared to conventional light microscopy, the essential advantages of confocal imaging are (i) an improved resolution in lateral (x/y) and in axial (z) direction, and (ii) an improved image contrast due to the reduction of background information by omitting out-of-focus information. Moreover, the better resolution in z -direction also allows optical sectioning of solid samples and thus enables three-dimensional reconstruction of a given structure. On the other hand, the initial costs for setting up the technique are relatively high, and the number of available laser lines is limited, especially in the ultraviolet (UV) range. Moreover, for living cells the high laser radiation dose in the UV-visible wavelength range might be harmful.

The basis of all confocal microscopy modes is the confocal principle. Compared to conventional bright field microscopy, the whole sample volume is not continuously illuminated but scanned with a point-like light source. The excitation light is pointed at the sample by a dichroic beam splitter, and the light returning from the sample, either by reflection or fluorescence emission, passes the beam splitter and is collected by a photomultiplier tube (PMT). The resulting image is displayed on a computer screen. Illumination, sample, and detector have all the same focus: they are called "confocal." In order to eliminate any out-of-focus light throughout the optical pathway, spatial filters or apertures, also known as "confocal pinholes," are placed behind the light source and in front of the PMT detector (Fig. 1).

In this imaging mode, only one thin plane within the sample is observed, i.e., the sample plane that is placed in the focal plane of the microscope; this plane is also called "optical section." The thickness of this virtual section depends on the spatial resolution of the system, which is the system's ability to resolve two adjacent point objects from each other. The lateral resolution mainly depends on the illumination wavelength and the numerical aperture of the objective and has been described by Abbe as (5): $d_{x/y} = \frac{0.61 \times \lambda}{NA}$, where $d_{x/y}$, smallest lateral distance between two adjacent points that are still distinguishable; λ , wavelength of the light used for imaging; NA , numerical aperture of the objective. The axial resolution in confocal systems is defined by: $d_z = \frac{1.4 \times \lambda \times n}{NA^2}$, where d_z , smallest axial distance between two adjacent points that are still distinguishable. Consequently, the theoretical lateral resolution for a confocal microscope equipped with a high-resolution objective (63x magnification, NA 1.4) and an excitation wavelength of 488 nm is approximately 210 nm; the axial resolution is slightly worse (approximately 400 nm).

TABLE 2 Confocal Laser Scanning Microscopy Fluorescence Imaging: Visualization of Skin Organization, Cellular Compartments, and Target Molecules

Staining technique	Staining mechanism	Examples	In vivo
Autofluorescence	Direct imaging of skin constituents with genuine fluorescence properties	NAD(P)H, lipofuscin; reinforcement of genuine protein autofluorescence by aldehyde fixation	+
Immersion staining	Immersion of whole skin samples in stain solution, followed by intense washing in buffer or solvent	Carmine staining	(+)
Histological staining	Specific binding of dyes to skin constituents by specific physicochemical interaction	Toluidine blue stain, Evans blue stain	–
Nucleic acid staining	Usage of dyes specifically designed for intercalation into the DNA double helix or strong interaction with nucleobases	DAPI (DNA stain), Sytox Green (DNA stain); Acridine orange (DNA and RNA stain)	–
Hybridization	Staining with small nucleic acids complementary to target sequences that are covalently bound to fluorescent dyes	Fluorescence in situ-hybridization	–
Toxin staining	Irreversible binding of toxins (e.g., from fungi or plants) to target proteins	Phalloidin (binding to F-actin); Taxol (binding to microtubules)	–
Antibody staining	Binding of antibodies specific for target molecules, normally visualized using fluorescent dyes coupled to the antibodies	Specific antibodies for many skin proteins are commercially available	–
Lipid/membrane staining	Staining with lipophilic dyes that mimic membrane lipids and thus are integrated into cellular membranes	Dil injection for neuron tracing in living tissue	+
Complexation/chelation	Staining with complexing agents specifically forming fluorescent complexes with the target ions	Morin staining of aluminum; Calcein staining of calcium	(+)
Enzyme immunoassays	Sample incubation with specific substrates containing a fluorescent molecule that is released by the target enzyme	Specific substrates for many different skin enzymes are commercially available	(+)
Milieu-dependent staining	Staining with dyes that show different fluorescence spectra depending on, e.g., local pH or ion strength	Visualization of pH in different epidermal-layers, e.g., by BCECF	+

Note: In this table, different approaches for fluorescent imaging of skin are listed together with a short description of the staining mechanism and some examples that might be used for staining. For each of these techniques, many different staining protocols have been described, adapted to the particular problem under investigation. Further information on the different staining techniques can be found in the references given at the end of this chapter. See also chapter 23 for more information.

After recording a single optical slice, the sample position is moved in z-direction relative to the focal plane of the microscope, and the next optical slice can be recorded from a different height within the sample. By moving the sample position stepwise along the z-axis, several optical sections from different sample planes can

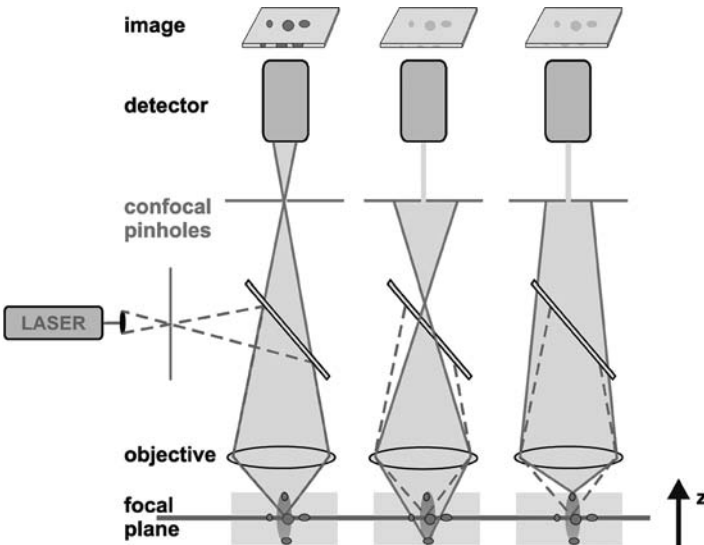


FIGURE 1 (See color insert) Image acquisition in confocal systems. In confocal microscopes, the image information is derived only from the focal plane but not from out-of-focus planes. This virtual cross-sectioning of the sample is reached by pinholes placed in the focal planes of the entrance optics and the objective lens, respectively, acting as a filter for out-of-focus-light. The illuminating light (*green broken line*) leaves the point-like light source and passes the illumination pinhole and is focused into the sample by the objective lens. The signal emitted from the sample (*red line*) is then collected by the objective lens and guided into the detector pathway. While signal from the focal plane can easily pass the detection pinhole and reach the detector for imaging (*left*), signal from below (*middle*) or above the focal plane (*right*) is filtered by the detection pinhole. Thus, the final image only shows signal information from the focal plane. For imaging different planes within the sample, the sample position relative to the objective lens has to be changed in z-direction.

be recorded (also known as “z-stack”) and put together to build a three-dimensional image volume. The maximum depth within the sample from which optical sections with acceptable signal-to-noise ratio can be recorded mainly depends on the imaging wavelength (excitation and emission), the working distance of the objective and the optical density of the sample. For the above-described system (objective 63x, NA 1.4, excitation wavelength 488 nm), it is about 70 μm . In modern confocal systems, z-stacks can also be recorded over time, enabling the observation of time-dependent processes within three-dimensional volumes (four-dimensional microscopy).

Technical Realization of Confocal Microscopy

Today, two fundamentally different types of confocal microscopes are commonly used: slow scan single-beam confocal microscopes and faster Nipkow systems using a multiple-beam approach. Single-beam instruments usually scan the sample point by point in a raster pattern, working with galvanometer-driven mirrors. Thus, the time for recording a single image (frame rate) is about one frame per second or longer. These instruments work with different laser lines for excitation, using, e.g., Argon ion lasers (488, 514 nm), Argon-Krypton lasers (476, 488, 576,

and 623 nm) and Helium–Neon lasers (543 and 632 nm). For detection, these systems use one or more PMT detectors; ideally, one separate detection channel for each dye is used. On the other hand, the Nipkow systems are equipped with a spinning disk behind the light source, containing an array of micro lenses or holes, which “cut” the light into multiple beams simultaneously focused at the sample. These multiple-beam instruments can work with normal arc-discharge lamps, and the signal can be captured in video rate with an ordinary CCD camera. Due to the better focal properties of the laser (no cross talk between multiple beams), single-beam instruments provide better results for scanning thick and dense tissue; for the investigation of rapid processes in living cells or tissues, the faster Nipkow systems are better suited.

For the evaluation and representation of confocal three-dimensional stacks, a variety of approaches with different complexity levels are available. While the maximum projection (MIP) and the average projection simply project the whole information from the image stack into one two-dimensional image, more complex algorithms lead to stereo views and three-dimensional projections which represent the sample in three-dimensional from different points of view. In order to get a good overview of the whole sample, several three-dimensional images from different angles can also be combined to a movie sequence. Using specialized rendering software packages, operations such as three-dimensional surface or volume measurement can also be calculated.

APPLICATIONS OF CONFOCAL MICROSCOPY: REFLECTANCE IMAGING

As already describe above, the reflection mode of confocal microscopes is very useful for the detailed visualization of skin and hair surfaces in their native state. In this operating mode, the topography of skin texture or the dimensions of skin folds, i.e., depth and width, can be measured up to a maximum resolution of 0.5 μm in axial direction; this resolution is sufficient, e.g., for investigating the structural changes of skin surfaces after treatment (Fig. 2). In addition to the static description and analysis of skin topography, it is also possible to follow dynamic processes on skin surfaces, e.g., the spreading behavior of emulsions directly after application (Fig. 3).

Measurement of Skin and Hair Texture

For the *ex vivo* measurement of skin topography changes after treatment, a precise protocol was developed in order to mimic the *in vivo* condition as far as possible: pork skin samples are fixed on wet filter paper and mounted on a heating stage, keeping the skin surface at a constant temperature of 32°C. This setup is placed in a tailor-made environmental chamber attached to the confocal microscope, allowing the controlled adjustment of air humidity between 30% and 90% water (w/w). Topography measurements are performed in a confocal laser scanning microscope (LEICA, Bensheim, Germany) operating in reflection mode with an excitation wavelength of 488 nm and a low magnification objective (10x, NA 0.4). Z-series are recorded with a spacing of 1 to 2 μm in z and a pinhole diameter of 1.5 airy units in order to reduce artifacts from edge effects. The final topography images are calculated using the center of mass method.

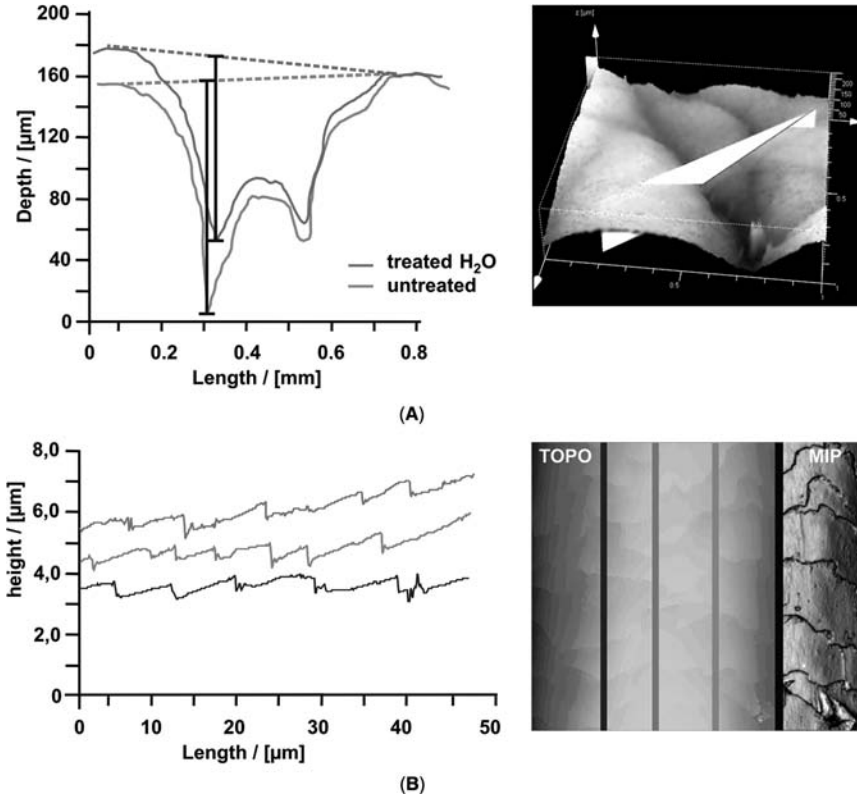


FIGURE 2 (See color insert) Three-dimensional measurement of skin surface topography and hair roughness. The reflection mode of the confocal laser scanning microscopy (CLSM) is very helpful to investigate skin surface topography and their changes after treatment. For this purpose, image stacks are taken with a spacing of 1 to 2 μm in z-direction. Afterwards, topographical images are calculated with the center of mass method. Using a standard objective (10x, NA 0.4), an axial resolution of 3 μm can be reached, and the precision of height measurement is in the range of 500 nm. **(A)** Using the above-described conditions, the depth of a skin fold is measured along the white section. Before treatment, the maximum depth is 150 μm (red line). After 10-minute treatment with tap water, the same skin fold is measured again and a reduction in depth of about 30 μm can be shown due to the swelling of the stratum corneum cells caused by water uptake. **(B)** When investigating hair surface topography, the depth profiles along the longitudinal axis of the hair only allow semiquantitative evaluation of hair roughness due to reaching the resolution limit of this setup. This is also clarified by the little structural contrast in the topography image (TOPO), while the maximum image projection (MIP) clearly outlines the single cuticle cells.

Based on this protocol, three-dimensional images of skin texture can be recorded as shown in Figure 2A. From such z-stacks of skin dimples, different profiles across the fold can be extracted to calculate the depth and the width of this fold. With the objective used in this setup, the axial resolution of the topographic measurement is approximately 3 μm , and the precision of height measurement is approximately 500 nm (i.e., height differences of ≥ 500 nm can be reproducibly distinguished). When measuring, very steep flanks of the fold should be excluded

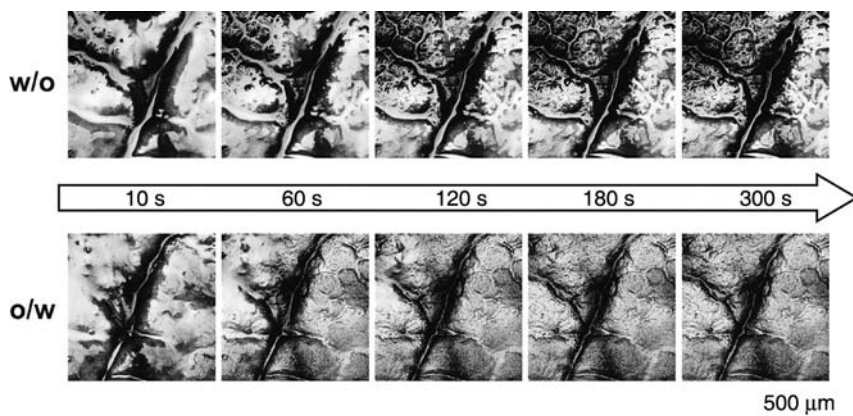


FIGURE 3 (See color insert) Spreading dynamics of different emulsion systems on skin surfaces. Remission confocal laser scanning microscopy (CLSM) imaging of emulsion films after application onto skin surfaces is a useful method to investigate the dwell time and uniformity of the respective emulsion films. In time-lapse series, the spreading and evaporation process of the emulsions can be visualized. In this example, the spreading dynamics of a water-in-oil emulsion (*w/o*, top line) is compared to an oil-in-water system (*o/w*, bottom line) on the same skin area. After skin cleansing with ethanol (70% in water), the emulsions have been applied to the same skin area (2 mg emulsion/cm²) and gently distributed. Image stacks have been recorded directly after distribution (10 seconds) and every 60 seconds for a total time of three minutes (300 seconds); later on, three-dimensional maximum projections were calculated for each time point. While the highly reflecting smooth areas on the skin surface indicate the emulsion film, uncovered surface areas reveal the skin's typical micro-roughness. Skin folds are characterized by long dark areas, often with a strongly reflecting line at their bottom. Comparing the spreading behavior of the different emulsion types, the *w/o* emulsion remains on the skin, longer than 300 seconds, surface leaving an oily film. In contrast, the *o/w* lotion has almost completely disappeared after 120 seconds.

from profile calculation. From these places, only a small fraction of the excitation light enters the objective, and the calculation of the z-profile causes outliers (6).

The skin sample shown in Figure 2A has been measured across the fold that is highlighted by the white box, before and after treatment with tap water for 10 minutes. When comparing these measurements, it can be seen that the depth of the skin fold is considerably reduced from originally approximately 150 μm (Fig. 2A, red profile) to approximately 120 μm after tap water treatment (Fig. 2A, blue profile). Presumably, the reason for this reduction is the swelling of the stratum corneum cells due to the uptake of water (7). Thus, the swollen stratum corneum at both flanks narrows the fold, resulting in the described reduction of depth.

Under the above-described controlled humidity conditions, also hair topography can also be easily measured in this setup (Fig. 2B). The recording of depth profiles along the longitudinal axis of the hair allows an assessment of the hair roughness. That way the adverse effects of repeated combing or bleaching can be estimated, as well as the visible repair effects after cosmetic hair treatment. Because the single steps between the individual cuticle cells are very small (approximately 0.3 μm, see also longitudinal profiles in Fig. 2B), the measured differences are near to the resolution limit of our setup. Thus, these measurements generate rather semiquantitative data for the comparison of different conditioning schemes than precise profiles of single hair fibers. This instance is also nicely

demonstrated by the little structural contrast of the topography image (TOPO) that is used for measurement (TOPO inset, Fig. 2B), while the MIP image used for topography visualization clearly outlines single cuticle cells (MIP inset, Fig. 2B).

Investigating the Spreading Behavior of Emulsions

Beyond static measurements of skin and hair topography, time-dependent processes can also be visualized by confocal reflection microscopy. That way the investigation of the dynamic spreading properties of emulsions on skin surfaces is a useful method for determining the dwell time and uniformity of the emulsion films after application (Fig. 3). For these measurements, one has to pay attention to the fact that the distribution properties of these products are strongly influenced by skin temperature and humidity: while the temperature influences the liquid dynamics of and within the emulsion, humidity regulates the vapor pressure of the water content and thus the evaporation speed. Therefore, the maintenance of constant ambient conditions (as described above for the static measurements) is essential for reliable measurements (8).

Figure 3 shows comparative time-lapse studies from two different basic emulsion systems [water in oil (w/o) vs. oil in water (o/w)]. After skin cleansing with 70% ethanol, the emulsion is applied to the skin and distributed with a gloved finger for five seconds. Starting directly after (10 seconds), sequential image stacks are recorded in a defined time-course using the time-lapse operating of the CLSM; the interval between the starting points of the respective stacks is set to 60 seconds. Subsequently, from each image stack a MIP image is calculated. The resulting time-dependent image series is then used for evaluation of the spreading behavior.

The time-dependent changes in surface topography of the emulsion-covered skin represent spreading and evaporation processes as well as the shine intensity of the remaining emulsions; these properties vary between different emulsions, dependent on their composition. While the highly reflecting smooth and bright areas on the skin surface display the emulsion film, uncovered surface areas show the typical skin micro-roughness. Skin folds are characterized by long dark areas, often with a strongly reflecting line at their bottom. As expected, the emulsion with an outer, low-volatile oil phase (w/o) remains on the surface even 300 seconds after application, leaving a caring oily film. In contrast, the more volatile outer water phase of the o/w emulsion is evaporated shortly after application, and the skin micro-roughness is visible again after 120 seconds.

APPLICATIONS OF CONFOCAL MICROSCOPY: FLUORESCENCE IMAGING

Staining is a popular approach for the specific visualization of skin structures. A large number of staining techniques for microscopic investigations have been developed, based on different approaches such as dyes preferably binding to tissue types with certain physicochemical binding properties or protein-specific antibodies coupled to marker dyes (Table 2). Based on these techniques, target structures of different dimensions can be addressed, ranging from the simple discrimination of different skin layers down to the sophisticated localization of single intracellular proteins (Fig. 4). In standard fluorescence microscopy, such investigations are mostly restricted to skin sections with a maximum thickness of approximately 10 μm because the superposition of stained structures in thicker

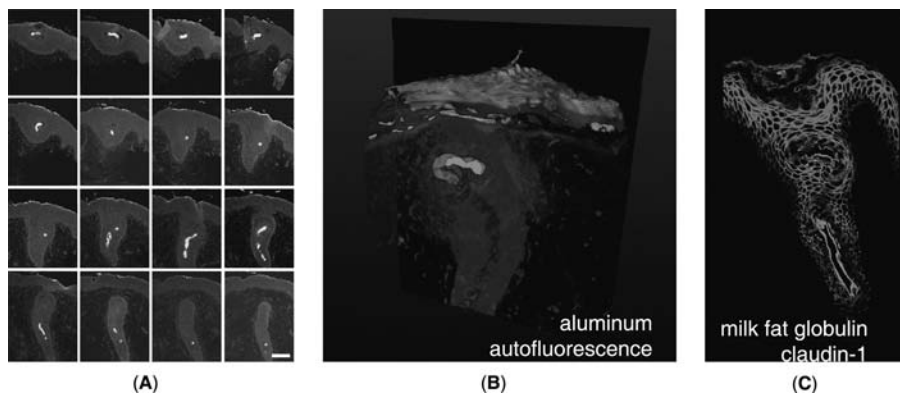


FIGURE 4 (See color insert) Specific labeling of molecular targets in two-dimension and three-dimension. In order to investigate the presence of aluminum in sweat ducts after application of antiperspirants containing aluminumchlorohydrate (ACH), samples of ACH-treated human skin (fixed in 2% paraformaldehyde and infiltrated with 30% saccharose) were plunge-frozen in liquid nitrogen. Then, serial vertical sections (thickness: 8 μm) were cut in a cryotome and incubated with morin, a complexing agent forming green fluorescent complexes with aluminum. (A) Two-dimensional confocal laser scanning microscopy (CLSM) images were taken from each serial section, recording the aluminum-morin fluorescence (yellowish-green) from the crosscut sweat duct as well as the autofluorescence (red) from the surrounding aldehyde-fixed epidermal skin. (B) Afterwards, the two-dimensional images were compiled to form an image stack for three-dimensional structural reconstruction of the aluminum distribution throughout the whole sweat duct. (C) For further elucidation of the interaction between antiperspirants and the sweat duct (right), the sections were immuno-labeled with specific antibodies, directed against a sweat-derived protein [milk fat globulin (MFG, green fluorescence)] and a potential constituent of the epidermal penetration barrier (claudin-1, red fluorescence). While the MFG signal is restricted to the luminal, i.e., the inner cell layers of the sweat duct, claudin-1 is present throughout the epidermis but not in luminal layers of the sweat duct. Scale bar: 100 μm .

samples impedes any discrimination of discrete labels. On the other hand, CLSM allows a more precise localization of target molecules due to the higher image contrast and the omission of out-of-focus fluorescence. The use of fluorescent dyes for skin staining even allows the three-dimensional investigation of the target structure in intact samples, e.g., skin biopsies, due to the possibility of optical sectioning in confocal systems; this approach is much easier and more precise than the classical approach based on serial sections. Hence, the CLSM investigation of samples stained with fluorescent labels enables the precise localization of cells or their constituents within an intact three-dimensional environment (Fig. 5).

Fluorescence-Labeling of Protein Targets in Skin Sections

Clear-cut identification of target molecules is an essential prerequisite for investigating their distribution within different skin layers as well as their subcellular localization. One possible approach for identification is the visualization of a target-specific fluorescence signals by confocal microscopy; while some target molecules already display intrinsic fluorescence properties [e.g., NAD(P)H or Ca^{2+}], most molecules have to be stained with a target-specific fluorescent label prior to investigation. In order to assure optimal accessibility of the target molecule for the fluorescent label, thin skin cross-sections are taken (thickness

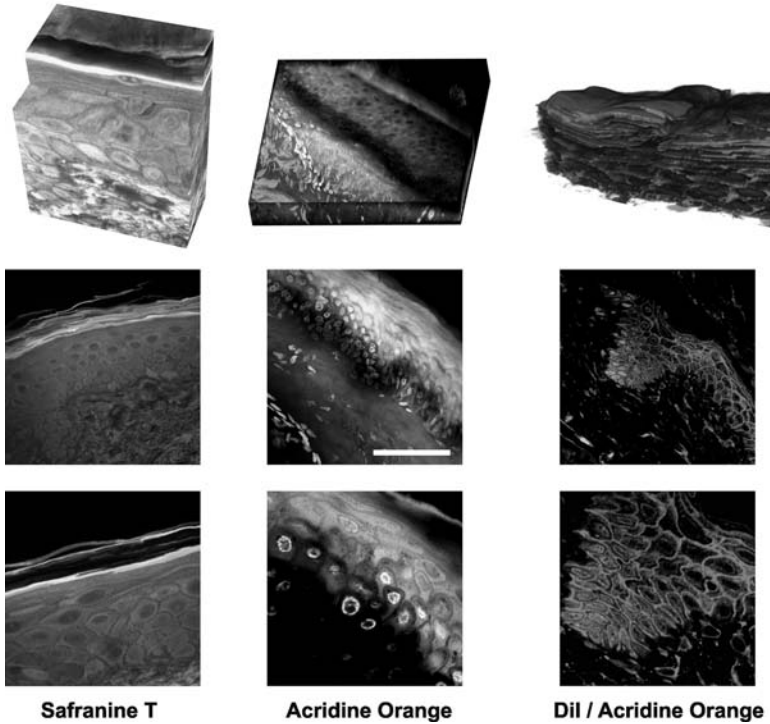


FIGURE 5 (See color insert) Blockface imaging of resin-embedded skin samples: optimal sample preservation for high-resolution three-dimensional light microscopy. Human skin biopsies were high-pressure frozen, freeze-substituted in the presence of fluorescent dyes and embedded in resin. After polymerization, excess surrounding resin was removed from the samples and plain sample surfaces (blockfaces) were produced using a diamond-trimming knife. Based on this preparation protocol, confocal image stacks can be recorded from the samples up to a maximum imaging depth of approximately 80 μm and used for three-dimensional reconstruction (*top row*). The high quality of sample staining and structural preservation allows the imaging of sample overviews (*middle row*) as well as of structural details (*bottom row*). “Safranin T” mainly stains the cytoplasm of the epidermal keratinocytes; nuclear staining is less prominent. Due to the lack of stain in the intercellular space, the cell borders are clearly visualized. Collagen and elastic fibers in the dermis are nicely outlined. “Acridine orange” stains cytoplasm and nuclei throughout the epidermis. Because the fluorescence signals from nuclei and cytoplasm show different emission maxima, these structures can be differentiated by color. The combination of “Dil and Acridine orange” leads to a clear discrimination of nuclei and lipophilic domains within the cytoplasm of viable epidermal cells, because these dyes have different binding and spectral properties. Scale bar: 100 μm .

approximately 5–20 μm); thus, the risk of a labeling failure due to impeded dye penetration is minimized. The sections then are incubated with the fluorescent label, which specifically binds to the target molecule and unbound dye is removed afterwards by washing. The specificity of the label-target bond can be assured by different binding mechanism, based on, e.g., ionic or hydrophobic interaction, chelation or high structural affinity between label and target molecule (Table 2).

In Figure 4, studies on the interaction between the active ingredient of antiperspirants, i.e., aluminumchlorohydrate (ACH), and axillary skin is shown.

For this purpose, axillary skin from volunteers was treated with ACH for three weeks and 2 mm punch biopsies were taken. From these samples, serial vertical sections (thickness: 8 μm) were cut and incubated with morin, a complexing agent that forms green fluorescent complexes with aluminum ions. The presence of aluminum can be nicely seen as yellowish-green signal along the course of the crosscut sweat duct in the serial sections, while no aluminum has penetrated into the living layers of the epidermis outlined by their autofluorescence signal (Fig. 4A). After three-dimensional structural reconstruction of the image series, the ACH distribution on the skin surface and throughout the sweat duct is even more apparent, clarifying that the antiperspirant effect is achieved by plugging the sweat duct (Fig. 4B). For further investigating possible interactions between ACH and skin proteins, the sections were immuno-labeled with specific antibodies directed against a sweat-derived protein milk fat globulin (MFG) and claudin-1, a potential constituent of the epidermal penetration barrier (Fig. 4C). It could be shown, that the MFG signal (green fluorescence) is restricted to the inner, i.e., luminal cell layers of the sweat duct, while claudin-1 (red fluorescence) is present throughout the epidermis but not in luminal layers of the sweat duct (9). Thus, any impairment of the skin barrier by ACH binding to barrier proteins can be ruled out.

Skin Morphology After Fluorescence Staining and Three-Dimensional Reconstruction of Tissue Structure

Microscopic resolution does not depend only on the physical parameters of the optical system but also on the structural preservation of the investigated sample—the interpretable resolution of a microscopic image cannot exceed the dimensions of the artifacts introduced during preparation.

Thus, for the three-dimensional visualization of skin samples at high resolution it is essential to preserve the skin structure in a near-to-life state. To determine the location of target structures with dimensions near to the resolution limit of the optical system, fixing techniques must be used that preserve the structures of the skin sample in their original position down to the nanometer range. This cannot be achieved with classical chemical fixation, because the cytoplasm is reorganized during the slow fixation process, and membranes are destabilized by osmotic gradients and chemical extraction. Also freezing in liquid nitrogen does not allow high-resolution structural microscopy because the growth of ice crystals within the sample squeezes the cytoplasm and also destroys cell membranes. High-pressure freezing, however, is one possible way to achieve low-artifact fixing of skin. In this method, formation of ice crystals during freezing (see above) is prevented by the buildup of extreme pressures (10). After freezing, these samples can then be freeze-substituted in the presence of fluorescent dyes and embedded in resin in their “vitrified” state (11).

The light microscopic information that can be obtained from such prepared samples strongly depends on the dye used during the freeze-substitution process. Figure 5 shows confocal two-dimensional images (optical sections) as well as three-dimensional reconstructions of whole skin samples freeze-substituted in the presence of selected dyes with different staining properties.

Using Safranin T, the cytoplasm is heavily stained and can be clearly distinguished from the nuclei. The cell borders become clearly outlined due to the lack of staining in the intercellular space. Because of cytoplasmic staining, individual cell layers in the stratum corneum can be distinguished. In the dermis, fibroblasts also

show a cytoplasmic staining, which can be differentiated from the detailed staining pattern of collagen and elastic fibers.

Acridine orange stains cytoplasm as well as nuclei. While the distinction between these two compartments can be clearly seen in the central and lower part of the stratum spinosum, the contrast becomes weaker in the upper layers of the epidermis. However, the stained nuclei emit light of a shorter wavelength (approximately 530 nm) than the surrounding cytoplasm (approximately 560 nm). Therefore, recording the fluorescence of the sample only in a narrow range of 525 to 540 nm allows precise visualization of the nuclei. With these filter settings no signal from the cytoplasm is detected. In the dermis, mainly nuclei of fibroblasts and epithelial cells can be seen. Structures reflecting collagen or elastic fibers are nearly unstained.

It is even possible to combine dyes with different staining properties, e.g., acridine orange as a nuclear stain (see above) and DiI, a lipophilic dye especially designed for membrane labeling. As these dyes have different excitation maxima (acridine orange approximately 500 nm, DiI approximately 550 nm), the fluorescence emitted by these molecules upon excitation can be easily discriminated with the confocal set-up. The combination of acridine orange with DiI leads to a very clear discrimination of nuclei and cell membranes or other lipophilic domains within the cytoplasm. The epidermis is homogeneously stained throughout all living layers, while the stratum corneum is stained only in the lower layers. In the dermis, nuclei and cytoplasmic structures of fibroblasts are well-defined, whereas collagen and elastic fibers show only diffuse or no staining.

The intense fluorescent labeling of such prepared skin shows clearly the high complexity of the tissue, and the optical sections recorded at higher magnification outline the excellent preservation of cellular organization (Fig. 5, bottom line). This preparation technique is especially suited to investigate the three-dimensional organization of skin and to describe interactions of different cells or cell groups in their natural environment.

FURTHER PROSPECTS OF CONFOCAL MICROSCOPY

This chapter only provides a small insight into the manifold possibilities of confocal microscopy, restricted to the examination and measurement of *ex vivo* skin samples in two-dimension, three-dimension, and four-dimension with up-to-date confocal laboratory research microscopes. Using such instruments with continuous wave lasers in the visible light range (350–700 nm), *in vivo* imaging is not possible due to the hazardous energy dose absorbed by the tissue. Moreover, there is a direct correlation between excitation wavelength and skin penetration depth: the shorter the wavelength, the smaller the skin depth that can be visualized. Thus, for *in vivo* imaging-specific microscopes have been developed using IR lasers (700–1000 nm) for confocal remission microscopy, which can be used for investigations of the cellular organization within the epidermis (see Chapter 8 and Chapter 12). However, in such microscopes both, signal-to-noise ratio as well as lateral and axial resolution, is inferior to that of laboratory research microscopes, because of the longer wavelength used for excitation and due to multiple scattering events in deeper skin layers.

Besides CLSM, multiphoton laser scanning microscopy (MPLSM) is another approach for optical sectioning of biological samples. Here, tunable femtosecond-pulsed NIR laser sources into the tissue produce fluorescence by nonlinear two- or

multiphoton fluorescence excitation of chromophores. Commonly used laser sources generate femtosecond radiation of 700 to 1000 nm, thus allowing the excitation of skin chromophores at approximately 350 to 500 nm (two photon excitation) or approximately 250 to 330 nm (three photon excitation), respectively. That way, a whole variety of fluorescence stains as well as the autofluorescence of intrinsic skin autofluorophores can be used for imaging. Because MPLSM is believed to be less harmful to the sample in terms of damaging the sample or bleaching the dye, it is also used for *in vivo* investigations of skin structure or the distribution and dynamics of intrinsic skin fluorophores (see Chapter 8 and Chapter 13).

In addition to straightforward fluorescence imaging, spectroscopic analysis of skin is also possible *ex vivo* and *in vivo*, and many different spectroscopic techniques have been developed for routine use in skin research over the last decade (see Chapters 16 and 17). For instance, FLIM allows very sensitive, concentration-independent investigations of fluorophore localization. Up-to-date, various technical approaches to measure and analyze FLIM-data are commercially available and/or under investigation (12). Because the chemical micro environment of the fluorophore is strongly influencing FLIM measurements, even specific information about the fluorophore's environment can be collected, e.g., ion or oxygen concentration and pH value.

Förster resonance energy transfer (FRET) is used to monitor interactions occurring at macromolecular distances, which actually cannot be otherwise investigated using light microscopy: upon excitation of a fluorophore, radiation-less energy transfer is possible to an appropriately positioned acceptor fluorophore over a very limited distance (1–10 nm) which subsequently emits fluorescence. Four conditions must be fulfilled for FRET to occur. Thus, FRET arises when a donor fluorophore is brought near to an acceptor dye, whose absorption spectrum significantly overlaps (>70%) with the donor emission spectrum (typically used pairs of dyes are, e.g., Cy3/Cy5, Cy5/Cy5.5, or CFP/YFP). The combination of CLSM and FRET in skin research was used, e.g., investigations on the stratum corneum lipid matrix (13) or connexin interaction patterns in keratinocytes (14).

Recently, another fluorescence-based technique has emerged that is used to investigate transport mechanisms and/or metabolic processes in living tissue: fluorescence recovery after photobleaching (FRAP). Here, an intracellular fluorophore is photobleached with high irradiation power at a localized sample area without harming the biological sample itself. After bleaching, a time-lapse series is recorded from the sample in order to monitor the reoccurrence of fluorescence in the bleached area. The time until full recovery of the fluorescence intensity at the bleached spot is used as a measure for either fluorophore diffusion speed or for the building rate of new endogenous fluorophore at the bleached site. In skin research, FRAP is mainly used for studies on penetration or diffusion processes (15).

CONFOCAL MICROSCOPY IN THE CONTEXT OF OTHER MICROSCOPIC TECHNIQUES

Structural description of tissue begins with the macroscopic view of the whole intact organ and ends with the localization of single molecules in their natural context. Depending on the question, different light microscopic approaches have to be combined with electron microscopic (EM) investigations and spectroscopic approaches in order to provide satisfactory data. While confocal microscopy is an efficient tool for studying skin samples ranging from *in vivo* studies of dynamic

processes (Figs. 2 and 3) to the *ex vivo* description of tissue organization in two-dimension and three-dimension (Figs. 4 and 5), only EM will deliver precise information on the macromolecular organization of single cells due to the higher resolving power (see Chapter 4).

Because the resolution of microscopic images is not only determined by the microscope itself but also by the artifacts introduced during sample preparation, it makes sense to develop preparation protocols that result in artifact-free samples suitable for many different microscopic approaches. Samples that have been prepared as shown in Figure 5 are suitable for three-dimensional examination by CLSM as well as for thin section analysis in transmission EM; high-pressure freezing provides optimal structural preservation and minimizes the number of artifacts. Hence, these samples allow the precise localization of subcellular compartments within the tissue environment. Moreover, these samples are also suitable for immuno light or electron microscopy. That way, skin samples can be continuously depicted from the macroscopic level to the EM level; the microscopy mode used for imaging is chosen according to the desired resolution (16).

The combination of different microscopic approaches on identically prepared skin samples will finally lead to multimodal datasets, which are a prerequisite for holistic analysis of skin structure. This will in fact close the gap between light and EM data on skin histology. For this purpose, CLSM has proven to be an essential tool.

ACKNOWLEDGMENTS

We thank K. Wilke, S. Pagel-Wolff, and K. Kawaschinski for excellent work on skin and sweat glands and to H. Wenck, K.P. Wittern, and U. Hintze for excellent support. Special thanks go also to F. Fischer for creative and challenging discussions about spectroscopy.

REFERENCES

1. Pawley JB. Handbook of Biological Confocal Microscopy. 2nd ed. New York: Plenum Press.
2. Diaspro A. Confocal and Two-Photon Microscopy: Foundations, Applications, and Advances. Hoboken: Wiley Press, 2001.
3. Matsumoto B. Methods in Cell Biology: Cell Biological Application of Confocal Microscopy. Vol. 70. 2nd ed. London: Academic Press, 2002.
4. Hibbs AR. Confocal Microscopy for the Biologists. New York: Kluwer Academic/Plenum Publishers, 2004.
5. Hecht E. Optics. 3rd ed. Boston: Addison Wesley, 2001.
6. Wessel S, Pagel S, Ritter M, Hohenberg H, Wepf R. Limitation of topographic measurements of real objects on reflection CLSM. In: Diaspro A, Brakenhoff F, Usai C, eds. Abstracts from Focus on Microscopy 2003.
7. Richter T, Peuckert C, Sattler M, et al. Dead but highly dynamic—the stratum corneum is divided into three hydration zones. *Skin Pharmacol Physiol* 2004; 17:246–257.
8. Wessel S, Pagel S, Lukas F, Hintze U, Wepf R. Dynamic Spread of Emulsions on Skin. *Imaging Microsc* 2001; 2:16–19.
9. Wilke K, Wepf R, Keil FJ, Wittern KP, Wenck H, Biel SS. Are sweat glands an alternate penetration pathway? Understanding the morphological complexity of the axillary sweat gland apparatus. *Skin Pharmacol Physiol* 2006; 19:38–49.
10. Pfeiffer S, Vielhaber G, Vietzke JP, Wittern KP, Hintze U, Wepf R. High-pressure freezing provides new information on human epidermis: simultaneous protein antigen and lamellar lipid structure preservation. Study on human epidermis by cryoimmobilization. *J Invest Dermatol* 2000; 114:1031–1038.

11. Biel SS, Kawaschinski K, Wittern KP, Hintze U, Wepf R. From tissue to (sub-) cellular fine structure: closing the gap between micro- and ultrastructural imaging. *J Microsc* 2003; 212:91–99.
12. Vo-Dinh T. *Biomedical Photonics Handbook*. Boca Raton: CRC Press, 2003.
13. Pechtold LA, Abraham W, Potts RO. Characterization of the stratum corneum lipid matrix using fluorescence spectroscopy. *J Invest Dermatol Symp Proc* 1998; 3:105–109.
14. Di WL, Gu Y, Common JE, et al. Connexin interaction patterns in keratinocytes revealed morphologically and by FRET analysis. *J Cell Sci* 2005; 118:1505–1514.
15. Johnson ME, Berk DA, Blankschtein D, Golan DE, Jain RK, Langer RS. Lateral diffusion of small compounds in human stratum corneum and model lipid bilayer systems. *Biophys J* 1996; 71:2656–2668.
16. Biel SS, Wilke K, Wepf R. From milli- to nanometer scale—no compromise in correlative microscopy. *Imaging Microsc* 2005; 7:26–29.

Histometry of the Skin by Means of In Vivo Confocal Microscopy

Kirsten Sauermann and Sören Jaspers

*Research and Development, Biophysics, Beiersdorf AG,
Hamburg, Germany*

INTRODUCTION

Histometric measurements are a quantitative approach to investigating skin changes that can not be described properly by qualitative histological parameters. Quantitative histometric parameters may be more helpful than qualitative histological features in describing subtle pathological changes, or changes in healthy skin due to environmental influences, ageing or effects of cosmetics or drugs.

In vivo histometric measurements using confocal laser scanning microscopy demonstrate worse resolution than those performed by means of histological sectioning. As compared with conventional histological sectioning, one of the main advantages of in vivo histometry is the lack of artifacts due to excision of the skin. The extent of shrinkage of the excised tissue varies. It depends, for example, upon the age of the donor (1,2). Tissue processing procedures such as dehydration and staining also contribute to distortion of the histological sections as compared with the original anatomical structures.

For this reason, it is not surprising to discover differences in histometrical parameters amongst studies using histological sectioning and in vivo methods (3). In spite of this, there are very few publications comparing in vivo histometrical techniques with other in vivo histometrical techniques, although the few existing studies show promising results (2,4,5).

The parameters described in the following are common tools used to describe skin dimensions and skin conditions.

VERTICAL PARAMETERS MEASURED WITH THE MICRONSCREW

Nouveau-Richard et al. compared skin thickness measurements to ultrasonic images and investigated the reproducibility of the respective parameters. They found that the feasibility of confocal measurements is limited to depths between 150 and 180 μm beneath the surface. Compared to ultrasonic A-scans, confocal measurements demonstrated less reproducibility. The authors explain this with the smaller field of view of the confocal microscope. The number of papillae contributing to the outcome of the measurement is smaller than with ultrasonic examinations, and biological variation of the height of the papillae has more influence on the variation of skin thickness measurements as a result. Neerken et al. compared skin thickness measurements performed by means of confocal laser scanning microscopy [especially minimum epidermal thickness (E_{min}) and maximum epidermal thickness (E_{max})] with measurements of the same sites performed with

optical coherence tomography and obtained good correlation, revealing a Pearson correlation coefficient of 0.91.

The following four parameters are measured using the micronscrew to determine the thickness of different layers of the skin: the thickness of the horny layer, the minimum thickness of the epidermis, the thickness of the viable epidermis and the maximum epidermal thickness.

Reducing the amount of water between cover slip and the skin makes investigation easier. It yields better results as the skin is oriented parallel to the glass and at a 90° angle to the z-axis of the microscope.

Thickness of Horny Layer (Dieke Stratum Corneum)

In confocal images, the healthy horny layer appears as a homogenous, highly reflective layer without any cellular structures (Fig. 1). If excessive amounts of immersion water are not used on the skin, it is easy to pinpoint the interface between the glass and the skin, and to measure the distance from this point to the layer where the first dark living cells appear in the granular layer when focusing down. Care has to be taken not to mistake nuclei in the parakeratotic horny layer following inflammation or other disturbances of final differentiation for nuclei in the granular layer. Cells in the granular layer have a bright border of cytoplasm which is full of bright, round-shaped granules (Fig. 2). Measurement of this parameter should be completed about three to five minutes after application of the water to the skin in order to avoid artifacts caused by swelling of the horny layer (6). Since, to some extent, the horny layer demonstrates irregular thickness, even within the small range of view typical of confocal microscopes, it should be measured at no less than four points per investigated area. The thickness of the horny layer, as well as its proportion of the overall thickness of the epidermis, varies over the surface of the body (Table 1). Chronological aging does not seem to influence this parameter (6). Changes from environmental influences such as thickening of the stratum corneum from repetitive UV exposure can be quantified by this

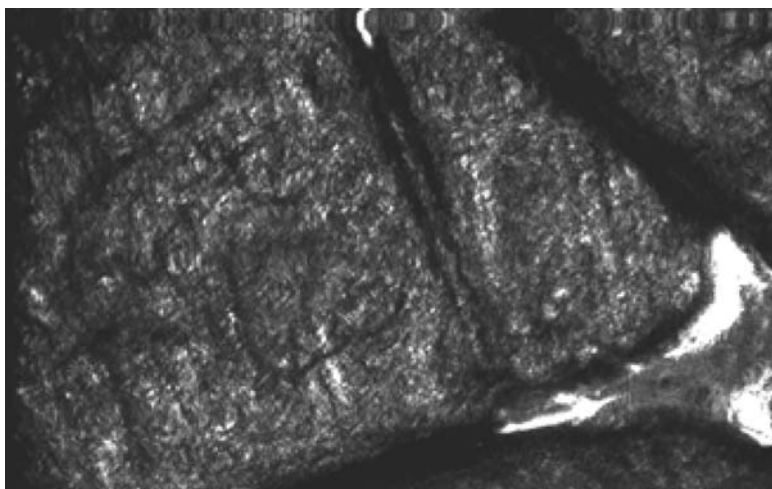


FIGURE 1 Image of the stratum corneum.

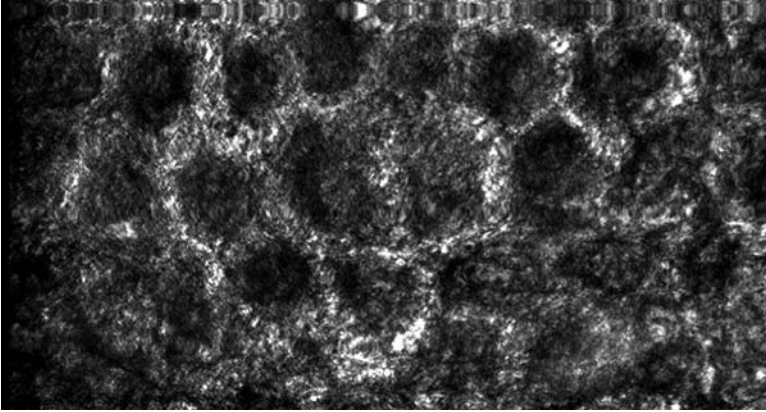


FIGURE 2 Image of the stratum granulosum.

method (7). Confocal laser scanning microscope (CLSM) seems to be more sensitive in detecting thickness of horny layer [Dieke Stratum Corneum (DSC)] changes than conventional tissue sectioning, because significant changes can be found in studies with smaller numbers of volunteers and at an earlier point in time after irradiation has begun as compared with studies using conventional histological sectioning (7). This can also be explained by the fact that in vivo confocal microscopy offers the opportunity of investigating the same defined area before treatment, and adjusting the measured changes to those of the untreated areas which lack artifacts such as the basket-weaving effect in the stratum corneum after dehydration.

Minimum Epidermal Thickness

Minimum epidermal thickness is the thickness of the epidermis down to the apical top of the dermal papillae (Fig. 3). It can be more easily and accurately measured than the overall thickness of the epidermis, because the basal parts of the rete pegs are imaged with unsatisfactory resolution and contrast. Minimum epidermal thickness may thus instead serve as an indicator of epidermal atrophy or hypertrophy and hyperplasia. It is defined and measured as the distance between the surface of the horny layer and the first appearance of the dark dermal portions of the tissue in the middle of bright shining circles of epidermal basal cells. It appears to depend upon topography, age, gender and phototype.

Huzaira et al. (8) have a different designation for this parameter, namely the "suprapapillary plate" (9). Kolbe et al. (5) measured the distance between the surface and the capillary loops (10). This parameter shows a better reproducibility than E_{\min} in slight pigmented skin, because in light skin there is less contrast between the basal layer and the underlying dermis than in more extensively pigmented skin. This might explain the slightly higher values resulting from their data as compared with other studies (Table 2). Huzaira et al. performed a study including 10 volunteers in order to investigate topographic variations of E_{\min} . Compared to most of the other studies, they came up with much higher values. This might be due to the wide range of prototypes included in their study (I–VI), with six out of ten volunteers classified as phototypes IV to VI, in contrast to most of the other studies which were restricted primarily to Caucasian skin.

TABLE 1 Thickness of Horny Layer

		DSC (μm)								
	No. of volunteers	Phototype	Volar forearm	Back	Leg	Dorsal forearm	Back of hand	Palm	Forehead	Cheek
Huzaira et al. 2001	10	I-VI	9.6 \pm 0.8	10.4 \pm 0.8	8.1 \pm 1.8	13 \pm 2.3			13.7 \pm 2.9	12.1 \pm 1.7
Gambichler et al. 2003	8	III	12.8 \pm 3							
Sauer mann et al. 2002	15	II-III	10.4 \pm 2.0							
Kolbe et al. 2001	24	I-III ^a	20 \pm 5							
Sauer mann et al. 2001 (>65 yr)	13	I-III	>65 yr: 11.2 \pm 1.9							
Neerken et al. 2004	15	I-III	18-25 yr: 10.4 \pm 3.2 Aged 19-24 yr: 29 \pm 3 Aged 54-57 yr: 29 \pm 4							19-24 yr: 27 \pm 3 54-57 yr: 28 \pm 5

^aPersonal communication.

Abbreviation: DSC, Dieke stratum corneum.

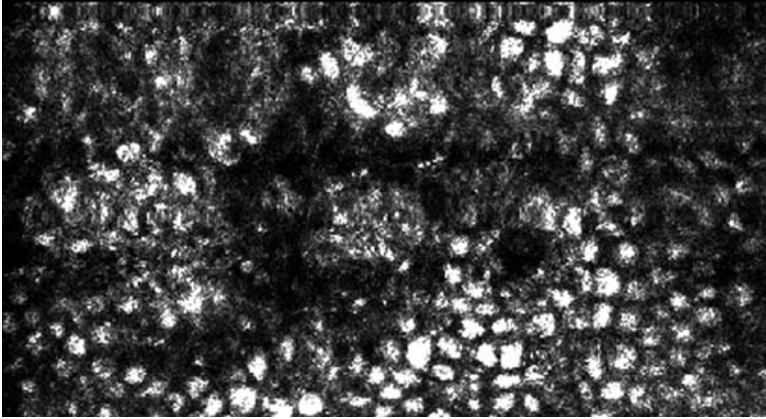


FIGURE 3 Image of the stratum basale.

E_{\min} is a sufficiently reasonable parameter for measuring epidermal hyperplasia due to UV exposure, as Gambichler et al. were able to show in a study on repeated UVA exposure. During the course of their study on topographical variations of histometric parameters, Huzaira et al. investigated 10 volunteers with wide-ranging phototypes (types I–VI) and ages (23–47 years). They were able to prove the existence of topographical differences, but based upon these observations, the authors were unable to arrive at the bold conclusion that these differences were due to chronic sun exposure in some of the investigated sites on the basis of available data. In spite of this, aging surely affects this parameter (6). Measured on the volar forearm, an area that is well protected from the sun even for Caucasian skin, E_{\min} increases slightly but significantly with age (6). Histological studies on the effects of chronological aging demonstrate change in the opposite direction, where the mean epidermal thickness decreases with age (10). This difference can be explained by looking at the anatomical differences of the parameter in question: The mean height of the epidermis is made up of the minimum height of the epidermis apical from the epidermal-dermal interdigitation, and half of the height of the undulation of the epidermal-dermal interdigitation. The epidermal-dermal interdigitation is known to flatten dramatically with age (10). This means that in aged skin, the decrease in the mean height of the epidermis is mainly due to the flattening of the epidermal-dermal interdigitation, and that this flattening must be more than twice the flattening of the overall epidermis E_{\max} (6,4).

In their study on only moderately photo-aged skin on the temple and on the volar portion of the forearm of Caucasian volunteers aged from 19 to 24, and those from 54 to 57 years, Neerken et al. were unable to detect any significant changes due to either chronological aging or photo-aging with regard to E_{\min} .

E_{\min} seems to increase for patients suffering from systemic sclerosis, although collagen deposition occurs in the dermis, not in the epidermis; but this finding is not specific enough to serve as a diagnostic criterion (11). In spite of this, drug related effects on the epidermis such as epidermal atrophy induced by topical treatment with corticosteroids or successful treatment of extragenital lichen sclerosis with topical calcipotriol can be evaluated by means of this parameter. After corticosteroid treatment, thinning of the epidermis results in a lesser distance

TABLE 2 Minimum Epidermal Thickness

		E_{\min} (μm)										
		No. of volunteers	Phototype	Volar forearm	Dorsal forearm	Back of hand	Palm	Back	Leg	Forehead	Cheek	Temple
Huzaira et al. 2001		10	I–VI	50.8 \pm 3.6	58.5 \pm 5.7			62.1 \pm 3.9	65.4 \pm 4.9	63.7 \pm 3.6	60.3 \pm 4.0	
Gambichler et al. 2003		8	III	39.0 \pm 2.9								
Sauer mann et al. 2002		15	II–III	39.4 \pm 5.5								
Kolbe et al. 2001		24	I–III ^a	68 \pm 9								
Sauer mann et al. 2001		2 \times 13	I–III	Aged > 65 yr: 40.0 \pm 5.6 Aged 18–25 yr: 35.5 \pm 4.2								
Nouveau-Richard et al. 2004		11	Not given		25–50	30–70	100–185					
Neerken et al. 2004		2 \times 15	I–III	Aged 19–24 yr: 47 \pm 5 Aged 54–57 yr: 50 \pm 8								19–24 yr: 53 \pm 5 54–57 yr: 56 \pm 6

^aPersonal communication.

between the skin surface and the capillary loops in the dermal papillae (5). The thickened epidermis measured as E_{\min} in extragenital lichen sclerosis was found to decrease after topical calcipotriol treatment (12).

As a short-term effect, changes in E_{\min} seem to reflect changes in the water content of the epidermis.

Thickness of the Viable Epidermis

Thickness of the viable epidermis (VE_{\min}) can be calculated either by subtracting DSC from E_{\min} for each single pair of measured heights, or by measuring it directly as the distance between the level of focus containing the most apical nuclei, and the apical top of the dermal papillae. Gambichler et al. calculated this parameter in their study on the effects of repeated sunbed exposures on human skin. No significant differences between UVA exposed and unexposed skin were discovered for this parameter during the course of the study, which means that the increase in E_{\min} appears to be primarily due to hyperkeratosis observed after UVA exposure. The mean level for the untreated volar forearm is specified as $26.2 \pm 2.4 \mu\text{m}$.

Overall Epidermal Thickness

As mentioned above, overall epidermal thickness can not be measured as accurately as minimal epidermal thickness by mean of confocal imaging, because the signal-to-noise ratio becomes too low as depth increases to clearly identify the bottom of the papillae. For this reason, Kolbe et al. used the distance between the surface of the skin and the upper dermal plexus to estimate overall epidermal thickness (E_{\max}). They identified the plexus as the level of focus showing vertical blood flow over large parts of the range of view (personal communication). Neerken et al. measure this height of the level of focus under the epidermis where no cells, but rather only fiber bundles could be observed, and do not mention any problems with the low signal-to-noise ratio in their investigations conducted on the volar forearm and the temple of Caucasians. In contrast, Nouveau-Richard et al. found that it was possible to obtain E_{\max} data from the back of the hands, but not to measure this height on the palm by means of confocal laser scanning microscopy. In spite of these different measuring criteria, the results are quite comparable except for the data obtained by Huzeira et al. and Rajadhyaksha et al. (Table 3) (8,13). This might be due to the ethnic differences of the volunteers involved in the studies.

As Neerken et al. point out, age seems to influence the E_{\max} parameter earlier than the E_{\min} , due to the dramatic decrease of the height of the epidermal-dermal interdigitation with age (4).

DISTANCE FROM PAPILLA TO CAPILLARY

In every dermal papillae, a single nutritive capillary can be visualized as two circles of low reflectivity, often with bright blood cells moving through the lumen. These capillaries rise from a network of arterioles at the interface between papillary and reticular dermis and lead to the numerous venules of the upper dermal plexus. The distance between the top of the dermal papillae and the first visible section of a capillary loop showing blood flow (PC) is quite constant in healthy skin. It is about $5 \mu\text{m}$ on the skin of the forearm (6,11).

TABLE 3 Overall Epidermal Thickness

	No. of volunteers	Phototype	E_{min} (μm)						
			Volar forearm	Dorsal forearm	Back	Leg	Forehead	Cheek	Temple
Huzaira et al. 2001	10	I-VI	130.36 \pm 26	134.55 \pm 18	101.6 \pm 8,5	110.6 \pm 9	130.25 \pm 11	115.25 \pm 13	—
Kolbe et al. 2001	24	I-III ^a	81 \pm 12	—	—	—	—	—	—
Neerken et al. 2004	2 \times 15	I-III	Aged 19–24 yr: 89 \pm 8	—	—	—	—	—	19–24 yr: 83 \pm 10
			Aged 54–57 yr: 75 \pm 7	—	—	—	—	—	54–57 yr: 76 \pm 6

^aPersonal communication.

This parameter is dramatically increased in the skin of patients suffering from systemic sclerosis. The papillae are filled with a reflective homogenous substance, probably collagen. The PC parameter might be useful in the diagnosis and staging of this disease (6,11).

HORIZONTAL PARAMETERS USING IMAGE ANALYSIS

Cell Size, Granular Layer

The size of the cells in the granular layer allows us to estimate changes in the speed of epidermal differentiation, and since this may correlate in healthy skin, of the epidermal proliferation rate as well. This parameter can not be used to compare the speed of epidermal turnover between different body sites or individuals, but only at one site over time, because both the speed of differentiation and the thickness of the epidermis vary between different body sites and individuals.

In general, large cells in the granular layer correspond with slow epidermal turnover, whereas small cell sizes indicate faster renewal of the epidermal structures (5,10).

Accordingly, the size of the cells in the granular layer increases with age as the time required for epidermal renewal increases (6). Cells in the most apical cell layer beneath the stratum corneum on the volar forearm lie within a range of $572 \pm 89 \mu\text{m}^2$ (5), $752.1 \mu\text{m}^2$ (7,14), $803 \pm 13 \mu\text{m}^2$ in younger individuals and $1004 \pm 120 \mu\text{m}^2$ in the skin of elderly volunteers (6,11). On the other hand, cell size decreases within two weeks of repetitive UV irradiation, which corresponds to the well-known development of hypertrophy and hyperkeratosis due to UV exposure (7,14). This phenomenon demonstrates that it is more likely the speed of differentiation than the epidermal turnover rate that influences the flattening of the keratinocytes during differentiation, because higher proliferation and faster differentiation in this physiological adaptation to UV leads to a thicker epidermis and stratum corneum, not to accelerated renewal of the epidermal tissue.

The influence of corticosteroids on the flattening of the keratinocytes in the process of differentiation seems to be paradoxical. In spite of a decrease in the proliferation rate, the cell size does not increase, but Kolbe et al. indicated a significant decrease in cell size after a three to four week period of daily topical application of corticosteroid. However, this observation, together with the well described atrophy of the epidermis due to corticosteroid treatment, is consistent with the hypothesis that cell size in the horny layer is influenced by the speed of differentiation of the keratinocytes on their way through the epidermal layers more than by the rate of mitosis in the basal layer.

Similarly, Huzeira et al. analyzed the number of cells per unit area in the spinous layer, and the number of basal keratinocytes per unit area of basal membrane, and found some topographic variations from one body region to the other for this parameter as well. The number of cells in the spinous layer seems to be quite high on the back compared to the leg, forehead and cheeks, whereas the opposite applies to the number of basal keratinocytes per unit area of basal membrane; this parameter has its lowest values in the skin of the back, and its highest values in the skin of the forehead.

OBJECT DENSITY PARAMETERS

Density of Dermal Papillae

In conventional histology, the epidermal-dermal junction is imaged as a more or less curved horizontal line. Epidermis and dermis show a strong interdigitation

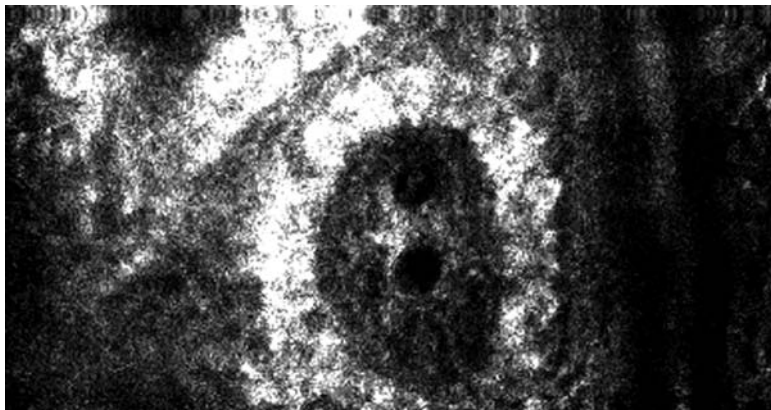


FIGURE 4 Image of the papillae (with section through capillary loop).

which probably has a function in connecting the epidermis with the dermis physically and, as it increases the interface between the two skin layers, it is important for the exchange of substances.

In order to quantify interdigitation between epidermis and dermis, Timar et al. have proposed using a parameter called the interdigitation index (15). They calculated this parameter in histological sections as the length of the winding borderline between epidermis and dermis divided by the length of the skin site investigated. Seite et al. used this parameter to evaluate changes to human skin resulting from topical application of a moisturizing cream containing retinol and vitamin C (16). The amplitude of the epidermal-dermal junction is not only a function of the height of each single dermal papilla reaching into the epidermis, but also of the density of dermal papillae in the skin, especially if they are rare as is the case with elderly skin, because it becomes less probable that a papilla is cut at its maximum height (6). In contrast to this, the density of the papillae counted by means of *in vivo* confocal microscopy is not influenced by the shape or height of the papillae.

As an *in vivo* parameter, the density of the dermal papillae can be estimated by counting the dermal papillae per viewed unit area (Fig. 4). This parameter is a measure for interdigitation of epidermis and dermis, and for the state of the nutritional function of the microvasculature of the papillary dermis: Each dermal papilla contains exactly one nutritive capillary loop (17). In 2001, Huzaira et al. announced that they found a higher papillae density in some areas that which are exposed to the sun, such as the dorsal forearm and the face, as compared with the lower back which is protected from the sun (8). This might have indicated that exposure to the sun leads to an increase in the density of dermal papillae. But Gambichler et al. and Sauermann et al., as well as Neerken et al., demonstrated that photo-aging, as well as aging, are associated with a decrease in the density of dermal papillae (4,7,6). Therefore, the differences in the size and density of the papillae observed by Huzeira et al. seem more probably to be topographical variations than changes due to exposure to the sun.

REFERENCES

1. Evans R, Cowdry EV, Nielson PE. Aging of human skin. *Anat Rec* 1943; 86:545-565.
2. Nouveau-Richard S, Monot M, Bastien P, de Lacharriere O. *In vivo* epidermal thickness measurement: ultrasonic vs. confocal imaging. *Skin Res Technol* 2004; 10:136-140.

3. Rajadhyaksha M, Gonzales S, Zavislan JM, Anderson RR, Webb RH. In vivo confocal scanning laser microscopy of human skin II: advances in instrumentation and comparison with histology. *J Invest Dermatol* 1999; 113:293–303.
4. Neerken S, Lucassen GW, Bisschop MA, Lendrink E, Nuijs TA. Characterization of age-related effects in human skin: a comparative study that applies confocal laser scanning microscopy and optical coherence tomography. *J Biomed Opt* 2004; 9(2):274–281.
5. Kolbe L, Kligman AM, Schreiner V, Stoudemayer T. Corticosteroid-induced atrophy and barrier impairment measured by non-invasive methods in human skin. *Skin Res Technol* 2001; 7(2):73–77.
6. Sauermann K, Clemann S, Jaspers S, et al. Age related changes of human skin investigated with histometric measurements by confocal laser scanning microscopy in vivo. *Skin Res Technol* 2002; 8(1):52–56.
7. Gambichler T, Sauermann K, Altintas MA, et al. Effects of repeated sunbed exposures on the human skin. In vivo measurements with confocal microscopy. *Photodermatol Photoimmunol Photomed* 2004; 20(1):27–32.
8. Huzaira M, Rius F, Rajadhyaksha M, Anderson RR, Gonzalez S. Topographic variations in normal skin, as viewed by in vivo reflectance confocal microscopy. *J Invest Dermatol* 2001; 116(6):846–852.
9. Lavker R, Gerberick F, Veres D, Irwin C, Kaidbey K. Cumulative effects from repeated exposures to suberythemal doses of UVB and UVA in human skin. *J Am Acad Dermatol* 1995; 32(1):53–62.
10. Lavker RM, Zheng PS, Dong G. Aged skin: a study by light, transmission electron and scanning electron microscopy. *J Invest Dermatol* 1987; 88(suppl 3):44–51.
11. Sauermann K, Gambichler T, Jaspers S, et al. Histometric data obtained by in vivo confocal laser scanning microscopy in patients with systemic sclerosis. *BMC Dermatol* 2002; 2(1):8 [Epub 2002 Aug 06].
12. Kreuter A, Gambichler T, Sauermann K, Jansen T, Altmeyer P, Hoffmann K. Extragenital lichen sclerosis successfully treated with topical calcipotriol: evaluation by in vivo confocal laser scanning microscopy. *Br J Dermatol* 2002; 146(2):332–333.
13. Rajadhyaksha M, Grossman M, Esterowitz D, Webb RH, Anderson RR. In vivo confocal scanning laser microscopy of human skin: melanin provides strong contrast. *J Invest Dermatol* 1995; 104(6):946–952.
14. Gambichler T, Sauermann K, Altintas MA, Altmeyer P, Hoffmann K. Acute effect of solar-simulated radiation on epidermal thickness assessed by confocal laser scanning microscopy in vivo. *J Europ Acad of Dermatol Venereol* 2004; 18(5):638.
15. Timar F, Soos G, Szende B, Horvath A. Interdigitation index – a parameter for differentiating between young and older skin specimens. *Skin Res Technol* 2000; 6(1):17–20.
16. Seite S, Bredoux C, Compan D, et al. Histological evaluation of a topically applied retinol-vitamin C combination. *Skin Pharmacol Physiol* 2005; 18(2):81–87.
17. Braverman IM. The cutaneous microcirculation [Review]. *J Investig Dermatol Symp Proc* 2000; 5(1):3–9.

Two-Photon Microscopy and Confocal Laser Scanning Microscopy of In Vivo Skin

Gerald W. Lucassen

Care & Health Applications, Philips Research, Eindhoven, The Netherlands

Rob F. M. Hendriks

Philips Research (WA11), Eindhoven, and Lumileds, Best, The Netherlands

INTRODUCTION

Noninvasive in vivo imaging of the upper skin layers has applications in dermatology and cosmetology. Here the importance lies in the ability to investigate the skin structure without taking skin biopsies. However, it is difficult to image skin optically due to the large extinction by scattering and the relatively short scattering lengths. In selecting an imaging technique, one has to make a trade-off between penetration depth and spatial resolution. Available techniques range (in order of decreasing penetration depth and increasing axial resolution) from magnetic resonance imaging, ultrasonography, photoacoustic imaging, optical coherence tomography, and optical coherence microscopy to confocal and multi-photon microscopy. The microscopic techniques have about 200 μm penetration depth and up to one-micrometer resolution and are therefore suitable for imaging the upper layers of the skin at the cellular level.

In this chapter we describe noninvasive in vivo skin imaging using confocal laser scanning microscopy (CLSM) (1–6) and two-photon fluorescence microscopy (TPFM) (7–15). CLSM and TPFM images provide complementary information. CLSM is based on elastic scattering (reflectance) of laser light in skin, originating from refractive index variations at the (intra) cellular level. TPFM is based on two-photon absorption-induced auto-fluorescence by endogenous fluorophores and proteins in the skin. The main endogenous fluorophores are extracellular components like collagen and elastin, or cellular nicotinamide adenine dinucleotide (NADH) and keratin (16–18). Some studies have been performed on using the two techniques on similar regions of the skin (7). We describe the combination of the two microscopes into one device to obtain images that contain complementary information of both reflectance and fluorescence of the exact same skin region (12). These methods have been used to study occlusion effects and skin layer thickness changes and for determination of mean epidermal cell sizes and orientation distribution of collagen in the dermal layer (19).

CONFOCAL LASER SCANNING MICROSCOPY

In CLSM a laser spot is laterally scanned in the focal plane of the objective lens in the skin using scanning mirrors. Three-dimensional resolution is obtained by limiting the detection volume using a pinhole in the detection path. The pinhole is used to only select light that originates from the image plane on the detector. Light that

is scattered from outside the image plane in the object is not focused onto the detection pinhole and is strongly suppressed. Penetration depth is limited to several hundred micrometers in skin.

In our experiments we used a modified VivaScope1000TM (Lucid Inc., Rochester, U.S.A.) specifically designed for *in vivo* skin investigations, which acquires images at a rate of 10 to 20 frames/sec (20). A gallium arsenide laser diode delivers light at a wavelength of 830 nm at a maximum power of 15 mW on the skin. The laser focus is continuously scanned in the X–Y lateral plane (parallel to the skin surface) with a field of view (FOV) of 480×640 pixels² and pixel size of $0.96 \mu\text{m}$. Part of the back-reflected light from the focus in the skin is picked up by the objective lens and separated from the incident beam using a polarizing beam splitter and detected on an avalanche photodiode through a pinhole for confocal detection. A piezo mechanical focusing drive (PIFOC, Physik Instrumente, Waldbronn, Germany) with $350 \mu\text{m}$ travel range and 60 nm resolution was used for accurate focal positioning of the microscope objective lens (a 30x, 0.9 NA, water immersion objective, Lomo, Vermont Optechs, Charlotte, Vermont, U.S.A.). Custom developed software in LabviewTM was used to control the microscope, to set the power of the diode laser, and for automatic depth scanning, data-acquisition, storage, and image processing. The images consist of a number of slices taken at different depths. In the control software, the user can select the number of slices, spacing between the slices, and the laser power used for each slice. Slices are saved as an 8-bit Windows bitmap. We generally choose the laser power such that at each depth the full 8-bit dynamic range is used. Averaging the images over four scans clearly improves the quality of the images. Furthermore, it is possible to select a region of interest within the full frame. For imaging we use a 14 Hz frame rate. The lateral images have a FOV of 586×652 pixels² with $0.96 \mu\text{m}/\text{pixel}$. To limit the total image file size and to increase speed, we frequently use a FOV of 250×250 pixels² and 170 slices at $2 \mu\text{m}$ step interval. Such a three-dimensional image of 170 slices takes approximately 40 seconds to acquire. For the experiments on skin, we used water immersion and a $170 \mu\text{m}$ cover glass slip. We tried oil and water to provide optical contact between skin and glass. Water leads to reflections at the boundary, which are absent when using oil due to the better refractive index matching with the skin stratum corneum and the glass.

TWO-PHOTON FLUORESCENCE MICROSCOPY

In TPFM the two-photon absorption-induced auto-fluorescence only occurs in the focal point of the excitation beam, where the intensity is at maximum. Therefore, in TPFM, the three-dimensional resolution is obtained through limiting the excitation volume. Hence, there is no need for a pinhole because no two-photon fluorescence is generated outside the focal volume. Compared to single-photon fluorescence microscopy, TPFM uses a longer excitation wavelength and, therefore, has increased penetration depth and has reduced photo damage to the excitation focal volume.

We have used a home-built two-photon fluorescence microscope, optimized for imaging *in vivo* human skin. The emphasis of the design is on a high-detection efficiency of the fluorescence, which leads to high imaging speed and reduces irradiation time as much as possible. We use a high quantum efficiency cooled photomultiplier tube (PMT) in photon counting mode (Hamamatsu H7421–40) for fluorescence detection. Lateral scanning is realized by two scan mirrors, while

for axial scanning the microscope objective is translated. For focusing of the excitation beam and collecting the fluorescence a high numerical aperture, long working distance microscope objective (Leica 40x, 0.8 NA water immersion) is used. A transparent gel with a refractive index close to that of water is used as immersion medium. Custom software has been written to control the lateral and axial scanning, and to synchronize these with the PMT readout. The two-photon microscope uses a titanium sapphire laser (Tsunami, Spectra-Physics). This laser generates 80 fsec pulses at a repetition rate of 80 MHz. A pre-chirp prism assembly is used to compensate for pulse spreading in the optical elements of the microscope. At the object location, we used an autocorrelation setup to determine the pulse length. Setting the pre-chirp to minimal pulse length resulted in 100 fsec pulses after the final microscope objective (without pre-chirp the final pulse length was 350 fsec). A dichroic beamsplitter separates fluorescence from the reflected excitation beam. This filter has high transmission between 400 and 600 nm, and a high reflection for wavelengths longer than 700 nm. The dichroic beamsplitter is placed between the microscope objective and the scan unit (nonscanned detection). For in vivo skin imaging, we use an excitation beam of 40 mW average power, consisting of 100 fsec pulses (0.5 nJ/pulse), at a wavelength of 760 nm. Lateral images have a FOV of $230 \times 230 \mu\text{m}^2$, and consist of 250×250 pixels². A three-dimensional image of 50 slices takes approximately one minute. For better image quality we take images of 250×250 pixels² at 5 kHz, taking approximately 15 minutes.

COMBINED TPFM AND CLSM

To combine the TPFM and CLSM we inserted a dichroic coupler just above the microscope objective in the confocal microscope (Fig. 1). The dichroic coupler was placed at a 45° angle with respect to the confocal reflectance laser beam. This introduced a lateral displacement of the confocal reflectance laser beam. To compensate for this displacement an antireflection coated compensator plate was used above the dichroic coupler (Fig. 1).

In the combined system where the TPFM and the CLSM share the same objective lens, one has the possibility to image the same spot in the skin at each depth position as selected by tuning the mechanical piezo stage coupled to the objective lens. Although some light loss in the CLSM was introduced by the insertion of the dichroic coupler and compensator plate, no significant decrease of CLSM imaging performance was observed. With the confocal laser beam switched off, the excitation spot of the TPFM was visible on the CLSM detector. This was used to determine the relative positions of the FOV of the two microscope systems. By imaging the fibers in a piece of highly fluorescent paper we checked the exact alignment of the systems.

Confocal reflectance and two-photon fluorescence images provide complementary information. In CLSM, the contrast depends on light scattering visualizing the interfaces where significant changes in refractive index occur such as cell membranes, collagen matrix interfaces, and melanin granules or nuclei. In TPFM the contrast is given by endogenous fluorophores-like collagen and elastin, or by NADH and keratin (16–18). The information content in the CLSM reflectance and TPFM images is thus rather different.

The combined microscope system allows for sequential imaging exactly of the same region of skin within a minimal time gap of minutes. This makes direct

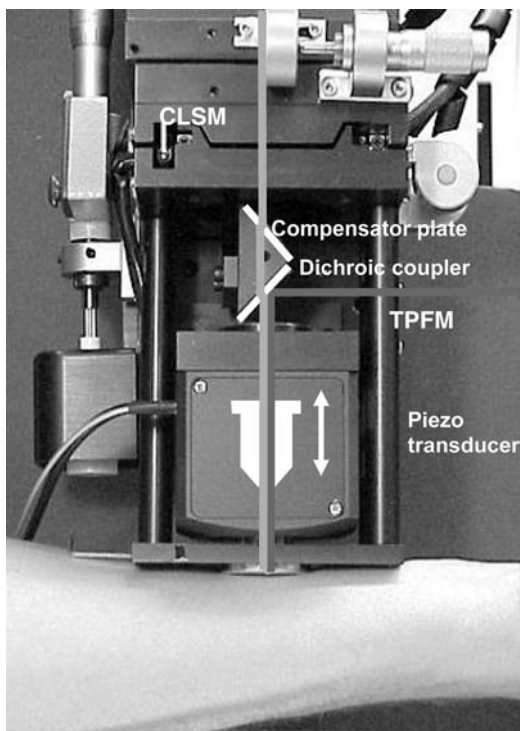


FIGURE 1 Experimental detail of the combined CLSM and TPFM microscope system; dichroic coupler and beam displacement compensator plate. *Abbreviations:* CLSM, confocal laser scanning microscopy; TPFM, two-photon fluorescence microscopy.

comparison of the methods possible. In the following, we describe results of the separate and combined methods applied to human skin *in vivo*.

RESULTS

Images of both microscopes are represented in 8-bit grey scale. Three-dimensional images are visualized by creating cross sections through the three-dimensional image stack using the software package Alice (Hayden Image Processing). Custom software (Labview) was used for making further analyzes on the images such as average image intensity versus depth profiles for determination of layer thickness and Fourier analysis for mean (epidermal) cell size (21).

CLSM and TPFM Images of Skin

Figures 2A and B depict the CLSM reflectance images of skin measured on the back of the hand and the TPFM images of volar forearm skin at various depths below the skin-glass interface, respectively. At the level of the stratum corneum light scattering is high and no structure of the corneocytes can be distinguished; however, in the epidermal skin layer cells are visible in the CLSM reflectance images. The bright scattering regions in the image indicate the epidermal-dermal basal cell-layer junction where high refractive index melanin granules are situated. At 74 μm depth the skin papillae region shows bright rings with dark inner regions. In the darker regions, collagen of the dermal papillae is present. In the live video

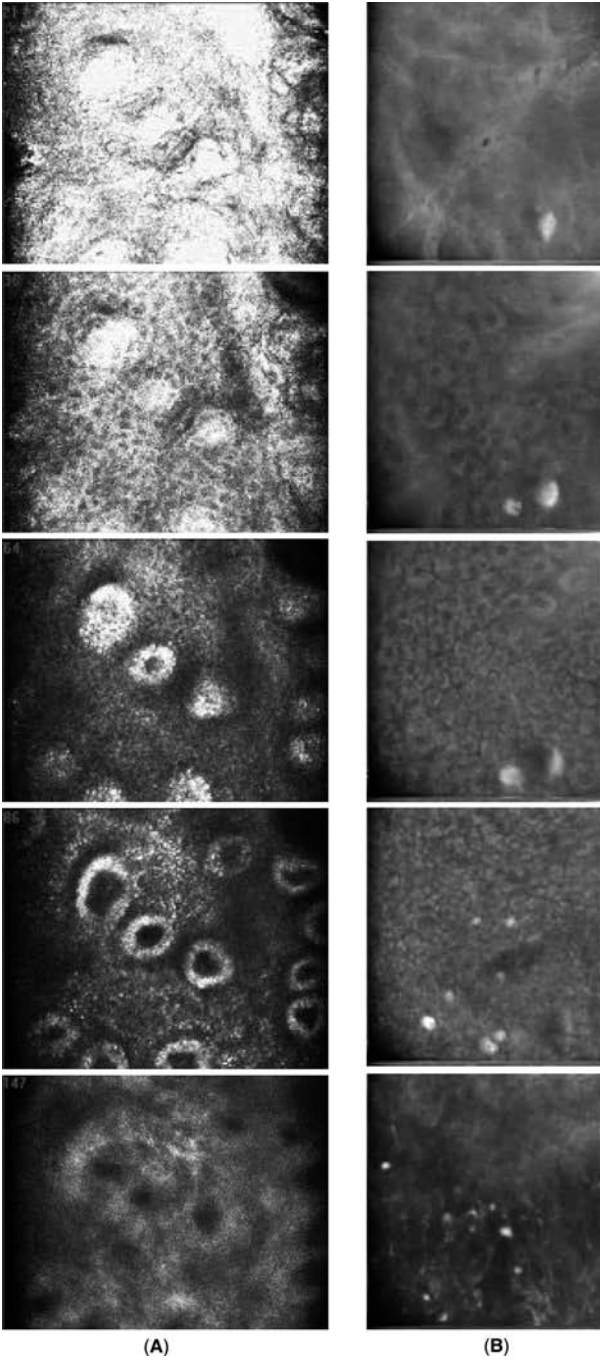


FIGURE 2 (Caption on next page)

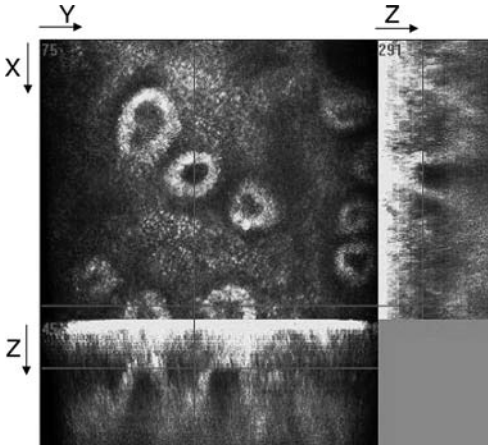


FIGURE 3 Confocal laser scanning microscopy cross-sectional image built from a three-dimensional stack of images. The lower panel shows the Y-Z plane cross-section, the right panel shows the X-Z cross-section. The epidermal-dermal junction in the skin is visible by the bright undulating band.

images in these regions often blood capillaries can be observed, with the individual red blood cells moving by. At $126\ \mu\text{m}$ depth the CLSM image represents scattering from collagen fibers in the dermal layer. At even greater skin depths, the images often darken and blur too much due to high extinction caused by light scattering and the contribution of multiple scattering events to the reflectance signal and decreased spatial resolution caused by aberrations. Cross-sectional views of the three-dimensional CLSM image stack are presented in Figure 3. The epidermal-dermal junction is visualized in the X-Z and Y-Z cross-sections by the bright undulating band.

In contrast to the CLSM images of the stratum corneum layer, in the TPFM images (Fig. 2B) individual corneocytes can be observed. In the epidermal layer the fluorescence signal arises from the cell cytoplasm, and not from the cell wall boundaries or the nucleus regions in the cells. The highly scattering melanin granules providing contrast in the CLSM images are not visible in the two-photon fluorescence images at $760\ \text{nm}$ excitation. In the upper dermal layer fibrous structures are observed, which represent the collagen and elastin network.

Combined CLSM and TPFM System

In the combined microscope system, reflectance and fluorescence images were taken of the same skin region for direct comparison of the information content of the methods. CLSM (top) and TPFM (bottom) images of epidermal skin are presented in Figure 4. From these images it can be seen that information from CLSM reflectance and TPFM are complementary. In the reflectance mode, light is scattered from the boundaries between the cells, i.e., the cell walls, whereas in

FIGURE 2 (Continued) (A) Confocal laser scanning microscopy reflectance images of human skin (back of the hand) in vivo at different depths. From top to bottom: 12, 26, 56, 74, and $126\ \mu\text{m}$ below the skin-glass interface as derived from the piezo focusing drive control. (B) Two-photon fluorescence microscopy images of human skin in vivo at different depths. From top to bottom: 16, 28, 55, 70, and $112\ \mu\text{m}$ below the skin-glass interface.

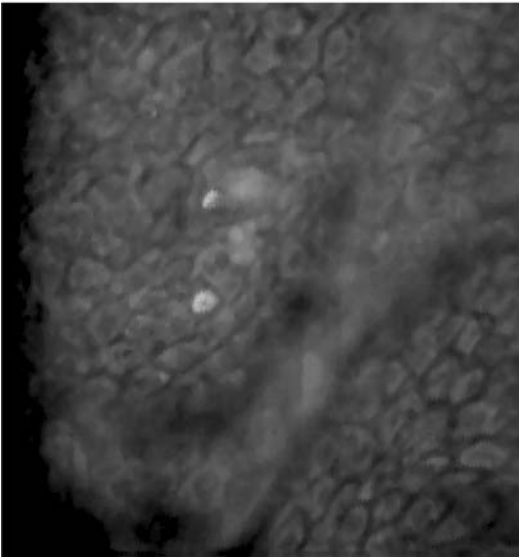
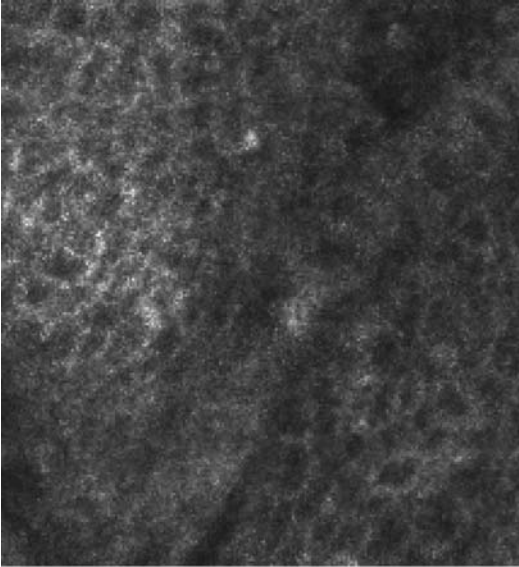


FIGURE 4 Complementary information from confocal laser scanning microscopy (CLSM) and two-photon fluorescence microscopy (TPFM) techniques of the same region in the epidermis layer in skin. CLSM (*Top*), TPFM (*Bottom*). In CLSM the signal is due to refractive index mismatches at interfaces of cell membranes. In TPFM the fluorescence signal originates from endogenous fluorophores such as NADH, keratin, and collagen. In the CLSM image the cell walls are visible, while contrastingly, in the TPFM image the cell content is fluorescing and the membranes and cell nuclei do not fluoresce.

two-photon fluorescence mode the cell boundary regions are dark. The cell cytoplasm does not scatter a lot of light in the reflectance mode but does give off a fluorescence signal. The nuclei do not seem to scatter enough light to be visualized in the reflectance image. In the fluorescence image the dark central regions in the cells most probably represent the nuclei. Rajadhyaksha et al. showed that the epidermal cell nuclei could be visualized by CLSM using acetic acid, which accumulates in the nucleus and enhances scattering by the increased refractive index mismatch of the nucleus with the cytoplasm (22).

Skin Layer Thickness Measurements

In Figure 5 an example of the TPFM image average intensity (normalized to the incident intensity) versus depth profile is presented. By visual inspection of the lateral images at the various depths the different skin layers can be identified. The regions in the intensity versus depth profile marked by I, II, and III correspond to stratum corneum, epidermis, and dermis, respectively. The high fluorescence signal in the stratum corneum originates from the keratin (16–18). In the confocal reflectance a similar intensity versus depth profile shows less distinctive structure in the stratum corneum, probably due to the more homogenous distribution of refractive index. Combined analysis of the depth profile and the lateral structure in the images allows automated determination of skin layer thickness from the images. Such analysis was performed on images of occluded skin, which will be described next.

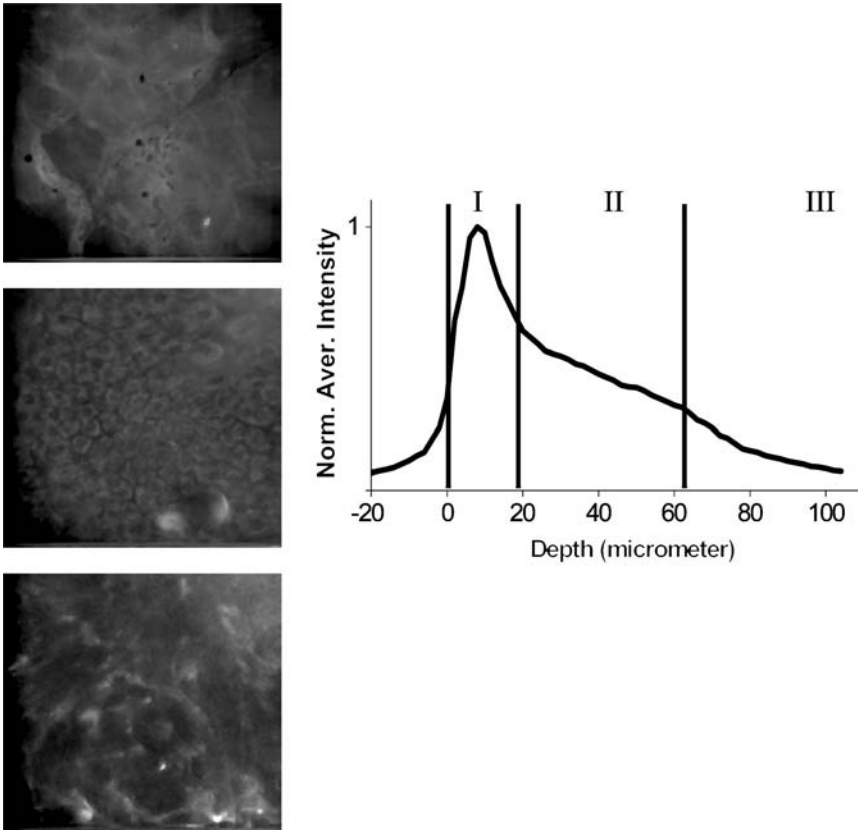


FIGURE 5 Layer thickness determination from the average image intensity profile across the skin depth as measured with two-photon fluorescence microscopy. The images at the left represent the stratum corneum (*top*), epidermis (*middle*), and dermis (*bottom*). By inspection of the images and the intensity depth profile we find markers indicated by I, II, and III to estimate layer thickness automatically.

Layer Thickness of Skin Under Occlusion

The combined CLSM and TPFM system were used to study the effects of occlusion on the skin. Under occlusion, water evaporation is blocked and a significant increase of the water content of the upper skin layers occurs. The occlusion experiments were performed on the volar forearm using a cover glass slip during 90 minutes. CLSM and TPFM measurements were done sequentially, each taking five minutes during a 45-minute period. A last data point was measured after 90-minute occlusion. The total time needed per data point for the two methods was three minutes. Between the first series of 45-minute measurements and the last measurement at 90-minute occlusion, the subject has been decoupled from the system; therefore, the position of this last measurement is not exactly the same. From the images, the stratum corneum thickness has been determined as a function of occlusion time as shown in Figure 6. The solid circles in Figure 6 correspond to the stratum corneum thickness determined by TPFM images and the open circles to that by CLSM images. The two-photon data has considerably lower variation compared to CLSM data due to the fact that the transitions between glass and stratum corneum and stratum corneum to epidermal cell layers can be better recognized in the two-photon fluorescence images. In the CLSM images, the glass-stratum corneum transition is unclear due to the strong scattering in the images even at lowest incident intensity. The solid line in Figure 6 is a fit to the two-photon data points. Using a single exponential decay model, we find a swelling time constant of about 25 minutes with $11\ \mu\text{m}$ stratum corneum thickness before occlusion and $25\ \mu\text{m}$ as a saturation value. In order to relate the measured thickness d' to the physical thickness d of the skin, a correction for the refractive index difference between the immersion medium (water, $n_0 = 1.33$) and the stratum corneum ($n = 1.5$) should be incorporated using (23)

$$d = \frac{n}{n_0} d' \quad (1)$$

yielding a physical thickness d , 12% larger than the measured thickness d' . A full correction would include also the actual changed refractive index profile due to hydration. From confocal Raman spectroscopy measurements on the effects of occlusion on the stratum corneum (24) it can be estimated that refractive index changes by 10% to 20% to lower values due to the higher water content after occlusion. Compared to data obtained from biopsies (where 30% swelling on average is reported) the swelling in our experiment is significantly larger (5,25). However, the experiment was repeated for six different subjects; with the result that, on average, the stratum corneum swelling was about 25% after 90 minutes in agreement with literature.

In the reflectance images we observed a remarkable change in the reflectance properties of the stratum corneum. In the cross-sectional view of the CLSM reflectance image after 90-minute occlusion in Figure 7 a bright band is clearly visible in the stratum corneum due to increased scattering from the stratum corneum. In Figure 6 (bottom) the maximum of the reflected intensity in the images is plotted versus occlusion time. The solid line is a single exponential fit to the data, yielding a time scale of 25 minutes scale by constant. The increased scattering is probably due to the increased contrast between high refractive index lipids and the lower refractive index of water that is inhomogeneously distributed in the stratum corneum.

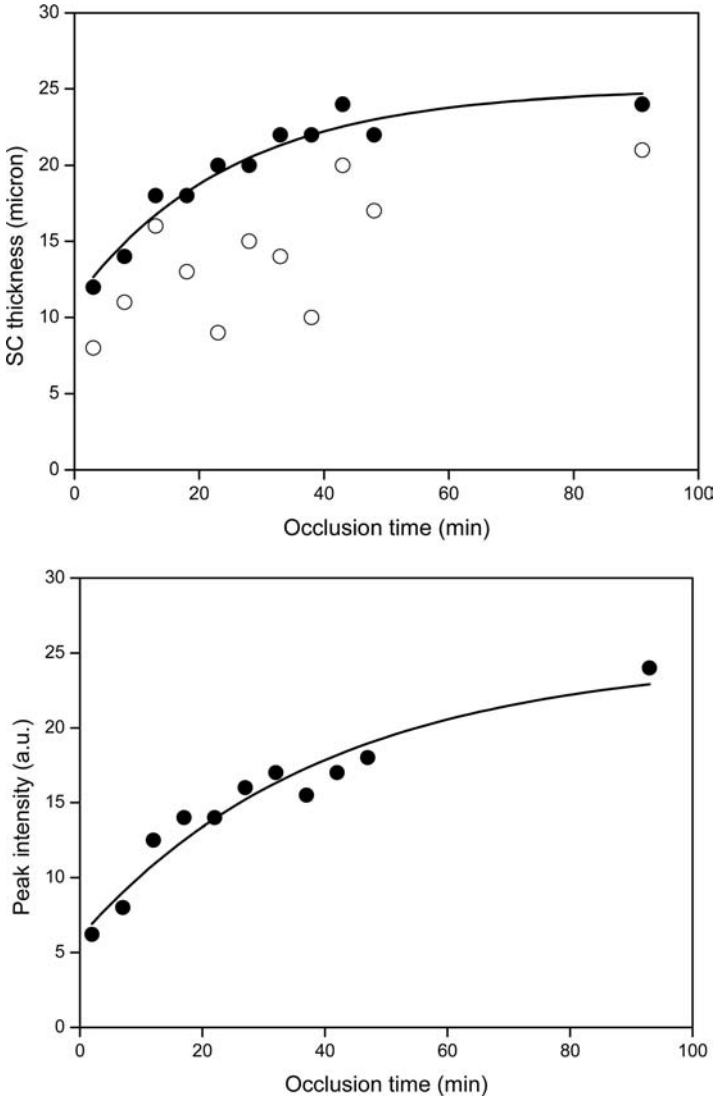


FIGURE 6 Effects of hydration to the stratum corneum. (*Top*) Increase in stratum corneum layer thickness versus occlusion time, measured by two-photon fluorescence microscopy. (*Bottom*) Increase in maximum average intensity in the reflectance image versus occlusion time.

Mean Cell Size from Fourier Analysis

Besides skin layer thickness determination also structural information can be extracted from the images, such as cell size and structural orientation of collagen in the dermis. We have used Fourier analysis (26) of the lateral images to *automatically* determine the mean cell size (MCS) in the epidermal skin layer CLSM images as a function of depth (21). This is done by calculating the power distribution $P(|k|)$

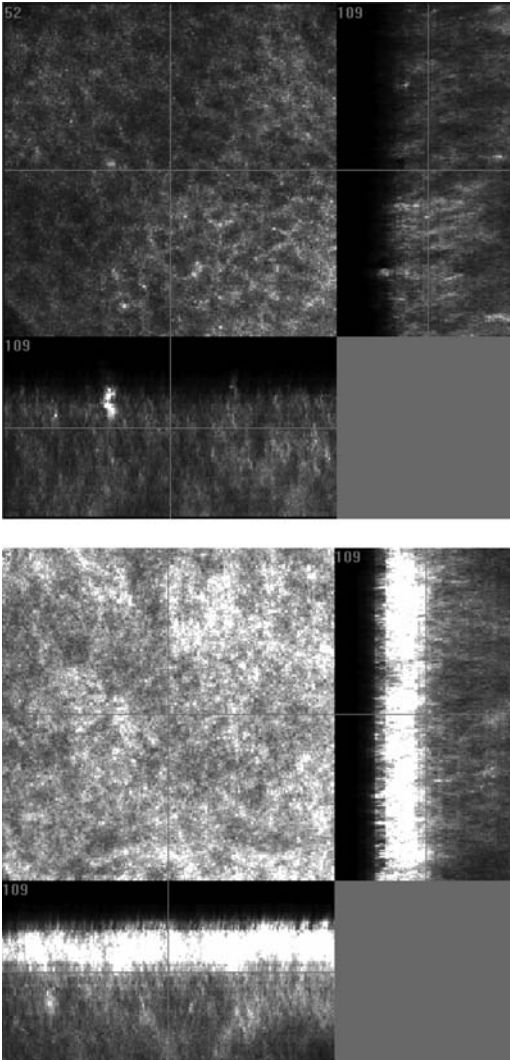


FIGURE 7 Confocal laser scanning microscopy images of skin after two minutes (*top*) and 90-minute (*bottom*) occlusion. Increased mismatching of refractive index interfaces in the stratum corneum between lipids and water leads to the increase in reflectance after 90-minute occlusion.

in spatial frequency length $|k|$ space. A peak in this distribution at spatial frequency length $|k|$ corresponds to the presence of a periodicity in the real space image. The periodicity is interpreted as the MCS and the peak width is related to the variation in the MCS. The spatial frequency length $|k|$ in cycles per image relates to a physical size L in the image by

$$L = \frac{S * p}{|k|} \quad (2)$$

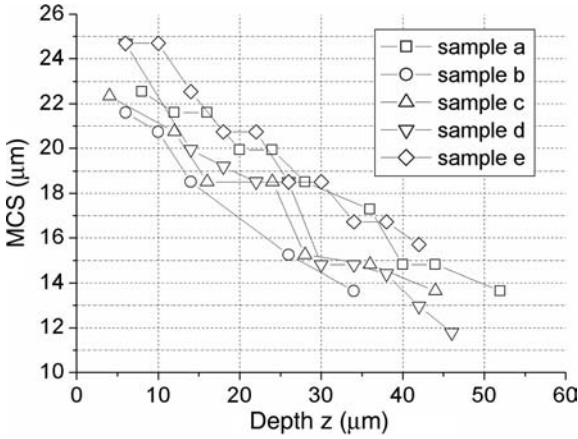


FIGURE 8 MCS as derived from confocal laser scanning microscopy images as a function of depth determined from the periodicity in the power spectrum for five different measurement positions at the back of the hand. *Abbreviation:* MCS, mean cell size.

where S is the image size in pixels, p is the pixel size (in our case $0.96 \mu\text{m}/\text{pixel}$, depending on the objective lens magnification). The measured depths are corrected for the refractive index mismatch to obtain the real physical depths.

In Figure 8 the result of MCS variation across the epidermal layer (for five repeats) is presented. From this figure, it can be seen that the mean epidermal size varies from about $25 \mu\text{m}$ at the top of the epidermis to about half this size at the basal layer at the bottom of the epidermis (Fig. 1). Such automated MCS (in two-dimension) or volume (three-dimension) determination could be used for estimating cellular swelling or detecting epidermal abnormalities.

DISCUSSION AND CONCLUSION

CLSM and TPFM images yield complementary information on the skin structure. CLSM reflectance images show a strong contrast in the epidermal layer by the melanin, whereas TPFM images show enhanced contrast and allow imaging of collagen and elastin fibers in the dermis. In the stratum corneum TPFM is capable of resolving individual corneocytes, and in CLSM the image of stratum corneum shows a homogenous distribution of the refractive index, without visible corneocyte structure. The combined microscope system allows for sequential imaging of the exact same region of the skin. This makes direct comparison of the methods feasible. In the combined microscope system, the advantages of both techniques can be exploited for skin studies. Using the averaged image intensity versus depth profiles, the skin layer thickness (changes) can be determined automatically and noninvasively. Structural analyzes of the images using Fourier methods yields MCSs as a function of epidermal skin depth and distribution of collagen orientation. Further potential of the techniques in the direction of using the spectral, and temporal (fluorophore life-time) characteristics of fluorescence in combination with structural imaging gives the device even more contrast mechanisms that can be used to study distribution of different chromophores locally in the skin. Some groups have already shown such developments (14,15). Full exploitation of the capabilities of confocal scanning and multiphoton microscopy is expected to find more application in clinical skin studies, such as in cell differentiation, skin morphological disorders, skin cancer research, and cosmetology.

REFERENCES

1. Corcuff P, Leveque JL. In vivo vision of the human skin with the tandem scanning microscope. *Dermatology* 1993; 186:50–54.
2. Corcuff P, Bertrand C, Leveque JL. Morphometry of human epidermis in vivo by real-time confocal microscopy. *Arch Dermatol Res* 1993; 285:475–481.
3. Rajadhyaksha M, Grossman M, Esterowitz D, Webb RH, Anderson RR. In vivo confocal scanning laser microscopy of human skin: melanin provides strong contrast. *J Invest Dermatol* 1995; 104:946–952.
4. Corcuff P, Gonnord P, Pierard GE, Leveque JL. In vivo confocal microscopy of human skin: a new design for cosmetology and dermatology. *Scanning* 1996; 18:351–355.
5. Corcuff P, Hadjur C, Chaussepied C, Toledo-Crow R. Confocal laser microscopy of the in vivo human skin revisited. 1st Colloque National d'ingenierie Cutanee, Franche-Comte, 1999.
6. Rajadhyaksha M, Anderson RR, Webb RH. Video rate confocal scanning laser microscope for imaging human tissue in vivo. *Appl Opt* 1999; 38(10):2105–2115.
7. Masters BR, So PTC. Multi-photon excitation microscopy and confocal microscopy imaging of in vivo human skin: a comparison. *Microsc Microanal* 1999; 5:282–289.
8. Masters BR, So PTC, Gratton E. Multi-photon excitation fluorescence microscopy and spectroscopy of in vivo human skin: a comparison. *Biophys J* 1997; 72:2405–2412.
9. Masters BR, So PTC, Gratton E. Optical biopsy of in vivo human skin: multi-photon microscopy. *Lasers Med Sci* 1998; 13:196–203.
10. Mueller M, Squier J, Brakenhoff GJ. Measurement of femtosecond pulses in the focal point of a high numerical aperture lens by two-photon absorption. *Opt Lett* 1995; 20(9):1038.
11. Kim KH, So PTC, Kochevar IE, Masters BR, Gratton E. Proceedings of SPIE-volume 3260, Optical investigation of cells in vitro and in vivo, Farkes DL, Leif RC, Tromborg BJ, eds 1998; 46–57.
12. Hendriks RFM, Lucassen GW. Two-photon fluorescence and confocal video microscopy of in-vivo human skin, *BiOS 2001*. SPIE 2001; 4262:287–293.
13. Bestvater F, Spiess E, Stobrawa G, et al. Two-photon fluorescence absorption and emission spectra of dyes relevant for cell imaging. *J Microsc* 2002; 208:108–115.
14. So PTC. Two-photon fluorescence light microscopy. *Encycl Life Sci* 2002; 1–5.
15. Konig K, Riemann I. High resolution multiphoton tomography of human skin with subcellular spatial resolution and picosecond time resolution. *J Biomed Opt* 2003; 8(3): 432–439.
16. Sterenborg HJCM, Motamedi M, Wagner RF, Duvic M, Thomsen S, Jacques SL. In vivo fluorescence spectroscopy and imaging of human skin tumours. *Lasers Med Sci* 1994; 9:191–201.
17. Sterenborg HJCM, Motamedi M, Wagner RF, Duvic M, Thomsen S, Jacques SL. In vivo fluorescence spectroscopy for the diagnosis of skin diseases. SPIE 1995; 2324:32–38.
18. Kollias N, Gillies R, Moran M, Kochevar IE, Anderson RR. Endogenous skin fluorescence includes ands that may serve as quantitative markers of aging and photoaging. *J Invest Dermatol* 1998; 111:776–780.
19. <http://www.perceptive.com/ALICE.HTM>.
20. <http://www.lucid-tech.com>.
21. Lucassen GW, Bakker BL, Neerken S, Hendriks RFM. Mean cell size and collagen orientation from 2D Fourier analysis on confocal laser scanning microscopy and two-photon fluorescence microscopy on human skin in vivo. SPIE 2003; 4964:106–114.
22. Rajadhyaksha M, Menaker G, Flotte T, Dwyer PJ, Gonzalez S. Confocal examination of nonmelanoma cancers in thick skin excisions to potentially guide Mohs micrographic surgery without frozen histopathology. *J Invest Dermatol* 2001; 117:1137–1143.
23. Neerken S, Lucassen GW, Bisschop M, Lenderink E, Nuijs AM. Characterization of age-related effects in human skin: a comparative study of confocal laser scanning microscopy and optical coherence tomography. *J Biomed Optics* 2004; 9(2):274–281.
24. Caspers PJ, Lucassen GW, Carter EA, Bruining HA, Puppels GJ. In vivo confocal Raman microspectroscopy of the skin: noninvasive determination of molecular concentration profiles. *J Invest Dermatol* 2001; 116:434–442.

25. Norlen L, Emilson A, Forslind B. Stratum corneum swelling. Biophysical and computer assisted quantitative assessments. *Arch Dermatol Res* 1997; 289:506–513.
26. Image Analysis Fundamentals <http://www.ph.tn.tudelft.nl/Courses/FIP/frames/fip.html>.

Chilwan Oh, Min Gi Kim, and Jong Sub Moon

Department of Electronics and Information Engineering, Korea University, Yeonkigun, Choognam, South Korea

INTRODUCTION

Bioengineering applications are becoming commonplace in many fields of medicine, including dermatology. The assessment of skin contours may be carried out to diagnose, to determine treatment efficacy, or to support pathophysiological experimentation. Many experimental methods have been used to study skin surface contours. Initially, only simple magnification methods were used; they were followed by the analysis of replicas under the scanning electron microscope (1). Later, other quantitative measurement techniques such as stylus profilometry, which was developed for surface metrological studies, were adopted to measure skin surface contours (2,3). Nevertheless, the stylus profilometer had limitations when it came to determining skin microtopographic changes due to the pressure exerted by the stylus on the skin. Moreover, it was a time-consuming procedure, and could not accurately measure minute skin surface contours due to the physical size of the stylus tip, as shown in Figure 1.

In order to overcome these limitations, a laser beam was used instead of a stylus. The use of the laser beam was referred to as laser profilometry (4). Nevertheless, this technique also had disadvantages because direct measurement of the three-dimensional (3-D) structures was made difficult by objective lens' auto focus constraints, and by the capital costs involved. Some researchers in Europe and America have used a conventional optical profilometer (COP) in combination with image analysis (5). This method was developed during the Apollo project, and was used to measure the height of moon's craters (6). Cop utilizes the formula $L \tan(\alpha)$, where L is the length of the shadow of the crater made by sunlight and α is the incident angle. The same principle may be applied to analyze skin surface contours, i.e., by creating replicas and analyzing the shadows of skin surface contours produced by illuminating surfaces with light at known angles. Yet, this technique also had disadvantages in that the obtained results are dependent only on the angle made by the incident light and by the two-dimensional (2-D) image produced. As Figure 2, illustrates two skin surfaces with different contours may show the same height. Also, shapes that appear to be identical in 2-D view usually differ in 3-D space.

Recently the stereoimage optical topometer (SOT) was invented to overcome the disadvantages of the above-mentioned profilometers (7). The SOT technique uses a 3-D algorithm based on the stereoimage principle. This technique is based on the phenomenon of stereopsis, and thus senses stereoimages by utilizing the slight differences between images taken simultaneously at two positions. This is the same technique used in creating virtual reality, which is also referred to as binocular disparity, or more commonly known as the "binocular effect" (8). SOT uses this stereoimaging principle to measure skin-surface contours; disparity maps indicate depth. The maps are constructed using a stereoimage matching process,

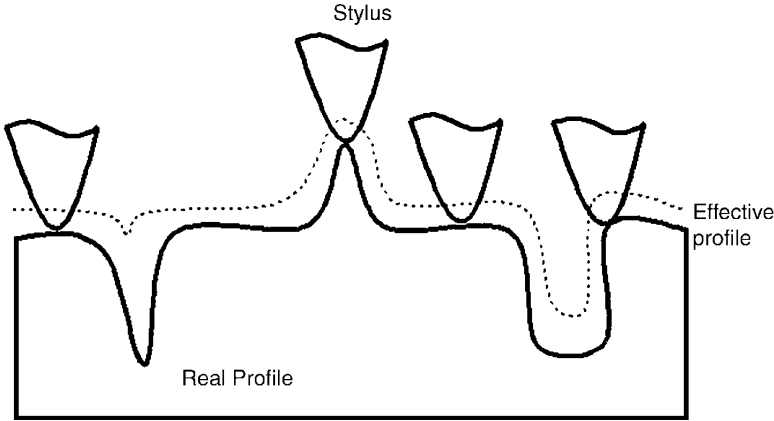


FIGURE 1 The stylus produces a filtering effect especially in a sharpened deep surface.

which uses two simultaneous skin-surface images taken with two CCD video cameras (9). 3-D stereoisimages can thus be composed of x , y , and z coordinates for all pixels in skin surface images by using two 2-D images.

METHODOLOGICAL PRINCIPLES

Basic Concepts of the Stereoimage Technique

The basic principle of stereoimaging is demonstrated by the binocular effect of the human eyes. The left and right eyes receive slightly different images of the same scene, and the brain produces 3-D information. These spatial differences between the left and right images are called disparity in the stereoimaging field, and the collective disparity of all spatial domains (x , y) in a stereoimage is referred to as its disparity (8).

The SOT technique requires a stereomicroscope, two CCD cameras, two frame grabbers, and a personal computer (Fig. 3).

The fundamental issue is in identifying points common to both 2-D images to allow disparity to be computed and the 3-D coordinates to be produced. Basically, two types of matching techniques have been devised: an area-based method and a feature-based method (10). Each of them naturally has its own advantages and

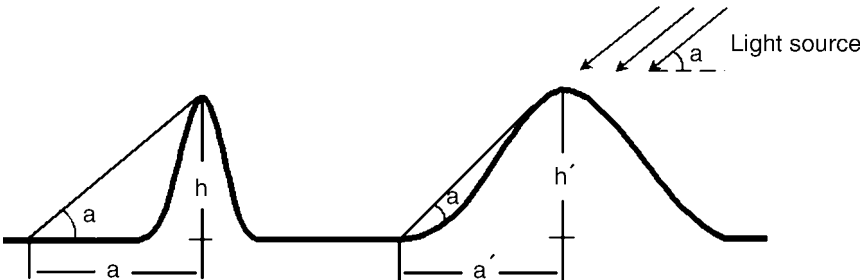


FIGURE 2 The same shadow area is produced by quite different skin contours.

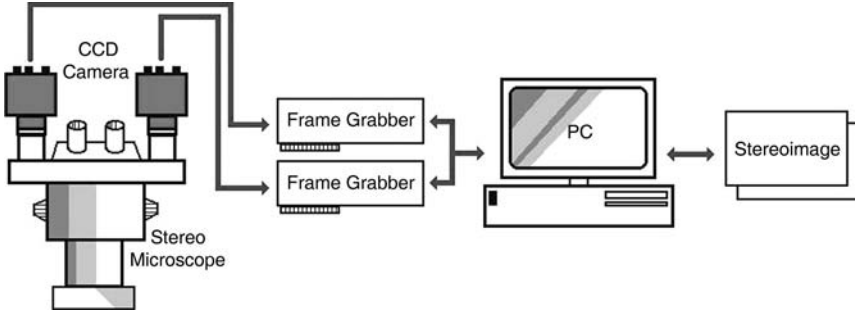


FIGURE 3 Schematic of the stereoinage optical topometer system.

disadvantages. The area-based method usually produces better results in smooth image changing intensities compared to the feature-based method. In the present study, we adopted the area-based method because skin surface contour images were comparatively smooth. In the area-based matching method, a point to in an image is essentially made the center of a small window of pixels, and this window is compared with a region of the same size in the paired stereoinage (11,12). To obtain the correct match, we used a mathematical tool that would provide a quantitative measure of the similarity between a window of pixels in one image and a window in its paired image.

To find these matching points in paired stereoinages, we applied various matching metrics, $Match(x, y; i, j)$, and two of these were considered for our application (13). These two functions, referred to as the absolute intensity difference (AID) and the zero mean sum of the squares of differences, are defined as follows:

$$AID(x, y; i, j) = \sum_{(m,n) \in W} |I_l(x + m, y + n) - I_r(x + m + i, y + n + j)|$$

$$ZSSD(x, y; i, j) = \sum_{(m,n) \in W} [(I_l(x + m, y + n) - \bar{I}_l) - (I_r(x + m + i, y + n + j) - \bar{I}_r)]^2$$

where $(i, j) \in S$

In the above equations, $I_l(x, y)$ and $I_r(x, y)$ represent the intensities of left and right images at position (x, y) , respectively. The search range used to identify a best matching point is defined as S . The mean value of the intensity in a window W is computed using the following equation:

$$\bar{I}_l = \sum_{(x,n) \in W} I_l(x + m, y + n) \text{ and } \bar{I}_r = \sum_{(m,n) \in W} I_r(x + n, y + n)$$

The corresponding problem is to find a point (x_r, y_r) in the right image that corresponds to a point (x_l, y_l) in the left image. The point that corresponds to (x_l, y_l) is defined as $(x_r, y_r) = (x_l + i^0, y_l + j^0)$, where (i^0, j^0) is the distance between the two corresponding points that satisfies the following equation:

$$(i^0, j^0) = \arg(\min_{(i,j) \in S} (Match(x, y; i, j))) \quad \text{for each } (x, y).$$

There are two types of stereopsis models: the convergence and nonconvergence types. In this paper, we chose the nonconvergence model, as shown in Figure 4 (15). This model shows the point (x_r, y_r) in the right image corresponding to the point (x, y) in the left image and is defined as $(x + i^0, y)$. This model enables a one-dimensional search problem in the x -direction rather than a 2-D search problem (Fig. 4).

However, the area that contains the 3-D information is smaller than the one in the convergence model when the distance between the camera and the object and the distance between the two cameras are the same.

To simulate matching metrics, the search window size and range were chosen to be $W = (7 \times 7)$ and $S = 20$ pixels, respectively. A stereoisage of a skin furrow was taken with an image size of 640×480 pixels, but we chose a 256×256 pixel-sized region from the original image, as shown in Figure 5A.

The result of a disparity map using AID is shown in Figure 5B. The set of disparities for all (x, y) points is called the disparity map. Once we found the disparity map, we obtained the 3-D topograph and $Z(x, y)$ using the following equations, which are based on the stereopsis in Figure 4.

$$\frac{d}{L} = \frac{f}{Z_p}$$

$$\frac{x_l}{f} = \frac{X_p}{Z_p} \quad \text{and} \quad \frac{x_r}{f} = \frac{X_p}{Z_p}$$

$$\frac{y_l}{f} = \frac{Y_p}{Z_p} \quad \text{and} \quad \frac{y_r}{f} = \frac{Y_p}{Z_p}$$

In Figure 4, L is the distance between the centers of the two cameras, f is the focal length of both cameras, d is the disparity of point (x_l, y_l) , and (X_p, Y_p, Z_p) denote the

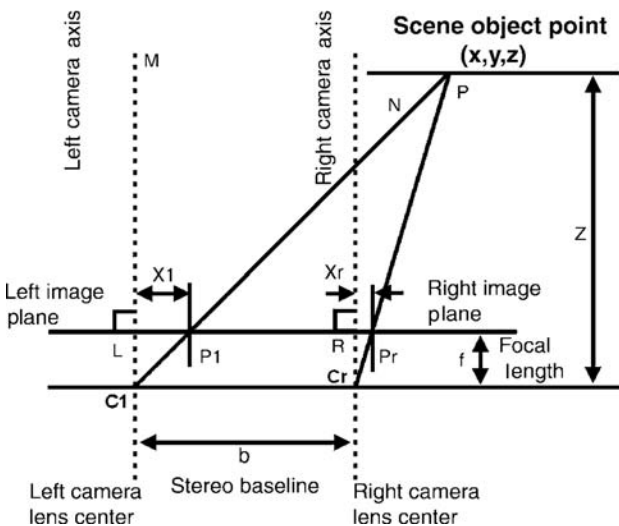


FIGURE 4 Stereopsis based on the nonconvergence model.

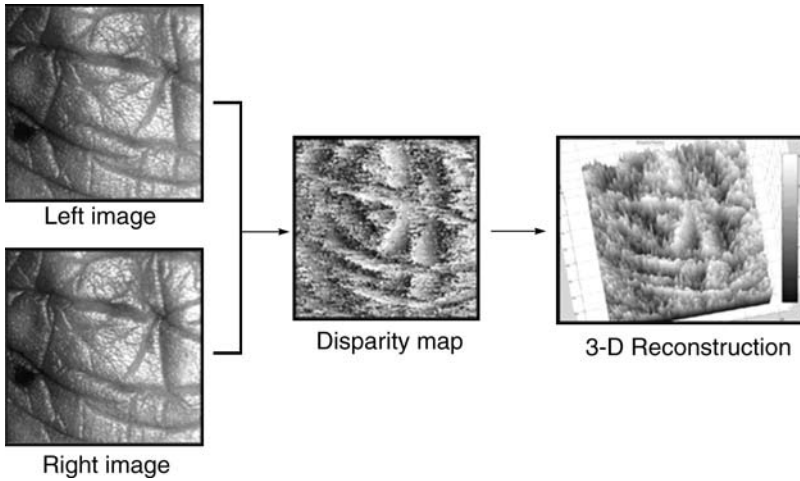


FIGURE 5 Sequence to construct three-dimensional information using stereoinage.

3-D coordinates of point (x_l, y_l) in the left image. In this paper, we considered the disparity map as a topograph.

The 3-D visualizations of the disparity map produced from using stereopsis are shown in Figure 4. In this figure, a 3-D object point (X_p, Y_p, Z_p) is projected onto a stereoinage at points P_l and P_r . Point P_r' is spatially the same point as P_l on the left image. The distance in the x -dimension between P_r' and P_l is the disparity of point (x_l, y_l) when using the nonconvergence camera model. The surface representation obtained using the normalized cross-covariance method was also considered with that obtained using the nonconvergence camera model (12). Visualizations of the disparity map are shown in Figure 5B, and Figure 5C shows a 3-D visualization of the stereoinage using Figure 5A.

So far we have assumed that the stereosystems have small baseline environments. However, over the last decade, researchers in this field of interest have developed means of solving wide baseline cases.

To solve matching problems for wide baseline cases we must find a scale or affine invariant points. Recently, Lowe et al. (16,17) tried to find scale invariant points and Mikolajczyk et al. (18,19) tried to find affine invariant points.

Development of Parameters for 3-D Surface Contour

The parameter of the mean height (R_a) profile and maximum peak-to-valley depth (R_z), which are used in COP, have been previously defined (5). In this paper, R_a and R_z are defined as:

$$R_a = \frac{1}{l} \int |R(x)| dx$$

where l is the scan length,

$$R_z = \frac{1}{n} \sum Z_i$$

Z_i is the maximum peak-to-valley depth within a segment of the profile, and n is the number of segments on the scan line.

We have developed some parameters during our research, such as the mean surface roughness (S_a), mean roughness depth (S_z), 3-D length (S_L), 3-D surface area (S_A) and 3-D volume (S_V).

The S_a parameter is defined as:

$$S_a = \frac{1}{A} \iint_{(x,y) \in A} |Z(x,y)| dx dy = \frac{1}{y_s} \int \frac{1}{x_s} \int |Z(x,y)| dx dy$$

where A is the 2-D area under consideration ($A = x_s \times y_s$) and $Z(x, y)$ is as defined in R_a .

In the equation, x_s and y_s are line segments in the x and y axis, respectively. Thus, R_a can be considered as a special case of S_a by letting a fixed scan line $y = y_f$. In the actual computation of S_a and R_a , the profile $Z(x, y)$ is adjusted to an average height equal to zero. Using the same idea, the mean height of profile R_z is also a special case of S_z by fixing (scaling) y . The 3-D length, S_L , between points at $P_1 = (x_1, y_1, z_1)$ and $P_2 = (x_2, y_2, z_2)$ on the surface is defined as:

$$S_L = \sqrt{(x_1 - x_2)^2 + (y_1 - y_2)^2 + (z_1 - z_2)^2}$$

This represents a surface consisting of a polygon. The simplest polygon is a triangle with three surfaces. For two points in a 3-D space, P_1 and P_2 , i.e., $x_{i+1} = x_i + 1$ and $y_{i+1} = y_i + 1$ for each i and j . A surface can be approximated by three points that lie on the surface. Here, we considered three points including $O_1 = (0, 0, a)$, $O_2 = (0, 1, c)$, and $O_3 = (1, 0, b)$. The length of two points becomes as shown in the following equation:

$$\overline{O_1O_3} = \sqrt{1 + (a - b)^2}, \overline{O_1O_2} = \sqrt{1 + (a - c)^2}, \overline{O_2O_3} = \sqrt{2 + (a - b)^2}$$

and the average length is denoted by:

$$S = \frac{\overline{O_1O_3} + \overline{O_1O_2} + \overline{O_2O_3}}{3}$$

Then the area of the triangle constructed by O_1 , O_2 , and O_3 becomes as shown in the following equation:

$$\sqrt{s \cdot (s - \overline{O_1O_3}) \cdot (s - \overline{O_1O_2}) \cdot (s - \overline{O_2O_3})}$$

The 3-D surface area (S_A) is the summation of all triangles for x and y , which vary by unit interval.

The volume of an object in 3-D space (S_V) can be approximated using the following equation:

$$\int \int \int_{(x,y,z) \in V} O(x, y, z) dx dy dz \cong \sum_{Z_i} \left[\iint Z(x, y) dx dy \right] \Delta Z_i$$

Based on an approximated 3-D volume, S_V , we used the following procedure. We assigned the referential plane $z = K$. This plane can translate all points such

as (x, y, z) above the referential plane to $(x, y, z - K)$ and can also translate all the points below the referential plane to $(x, y, K - z)$. After adjusting all points, we assumed three adjacent points to be $(0, 0, a)$, $(1, 0, b)$, and $(0, 1, c)$. The volume represented by these three points is then $(a + b + c)/6$.

Validity and Reliability

Validity and reliability tests were done with 103 nonsmoking male volunteers grouped into four age groups: 0 to 20 years; 21 to 40 years; 41 to 60 years; and over 61 years. Silicon Exafin (GC Co., Japan) skin replicas were produced from the upper lateral forearm area, 0.5 cm below the plane of the lateral condyle of the humerus. A stereomicroscope (Stereo Zoom 6-ST, Leica) was used to measure the skin contours under a magnification of 10x using 22° incident (measured from the surface normal) illumination on the silicone replica in the COP. R_z was calculated to analyze skin fold shadows using a computerized image analysis system (AIC Inc., Georgia, U.S.A.). SOT generated 3-D information of the skin replicas using the stereomatching algorithm.

To test the validity, we used S_z and R_z parameters to compare the accuracy of SOT and COP. The R_z value of COP was calculated from one horizontal line. The height of a furrow was determined from the grey level degree along a horizontal line, i.e., by fixing $y = y_F$. The S_z value of SOT was calculated as described. The coefficients of variation (CVs) of R_z and S_z were for COP and SOT. SOT reproducibility testing was performed by obtaining two replicas from the same subjects four weeks apart.

The SOT was found to be the more precise method as judged using CV values of R_z of COP, which were between 14.76 and 16.56, while the S_z values of SOT were between 2.18 and 2.68 (Table 1). Reproducibility was tested using two skin replicas from the same person, taken four weeks apart, but no significant difference was found.

CLINICAL APPLICATIONS

The objective quantification of the severity in various types of cutaneous disorders is important because it is a fundamental aspect of the proper clinical evaluation of cutaneous disorders. This type of quantification is essential, not only for etiological studies of cutaneous disorders, but also for the determination of the most effective treatment modalities.

Determination of the Severity of Atopic Dermatitis

It is important to objectively measure and record the severity of atopic dermatitis (AD) in routine clinical practice and research. Many clinical severity scales such as baseline grading, AD area and severity index, and the severity scoring of the AD

TABLE 1 Comparison of the Coefficient Variation of R_z (COP) and S_z (SOT) in the Four Age Group

	0-20	21-40	41-60	Over 61
CV of S_z (SOT)	2.68	2.47	2.43	2.18
CV of R_z (COP)	15.76	16.56	14.76	15.07

Abbreviations: COP, conventional optical profilometer; SOT, stereoinage optical topometer.

(SCORAD) index have been proposed to evaluate AD severity. The SCORAD index is the most extensively tested and employed system (20,21). Although clinical severity scales can be economically and conveniently applied, they can show significant drawbacks due to inter- and intraobserver variability. In order to objectively quantify the severity of AD, some bioengineering techniques have been used, such as D-Square[®] (Cuderm, Texas, U.S.A.), Corneometer[®] (Dermalab, Cortex, Denmark), and Evaporimeter[®] (Courage-Khazaka Elect., GmbH, Germany) (22,23). However, because these methods measure physiologic changes on the skin surface, they cannot measure skin contour changes.

The purpose of this study was to determine if morphologic studies of skin contours are helpful in objectively quantifying the severity of AD by comparing SOT, other bioengineering methods, and the SCORAD index (24).

To evaluate the degree of change in skin contours and to compare bioengineering methods with clinical severity, moisturizer was applied twice daily for two weeks. Measurements using bioengineering methods such as D-Square, Corneometer, Evaporimeter, and Spectrophotometer[®] (PSI Inc., Korea) were taken on an area of 2 cm below the antecubital crease. Initial measurements were taken at the start of the study and follow-up measurements were taken after one and two weeks. The SCORAD index was evaluated by the same observer at each visit during the clinical assessment of AD patients.

In addition, measurements using bioengineering methods were taken three hours after moisturizer application to evaluate the rapid effect of moisturizations.

We studied scaling patterns using D-Square tape. This tape was applied gently to the test areas and pressed evenly. The scaling patterns were evaluated using a video camera (Pulnix Inc., U.S.A.). Desquamation (DI) and scaling indices (SI) were calculated using computerized image analysis (AIC Inc., Georgia, U.S.A.).

$$DI = \frac{2A + \sum_{n=1}^5 Tn(n-1)}{6}$$

where A is the percentage of skin area covered by corneocytes, Tn is the percentage of corneocytes, and n is the thickness (25),

$$SI = \frac{1}{(w \times h)} \times \sum_{x=1, y=h}^{x=w, y=h} \frac{D(x, y) - B(x, y) - [W(x, y) - B(x, y)]T\%}{W(x, y) - B(x, y) - [W(x, y) - B(x, y)]T\%}$$

and where $D(x, y)$ is the D-Square image of each pixel (x, y) , $W(x, y)$ the white calibrate image of each pixel (x, y) , $B(x, y)$ the black calibrate image of each pixel (x, y) , and T the 10% threshold level.

Transepidermal water loss (TEWL) was measured using an Evaporimeter. The water vapor pressure gradient was measured using sensors at two different levels above the skin surface.

The Corneometer CM 825 measures the electrical capacitance of the epidermis, expressed in arbitrary units. We analyzed the averages of three measurements taken at each site with this appliance.

The Darsa Pro 3000 System Spectrophotometer consists of an optical fiber, components, and an A/D board with software. The incident light from the sample goes through the fiber, reflected by a mirror and collided with the grating.

The composite light is resolved in a range between 220 to 1100 nm at the grating and the resolved light source energy is converted to electric energy at the

sensor. The “X” value of the International Commission on Illumination XYZ tristimulus values was measured to evaluate the severity of the erythema.

Clinical assessment of AD patients was calculated as the following equation according to the guidelines of the European Task Force on AD (21).

SCORAD = extent/5 (0–20) + 3.5 x intensity (0–63) + subjective symptoms (0–20).

The SCORAD index used the rule of nine to grade extent, based on front-back drawings on a 0–100 scale. A list of six intensity items (erythema, edema/papulation, oozing/crust, excoriation, lichenification, dryness) graded 0–3 (0–18 scale) and two subjective items (pruritus, sleep loss), were each measured on a 0–10 analog scale (0–20 total scale).

Results of 3-D parameters measured by SOT are shown in Figure 6. S_z , S_A , S_V and S_L were significantly reduced after three hours of moisturizer application in comparison to the baseline ($p < 0.05$). All of four parameters of SOT were significantly reduced after one and two weeks of comparing to the baseline ($p < 0.01$).

We calculated the values of DI and SI using D-Squares and obtained the values after three hours, a week, and two weeks. TEWL, determined by Evaporimeter, showed a significant difference after two weeks of application, but not after one week. After three hours, a week, and two weeks, results determined by Corneometer showed a significant difference. After one and two weeks, significant differences were also observed in results determined by Spectrophotometer. However, there was no significant difference after three hours.

The results measured by D-Square and the Corneometer were significantly altered after three hours of moisturizer application compared to the

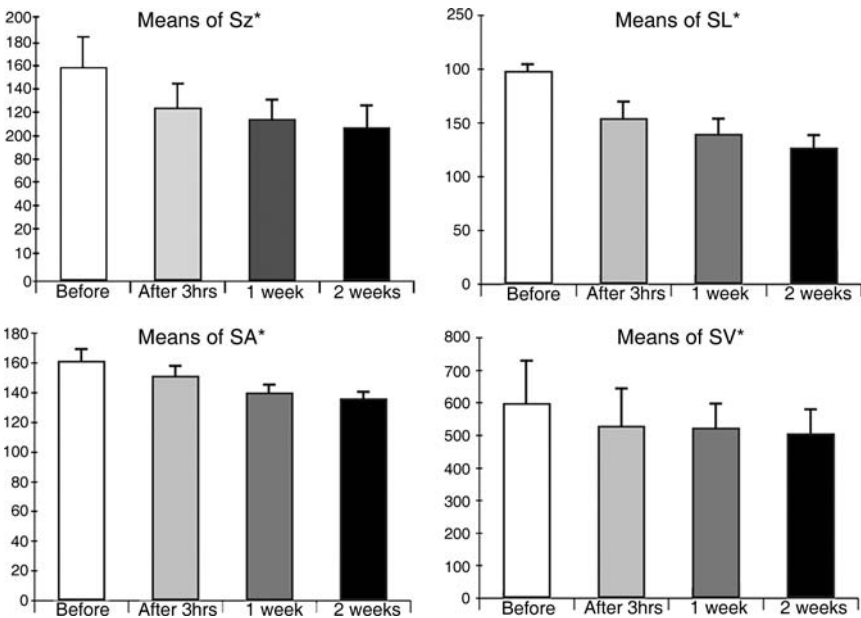


FIGURE 6 Comparison of the results to measure the severity of atopic dermatitis before, three hours after, one week after and two weeks after the moisturizer applied measuring by stereoinage optical topometer (* $p < 0.01$).

baseline. However, results by Evaporimeter and Spectrophotometer showed no significant difference after three hours. After one and two weeks of application, significant changes were observed in the results determined by D-Square, Corneometer, and Spectrophotometer (data are not shown).

The severity of AD scores according to the SCORAD index are shown in Figure 7. After one and two weeks, SCORAD indices were significantly reduced ($p < 0.05$).

In correlation analysis, we used the S_z of SOT, DI of D-Square test, Evaporimeter, Spectrophotometer, and the SCORAD index. These values were negatively correlated with Corneometer results (Table 2). Highly significant correlations were found between the bioengineering methods and the SCORAD index ($p < 0.05$).

The electrical capacitance correlates negatively with D-Square tape, indicating that skin with a higher capacitance has fewer scales. In our study, D-Square tape was also found to be negatively correlated with Corneometer. This study demonstrates that D-Square tape method is sensitive and reliable for the quantitative evaluation of dry skin of AD.

The TEWL, which demonstrates diffusional water loss through the skin, is often used as a parameter reflecting the functional state of the epidermal diffusion barrier. The TEWL is increased both in dry noneczematous skin and in the clinically normal skin of AD patients. Chamlin et al. showed that TEWL rates declined parallel to SCORAD values during treatment of the skin barrier repair preparation, suggesting that TEWL could provide an objective measure of AD severity. Our results showed a progressive reduction in TEWL at the test area during the study, although there was a statistically significant difference only after two weeks.

Linde showed that the water content was reduced in dry atopic skin when measured with Corneometer (26). Sugarman et al. observed that stratum corneum function was correlated to clinical estimates of disease severity and that Corneometer was a meaningful method of AD activity (22). The results of this study

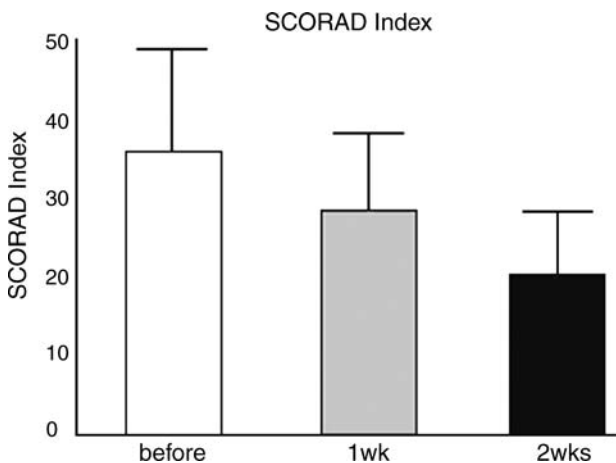


FIGURE 7 Comparison of the results to measure the severity of atopic dermatitis before, three hours after, one week after and two weeks after the moisturizer applied measuring by SCORAD index ($*p < 0.01$). *Abbreviation:* SCORAD, severity scoring of the atopic dermatitis.

TABLE 2 The Results of Correlation Coefficients Between Bioengineering Methods and the SCORAD Index

	SOT (S_z)	SCORAD	D-Square (DI)	Corneometer	TEWL	Spectrophotometer
SOT(S_z)	1	0.87	0.94	-0.91	0.85	0.89
SCORAD		1	0.90	-0.93	0.94	0.94
D-Square (DI)			1	-0.93	0.89	0.92
Corneometer				1	-0.93	-0.95
TEWL					1	0.95
Spectrophotometer						1

Abbreviations: SOT, stereoinage optical topometer; DI, desquamation; SCORAD, severity scoring of the atopic dermatitis; TEWL, transepidermal water loss.

suggest that Corneometer is an effective and sensitive tool to determine skin surface hydration by measuring the electrical capacitance of the stratum corneum.

The skin color is one of the most important elements by which we can evaluate the state of skin. The greatest influence on the variability between repeated measurements using Spectrophotometer can be caused by the accidental inclusion of unshaven hair in the test area. The antecubital fossa of our test area is a good place for cutaneous erythema assessments using Spectrophotometer (23). The X values were measured to evaluate the severity of erythema and the significant correlation with the SCORAD index.

Corneometer, D-Square, and SOT results were significantly changed ($p < 0.05$), but Evaporimeter, Cutometer[®] (Courage-Khazaka Elect., GmbH), and Spectrophotometer results did not show any significant difference.

In conclusion, this data indicates that the morphological study of skin surface contours is useful in evaluating AD severity. We consider noninvasive bioengineering methods to be sensitive, particularly SOT, D-Square, and Corneometer. If we could combine methods to evaluate the physiological changes, and use SOT to measure the morphological changes of the skin surface, we could evaluate the severity of AD more objectively and quantitatively.

Determination of Psoriatic Lesion Severity

Psoriasis area and severity index (PASI) scores, psoriasis severity scores, and lesional severity scores can be used to objectively evaluate the degree of clinical manifestations of psoriasis. Although this system shows significant interobserver differences (27,28), the PASI-scoring system is the most commonly used method (15) among others. Various studies which have used severity evaluations have experienced difficulties because psoriasis severity and treatment efficacy evaluations were accomplished using subjective measurements. Therefore, we need further studies on more objective and quantitative evaluation methods.

In order to objectively quantify severity criteria in the case of psoriasis, 3-D skin contours were measured using SOT (29).

Two evaluation methods were used to determine the severity of psoriatic lesions. For the first one we quantified the skin-surface contours, and for the second method we used PASI visual scoring system. They were then compared by SOT.

After observing the two characteristic clinical findings (infiltration and scaling), the evaluation was performed by awarding five visual scores: grade 0 (none),

grade 1 (mild), grade 2 (moderate), grade 3 (severe), and grade 4 (very severe). This scoring method used the five stages defined in the PASI-scoring system for the severity evaluation of psoriasis lesions.

Of a total of 134 psoriatic lesions in 30 patients, the degree of infiltration did not reach grade 4 for any lesion, and no case showed a degree of scaling of grade 3 or 4. Changes in the 3-D parameters of SOT were found to be closely related to the visual scores of infiltration and scaling. The mean values of each parameter (S_a , S_A , S_L , and S_V) according to the degree of infiltration significantly decreased as the visual scores increased, whereas the coefficient of the variation significantly increased as the visual scores increased (Fig. 8A and B).

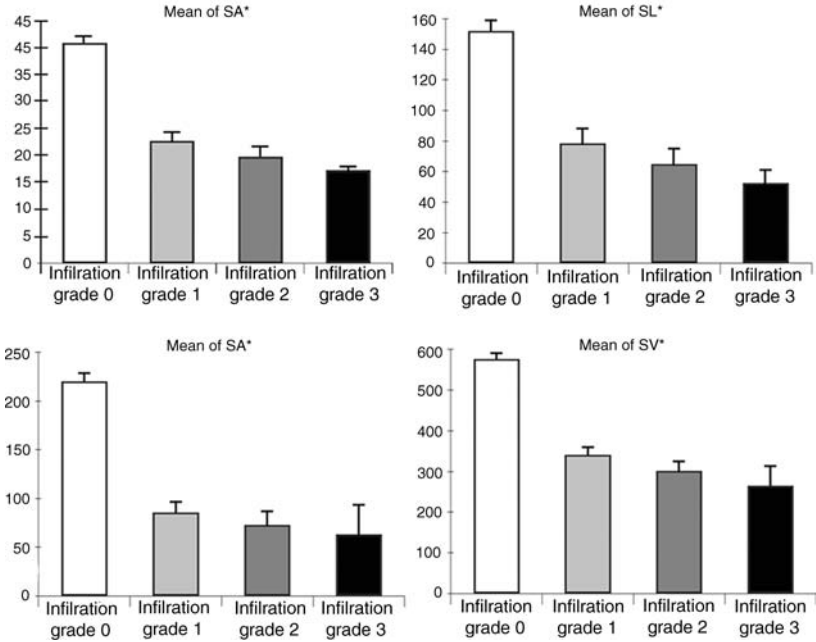
On the other hand, the mean values of each parameter (S_a , S_A , S_L , and S_V) according to the degree of scaling significantly decreased as the visual scores increased, and the coefficients of variation significantly increased as visual scores increased (Fig. 9A and B). This study shows that the mean values of each parameter (S_a , S_L , S_A , and S_V) increased as the degree of infiltration and scaling decreased with the visual scores, i.e., the severity (Figs. 8 and 9A), whereas the coefficients of variation of each parameter (S_a , S_L , S_A , and S_V) increased as the severity increased (Figs. 8 and 9B). Therefore, all the mean values and coefficient variations of the four parameters used for scaling measurement in this study can be used as appropriate parameters to evaluate the severity of psoriasis. This result indicates that although the degree of skin furrowing decreases as the severity in psoriasis lesions increases, the variation between each skin furrow is high. The pathomechanism of this finding is that the decrease in the degree of furrowing are accompanied by an increase in psoriasis lesion severity. This may result from a disappearance of normal furrows from the skin-surface contours as a result of lesion progression. These findings show that the mean values of 3-D parameters are high in normal skin. Furthermore, an increased coefficient variation means an increase in the irregularity of the skin-surface contour. Therefore, this study shows that SOT can be useful for overcoming previous objective and quantitative difficulties associated with evaluating skin contours in different cutaneous disorders.

Determination of Sodium Lauryl Sulfate-Induced Edema Severity

The visual scoring system (-, ?, +, ++, +++) recommended by the International Contact Dermatitis Research Group is used to determine the results of patch testing, which is an important diagnostic tool in allergic contact dermatitis. The visual scoring system is both economical and convenient. However, it is subjective and can be interpreted differently by even the most experienced dermatologists.

Based on different physiological principles methods for interpreting patch test results objectively and quantitatively had been applied. These include Laser Doppler Velocimeter, reflectance spectrophotometer (or Colorimeter), TEWL, and a Corneometer. These measurement methods, which rely on additional physiologic phenomenon related to skin surface changes have been researched for many years, because they are noninvasive and objective (30–34). Furthermore, high-frequency pulsed ultrasound and magnetic resonance imaging are also being investigated as skin thickness measuring tools (35). However, these methods are intrinsically unable to describe the external contour of the skin accurately. In an attempt to apply the interpreting criteria to patch test results with respect to contour changes of skin, some studies have used skin replicas to observe the skin contours. It was

(A)



(B)

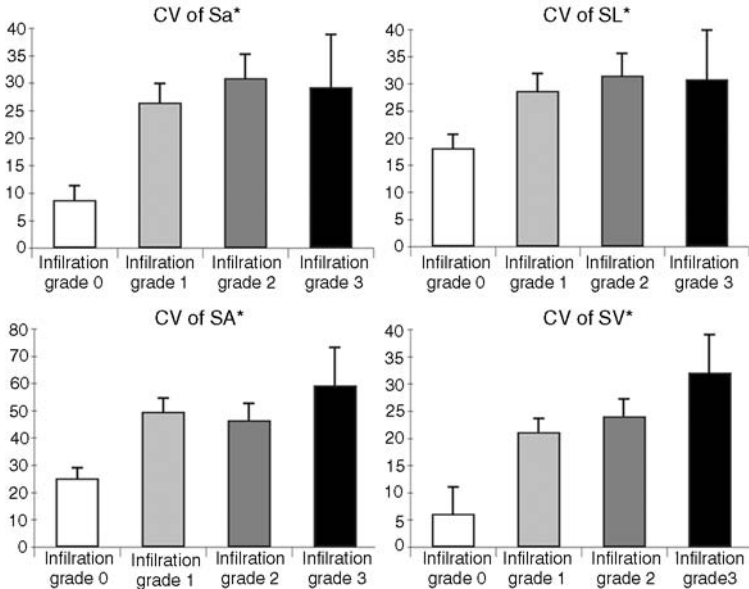


FIGURE 8 (A) Comparison of the results to measure the severity of infiltration in psoriatic lesions between visual score, the mean of the four SOT parameters ($*p < 0.01$). (B) Comparison of the results to measure the severity of infiltration in psoriatic lesions between visual score, coefficient variations of the four SOT parameters ($*p < 0.01$). *Abbreviation:* SOT, stereoimage optical topometer.

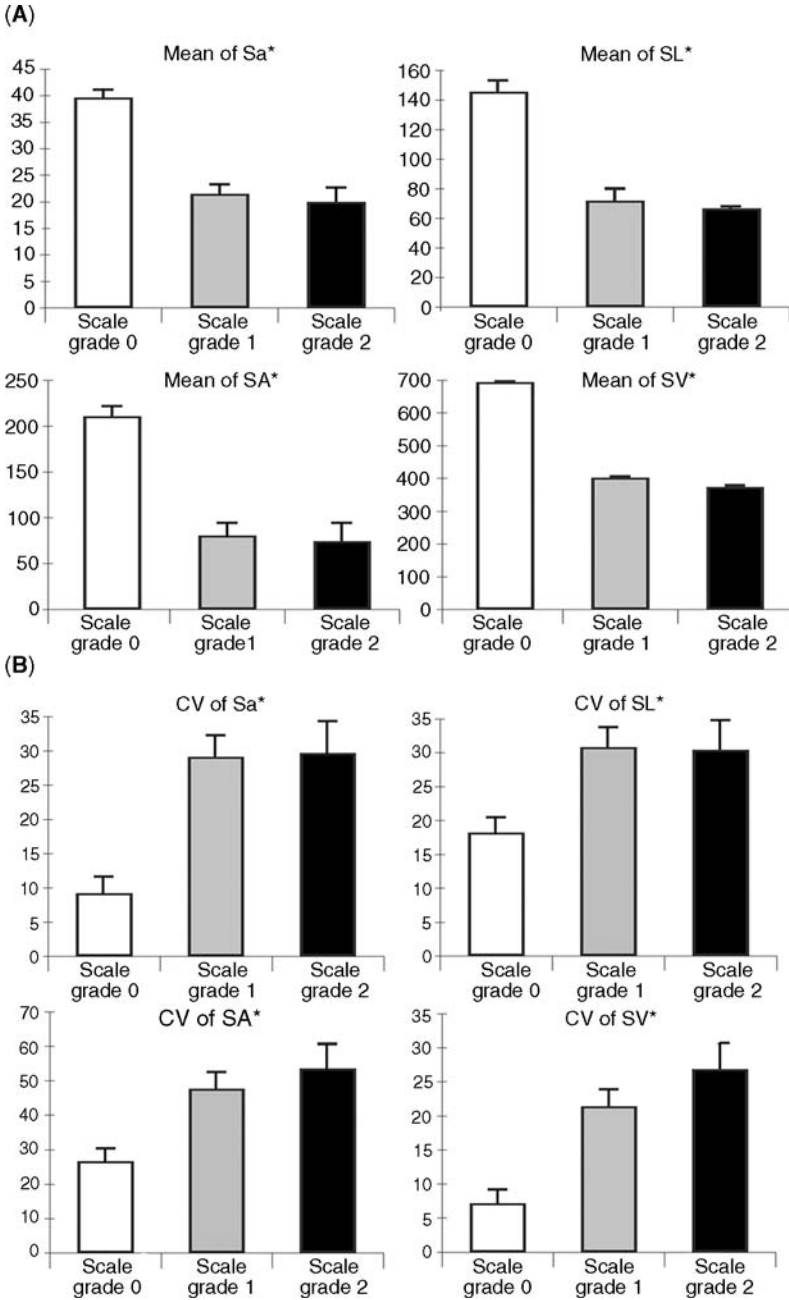


FIGURE 9 (A) Comparison of the results to measure the severity of scale in psoriatic lesions between visual score, the mean of the four SOT parameters ($*p < 0.01$). (B) Comparison of the results to measure the severity of scale in psoriatic lesions between visual score, coefficient variations of the four SOT parameters ($*p < 0.01$). *Abbreviation:* SOT, stereomage optical topometer.

claimed that using skin replicas is more sensitive than the visual scoring system. The studies involving skin replicas were comparative in nature and were based on simple visual observations of a replica rather than being reliant upon specific quantitative study (36).

Thirty two healthy male volunteers gave their consent to be included in the study (37) as the subjects. The skin area used for the experiment was the inner side of the forearm, located 3 cm below the medial condyle of the ulna.

The patch test was done with 0.5%, 1%, and 3% sodium lauryl sulfate (98% purity, Fluka Chemie, Buchs, Switzerland) solutions that were diluted with distilled water. We used distilled water as the control. Skin occlusion was performed using 50 mL of the sodium lauryl sulfate solution with Scanpor tape in a Finn Chamber for 24 hours. Thirty minutes after being removed from the chamber, the degree of edema was scored visually as: 0: no edema, +: mild (under 25%), ++: moderate (under 50%), or +++: severe (over 50%).

On comparing the means of the five parameters (i.e., S_{0r} , S_{zr} , S_{Lr} , S_{Ar} , and S_{Vr}) for visual grades 0 and 1+, a significant increase in means levels was found in grade 1+ compared to grade 0. Thus, skin with mild edema showed deeper skin furrowing than normal skin. Comparing the visual grades 1+, 2+, 3+ versus these five parameters (i.e., S_{0r} , S_{zr} , S_{Lr} , S_{Ar} , and S_{Vr}) statistically significant decreases were seen in all parameters at the higher visual grades. In other words, skin furrow dimensions reduced with severe edema, starting with grade 1+ (Fig. 10A).

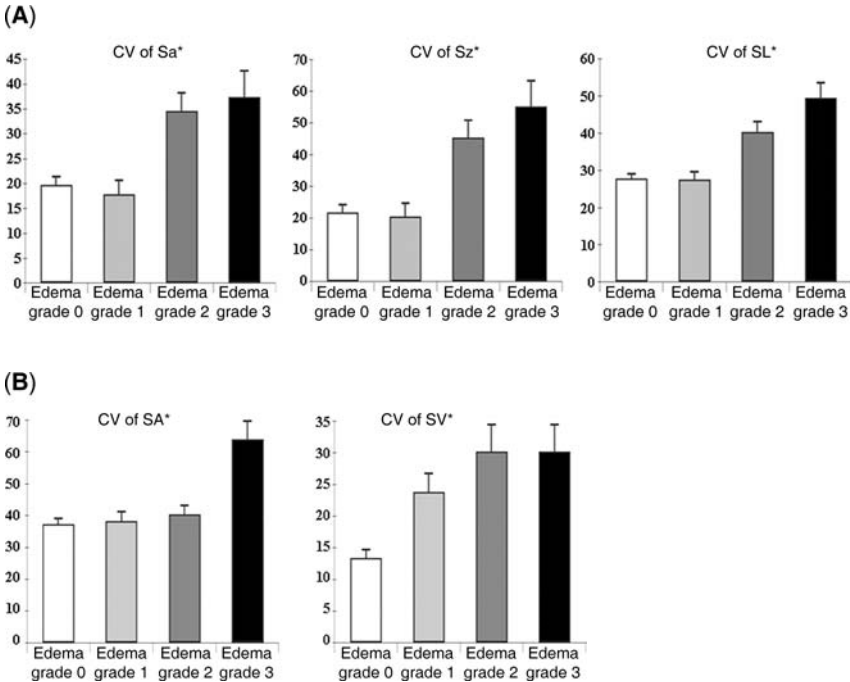


FIGURE 10 (A) Comparison of the results to measure the severity of SLS-induced edema between visual score, the mean of the four SOT parameters. (* $p < 0.01$). (B) Comparison of the results to measure the severity of SLS-induced edema between visual score, coefficient variations of the four SOT parameters. (* $p < 0.01$). *Abbreviations:* SOT, stereoimage optical topometer; SLS, sodium lauryl sulfate.

The coefficient of variation of each parameter showed a gradual statistically significant increase on moving from a visual score of 1+ to 3+ in each grade. Thus, on increasing the visual score from 1+ to 2+ and to 3+, the degree of skin furrows reduced but the irregularity of the skin surface contours (coefficient of variation) increased significantly from grade 1+ to 3+ (Fig. 10B); however, no significant difference was found between grade 0 and 1+.

Skin Contour Changes Due to the Aging Process

Changes to the skin surface contour due to aging were evaluated using stereoinaging (9). The volunteers, made up of 103 nonsmoking men at the Korea University Medical Center, were grouped into four age groups: 0 to 20 years 21 to 40 year, 40 to 60 years and over 61 years. The replicas, which were made of silicon (Exafin, GC Co, Japan), were sampled on the upper lateral forearm area, 0.5 cm below the plane of the lateral condyle of the humerus. The results of the 3-D data of changes to the skin contour with increasing of age were analyzed. There was a trend of increasing S_a values with increasing age. A statistically significant increment of S_a was noted in the over-61 age group, when compared to the under-60 age group. The increment in the value of S_z was seen with increasing of age. There were significant differences when comparing the under 20, 21 to 60, and over 61 age groups. Regular increments in the values of S_L and S_A were seen with increasing age and a statistical significance ($p < 0.05$) was present in the over 61 age group, in comparison with the under 60 age group. There was no significant change in the value of S_V values with aging (Fig. 11).

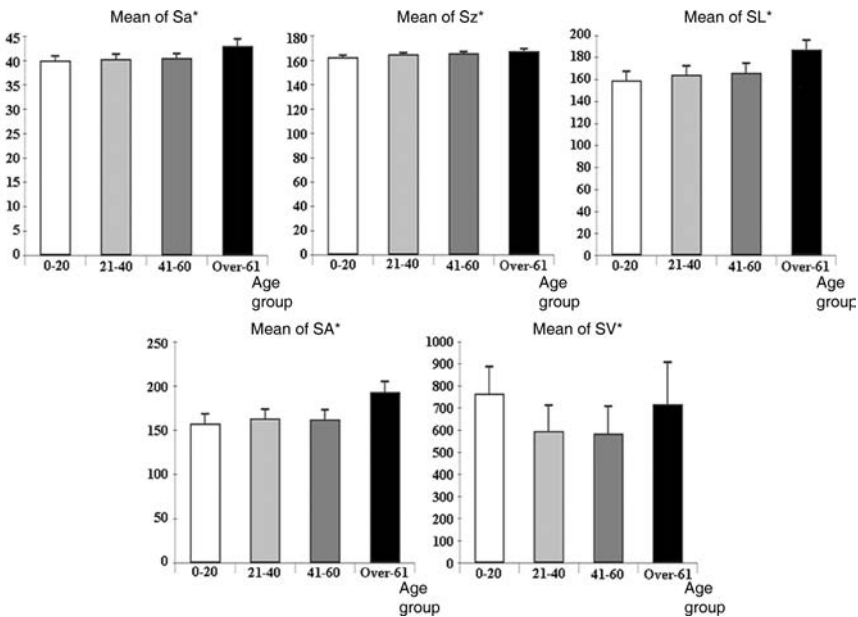


FIGURE 11 Comparison of the results of five stereoinage optical topometer parameters among the four age group (* $p < 0.01$).

REFERENCES

1. Tsuji T. Light and scanning electron microscopic studies on wrinkles in aged persons' skin. *Br J Dermatol* 1986; 114:329–335.
2. Corcuff P. The impact of aging on the microrelief of peri-orbital and leg skin. *J Soc Cosmet Chem* 1983; 82:145–152.
3. Makki S, Agache P. Statistical analysis and three-dimensional representation of the human skin surface. *J Soc Cosmet Chem* 1984; 35:311–315.
4. Efsen J, Hansen HN, Christensen S. et al. In: Serup J, Jemec GBE, eds. *Laser Profilometry, Handbook of Non-Invasive Methods and the Skin*. 1st ed. Boca Raton, FL: CRC Press, 1995:97–106.
5. Grove GL, Grove MJ, Leyden JJ. Skin replica analysis of photodamaged skin after therapy with tretinoin emollient cream. *J Am Acad Dermatol* 1991; 25:231–237.
6. Schurmeier HM, Heacock RL, Wolte AE. The ranger missions to the moon. *Sci Am* 1966; 214:52–56.
7. Oh CH. Evaluation of skin furrows according to aging process by using an image analysis system. *J Invest Dermatol* 1995; 104(4):618.
8. Cochran S, Medioni G. Three-dimensional surface description from binocular stereo. *IEEE Trans Pattern Anal Mach Intell* 1992; 14:981–994.
9. Moon JS, Oh CH, Kim MG. A new technique for 3-D measuring of the skin surface contours: evaluation of skin surface contours according to the aging process by using stereoimage optical topometer. *Physiol Meas* 2002; 23:247–259.
10. Grimson WEL. Computational experiments with a feature bases stereo algorithm. *IEEE Trans Pattern Anal Mach Intell* 1985; 7–17.
11. Oh CH, Kim IH, Hong SH, et al. Evaluation of skin furrow in aging process using stereoimage. *J Invest Dermatol* 1997; 108(4):537.
12. Kim MG, Moon JS, Oh CH. A study of skin furrows using image matching. *J Sci Technol* 1996; 14:93–104.
13. Weng T, Ahuja TS. Matching two perspective views. *IEEE Trans Pattern Anal Mach Intell* 1992; 14:806–825.
14. Stout KJ, Sullivan PJ, Dong WP, et al. Parameter for characterizing 3-D surface. Commission of the European Communities. The Development of Methods for the Characterization of Roughness in Three Dimensions. Publication no Eur 15178, EN. Birmingham: Printing section of Birmingham University, 1994; 216–246.
15. Fleischer AB, Feldman SR, Rapp SR, et al. Disease severity measures in a population of psoriasis patients: the symptoms of psoriasis correlate with self administered psoriasis area severity index scores. *J Invest Dermatol* 1996; 107:26–29.
16. Brown M, Lowe DG. Invariant features from interest point groups. *British Machine Vision Conference, Cardiff, Wales, 2002:656–665*.
17. Lowe, David G. Distinctive image features from scale invariant features. *Int J Comput Vision* 2004; 60(2):91–110.
18. Mikolajczyk K, Schmid C. An affine invariant interest point detector. *Proc 7th Eur Conf Comput Vision* 2002; 1:128–142.
19. Mikolajczyk K, Schmid C, et al. Scale and affine invariant interest point detectors. *Int J Computer Vision* 2004; 60(1):63–86.
20. Charman C, Williams H. Outcome measures of disease severity in atopic eczema. *Arch Dermatol* 2000; 136:763–769.
21. The European Task Force on Atopic Dermatitis. Severity scoring of atopic dermatitis: the SCORAD index. *Dermatology* 1993; 186:23–31.
22. Sugarman JL, Fluhr JW, Fowler AJ, et al. The objective severity assessment of atopic dermatitis scores. *Arch Dermatol* 2003; 139:1417–1422.
23. Seitz JC, Whitmore CG. Measurement of erythema and tanning responses in human skin using a tri-stimulus colorimeter. *Dermatologica* 1988; 177:70–75.
24. Son SW, Park SY, Ha SH, et al. Objective evaluation for severity of atopic dermatitis by morphologic study of skin surface contours. *Skin Res Technol* 2005; 11:272–275.
25. Yoon HS, Baik SH, Oh CH. Quantitative measurement of desquamation and skin elasticity in diabetic patients. *Skin Res Technol* 2002; 8:250–254.

26. Linde YW. Dry skin in atopic dermatitis. *Acta Dermatol Venereol (Stockh)* 1992; 177: 9–13.
27. Marks R, Barton SP, Shuttleworth D, et al. Assessment of disease progress in psoriasis. *Arch Dermatol* 1989; 125:235–240.
28. Moon JS, Kim MK, Oh CH, et al. Objective assessment of involved surface area in patients with psoriasis. *Skin Res Technol* 2003; 9:339–342.
29. Moon JS, Kim MK, Oh CH, et al. Quantitative evaluation of severity in psoriatic lesions using three-dimensional morphometry. *Exp Dermatol* 2004; 13:223–228.
30. Van Neste D, De Brouwer B. Monitoring of skin response to sodium lauryl sulphate: clinical scores versus bioengineering methods. *Contact Derm* 1992; 27:151–156.
31. Kollias N, Gillies R, Muccini JA, et al. A single parameter, oxygenated hemoglobin, can be used to quantify experimental irritant-induced inflammation. *J Invest Dermatol* 1995; 104(3):421–424.
32. Berardesca E, Maibach HI. Bioengineering and the patch test. *Contact Dermatitis* 1988; 18:3.
33. Agner T, Serup J. Individual and instrumental variations in irritant patch-test reactions—clinical evaluation and quantification by bioengineering methods. *Clin Exp Dermatol* 1990; 15:29–33.
34. Serup J. Characterization of contact dermatitis and atopy using bioengineering techniques. A survey *Acta Dermatol Venereol* 1992; 177:14–25.
35. Serup J, Staberg B, Klemp P. Quantification of cutaneous oedema in patch test reactions by measurement of skin thickness with high-frequency pulsed ultrasound. *Contact Derm* 1984; 10:88–93.
36. Kawai K, Nakagawa M, Kawai J. Evaluation of skin irritancy of sodium lauryl sulphate: a comparative study between the replica method and visual evaluation. *Contact Derm* 1992; 27:174–181.
37. Kim MG, Park SY, Ha SH, et al. Objective interpretation of the severity of SLS induced edema by stereo-imaging. *J Dermatol Sci* 2004; 35:125–131.

Development of a Digital Imaging System for Objective Measurement of Hyperpigmented Spots on the Face

Kukizo Miyamoto

Department of Dermatology, School of Medicine, The University of Tokushima, Kuramoto-cho, Tokushima, and Research and Development, Personal Beauty Care, Tokushima, and Procter & Gamble Company, Higashinada-ku, Kobe, Japan, and Procter & Gamble Company, Cincinnati, Ohio, U.S.A.

Hirotsugu Takiwaki and Seiji Arase

Department of Dermatology, School of Medicine, The University of Tokushima, Kuramoto-cho, Tokushima, Japan

Greg G. Hillebrand

Procter & Gamble Company, Higashinada-ku, Kobe, Japan, and Procter & Gamble Company, Cincinnati, Ohio, U.S.A.

INTRODUCTION

One of the most visually prominent features of photoaged skin is a mottled and irregular pigmentation due to the irregular distribution of melanocytes in the epidermis (1) and local differences in melanogenesis rates. It has been well-known that various types of chemical agents can inhibit melanogenesis (2,3). Most of the effects of these "skin-lightening ingredients," however, have been demonstrated through in vitro study design. It is true that several clinical studies have been performed by means of visual assessment (4) and/or histological evaluation in which only narrow areas of hyperpigmented spots have been examined (5,6). However, there are few objective and quantitative methods available for evaluating the degree of hyperpigmented spots in the entire face. We developed an image analysis system that was capable of capturing a wide area of the face in order to quantify overall improvement of hyperpigmented spots through the treatment with skin-lightening materials. This is the report on the design, capability, and limitation of our system.

MATERIAL AND METHODS

Digital Imaging System Equipment

The facial imaging system used in the present study is shown in Figure 1. This system was placed in a room free from ambient light. Illumination was provided by (i) a 3200K Balcar Fluxlite[®] tungsten light source (OSRAM 36 Dulux 36W/12 Lamp) that was mounted on a video camera at a 55° angle to the table, and (ii) a 3500K Balcar Duolite tungsten light source mounted below the video camera at a 65° angle to the table in order to provide uniform illumination on the subject's face. The intensity of both lights was controlled by a dimmer (Dove Systems SceneMaster SM1).



FIGURE 1 Facial imaging system composed of a light source, dimmer switch, 3-CCD video camera, computer, and positioning device for accurate alignment of the subject's face.

The distance from the camera head to the subject's face was 460 mm. Image magnification was $30 \text{ mm} = 95 \text{ pixels}$ ($\pm 1\%$). Voltage fluctuation was minimized by using a voltage stabilizer. A Sony DXC-537H 3-charge-coupled device (CCD) camera, containing 640 (horizontal) \times 582 (vertical) effective picture elements (pixels), equipped with a Canon J15 \times 9.5 BKRS Lens was used, and the collected images were digitally transferred to the computer. A Tiffin Series 9 Polarizing Filter in combination with polarizing sheets on the lights was set to produce a cross-polarized image. The positioning device was placed on the imaging system to align the position of the subject's face with the camera and illumination during the image acquisition. We customized a dental device that was originally used for taking an X-ray picture of the teeth. Once the subject's head was positioned with the device, the camera and illumination mount were rotated to the table at an angle of 45° either left or right to the subject in order to capture the left or right side of facial images.

Quantification of Color

After white balancing of the camera, brightness values of red, green, and blue channels [RGB values: 0 (min.) – 255 (max.)] were converted into colorimetric values as follows: 24 color chips (each chip size was 9 mm^2) on a mini GretagMacbeth ColorChecker were measured with a tristimulus colorimeter (Minolta CR-300 Chromameter[®], Osaka, Japan) to obtain CIE (Communication Internationale de l'Éclairage) $L^*a^*b^*$ values for each color chip. These chips were then placed on the subject's positioning device and captured by the imaging system to measure the mean RGB value of each color chip. These RGB values were also used thereafter as targeted standard values for calibrating the color of the system. CIE $L^*a^*b^*$ values were approximated by three different cubic equations of RGB values using multiple regression analysis. (The approximated $L^*a^*b^*$ values derived from the three equations will be called quasi $L^*a^*b^*$ values thereafter.)

System Calibration Before Measurement

A GretagMacbeth neutral 8.0 gray color board was used for white balancing of the camera. Color calibration was performed using the mini GretagMacbeth ColorChecker placed on the subject's positioning device as mentioned above.

The intensity of the illumination was then adjusted with the dimmer until the mean *RGB* values were obtained within $\pm 5\%$ of the targeted standard values. On each measurement day, white balance and color calibration were performed twice, once in the morning and again in the afternoon (approximately four hours after the first calibration).

Image Collection and Analysis Procedure

For a series of long-term evaluation of pigmented spots, a baseline image was always taken, and this image was used to accurately reposition the subject's head for subsequent images as follows: During image capture at each point in time, the baseline image was displayed on a monitor simultaneously with the subject's live image to adjust her head so that her live image would be exactly superimposed upon the baseline image. The software image analysis was developed by us using Visual Basic (Version 5.0 Microsoft). Roughly speaking, the algorithm of this software is composed of two sequences, the first part is designed for the detection of hyperpigmented spots based on the local contrast between a spot and its surrounding area, and the second part is for measuring averaged color tone of both detected spots and normal skin as a background. The algorithm for extraction of hyperpigmented spots is as follows: Of three monochromatic images of *RGB* channels, the blue channel image was employed for the detection of pigmented spots because blue light is absorbed well by melanin. The region of interest that was manually selected in the image was processed by high-pass filtering using a Gaussian smoothing on every 3×3 pixels area in the image. Candidates for hyperpigmented spots were then extracted, by subtracting the resultant image from the original blue channel image, when the difference of the brightness values between two images was more than 15. After transcribing the candidate spots to the original full color image, the mean quasi $L^*a^*b^*$ values in the area of all candidate spots and those of surrounding areas were calculated. The color contrast between each candidate spot and its surrounding area was measured in ΔE units as noted below

$$[\Delta]E = \sqrt{\left(\text{mean}L^*_{\text{spot}} - \text{mean}L^*_{\text{surrounding}}\right)^2 + \left(\text{mean}a^*_{\text{spot}} - \text{mean}a^*_{\text{surrounding}}\right)^2} + \sqrt{\left(\text{mean}b^*_{\text{spot}} - \text{mean}b^*_{\text{surrounding}}\right)^2}$$

where “ $\text{mean}L^*_{\text{spot}}$ ” is the $\text{mean}L^*$ value of a candidate spot and “ $\text{mean}L^*_{\text{surrounding}}$ ” is the $\text{mean}L^*$ value of the area surrounding the candidate spot. These values were calculated in a similar way for a^* and b^* values as well. When ΔE was greater than three and the minimum size of candidate spots were larger than a 4mm^2 circular shape, these spots were defined as hyperpigmented spots. This definition was based on the results of our preliminary study showing that most spots darker and larger than these thresholds were recognized as “hyperpigmented spots” by the inspection of all of 10 image examiners, while brighter or smaller ($\Delta E < 3$ or area $< 4\text{mm}^2$) spots tended to be missed by more than 40% of them. In this way, we determined the entire area (mm^2) of hyperpigmented spots. The area of the spots were then subtracted from region of interest (ROI) in the original image to extract the background normal skin area and to measure its mean $L^*a^*b^*$ values. The flowchart for overall algorithm is shown in Figure 2. This image analysis was

Hyperpigmented Spots Detection Flowchart

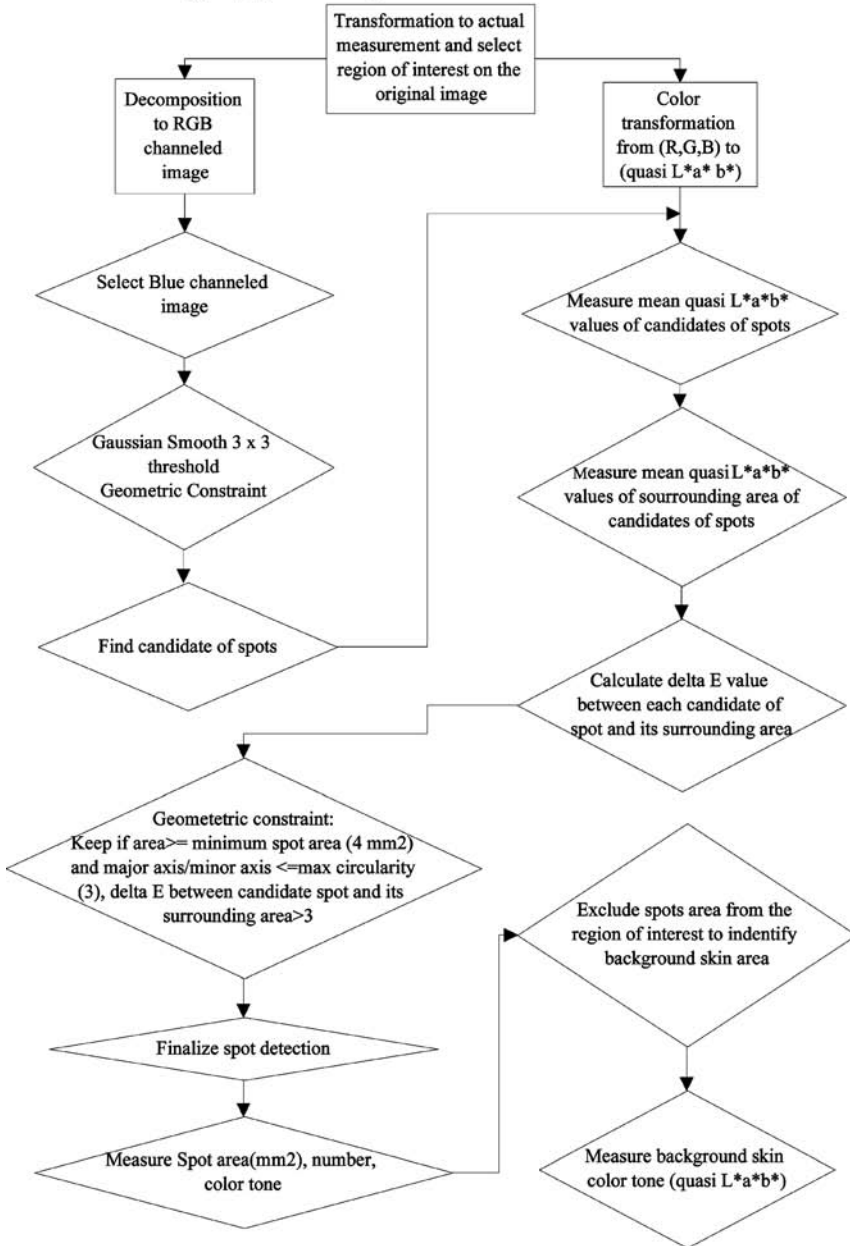


FIGURE 2 Algorithm of the image analysis for measuring hyperpigmented spots on the face.

executed automatically except for selecting ROI, and the results obtained can be stored on the computer for later retrieval and analysis.

Method Validation

The accuracy and reliability of the system was determined using a mannequin head attached with six standard color chips on the face for the measurement of skin color tone and circular artificial brown spots of known area on the face for the measurement of the area of hyperpigmented spots.

Skin Color Tone

A small color board with six skin color standards [(i) very light skin color (2.5YR 8/4 in Munsell Color Chart), (ii) light skin color (2.5YR 7/6), (iii) medium skin color (2.24YR 6.5/4.1), (iv) medium dark skin color (2.5YR 6/6), (v) dark skin color (3YR 3.7/3.2), and (vi) very dark skin color (10R 3/4) chips obtained from the GretagMacbeth Munsell Color Sheets] was attached to four facial regions of the mannequin head (forehead, cheek, mandibular area, and lateral periorbital area) (Fig. 3). Quasi $L^*a^*b^*$ values were measured using the image analysis. As the lateral periorbital area was in the center of the image and at the same distance from the camera during color calibration of this system, the quasi $L^*a^*b^*$ values measured in this area (i) were regarded as the real color values. Therefore, the rates of error (%) in the quasi $L^*a^*b^*$ values in forehead, cheek, and mandibular region (ii) were defined as: $\frac{(B)-(A)}{(A)} \times 100$

Area of Hyperpigmented Spots

Two types of brown circular patches, with diameters of 8 and 5 mm, were attached to the forehead, cheek, mandibular area, and lateral periorbital area on the mannequin head (Fig. 3). Images of the mannequin face were then captured and the areas measured by the image analysis were compared to the true sizes to detect the range of error and determine the zone of accuracy.

Stability of the System

Stability of the system was evaluated by examining the variances in facial color values and the area of brown patches attached to the cheeks and lateral periorbital

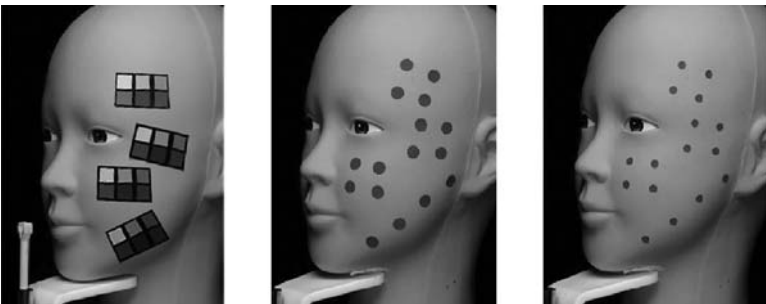


FIGURE 3 (See color insert) Simulation using a mannequin head. Six color chips (*left*) and brown circular patches (5 mm in diameter: *right*) placed on the forehead, in the lateral periorbital region on the cheek and in the mandibular areas.

areas of the mannequin head. We repeated image capturing five times every hour. The coefficient of variation for background color tone (quasi $L^*a^*b^*$) of the mannequin heads and for spot areas were then examined.

*Correlation Between Communication Internationale de l'Eclairage $L^*a^*b^*$ and Quasi $L^*a^*b^*$ Values of the Facial Skin*

A total of 187 Japanese females were measured for their facial skin color tone in both the CIE $L^*a^*b^*$ values with the Chromameter and quasi $L^*a^*b^*$ values using the image analysis. Because the aperture of the probehead of the Minolta Chromameter was approximately 1/20 of the objective area of the image analysis, color measurement with the chromometer was repeated 20 times to completely cover the lateral periorbital and cheek regions of the face. From these scans the mean CIE $L^*a^*b^*$ values were obtained and then, compared to the quasi $L^*a^*b^*$ values obtained by the image analysis. Correlations between the two types of $L^*a^*b^*$ values were then examined.

RESULTS

The Equation for Transforming RGB Values to Quasi $L^*a^*b^*$ Values

The equations for transformation from RGB values to quasi $L^*a^*b^*$ values were determined as follows:

$$\begin{aligned} \text{Quasi } L^* &= 23.2753298 + 0.09189237 \times R + 0.34734768 \\ &\quad \times G - 0.0018069 \times G^2 + 0.00000464 \times G^3 \quad (r^2 = 0.9984) \end{aligned}$$

$$\begin{aligned} \text{Quasi } a^* &= -4.6472575 + 0.40731244 \times R - 0.4905761 \\ &\quad \times G + 0.31679128 \times B - 0.0014044 \times R \times B - 0.0010724 \\ &\quad \times G \times B + 0.00000657 \times RGB \quad (r^2 = 0.9946) \end{aligned}$$

$$\begin{aligned} \text{Quasi } b^* &= 0.3708721 + 0.18277815 \times R + 0.23190101 \\ &\quad \times G - 0.4344087 \times B \quad (r^2 = 0.9951). \end{aligned}$$

Accuracy of Color and Area Measurement

The error of color values of the color chips in the cheek was less than 2% in each measurement of L^* , a^* , and b^* although more than 2% in the forehead and mandibular area (Fig. 4). The difference in quasi L^* values of lighter skin color chips between on the forehead or mandibular area and on the lateral periorbital area tended to be larger than that of darker skin color chips. Also, the difference in quasi a^* values of darker skin color chips between on the forehead or mandibular area and on the lateral periorbital area tended to be larger than that of lighter skin color chips. This seems to be mainly due to the difference between the intensity of illumination on the forehead or mandibular area and on the lateral periorbital area, which was determined by the distance and angle between the light source and the anatomical area. The error of area of brown patches in the cheek and lateral periorbital area was less than 5% when compared to real spot sizes, regardless of their diameters. However, the variability of spot areas measured on the forehead

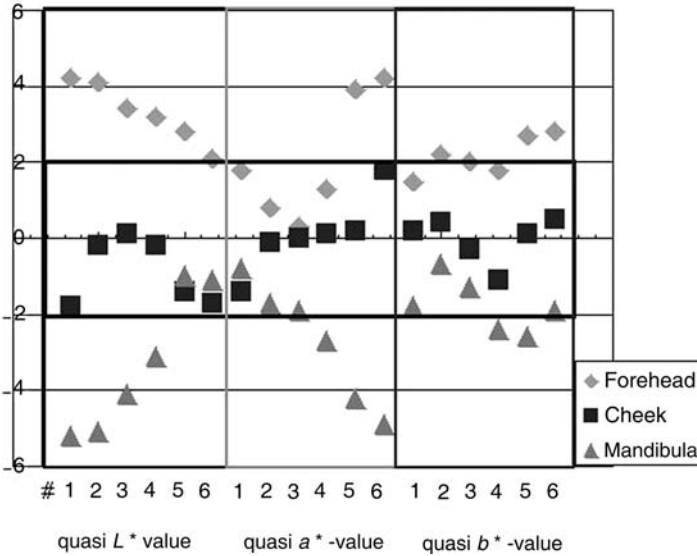


FIGURE 4 Errors in measurement of color values of six color chips placed on three regions of a mannequin face. The rate of error was defined by the difference from the color values of the chips placed in the lateral periorbital area.

and mandibular areas was more than 5% (Fig. 5). Judging from these results, the periorbital and cheek areas were regarded as the best locations to accurately measure the skin color and the area of hyperpigmented spots with this system (Fig. 6).

System Stability

The coefficient of variation over the course of all the measurements of quasi L^* , a^* , and b^* values in the cheek and lateral periorbital areas of the mannequin head were 0.3%, 1.2%, and 1.2%, respectively. The coefficient of variation for the measurement of the areas of brown spots in the cheek and lateral periorbital regions was 0.4%.

Correlation Between Communication Internationale de l'Eclairage $L^*a^*b^*$ Values and Quasi $L^*a^*b^*$ Values of the Facial Skin

Pearson's correlation coefficients (r) between quasi $L^*a^*b^*$ values and CIE $L^*a^*b^*$ values were 0.897, 0.815, and 0.817, respectively. The regression line equations were as follows: (Fig. 7)

$$(\text{quasi } L^* \text{ value}) = 0.884 (\text{CIE } L^* \text{ value}) + 10.47$$

$$(\text{quasi } a^* \text{ value}) = 1.082 (\text{CIE } L^* \text{ value}) + 1.039$$

$$(\text{quasi } b^* \text{ value}) = 1.231 (\text{CIE } L^* \text{ value}) - 0.712$$

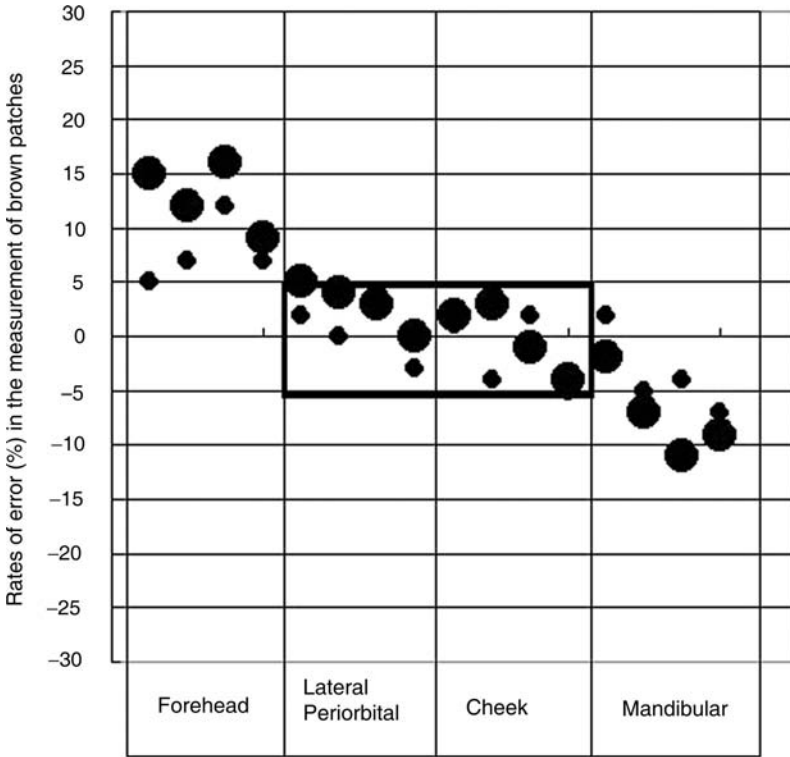


FIGURE 5 The rate of error (%) in the measurement of the area of brown patches (small circle: 5 mm, large circle: 8 mm in diameter) using image analysis.

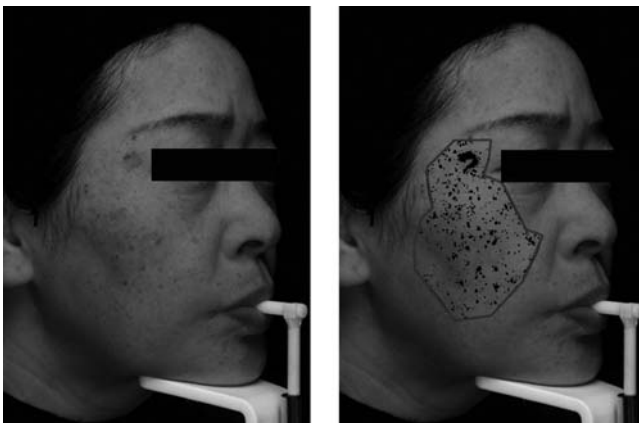


FIGURE 6 (Left) A sample image and recommended region of interest for most accurate measurement. (Right) Hyperpigmented spots detected automatically by the image analysis.

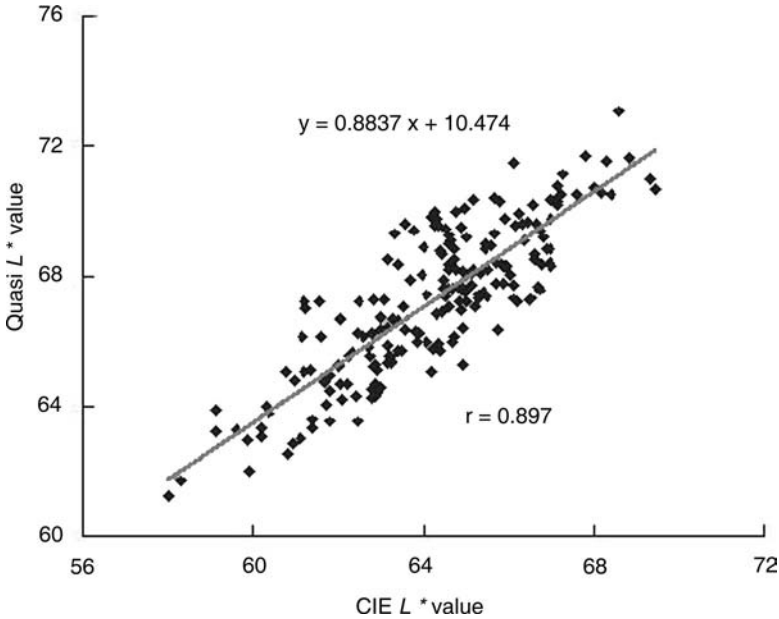


FIGURE 7 Correlation between quasi L^* values measured by the image analysis and the mean Communication Internationale de l'Eclairage L^* values measured with a tristimulus colorimeter. *Abbreviation:* CIE, Communication Internationale de l'Eclairage.

DISCUSSION AND CONCLUSIONS

We have demonstrated here a measurement methodology to quantify the area of hyperpigmented spots and the background skin color of the face by using high-resolution digital imaging technology. We confirmed by several validation studies that this system was sensitive enough to detect hyperpigmented spots and offered excellent data reproducibility for practical use. This reliability seemed to result from the strict system calibration and appropriate face positioning procedures.

Current measurement methods to evaluate skin color tone or color of hyperpigmented spots are mostly through the use of colorimetric instruments such as chroma- or colormeters, spectrophotometers (7–9), and/or video microscopes (10,11). Although skin color tone measured with these instruments seems to be accurate, it may be a disadvantage as the measurement area is too narrow (smaller than approximately 10 mm in diameter) to evaluate color of wide region. For instance, it is necessary to carry out at least 20 measurements in order to evaluate the average color tone of the facial skin from lateral periorbital region to the cheek. Although visual assessment has been performed conventionally for this purpose, it appears to be a less objective method.

To overcome these disadvantages of conventional methods, we developed a new imaging system that was capable of both extracting pigment spots from facial images and comparing the area of these spots between two images in a quantitative and automatic fashion. We employed full polarization to reduce reflected shine and strictly control calibration procedure under constant illumination to avoid artificial or false changes in skin color. Moreover, we developed a device to correctly

reposition the face as well as the image blending system to superimpose a live image onto a previous image via computer software.

There are two major methods for the evaluation of hyperpigmented spots by image analysis. The first one is to count the number of pixels whose *RGB* brightness intensities are distributed in a certain level threshold using the histograms analysis of the frequency distribution on all pixels within ROI. The second method is to extract pigmented spots from the image and measure the total area of them if color difference between a spot and its surrounding skin area is higher than a certain level. In our experience, the first method is suitable for color and area analysis of an image in which a single and relatively large spot is captured. This is the case with the image collected with a video-microscope. The results of our preliminary studies revealed that the first method was far less sensitive than the second one in evaluating total area of pigmented spots if facial images with a large number of small spots were analyzed. If the total area of pigmented spots is far smaller than that of the background skin, the frequency distribution of *RGB* brightness intensity of the former may be hidden by that of the latter in spite of their significant low brightness levels in histogram analysis. This is because the background skin image contains pixels with a variety of low brightness intensities, reflecting the inevitably produced noises in electric signals and the shadows caused by facial curvature of furrows. Consequently, it becomes difficult to set the threshold level to distinguish pigment spots from the background skin. As the main purpose of our imaging system was to quantify the total area of a number of small hyperpigmented spots that are distributed in the wide area of the face, namely solar lentigo, we employed the second algorithm for the software of this system. Besides solar lentigo, this algorithm is suitable for detection of discrete, small pigmented spots such as ephelides, simple lentigo, and pigmented nevi. However, large pigmented spots covering a wide area, such as melasma, are not readily detected by this algorithm. In addition, there is a disadvantageous limitation in our system that a hyperpigmented spot is not automatically judged as being improved unless color difference between the spot and its surrounding area (ΔE) becomes less than three units. It would be better that we should develop a better algorithm to detect the larger and irregular shaped spots and measure their color tone to evaluate various types of facial hyperpigmented spots in the future. Judging from the simulation results using a mannequin head and data comparison with Chromameter, the reliability and reproducibility of this system for measuring facial skin color and the area of small pigmented spots were validated unless the objective area is located at the peripheral region of the face. Although the obtained data with this system tended to be comparatively inaccurate in the forehead and chin areas, as probably influenced by longer distance from the camera and anatomical curvature of the skin surface, there seems to be few problems if we compare two images including those areas not in an absolute but in a relative manner. The advantages of this imaging system are that it enables us to quantify the total area of small hyperpigmented spots scattered in a wide area of the skin in a very short time. However, in order to utilize this imaging system effectively, it is important to provide constant conditions for measurement throughout the measurement period, such as cleansing the face to remove make-up and maintaining a constant room temperature and humidity to avoid variation in cutaneous circulation resulting in temporary skin color change. In conclusion, this digital imaging system seems to be a more reliable and time-saving measure than conventional methods for objective and quantitative evaluation of the degree of some kinds of facial pigmentary disorders,

such as a face with a large number of solar lentigines, and for the fair judgment of the overall responses to treatments.

REFERENCES

1. Breathnach AS, Nazzaro-Porro M, Passi S, Picardo M. Ultrastructure of melanocytes in chronically sun-exposed skin of elderly subjects. *Pigment Cell Res* 1991; 4:71-79.
2. Madhosingh C, Sundberg L. Purification and properties of tyrosinase inhibitor from mushrooms. *FEBS Lett* 1974; 49(2):156-158.
3. Curto EV, Kwong C, Hermersdorfer H, et al. Inhibitors of mammalian melanocyte tyrosinase: in vitro comparisons of alkyl esters of gentisic acid with other putative inhibitors. *Biochem Pharmacol* 1999; 57(6):663-672.
4. Newman N, Newman A, Moy LS, Babapour R, Harris AG, Moy RL. Clinical improvement of photoaged skin with 50% glycolic acid. A double-blind vehicle-controlled study. *Dermatol Surg* 1996; 22(5):455-460.
5. Schindewolf T, Schiffner R, Stolz W, Albert R, Abmayr W, Harms H. Evaluation of different image acquisition techniques for a computer vision system in the diagnosis of malignant melanoma. *J Am Acad Dermatol* 1994; 31(1):33-41.
6. Ascierto PA, Palmieri G, Celentoro E, et al. Sensitivity and specificity of epiluminescence microscopy: evaluation on a sample of 2731 excised cutaneous pigmented lesions. The Melanoma Cooperative Study. *Br J Dermatol* 2000; 142(5):893-898.
7. Green A, Martin N, Pfitzner J, O'Rourke M, Knight N. Computer image analysis in the diagnosis of mela. *J Am Acad Dermatol* 1994; 31(6):958-964.
8. Pierard GE. EEMCO guidance for the assessment of skin colour. *J Eur Acad Dermatol Venereol* 1998; 10(1):1-11.
9. Adhoute H, Grossman R, Cordier M, Soler B. Chromametric quantification of pigmentary changes in the solar lentigo after sunlight exposure. *Photodermatol Photoimmunol Photomed* 1994; 10(3):93-96.
10. Tomatis S, Bono A, Bartoli C, Tragni G, Farina B, Marchesini R. Image analysis in the RGB and HS colour planes for a computer-assisted diagnosis of cutaneous pigmented spots. *Tumori* 1998; 84(1):29-32.
11. Takiwaki H, Shirai S, Watanabe Y, Nakagawa K, Arase S. A rudimentary system for automatic discrimination among basic skin spots on the basis of color analysis of video images. *J Am Acad Dermatol* 1995; 32(4):600-604.

Skin Documentation with Multimodal Imaging or Integrated Imaging Approaches

Nikiforos Kollias

Methods and Models, Johnson and Johnson Consumer and Personal Products Worldwide Co., Skillman, New Jersey, U.S.A.

INTRODUCTION

Documentation of skin and facial skin, in particular, has evolved with the developments of digital imaging camera equipment and the explosive miniaturization and exponential growth in personal computing power. In the past, a camera with some light source, typically a flash or daylight, was adequate for recording the attributes of the skin or of skin lesions. Dermatologists developed extensive personal libraries of 35 mm slides depicting skin conditions of interest and published books (atlases) with collections of images for educational purposes. These images have scientific value and many dermatology departments hired medical photographers to ensure consistent image quality. In the last 5 to 10 years, photographic film has become all but obsolete as digital image sensor pixel counts have increased and magnetic disk storage and computer memory costs have dramatically decreased. Computers have been developed, which are fast and with essentially limitless memory, making it possible to store large collections of images in small footprint instruments—desktop and laptop computers. The developments in memory media make it possible to have access to very large image caches at the personal level, gigabyte to terabyte.

It has been recognized that standard photography with a flash or daylight is inadequate to produce images that have the same sensitivity in retrospective evaluation as a clinical examination. Specialized photographic techniques that have similar sensitivity to clinical evaluation have been developed, with each modality contributing information enhancement in specific skin attributes; simultaneous use of several modalities has been found to yield a further increase in the information content. No single image can provide an examiner with adequate information to allow a retrospective examination of the skin from the image alone, which would yield results equivalent to a clinical assessment. The specialized techniques include polarized light imaging (parallel and perpendicular polarization) and fluorescence imaging [excitation in the blue and in the long wavelength ultraviolet (UV) part of the electromagnetic spectrum]. These techniques allow visualization and quantification of many skin features and attributes that taken together may provide information equivalent to a clinical assessment. These methods provide enhancement of specific skin features in each mode and suppression of others, thus providing a means to concentrate on certain features with adequate sensitivity. For the imaging techniques to be complementary, the images need to be collected simultaneously or in rapid succession to minimize subject motion artifacts and possible skin changes between exposures. Thus multimodal systems have been developed, which acquire high-resolution images in several modalities in rapid

succession, which are capable of resolving features that are each 0.3 mm. High-resolution facial images are currently six megapixels (Mp), which require 18 Mb of memory space each (pixel stands for picture element). Thus, while collecting the multimodal images from a subject, a large volume of data is obtained, which is not unlike the collection of observations that the clinician does mentally during a patient visit.

In this chapter, the concepts and the execution of multimodal imaging will be discussed and the skin attributes that are enhanced in the various modalities will be described. Furthermore, the discussion will be restricted to the description of systems that allow the evaluation of skin areas such as the entire face; the techniques discussed may be used for both macroscopic imaging of the whole body and microscopic imaging of individual lesions as in dermoscopy. These topics will be discussed elsewhere. The terms “multimodal” and “integrated” imaging will be used interchangeably throughout. Two imaging modes will be considered: reflectance imaging with visible light (including polarized light) and fluorescence imaging excited with either long wavelength UVA (360–400 nm) or with blue light (400–450 nm). Imaging of the skin with these methods have been lately widely used; therefore there is an extensive clinical database to draw on.

An image is a two-dimensional (2D) table of intensity and color values where the distance between measurement points is such that it allows the discrimination of subject attributes that are thus recorded. An image of the skin (or of any other object) is the result of light (electromagnetic radiation) being directed onto the object and some of the remitted light by that object being directed to our eyes so that an image may be formed on our retinas; imaging involves the replacement of the cornea–lens–retina combination by a focusing lens and recording on a sensitive detector of what was the retinal image. The elements necessary to obtain an image are (i) a light source for illumination, (ii) optical elements that may define the direction and quality of light radiating from the source, (iii) an object to be imaged, (iv) some collection optics that may include filters and lenses, and (v) a detector. Imaging is a scientific process when the technical specifications of each element are precisely known and may be duplicated to obtain reproducible images. An image of the skin is obtained by photons (light particles) that have been reflected by surface and subsurface elements or remitted following absorption by some chromophore in the skin (chromophore: any chemical entity in the skin that absorbs light, such as melanin or hemoglobin).

THE INTERACTION OF LIGHT WITH THE SKIN

The interaction of visible light with the skin may be described in terms of a number of processes—absorption, elastic scattering, fluorescence, or inelastic scattering. There are also a number of nonlinear processes that require very high intensity light sources as two-photon conversion, second harmonic generation, etc; these are beyond the scope of this discussion because they require light sources (lasers) of high power and short pulse width (femtosecond– 10^{-15} sec). At low powers (such as those produced by ordinary photography flashes), light interacts with skin by (i) being absorbed by chemical species followed by a conversion of the light energy into heat—absorption, (ii) changing the direction of travel of light by differences in index of refraction within the skin—elastic scattering, (iii) being absorbed in an electron transition followed by the emission of a photon of lower energy, longer wavelength—fluorescence, and (iv) inelastic scattering where photons

may lose energy to vibrational states followed by emission of lower energy photons or longer wavelength. Of these, the most likely interactions are absorption and elastic scattering; fluorescence is likely to occur, yielding intensities that are weaker by a factor of 10 to 100 times. Inelastic scattering may be assessed with elaborate instrumentation and is not detectable in the recording of routine reflectance images. The images obtained due to absorption and elastic scattering are called reflectance images or, to be more precise, they should be called diffuse reflectance images; this includes images obtained through ordinary photography. Diffuse reflectance refers to light that reemerges from the skin after having suffered some absorption and some scattering; i.e., it is color modified and may travel in any direction away from the skin.

Light is defined as the part of electromagnetic radiation that is visible to the eye and has wavelengths in the range of 400–700 nm; electromagnetic radiation of shorter wavelengths constitutes the UV spectrum and electromagnetic radiation of longer wavelengths constitutes the near infrared. Photons are particles of light each having energy of $E = h\nu$, where E is the energy content, h is Planck's constant (6.6×10^{-34} J/sec), and ν is the frequency of the photons. Thus the energy content of a green photon of wavelength of 500 nm (frequency of 6.0×10^{14} Hz) is 4×10^{-19} J; photons may be thought of as "fuzzy" little spheres of a diameter corresponding to their wavelength and very small energy content each. The chromophores (absorbing species) mentioned (i.e., melanin and hemoglobin) have absorption properties in both the UV and the near infrared; in the present discussion, only their absorption properties in the visible will be considered, in how they may affect the visible appearance of the skin. The processes of absorption and scattering attenuate the incident light with the effect of limiting the depth to which visible radiation may penetrate (Fig. 1). The penetration depth of light in skin is defined as the depth at which the incident intensity has been attenuated to $(1/e)$ or 37% of its value outside the skin. It should be kept in mind that usual intensities,

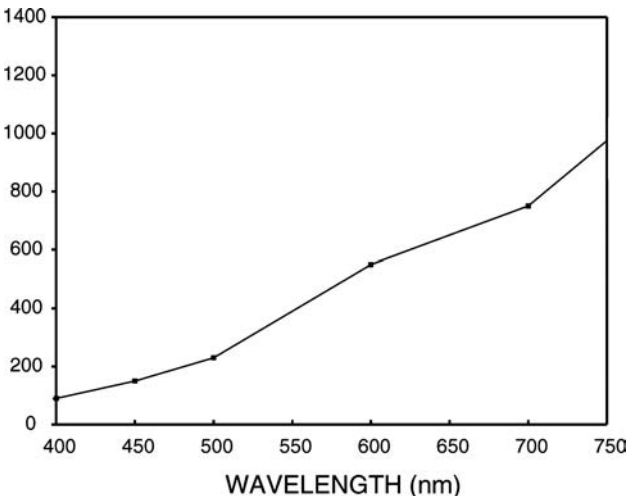


FIGURE 1 The penetration depth of visible light as a function of wavelength. Note that the depth varies by a factor of 10 (10 times) between 400 nm (deep blue) and 700 nm (far red). These data were obtained from bloodless dermis *ex vivo*; therefore the effect of hemoglobin is not considered here.

as in sunlight, correspond to 10^{17} to 10^{18} photons per second per square centimeter (which corresponds to 150 mW/cm^2 of green light—an intensity similar to that of sunlight in the visible) and 37% of these values corresponds still to a very large number of photons; thus the penetration depth is an indication of the rate at which the intensity of the incident light is attenuated in tissue and does not indicate the depth beyond which there are no more photons!!

Photons that enter through the stratum corneum into the skin need to suffer a large number of scattering events before they come back out of the skin in order to be observed. Because the average deflection angle per scattering event for photons in tissue is 10° , a minimum of 18 interactions have to take place for light to exit the skin (a change of 180° in the direction of travel); in general, it takes close to 360 scattering events before light exits because the scattered beam is not confined to one plane. The larger the number of interactions the larger the path length that the light travels in the skin and the greater the probability that it will be attenuated by an absorbing chromophore. For single-particle scattering, the intensity of the scattered light varies with the direction at which it is viewed (it depends on the size of the scattering particles) and with the wavelength of the photons. For particles or even molecules much smaller than the wavelength of visible light (smaller than one tenth of the wavelength, i.e., $< 50 \text{ nm}$), the scattering is isotropic and weak, i.e., scattered equally in the forward and the backward directions and scattering is very strongly wavelength dependent (λ^{-4}), resulting in much stronger scattering of the shorter wavelengths (i.e., the blue) (Fig. 2).

If light was scattered by an optically thin^a suspension of particles with dimensions $< 0.1 \lambda$, placed against a black background, it would appear blue, while placed against a bright white background it would appear yellow. When illuminated from the front, it appears blue because this is the wavelength that is scattered the most strongly toward the eye while when back illuminated, blue is still the wavelength that is scattered most strongly this time out of the beam reaching the eyes; therefore the loss of blue results in a yellow appearance. It is because of this that the sky appears blue (Rayleigh scattering). For particles of dimensions similar to the wavelength range of visible light (500 nm), scattering achieves maximum intensity and is mostly in the forward direction. Scattering by particles of dimensions of 500 nm and larger depends weakly on the wavelength ($\lambda^{-2} - \lambda^{-1}$), (Mie scattering). Scattering by bloodless dermis, *ex vivo*, has a weak dependence on wavelength ($\lambda^{-1.5}$) (Fig. 2). It is important to remember that both types of scattering occur in tissue because of the large variety of scattering centers from organelles to cells and collagen bundles.

The color of the resulting radiation from the scattering of light by particles of various sizes is accurately given by the above rules when dealing with single scattering events and media that are not optically thick.

When visible radiation falls on the surface of the skin, it is reflected at the stratum corneum–air interface because of the change in index of refraction (index of refraction of air $n_{\text{air}} = 1$ and index of refraction of stratum corneum $n_{\text{sc}} = 1.45$)

^a An optically thick medium is one that we cannot see through. In the case of optically thick scattering media with very weak absorption (i.e., long path lengths), scattering of incident white light results in white light irrespective of the size of the individual particles responsible for the scattering. This is because although red wavelength photons travel further than blue wavelength photons; they both eventually escape the medium, because there is little absorption. Bloodless dermis is such a medium.

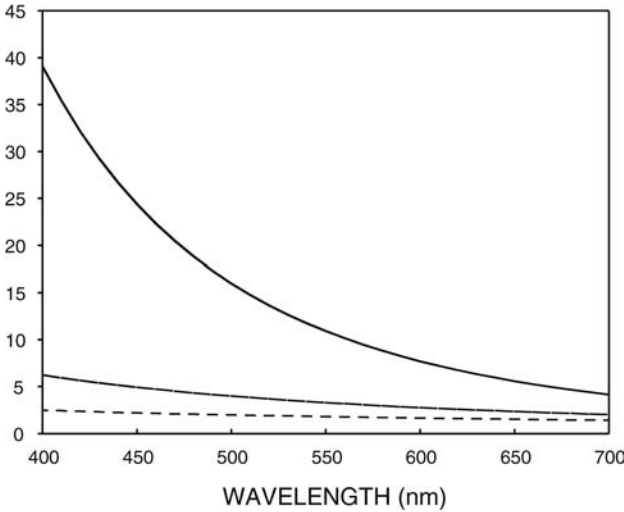


FIGURE 2 Comparison of the “strength” of scattering as a function of wavelength for three different types of scattering; the lowest curve corresponds to a λ^{-1} dependence (large particles, $d > \lambda$), the middle curve to a λ^{-2} dependence, and the highest curve to a λ^{-4} dependence (scattering by very small particles/molecules, $d > 0.1\lambda$), where d is the diameter of the particles and λ the wavelength of light.

(Fig. 3). This reflected radiation, 4% to 8% of the intensity of the incident light, has not interacted with the interior of the skin and thus has not been color modified by color substances in the skin (such as hemoglobin and melanin). Stratum corneum is a clear material and only slightly colored (yellow) in dark subjects or following exposure to UVB radiation (290–320 nm). The remainder of the light enters and

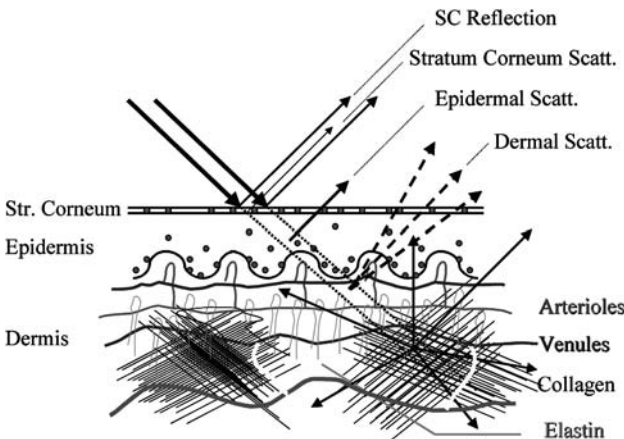


FIGURE 3 (See color insert) A schematic drawing of the skin and how visible light might interact with it. Abbreviation: Scatt., scattering.

traverses the stratum corneum, being scattered only by the melanin “dust” (degraded melanosomes) that is found in the flattened corneocytes.

The light then enters the viable epidermis where it is absorbed and scattered by the epidermal melanin pigment. The direction of travel of the light is changed whenever a change in the index of refraction occurs in its path of travel. Cell membranes and organelles have slightly different indices of refraction than the bulk index of the epidermis and therefore will cause slight changes in the direction of travel; melanin granules have the largest index of refraction in tissue, $n=1.7$. The normal human epidermis of a fair-skinned subject appears as a fairly transparent and slightly colored medium. This is because the epidermis is thin (100 μm) and does not produce a lot of scattering. The epidermis of a black person will be as black as the person appears because all the melanin resides in the epidermis; the dermis of either a black- or a white-skinned person will be white if devoid of blood. A dry and scaly stratum corneum on the other hand can produce considerable scattering by the disoriented and dry corneocytes, to the point that it hides the subsurface features of the skin by proportionally reducing the light that enters the epidermis—as in the case of scale on a psoriatic plaque. The color appearance of the epidermis of the darkest African subjects becomes silver because of the strong scattering of light by the large number of melanin granules present. The light that traverses the epidermis enters the dermis where it is strongly scattered by the collagen bundles and is absorbed by oxy- and deoxyhemoglobin in the capillaries and the superficial venular and arteriolar plexi. It is important to note that the light-absorbing species in the skin are not uniformly distributed as in a solution but are confined in melanosomes (for melanin) and in vessels and erythrocytes (for hemoglobin).

It helps to have a simplified model of the skin in mind when considering how light interacts with the skin. We can think of the stratum corneum as a transparent thin layer that absorbs like melanin only and can have a rough surface. This sits on top of a transparent layer, the viable epidermis, with absorption properties like that of melanin and some weak scattering. The dermis may be considered as a strongly scattering medium (like a glass of milk), with blood (or hemoglobin) dispersed uniformly within it. Occasionally, we have to consider other absorbing species such as methemoglobin, bilirubin or β -carotene but those form exceptions rather than the rule. Thus light incident on the skin model will either be reflected or scattered at the interface of the stratum corneum with air. It will then traverse the melanin filter in the epidermis and the hemoglobin filter in the dermis and will be scattered back by the collagen matrix. The scattering is not equally strong from all human skin and certainly varies with edema (as the distance between individual scatterers changes) and with age. Back-scattered light will then traverse the hemoglobin filter and the melanin filter and will again be reflected and scattered some by the air interface and escape the skin. The light we detect (photograph) has traveled twice through the melanin and the hemoglobin filters.

Light that has interacted with human skin carries information first about the surface of the skin (this light has the same color as that of the light source) and secondly about the subsurface absorbers and scatterers as light that has entered the skin has been color modified by the resident pigments. Thus in this simple approach we have two components to analyze, which hold the information on the appearance of the skin. Skin appendages also affect the appearance of the skin, although they have been ignored in this simple model. Hair follicles are the most prominent appendage that has an effect on the appearance of the skin; sebaceous

glands and sweat glands affect it as well. In this simplified model, we ignore the glyptic patterns that characterize the surface of the skin. Unfortunately, there is no way to incorporate these into a simple model. These structures and the information we may obtain about them from different imaging modes need to be considered individually, because they affect the appearance of the skin. For example, vellous hairs on the face may affect the appearance of facial skin because they act as a scattering layer before the incident light strikes the stratum corneum, vellous hair of the right length may serve a purpose similar to makeup while long vellous hairs may become visible and a distracting feature on the surface of the skin.

In fluorescence, an incident photon is absorbed by a molecule, exciting the molecule to its first electronic excited state; the molecule may then return to its ground state or may undergo a change in spin (intersystem crossing), lose some energy, and then decay to the ground state with a delay and emitting a photon of lower energy (longer wavelength). To produce a fluorescence signal, the incident light needs to be absorbed and the absorbing molecule needs to have a reasonably high conversion efficiency for fluorescence; there also needs to be a high enough concentration of fluorescing species for a fluorescence signal to be recorded on the detector (camera). Just as absorbing species have specific wavelength bands where they absorb the strongest (absorption maxima), fluorescing species have pairs of wavelength bands where they first excite the strongest and then emit the strongest. Unlike the absorption process, the fluorescence process is very much dependent on the environment of the species; e.g., dehydrated corneocytes have a strong fluorescence that may be used to detect scale; hydrated corneocytes—those closely attached to the stratum corneum—show no such fluorescence. We call this phenomenon fluorescence quenching. In fluorescence imaging, the source of light that is incident on the skin is filtered completely out of the recorded image. Fluorescence detection of chemical species is a sensitive technique because the fluorescence signal is detected on a black background (in order to “see” the fluorescence we have to filter out completely the excitation signal, i.e., produce a black background against which the fluorescence signal is measured) while in the case of absorption we measure the attenuation of the incident light, i.e., a measurement in the presence of a strong signal. We always do better in detecting small signals on a black background than small signals on a strong background—stars are visible at night against a dark sky.

There are a number of fluorescing compounds that may be visualized in or on the skin with fluorescence imaging, this includes both endogenous (native) fluorescing species as collagen cross-links, elastin cross-links, keratin, “horn,” porphyrins (coproporphyrin and protoporphyrin IX), and others that are not prominent (Table 1) and exogenous (topically applied) fluorescing species as salicylic acid, some sunscreens, retinol as well as dyes as methylene blue, fluorescein, indocyanine green, and others. We will focus our attention here on endogenous materials; these may be excited with long wavelength UV radiation or short wavelength visible radiation. The reason for this choice of excitation bands is safety—it is difficult to produce any damage in the skin with wavelengths longer than 375 nm neither in terms of a sunburn nor pigmentation. Fluorescence imaging has also been used to delineate pigmented lesions because of the enhancement obtained in melanin absorption by going in the UV range of wavelengths—more on this later. The species that have been found to fluoresce the strongest in the skin when excited at their excitation maximum are collagen cross-links excited at 375–380 nm, elastin cross-links (isodesmosine) excited at 400–410 nm, porphyrins

TABLE 1 The Principal Chromophores of Human Skin

Skin chromophore	Spectral range of activity	Abs/Scat/Fluo	Principal spectral features—maxima, (nm)
Oxyhemoglobin	UV–Vis	Abs	412, 542, 577
Deoxyhemoglobin	UV–Vis	Abs	430, 555, 760
Melanin	UV–Vis	Abs/Scat	Monotonic increase to short wavelengths
Water	Vis–near infrared	Abs	760, 900, 1250, 1400, etc
Porphyrin	Vis	Fluo/Abs	Ex: ~405; Em: 620
Bilirubin	Vis	Abs	460
Nicotinamide adenine dinucleotide/reduced form of nicotinamide adenine dinucleotide	UV–Vis	Fluo/Abs	Ex: ~350; Em: 460
DNA/RNA	UV	Abs	260 (principal), 290 (weak)
Tryptophan	UV	Fluo/Abs	Ex: ~295; Em: 340–350
Urocanic acid	UV	Abs	280
Collagen cross-links	UV–Vis	Fluo/Abs	Ex: 335; Em: 380 Ex: 370; Em: 460
Elastin cross-links	UV–Vis	Fluo/Abs	Ex: 420; Em: 500 Ex: 460; Em: 540
Keratin (in corneocytes)	UV	Fluo/Abs	Ex: 370; Em: 460
Keratin (in horn)	UV–Vis	Fluo/Abs	Ex: ~405; Em: 460–650; Ex: ~370; Em: 460
Erythrocyte ghosts	UV–Vis	Scat	Broad over UV–Vis
Corneocytes	UV–Vis	Scat	Broad over UV–Vis

excited at 405–410 nm, and horn (a mixture of sebocyte ghosts, keratinocytes, sebaceous lipids, and water) excited at 380–400 nm. Other fluorescing species, such as the reduced form of nicotinamide adenine dinucleotide and flavin adenine dinucleotide, which are part of the cellular makeup, do not give strong signals in the skin. Thus by exciting at 370–390 nm, we may obtain strong signals from collagen cross-links and horn, and by exciting at 400–420 nm, we may obtain strong signals from porphyrins, elastin cross-links, and to a lesser extent horn. There are other fluorescing species that may be excited by shorter wavelength radiation but imaging of those requires specialized equipment as the available light sources (xenon flash) do not produce a high enough intensity and there are concerns about safety as shorter wavelengths present an increased risk of damage to the skin, such as sunburn or photoaging with multiple exposures. It cannot be overemphasized that the absence of a fluorescence signal does not necessarily mean the absence of a specific species. It may be that the environment of the species is such that it quenches the fluorescence; therefore we may need to run a parallel test with fluorescence detection to confirm the absence of the particular species.

MACROIMAGING OF THE SKIN

Imaging is an attempt to document the visual appearance of the skin; it may also be an attempt to obtain 2D data or a measure of the variation of certain parameters over the surface of the skin and over time. Imaging goes well beyond simply the accumulation of information in 2D, although it is just that when we consider an image as what is stored in the memory of a computer—a 2D matrix of numbers

representing color and intensity at each point. The reason an image is more than just a matrix of numbers is because not only do we automatically obtain measures of what occurs at every point in a plane but we are also able to generate relational information by measurements of contrast among points on the plane and principally between adjacently located points. Imaging is thus more than the accumulation of 2D information because we automatically start processing the information obtained by the use of contrast within the image and with other images in our particular mental library because we are accustomed to obtain, retain, and interpret information obtained through our vision. Our vision does not simply generate optical signals over space and the relation among these but goes beyond these to generate a look-up table (a continuously updatable library of images against which our current perception is compared). For example, the image of a face is quickly recognized as such. What follows in a rapid succession is the formation of a value judgment on the obtained image both by evaluating the quality of the image, i.e., clarity, color, and contrast, and by evaluating the experience that this image generates, i.e., pleasure, disgust, interest, affection, etc. In other words, an image forms the link between the documentation of objective evidence and the emotional state—*aspirations*—of the observer. In forming a value judgment, we first go through our library of images together with the emotions that these stimulate; e.g., an image of a woman that resembles our mother might elicit positive emotions because of this association. On the other hand, images may be analyzed on the basis of the beauty quotient, no matter how this is defined. Therefore the quality of the image needs to be assessed not simply in the physiological domain, i.e., the information it carries about the biological system in question as measures of physical attributes, but also in the psychological domain, i.e., in elicitation of emotions. The two are never separated especially when one is viewing human faces and especially his/her own image.

In imaging subjects in clinical or consumer studies—where many facial images are collected in order to assess facial skin—we have used certain techniques in order to minimize the role of emotions from our evaluation of images of the skin; these include expressionless faces, imaging of small areas of the face, using headbands to eliminate the contribution of hair and always trying to evaluate persons whom we are unfamiliar with. It is interesting to note that under such conditions, individuals are frequently unrecognizable as acquaintances. Thus by elimination of expressions and by focusing-in on the particular skin site of interest we succeed in minimizing the influence of the accompanying emotions in viewing the image and are able to assess skin benefits from the use of products. However, in this type of analysis, we may provide an accurate assessment of skin benefits but we miss the benefits to the overall picture—do these benefits actually contribute positively in improving the “appearance” of the person? It should be remembered that appearance is related to the emotions that a face or other skin site might elicit when viewed under a particular set of circumstances.

INTEGRATED IMAGING: MODE—WAVELENGTH

Integration

There exist several ways of imaging, e.g., reflectance imaging, the most familiar “picture taking” mode, polarization imaging with parallel or perpendicular polarizers, etc. One of the principal goals of imaging is to document consumer/patient

or physician perception of the skin under study. Different modes of imaging have been developed to enhance the assessment of the state of the skin because it is impossible to document physician assessment with a single image no matter how it is obtained, because the perception of the physician is not generated by a single view but by a series of images obtained by either moving the head or by moving the light source in order to minimize glare and to obtain a three-dimensional view of the lesion contour. Beyond the observation, the physician compares the images he/she obtains with the library of images in his/her mental library to arrive at a diagnostic judgment by the end of the observation period noting similarities and differences from his/her mental "average" for a recognized condition. It is clear that all this information may not be generated and contained within any one image. A number of imaging techniques have been developed to enhance selected features of the skin so that they may facilitate perception and evaluation of single features at a time and make it possible to integrate images obtained through different modalities to arrive at a more complete "picture"—assessment of the state of the skin. Integration of information obtained through different modes of imaging is thus necessary if we are to approach the objective perception of a professional or the visual emotional state elicited by a well-documented set of images in the mind of the consumer. Besides integration of images (reflectance and fluorescence) that may result in a better perception of the skin, there may be integration (in wavelength) that may lead to the relative contribution of the molecular absorbers and scatterers in the skin, which are responsible for the color appearance of the skin.

Integration of Imaging Modes

Imaging modes that document the state of the skin include reflectance and fluorescence modes. In reflectance mode, we can use illumination with visible light at an angle that simulates room illumination, i.e., from a slightly overhead direction. This directional lighting enhances largely horizontal surface features such as crow's feet wrinkles in the periorbital area and fine lines in the upper cheek area and under the eyes; it also gives the perceived appearance of dark circles under the eyes—"dark circles" tend to be minimized with head-on illumination. It also gives a good impression of the facial contours because of the shadows that are cast on the side of the face. In imaging faces, positioning of the face is important and allows improved evaluation of certain features; e.g., the three angles that have been used most frequently are head-on, and 45° on either side of the face. The head-on view allows (i) evaluation of shape and contours, (ii) perception of overall appearance and documentation of what a person sees for themselves in a mirror, (iii) evaluation of the features that are important in recognition—the eyes area, the mouth area, the overall beauty quotient of each face, i.e., ratios of different facial dimensions, (iv) evaluation of cheek and forehead pores, (v) evaluation of forehead furrows, and (vi) the distribution of hyperpigmented macules or freckles and redness on the face. The 45° views on either side of the face allow evaluation of skin attributes used in the assessment of aging and photodamage, i.e., (i) crow's feet wrinkles, (ii) fine lines under the eye and on the bony prominence under the eye, (iii) cheek skin texture including fine lines and wrinkles, (iv) freckles or hyperpigmented macules, (v) acne—inflammatory lesions as well as noninflammatory, (vi) pores, (vii) redness, (viii) overall skin color and sallowness, (ix) laxity, and (x) overall tone (uniformity of color). The 45° views are valuable in assessing acne although the distribution of acne lesions is concentrated in the center of the face.

Image Capture

In flash photography, we assume that the flash or set of flashes is the only source of light in the image because we can then control both the direction of the illumination and the intensity of the flash. Care must be exercised to record both direction and intensity in producing reproducible conditions. In normal room lighting conditions, the intensity of the flash is usually much higher than ambient lighting; if there is direct sunlight in the area of the image then reproducibility will become compromised. It is customary to record images with subdued room lighting and in a room that does not have windows. There are many references that discuss photographic lighting.

Image Viewing

Images may be viewed either in print form or on a computer monitor. It should be kept in mind that viewing is done under room lighting conditions; so for reproducible evaluation of images, the lighting will need to be well defined both in terms of its intensity and the color temperature of the source—different types of room lighting such as that produced by incandescent or fluorescent lamps may produce widely different color appearance of the images. Prints ideally should be viewed in special booths with well-prescribed lighting in order to avoid color shifts from time point to time point. Nowadays, with digital image capture, the predominant mode of image acquisition, most image viewing is conducted on computer monitors. Again, caution should be exercised in the selection of monitors because they may produce unwanted artifacts. It is important to know the uniformity of the illumination of the screen and ideally the screen should be color calibrated over its surface and from time to time to ensure reproducibility. Some monitors, especially liquid crystal display (LCD) screens, are sensitive to the direction in which they are viewed both in the horizontal and in the vertical direction; e.g., recently, we were able to reduce redness from the face on an LCD screen simply by standing up and viewing the same monitor! There are monitors that can be calibrated and screens that are not sensitive to the direction they are viewed—there are both personal preferences and technical preferences. In general, when a good monitor is used to evaluate images it is necessary to control the room lighting as well—ideally, room lighting should be at a minimum.

POLARIZED LIGHT IMAGING OF SKIN

Other reflectance images may use polarized light to selectively enhance either surface or subsurface features; surface features are enhanced with parallel polarized light and subsurface features are enhanced with cross polarized light because in this mode we minimize the surface glare and therefore the information from the surface of the skin.

An Introduction to the Physics of Polarized Light

Light is made up of photons, which are packets of electromagnetic waves. Each photon is characterized by its frequency or wavelength. Electromagnetic waves are transverse waves, i.e., the oscillations are perpendicular to the direction of propagation and are made up of an oscillating electric field and an oscillating magnetic field oscillating in mutually perpendicular planes (Fig. 4A). To minimize

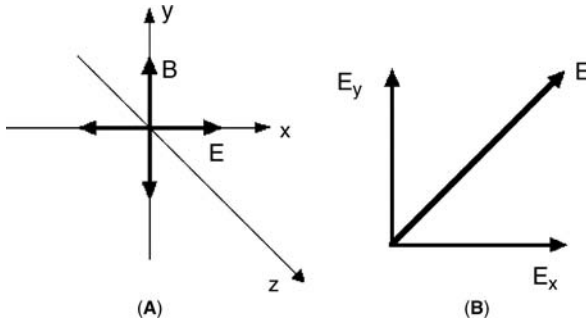


FIGURE 4 (A) A drawing of the oscillating electric and magnetic fields associated with an electromagnetic wave propagating along the z -axis. (B) An electric field is shown decomposed into two perpendicular directions (i.e., x and y). *Abbreviations:* B, magnetic field; E, electric field.

complexity, we can describe the waves in terms of only the electric field, keeping always in mind that there is an associated magnetic field. If we were to place ourselves in the direction of propagation of a photon then we can visualize the electric field oscillations either in a vertical or in a horizontal plane relative to the direction of travel.

In general, the electric field will oscillate in any direction (which is defined by the direction of oscillation of the charge that creates the electromagnetic wave) as long as the oscillations lie within a plane that is perpendicular to the direction of travel of the photon. We can describe the electric field of any photon in terms of two components—one that lies in the horizontal plane and one in the vertical plane (Fig. 4B). To distinguish these two directions of oscillation, we say that photons may be polarized in a vertical or a horizontal plane. This description accounts for linearly polarized photons (light), i.e., photons whose electric field oscillations are confined to a single plane. Photons may be circularly polarized or elliptically polarized—the latter being the most general case. In the case of circularly polarized photons, the electric field still oscillates in a plane that is perpendicular to the direction of travel; however, this plane rotates about the direction of travel. We shall confine our discussion here to linearly polarized waves—the results of our discussion will be equally valid for circularly and elliptically polarized light.

When a photon comes in contact with any material medium (shining light on a piece of glass), the oscillating electric field causes the electrons in the material to oscillate producing a reflected wave. Malus discovered in 1808 that if a beam of white light is incident on the polished surface of a plate of glass at an angle, e.g., 45° , the reflected beam is polarized. Although this light beam appears identical to the incident beam (in terms of its color), its polarization can be determined by reflecting it off a second polished glass surface. When the orientation of the second surface is parallel to the first, light will emerge from the second reflection; when the second glass surface is perpendicular to the first, very little light will emerge from the second reflection (Fig. 5). We may understand Malus's observations by realizing that when an oscillating electric field comes in contact with a material medium, it causes the electrons in the medium to oscillate. Surface electrons are more free and therefore the component of the electric field that is parallel to the surface induces motion of the electrons, causing the reflection of that

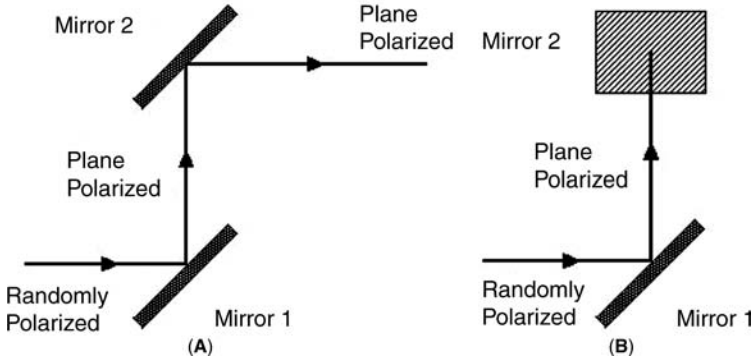


FIGURE 5 In diagram (A), randomly polarized light reflects off mirror 1 resulting in a linearly polarized beam. When this beam is reflected from a second mirror aligned parallel to the first one, a linear polarized beam emerges with the same polarization as after the first reflection. In diagram (B), randomly polarized light reflects off mirror 1 as in diagram (A), resulting in a linear polarized beam of light. When this linearly polarized beam is reflected from mirror 2, which is oriented in a perpendicular orientation to mirror 1, there is total attenuation of the light beam, no light emerges from the second reflection.

component. At a certain angle, the polarizing angle, 100% of the reflected light is linearly polarized. The value of the polarizing angle depends on the index of refraction of the material (plate of glass) and of the medium in which the material exists (air). The polarizing angle, also called Brewster's angle, is given by $\theta = \tan^{-1}[n_{\text{glass}}/n_{\text{air}}]$.

Light that is emitted by incandescent lamps, xenon flash, or fluorescent lamps is randomly polarized, i.e., the direction of oscillation of the electric field of the emitted photons are at random but always perpendicular to the direction of travel of the photons. A well-polished glass or metallic surface may be used to select photons of one direction of polarization. Lasers may produce light of a single polarization if the output windows are set at Brewster's angle. A beam of light produced by an incandescent lamp may be polarized by placing a linear polarizing filter in its path. The resulting beam will be linearly polarized and will have less than half the intensity of the original beam (Fig. 6).

When a second linear polarizing filter is placed in the path of a linearly polarized beam of light, then if the second polarizer is in the same orientation as the first, light will come through, linearly polarized and with reduced intensity. If on the other hand the second polarizer is oriented perpendicular to the orientation of the first one, then no light will come through the second polarizer (Fig. 6). We can thus select which polarization direction our detector measures. The component of light that is the easiest to eliminate is the surface reflection or the glare, which is easily accomplished with polarizing sunglasses. Let us consider the situation when light is reflected from the surface of water. The reflected beam is polarized to a great extent. Thus we can eliminate the surface glare by orienting a polarizing filter so that the photons reflected by the surface are filtered out. Eliminating the photons reflected by the surface of the water from the beam makes it impossible to "see" the surface of the water (there is no light coming to our eyes from the surface). The only photons arriving at our eyes then are those scattered by particles

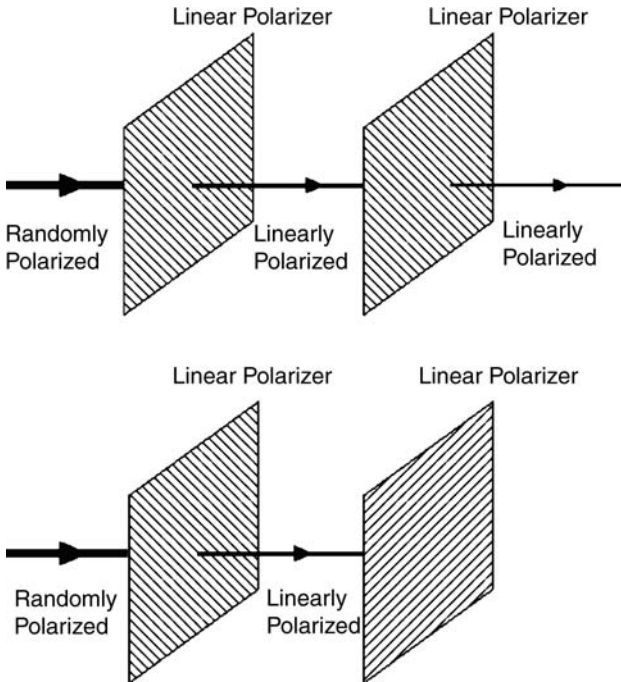


FIGURE 6 Light that is randomly polarized passes through a linear polarizer. The transmitted beam is reduced in intensity and is linearly polarized. If the polarized beam is incident on a second polarizer that is oriented with its polarization direction parallel to the first, light is transmitted, with further reduced intensity. If the linearly polarized beam is incident on a second linear polarizer that is oriented with its polarization direction perpendicular to the first polarizer, the beam is totally attenuated, no light is transmitted.

inside the water. We would thus be able to “see” the pool without the distraction of the surface glare and be able to see any reflecting or scattering object in the water, such as a swimmer.

The glare, or light that is reflected by the surface of any material object, is not color modified by the object because it has not interacted with absorbing chromophores in the material (it has not entered the material). It has therefore the same spectral composition (color) as the incident light. Thus the glare from any object has two characteristic properties: it is polarized (to a great extent) and it has the same color as the light source (usually white).

The Interaction of Polarized Light with the Skin

When polarized light is incident on the skin, it interacts with the stratum corneum exactly as it interacts with a plate of glass, i.e., the light that is reflected by the stratum corneum is polarized in the same direction as the polarization of the incident light. The reflected intensity by the stratum corneum is maximum when the angle of incidence is approximately 50° and the plane of oscillation of the electric field is parallel to the surface of the stratum corneum (Fig. 7) (the angle of incidence is the angle defined by the incident beam and the normal to the surface). The reflected

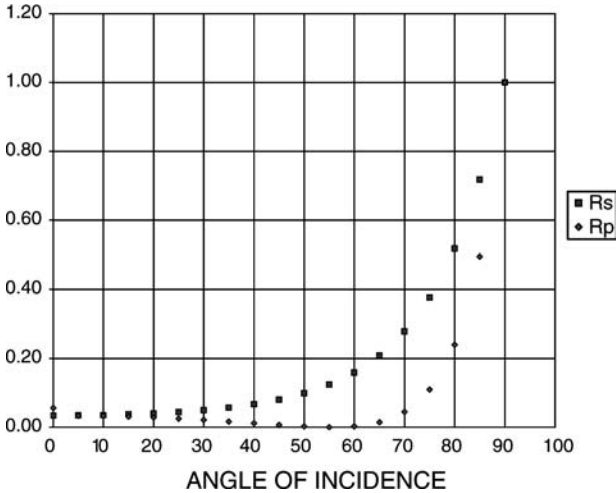


FIGURE 7 The reflectance of a linearly polarized beam of light depends on the angle of incidence and the direction of polarization. When the electric field oscillates in a plane perpendicular to the plane of incidence (a plane parallel to the surface it is incident on) (R_s), the reflectance increases as the angle of incidence increases. When the electric field oscillates in a plane perpendicular to the plane of the surface it is incident on (R_p), the reflectance first decreases to zero—all the light penetrates past the interface (at the polarizing angle or Brewster's angle) and then increases.

intensity of a collimated light beam at normal incidence to a polished surface with index of refraction equal to that of the stratum corneum is approximately 3%, while the reflected intensity of polarized light at an angle of incidence of 50° with the normal and with the electric field vector oscillating parallel to the surface of the medium is 15%. On the other hand, if the electric field is oscillating in the plane of incidence and the beam is at 50° to the normal then the reflected intensity approaches zero. Thus the surface reflection can be maximized or eliminated by careful selection of the polarization direction and the angle of incidence.

The component of the incident light that is not reflected by the stratum corneum–air interface enters the skin and is scattered in the dermis. As the collagen bundles in the dermis are randomly oriented, multiple scattering will cause the light to become randomly polarized. Thus the light that exits the skin after being scattered by the dermis is randomly polarized; i.e., all orientations of polarization are equally represented in the reflected beam. Thus there are two components of light that are reflected by the skin, one that maintains the orientation of polarization of the incident beam and another component that is randomly polarized. We can then select one or the other by placing a second polarizer in front of the camera lens (Fig. 6). When the polarizer in front of the camera lens has the same orientation as the orientation of the incident beam, the image recorded on film is that of the surface of the stratum corneum, because the lens polarizer selects one polarization (the light scattered by the dermis in this orientation has an intensity of at most 20% of that of the stratum corneum; therefore it does not interfere). Conversely, the reflection of the stratum corneum surface can be eliminated from the image by placing the camera polarizer in a direction perpendicular to the orientation of the light

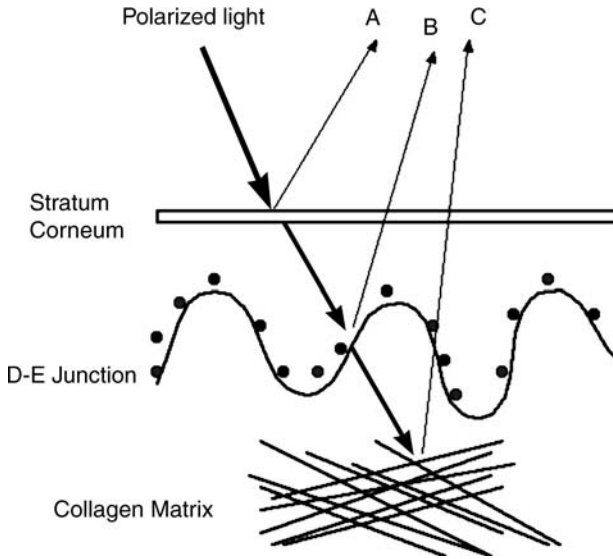


FIGURE 8 A schematic diagram of the interaction of linearly polarized light with the skin. (A) The beam that is reflected by the surface of the stratum corneum and it is polarized in the same direction as the incident beam; (B) partially depolarized because it has undergone a few scattering events; (C) randomly polarized because it has undergone many scattering events. Thus by setting a linear polarizer in front of the camera, we can select to view light that is polarized in the same direction as the incident beam or we can reject this component, which allows us to view light coming from structures that are deeper than the stratum corneum. *Abbreviation:* D-E, dermal-epidermal.

source polarizer. Now only the light that has been depolarized by multiple scattering in the dermis will be recorded (Fig. 8).

What Information May Be Gained in Imaging with Polarized Light?

In imaging with polarized light, we can selectively record surface or subsurface features that contribute to the appearance of the skin; this is demonstrated in Figure 8. Surface features may be viewed without interference by pigmented lesions and underlying erythema; thus the surface features may be evaluated without the disruption by the distribution and intensity of subsurface features. On the other hand, when the polarizers are perpendicular to each other, the surface features (such as scale, wrinkles, pore openings, etc.) are eliminated from the image, allowing the selective evaluation of pigment distribution and erythema. It has been demonstrated that polarized light imaging, with perpendicularly oriented polarizers, is more sensitive than standard flash photography. The visualization of distribution of erythema and extent of inflammatory lesions is much better realized in imaging with polarized light, so much so that retrospective evaluation of images yields results that have at least equal sensitivity with clinical assessment. Polarized light photography/imaging has been widely used in clinical settings and has been incorporated in commercial systems. In our hands, it has been used to record and evaluate ultraviolet reactions, the response of psoriatic lesions to treatment, the distribution of inflammation in acne, photodamaged skin,

and irritancy. Evaluations carried out with polarized light on black skin have shown the applicability of this method for the documentation of the distribution and intensity of erythema and pigmentation in darkly complexioned individuals as well.

Some Important Technical Details

The easiest way to obtain polarized light photographs is by placing a linear polarizer in front of the flash unit that is used for standard photography and a polarizer in front of the camera lens. These polarizers will, in general, affect both the amount of light that reaches the film and the color quality of the light. Because a linear polarizer eliminates all light that is not polarized in a specific orientation, at least 50% of the incident light from the flash unit will be attenuated and because a polarizer is also necessary on the camera, reflected light from the subject will also be attenuated. To obtain a good quality image, a lower f /stop will have to be used than before placement of polarizers, i.e., the aperture should to be opened by one f /stop; this results in diminution of depth of field. A way around the problem is to use a stronger flash unit or multiple flash units. When using multiple flash units, it is important to make sure that the polarizers in front of each are aligned in the same direction. One way to maintain the same depth of field (which is necessary for close-up photography) is to use film of higher speed (higher ISO number, greater than 100) or a digital camera with a sensitive detector (high ISO).

By placing a polarizer in front of the flash and the camera, we are making the implicit assumption that they do not color modify the images. What we need are polarizers that are equally absorbing at all the wavelengths of the visible spectrum. This is almost the case with the polarizers that are available either through companies that make optical filters (Hoya, Schott, etc.) or manufacturers of polarizers as Polaroid. Because the polarizer in front of the flash absorbs at least half of the emitted light by the flash, it may photodegrade with time. This is not the case with standard flash units used in photography. However, it is possible to degrade the polarizers when using intense light sources, and especially with lamps that stay on for the entire photo session. These polarizers will heat up and will start to deform. When this happens the polarizers start losing their ability to polarize light and therefore the conditions of illumination are changed in the images obtained. Fortunately polarizers are easy to test; first a quick inspection will show if they have deformed and secondly their ability to polarize light can be tested with an additional piece of polarizer. When the two pieces are held one after the other and a distant source of light is viewed through the combination, rotation of one relative to the other should result in essentially complete and uniform extinction of the light at a particular angle (Fig. 6). If this does not happen, the light source polarizer should be replaced with a new one and cooling of the light source or the polarizer may be desirable with a small fan. Lately a number of companies are manufacturing "wire polarizers;" these are made of a fine set of wires printed onto a substrate with the spacing of the wires smaller than the wavelength of visible light (i.e., 500 nm). These objects are essentially gratings partially coated with metal.

The flash unit is usually mounted on the camera body either on a hot shoe on top of the viewfinder or as a ring light around the lens. Both these arrangements will produce excellent images with perpendicularly oriented polarizers. Although the angle of incidence is small the reflected light by the surface of the skin demonstrates the qualities described and clearly evident. The surface reflection is much

better visualized when the polarized light is incident at larger angles (Fig. 7). The subsurface features are of similar intensity with any of the proposed arrangements of electronic flash units.

To obtain photographs with both orientations (the polarizers in parallel and perpendicular orientations to each other), one polarizer has to be able to be rotated with respect to the other. This is easily attainable with the linear polarizing filters sold in camera shops. The only modification is that a permanent mark has to be made indicating when the relative orientation of the filters is parallel or perpendicular. This again may be determined by placing the flash polarizer and the lens polarizer on top of each other and by viewing a distant source of light. When the transmission through the two polarizers is minimum (ideally zero), they are oriented perpendicular to each other. A problem that may occur with some ring flash units is when the polarizer is mounted in front of the ring flash, some light might reflect off the back surface of the polarizer into the lens; it is easy to know when this occurs because all the photographs will be seriously overexposed, because the photograph records a diffuse image of the flash. On flash units in which the flash intensity is adjusted by detecting the reflected intensity from the object, the detector has to be filtered by a polarizer as well to compensate for the lens polarizer.

FLUORESCENCE IMAGING OF THE SKIN WITH EXCITATION IN THE ULTRAVIOLET-A RADIATION OR THE BLUE

The fluorescence imaging modes generate images of skin features that are either difficult to see under visible light illumination or impossible to see because they do not absorb strongly or scatter visible light, although they do absorb enough to generate a detectable fluorescence signal. The wavelength bands used to excite skin fluorescence include long wavelength ultraviolet A (UVA) (360–380 nm) and blue light (400–420 nm) because these bands selectively excite structures/elements, i.e., collagen cross-links, elastin cross-links, horn, porphyrin, etc. (Table 1). It should be kept in mind that the fluorescence emission signal is much weaker than the reflectance signal (10 to 100 times weaker), requiring both a more intense light source for excitation and an enhanced sensitivity in the imaging system capture and subdued environmental lighting, because the fluorescence signal may be as weak or weaker than room lighting.

Fluorescence Excitation with UV Radiation

In fluorescence, there needs to be an excitation light (radiation) that induces the molecules to produce fluorescence emission at longer wavelength than the excitation; in this case, the UVA excitation source includes wavelengths in the long wavelength UVA (370–400 nm) and the emission wavelength band includes wavelengths 420–600 nm. Both the excitation band and the emission band are selected by placing appropriate filters in front of the light source and in front of the detector; in fluorescence, care must be taken that there is no overlap between the excitation and emission bands because typically the emission fluorescence signal is 10 to 100 times weaker than the excitation signal. In fluorescence (Fig. 9), the excitation radiation impinges on the stratum corneum where it may excite fluorescence of dry corneocytes; thoroughly dry corneocytes or scale, fluoresce rather strongly when excited with UVA radiation. The corneocytes that are well attached

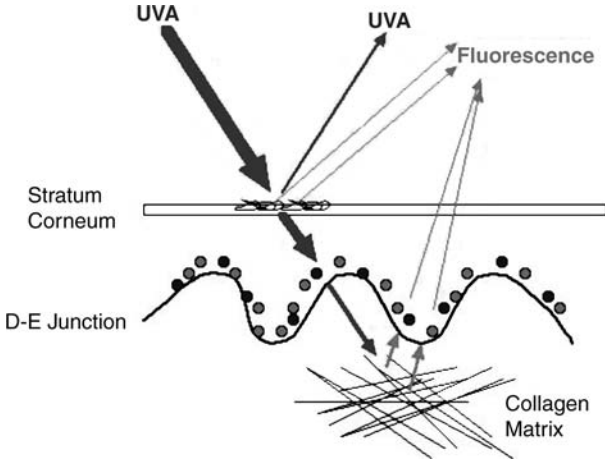


FIGURE 9 A beam of UVA radiation falls on the surface of the stratum corneum, some of this is reflected and the rest may induce dry corneocytes to fluoresce in the visible or enters the epidermis where it may be attenuated by melanin; the radiation that is not absorbed by melanin enters the dermis where it induces the collagen cross-links to fluoresce. The light emitted by the collagen cross-links is in the visible and is attenuated by the epidermal melanin before it exits the skin's surface and is detected. *Abbreviations:* UVA, ultraviolet A, D-E, dermal-epidermal.

to the rest of the stratum corneum and, as a consequence, are somewhat hydrated do not produce a fluorescence signal. The incident UVA radiation may then enter the stratum corneum, and from there the viable epidermis, producing little fluorescence signal in either; however, UVA radiation is attenuated in the epidermis by resident melanin pigment which has a stronger absorption in the UVA than in the visible—the absorbance of melanin at 370 nm is approximately five times stronger than that at 520 nm. UVA radiation then enters the dermis where it is absorbed by collagen cross-links and elastin cross-links and causes these molecular species to fluoresce. UVA radiation is attenuated in the superficial (papillary) dermis by hemoglobin resident in blood vessels, because it absorbs strongly in this wavelength range. Fluorescence is produced isotropically, i.e., with equal intensity in all directions, and the principal sources of native (endogenous) fluorescence due to UVA excitation are scale on the surface of the stratum corneum and collagen cross-links in the superficial dermis; the elastin cross-link fluorescence is considerably weaker than the signal due to collagen. The reflected UVA radiation from the skin together with the fluorescence signals is collected by the camera optics for recording. The reflected signal (the same wavelength band as the excitation) is eliminated by the emission filter in front of the detector (camera). These images are typically black and white because the fluorescence is viewed in the blue channel of a red, green, and blue (RGB) image; there are good reasons for doing this. First, the fluorescence signal is strongest in the blue and melanin absorption is stronger in the blue (the absorbance of melanin at 420 nm is approximately two times stronger than at 520 nm) than in the other two channels (green and red); so it is optimal for viewing pigmented macules and freckles in light-complexioned skin because it provides the highest contrast. The green channel image provides less contrast and the red channel includes a partially transmitted reflectance signal

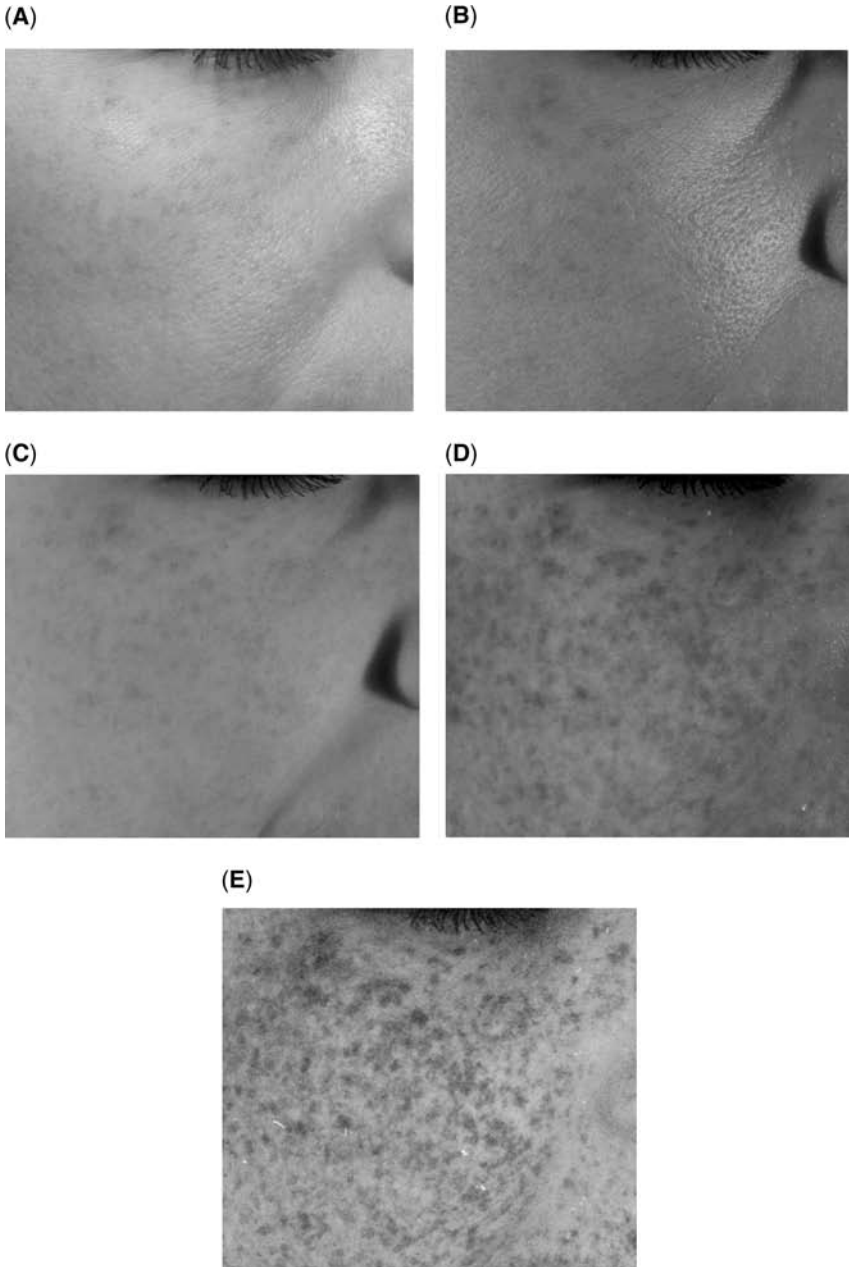


FIGURE 10 (Caption on facing page)

because of a secondary transmission band in the red by the usual UVA glass filters (Schott UG11 or Kodak 18A glass filters); the red reflectance signal becomes progressively more prominent as we go to darker-complexioned individuals.

In the UVA-induced fluorescence image of the face (Fig. 10), the bright background is due to the fluorescence of collagen cross-links. Variation in the intensity of the fluorescence can provide information on the density of cross-links as well as structures such as fine wrinkles that become more apparent as they also become more permanent. This image may be used to “see” and distinguish wrinkles and folds as they become permanently imprinted in the dermal matrix often before they become visually apparent/disturbing. Melanin pigmentation has been documented in these images, especially on Caucasian skin because the melanin absorption is larger both at the excitation and the emission wavelengths of the collagen fluorescence compared to the absorption of melanin in the visible (2 times in the emission wavelength and 5 times in the excitation, yielding and enhancement factor of 10 times). This has been used to document pigmented macules (flat pigmented lesions or “spots”) as well as diffuse hyperpigmentation as in melasma. Because the enhancement factor is so great, it has been used to document the intensity and distribution of epidermal pigment and it has been related to photodamage by making the assumption that pigmented macules on the face are strictly the result of multiple solar exposures. Macules that appear equally dark in these images might be due to erythematous (red) lesions of similar dimensions as the pigmented lesions (freckles). To distinguish between pigmented and erythematous macules, we need to place a cross-polarized image next to the UVA fluorescence image and compare the color and intensity of the lesions in the two. Because both pigmented and erythematous lesions in UV fluorescence images are usually characterized by a signal void (appearing totally dark in the images), it is difficult to assess how dark or intense the absorption is and for this reason they are not very useful in assessing the effectiveness of depigmenting agents because a small change in the intensity of the absorption by the pigment will still most likely produce a signal void.

This type of imaging has also been proposed to differentiate between epidermal and dermal pigmentation (Fig. 11). Epidermal pigmentation may be assessed by attenuation of the transmission of UVA to the dermis by the resident epidermal pigment and the attenuation of the collagen fluorescence by the epidermal pigment on its way to the camera. In the case of dermal pigmentation, UVA yields no enhancement factor or makes the lesion indistinguishable from background because neither the excitation radiation nor the emitted fluorescence is attenuated by the dermal pigment; the collagen cross-links that lie above the dermal pigment fluoresce upon excitation, thus “hiding” the underlying pigment. Because the epidermis–dermis interface is not perfectly flat, there may be cases of increased pigmentation in basal keratinocytes or very superficially within the dermis, which

FIGURE 10 (See color insert) (Figure on facing page) Five facial images obtained in rapid succession (in approximately five seconds); (A) is a visible light reflectance image with slightly overhead illumination, (B) is a reflectance image obtained with the light source (flash) and camera polarizers oriented parallel to each other, enhancing surface details, (C) is a reflectance image obtained with the light source and camera polarizers oriented perpendicular to each other enhancing subsurface details, (D) is a fluorescence image obtained with excitation in a band centered at 405 nm and emission longer than 450 nm where the surface features are absent and pigmentation is enhanced, as well as some porphyrins in the nasolabial fold, and (E) is a fluorescence gray scale image obtained with excitation centered at 380 nm and emission in the 400 to 470 nm range (blue) where surface features are absent (no scale) and pigment distribution is further enhanced; this last image is good for evaluating the distribution of pigment but not the concentration as the macules become essentially black. *Abbreviation:* UVA, ultraviolet A.

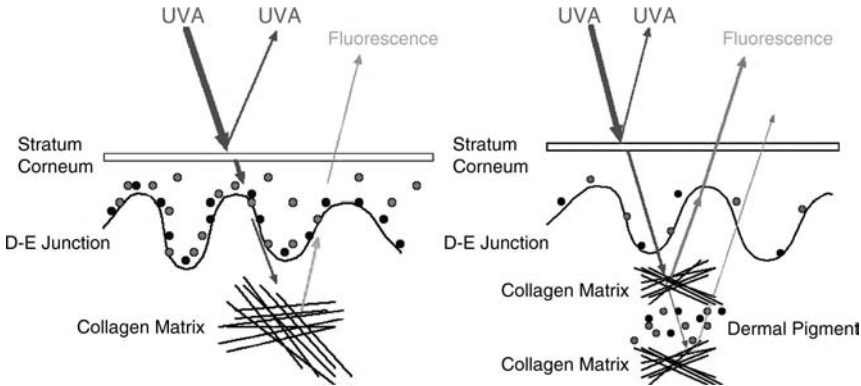


FIGURE 11 Examples of how the collagen cross-link fluorescence and the melanin absorption may be used to distinguish between epidermal and dermal pigmentation. Epidermal pigmentation is evident in a UVA fluorescence image by the loss of signal, appears dark just as it does in the visible image; dermal pigmentation in the UVA fluorescence image may be almost entirely hidden by the fluorescence of the overlying collagen, causing the pigmented lesion to essentially disappear—become not perceptible, in contrast to the visible image. *Abbreviations:* UVA, ultraviolet A; D-E, dermal-epidermal.

may yield confusing results; care is necessary in applying these rules in clinical practice. UVA fluorescence imaging is also very useful in documenting the application of UVA-absorbing or -fluorescing products, as well as in the evaluation of the persistence of such products with time.

Fluorescence Excitation with Blue Light

As above in fluorescence, there needs to be an excitation light (radiation) that induces the molecules to produce fluorescence emission at longer wavelengths than the excitation; in this case, the blue light excitation source includes wavelengths in the short wavelength range of the visible (400–420 nm) and the emission wavelength band includes wavelengths 440–650 nm. Both the excitation band and the emission band are selected by placing appropriate filters in front of the light source and in front of the detector; in blue light–induced fluorescence, care must be also taken to ensure that there is no overlap between the excitation and emission bands because, typically, the emission fluorescence signal is 10 to 100 times weaker than the excitation signal and, in this case, there are a number of molecular species that fluoresce in this band, with varying intensities. The blue excitation radiation (Fig. 12), impinges on the stratum corneum where it may excite fluorescence of porphyrins produced by resident bacteria such as *Propionibacterium acnes*. Porphyrins fluoresce in the red (coproporphyrin at 620 nm) and are localized in pores because the bacterium colonizes the sebaceous gland. Porphyrins may be frequently perceived together with horn; horn has the consistency of butter and is a mixture of keratinocyte ghosts that come from the lining of the sebaceous glands, sebaceous lipids, and sebocyte ghosts; the mixture also includes approximately 50% water. The incident blue light may then enter the stratum corneum and from there the viable epidermis, producing little fluorescence signal in either; however, blue light is attenuated in the epidermis by the resident melanin pigment, which has a stronger absorption in the blue than in the middle of the visible—the

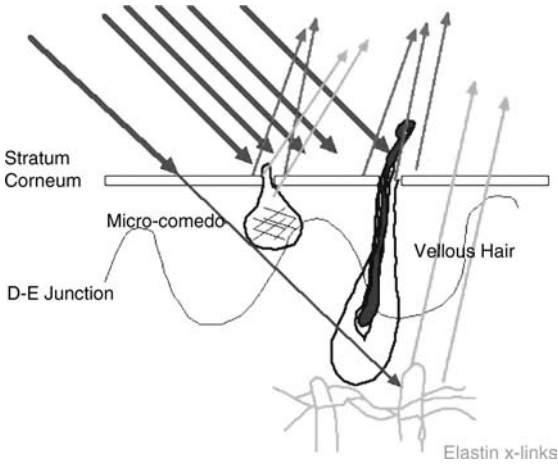


FIGURE 12 (See color insert) A beam of blue light (405 nm) is incident on the surface of the stratum corneum; there, it may interact with coproporphyrin, produced by *Propionibacterium acnes*, producing a red fluorescence signal, which, in images, has a punctate appearance around pores or microcomedones or hair follicles; the microcomedones may fluoresce in the visible with a broad emission (yellow appearance). Blue light that enters the skin is absorbed strongly by hemoglobin in the superficial dermis where it may also encounter elastin networks and stimulate fluorescence of elastin cross-links; this signal is fairly strong and may be documented even in darkly pigmented skin. *Abbreviation:* D-E, dermal-epidermal.

absorbance of melanin at 410 nm is approximately two times stronger than that at 520 nm. Blue light then enters the dermis where it is absorbed by elastin cross-links and collagen cross-links causing, these molecular species to fluoresce; in this spectral range the elastin cross-link signal is larger than the collagen cross-link signal. Blue light is also attenuated in the superficial (papillary) dermis by hemoglobin resident in blood vessels. Hemoglobin absorbs very strongly (!) in this wavelength range; because of the strength of the absorption, very fine vessels that run parallel to the skin's surface may be easily visualized under magnification (2–5X). Erythematous (red) lesions such as inflammatory acne or diffuse redness may be visualized as well and appear slightly red in the images, allowing, thus, discrimination from melanin pigmentation; it proves very helpful in viewing the blue fluorescence image of a face simultaneously with the cross-polarized image (side-by-side) to better determine the source of the dark-appearing regions in the blue fluorescence image. Blue light-induced fluorescence of faces (Fig. 10) is characterized by the overall green color of the image; this is primarily due to the excitation of elastin cross-links. These images appear green because they lack the blue channel—the excitation source lies in the range of the blue channel; thus the signal in the blue channel would represent the reflectance in the blue. Therefore, in blue fluorescence imaging, the blue channel information is filtered out in order to be able to detect the fluorescence emission, which is weak.

Thus there are a number of imaging modes, in reflectance and in fluorescence, where each may enhance the information obtained from the other. Each imaging mode adds information beyond what is obtained by the other and, in totality, they allow us to assemble a great deal of information that may be used to provide an accurate record of the professional and/or consumer perception of the skin status.

Some Important Technical Details

In choosing filters for excitation and emission, it is critically important that they do not overlap, i.e., that none of the excitation light is transmitted by the emission

filter, because as the excitation is in the visible, it will be recorded by the detector. Furthermore, the emission filter needs to be placed in such a way that no source light (white light) may arrive at the detector by going around the filter. More than 98% of the output of a typical flash needs to be attenuated by the excitation filter; therefore even a small leak of white light will be easily picked up by the detector. Because the filter absorbs a great deal of the excitation flash light output, it is not unusual for the filter to degrade with time, thus allowing light beyond the desired band to pass through it; this will tend to make the images brighter and progressively more yellow in appearance. The best practical way to make sure that the excitation and emission filters do not overlap is to hold them together and view a bright visible source—there should be no light coming through. The spectral characteristics of the filters may of course be evaluated with a spectrophotometer that has an adequately large sample compartment for the filters to go in one at a time; again care needs to be exercised in viewing the transmission curves of the filters to ensure that no light will make it through both of them. Finally, it should be kept in mind that the fluorescence images contain both fluorescence and absorption information and at times the two may overlap; therefore it is important to view fluorescence images in parallel with some visible image recorded at the same time as the fluorescence image.

WAVELENGTH INTEGRATION

We only briefly describe here this upcoming imaging technology; wavelength integration is also called spectral imaging or hyperspectral imaging. This technology has been used in mapping the earth's surface, in studying old manuscripts including the Dead Sea scrolls, and in microscopy. So far it has found limited use in skin documentation. In this imaging approach, a series of gray scale (black-and-white) images are obtained each at a different wavelength while the light source may be an extended white light source that might also be polarized to minimize surface reflections. Such a series of black-and-white images is called an image stack (Fig. 13). The number of wavelengths can be as small as two to five—to quantify concentrations of specific chromophores—or as high as several dozen—to obtain a detailed spectrum at each pixel. By obtaining a series of images at various wavelengths, one arrives at having a full reflectance spectrum for each pixel in the image corresponding to a skin site.

Reflectance spectra from the skin have been successfully analyzed for the concentration of the contributing absorbers in the skin site under investigation. One may thus think of spectral imaging as a way of obtaining an absorption spectrum at each pixel in an image—a job that is prohibitively time consuming with a single point measuring system. For example the equivalent of a 1000 x 1000 array of measuring elements in a one megapixel charge-coupled device (CCD) camera would otherwise require one million measurements of the reflection spectrum of each skin site within the image. The goal of this approach is to use the spectral features of the absorbers in order to separate each reflection spectrum into its molecular constituents to arrive at a concentration map for each absorber. Maps of oxyhemoglobin, deoxyhemoglobin, and melanin, as well as dermal scattering and extracellular water may be obtained in less than one minute and may be used to document the distribution of these important molecules in the skin and how they contribute to skin appearance. As these data are studied further, they

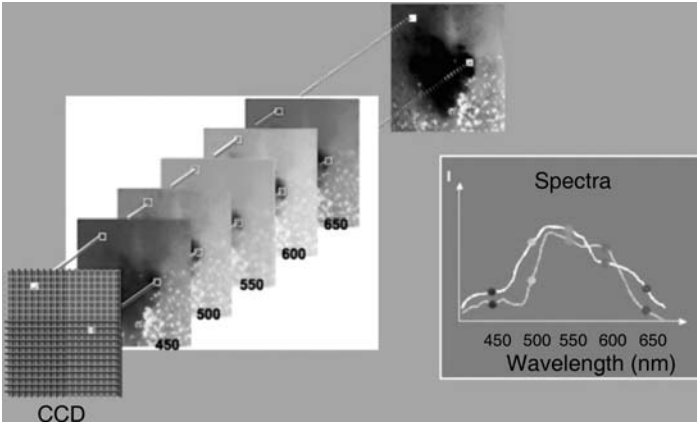


FIGURE 13 (See color insert) A schematic representation of spectral imaging. The tissue that is imaged is shown in the color image in the middle of the frame, a pigmented lesion. To the lower left is shown the CCD camera sensor followed by a stack of gray scale images at each of the wavelengths shown at the right lower corner of each frame. If we were to consider two pixels (picture elements) on the image and follow them through the image stack, we may obtain the spectral features of these locations on the image and the spectra identifying these are shown on the right of the frame and the information from each image plane is color coded for clarity. In principle, this method of imaging can separate out dyes that have very close color appearance even in cases of metamerism. To perform analysis, we would need to align the images obtained at each wavelength with respect to each other so that image details match as we go from one image to the next and then mathematical analysis (calculation of the contribution of each chromophore at each pixel) may be used to generate distribution maps of each chromophore in the image. *Abbreviation:* CCD, charge-coupled device. *Source:* Courtesy of Dr. R. Levinson, CRI Inc., MA, U.S.A.

may shed light on colocalization of absorbers and guide treatments following identification of vascular versus pigmented lesions or the evaluation of the contribution of each of the vascular compartments and/or the pigmented compartments to a skin lesion. This imaging approach allows the development of understanding of the molecular species that are responsible for the appearance of the skin not simply as in the Integration of Modes Analysis in terms of colors (Fig. 14).

Wavelength integration or spectral imaging has proved valuable in analyzing the persistence of inflammatory acne lesions, which clinically may be assessed by their redness. With spectral imaging, we obtain delineation of the lesions in oxyhemoglobin maps and of the edema involvement in each lesion by calculating the absorption of extracellular water. Spectral imaging has been used to document the extent and intensity of redness in chronically inflamed skin and its variation with season; similar studies have been conducted to document the colocalization of hemoglobin and melanin in what appears to be pigmented macules. This imaging modality is still in its infancy and will advance fast once cheaper and faster cameras become available and the minimum number of necessary filters that will yield all the required information have been identified. Finally, it should be mentioned that from a spectral image stack, the ordinary RGB image may also be reconstructed; i.e., this imaging modality has an overlap with mode integration.

In conclusion, image integration is essential in obtaining a precise assessment and documentation of the state of the skin and of the effects of treatments with

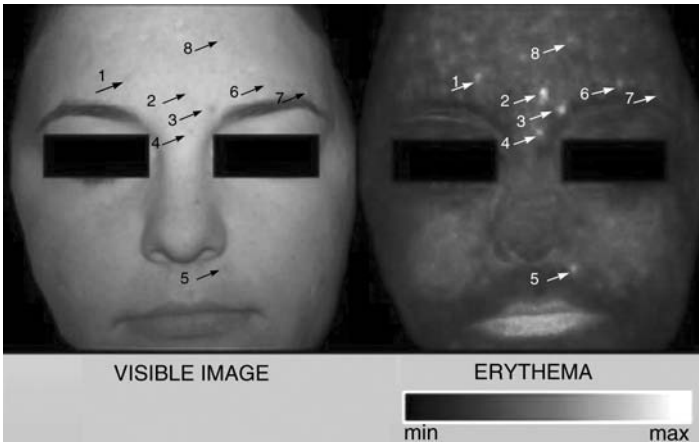


FIGURE 14 An example of image analysis to generate concentration and distribution maps of chromophores in the skin; in this particular example, the concentration and distribution of oxyhemoglobin is shown for a subject that has mild acne. It is interesting that in the oxyhemoglobin image, we can perceive both the inflammatory lesions and variations in concentration on the cheeks and the forehead, which are difficult to perceive in the visible red, green, and blue image on the left.

time. Two types of integration have been considered, which provide documentation of “color” bearing structures, where color means wavelength modification of the incident light at a resolution of 0.3 mm while recording images of the entire face. In these approaches, the magnification remains constant and is limited by the resolution of the camera (number/size of pixels) and the focal length of the lens. In mode integration, we considered reflectance and fluorescence imaging, the first to provide detailed documentation of visible structures and the second to investigate the distribution of chromophores that are either difficult to perceive in a visible image or simply do not have a distinct visible signature. In spectral imaging, we considered an approach to quantification and distribution of the molecules that are responsible for the color appearance of the skin. A third type of imaging, not considered here, involves obtaining information at an ever-increasing magnification and in depth beyond the surface of the skin. It is clear that here we could incorporate elements of the first two approaches to enhance the detailed information and new tools, e.g., confocal microscopy, video microscopy, two-photon microscopy, optical coherence tomography, Raman imaging, and others.

SUGGESTED READING

- Hecht E, Zajac A. Optics. Reading, MA: Addison-Wesley Pub. Co., 1979.
- Sinichkin YP, Kollias N, Zonios GI, Utz SR, Tuchin VV. Reflectance and fluorescence spectroscopy of human skin in vivo. In: Tuchin VV, ed. Handbook of Optical Biomedical Diagnostics. SPIE Press, 2002:725–786.
- Vetter JP. Biomedical Photography. Boston: Butterworth-Heinemann, 1992.

Combined Raman Spectroscopy and Confocal Microscopy

Peter J. Caspers and Gerwin J. Puppels

Department of General Surgery, Center for Optical Diagnostics and Therapy, Erasmus MC, and River Diagnostics B.V., Rotterdam, The Netherlands

Gerald W. Lucassen

Care & Health Applications, Philips Research, Eindhoven, The Netherlands

INTRODUCTION

A wide variety of imaging techniques has been developed to study the properties of the human skin. Many of these techniques are described in detail in section “Confocal Scanning Laser Microscopy.” A general characteristic of these imaging techniques is that they uncover the skin morphology. Variations in the physical properties of the tissue are detected and visualized as contrast in an image, revealing skin texture, layers, structures such as sweat ducts and hair follicles. At a higher magnification, cells and subcellular structures become visible. Spectroscopic techniques provide a window to the molecular properties of tissue. Rather than showing skin morphology, spectroscopic techniques reveal molecular composition, structure, and interactions within the tissue. The two modalities, skin imaging and skin spectroscopy, make a powerful combination. Together, they enable qualitative and quantitative assessment of molecular properties of various skin layers and structures, and add a morphological context to the molecular properties of the skin.

This chapter describes the combination of confocal scanning laser microscopy and confocal Raman microspectroscopy in a single instrument. Confocal images and confocal Raman spectra are acquired simultaneously, or with only a small delay between both modalities. Therefore, a Raman spectrum can be matched to a precise location in a confocal image. The combined technique is applied noninvasively, providing *in vivo* spectroscopic information about skin structures such as blood capillaries and sweat ducts, as well as detailed molecular concentration profiles of water and free amino acids in direct relation to the layered skin architecture.

RAMAN SPECTROSCOPY

Introduction to Raman Spectroscopy

Raman spectroscopy is a powerful nondestructive method to assess the molecular composition, molecular structure, and molecular interactions of matter. Many textbooks are available, in which the theoretical and experimental aspects of Raman spectroscopy are extensively described, including applications in biology (1,2). An introduction will be given in this chapter.

When the electric component of light interacts with matter, part of the light will be deflected from the direction of the incidence. This is called light scattering.

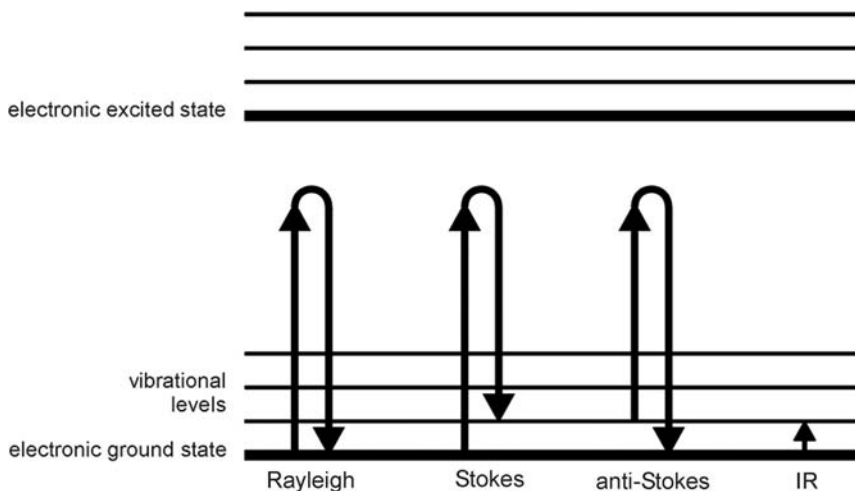


FIGURE 1 Energy level diagrams showing inelastic scattering (Rayleigh), elastic scattering (Stokes and anti-Stokes), and IR. *Abbreviation:* IR, infrared absorption.

The dominant type of light scattering is elastic or Rayleigh scattering, in which the scattered light has the same frequency as the incident light. The two other types of light scattering are inelastic, with a frequency different from the incident light. When the frequency or energy of the scattered photons has decreased, the process is called Stokes Raman scattering. An increased frequency is called anti-Stokes Raman scattering (Fig. 1).

In terms of classical mechanics, a molecule can be described as a harmonic oscillator that can store energy by increasing its internal vibrational motion. When two particles are connected by a spring and the spring is stretched and released, the particles start to oscillate. Adding vibrational energy will increase the amplitude of the oscillation. In analogy, a molecule can increase its vibrational motion by absorption, and decrease its vibrational motion by dissipation of electromagnetic energy. The laws of Quantum Mechanics state that the internal vibrations of a molecule possess discrete energies. Therefore, a molecule absorbs or dissipates energy in discrete units, as it changes from one vibrational state to another. In a Raman scattering event, a change in the vibrational energy of a molecule results in an equal shift of energy of the scattered photon. A decrease of vibrational motion of a molecule adds to the energy of the scattered photon, and shortens the wavelength. An increase of vibrational motion of a molecule is subtracted from the energy of the scattered photon, resulting in a longer wavelength. The exact shift in frequency is determined by the energy of the excited vibrational mode, which in turn depends on the atom masses and the type of chemical bonds between the atoms involved in the process. The energy may be influenced by molecular structure, interactions between molecules and the chemical microenvironment of groups of atoms involved in the vibration. Molecules generally have a great number of independent vibrational modes ($3N-6$ for a molecule consisting of N atoms), many of which can be excited by a Raman scattering event. This means that a molecule has a unique combination of vibrational levels and that its Raman spectrum is highly molecule specific. In addition, Raman scattering is a linear

process. The number of Raman scattered photons is directly proportional to the number of irradiated molecules. Hence, the intensity of a Raman band is proportional to the concentration of the respective compound, and can be used to quantify molecular concentrations in a sample.

The Indian physicists Raman and Krishnan first described the Raman scattering process in 1928 (3). Interest in the new phenomenon was great, and numerous publications devoted to the Raman effect appeared in the first decade after its discovery. Then, after a rapid initial growth, the popularity of Raman spectroscopy as an analytical method declined because of the technical hurdles that could not be solved with the technology of that time. The technique required an intense monochromatic light source to generate the Raman signals, which are generally extremely weak. Spectroscopists at the time used a mercury lamp and photographic paper. Exposure times were very long: hours or even days. Interest renewed after the invention of the laser in the 1960s. The invention sensitive detection equipment such as Fourier transform (FT) Raman spectroscopy and later of sensitive multichannel detectors further extended the applications to the field of biology. Recent developments in hardware and software by companies such as River Diagnostics (River Diagnostics, Rotterdam, The Netherlands) have further improved optical efficiency and speed of detection, which makes the technique ready for real-time *in vivo* application, including bioengineering of the human skin.

Raman Instrumentation

A Raman spectrometer essentially consists of a monochromatic light source, a sample stage, and a spectrometer. Upon irradiation of a sample, scattered light is collected in the sample stage and directed toward a spectrometer. In the spectrometer, the different frequency components are separated and recorded. The two types of Raman spectrometers that are in use today are FT and charge-coupled device (CCD)-based systems, also called dispersive or multichannel Raman systems. Raman signals are generally weak due to the low efficiency of the Raman scattering process. Therefore, efficient detection of the Raman signal is important, particularly for *in vivo* applications, when long signal collection times are generally not opportune. The first choice of instrument for most *in vivo* applications is CCD based. In a CCD-based spectrometer, the different wavelengths of the scattered light are dispersed by an optical grating and projected on a CCD detector. This is essentially a large array of detectors that enables recording of a complete Raman spectrum in a single exposure. The different frequency components of a Raman spectrum are recorded simultaneously on the pixels or "channels" of a CCD detector, hence the description "multichannel." The resulting detection efficiency is roughly two orders of magnitude better than that of the FT Raman systems initially used in Raman investigations of the skin (4).

In Vivo Confocal Raman Microspectroscopy of the Skin

Sufficient spatial resolution in the depth direction is a prerequisite for discriminating between the different skin layers and to study molecular variations within the stratum corneum (SC). Raman microspectroscopy exploits the principles of confocal microscopy to obtain spectra from specific regions in a sample. Laser light is focused on the sample with a microscope objective. A confocal pinhole in the detection patch rejects light from out-of-focus regions. The focus from which

scattered light is detected and the focus irradiated by the laser coincide, hence the name "confocal."

In vivo Raman microspectroscopy enables spatially resolved Raman measurements from the different layers of the skin and in particular, from different portions of the SC. A series of Raman spectra recorded at different distances from the skin surface provides a series of "snapshots" of the local molecular composition of the skin as a function of depth. This approach can be used to obtain in vivo molecular gradients or depth profiles of various molecular components across the SC, such as water, free amino acids, lipids, or topically applied substances (5–7).

CONFOCAL SCANNING LASER MICROSCOPY

Confocal scanning microscopy is a well-known technique for imaging of thin sections of the tissue without physically dissecting the tissue. Corcuff and Leveque have demonstrated confocal microscopy of the human skin in vivo, using a tandem-scanning microscope (8). Rajadhyaksha et al. have described a video-rate confocal scanning laser microscope (CSLM), which enables real-time confocal imaging of the human skin at subcellular level (9). CSLM uses a near-infrared laser that is focused in the skin using a microscope objective. The laser focus is scanned laterally in the confocal plane, which is located in the skin. The reflected light is focused with an avalanche photodiode. A confocal pinhole is inserted in the light path to reject light originating outside the focal plane, thus enabling optical sectioning of the tissue. The output signal of the photodiode is converted into a video signal that is displayed on a monitor in real time. With a frame grabber images can be captured from the video signal, digitized, and stored for later analysis. Chapter 11 gives a more detailed description of the same CSLM instrument that was used for the experiments in this chapter.

COMBINED RAMAN AND CSLM

Instrumentation

A combined Raman–CSLM system was built, composed of a confocal Raman microspectrometer dedicated to in vivo examination of the skin [in-house design (10)], and a modified CSLM type VivaScope 1000 (Lucid Inc., Rochester, New York, U.S.A.) (Fig. 2). The optical design of the CSLM was largely the same as described by Rajadhyaksha et al. (9). The main difference is that a piezo mechanical focusing drive (Physik Instrumente, Waldbronn, Germany) with 350 μm travel range and 60 nm resolution was used for accurate focal positioning of the microscope objective lens. Furthermore, custom developed software in LabviewTM was used to control the CSLM. This included control of the output power of the laser diode during automatic depth scanning, data acquisition, data storage, and advanced image processing.

The Raman system used a liquid nitrogen cooled CCD (Princeton Instruments, Trenton, New Jersey, U.S.A.) connected to an in-house design spectrometer with a spectral resolution of 6 cm^{-1} . The laser source was an argon-ion pumped titanium-sapphire laser (Spectra-Physics, Mountain View, California, U.S.A.) operating at either 850 or 720 nm. The laser was tuned to 850 nm for Raman experiments in the so-called "fingerprint region" (up to 2000 cm^{-1}). A 720 nm excitation was used for Raman experiments in the OH-stretch or "high wave number" region (2500–4000 cm^{-1}). The advantage of using different excitation wavelengths

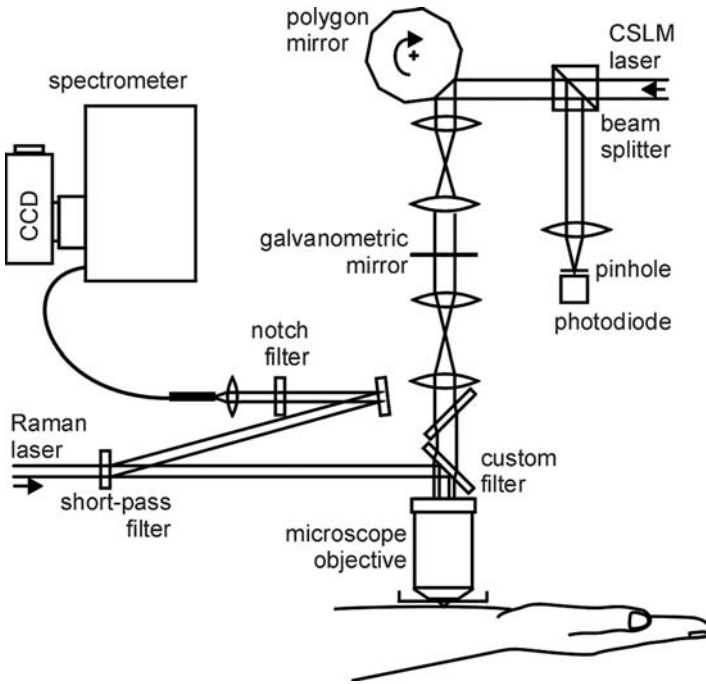


FIGURE 2 Schematic overview of the combined CSLM and confocal Raman spectrometer for in vivo study of the skin. Light from the Raman laser at 720 or 850 nm is reflected by the custom-designed coupling filter and focused in the skin with a 30x NA 0.9 water immersion microscope objective. Raman scattered light at wavelengths above 880 nm is reflected by the coupling filter and, after passing a laser rejection notch filter, focused onto an optical fiber using an $f = 149$ mm achromat. The output of the fiber connects to the spectrometer. Laser light from the CSLM, produced by an 830 nm diode laser, and the reflected light are transmitted by the coupling filter. A polygon and a galvanometric mirror are used to scan the laser focus across the focal plane. *Abbreviation:* CSLM, confocal scanning laser microscope. *Source:* From Ref. 10.

is that the detected Raman signal is between 880 and 1010 nm for both spectral regions. This enables a fixed grating position, which is intrinsically more stable than a moving grating. More importantly, the OH-stretch region is not truncated by the rapid decrease in quantum efficiency above 1000 nm, which is typical for silicon-based CCD detectors. Raman measurements and skin imaging used a single water immersion microscope objective (30x NA 0.90, Lomo, Vermont Optechs, Charlotte, Vermont, U.S.A.). The original sample stage of the VivaScope was slightly modified to incorporate a piezo focusing drive (Physik Instrumente, Waldbronn, Germany) and a coupling filter (Fig. 3).

The piezo drive enabled automated setting of the focusing depth in the skin. This feature was valuable for rapidly generating three-dimensional (3D) stacks of confocal images and acquisition of Raman depth profiles. The coupling filter (custom) was designed in such a way that the imaging laser beam from the CSLM (830 nm), the excitation laser from the Raman system (850 or 720 nm) and the Raman signals at wavelengths greater than 850 nm could all be combined using a single microscope objective. Figure 4 shows the filter characteristics: light at

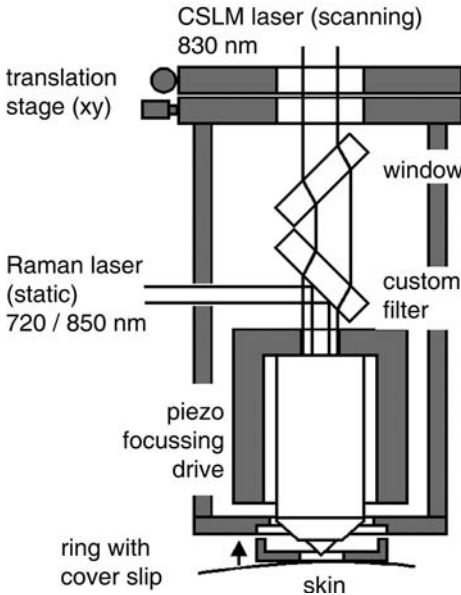


FIGURE 3 Detailed view of the modified measurement head with the optical coupling between the CSLM and the Raman system. Abbreviation: CSLM, confocal scanning laser microscope. Source: From Ref. 10.

830 nm is transmitted for confocal imaging, whereas light at 720 and 850 nm and above is reflected to enable Raman spectroscopic measurements.

Methods

The mode of operation was as follows. A target or skin region of interest was located using the normal real-time CSLM functionality of the system. Using the

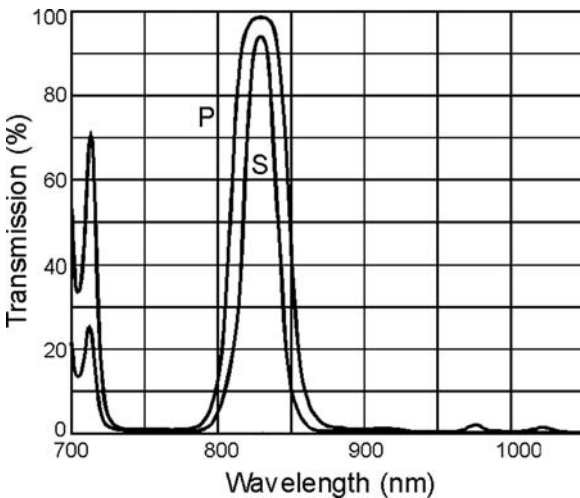


FIGURE 4 Transmission curve of the custom-designed coupling filter between the CSLM and the Raman spectrometer for parallel (P) and normal (S) polarization. Angle of incidence: 45°. Source: From Ref. 10.

static Raman excitation laser confocal Raman spectrum could be recorded from the center of the confocal plane at any time. The precise location of the Raman focus was indicated by a cross hair overlaid on the video image. By lateral and axial adjustment of the focal plane, any skin layer or structure that was visible in the confocal image could be brought into the Raman focus and a spectrum could be measured. In addition, the system could be focused automatically to a range of predefined depths in order to acquire stacks of images and to obtain automated depth profiles of both Raman measurements and confocal images.

Data Processing

Spectral data were processed using routines that were developed in-house using Matlab[®] (MathWorks, Natick, Massachusetts, U.S.A.). Spectral processing involved wave number and intensity calibration (11), integration of Raman bands, and spectral fitting. Water content was determined from the water to keratin ratio, which follows from the ratio between OH band of water around 3400 cm^{-1} , and the CH band of keratin around 2930 cm^{-1} . Natural moisturizing factor (NMF) content was determined semiquantitatively as an NMF to keratin ratio, using a least squares fit of the complete spectrum with a set of model spectra including the spectra of keratin and NMF. The NMF content was expressed as the ratio between the fit coefficients found for NMF and keratin. Details about the water content calculations and spectral fitting have been published elsewhere (7). Confocal images were processed using Alice (Hayden Image Processing) and Matlab in order to convert 3D stacks of grayscale images into two-dimensional cross-sectional images.

RESULTS

Water Distribution

The SC is an efficient barrier to water, potentially harmful agents, and microorganisms. It also plays an important cosmetic role. Both the barrier function and the perception of smooth and healthy skin are thought to critically depend on the appropriate water content in the SC. Water content is not an overall property of the SC, because the water content in the SC varies from approximately 20% (mass percent) at the surface to 70% near the stratum granulosum (SG). To study the local water content across the SC, a measurement technique is required that can quantify SC hydration with sufficient spatial resolution.

Raman measurements were performed on the palm of the hand of healthy volunteers. Measurements were performed using the OH-stretch spectral region ($2500\text{--}4000\text{ cm}^{-1}$) to determine the water content. Spectra were measured every $10\text{ }\mu\text{m}$, starting at the skin surface down to a depth of $270\text{ }\mu\text{m}$. This range covers the entire SC and part of the viable epidermis, because the SC on the palm is about 10 times thicker than the regular SC thickness on the rest of the body. Exposure time was one second per spectrum, which yields a total measurement time of about 30 seconds for a single depth profile. A 3D image stack was recorded directly before recording of the Raman profile. The size of the images was $250 \times 250\text{ }\mu\text{m}$ and the axial spacing was $1\text{ }\mu\text{m}$ and the frames rate was 14 frames per second. The complete stack of 300 images was recorded in about 22 seconds. In this way, a complete profile of Raman and CSLM recordings on the same part of the skin was carried out in less than a minute. An example is shown in Figure 5A, which is an *in vivo*

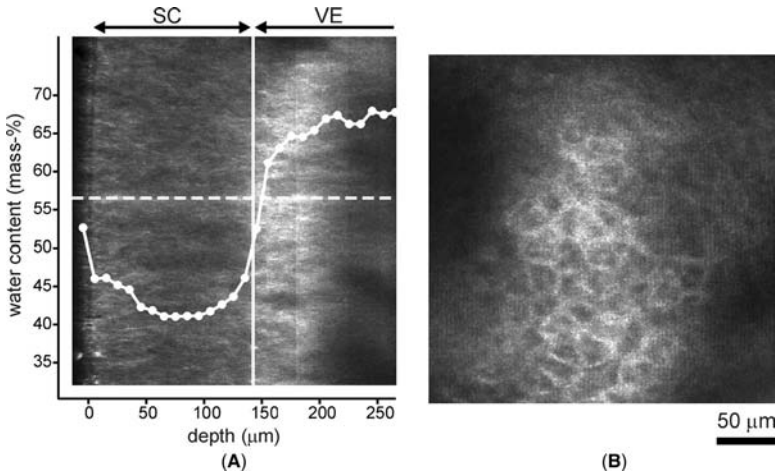


FIGURE 5 In vivo cross section and water concentration profile of the SC of the palm, based on combined CSLM and Raman measurements. **(A)** Cross section of the skin (xz -plane: SC, VE). Raman measurements were performed on the dashed line. The depth-axis is the distance to the skin surface and applies to both the image and the graph. The vertical-axis is the water concentration in mass percentage (gram water/100 g wet tissue). The solid line indicates the location of image **(B)**; **(B)** CSLM image (xy -plane) recorded at $145\ \mu\text{m}$ below the skin surface. *Abbreviations:* CSLM, confocal scanning laser microscope; SC, stratum corneum; VE, viable epidermis. *Source:* From Ref. 10.

cross-sectional image (xz -plane) of part of the upper epidermis on the palm of the hand. The overlaid curve shows the water concentration in mass percent (gram water/100 g tissue) derived from Raman measurements on the very same location. The axis on which the Raman measurements were done is indicated with a dashed line. The solid line demarcates the boundary between the SC and the SG, at a depth of $145\ \mu\text{m}$ below the skin surface. This boundary could be clearly distinguished in both the cross section (Fig. 5A), and the confocal images in the xy -plane. Figure 5B is a confocal image of the SC-SG boundary at $145\ \mu\text{m}$. The uppermost cells of the SG are easily recognized. In the cross section (Fig. 5A), the SG lights up as a bright band, caused by strong scattering from the keratohyalin granules.

In spite of the various techniques that have been developed to assess skin hydration, confocal Raman microspectroscopy is the only in vivo technique to date, capable of quantitative and spatially resolved determination of the local water content in the SC. The results from combined CSLM/Raman spectroscopy clearly show that the steep water gradient in palmar SC in vivo is not evenly distributed across the SC. The water content throughout most of the SC is relatively constant but rapidly changes around the SC/SG junction. This implies that the water barrier is not homogeneously distributed, but predominantly localized at the SC/SG junction.

NMF Distribution

For assessment of the NMF Raman measurements were performed on the palm of the hand using the fingerprint spectral region (below $2000\ \text{cm}^{-1}$). Spectra were measured every $10\ \mu\text{m}$, starting at the skin surface down to a depth of $170\ \mu\text{m}$.

Exposure time was 10 seconds per spectrum, totaling 180 seconds for the complete Raman profile. CSLM measurements were done directly before the start of the Raman profile. A complete profile of Raman and CSLM recordings on the same part of the skin was carried out in about 3.5 minutes. An example is shown in Figure 6A, which is an *in vivo* cross-sectional image (*xz*-plane) of part of the upper epidermis on the palm of the hand. The overlaid curve shows the content of the NMF, which was derived from the Raman measurements on the very same location.

The NMF content, which was the ratio between NMF and keratin (arbitrary units), has been normalized on the maximum value. The axis on which the Raman measurements were done is indicated with a dashed line. The solid line demarcates the boundary between the SC and the SG, at a depth of 135 μm below the skin surface. The SG/SC boundary could be clearly distinguished in both the cross section and the confocal images in the *xy*-plane. Figure 6B shows the confocal image of the SC–SG boundary at 135 μm below the skin surface.

Although skin hydration and the highly hygroscopic NMF must be closely related, the *in vivo* profiles of water (Fig. 5) and NMF (Fig. 6) are very different. However, these results are in agreement with the work by Rawlings et al. (12,13). NMF is a breakdown product from the proteolysis of the protein filaggrin. The process is controlled by hydrolytic enzymes, which are modulated by the water content in the tissue. Radio labeling and immunohistochemical studies in rats have shown that a high water content blocks filaggrin hydrolysis. In the *in vivo* situation, the high water content in the viable cells blocks the hydrolytic processes. Only when

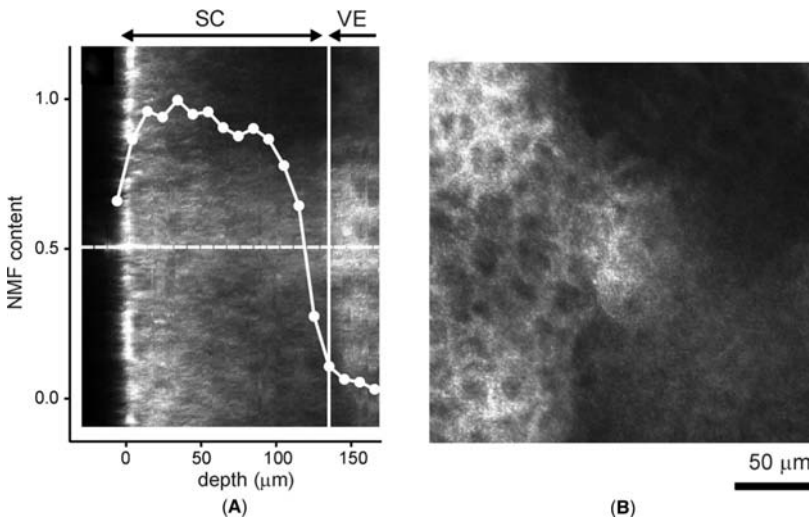


FIGURE 6 *In vivo* cross section and NMF profile of the SC of the palm, based on combined CSLM and Raman measurements. **(A)** Cross section of the skin (*xz*-plane: SC, VE). Raman measurements were performed on the dashed line. The depth-axis is the distance to the skin surface and applies to both the image and the graph. The vertical-axis is the relative amount of NMF, normalized on its maximum value. The solid line indicates the location of image **(B)**; **(B)** CSLM image (*xy*-plane) recorded at 135 μm below the skin surface. *Abbreviations:* NMF, natural moisturizing factor; CSLM, confocal scanning laser microscope; SC, stratum corneum; VE, viable epidermis. *Source:* From Ref. 10.

the water content has decreased in the deepest part of the SC, as shown by the water gradient in Figure 5, the hydrolytic enzymes are triggered and filaggrin is converted into the free amino acids that constitute the NMF (12). This is in agreement with Figure 6, in which NMF is absent from the SG and the in the deepest layers of the SC and a rapid increase of NMF is observed at a distance of about 10 μm from the SC/SG junction.

Targeting of Skin Structures

In vivo targeting of morphological structures is demonstrated by two examples. Figure 7 shows a CSLM image of the SC on the thenar at 30 μm below the skin surface. The bright area in the center is a sweat duct. Several Raman spectra were recorded in and around the sweat duct. The panel on the right shows a spectrum from the center of the sweat duct and a spectrum from the surrounding area. The large spectral differences reflect the difference in molecular composition between the two locations. Most prominent are the peaks at 856 cm^{-1} (*asterisk*) and 1002 cm^{-1} (*solid circle*). Based on difference spectra between spectrum (A) and (B) and spectral fitting the peaks were assigned to lactate (C) and urea (D). Clearly, measurements inside the sweat duct exhibit a higher lactate and urea signal than measurements in the surrounding area. This result demonstrates that information about the molecular composition of sweat can be obtained from a sweat duct in situ, which offers the possibility to study the effects of antiperspirants in situ in cosmetic research.

Another example of in vivo Raman spectroscopy of morphological structures is demonstrated in Figure 8. Capillary loops can easily be identified with video-rate CSLM, with erythrocytes showing as moving bright dots. The combined CSLM/Raman system was used to identify capillary loops and obtain high quality

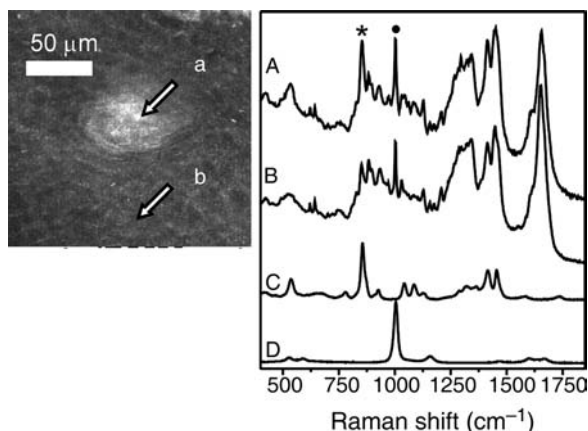


FIGURE 7 In vivo CSLM image and Raman spectra of a sweat duct on the palm of the hand, 30 μm below the skin surface. The bright area is the sweat duct. The arrows (*left*) mark the spots from which the Raman spectra were obtained. The asterisk marks the lactate peak at 856 cm^{-1} . The solid circle marks the urea peak at 1002 cm^{-1} . (A) Raman spectrum measured in the sweat duct. (B) Raman spectrum measured outside the sweat duct. (C) Raman spectrum of lactate. (D) Raman spectrum of urea. *Abbreviation:* CSLM, confocal scanning laser microscope. *Source:* From Ref. 10.

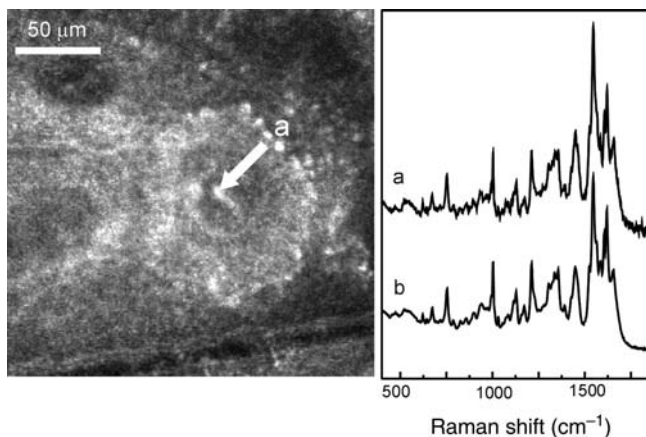


FIGURE 8 In vivo CSLM image and Raman spectrum of blood, measured in a dermal capillary in the skin of the lower forearm at 60 μm below the skin surface. The arrow indicates the location from which the Raman spectrum was obtained. **(A)** In vivo Raman spectrum of blood. Signal integration time: 30 seconds. **(B)** In vitro Raman spectrum of blood. *Abbreviation:* CSLM, confocal scanning laser microscope. *Source:* From Ref. 10.

Raman spectra of circulating blood inside. Figure 8 shows an in vivo spectrum of blood inside a capillary, and for comparison, an in vitro spectrum of blood measured in a fused silica capillary. The collection time was only 30 seconds, demonstrating that high quality Raman spectra of blood can be rapidly measured noninvasively. This opens many possibilities for noninvasive analysis of blood and blood analytes.

DISCUSSION AND CONCLUSIONS

Raman spectroscopy combined with an imaging technique is a powerful tool to investigate the human skin in vivo, which was demonstrated by a combination of confocal Raman spectroscopy and confocal scanning laser microscopy. The detailed in vivo concentration profiles of water and NMF in relation to the skin morphology provide new possibilities to investigate the barrier and water holding properties of the SC. This is relevant for the cosmetic industry (e.g., moisturization) and pharmaceutical industry (e.g., transdermal drug delivery) and for better understanding of barrier-related problems and the effects of treatment (e.g., dry skin, psoriasis). Precise targeting of morphological structures for spectroscopic investigation offers numerous possibilities from fundamental to applied study of the skin.

The instrumentation described in this chapter was a prototype, designed to demonstrate the feasibility of in vivo confocal Raman spectroscopy and confocal scanning laser microscopy combined in a single instrument. The Raman microspectrometer was built in-house, and not commercially available. The technique and the availability have progressed since then. River Diagnostics (Rotterdam, The Netherlands) has developed the first commercial confocal Raman system for in vivo skin applications. A new optical and mechanical design and dedicated software deliver increased sensitivity, ease-of-use and speed, in comparison to the Raman system

that was described in this chapter. At present, *in vivo* confocal Raman spectroscopy is being used in cosmetology on a moderate scale. It is to be expected that applications in cosmetology will increase and that the technique will find application in fundamental and clinical dermatology and pharmacy, in particular when combined with an *in vivo* imaging technique such as CSLM.

REFERENCES

1. Koningstein JA. Introduction to the Theory of the Raman Effect. Dordrecht: D. Reidel Publishing Company, 1971.
2. Tu AT. Raman Spectroscopy in Biology. New York: John Wiley & Sons, 1982.
3. Raman CV, Krishnan KS. A new type of secondary radiation. *Nature* 1928; 121:501–502.
4. Barry BW, Edwards HGM, Williams AC. Fourier transform Raman and infrared vibrational study of human skin: assignment of spectral bands. *J Raman Spectrosc* 1992; 23:641–645.
5. Caspers PJ, Lucassen GW, Wolthuis R, Bruining HA, Puppels GJ. *In vitro* and *in vivo* Raman spectroscopy of human skin. *Biospectroscopy* 1998; 4:S31–S39.
6. Caspers PJ, Lucassen GW, Bruining HA, Puppels GJ. Automated depth-scanning confocal Raman microspectrometer for rapid *in vivo* determination of water concentration profiles in human skin. *J Raman Spectrosc* 2000; 31:813–818.
7. Caspers PJ, Lucassen GW, Carter EA, Bruining HA, Puppels GJ. *In vivo* confocal Raman microspectroscopy of the skin: noninvasive determination of molecular concentration profiles. *J Invest Dermatol* 2001; 116:434–442.
8. Corcuff P, Leveque JL. *In vivo* vision of the human skin with the tandem scanning microscope. *Dermatology* 1993; 186:50–54.
9. Rajadhyaksha M, Grossman M, Esterowitz D, Webb RH, Anderson RR. *In vivo* confocal scanning laser microscopy of human skin: melanin provides strong contrast. *J Invest Dermatol* 1995; 104(6):946–952.
10. Caspers PJ, Lucassen GW, Puppels GJ. Combined *in vivo* confocal Raman spectroscopy and confocal microscopy of human skin. *Biophys J* 2003; 85:572–580.
11. Wolthuis R, Bakker Schut TC, Caspers PJ, et al. Raman spectroscopic methods for *in vitro* and *in vivo* tissue characterization. In: Mason W, ed. *Fluorescent and Luminescent Probes for Biological Activity*. London: Academic Press, 1999:433–455.
12. Scott IR, Harding CR. Filaggrin breakdown to water binding compounds during development of the rat stratum corneum is controlled by the water activity of the environment. *Dev Biol* 1986; 115:84–92.
13. Rawlings AV, Scott IR, Harding CR, Bowser PA. Stratum corneum moisturization at the molecular level. *J Invest Dermatol* 1994; 103:731–741.

Friedrich A. Bahmer*Department of Dermatology, Central Hospital, Bremen, Germany***INTRODUCTION**

In dermatology, the size and the form of skin lesions is an important part of any description of skin disease. However, size is rarely measured and the complexity of a lesion usually is not quantified, e.g., using something like a form factor. Instead, lesions are compared to daily used items such as coins, fruits, and plant seeds. A paper with pictures of commonly used items together with their approximate size, published more than 100 years ago, proves that the problem of quantifying skin lesions is quite old (1).

Even more irritating is the fact that very often essentially two-dimensional (2-D) skin lesions such as nevi or melanomas are compared to three-dimensional (3-D) botanical objects. Statements like "nevus of the size of a peanut" are not uncommon. Apart from the fact that it does not make sense to compare 3-D to 2-D objects, there are very few persons able to state the diameter or the volume of a peanut spontaneously. To make things worse, there are considerable volume differences in most items of botanical origin, making comparisons even more vague (2).

During the past century or so, a solid body of methods has been developed in the field of morphometry (2-4). These methods allow one to solve the problem of easy and simple quantification both in clinical and experimental dermatology without costly equipment. Because in many parts of the world image analysis systems are not available, the importance of "classical" morphometry and stereology cannot be overemphasized. For dermatological purposes, however, these methods have been adopted only recently (5).

Very often, the terms "morphometry" and "stereology" are used synonymously. In the context of this paper, "morphometry" denotes the methods used to obtain quantitative data of morphological structures. The term "stereology" is used according to the definition: "a body of mathematical methods, relating 3-D parameters defining the structure to 2-D measurements obtainable on sections of the structure (2)." Thus, stereology consists mainly of mathematical and statistical methods, based on stochastic geometry, which allow us to extrapolate from 2-D into 3-D.

It should be mentioned at the very beginning that stereology is not synonymous with image analysis, being automatic or semiautomatic. The data necessary to calculate stereological parameters might be obtained by image analysis or by the use of test systems ("grids"). In fact, the strength and beauty of morphometric 2-D (and stereological 3-D) methods lies in their simplicity and ease of use. The 2-D methods are advantageous, because they usually do not require intermediate steps to be taken, such as outlining the contour of an object on transparent paper. The following pages contain some basic knowledge on morphometry, as well as some applications of morphometric methods in clinical and experimental dermatology

with emphasis on quantification of 2-D structures. For the interested reader, some extensions of these methods into 3-D are given.

MORPHOMETRY: PRINCIPLES AND APPLICATIONS IN 2-D

Area

For a number of geometric figures such as squares, circles, and ellipses, equations exist which allow calculation of their area on the basis of few length parameters and π , respectively. No such equations exist for irregularly shaped areas, making area determination somewhat tedious.

A simple solution for area determination is to fill it with squares of known area a . Then, the total area equals the sum of the squares (Fig. 1). The precision of this estimation method obviously depends on (i) the complexity of the figure, and (ii) on the size of the squares used: the smaller the squares, the more precise the estimation. This principle is used in automatic image analyzers with very small squares in the form of pixels (picture elements), counted at computer speed.

For clinical purposes, however, computer analysis of areas is not suitable, because an intermediate step is required with the boundaries outlined on a transparent foil, which in turn has to be subjected to the image analyzing process.

Remarkably, instead of using tiny pixels, a comparatively coarse grid might be employed. Here, the crossovers of the grid lines are regarded as representative of one square (Fig. 1). Then, only the crossover-points within the area have to be counted. The area can be calculated then by the simple equation:

$$A_{\text{str}} = \sum P \cdot a \quad (1)$$

where A_{str} denotes the area of the structure, $\sum P$ the number of points counted, and a the area associated with one point (in the case of a square lattice grid, $a = d^2$ with d = distance of the grid lines) (Fig. 1).

Besides the complexity of the structure, the precision depends on the characteristics of the test system ("grid"). Because the figures encountered on the skin

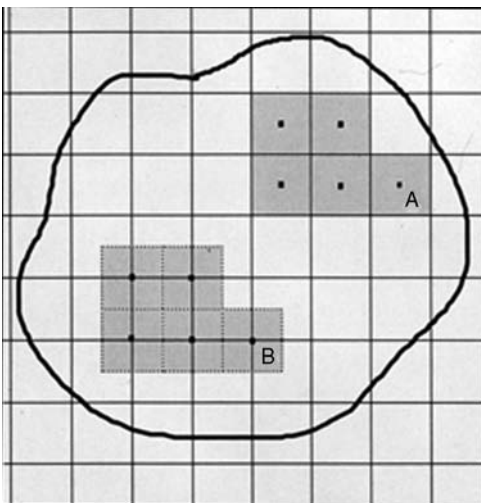


FIGURE 1 Principle of point counting. Instead of counting the squares contained in the figure (A), the crossover-points are counted (B), because they can be regarded as representatives of the squares.

usually are quite simple, the number of points necessary for a rather high precision is surprisingly low (2). Very often, the accuracy of an image analyzer is considered to be superior to ordinary point counting. However, it should not be forgotten that the precision of the estimation method by pixel counting depends on the precision with which the boundaries of an area are brought into the machine. Because the accuracy of tracing the boundaries of the area of interest, e.g., of a leg ulcer, is rather low, the overall precision cannot particularly be high. This in turn is due to the fact that it is rather difficult to trace such boundaries exactly by a pen on a digitizing tablet, or by a cursor on a computer screen.

Studies have shown convincingly that the precision of the point counting procedure is rather fair, combined with a comparatively low workload at a fraction of the costs compared with those of an image analyzing system (2,6). Furthermore, a high precision is not necessary for most purposes. If the area of, e.g., a leg ulcer has to be determined during the course of the treatment, an estimation with a precision of $\sim 1 \text{ cm}^2$ usually suffices. This precision might be accomplished with a rather coarse grid with about 10 points counted on the ulcer.

It is possible to estimate the precision of point counting by calculus (2). For ease of use, nomograms have been published which allow reading of the number of points necessary at a given error level (2,7). More theoretical considerations concerning the precision of point counting are also available (8,9).

The grids used for point counting in a clinical setting can easily be drawn by use of a spreadsheet calculation program and printed with a laser printer. From these printouts, copies are made with any photocopier on transparent foil. It is clear that the original drawing might be enlarged or downsized to obtain the desired grid characteristic.

Applications

One object of clinical size determination are nevi, because the rate of malignant transformation of congenital nevi seems to be related to the size of the lesion. To get valuable data on whether the development of malignancy is related to the size of the nevi, their area should be determined accurately. Area determination by the use of such a grid is very easy with a grid, which can be carried in the pocket, even during daily work, despite the fact that these nevi are very often irregularly shaped (10). If area determination is performed in this way, there is no need to classify nevi according to their maximum diameters. If large body areas are covered by the nevus, the fraction of the whole body surface might be estimated on photos from the upper and lower parts of the body, taken from the front and back (see below).

In scientific studies, the size of *malignant melanomas* might be of interest (Fig. 2). Especially in studies requiring exact documentation of clinical features, estimation of the area of the melanoma is necessary (10). This in turn would allow one to calculate the average thickness of the tumor. As outlined below, it is possible to calculate the total volume of the lesion by the principle of Cavalieri (see below), however.

As already mentioned, area determination by point counting is very simple. For the determination of the area of *leg ulcers*, we use a double square-lattice grid with coarse lines 2 cm apart, and fine lines 1 cm apart (Fig. 3). If the size of small- to medium-sized ulcers has to be determined, all crossover-points of both the coarse and the fine lines are counted and simply multiplied by 1 cm^2 . On large ulcers, only the coarse points are counted and multiplied by 4 cm^2 , because one

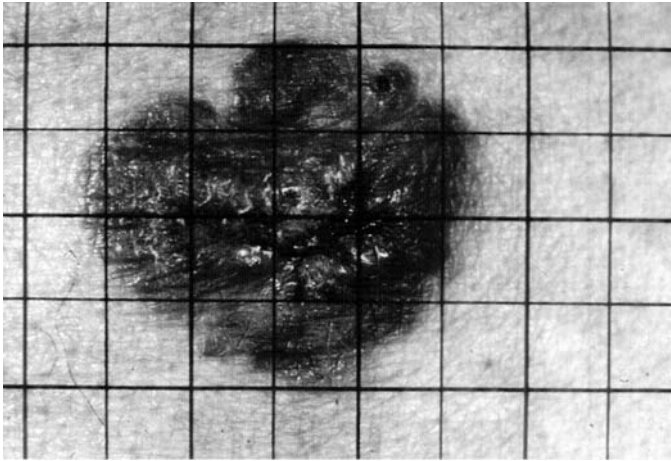


FIGURE 2 Malignant melanoma with a square lattice grid superimposed. Originally, the grid lines are $d=0.5$ cm apart. Thus, one point of the grid represents 0.25 cm². Total area of the melanoma is 14×0.25 cm² = 3.5 cm².

coarse crossover-point represents 2 cm \times 2 cm = 4 cm². Because leg ulcers are very often infected, the ulcer is covered with a piece of the very thin transparent wrap foil used in the household before the counting grid is applied, to avoid contamination.

To evaluate the efficacy of antihistamines, *prick-* or *intracutaneous tests* are used, usually in comparison to the reaction to a diluted histamine solution. The change in the size of the wheal and flare reactions is used as variable. Usually, the diameter of the wheal in two opposite directions a and b is measured, and the "mean diameter" is calculated by dividing the sum of a and b by 2. Unfortunately, the wheal and flare reactions are not always as regular as in Figure 4. Because the erythema and the wheal are of a different size, it could be wise to use a double lattice grid to assess both areas simultaneously (11).

The same principle is applicable for the estimation of *lymphocyte* and *macrophage migration area* (12), as well as for the thallus area in dermatophyte cultures (12a). Here, the areas to be measured are rather small. Thus, an appropriate small grid is used under a stereomicroscope or under a good enlarging lens. The making of such a grid is very easy, just by contact copying the negative with the grid onto high contrast film.

Area Fraction

Because the eye is notoriously poor as an estimator of area fractions (13), methods are needed which accomplish this task in a variety of settings. Point counting allows one to estimate not only areas, but also area fractions.

Geologists always had the problem of determining how many different minerals constituted a rock without the possibility of physically separating these minerals from one another. Within the last 150 years, it has been demonstrated various times that the points hitting an area contained in another area corresponds to the ratio of the points falling on these two areas.



FIGURE 3 Leg ulcer with superimposed double square lattice grid. There are five points of the coarse grid (each representing 9 cm^2 originally), and 42 points of the fine grid lines (each representing 1 cm^2 originally). Thus, ulcer area estimation by the rapid but “coarse” procedure is 45 cm^2 , by the “fine” procedure is 42 cm^2 .

In a formalized manner and in stereological notation:

$$\frac{A_{\text{str}}}{A_{\text{ref}}} = \frac{P_{\text{str}}}{P_{\text{ref}}} \quad (2)$$

where A_{ref} is the reference area, A_{str} the area contained in the reference area, P_{ref} number of points on the reference area, and P_{str} the number of points on the area contained in the latter.

Applications of Area Fraction Determination

In the example of the prick test reaction, the number of points on the wheal divided by the number of points on the whole reaction (wheal and flare), equals the area fraction of the wheal. In a variety of clinical settings, the area fraction of a large lesion or multiple smaller lesions is of interest. If photographs of the body

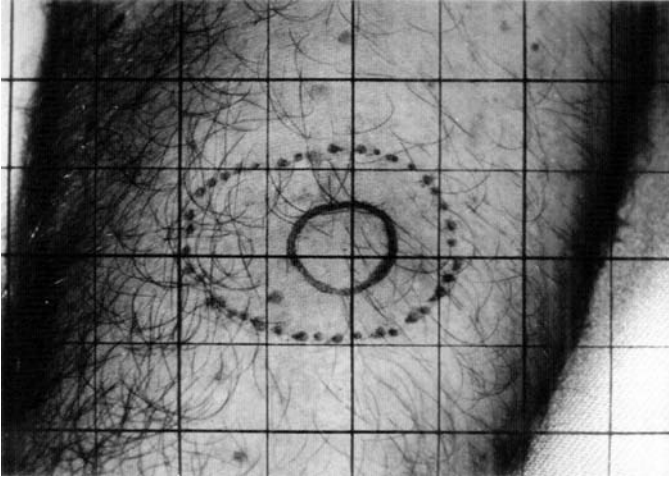


FIGURE 4 Wheal and flare reaction (boundaries outlined for better visibility) with superimposed square lattice grid. Originally, one crossover-point represents 1 cm^2 , because the grid lines are 1 cm apart. Thus, wheal area is 1 cm^2 (1 point), erythematous flare area 4 cm^2 (4 points).

are taken, the fraction of the lesions on the body surface can be estimated by point counting. To facilitate evaluation and comparisons, the photos should be taken in a standardized manner (upper half body front and back, lower half body front, and back, separated by a line, e.g., in the height of the iliac crest). The exact magnification does not need to be known, because area fractions and not absolute areas are determined (Fig. 5). We have proposed to determine the extent of skin lesions in atopic dermatitis by the use of body schemes, with the lesions outlined by different colors (14). Because this intermediate step is liable to subjective assessment, it is better to determine the area fraction using projected slides (unpublished results).

Sebum excretion can be determined using the *Sebutape*[®]. On this tape, sebum excreted by follicle orifices is made visible as transparent spots, which appear black on a black background. For quantification, a semiquantitative approach is used by comparing the sebum spots to reference patterns supplied by the manufacturer. This method lacks accuracy, because the spots differ considerably in size and are of rather irregular form (Fig. 6). Sometimes, the spots even show confluence.

Semiautomatic (interactive) morphometry by tracing the outlines of the spots for measurement allows a fairly exact quantification (15). However, this method is rather time consuming and has thus not gained wide acceptance. If a simple grid is used together with a magnifying lens or a stereomicroscope, quantification is a matter of minutes (Fig. 6). The number of grid points on the spots, divided by the total number of points on the grid, yields an estimate of the area fraction the sebum spots occupy (16).

The average spot size, corresponding somewhat to the follicle orifices, can be estimated conveniently by counting the number of spots contained within the inner frame. To obtain the unbiased number of spots, the rule of the "forbidden lines" has to be respected. This means that only those spots are counted which are within the inner frame provided that they are not intersected by the full-drawn ("forbidden") lines on two sides of the frame (17).

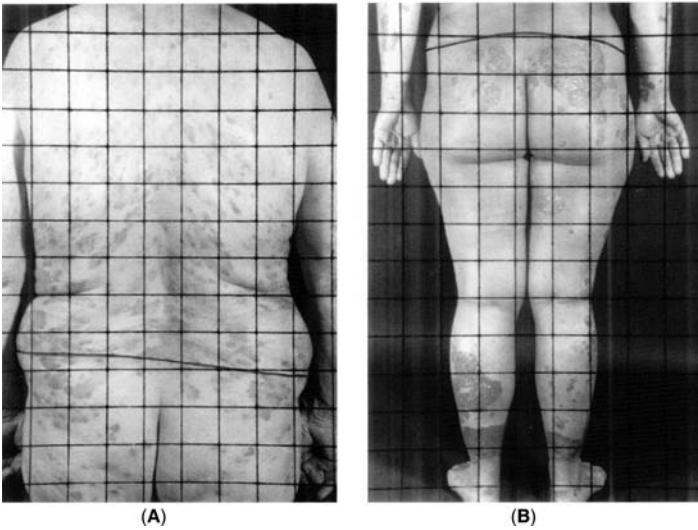


FIGURE 5 (A) Photo from the upper and (B) from the lower dorsal part of a patient with psoriasis. There are 126 points over the body counted on both photos. From these, 20 points are on the psoriatic lesions. Thus, the area fraction of the psoriasis lesions is $20/126$ (15.9%).

This morphometric estimation can also be used to quantify *corneocytes* obtained by tape stripping. Here too, the area fraction of the corneocytes contained within the reference area is determined by point counting. The number of corneocytes is estimated respecting the forbidden lines, and the average corneocyte area is calculated as stated for sebutape evaluation.

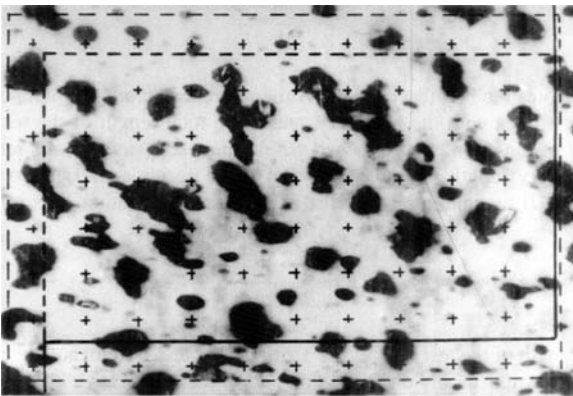


FIGURE 6 Original Sebutape at a magnification of fourfold and with a superimposed grid containing the counting frame with the forbidden lines according to Gundersen (17). The area fraction of the sebum spots is 27.5% ($22/80$ points). There are 55 spots within the inner frame of the counting area. Because originally the frame area was 2.16 cm^2 , average spot size is 0.04 cm^2 ($2.16 \text{ cm}^2/55$).

Length

Not only the area of a 2-D object, but also the length of a boundary can be estimated simply by the number of intersections formed with test lines. The formula is as follows (2):

$$\frac{B}{A} = \frac{\pi}{2} * \frac{I}{L} \quad (3)$$

Here, B denotes the boundary length, A the reference area, I the number of intersections of the test lines with the boundary, and L the total length of the test lines. If the total length B of the boundary contained within the test system area is required, rather than the boundary length per area unit B/A as in formula 3, Eq. (3) is simply multiplied by A . If magnified pictures are used, the magnification M is introduced:

$$B = \frac{\pi \cdot A}{2 \cdot L \cdot M} \cdot I \quad (4)$$

Because the length of the test lines L , the area A of the test system, and the magnification M have to be determined only once, the first part of the equation yields a constant. Thus, for length determination, only the intersections, I , with the boundary or the lineal structure have to be counted and multiplied with the constant. Another method of length determination is based on the famous "Needle-problem of Buffon (3)." In the 18th century, the Compte de Buffon provided a mathematical solution to the problem of the probability for a needle of length l thrown on lines d units apart to hit these lines with $l < d$. If the formula provided by Buffon is rearranged, the boundary length of a structure can be determined with superimposed parallel lines according to the formula

$$l = \frac{\pi}{2 \cdot M} \cdot d \cdot I \quad (5)$$

with l length of the boundary, M magnification, d distance of the parallel lines, and I number of intersections of the lines with the boundary.

Application of Length Determination

In clinical experimental dermatology, length determination might be useful for quantification of *telangiectatic vessels* in corticosteroid assays. If corticosteroids are applied topically over prolonged periods of time, permanent vessel dilatation might be a prominent feature. Usually, a "semiquantitative" method is used such as counting the number of vessels, or grading them on an ordinal scale. However, both methods are rather inaccurate, because the "number" of vessels per area is not meaningful, and reading is subjective because of the fact that the human eye is poor as a measuring device. An example is found in Figure 7 with a grid consisting of line segments superimposed to telangiectatic vessels (2).

Obviously, length determination might be performed correctly with a semi-automatic or an automatic image analyzer. However, these devices are expensive and not readily available in many parts of the world. In experimental dermatology, working on *angiogenic assays*, quantification of new vessel formation by lineal analysis is as easy as quantification of telangiectatic vessels in corticosteroid assays.

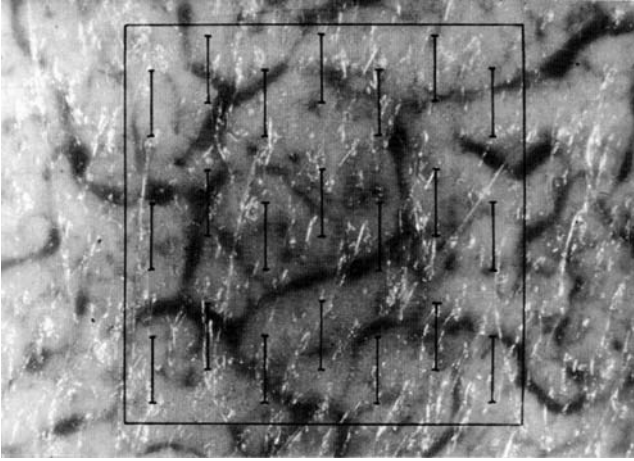


FIGURE 7 Network of telangiectatic vessels with a superimposed test grid containing 21 segments with a total length of 37.8 cm, contained in an area of 110.3 cm² at a magnification of 21.5-fold. There are 17 intersections between grid lines and vessels. According to Eq. (4), total vessel length is 3.62 cm.

Irregularity

A characteristic feature of malignancy is a certain degree of anisotropy, i.e., deviation from a regular pattern. Good clinical examples are malignant melanomas, which very often show, apart from other features, a rather irregular border compared to benign nevi. Thus, it could be desirable to assess the degree of irregularity. From the large number of form factors (18), a convenient measure of irregularity is provided by the relation

$$FF = \frac{B}{\sqrt{A}} \quad (6)$$

B denotes the length of the boundary, divided by the square root of the area A . Boundary length can be determined using Eq. (4) or (5), area by simple point counting. It is obvious, that the more irregular a structure is, the larger is the (dimensionless) figure of this form factor. An example is shown in Figure 8.

STEREOLOGY: FROM 2-D TO 3-D

Volume Estimation

One important application of morphometry is to provide 2-D information which in turn yields 3-D parameters if subjected to stereological analysis. To obtain information on numeric quantities contained within a volume, such as the number of cells, length of vessels, etc., this reference volume has to be known. Contrary to common belief and widespread usage, it is not possible to equate the cell profiles seen in a section with the number of cells contained in 3-D, because cell profiles on a section constitute a weighted sample. This is due to the fact that the probability that a cell is hit during the cutting process depends on its extension along the cutting axis (2,19).

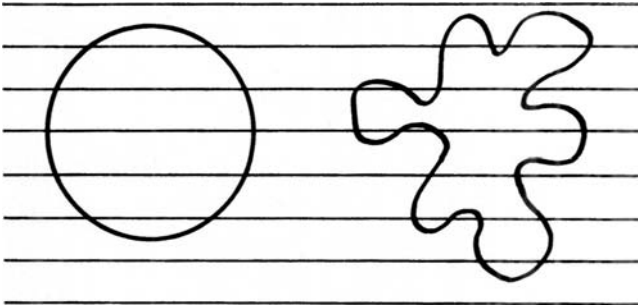


FIGURE 8 Circle and irregular area of about the same size (originally $\sim 10 \text{ cm}^2$). There are 10 intersections of the parallel lines with the circle, and 20 intersections with the irregular area. According to Eq. (6), the form factor for the circle is 3.54 and 6.91 for the irregular area, respectively.

The volume of a malignant melanoma is considered to be of prognostic significance (20). It has been postulated that it is difficult and time consuming to assess the volume of a malignant melanoma (20). However, if the old principle of Cavalieri is combined with area determination, e.g., by point counting, the volume of any tumor, irrespective of its shape, can be determined with ease. One provision is that the tumor cells can be distinguished from the surrounding tissue, a prerequisite that in most cases is easy to fulfil by conventional staining methods or by modern immunostaining procedures. The volume estimation is based on slabs of equal thickness and the estimation of the area of each slab according to the equation

$$V = \sum P \cdot a_p \cdot t \quad (7)$$

The sum of the points, P , on the slabs, times the area "associated" with one point (see above), a_p , and the (average) thickness of the slabs, t , yields an unbiased estimate of the volume of the body. It should be emphasized that it is very important that the starting point for cutting the slabs within the interval $\langle t \rangle$ has to be random (7).

Application of Volume Estimation

As mentioned briefly, the *volume of any tumor* such as melanoma, squamous cell carcinoma, and basal cell carcinoma might be of interest if (i) the amount of a structure (e.g., cells, vessels) contained within the tumor tissue has to be quantified, and (ii) with respect to the opinion that the volume of a tumor might be important for its metastasizing property. We have shown that melanoma volume can be estimated quite accurately and with little time spent, if the principle of Cavalieri is used (21). Another application are multicellular tumor spheroids which might serve as a model for avascular tumor parts (22).

CONCLUSIONS

Morphometric and stereologic methods have not gained wide acceptance so far in clinical and experimental dermatology. The most likely explanation is the fact that these methods require a certain amount of mathematical knowledge. It is true

that morphometry and stereology are based on stochastic geometry, probability theory, and statistics. However, neither the measurements nor the estimations are difficult; they can be performed manually or, if desired, with an automatic or semiautomatic image analyzing or morphometric system, respectively.

Morphometry provides the facilities for convenient quantification even during daily work in the hospital or in private practice. They render the frequent guessing concerning the size of lesions, and the more or less curious comparisons with biological objects obsolete.

Furthermore, morphometry and stereology provide the tools to assess even rather subtle differences if comparisons have to be made, e.g., quantity before and after treatment, diseased versus nondiseased tissue, malignant versus benign tissue. The great value of morphometry and stereology has been emphasized about 25 years ago by Weibel with respect to other disciplines like biochemistry, where measurements and not guesses are made: "... one would [therefore] expect [the associated] morphological studies ... to be quantitative as well (23)."

Last but not least, the methods outlined here are very economic, both in terms of time and money spent. For most purposes, nothing more than a selection of test systems on transparent foil, and a pocket calculator is required. Thus, it seems to be about time to quantify in clinical and experimental dermatology by unbiased morphometric and stereologic methods.

REFERENCES

1. Metrology a century ago. *Arch Dermatol* 1991; 127:503.
2. Weibel ER. *Stereological Methods. Vol. I. Practical Methods for Biological Morphometry.* London: Academic Press, 1979.
3. Aherne WA, Dunnill MS. *Morphometry.* London: Edward Arnolds, 1982.
4. Elias H, Hyde DM. *A guide to practical stereology.* Basel: Karger, 1983.
5. Bahmer FA, Smolle J. Morphometry in clinical dermatology. *Acta Derm Venereol (Stockh)* 1992; 2:52-57.
6. Gundersen HJG, Boysen M, Reith A. Comparison of semiautomatic digitizer-tablet and simple point counting performance in morphometry. *Virchows Arch [Cell Pathol]* 1981; 37:317-325.
7. Gundersen HJG, Jensen EB. The efficiency of systematic sampling in stereology and its prediction. *J Microsc* 1987; 147:229-263.
8. Cruz-Orive LM. The use of quadrats and test systems in stereology, including magnification corrections. *Microscopy* 1982; 125:89-102.
9. Mattfeldt T. The accuracy of one-dimensional systematic sampling. *J Microsc* 1989; 153:301-313.
10. Bahmer FA. Measurements and figures in dermatology. *Arch Dermatol* 1986; 122:501.
11. Bahmer FA. Quantifizierung allergischer Sofortreaktionen mittels Punktzählmethode. *Allergologie* 1986; 9:411-412.
12. Bahmer FA, Körner R. Simple methods for the assessment of migration areas in lymphocyte migration under agarose. *J Immunol Methods* 1986; 95:289-290.
- 12a. Bahmer FA, Lorenz E. Evaluation of the growth dynamics of *Trichophyton rubrum* cultures by morphometry and non-linear curve fitting analysis. *Mycoses* 2000; 43:25-28.
13. Russ JC. *Practical Stereology.* New York: Plenum Press, 1986.
14. Bahmer FA, Schäfer J, Schubert HJ. Quantification of the extent and severity of atopic dermatitis: the ADASI-score. *Arch Dermatol* 1991; 127:1239-1240.
15. Pierard GE. Follicle to follicle heterogeneity of sebum excretion. *Dermatologica* 1986; 172:31-35.
16. Bahmer FA, John S, Zaun H. Quantifizierung der mittels Sebutape bestimmten Talgsekretion mit einer einfachen morphometrischen Methode. *Ärztl Kosmetol* 1990; 20: 219-221.

17. Gundersen HJG. Estimators of the number of objects per area unbiased by edge effects. *Microsc Acta* 1978; 81:107–117.
18. Oberholzer M. *Morphometrie in der klinischen Pathologie. Allgemeine Grundlagen.* Berlin: Springer, 1983:105–111.
19. Gundersen HJG. Stereology of arbitrary particles. A review of unbiased number and size estimators and the presentation of some new ones, in memory of William R. Thompson. *J Microsc* 1986; 143:3–45.
20. Maize JC. Primary cutaneous malignant melanoma. An analysis of the prognostic value of histologic characteristics. *J Am Acad Dermatol* 1983; 8:857–863.
21. Bahmer FA, Hantirah S, Baum HP. Rapid and unbiased estimation of the volume of cutaneous malignant melanoma using Cavalieri's principle. *Am J Dermatopath* 1996; 8:159–165.
22. Bauer J, Gries W, Bahmer FA. Volume estimation of multicellular colon carcinoma spheroids using Cavalieri's principle. *Path Res Pract* 1995; 191:1192–1197.
23. Weibel ER. Stereological methods in cell biology: where are we—where are we going? *J Histochem Cytochem* 1981; 29:1043–1052.

Dominique van Neste*Skinterface, Tournai, Belgium***INTRODUCTION**

The present review will focus on basic principles involved in human hair evaluation using imaging, i.e., photographic and computerized methods. The visibility of hair will depend not only on the resolution power of the optics and charge coupled device (CCD) camera but also on the natural contrast between the object, i.e., hair (with every variation of the fiber components and optical interfaces) and background (including skin as a heterogeneous and variable background and extraneous material).

BASICS ABOUT HAIR STRUCTURE AND FUNCTION

Here we shall briefly review some basics about hair follicle structure and function necessary for the understanding the fine tuning of technical aspects of hair photography. Those who are acquainted with growth of hair and hair follicle cycling may easily proceed to the next section. Scalp hair is an appropriate example to introduce the concept of global and analytical methods while “zooming” into the field of hair (Fig. 1). Scalp hair appears as a stable mass of hair. It actually represents the cumulative end result of discrete changes of individual hair follicle dynamics: hair shedding and replacement resulting in global maintenance. The key to the appropriate assessment of hair maintenance lays first in a thorough understanding of the hair cycle (3). This is shown schematically in Figure 2 for one single hair follicle. On the scalp, there are about 100,000 follicles. Importantly, not all follicles are active at the same time: some produce a hair while others are resting. After this resting phase also named telogen, the club hair is processed (exogen phase of the hair follicle and hair cycle) for its programmed release. Exogen phase terminates with the shedding of the hair and eventually a new hair shows up. After a short time necessary to reach the scalp surface, hair becomes visible. Each follicle appears to function independently from its neighbors, i.e., the process of scalp hair growth is not synchronized. However, follicles in a certain field may express a common phenotype after exposure of some compounds, i.e., sex hormones. Some scalp areas, in genetically predisposed individuals, will show a phenotype of defective hair replacement, i.e., patterned balding (Fig. 3). In other areas (axilla, face, chest, genital skin, etc.), other “patterns” will be expressed: the very thin hair follicles will now grow longer and coarser, such hair usually grows during limited periods of time and is retained as telogen hair for prolonged periods of time as compared to the scalp hair. As such, the clinical appearance of “hairiness” depends as much on regional modulation of the hair follicle activity and of its cycle in particular as on the number of hair follicles.

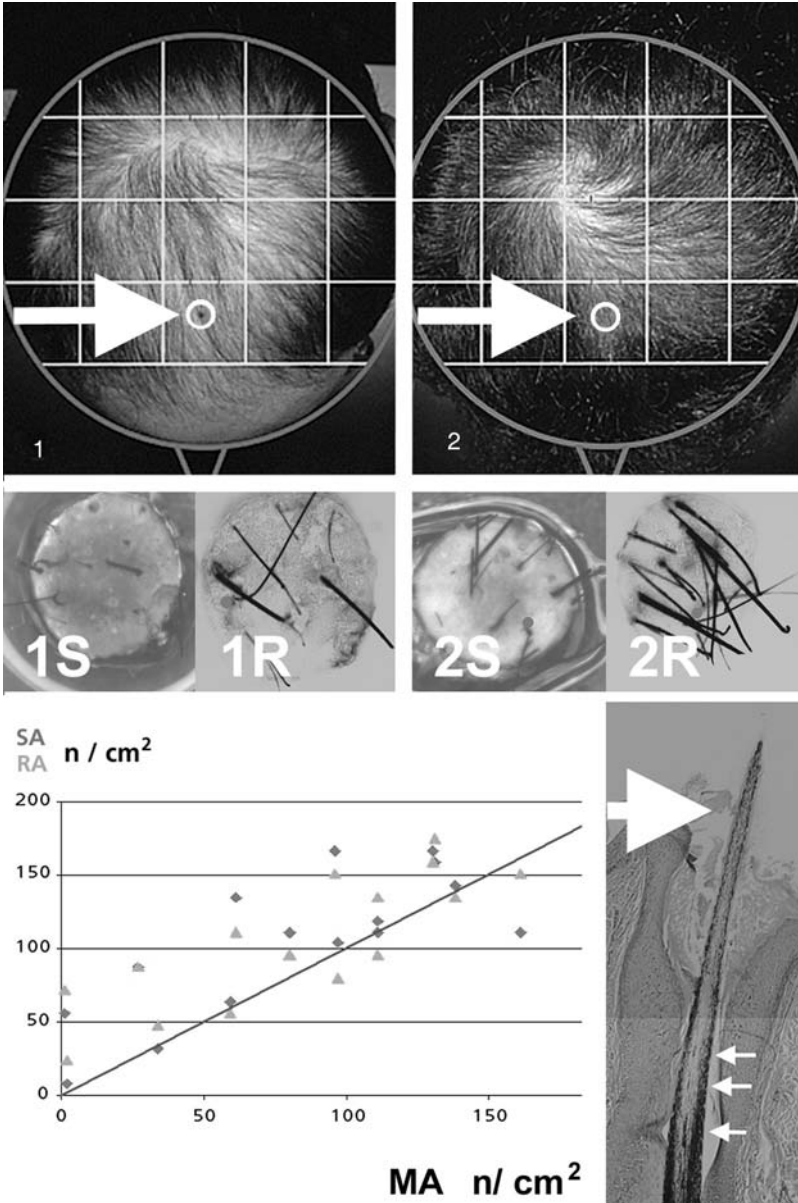


FIGURE 1 (Caption on facing page)

HAIR PHOTOGRAPHY AND IMAGING

Search for “Golden Standards”

There is not a single technical modality that will encompass with a sufficient degree of precision the many dimensions of hair (4,5). At one end of the spectrum,

global viewing is very often used for “demonstration” purposes, i.e., to document the views of health authorities or individual patients. A simple hair cut can have dramatic effects and possibly “ruin” a clinical file during a clinical study on a hair growth promoter! Global viewing, even when highly standardized procedures are being used, does not resolve the question of hair cycling changes.

At the other end of the spectrum, microscopes have a superb resolution power when a single hair fiber or a follicular unit or even single cells are concerned. A comparison between stereomicroscopic viewing of scalp samples and photographs of the same sites taken with a commercially available macrophotographic equipment showed that the number of growing hair counted on the surface view or from the root view were always higher when compared to counts generated from large photographic printouts (2). In order to be “clinically representative,” a field containing around 100 hair fibers would be considered as a representative (6). The analysis would be valuable only if “exhaustive” sampling took place (7). We have shown this with scalp biopsies but (Figs. 1 and 4), taking repeat images from the scalp surface seems acceptable while repeatedly taking biopsies seems definitely not practical for hair growth monitoring purposes.

Hair density or number of hair per unit area is usually reported as number/cm². It reflects the number of functionally active follicular units, whether growing (anagen) or not (telogen). Under physiological conditions, i.e., the long duration of anagen phase and the comparatively short duration of telogen, we know that most scalp follicles are engaged in anagen. This will produce long and clearly visible hair at the scalp surface, but this may change dramatically in some hair disorders leading to hair loss and balding.

The percentage of anagen follicles properly reflects the time during which hair follicles are engaged into the growth phase. The anagen/telogen ratio is also often found in the literature. Many clinicians are not aware that this is true only when an exhaustive count of hair and/or hair follicles is made. Hair has been classified into terminal, intermediate, and miniaturized, but there is no consensus on the definition of these categories.

FIGURE 1 (Figure on facing page) Zoom concept from global view to hair folliculogram. Global view of the top of the head in two male subjects with male pattern baldness (1,2). The top of the head is fragmented into smaller areas (*squares*) for scalp coverage scoring [scalp coverage scores (SCSs); for more details on SCS, see text and other figures]. Clipping hair allows a more detailed record using close-up (or macro-) photographs. Depending on the technique, the area of the target site ranges from 5 to 1 cm² (*white arrows*; clipping and close-up photographs not shown). A small tattoo allows relocation of the target area (*middle of white ring*). Such tattoos can also be removed by a small 4 mm punch biopsy (not shown). We show images taken with a video microscope of the surface of the biopsy. This shows very small number of hairs (1S < 2S for surface view). The same scalp specimens are marked (*dots*) and processed for the isolation of the dermal part of the hair fiber (1R and 2R for root view). In the *lower left panel*, we show the results of a “validation” test of a macrophotographic equipment and analysis system. After taking a macrophotograph for anagen hair counts [macrophotography anagen (MA), n/cm² (1)], tattoos were punched out and specimens were tested for “anagen” hair counts with a stereomicroscope on the surface or on the root view [respectively surface anagen (SA) and root anagen (RA); n/cm²]. In most cases (three out of four) counts of SA and RA were higher than those obtained with a close-up photograph (MA, n/cm²) showing that the macrophotographic system was less than optimal to detect all growing hair in vivo on the human scalp (2). Finally, the light microscope (*lower right panel*) gives a very detailed view of the hair as it emerges at the scalp surface (*thick arrow*) from the deeper parts of the hair infundibulum (*three small arrows*).

Many based their assumptions on the thickness of hair fibers, but we argue that enough attention has not been devoted in the past to variables, such as growth rate, natural pigmentation (8), and other factors (9,10) such as the duration of the lag phase. From the above sections it becomes clear that the results of an assay largely depend on the technology that was used for measuring hair parameters. Before discussing the aims of computerizing, we wish to illustrate some tools that are commercially available or systems that can be delivered in the context of the installation of a hair clinic with licensing of technology or on the occasion of a clinical trial project (Fig. 5).

Improving Hair Photography for Computerized Measurements

Computers may help perform routine tasks but need to be fed properly in order to generate acceptable numbers out of figures for clinical interpretation! In the description of noninvasive photographic methods that can be used in vivo in human subjects, we propose to distinguish between global and analytical methods. Global methods apprehend at once various factors responsible for the hair covering.

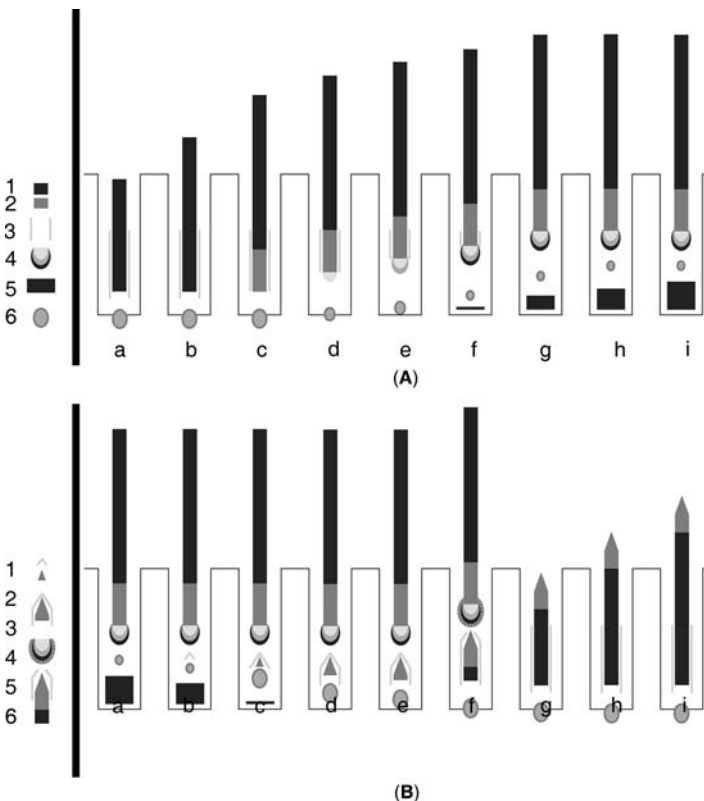


FIGURE 2 (Caption on facing page)

Global Vision and Imaging Methods

Categorical Classification Systems

Distinctive patterns of defective scalp skin coverage or alopecia have been identified by clinicians as patterns. One could practice in any public space (mall, theatre, etc.) and see for himself/herself what the limits of this method are (Figs. 1 and 3). In the authors' hands, there is a very large variation between sessions when the same views of the top of the head of male subjects with patterned hair loss were presented several times in a randomized sequence (unpublished observations). Also, intervals between successive severity scales may not be equal. The consensus among experienced clinicians is that the schemes are of little help in measuring the dynamics of hair changes—whether growth or loss—over time.

Based on these patterns, fragmentation of the scalp was proposed on the basis of anatomical criteria (11). However, no evidence was presented to support this “new” belief. The fact that the use of noncalibrated density scale casts some doubts as to the practical application in real time or “as a bedside” measurement

FIGURE 2 (*Figure on facing page*) Hair cycle: The hair growth phase (anagen) during which hair is visible at the skin surface and growing are shown in (A) while the apparent resting phase of the hair cycle (telogen) is shown in (B). (A) From growth to rest: The same hair follicle is represented at various times (days) at the very end of the growth phase. At the skin surface, there is a normal pigmented hair production (days a–b and b–c) representing the constant daily hair production. Then, the pigmentation of the newly synthesized hair shaft (appearing at the bottom of the hair follicle) is decreased (c). This early event announces the regression of the impermanent portion of the hair follicle and is followed by terminal differentiation of cells in the proliferation compartment (d) that will turn into the club hair formation. The shrinking dermal papilla (d) begins an ascending movement together with the hair shaft (d–h; 21 days). This characterizes the catagen phase (d–h) with an apparent elongation of the hair fiber. This reflects the outward migration of the hair shaft which is much smaller than the daily growth rate. What is left after disappearance of the epithelial cells from the impermanent portion of the hair follicle is basement membranes followed by dermal connective tissue usually referred to as streamers or stellae (f–i). The true resting stage begins when catagen is completed, i.e., when the dermal papilla abuts to the bottom of the permanent portion of the hair follicle (i). In the absence of physical interaction between dermal papilla and bulge the next cycle (see B) is definitely compromised. As from now, no hair growth is observed at the surface (g–i). (B) From rest to growth: During this stage, one notices absence of hair growth at the skin surface (a–e) but significant changes occur in the deeper parts of the hair follicle. The dermal papilla expands and attracts epithelial cells from the bulge (stem cell zone) in a downward movement (a–b). To create space, previously deposited materials have to be digested (a–c). The epithelial cells then start differentiation in an orderly fashion starting with the inner root sheath [forming the initial cone in (b) and then a funnel in (c)] containing the tip of the cuticle and hair cortex of the newly formed unpigmented hair fiber (c–e). The resting hair remains in the hair follicle for approximately one to three months (a–e), then a detachment process transforms the old follicle into exogen and releases the exogen hair (f) that may stick in the follicle for a short time before being shed (f–g). The shiny root end of the shed hair is the club. Before, during, or after hair shedding, there may be replacement by a new gradually thicker and more pigmented hair shaft (e–f–g). Indeed, under physiological conditions, the follicle may proceed immediately or only after some lag time with new hair production (from b to g; up to 90 days). In conditions like androgenetic alopecia, the shed hair may stick in the follicle for a longer time (stasis of exogen hair may turn into trichostasis due to abnormal accumulation of nonadherent or loosely attached elements) and there may be a much longer interval before regrowth is recorded at the scalp surface. At the earliest visible stages, i.e., when the new anagen follicle is again deeply set into the dermis, one notices at the scalp surface, a thin usually nonpigmented hair tip that is seen first (h) soon followed by a thicker more pigmented and faster growing hair fiber (i). This sequence of course depends on the many regulatory factors controlling the hair follicle activity during its replacement.

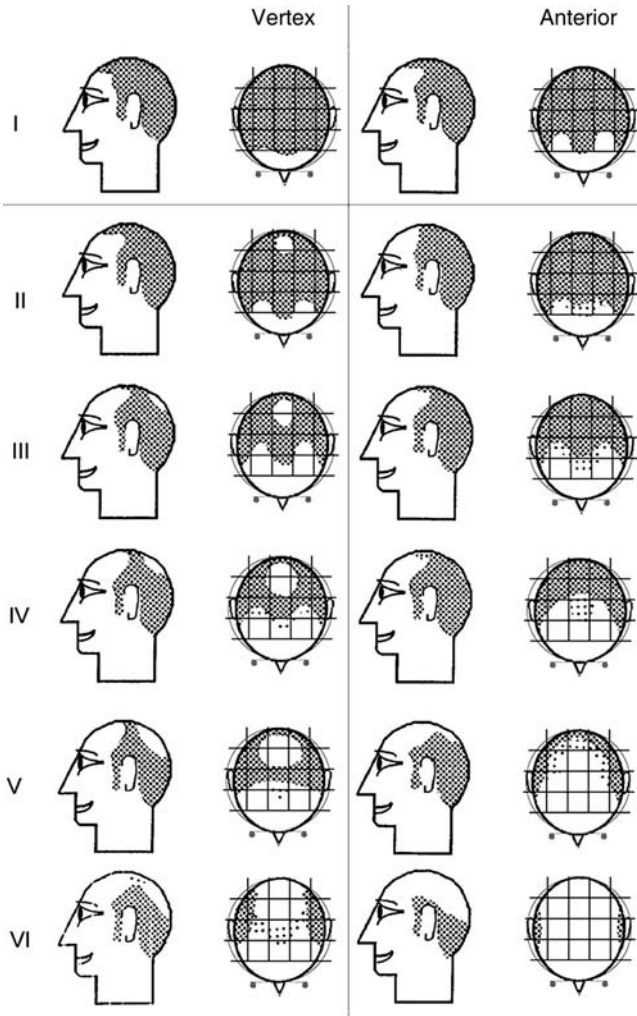


FIGURE 3 Hair pattern analysis and quantification: The present classification shows patterns that affect the scalp of genetically predisposed male subjects. Such patterns develop after puberty, when deficient hair replacement ultimately results in bald appearance. They are subdivided into six categories of increasing severity (I–VI) from mild to severe balding. The anterior pattern indicates a backward progression of hair follicle miniaturization that starts from the frontal hairline. The vertex type indicates isolated regression occurring on the vertex but this is usually combined with some involvement of the frontal temporal areas. As in Figures 1 and 6, fragmentation of the scalp view (*square areas*) helps in evaluating the severity of the balding process in terms of extension or progression.

tool (11). In order to circumvent several of the weaker aspects of these methods (lack of standardization, lack of calibration, transposing shaved hair density, i.e., “skinhead” type of density patterns onto real heads of patients with a great diversity of hair styles, etc.), we proposed, as shown in Figures 1,3 and 6 the top of the head into a number of fixed and predefined subunits. This helps focusing the attention of the observer in clearly outlined spaces where patterning results

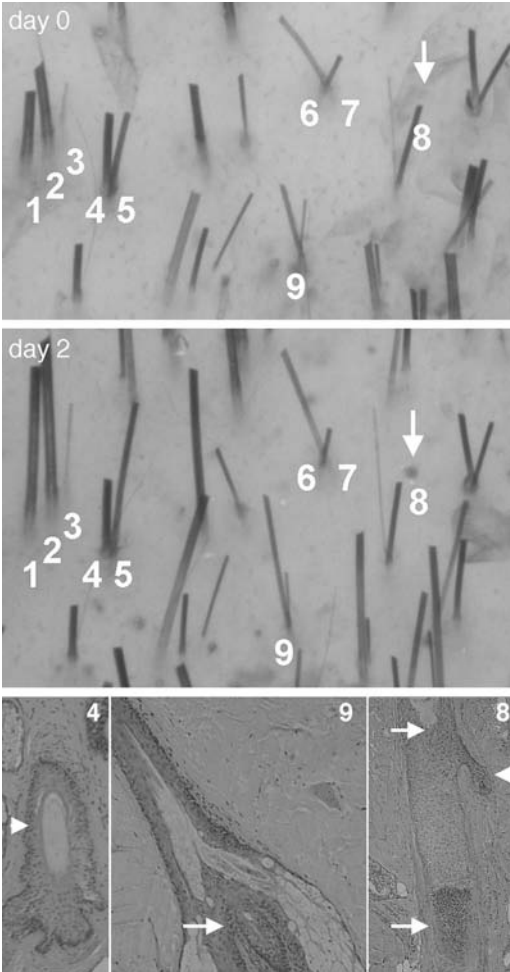


FIGURE 4 Phototrichogram (PTG) in a young male with patterned alopecia: The contrast-enhanced (CE) PTG technique (*upper panels*) matches perfectly histology (*lower panels*) for hair growth measurement. Evaluation of hair growth with the PTG. At time 0 (day 0), the hairs are clipped close to the scalp surface and photographed. After a given time (48 hrs in the authors' experience, day 2), the same scalp site is photographed again. Substantial elongation at day 2 reflects hair growth and indicates anagen in thick (1,2,5) and thin (7) hair. Moderate elongation reflects catagen in a thinning hair (3). No elongation reflects resting in thick (4) and thinning hair (6). After shedding the thick (4) or the typical tiny (9) resting hair, an empty follicle in the exogen stage will remain visible (8 *arrows* at day 0 and day 2 and *upper arrow* in histology 8, *lower right panel*). The formation of new follicles is shown in the same panel where follicles initiate anagen for a thick (*lower arrow*) and thin hair (*upper right arrowhead*) can be seen only with histology (8). Tracking of such empty follicles with CE-PTGs will show newly growing hair in some days or weeks (see later).

in various degrees of defective scalp coverage. We will describe results obtained using this novel approach in greater detail in the next section. Using analogical reasoning with mathematics, one could use the term of fractal approach from quantifying the most global perception and stepwise scaling down to the measurements of single cycling hair follicles and finally to cellular and genetic controls of its structure–function. In this chapter, we will limit ourselves to global methods and analytical methods where detailed measurements of single hair follicle activities are provided.

Calibrated Scoring Systems

A system has been developed where examination of the scalp surface proceeds through fixed external standards. The top of the head is separated into small units (equal size in the projection plane) with no anatomical correspondence of the bones of the skull (e.g., frontal, parietal, etc.) or the substantial variation of patterning in human subjects. The relative difficulty to detect scalp skin between the hair is

translated into scalp coverage scores (SCSs) (SCS 0 means there is no difficulty and score 5 means that it is barely possible to detect scalp skin through the hair). This is rated—under strict distance and angle control—against objective rulers of density (method and equipment for measuring coverage density of a surface—Skinterface, application patent no. PCT/EP 01/06970, 2001). The reproducibility (intra- and interobserver) is very high (correlation factors > 0.9) (12). Several studies using scores generated in the clinic (real time measurement) and on global photographs have now been performed either as a single center or in the context of multicenter, placebo-controlled trials (H.A.I.R. Technology[®] protocols 02P08, 03P17, and 03P22) using known drugs or new compounds (phase II–III).

When all identified sources of variation are kept under control, the variation of scores is less than 5% (12). During calibration studies, the SCS was also correlated with clinically relevant hair parameters such as proportion of anagen hair or density of thinning hair (13). As such, SCS measures clinically relevant changes (Fig. 3).

In a one-year period, a clinician is able to disclose hair loss in untreated (randomized, placebo-controlled study in vivo) patients (14–16), but standardized global scalp photographs may be an interesting alternative that will be discussed in the next section.

Global Photographs

Global photography has been a significant step forward in scalp hair documentation by creating a permanent record (17). Processing and rating has to be performed under controlled (e.g., blinded as to treatment and/or time) conditions. Trained experts could generate reproducible data. It appears that paired comparison of global photographs is more realistic in the appreciation of hair growth effects after drug treatment as compared with subjective evaluations of investigators and patients (18).

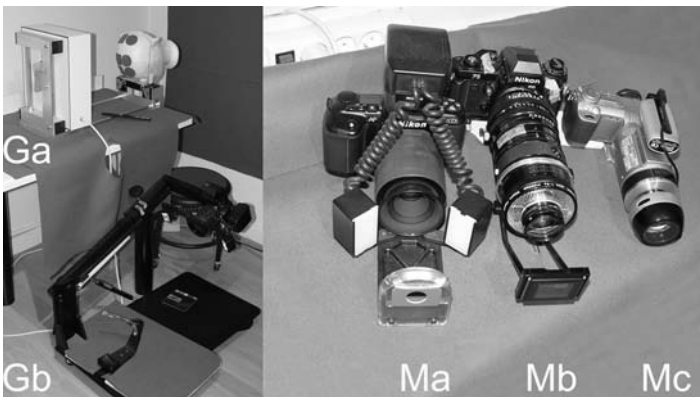


FIGURE 5 Equipment for global and close-up hair photography: Equipment for global scalp viewing (Ga from Skinterface or Gb from Canfield) or for macrophotography [Ma from Canfield or Mb–Mc (Mb, historical) and Mc from Skinterface]. Ga also shows a model used for calibration purposes and the comb that is always necessary to organize the mass of scalp hair properly. Such materials are commercially available at Canfield or can be licensed by Skinterface on the occasion of a clinical trial project. Ga and Mc (developed in 2002) show the recent trend toward miniaturization (compare with Gb, Ma, and Mb).

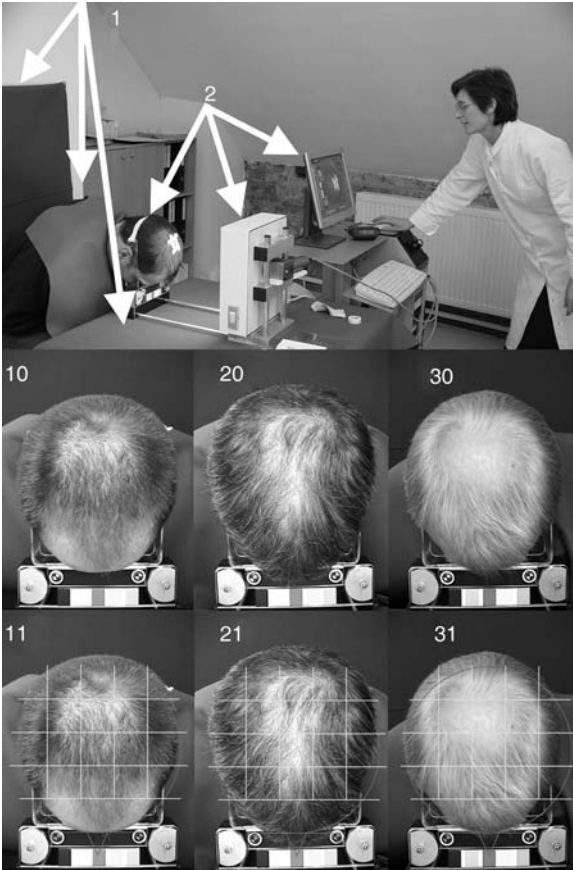


FIGURE 6 How to standardize global scalp hair imaging: In this setting, great care has been taken in the preparation of the background and positioning of the patient (1). Imaging (2), involves adjusting the subject with the headgear to the positioning device. Once the “light box” is switched on and the camera properly inserted into the “light box,” one captures an image appearing on the computer screen. Examples show the views of the top of the head (10–30) on which a grid can be placed as an overlay (11–31).

Global images taken from the top of the head can also be scored individually with the SCS system. Some computer approaches have already been published (19,20). Standardization remains the key! (Fig. 7).

Analytical Methods

Phototrichogram: From Conventional Phototrichograms to Contrast-Enhanced Phototrichograms

What Did We Learn with the Conventional Phototrichogram?

The basic principle of the phototrichogram (PTG) consists of taking a close-up photograph of a certain area of the scalp. The hair is cut very close in preparation

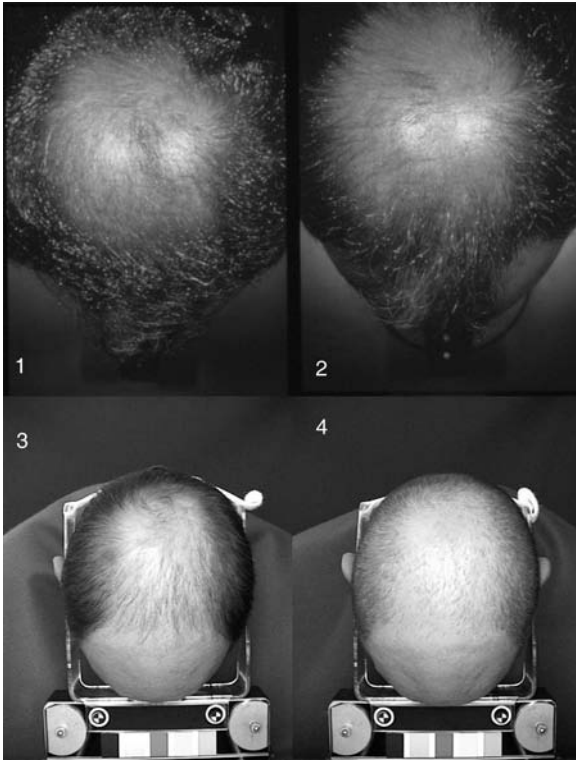


FIGURE 7 Coping with technical and styling variability of global photographs: These two sets of before and after pictures illustrate difficulties encountered in evaluation of time or treatment related changes of scalp coverage. The commercially available Canfield system (1,2) and clinical trial set developed at Skinterface (3,4) illustrate some differences between the systems (backscattering of light, background, inclusion of color codes during imaging, etc.). The vertex view (1) turned into a top of the head view (2) at the follow-up visit. The technician did not position properly the head of the patient on the two sessions (estimated angle error $\pm 45^\circ$). The two top of the head views (3,4) illustrate the difficulty of managing properly the hairstyle. Although the technical quality is almost perfect (see overlay of targets, distance, angle, color codes, etc.) any possible change of hair growth can be masked by a hair cut or a subtle change in hairstyle.

for the first photograph, followed by repeat photographic documentation after a certain time period. This period of time should be long enough to allow the growth of a hair segment (time window which is usually between 24 and 72 hrs) but not too long in order to prevent outgrowth or too much overlapping of growing hair. The growth is then evaluated by comparing the two pictures. Hairs that have grown are in anagen phase and those, which have not, are in telogen phase (Fig. 4).

Analytical methods that document major aspects of the hair cycling process have been developed over the years (21–27) and are subject to continuous reevaluation and improvement (28–30). Some PTG data have been computed for mathematical modelling so as to develop virtual patterns of defective hair replacement mimicking those observed in the hair clinic (31). The conclusions of these

statistical studies may not reflect biological events because some were unraveled in recent assays (10). This suggests that neither all hair fibers nor all productive hair follicles were taken into account during the conventional PTG procedures. In some assays, we noticed that the length of hair significantly affected its visibility. As growing hair will become more visible on the second photograph, a bias was detected (unpublished data). Between 1989 and 1992 we used scalp immersion photography (32) or proxigraphy (23) well before epiluminescence microscopy became eventually the accepted term. After comparison with another more invasive method (29), some weaknesses have been considered with great care and considered contrast enhanced (CE) as a further improvement (7,28). This brought the CE-PTG technique to an almost equal resolution as transverse microscopy of scalp biopsies, which are usually considered as the golden standard (33–38). So far, the CE-PTG remains the only method that has documented all transitions of thick and thinning follicles from anagen through catagen into telogen phases on a follicular basis (7).

In early stages of androgenetic alopecia (AGA) in man, this sensitive method (10) was able to detect a preclinical phase of AGA with obvious shortening of the anagen phase in the absence of hair miniaturization. This preclinical stage evolves into patterning, i.e., the full-blown phenotype associated with a further shortening of the growth phase along with reduction in hair diameter (23–30,39–43). The follicular regression process finally results in production of clinically nonvisible hair (44).

What Can We Learn to Measure with the CE PTG?

The data that can be generated from a CE-PTG are total number of hair present in a certain area, i.e., hair density (n/cm^2), the percentage of hair in the growth phase (anagen, %), the linear hair growth rate ($\mu m/day$), and the hair thickness (hair width, μm).

Thickness can be measured on hair clippings, scalp biopsies, and on scalp hair photographs. It may seem trivial to state that the hair diameter evaluation is more precise with the microscope. These measures reflect diameter almost exactly whenever the fiber section is circular (typically Asian hair) like in hair (no ethnic variation) that is thinner than 40 μm (45). In Caucasians, thicker hair loses this property and the section becomes elliptical. In Africans, the hair flattens even more. The same comment holds true for other body sites where curly and flattened hair is the rule rather than the exception.

Nevertheless, we found a significant correlation between paired microscopic measurements and thickness evaluation on Caucasian scalp hair photographs in the range of less than 20 to greater than 100 μm thick hair fibers (<1% variation in a test using multiple technicians; personal unpublished data) so reducing methodological errors of other approaches (46).

The method was applied with success to various genetic conditions including male pattern baldness in vivo (5,7–10). This technique was able to document the earliest changes of hair growth in AGA in man. From shortening of anagen duration of thick hair, regression appears to evolve in sequence into a phase of further shortening associated with slower growth rates and more severe thinning turning finally into a stage of reversible miniaturization without production of any visible hair. At this stage, one speculates that drug response is still possible before the follicle drops into total irreversible atrophy, though without scarring (10).

Variants of Phototrichogram Methods

Subtle modifications in the preparation of target site can help identification of the hair in the growing from resting phase, especially when less than optimal magnification lenses are used [e.g., less than $\times 3$ (25)]. Indeed after clipping the hair short (first step of the PTG as control for density or hair counts), a close shave will further reduce the visible length of the hair fiber. Then, usually three rather than two days later, the second photograph is taken. A new hair count of the long hair fibers reflects anagen hair follicles. This procedure has been used to monitor changes occurring after finasteride in man with AGA demonstrating a significant induction of growth as compared with placebo (1).

When the photographic camera is replaced by a video or CCD camera equipped with specific lenses, other variants of PTG recording are obtained. In fact, reports on Orientals and Caucasians were published. In the latter subjects, the contrast between hair and scalp seems favorable for the application of this method and the low figures of hair density could possibly be racial in origin (22). As shown already (28,46), the use of CE is advisable—especially for Caucasian hair—even when the use of computer applications for textile fiber analysis (47) or hair recognition software—already developed for other applications (48). Such a system has been proposed (49) and the promoters of the method recognize that the explored area is small ($<0.25\text{ cm}^2$). This is yet another source of variability, because the number of hair so analyzed is definitely less than 100 and drops below statistically acceptable population sample size (6).

Furthermore, all of these automated systems generate numbers without securing that all hairs in the field were detected. Various commercial brands have been proposed such as Trichoscan (49) or Capillicare (data in file) and customers reported lack of satisfaction with such methods because the dream of an easy and fast method vanishes as it remains time consuming. The method analyzes only a limited number of clinical situations and even when all clinical conditions are suitable for the computer, it does not generate all data that may be of interest to the observer in terms of diagnosis, prognosis, or any other clinically relevant information (50). More importantly, independent clinical observers (51) also state that “the potential of computer-assisted technology in this field is yet to be maximized and the currently available tools are less than ideal.”

Future Trends in Computerized Methods

More than a decade ago, we listed the different problems arising when automated computer-assisted image analysis comes into the scope of hair growth measurement (52). Some problems have been solved. Accurate analysis still requires expert human intervention during the sampling and processing of images. Today we are easily coping with the three dimensions involved in hair, we master the requirements in terms of enlargement factor or pixel size, immersion and polarized light. We also wiped out the problem of backscattering of light and other problems linked to presence of sebum droplets, sweat, and scales. More recent developments helped us to clear the scene from any other loosely attached elements such as exogen hair (application patent process, method, and apparatus for removing nonadherent elements from the skin of living beings and measuring the hair loss of living beings—Skinterface—PCT/EP02/06434; June 12, 2002) and add information on “trichostasis” a largely unsuspected phenomenon that influences

significantly hair counts. Increasing contrast between scalp and hair allows us to express data in a single case observation or to perform accurate time-course studies of hair growth changes using highly standardized operating and monitoring procedures. As an example of the technological resolving power, we discussed recently on hair pigmentation during aging and how it might affect the outcome of a clinical trial (8,53). Initially nonvisible hair under conventional PTG may become visible due to drug effects such as increased pigmentation, initiation of short-lived but thick anagen hair, etc. The spectrum of follicular bioresponses is actually underestimated and requires sophisticated investigations.

Detection of “Nonvisible” Hair: Less Contrasted and Thinning Hair

Clinicians occasionally express their fears about new information generated by these up-to-date technologies such as taking into account that thin hair is becoming visible (11). This clearly illustrates that the message telling that contrast enhancement makes also thick hair more visible did not come through. In order to know whether a miniaturized hair has any potential meaning or is just useless as a potential site for drug action, there is only one way: Use a method that is able to measure their presence and monitor their potential modification over time. Anything else should be considered as speculative issues contributing to maintaining hair science and technology in the marshlands of trichoquackery.

As a practical example of a critical comparative study, we refer to illustrations and comments in Figure 8. Therefore, we conclude that fully automated analysis systems (32), notwithstanding the apparent easiness and speed of analysis of more recent systems (49), remain generally unsatisfactory (50) when detailed description of hair variables such as hair counts, diameter—especially for thinning hair—and growth rate is required. Biologically significant data in terms of follicle distribution, productivity, cycling, regression, or progression are not yet published—but will be in the recent future—with our updated technologies. We do hope that the work done during the last decade will definitely bring such systems to the status of medically acceptable as diagnostic, prognostic, and therapeutic monitoring tools.

CONCLUSION

A bold statement would be to say that the assessment of hair loss requires some experience and a lot of technological effort in order to grasp all the parameters involved in hair measurement. There was a time, when some colleagues argued that measurement methods were not necessary as the patient could tell when hair is growing or not. It is obvious that this is untrue as soon as one enters the continuum of the hair replacement process especially when some hair is still present. Such a statement also looks outdated when one acknowledges the importance of the placebo effect. Indeed, subjective evaluation may reach 60% or more satisfaction while significantly decreased hair counts clearly document the natural worsening of the condition (18). Our experience points to the fact that a combination of a highly sensitive and precise analytical approach together with a global calibrated method seems advisable in the context of kinetic monitoring of hair growth and hair loss in the hair clinic in general and this is warmly recommended in the context of efficacy analysis of new (and recognized!) compounds in future clinical trials.

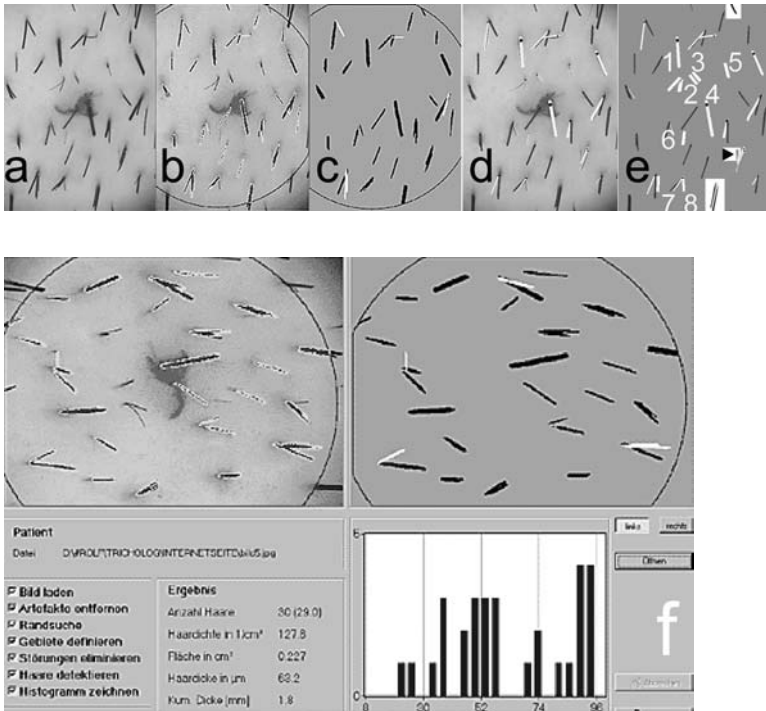


FIGURE 8 Quality process evaluation comparing manual versus automated hair analysis software: Here we show a typical example of quality process evaluation—as it is usually practiced in our laboratory—comparing results of our routine hair processing method versus those generated by the automated hair analysis software. *Image processing results:* An image (a: source image) was downloaded in July 2003 from a website (trichoscan.com) displaying a full automatic system for hair analysis. Accordingly, after the automated hair selection (b: clear outline of selected elements by software) and analysis (c: binary image of selected elements). The same “source” document (a) was also submitted to a technician for routine processing in our laboratory. The technician had no information about the origin of the document or results of automated analysis. This modality is part of our routine processing quality control (d). Our technician identified 43 hair segments in the circular outline of that image. Fourteen hair fibers had a thickness estimated to be less than 40 µm and 29 were considered as thicker hair (≥ 40 µm). *Quality analysis of process:* At the final revision by the author, the discrepancies were noted between the two processing modalities. They are outlined visually in (e) against a white background. One very thin hair partly hid within a trio (white rectangle with arrowhead) was missed by both measurement systems. A display of hair results from automated analysis of image (a) is shown in (f): 29 hairs were counted in the 0.227 cm² area (parts of circular outline) generating a density of 127.8 hairs per cm². The automated system also missed seven other hairs that were identified by our technician [empty numbered spaces in (e)]. Automated counts also included three hairs crossing the edges [white rectangles top (one hair) and bottom (two hair) of (e)]. Hairs that stick together were not individualized by the automated system. *Results:* While the automated analysis counted 29 hairs we found 42 in the same area. Technicians’ error (1/43) is much lower than automation error (12 or 13/43), i.e., 2.3% instead of 30.2% of the total sample. *Conclusion:* Hair evaluation as performed with automated systems does not match the quality standards prevailing in our laboratory. Many problems identified in 1989 (51) still cause concerns for automatic evaluation in 2004! Truëb and Van Neste (50) conducted a more refined study with original documents: the demonstration that error rates over 50% in terms of hair counts actually confirmed the present comments.

REFERENCES

1. Van Neste D, Fuh V, Sanchez-Pedreno P, et al. Finasteride increases anagen hair in men with androgenetic alopecia. *Br J Dermatol* 2000; 143:804–810.
2. Van Neste D. Folliculogram demonstrates more anagen hair roots in male androgenetic alopecia after one year treatment with finasteride 1mg/d. In: Van Neste D, Blume-Peytavi U, Grimalt R, Messenger A, eds. *Hair Science and Technology*. Tournai, Belgium: Skinterface sprl, 2003:311–316.
3. Stenn KS, Paus R. Controls of hair follicle cycling. *Physiol Rev* 2001; 81:449–494.
4. Sinclair R, Jolley D, Mallari R, et al. Morphological approach to hair disorders. *J Invest Dermatol Symp Proc* 2003; 8:56–64.
5. Van Neste D, Blume-Peytavi U, Grimalt R, Messenger A. *Hair Science and Technology*. Tournai: Skinterface sprl, 2003.
6. Van Neste DJJ. Hair growth evaluation in clinical dermatology. *Dermatology* 1993; 187:233–234.
7. Van Neste DJJ. Contrast enhanced phototrichogram (CE-PTG): an improved non-invasive technique for measurement of scalp hair dynamics in androgenetic alopecia—validation study with histology after transverse sectioning of scalp biopsies. *Eur J Dermatol* 2001; 4:326–331.
8. Van Neste D. Thickness, medullation and growth rate of female scalp hair are subject to significant variation according to pigmentation and scalp location during ageing. *Eur J Dermatol* 2004; 14:28–32.
9. Van Neste D. Female patients complaining about hair loss: documentation of defective scalp hair dynamics with contrast enhanced phototrichogram. *Skin Res Technol* 2006; 12:83–88.
10. Van Neste D. Natural scalp hair regression in preclinical stages of male androgenetic alopecia and its reversal by finasteride. *Skin Pharmacol Physiol* 2006; 19(3):168–176.
11. Olsen EA. Current and novel methods for assessing efficacy of hair growth promoters in pattern hair loss. *J Am Acad Dermatol* 2003; 48:253–262.
12. Van Neste D, Leroy T, Sandraps E. Validation and clinical relevance of a novel scalp coverage scoring method. *Skin Res Technol* 2003; 9:64–72.
13. Sandraps E, Leroy T, Demortier Y, Van Neste D. Validation and clinical relevance of a novel scalp coverage scoring (SCS) method. In: Van Neste D, Blume-Peytavi U, Grimalt R, Messenger A, eds. *Hair Science and Technology*. Tournai, Belgium: Skinterface sprl, 2003:255–270.
14. Van Neste D. My management plan of the male patient with androgenetic alopecia. In: Van Neste D, Blume-Peytavi U, Grimalt R, Messenger A, eds. *Hair Science and Technology*. Tournai, Belgium: Skinterface sprl, 2003:301–310.
15. Van Neste D. Scalp coverage scoring (SCS) documents natural worsening within less than 12 months in a majority of men with androgenetic alopecia (AGA). In: Van Neste D, Blume-Peytavi U, Grimalt R, Messenger A, eds. *Hair Science and Technology*. Tournai, Belgium: Skinterface sprl, 2003:271–276.
16. Van Neste D, Sandraps E, Herbaut D, Lelubre P, Leroy T. Validation of scalp coverage scoring methods for scalp hair loss in male pattern hair loss (androgenetic alopecia). *Skin Res Technol* 2006; 12:89–93.
17. Canfield D. Photographic documentation of hair growth in androgenetic alopecia. *Dermatol Clin* 1996; 14:713–721.
18. Kaufman KD. Long-term (5-year) multinational experience with finasteride 1 mg in the treatment of men with androgenetic alopecia. *Eur J Dermatol* 2002; 12:38–49.
19. Gibbons RD. Computer-aided quantification of scalp hair. *Comp Dermatol* 1986; 627–640.
20. Gibbons RD, Fiedler-Weiss VC, West DP, Lapin G. Quantification of scalp hair—a computer-aided methodology. *J Invest Dermatol* 1986; 86:78–82.
21. Guarrera M, Ciula MP. A quantitative evaluation of hair loss: the phototrichogram. *J Appl Cosmetol* 1986; 4:61–66.
22. Hayashi S, Miyamoto I, Takeda K. Measurement of human hair growth by optical microscopy and image analysis. *Br J Dermatol* 1991; 125:123–129.

23. Van Neste DJJ, Dumortier M, De Brouwer B, De Coster W. Scalp immersion proxigraphy (SIP): an improved imaging technique for phototrichogram analysis. *J Eur Acad Dermatol Venerol* 1992; 1:187–191.
24. Courtois M, Loussouarn G, Hourseau C, Grollier JF. Hair cycle and alopecia. *Skin Pharmacol* 1994; 7:84–89.
25. Van Neste D, De Brouwer B, De Coster W. The phototrichogram: analysis of some technical factors of variation. *Skin Pharmacol* 1994; 7:67–72.
26. Guarrera M, Rebora A. Anagen hairs may fail to replace telogen hairs in early androgenic female alopecia. *Dermatology* 1996; 192:28–31.
27. Guarrera M, Semino MT, Rebora A. Quantitating hair loss in women: a critical approach. *Dermatology* 1997; 194:12–16.
28. Blume U, Ferracin I, Verschoore M, Czernielewski JM, Schaefer H. Physiology of the vellus hair follicle: hair growth and sebum excretion. *Br J Dermatol* 1991; 124:21–28.
29. Rushton DH, De Brouwer B, De Coster W, Van Neste D. Comparative evaluation of scalp hair by phototrichogram and unit area trichogram analysis within the same subjects. *Acta Derm Venereol (Stockh)* 1993; 73:150–153.
30. Van Neste DJJ, Rushton DH. Hair problems in women. *Clin Dermatol* 1997; 15:113–125.
31. Halloy J, Bernard BA, Loussouarn G, Goldbeter A. Modeling the dynamics of human hair cycles by a follicular automaton. *Proc Natl Acad Sci USA* 2001; 97:8328–8333.
32. Van Neste D, Dumortier M, De Coster W. Phototrichogram analysis: technical aspects and problems in relation to automated quantitative evaluation of hair growth by computer-assisted image analysis. In: Van Neste D, Lachapelle JM, Antoine JL, eds. *Trends in Human Hair Growth and Alopecia Research*. Lancaster: Kluwer Academic Publishers, 1989:155–165.
33. Headington JT. Histological findings in androgenic alopecia treated with topical minoxidil. *Br J Dermatol* 1982; 107(suppl 22):20–21.
34. Headington JT, Novak E. Clinical and histologic studies of male pattern baldness treated with topical minoxidil. *Curr Ther Res* 1984; 36:1098–1106.
35. Whiting DA. The value of horizontal sections of scalp biopsies. *J Cutan Aging Cosmet Dermatol* 1990; 1:165–173.
36. Headington JT. Telogen effluvium. New concepts and review. *Arch Dermatol* 1993; 129:356–363.
37. Whiting DA. Diagnostic and predictive value of horizontal sections of scalp biopsy specimens in male pattern androgenetic alopecia. *J Am Acad Dermatol* 1993; 28:755–763.
38. Whiting DA. Scalp biopsy as a diagnostic and prognostic tool in androgenetic alopecia. *Dermatol Ther* 1998; 8:24–33.
39. Tsuji Y, Ishino A, Hanzawa N, et al. Quantitative evaluations of male pattern baldness. *J Dermatol Sci* 1994; 7:136–141.
40. Courtois M, Loussouarn G, Hourseau C, Grollier JF. Ageing and hair cycles. *Br J Dermatol* 1995; 132:86–93.
41. Courtois M, Loussouarn G, Hourseau S, Grollier JF. Periodicity in the growth and shedding of hair. *Br J Dermatol* 1996; 134:47–54.
42. Ishino A, Uzuka M, Tsuji Y, Nakanishi J, Hanzawa N, Imamura S. Progressive decrease in hair diameter in Japanese with male pattern baldness. *J Dermatol* 1997; 24:758–764.
43. Rushton DH. Androgenetic alopecia in men: the scale of the problem and prospects for treatment. *Int J Clin Pract* 1999; 53:50–53.
44. Dawber R, Van Neste D. Hair and scalp disorders. In: *Common Presenting Signs, Differential Diagnosis and Treatment*. London: Martin Dunitz, 1995.
45. Rushton DH. *Chemical and Morphological Properties of Scalp Hair in Normal and Abnormal States*. UK: University of Wales, 1988.
46. Leroy T, Van Neste D. Contrast enhanced phototrichogram pinpoints scalp hair changes in androgen sensitive areas of male androgenetic alopecia. *Skin Res Technol* 2002; 8:106–111.
47. Van Neste D, De Coster W. Phototrichogram: technical problems in relation with automated quantitative evaluation of hair growth by computer assisted image analysis. *Nouv Dermatol* 1988; 7(suppl 1):56.

48. Lee T, Vincent NG, Gallagher R, Coldman A, McLean D. Dullrazor[®]: a software approach to hair removal from images. *Comput Biol Med* 1997; 27:533–543.
49. Hoffmann R. TrichoScan: combining epiluminescence microscopy with digital image analysis for the measurement of hair growth in vivo. *Eur J Dermatol* 2001; 11:362–368.
50. Van Neste D, Trüeb RM. Critical study of hair growth analysis with computer-assisted methods. *J Euro Acad Dermatol Venereol* 2006; 20:578–585.
51. Chamberlain AJ, Dawber RP. Methods of evaluating hair growth. *Australas J Dermatol* 2003; 44:10–18.
52. Van Neste D. Dynamic exploration of hair growth: critical review of methods available and their usefulness in the clinical trial protocol. In: Van Neste D, Lachapelle JM, Antoine JL, eds. *Trends in Human Hair Growth and Alopecia Research*. Lancaster: Kluwer Academic Publishers, 1989:143–154.
53. Van Neste D, Tobin DJ. Hair cycle and hair pigmentation: dynamic interactions and changes associated with aging. *Micron* 2004; 1:193–200.

Marie Lodén

*ACO HUD AB, Research & Development,
Upplands Väsby, Sweden*

INTRODUCTION

For centuries, dermatologists have depended on their eyes and fingers to assess visible and tactile changes of the skin. In most cases, this is sufficient for making a clinical diagnosis. An increased understanding of the skin surface is obtained using macrophotography (1) and scanning electron microscopy (SEM) of skin replicas (2). Skin surface topography is a mirror of the functional skin status and its evaluation is of great interest for dermatological research. Surface features of the skin can be quantified using computerized digital image analysis.

Visualization of morphological features not seen by the naked eye can be obtained using dermoscopy, which is a noninvasive diagnostic technique that links clinical dermatology and dermatopathology. Questions about deeper dermal or subdermal structures can be answered noninvasively by using imaging systems that do not rely on visible light, such as ultrasound, magnetic resonance imaging, and confocal laser scanning microscopy. Ultrasound measurements have been used to evaluate a variety of conditions affecting the thickness of the skin, such as acrosclerosis, morphea, psoriasis plaques, cutaneous edema in patch test reactions, and skin-prick histamine wheals (3–7). Ultrasound has also been utilized in the diagnosis and pretreatment evaluation of melanomas, vascular neoplasms, and basal cell carcinomas (BCCs). Structural data on the entire tissue volume can be displayed using three-dimensional (3D) ultrasonography (8).

One obvious advantage of noninvasive biophysical method is that they allow enhanced clinical examination and improved methods of analyzing, grading, and standardizing the results of the therapeutic effects without interfering with the studied area. The numerical data that are generated can be analyzed with more powerful statistical methods than can interval scales with fixed set of categories. Thus, the methods may reduce some of the problems that constitute a basic reason for the need for extensive clinical studies, and thus they may have a resource-saving effect. In this chapter, we will provide some insight into how visible and tactile changes of the skin surface in different diseases can be objectively quantified.

DRY SKIN IN ATOPIC PATIENTS

Clinical Presentation

Atopic dermatitis is a common, chronically relapsing skin disorder, usually beginning in childhood. The cardinal symptom is itching; and scratching may account for much of the clinical picture. In many patients with atopic dermatitis, the skin in noneczematous areas has a dry-looking appearance, i.e., a finely scaling, noninflamed skin surface, which feels rough to the touch (9). The feeling of roughness reflects a structural abnormality of the skin surface, with changes in the surface

morphology, as may be visualized by use of a replica technique and SEM (10). Dry skin of atopic patients is characterized by increased transepidermal water loss, reduced frictional resistance, and reduced skin capacitance (indicative of low skin hydration) (11).

Quantification of Skin Surface

A new image analysis device was recently developed which can collect the micro-relief lines and provide values of local skin capacitance (12). Moreover, the surface features of dry atopic skin have been quantified and compared with those of nonatopic, clinically normal skin using a replica technique (10). The replicas were taken on the back in 10 females (aged 18–40 years, mean 29). All atopic subjects, as assessed by the criteria of Hanifin and Rajka (13), had dry skin in that area, defined as a rough, finely scaling, noninflamed skin surface. Ten females (aged 18–40 years, mean 29) without any kind of atopy or dry skin served as controls. The replicas were analyzed by collecting 75 parallel profile traces (interval 40 μm) within an area of 6.0 mm \times 3.0 mm. These data were then used to calculate texture parameters and to build up a 3D reconstruction of the skin microtopography (10).

SEM of replicas and 3D reconstruction of the topography showed that the dry atopic skin was rougher than normal skin (Fig. 1). The dry atopic skin had a significant increase in the roughness parameters R_a , R_{qz} and R_y and a decrease in the number of peaks/cm (R_n), indicating higher but fewer peaks than in normal skin. Both atopic and normal skin exhibited a negative skewness, indicating that

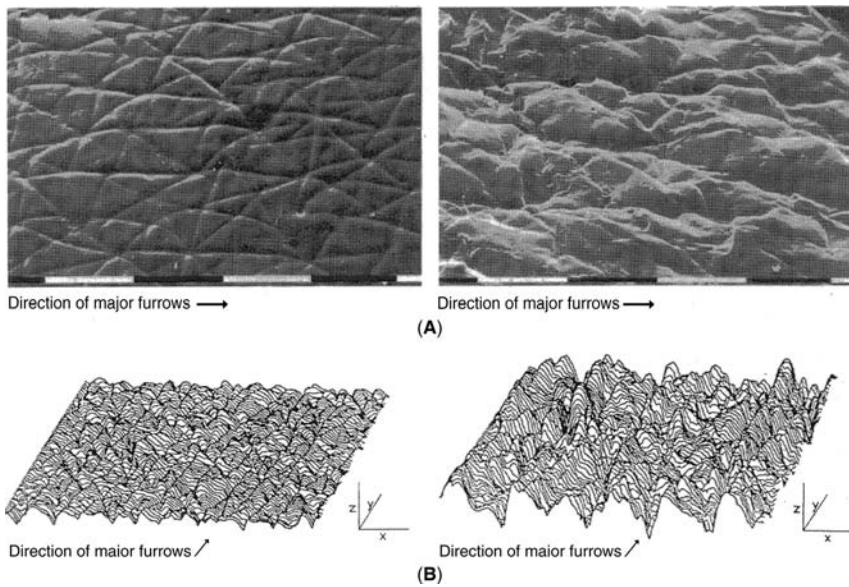


FIGURE 1 (A) Scanning electron micrographs of replicas from normal (*left*) and dry atopic (*right*) skin (bar 1 mm). (B) Three-dimensional reconstruction of the same replicas ($X = x9$, $Y = x9$, $Z = x45$). Note that the major furrows in the micrographs are perpendicular to those in the three-dimensional reconstructions. *Source:* From Ref. 10.

the skin relief is mainly formed of plateaus, as may be expected from the visual appearance of the skin topography. No significant difference was found between atopic and normal skin regarding skewness. Also, the values for Δa and kurtosis were similar. These results indicate that normal and dry atopic skin have approximately the same profile, which is further substantiated by the finding that the two bearing area curves were almost overlapping (10).

The resolution of atopic eczema has been studied in a patient by means of negative surface impressions with a rubber-based dental impression material (14). Electron micrographs and a programmed computer-assisted image analysis of the topographical changes were found to be sufficiently sensitive to show a numerical difference between grossly lesional and clinically normal skin. The middle range values representing the triangular unit structures were lost, but returned as the skin became clinically normal (14).

The roughness parameters R_a , R_z , and R_{max} have also been shown to differ between healthy areas and chronic eczema using fast optical *in vivo* topometry of human skin (15). The method uses computer-assisted strip analysis to process information gathered from high-speed, noncontact scanning of the 3D microstructures of the skin (15). Moreover, a significant correlation was found between changes in "positive" and "negative" volume of the skin and a smoothing of the skin was seen after 14 days of treatment with standard ointments (15).

No differences in surface topography (R_a and R_y) were found between clinically normal skin of patients with atopic dermatitis and nonatopic normal skin in a study with use of profilometry (16). However, in another study on atopic patients with high disease activity, it was found that clinically normal-appearing skin differed from nonatopic normal skin in surface morphology, as characterized with a video-microscope. A variation coefficient score that reflected the irregularity of skin ridges, named the surface irregularity index, differed between the normal-appearing skin in the atopics and normal skin in nonatopics (17).

PSORIATIC PLAQUES

Clinical Presentation

Psoriasis has many different clinical forms, the most common being "psoriasis en plaque," with characteristic scaling and a well-defined edge. The size of the lesions may vary from a few millimeters to very extensive plaques. The thick plaque displays a waxy appearance upon scratching. The clinical spectrum of psoriasis also includes variants, which lack the characteristic scaling, such as inverse psoriasis, napkin psoriasis, pustular lesions, and erythrodermic psoriasis.

Quantification of the Skin Surface

The skin roughness in psoriasis has been examined by taking a skin surface biopsy sample by placing cyanoacrylate adhesive on a glass microscope and then pressing this glass slide against the area to be sampled (18). The biopsy sample, consisting of a layer of stratum corneum several cell layers thick, was then analyzed with a surfometer by moving a stylus along the surface and recording the movements on a moving chart. On analysis of such skin surface, biopsy samples from psoriatic lesions in six patients, a considerable difference in the topography was found compared to normal skin (18). The tracings were irregular and "spiky."

By means of skin profilometry, other authors studied the roughness parameters in psoriatic skin of five patients (mean age 46 years) (19). Examination of negative silicone rubber dental impression replicas of the plaques showed that R_a was significantly lower in psoriatic skin than in uninvolved skin (19). After 10 days of monotherapy with topical crude coal tar, no significant differences in the analyzed roughness parameters were observed, suggesting that profilometric analysis of psoriatic skin can be useful to follow the effects of topical therapy (19).

The degree of erythema of the psoriatic plaques has been measured with a narrow-band reflectance spectrophotometer (Derma-Spectrometer[®], Cortex, Hadsund, Denmark) and a tristimulus colorimeter (Choma Meter CR-200[®], Minolta, Osaka, Japan) (20). Fifty psoriatic plaques were studied in 10 patients after scoring the degree of scaling on them by visual inspection. In psoriasis with little scaling, the measured amount of erythema (E index and a^*) was about twice that on normal skin. As the scales became thicker, the lesions were significantly less reddish (decrease in E index and a^*) and brighter (increase in L^*). Thus, these parameters can be used for comparative studies of the therapeutic effects of topical agents when two or more plaques with the same degree of erythema and scaling have to be selected. However, the authors suggest that the parameters in themselves cannot be used as markers of the severity of the plaque, because they become rather close to those of the normal skin as the erythema becomes covered by thicker scales (20).

Color measurements have been used to follow the effects of a standardized treatment regimen with dithranol, sole-baths, and UV radiation (21). Fifty patients with stationary plaque-type psoriasis were studied. An increase in the L -value and a decrease in the a -value were found during the treatment, but the changes were not statistically significant. Possible reasons for these findings are that the UV therapy and the applied substances interfered with the color changes of the skin that resulted from the resolution of the plaques. However, measurement of the plaque size with the aid of computer-based image analysis proved useful for monitoring treatment effects (21).

Reflectance spectrophotometry has been used to measure changes in the skin hemoglobin and melanin contents during psoralens and ultraviolet A (PUVA) therapy (22). The results suggest that the nonvisible change in the erythema response pattern of the lesion can be measured and used as a basis for terminating PUVA therapy despite the presence of some psoriasis clinically.

THE ICTHYOSES

Clinical Presentation

The ichthyoses are a group of disorders of stratum corneum formation and desquamation, which share, as their main feature, marked scaling in the absence of inflammation. This gives rise to a pronounced change in the surface structure. There are several types, with differing modes of inheritance and clinical pictures. In *ichthyosis vulgaris* (autosomal dominant), the scales are usually small and whitish, and are most clearly observed on the limbs and back. In *lamellar ichthyosis* (autosomal recessive), the skin changes seen at birth consist of a smooth and shiny stratum corneum, which later on turns into persistent, large dark scales with little or no erythema.

Quantification of the Skin Surface

Attempts have been made to study the skin topography of patients with ichthyotic disorders by simple surfometry (18). In one patient with *lamellar ichthyosis*, a distinctive

surfometer tracings were obtained, whereas in one patient with dominant ichthyosis, one with "xeroderma," and one with ichthyosiform erythroderma the surfometer profiles were not easily distinguishable from those of normal skin (18).

PLAQUES OF MORPHEA

Clinical Presentation

Morphea is a localized form of scleroderma with pale indurated areas of the skin, which, especially in the central parts, have an ivory color with a smooth and shiny surface. On biopsy, the epidermis and the skin appendages in the mature lesions are atrophic and the collagen of the dermis hypertrophic. On stereomicroscopy of skin replicas of the plaques, smoothing and loss of the normal crease function can be observed, together with impaired sweat gland function (3).

Quantification of the Skin Surface

The skin relief of morphea plaques has been evaluated quantitatively by a stylus method on negative skin surface rubber base impression material (6). Eight patients with localized plaques and four with generalized morphea were studied (aged 33–77 years, mean 50). The mean duration of the morphea was 2.4 years and only plaques with the classical signs of scleroderma, i.e., a white color, induration, and thickening of the skin, were studied.

All the morphea plaques had a significantly lower value of roughness than their respective regional controls. The mean reduction in roughness was almost 60%. The roughness values of scleroderma skin were not correlated to the thickening or the duration of the plaques. It was proposed that the method could be useful in the clinical diagnosis of scleroderma and for documenting remission of morphea (6).

MELANOMA

Clinical Presentation

Melanoma is a malignant tumor of melanocytes, which normally give the skin its characteristic color. Initially the tumor spreads rapidly in the superficial skin layers, but soon vertical infiltration occurs into the dermis. Early detection and treatment are crucial for the prognosis.

The diagnosis of skin tumors using noninvasive diagnostic tools are becoming increasingly reliable and popular among physicians and patients (23). Dermoscopy and sonography add useful information to the clinical constellation, improving the diagnostic performance for early diagnosis of melanoma, and for differentiating various melanocytic and nonmelanocytic pigmented lesions (23,24). A recent survey study among 1200 U.S. dermatologists showed that 57% used a magnifying lens and only 17% used a dermoscope to aid in clinical assessment. A large percentage of physicians (78.9%) preferentially used dermatopathologists for the evaluation of the majority of pigmented lesions. Considerable variability existed in the clinical concept and management of melanoma in situ (25).

Quantification of the Skin Surface

Potential diagnostic characteristics of malignant melanoma include color, shape, size, regularity of outline, and distinctness of the boundary with the surrounding

skin. Dermatoscopy allows the physician to discriminate between melanocytic and nonmelanocytic lesions with high diagnostic accuracy and to detect initial malignant melanomas (23,24). The overall shape of the lesions can be expressed by the "bulkiness" measure, and the irregularity of the border by two fractal dimension measures. The method was reported to produce correct classification with a sensitivity of 91% and a specificity of 69% (26). In another study, 16 of 18 melanomas, and 89% of pigmented lesions overall, were correctly classified by the image analysis system, compared with 83% on the basis of clinical grading of lesion characteristics (27). In the latter study, features relevant to size, color, shape, and boundary of each lesion were analyzed.

Tumor thickness is the most important prognostic factor for the prognosis of the malignant melanoma and the use of epiluminescence microscopic (ELM) dermatoscopy enhances the ability to study deeper structures in the skin. In epiluminescence microscope, oil is applied to the cutaneous lesion and a transparent material is then pressed over the lesion, which is examined under tangential illumination with magnification. This technique renders the epidermis more transparent so that structures at the dermal-epidermal junction and upper dermis may be visualized. The magnification power of these instruments is mostly up to 40-fold. The images can be captured and analyzed by a television camera attached to a computer; for a review see Ref. 28. The technique offers a variety of potential applications, such as assistance in the diagnosis of melanoma during screening, and maintenance and retrieval of images in patients with pigmented lesions who are being followed up clinically (28,29).

In addition to ELM, high-frequency ultrasound may improve the diagnostic accuracy by providing information about the depth and topographic location of skin tumors (30,31). More recently, near-infrared reflectance-mode confocal scanning laser microscopy (RCM) has been introduced for microscopic analysis of skin lesions, which enable a noninvasive modality for the diagnosis of BCC (32). Evaluation of clinically equivocal lesions by RCM revealed features characteristic of BCC, including tightly packed nests of elongated, monomorphic, polarized nuclei, and subjacent ectatic blood vessels with lymphocytes undergoing margination and rolling. Conventional histology confirmed the presence of BCC in all cases (32).

The reproducibility and validity of the diagnostic algorithms in assessing pigmented skin lesions have been evaluated via the Internet by 40 experienced dermatoscopists using a two-step diagnostic procedure. The first-step algorithm distinguished melanocytic versus nonmelanocytic lesions. The second step in the diagnostic procedure used four algorithms (pattern analysis, ABCD rule, Menzies method, and seven-point checklist) to distinguish melanoma versus benign melanocytic lesions. The results showed fair to good interobserver agreement for all diagnostic methods, but it was poor for the majority of dermatoscopic criteria. Intraobserver agreement was good to excellent for all algorithms and features considered. Pattern analysis allowed the best diagnostic performance (positive likelihood ratio: 5.1), whereas alternative algorithms revealed comparable sensitivity but less specificity. Interobserver agreement on management decisions made by dermatoscopy was fairly good.

MICROCOMEDONES

Clinical Presentation

Microcomedones are noninflammatory lesions consisting of follicular horny material that are visible upon close examination of the skin with a magnifying lens. They are present in acne patients and may also be found in persons without acne.

Quantification of the Skin Surface

Digital image analysis of skin surface biopsies has been developed for determining the number and size of follicular casts and microcomedones (33). The effects of a cosmetic product on comedogenesis and comedolysis were compared with those of benzoyl peroxide and miconazole nitrate. Evaluations were made on follicular biopsy samples taken every second month from the cheek at a site devoid of comedones on 31 men with acne (aged 18–23 years). As controls, 20 age- and sex-matched volunteers who had never had acne were enrolled. It was found that application of a cosmetic product increased the number and size of microcomedones, whereas treatment with benzoyl peroxide and miconazole nitrate resulted in microcomedolysis. Thus, digital image analysis of skin surface biopsy samples appears to be a sensitive method for documenting microcomedo formation and dissolution (33).

CONCLUSIONS

The inconvenient biopsy of the skin to obtain deeper information on skin pathology can often be replaced by the new highly developed noninvasive methods for evaluation of the skin physiology and pathology. For example, color changes of the skin surface can be analyzed by digital imaging of the skin and the topography of the skin can be quantified by digital imaging of shadows or profilometry.

Once a lesion is found and characterized in a patient, the techniques can provide numerical data to demonstrate a possible progression from diseased to healthy skin. However, the discipline is still young, and even the skilful researcher faces problems of relevance and interpretation of data. In other chapters of this book, valuable information about potential sources of error when employing the methods can be found. Validation, standardization, and controlled conditions will continuously enhance the benefit with the new important techniques.

REFERENCES

1. Wagner G, Goltz RW. Human cutaneous topography a new photographic technique: observations on normal skin. *Cutis: Cutan Med Pract* 1979; 23(6):830–842.
2. Ryan RL, Hing SA, Theiler RF. A replica technique for the evaluation of human skin by scanning electron microscopy. *J Cutan Pathol* 1983; 10(4):262–276.
3. Serup J. Localized scleroderma (morphoea): studies of eccrine gland function and skin microtopography. *J Dermatol* 1984; 11(3):269–276.
4. Serup J. Localized scleroderma (morphoea): thickness of sclerotic plaques as measured by 15 MHz pulsed ultrasound. *Acta Derm Venereol* 1984; 64(3):214–219.
5. Serup J, Staberg B, Klemp P. Quantification of cutaneous oedema in patch test reactions by measurement of skin thickness with high-frequency pulsed ultrasound. *Contact Dermatitis* 1984; 10(2):88–93.
6. Serup J. Assessment of epidermal atrophy in localized scleroderma (morphea). *Dermatologica* 1986; 172(4):205–208.
7. Serup J. Non-invasive quantification of psoriasis plaques—measurement of skin thickness with 15 MHz pulsed ultrasound. *Clin Exp Dermatol* 1984; 9(5):502–508.
8. Stiller MJ, Driller J, Shupack JL, Gropper CG, Rorke MC, Lizzi FL. Three-dimensional imaging for diagnostic ultrasound in dermatology. *J Am Acad Dermatol* 1993; 29(2 Pt 1): 171–175.
9. Linde YW. “Dry” skin in atopic dermatitis. A clinical study. *Acta Derm Venereol (Stockh)* 1989; 69:311–314.

10. Linde YW, Bengtsson A, Lodén M. "Dry" skin in atopic dermatitis. II. A surface profilometry study. *Acta Derm Venereol* 1989; 69(4):315–319.
11. Lodén M, Olsson H, Axell T, Linde YW. Friction, capacitance and transepidermal water loss (TEWL) in dry atopic and normal skin. *Br J Dermatol* 1992; 126(2):137–141.
12. Leveque JL, Querleux B. SkinChip, a new tool for investigating the skin surface in vivo. *Skin Res Technol* 2003; 9(4):343–347.
13. Hanifin JM, Rajka G. Diagnostic features of atopic dermatitis. *Acta Derm Venereol* 1980; 44(suppl 92):44.
14. Murphy R, Cotton DW, Wright AL, Bleehen SS. Computer-assisted image analysis of skin surface replicas. *Br J Dermatol* 1991; 124(6):571–575.
15. Piche E, Hafner HM, Hoffmann J, Junger M. FOITS (fast optical in vivo topometry of human skin): new approaches to 3-D surface structures of human skin. *Biomed Tech (Berl)* 2000; 45(11):317–322.
16. Gloor M, Nolzen F, Wirth H, Stuhler T. Hautoberflächenprofil, hautoberflächen lipide und zell-kinetische parameter in der epidermis. Untersuchungen an gesunden versuchspersonen und patienten mit neurodermitis atopica. *J Soc Cosmet Chem* 1985; 36:153.
17. Suehiro M, Hirano S, Ikenaga K, Katoh N, Yasuno H, Kishimoto S. Characteristics of skin surface morphology and transepidermal water loss in clinically normal-appearing skin of patients with atopic dermatitis: a video-microscopy study. *J Dermatol* 2004; 31(2):78–85.
18. Marks R, Pearse AD. Surfometry. A method of evaluating the internal structure of the stratum corneum. *Br J Dermatol* 1975; 92(6):651–657.
19. Monti M, Bozzetti M, Motta S, Barbareschi M. Usefulness of surface topography analysis in psoriatic skin. *Acta Derm Venereol Suppl (Stockh)* 1989; 146:81–83.
20. Takiwaki H, Serup J. Measurement of color parameters of psoriatic plaques by narrow-band reflectance spectrophotometry and tristimulus colorimetry. *Skin Pharmacol* 1994; 7(3):145–150.
21. Hoffmann K, Dirschka T, Schwarze H, et al. 20 MHz sonography, colorimetry and image analysis in the evaluation of psoriasis vulgaris. *J Dermatol Sci* 1995; 9(2):103–110.
22. Ryatt KS, Feather JW, Dawson JB, Cotterill JA. The usefulness of reflectance spectrophotometric measurements during psoralens and ultraviolet. A therapy for psoriasis. *J Am Acad Dermatol* 1983; 9(4):558–562.
23. Ruocco E, Argenziano G, Pellacani G, Seidenari S. Noninvasive imaging of skin tumors. *Dermatol Surg* 2004; 30(2 Pt 2):301–310.
24. Stolz W, Semmelmayr U, Johow K, Burgdorf WH. Principles of dermatoscopy of pigmented skin lesions. *Semin Cutan Med Surg* 2003; 22(1):9–20.
25. Charles CA, Yee VS, Dusza SW, et al. Variation in the diagnosis, treatment, and management of melanoma in situ: a survey of US dermatologists. *Arch Dermatol* 2005; 141(6):723–729.
26. Claridge E, Hall PN, Keefe M, Allen JP. Shape analysis for classification of malignant melanoma. *J Biomed Eng* 1992; 14(3):229–234.
27. Green A, Martin N, Pfitzner J, O'Rourke M, Knight N. Computer image analysis in the diagnosis of melanoma. *J Am Acad Dermatol* 1994; 31(6):958–964.
28. Sober AJ. Digital epiluminescence microscopy in the evaluation of pigmented lesions: a brief review. *Semin Surg Oncol* 1993; 9(3):198–201.
29. Saida T, Oguchi S, Ishihara Y. In vivo observation of magnified features of pigmented lesions on volar skin using video microscope. Usefulness of epiluminescence techniques in clinical diagnosis. *Arch Dermatol* 1995; 131(3):298–304.
30. Tacke J, Haagen G, Hornstein OP, et al. Clinical relevance of sonometry-derived tumour thickness in malignant melanoma—a statistical analysis. *Br J Dermatol* 1995; 132(2):209–214.
31. Dummer W, Blaheta HJ, Bastian BC, Schenk T, Brocker EV, Remy W. Preoperative characterization of pigmented skin lesions by epiluminescence microscopy and high-frequency ultrasound. *Arch Dermatol* 1995; 131(3):279–285.
32. Marra DE, Torres A, Schanbacher CF, Gonzalez S. Detection of residual basal cell carcinoma by in vivo confocal microscopy. *Dermatol Surg* 2005; 31(5):538–541.
33. Pierard GE, Pierard-Franchimont C, Goffin V. Digital image analysis of microcomedones. *Dermatology* 1995; 190(2):99–103.

Differentiation Between Benign and Malignant Skin Tumors by Image Analysis, Neural Networks, and Other Methods of Machine Learning

Michael Binder, Harald Kittler, and Hubert Pehamberger

Division of General Dermatology, Department of Dermatology, Medical University of Vienna, Währingergürtel, Vienna, Austria

Stephan Dreiseitl

Department of Software Engineering, Upper Austria University of Applied Sciences, Upper Austria, Austria

INTRODUCTION

Malignant melanoma of the skin is the fastest growing cancer in the Western world, with incidence rates in Caucasian populations increasing between 3% and 7% in recent years. This means that incidence rates will double every 10 to 25 years (1).

The most recent available data comparing global figures (2) shows, e.g., for Austria, an incidence rate (per 100,000 population) of 13.0 in males and 18.7 in females, respectively. This compares to the region with the highest rates in the world (Australia/New Zealand), at incidence rates of 49.0 in males and 38.7 in females. In this region, the cumulative lifetime risk of developing melanoma has been estimated to be as high as 5.7% (3).

An increased awareness of skin cancer and early detection methods have resulted in decreased mortality levels in some, but not all populations. While Australian, Northern American and Northern European populations have exhibited stable mortality rates (even though incidence rates are increasing), the same cannot be said for Central and Southern European populations, where mortality rates continue to rise, although at a slower pace than incidence rates (4).

While the early diagnosis of melanoma is beneficial for the patient, it is by no means easy for the dermatologist. Several studies have shown the unaided diagnostic performance of dermatologists to vary between 65% and 80% sensitivity (true positive rate) (5). Specificity values (true negative rates) are usually even lower. It is much more harmful to overlook an existing melanoma than to excise a suspicious lesion that then turns out to have been benign.

The correct diagnosis of pigmented skin lesions is further complicated by the fact that diagnosing lesions is not a purely dichotomous task. There are not only benign lesions (common nevi) and malignant lesions (cutaneous melanoma), but there also is a third class of atypical lesions. These lesions that are not (yet) malignant, but function as a precursor to melanoma or may at least be indicative to a higher melanoma risk.

Motivated by this uncommon diagnostic task and the unsatisfactory level of diagnostic performance, physicians developed new techniques that help them to

make more accurate diagnoses. Most prominent among these techniques is pattern analysis by epiluminescence microscopy or dermatoscopy (6–10). Nowadays dermatoscopy uses digital devices that are generally bundled with computer systems that serve as digital image repositories. The advantage of this approach is the ease with which the images can be manipulated (e.g., enlarged), archived and retrieved for follow-up consultations, and the ability to include computer decision support systems in the diagnostic process. A recent review of research findings using dermatoscopy is given as reference (11).

In numerous controlled experiments, it has been shown that dermatoscopy is well-suited to increase the diagnostic performance of dermatologists (11–13). It has however been noted that some training and experience is required to actually reap the benefits of this technology (14,15). As an added value, the simple availability of large data sets has led to the structured analysis of lesion images and subsequently to the derivation of a number of rules that aid in the diagnosis of cutaneous melanoma (16,17).

The most prominent of these rules, the ABCD rule (18), has become known even outside the field of dermatology, and is easy to apply for a broader medical community.

The benefit in diagnostic performance using dermoscopy has been observed in a number of studies (increase in sensitivity between 10% and 27%); a review is given in Ref. 17. There a comparison of the various rules show to have sensitivities in the range of 87% to 95% and specificities between 72% and 89% (with high sensitivities corresponding to low specificities and vice versa). The benefit of dermoscopy has created a demand for medical devices that provide the hardware (camera equipped with polarized light source, computer backend) for this diagnostic technique. As a result, a number of commercial vendors now offer these devices.

The availability of electronic data repositories quite naturally led to the goal of automated analysis of the lesion images. In fact, the first investigations into finding structures in lesion images predate the use of digital imaging technology (6,9). The rise of dermoscopy coincided with the rise in interest in using neural network algorithms for medical applications. The first diagnostic model in this domain was a neural network model (19). Since then, numerous machine learning algorithms were applied to this problem, with varying degrees of success.

DATA ACQUISITION AND PREPROCESSING

Image data is generally acquired using a commercially available digital epiluminescence microscopy device. Most of the systems available use a fixed-focus hand-held charge coupled device camera with polarized or nonpolarized light sources and suitable magnification ranging between 15- and 30-fold. In the computer system that supports the camera, a frame grabber card converts the images to digital format. At the time of writing, the majority of systems are using analog technology.

IMAGE SEGMENTATION

For the automated diagnosis of such lesions, a segmentation step of the area of interest (i.e., the pigmented lesion) is necessary to identify regions of interest in the images. In general, region-growing methods and in particular, thresholding

operations are suitable for the automated segmentation of lesion images. This is of importance since the lesions themselves tend to be darker than the surrounding skin (20). Attention must be given to hair that may obstruct the lesion and complicate the segmentation process. Some of the algorithms used are capable of eliminating these artifacts. In general, the automated segmentation method implemented, provides satisfactory results in more than 90% of all analyzed lesions. A similar level of performance was also achieved by our local research group (20).

FEATURE EXTRACTION

After the segmentation step has identified the lesion portion of the image. Image analysis methods are required to transform the RGB color information of the pixels into information that can be used by machine learning algorithms. Most of the features are motivated by the early pattern analysis literature of pigmented skin lesions (6). Generally, the features can be grouped into global and local descriptors (21). Global descriptors are mostly those that relate to size (perimeter, area, and diameter), shape (elongation, asymmetry, and roundness), border characteristics (gradient of color information between lesion and skin), and number of discernible colors. Local descriptors are statistical measures of local shape and color distributions (maximum, minimum, mean, standard deviation), calculated for each of the four quadrants obtained by dividing the lesion along its major and minor axis. Overall, more than 100 different features have been described and published extracted for each of the lesion images (20,22).

FEATURE SELECTION

In any finite data set for predictive modeling, there may be spurious correlations between the input variables (independent) and the target variables (dependent). Model quality may be improved by removing these variables, as the correlation (if it is indeed spurious) will not be exhibited by new data, and thus may limit the ability of the model to generalize well.

There is a large amount of literature on feature selection methods, both as a preprocessing step (independent of any specific model building algorithm) and as a component of some machine learning algorithms.

VALUE OF CLINICAL INFORMATION

The diagnosis of pigmented skin lesions can be thought of as a visual discipline. The physician assesses the malignancy of a lesion by visual inspection, without the need to consult laboratory tests or other sources of information. This impression, however, is only partly correct. A patient presenting to a physician conveys a wide range of information, even before particular lesions are shown. Information of this sort (among others: age, skin condition, skin type, or number of visible lesions) is not available when the lesion (or a lesion image) is the only source of diagnostic information. It is therefore not surprising that the study (23) in *in vivo* dermoscopy is found to perform better than that done in purely image-based dermoscopy, where the patient is not present and his or her clinical information can therefore not be included (even subconsciously) in the diagnostic process. Our own study (24) had come to the same conclusion. A neural network using clinical information as additional input was able to distinguish more

accurately between benign and malignant lesions rather than a neural network using only lesion-specific features. This is an important finding for telemedical applications of dermoscopy, both with and without computer decision support.

MODEL BUILDING

In medical decision support settings, two models have traditionally been favored over all others; decision trees and logistic regression models. This can be attributed to the fact that both models are in some sense “interpretable,” i.e., a human can look at the model (and not just the model output!) and choose to agree or disagree with it. For decision trees, translating the branching structure into explicit “if-then rules” yields an immediate humanly understandable format. Unfortunately, in a comparative study of different machine learning algorithms on the pigmented skin lesion (PSL) classification task (25) we found that the performance of decision trees is not comparable to that of other machine learning algorithms. This may, among others, be due to the fact that the discretization step required for tree construction removes too much information from the continuous-valued features in the PSL data set. Logistic regression models performed rather well in this study. The major characteristics of this model class are briefly summarized below.

The two other machine learning models that are currently considered state-of-the-art for classification problems, and which also performed well in the study (25), are: (i) artificial neural networks (ANNs), and (ii) support vector machines (SVMs). In contrast to logistic regression, these two models do not have interpretable parameters; the validity of such models cannot, therefore, be checked by human inspection. Nevertheless, the impressive classification performance of ANNs on a variety of medical data sets have made them, along with logistic regression, the de-facto standard for medical classification problems. A methodological review and hints to their correct use in modeling problems is given in the paper (25). Given the only recent addition of SVMs to the tool set of machine learning, it is not surprising that there have not been many studies using SVMs on medical databases.

LOGISTIC REGRESSION

Logistic regression modeling techniques have a long and rich tradition of applications in the medical domain (26). Logistic regression is a linear model in the sense that the decision boundary of points separating the two classes is an $(n-1)$ -dimensional affine hyperplane in the data space.

Therefore, the coefficients give an indication of how important the covariates are for the model. Even large changes in the corresponding covariate will have little effect on the model output, and vice versa. It is this interpretation that makes logistic regression modeling valuable for medical applications, because it allows a physician to check the plausibility of the model by cross-validating it with his or her own assessments and prior knowledge.

ARTIFICIAL NEURAL NETWORKS

From a statistical point of view, ANN models can be seen as generalizations of logistic regression models. Of course this was not the motivating factor for ANN

research which, starting with the seminal work (27), even predates other artificial intelligence research directions. Rather, the motivation was taken from organic brains, and the way that they store and process information. In this work, the focus will be on feedforward multilayer perceptrons. This is the most common ANN paradigm in medical applications, to the point that ANNs and multilayer perceptrons are being used synonymously in most of the biomedical informatics literature.

A comparison of the relative merits of the ANN and logistic regression modeling paradigm in medical application areas is given in (26). Actual health benefits arising from the use of neural networks in medicine are discussed in (28). In its mathematical abstraction, a single neuron (perceptron) calculates its output as an activation function of the weighted sum of inputs it receives. In most applications, the activation function is either a sigmoidal function (the logistic function $f(x) = 1/(1 + e^{-x})$) or the hyperbolic tangent or the identity function. The functional form of a single neuron with logistic activation function is thus exactly the same as the logistic regression model.

The nonlinear nature and higher flexibility of ANNs is due to the interaction of several neurons. In feedforward multilayer perceptrons and the signal flow is in one direction only.

Because the inputs to the output neuron depend on the network inputs in a nonlinear manner, the decision boundary for ANNs is nonlinear.

Compared to logistic regression, the problem of overfitting the model is even more pronounced with neural networks, given their nonlinear and thus more flexible functional form.

SUPPORT VECTOR MACHINES

SVMs are the most recent addition to the set of machine learning algorithms considered here. Interest in this paradigm has been rising steadily since the first technical papers were published in the 1990s. Several of the key concepts of SVMs had been considered earlier, but not in combination. The classical works on statistical learning theory is the theory underlying the SVM algorithm (29). Due to the generally slower nature of the medical researchers in using new algorithms, there are not many applications of SVMs on medical data sets, and no review is yet published. Our own work (25) and another publication (30) were the first to compare SVMs with other learning paradigms in a medical domain. The bioinformatics field however, has been faster in adopting SVMs, mainly for the promise of being able to build robust models from data sets with many more variables than cases. A review of SVM models in bioinformatics applications is given in (29,31,32).

APPLYING COMPUTER DIAGNOSIS ON MELANOMA AND PIGMENTED SKIN LESIONS

The most important question for the practicing clinician is less theoretically oriented. How well do computerized systems perform? Is their application useful, efficient and safe? Recent research developments have raised expectation that in the near future there will be the strong diagnostic support by a machine available (22,33). Ideally this machine should be equally or better than an experienced clinician.

During the last few years, numerous articles have been published in this field. This led our group to perform a formal meta-analysis in order to critically

review the contemporary literature on computer diagnosis of melanoma. The main advantage of formal meta-analysis is the provision of quantitative data on the issue investigated (34).

A total of 30 studies (the original articles are not listed here, but can be easily reviewed in our paper) met the inclusion criteria for this metaanalysis. The pooled sample size included 11,849 lesions. The prevalence of melanoma ranged between 1.8% and 60% depending on the study. Nineteen out of 30 studies (63%) included atypical/dysplastic nevi. Only eight studies reported the average thickness of melanoma according to Breslow, which ranged from 0.5 to 0.75 mm. Ten studies included also melanoma in situ. Seventeen (57%) studies used dermoscopic images. Histopathologic diagnosis by consensus was established by just three studies. As shown above, the image analysis approach is no longer a substantial problem. Twenty studies (67%) used fully automatic segmentation. The number of extracted features ranged from 3 to 822 (1 study). The median of extracted features was 18. About half of the studies (16 studies, 53%) used the classic approach of training set and test set. Eleven studies (37%) used cross-validation. Only four studies used ANNs for the analysis of data. The remaining studies applied various other methods such as discriminant analysis, logistic regression, k-nearest neighbor and regression trees.

The summary logit of the computer diagnosis for melanoma calculated with a fixed-effect model was 3.36 (95%, confidence interval 1.97–4.74).

Based on 10 studies, which provided sensitivity and specificity directly, the performance of the computerized systems was statistically not different from human performance.

Another interesting study has been published in 2003 (33). Hoffmann et al. report the results from a large European multicenter study called Diagnostic and Neural Analysis of Skin Cancer. Based on a training dataset of 2218 pigmented skin lesions, 2465 dermoscopic images were used for segmentation and analysis. The performance is given as area under the receiver-operator curve and reaches 0.844 for all lesions the set.

Recently the trend goes towards the analysis of more subtle feature of pigmented skin lesion and melanoma. The value of color information has been underestimated so far. Seidenari and coworkers recently published a set of studies focusing on distinct features of color within the lesion which are not discernible by the human eye (35–37).

CONCLUSION

A superficial analysis of the current literature could suggest that computer-aided diagnosis of pigmented lesions is ready for routine application. A more critical approach suggests that many of the studies need to be interpreted with caution. Many of the studies still have a number of methodological flaws, which do not allow generalizing their optimistic results. In most of the studies, a preselection of melanocytic pigmented skin lesions has been made. In most studies, pigmented seborrheic keratoses have been excluded a priori. Clinically however, even specialists may mistake pigmented seborrheic keratosis for melanocytic lesion. Selection bias is another problem of most current studies. In many cases, the lesions fed into the computerized system have been preselected for technical or practical reasons. For instance, hypopigmented lesions will hardly achieve sufficient results during the segmentation step and are therefore less frequently used.

For future experiments, we suggest the development of a unifying study guideline. Such a guideline should be developed mutually by the "dermoscopic" community.

During the last decade, substantial progress has been made in the field of computer aided diagnosis of pigmented skin lesions. It is, however, too early to implement these system into clinical routine. Controlled multicenter trials should be carried out to evaluate the validity of such systems

REFERENCES

1. Garbe C, McLeod GR, Buettner PG. Time trends of cutaneous melanoma in Queensland, Australia and Central Europe. *Cancer* 2000; 89(6):1269–1278.
2. Cancer Incidence, Mortality and Prevalence Worldwide. IARC Cancer Base No. 5, Version 2.0, 2005.
3. Jones WO, Harman CR, Ng AK, Shaw JH. Incidence of malignant melanoma in Auckland, New Zealand: highest rates in the world. *World J Surg* 1999; 23(7):732–735.
4. Severi G, Giles GG, Robertson C, Boyle P, Autier P. Mortality from cutaneous melanoma: evidence for contrasting trends between populations. *Br J Cancer* 2000; 82(11):1887–1891.
5. Miller M, Ackerman AB. How accurate are dermatologists in the diagnosis of melanoma? Degree of accuracy and implications. *Arch Dermatol* 1992; 128(4):559–560.
6. Pehamberger H, Steiner A, Wolff K. In vivo epiluminescence microscopy of pigmented skin lesions. I. Pattern analysis of pigmented skin lesions. *J Am Acad Dermatol* 1987; 17(4):571–583.
7. Pehamberger H, Binder M, Steiner A, Wolff K. Early recognition and prognostic markers of melanoma. *Melanoma Res* 1993; 3(4):279–284.
8. Pehamberger H, Binder M, Steiner A, Wolff K. In vivo epiluminescence microscopy: improvement of early diagnosis of melanoma. *J Invest Dermatol* 1993; 100(3):356S–362S.
9. Steiner A, Pehamberger H, Wolff K. In vivo epiluminescence microscopy of pigmented skin lesions. II. Diagnosis of small pigmented skin lesions and early detection of malignant melanoma. *J Am Acad Dermatol* 1987; 17(4):584–591.
10. Steiner A, Binder M, Schemper M, Wolff K, Pehamberger H. Statistical evaluation of epiluminescence microscopy criteria for melanocytic pigmented skin lesions. *J Am Acad Dermatol* 1993; 29(4):581–588.
11. Massone C, Di SA, Soyer HP. Dermoscopy for skin cancer detection. *Curr Opin Oncol* 2005; 17(2):147–153.
12. Bafounta ML, Beauchet A, Aegerter P, Saiag P. Is dermoscopy (epiluminescence microscopy) useful for the diagnosis of melanoma? Results of a meta-analysis using techniques adapted to the evaluation of diagnostic tests. *Arch Dermatol* 2001; 137(10):1343–1350.
13. Pizzichetta MA, Argenziano G, Talamini R, et al. Dermoscopic criteria for melanoma in situ are similar to those for early invasive melanoma. *Cancer* 2001; 91(5):992–997.
14. Binder M, Schwarz M, Winkler A, et al. Epiluminescence microscopy. A useful tool for the diagnosis of pigmented skin lesions for formally trained dermatologists. *Arch Dermatol* 1995; 131(3):286–291.
15. Kittler H, Pehamberger H, Wolff K, Binder M. Diagnostic accuracy of dermoscopy. *Lancet Oncol* 2002; 3(3):159–165.
16. Argenziano G, Soyer HP, Chimenti S, et al. Dermoscopy of pigmented skin lesions: results of a consensus meeting via the Internet. *J Am Acad Dermatol* 2003; 48(5):679–693.
17. Blum A. Pattern analysis, not simplified algorithms, is the most reliable method for teaching dermoscopy for melanoma diagnosis to residents in dermatology. *Br J Dermatol* 2004; 151(2):511–512.
18. Stolz W, Landthaler M. Classification, diagnosis and differential diagnosis of malignant melanoma. *Chirurg* 1994; 65(3):145–152.

19. Binder M, Steiner A, Schwarz M, Knollmayer S, Wolff K, Pehamberger H. Application of an artificial neural network in epiluminescence microscopy pattern analysis of pigmented skin lesions: a pilot study. *Br J Dermatol* 1994; 130(4):460–465.
20. Ganster H, Pinz A, Rohrer R, Wildling E, Binder M, Kittler H. Automated melanoma recognition. *IEEE Trans Med Imaging* 2001; 20(3):233–239.
21. Seidenari S, Pellacani G, Martella A. Acquired melanocytic lesions and the decision to excise: role of color variegation and distribution as assessed by dermoscopy. *Dermatol Surg* 2005; 31(2):184–189.
22. Blum A, Luedtke H, Ellwanger U, Schwabe R, Rassner G, Garbe C. Digital image analysis for diagnosis of cutaneous melanoma. Development of a highly effective computer algorithm based on analysis of 837 melanocytic lesions. *Br J Dermatol* 2004; 151(5):1029–1038.
23. Carli P, De Giorgi V, Nardini P, Mannone F, Palli D, Giannotti B. Melanoma detection rate and concordance between self-skin examination and clinical evaluation in patients attending a pigmented lesion clinic in Italy. *Br J Dermatol* 2002; 146(2):261–266.
24. Binder M, Kittler H, Dreiseitl S, Ganster H, Wolff K, Pehamberger H. Computer-aided epiluminescence microscopy of pigmented skin lesions: the value of clinical data for the classification process. *Melanoma Res* 2000; 10(6):556–561.
25. Dreiseitl S, Ohno-Machado L, Kittler H, Vinterbo S, Billhardt H, Binder M. A comparison of machine learning methods for the diagnosis of pigmented skin lesions. *J Biomed Inform* 2001; 34(1):28–36.
26. Dreiseitl S, Ohno-Machado L. Logistic regression and artificial neural network classification models: a methodology review. *J Biomed Inform* 2002; 35(5–6):352–359.
27. McCulloch W, Pitts W. A logical calculus of ideas immanent in nervous activity. *Bull Math Biophys* 1943; 1(5):115–133.
28. Lisboa PJ. A review of evidence of health benefit from artificial neural networks in medical intervention. *Neural Net* 2002; 15(1):11–39.
29. Vapnik V, Chapelle O. Bounds on error expectation for support vector machines. *Neural Comput* 2000; 12(9):2013–2036.
30. Miwakeichi F, Ramirez-Padron R, Valdes-Sosa PA, Ozaki T. A comparison of non-linear non-parametric models for epilepsy data. *Comput Biol Med* 2001; 31(1):41–57.
31. Wei L, Yang Y, Nishikawa RM, Jiang Y. A study on several machine-learning methods for classification of malignant and benign clustered microcalcifications. *IEEE Trans Med Imaging* 2005; 24(3):371–380.
32. Yang ZR. Biological applications of support vector machines. *Brief Bioinform* 2004; 5(4):328–338.
33. Hoffmann K, Gambichler T, Rick A, et al. Diagnostic and neural analysis of skin cancer (DANAOS). A multicentre study for collection and computer-aided analysis of data from pigmented skin lesions using digital dermoscopy. *Br J Dermatol* 2003; 149(4):801–809.
34. Rosado B, Menzies S, Harbauer A, et al. Accuracy of computer diagnosis of melanoma: a quantitative meta-analysis. *Arch Dermatol* 2003; 139(3):361–367.
35. Pellacani G, Grana C, Cucchiara R, Seidenari S. Automated extraction and description of dark areas in surface microscopy melanocytic lesion images. *Dermatology* 2004; 208(1):21–26.
36. Seidenari S, Pellacani G, Grana C. Pigment distribution in melanocytic lesion images: a digital parameter to be employed for computer-aided diagnosis. *Skin Res Technol* 2005; 11(4):236–241.
37. Seidenari S, Pellacani G, Grana C. Colors in atypical nevi: a computer description reproducing clinical assessment. *Skin Res Technol* 2005; 11(1):36–41.

Early Detection of Melanoma by Image Analysis

Stefania Seidenari and Giovanni Pellacani

Department of Dermatology, University of Modena and Reggio Emilia, Italy

Costantino Grana

*Department of Computer Engineering, University of Modena
and Reggio Emilia, Italy*

The worldwide incidence of cutaneous melanoma has increased dramatically over the past decades (1). It is well known that a good prognosis of melanoma is only expected for thin lesions. Preventive effort has therefore been concentrated on identification of early lesions facilitated by the introduction and dissemination of standardized clinical criteria and by the use of dermoscopy (epiluminescence microscopy) (2). However, the interpretation of dermoscopic criteria is often confusing especially for the inexperienced observer (3), and whereas in specialized centers the diagnostic accuracy doesn't seem to be higher than 60% to 85% (4), for untrained dermatologists it is often considerably lower (5).

To further improve diagnostic accuracy and develop better diagnostic technology for the assessment of pigmented skin lesions, digital imaging associated to image analysis has been introduced. Systems for machine-aided diagnosis are based on the translation of morphological parameters into mathematical terms (6–8). These provide the quantitative characterization of significant features of melanocytic lesion images, introducing objectivity and reproducibility in the diagnostic process. Image-generated data undergo statistical classification as a basis for differentiation between malignant and benign lesions. When employed by expert dermatologists, computer-assisted imaging systems may provide a support to dermoscopic diagnosis leading to further improvement in diagnostic accuracy for melanoma.

What does a computer-made diagnosis rely on, and which image features are most important in mathematical terms for the diagnostic process? To answer these questions, we can compare the way dermatologists make a diagnostic decision to the manner mathematical parameters extracted by image analysis are transformed into a global score suggesting a diagnosis or an operational decision.

Human diagnosis on a melanocytic lesion image is based initially on a global evaluation of the image and its comparison with mental stereotypes corresponding to different diagnostic groups. Mental categories derive from experience and elaboration, i.e., observation of lesion images, selection and memorization of determinant features, correlation of the latter to diagnostic standards (histology) and, finally, lesion classification for diagnosis. Especially when experience is lacking, a systematic analysis of the image with the attribution of scores to general features or particular patterns, followed by the summing up of single numbers to reach a global score indicating a diagnosis, may be helpful and instructive (9–13). Human diagnosis achieved employing these semiquantitative methods

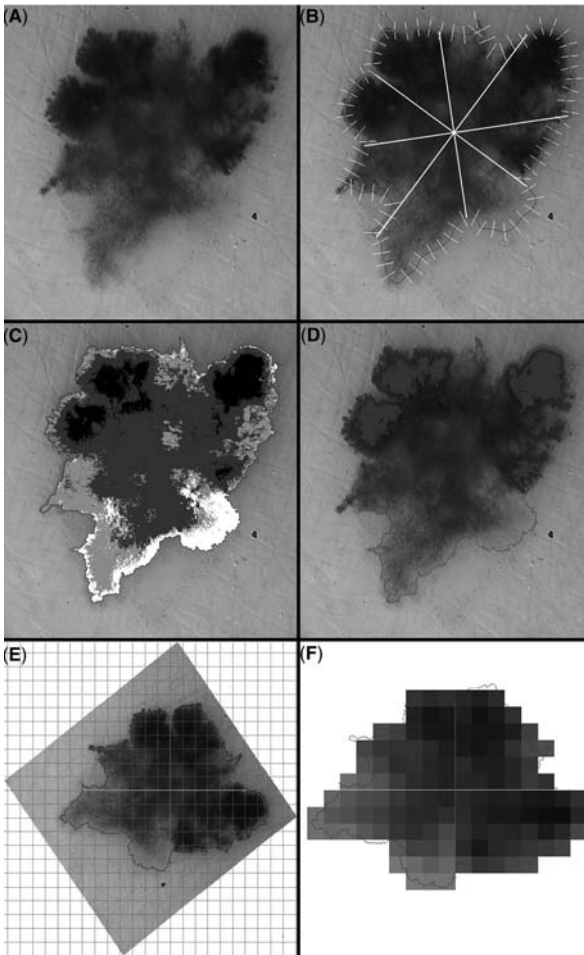


FIGURE 1 (See color insert) (A) Image analysis of a thin melanoma (Breslow's thickness 0.30 mm). (B) Border analysis. The red outline represents the sectors with an abrupt cut-off. (C) Color areas identification: the six main color groups are highlighted by false colors. (D) Absolute dark areas are highlighted in blue false-color. (E) For color asymmetry calculation, the lesion is oriented according to the major axis and divided in blocks with a predetermined area. (F) Each block belonging to the lesion is converted to the mean RGB color of that area for the calculation of the asymmetry parameters.

bears some similarities with the way computer programs perform the analysis of an image. In fact, computer diagnosis is based on the extraction of image features and their numerical description employing dedicated algorithms. Thus, not only is the presence/absence of certain aspects objectively described, but their quantitative evaluation is also given. A new mathematical semiology has been introduced for pigmented skin lesion image analysis, defining geometry, texture, pigment distribution and colors. Statistical elaboration of image-derived data based on neural networks or discriminant analysis, is then applied for translation of numbers into information easily accessible to the dermatologist (6–8).

The ABCD rule of dermoscopy, introduced by Stolz et al., represents the first semiquantitative algorithm and one of the most popular diagnostic methods. Four main diagnostic features for the calculation of a final score were identified, i.e., (i) asymmetry, (ii) abrupt border cut-off, (iii) colors, and (iv) differential structures (9).

Let us follow these diagnostic steps to make a comparison between clinical diagnosis and computer image analysis (Fig. 1).

THE "A" OF THE ABCD RULE: ASYMMETRY ASSESSMENT

Symmetry evaluation is considered crucial for melanoma diagnosis, both on a macroscopic and dermoscopic basis (9). In the ABCD rule for dermoscopy, the minimum final score indicating possible melanoma corresponds to 4.75, and asymmetry of microscopic features contributes by one-third (1 axis-asymmetry = 1×1.3) or two-thirds (2 axis-asymmetry = 2×1.3) to melanoma diagnosis. In the Tuebingen method for asymmetry assessment, both asymmetry of the outer shape and of the internal structure of the lesion are considered, and contribute by 25% to the overall score for a lesion to be classified as a melanoma (13).

According to ABCD rule, asymmetry is defined as the asymmetric distribution of shape, colors and dermoscopic structures with regard to two orthogonal axes. However, since for biological structures perfect symmetry does not exist, no definition of asymmetry can be precise enough to be unequivocally interpreted by different observers. Thus, the discriminating process is highly subjective, and different observers may have personal thresholds for asymmetry, and may disagree in a variable percentage of cases. Although the simultaneous consensus of several observers may probably establish a correct diagnosis, reproducibility of clinical judgment is often unsatisfactory. In a consensus net meeting on dermoscopy comparing the diagnostic accuracy of 40 observers, interobserver agreement on asymmetry showed a kappa value of 0.41, which is barely satisfactory, demonstrating that this way of assessing asymmetry is scarcely reproducible (4). Asymmetry assessment also represents a diagnostic clue for computer diagnosis. Similarly to the clinician, the computer evaluates shape, pattern, and color symmetry.

Shape Asymmetry

Shape symmetry can be calculated as the proportion of coincident points between the two halves of the image obtained along the major and minor axes (14). For defining a lesion asymmetric in shape, we have to set a threshold, e.g., 90% of coincident pixels, and a score can then be automatically attributed to each axis: 0 if equal or greater than 90% and one if lower. For each of these axes, a symmetry measure is then calculated, defined as the number of points that have a corresponding symmetric point with respect to the considered axis.

Pigmentation Asymmetry

The distribution of pigmentation too can be assessed by asymmetry measures. One possible method for its description is based on the quantification of the difference in brightness between the two halves of the lesion along the two main axes. The lesion is first converted into a luminance image. Subsequently, the mean luminance is obtained for each half lesion along the two main axes and the difference is calculated along the major and minor axes. Differences in brightness equal or greater

than 6 out of 256 luminance levels (gray scale) are considered the threshold for pigment asymmetry and one point score is automatically attributed to each axis (14).

Another method to assess pattern asymmetry is the evaluation of "relative" and "absolute" dark areas (15). These areas correspond to regions where pigmentation is more intense, and their presence greatly contributes to human perception of a lesion to be asymmetric. Image analysis programs easily extract absolute dark areas, corresponding to areas that are darker than the surrounding skin, and relative dark areas, corresponding to the darkest region in respect of the overall lesion brightness. Absolute dark areas describe the hyperpigmented regions inside the lesion and are not necessarily present (Fig. 1D), whereas relative dark areas describe the pigment distribution representing the darkest quartile of the lesion area and are always present (15).

The latter dark areas are obtained dividing the gray level histogram into four zones following an iterative process, that begins by partitioning the gray level histogram along the median value, and proceeds selecting the largest of the two halves. The process is repeated until the number of required zones is obtained. The zone corresponding to the lowest gray levels is considered the "relative dark area." In order to describe the dark area properties and extract a set of parameters, the lesion is divided into three zones each comprising eight sectors formed by the division along the major and minor axis and along directions shifted 45° to the left and to the right of the axes. This allows the search for correspondences between inner structures or between peripheral structures. The number of dark area pixels present in each sector and their distribution on each side of the axes are then evaluated, highlighting differences between benign and malignant lesions (15).

Color Asymmetry

Color asymmetry is also crucial for asymmetry assessment in the ABCD rule of dermoscopy. By image analysis this can be evaluated comparing average colors referring to image blocks situated at the two sides of the major and minor symmetry axes (Fig. 1E and F). To describe image color asymmetry, the average color inside each block is computed, considering only pixels belonging to the lesion. Subsequently, the Euclidean distance in the RGB color space of all symmetric blocks is compared. Since blocks of different size and different symmetry axes can be considered, the comparison of block colors at the same time provides information referring both to structure asymmetry (large blocks) and to lesion texture (small blocks) (16).

THE "B" OF THE ABCD RULE: BORDER EVALUATION

According to the ABCD rule of dermoscopy, to assign a dermoscopic score to the border, this should first be divided into eight segments; then the abrupt interruption of the border of the lesion for each segment should be established and a score of one for each abrupt interruption of the border segment should be assigned, whereas when the border segment gradually shades to the periphery no score points are attributed. However, it is sometimes difficult to establish if the border of a lesion is abrupt or if it shades into adjacent skin, and this uncertainty is expressed by the poor interobserver agreement reported by the consensus net meeting (4).

For computer assessment of lesion borders a similar method can be employed. An algorithmic reproduction of the "B" parameter of the ABCD rule

of dermoscopy, that automatically measures the number of segments with sharp cut-off was recently proposed by us (Fig. 1B) (17). In order to enable a correct evaluation of the contours also of lesions with deep indentations and irregular shape, luminance values along a direction normal to the contour at each point are considered. An interpolation approach based on Catmull-Rom spline curves is employed, to obtain a smoother outline. Skin lesion gradient is defined as the change in brightness from the lesion to the skin at each boundary point along a normally oriented segment centered on the boundary point. The "lesion slope" and "lesion slope regularity" are calculated on the entire boundary and on eight sectors for each lesion. "lesion slope," a descriptor of the overall intensity at the border, and "lesion slope regularity," related to the "nonhomogeneity" of the border cut-off, are higher in melanomas, objectively showing that malignant lesions are characterized by more abrupt and nonhomogeneous margins (14,17).

THE "C" OF THE ABCD RULE: COLORS

The assessment of colors is essential for melanoma diagnosis, both for pattern analysis on dermoscopic images, and when employing semiquantitative methods such as the ABCD rule of dermoscopy. According to this rule, we have to evaluate the presence of six possible colors (black, dark brown, light brown, red, white, and blue-gray); each color is scored one point and the sum is multiplied by 0.5. A blue, red, or white color component is more often present in melanomas with respect to nevi. Therefore, the detection of these colors within an image may have great diagnostic importance. Moreover, malignant lesions frequently show more than three colors, whereas in nevi, three or less than three colors are usually observed (18).

Our computer program assesses the number of colors which are included in an image with an approach mimicking the human perception of colors (Fig. 1C) (19). Moreover, it evaluates areas pertaining to homogeneous colors, describing their shape and distribution (20). The color palette employed in our image analysis program was interactively created by manually selecting square color patches of arbitrary size on different regions of interest pertaining to sample images, unequivocally showing black, dark brown, light brown, red, white, and blue-gray color components. For each selected color patch, an average RGB color was extracted by the program. Subsequently, color groups were formed, putting together color patches corresponding to the same color as perceived by the human observer, including a minimum number of color shades (patches) permitting a sufficiently accurate description of the color. The palette is then used to extract color regions from the images to be examined. Each pixel of the image is assigned to the color patch that minimizes its Euclidean distance in the RGB color space, then pixels belonging to the same group are merged together to form the region corresponding to a particular color. Thus, the presence/absence of a certain color region can be objectively described. Moreover, the color region can be characterized by extracting a set of parameters corresponding to its properties, e.g., extension, distance from the barycentre, spread, distribution in the internal and the external part of the lesion, and asymmetry (20,21).

THE "D" OF THE ABCD RULE: DIFFERENTIAL STRUCTURES

Pattern analysis and the identification of "differential structures" according to the ABCD rule of dermoscopy represent the basis for dermoscopic diagnosis of

melanoma, however, at present, no computer program for melanoma diagnosis is based on the identification of aspects such as globules, dots, vessels, regression etc. Software for the characterization of the net has recently been introduced, but its usefulness for differentiation of benign and malignant lesions has not been demonstrated so far (22). Moreover, in early melanoma, differential structures which are diagnostic for melanoma may be lacking, and architectural modifications often represent the earliest signs of malignant change (23,24).

Our method for assessment of "differential structures" is based on the evaluation of color distribution (25). The image is initially subdivided into homogeneous regions or blocks, which are obtained by a spatial reduction of the image and by its subdivision with a grid, to identify the blocks, which may be different in size and number. This procedure is similar to a reduction up to 1% of the original size. Thus, structural differences (i.e., details such as globules, dots, regression structures, areas of increased vascularization, or gray-blue areas etc.) are translated into color differences, and differential structures contribute to the color values within the image region/block they are included in. The distribution of these structures is then assessed by comparing the color distributions pertaining to different regions/blocks. Mean color distance, its variance, and maximum color differences are considered parameters useful for the differentiation of benign and malignant lesions. A large color distance between areas means that the lesion structure is nonhomogeneous and the architecture is complex. This corresponds to the presence of many different structures as assessed by the clinician when employing semi-quantitative methods.

COMPARISON BETWEEN HUMAN AND COMPUTER ASSESSMENT

When evaluating the diagnostic potential of a software for diagnosis and automated classification of melanocytic lesions, it is of utmost importance to compare its diagnostic performance with that of human observers.

Since 1995, we have studied the application and the generation of programs for image analysis for the elaboration of pigmented skin lesion images acquired by means of surface microscopy tools (7,14–17,19–21,25–28). Our first image analysis program, based on the numerical description of geometrical and color aspects of pigmented skin lesions, enabled the discrimination between malignant and benign pigmented skin lesions with a diagnostic accuracy greater than the one of an untrained clinician (7,27). Subsequently, we aimed at the creation of numerical descriptors of dermoscopic features mimicking the human perception of lesion images, thus more usable and intelligible by nonexpert clinicians. Algorithms for quantification of border gradient, segmentation of the lesion image into significant dark and color areas, and evaluation of structure and texture were developed, enabling a good distinction between malignant and benign lesions. To assess their diagnostic capacity and comprehensiveness, newly introduced algorithms were always compared with clinical judgment.

In a study assessing geometric descriptors of shape and lightness and employing clinical judgment of two experienced observers attributing scores to shape, pigment distribution and structure asymmetry, a good concordance between clinician and computer evaluation was achieved for both asymmetry parameters, with 89% and 75% concordant evaluations, respectively (14). For melanoma diagnosis, the pigment distribution asymmetry along two axes seemed the most striking parameter both for clinicians and computer. The human-computer

concordance for pigment distribution asymmetry was lower than the one observed for shape symmetry, since human and computer procedures were not directly comparable due to the fact that chromatic differences and pattern asymmetry were not taken into account.

An image analysis program for the numerical assessment of asymmetry in melanocytic lesions, based on evaluation and comparison of CIE $L^*a^*b^*$ color components inside image color blocks, describing color and structure variegation inside the lesion, was compared with the clinical judgment of asymmetry on 459 dermoscopic digital images of melanocytic lesions. Although human and computer evaluations showed a fair to good agreement, the software was able to better discriminate between benign and malignant lesions, indicating that 82% of melanomas and 33% of atypical nevi were asymmetric, in contrast with the clinical evaluation, which attributed 62% of melanomas and 45% of atypical nevi (25) to the "asymmetry" group.

To study the border and compare clinical and computer assessment, we analyzed 331 dermoscopic images investigating the border cut-off (14). An excellent concordance was observed between our computer method and the clinical evaluation, the computer B score not diverging much from the clinical one for the majority of cases, with 89.5% coincident evaluations.

Dermoscopic digital images of 331 melanocytic lesions underwent human assessment for the presence of the six colors of the ABCD rule of dermoscopy (19). Computer evaluation of type and number of colors was performed by the above mentioned color palette. A good concordance was obtained for computer and human evaluation, with the highest correlation coefficients observed for black, white and blue-gray, which also represented important colors for diagnosis.

In conclusion, it may be said that these data suggest that elaboration of melanocytic lesion images by means of a dedicated software improves diagnostic accuracy with respect to the simple examination of pigmented skin lesions by means of dermoscopic systems, and that this method could represent a useful tool for screening melanomas, to be used in outpatient locations not associated with expert centers, both minimizing unnecessary surgery for benign pigmented lesions, and enabling an accurate quantification of changes in size and shape of skin lesions during follow-up studies. It should be kept in mind, however, that computer-assisted diagnostic systems have been developed in order to assist (and not to replace) physicians in making a diagnosis, and that the decision making process becomes ideal when machine-derived information is managed by an experienced clinician.

REFERENCES

1. Hall HL, et al. Update on the incidence and mortality from melanoma in the United States. *J Am Acad Dermatol* 1999; 9:178.
2. Bafounta ML, et al. Is dermoscopy (epiluminescence microscopy) useful for the diagnosis of melanoma? Results of a meta-analysis using techniques adapted to the evaluation of diagnostic tests. *Arch Dermatol* 2001; 137:1343.
3. Stanganelli I, et al. Intraobserver agreement in interpretation of digital epiluminescence microscopy. *J Am Acad Dermatol* 1995; 33:584.
4. Argenziano G, et al. Dermoscopy of pigmented skin lesions: results of a consensus meeting via the internet. *J Am Acad Dermatol* 2003; 48:679.
5. Binder M, et al. Epiluminescence microscopy. A useful tool for the diagnosis of pigmented skin lesions for formally trained dermatologists. *Arch Dermatol* 1995; 131:286.

6. Binder M, et al. Epiluminescence microscopy-based classification of pigmented skin lesions using computerized image analysis and an artificial neural network. *Melanoma Res* 1998; 8:261.
7. Seidenari S, Pellacani G, Pepe P. Digital videomicroscopy improves diagnostic accuracy for melanoma. *J Am Acad Dermatol* 1998; 39:175.
8. Ganster H, et al. Automated melanoma recognition. *IEEE Trans Med Imaging* 2001; 20:233.
9. Stolz W, et al. ABCD rule of dermoscopy: a new practical method for early recognition of malignant melanoma. *Eur J Dermatol* 1994; 4:521.
10. Nachbar F, et al. The ABCD rule of dermoscopy. *J Am Acad Dermatol* 1994; 30:551.
11. Menzies SW, Ingvar C, McCarthy WH. A sensitivity and specificity analysis of the surface microscopy features of invasive melanoma. *Melanoma Res* 1996; 6:55.
12. Argenziano G, et al. Epiluminescence microscopy for the diagnosis of doubtful melanocytic skin lesions. Comparison of the ABCD rule of dermoscopy and a new 7-point checklist based on pattern analysis. *Arch Dermatol* 1998; 134:1563.
13. Blum A, Rassner G, Garbe C. Modified ABC-point list of dermoscopy: a simplified and highly accurate dermoscopic algorithm for the diagnosis of cutaneous melanocytic lesions. *J Am Acad Dermatol* 2003; 48:672.
14. Pellacani G, Grana C, Seidenari S. Algorithmic reproduction of asymmetry and border cut-off parameters according to the ABCD rule for dermoscopy. *J Eur Acad Dermatol Venereol*. In press.
15. Pellacani G, et al. Automated extraction and description of dark areas in surface microscopy melanocytic lesion images. *Dermatology* 2004; 203:21.
16. Seidenari S, Pellacani G, Grana C. Asymmetry in melanocytic lesion images: a computer description based on colour distribution. *Acta Dermatol Venereol* 2006; 86:123.
17. Grana C, et al. A new algorithm for border description of polarized light surface microscopic images of pigmented skin lesions. *IEEE Trans Med Imaging* 2003; 22:959.
18. MacKie RM, et al. The use of the dermatoscope to identify early melanoma using the three-colour test. *Br J Dermatol* 2002; 146:481.
19. Seidenari S, Pellacani G, Grana C. Computer description of colours in dermoscopic melanocytic lesion images reproducing clinical assessment. *Br J Dermatol* 2003; 149:523.
20. Pellacani G, Grana C, Seidenari S. Automated description of colours on surface microscopic images of melanocytic lesions. *Melanoma Res* 2004; 14:125.
21. Seidenari S, Pellacani G, Grana C. Colors in atypical nevi: a computer description reproducing clinical assessment. *Skin Res Technol* 2005; 11:36.
22. Anantha M, Moss RH, Stoecker WV. Detection of pigment network in dermoscopy images using texture analysis. *Comput Med Imaging Graph* 2004; 28:225.
23. Kittler H, et al. Follow-up of melanocytic skin lesions with digital epiluminescence microscopy: patterns of modifications observed in early melanoma, atypical nevi, and common nevi. *J Am Acad Dermatol* 2000; 43:467.
24. Menzies SW, et al. Short-term digital surface microscopic monitoring of atypical or changing melanocytic lesions. *Arch Dermatol* 2001; 137:1583.
25. Seidenari S, Pellacani G, Grana C. Pigment distribution in melanocytic lesion images: a digital parameter to be employed for computer-aided diagnosis. *Skin Res Technol* 2005; 11:236.
26. Seidenari S, et al. Computerized evaluation of pigmented skin lesion images recorded by a videomicroscope: comparison between polarizing mode observation and oil/slide mode observation. *Skin Res Technol* 1995; 1:187.
27. Seidenari S, Pellacani G, Giannetti A. Digital videomicroscopy and image analysis with automatic classification for detection of thin melanomas. *Melanoma Res* 1999; 9:163.
28. Pellacani G, Martini M, Seidenari S. Digital videomicroscopy with image analysis and automatic classification as an aid for diagnosis of Spitz nevus. *Skin Res Technol* 1999; 5:266.

Martin J. Behne

*Department of Dermatology and Venerology, University of Medical Center
Hamburg-Eppendorf, University of Hamburg, Germany*

INTRODUCTION

First descriptions of the surface acidity of human epidermis date back to the late 19th century (1). Initially, these reports describe pH as a physiologic variable (2), and later systematic observation of this parameter both in physiology and in disease revealed its connection to biochemical processes in epidermis (3–6). Similarly, a large section of literature is dedicated to pH variations in bodily areas (7), various population groups (8), and the influence of cosmetics and detergents on pH (9). Further, a number of animals display a similar surface acidity, justifying their frequent use as study objects in this field (10,11).

The importance of pH is illustrated through its role in the regulation of enzyme activity surrounding processes in epidermal barrier homeostasis (12–14). The formation of a competent epidermal barrier involves enzymatic processing of lipids secreted from lamellar bodies into the lower stratum corneum (SC) interstices. While this secretion is controlled by Ca^{2+} and K^{+} concentrations (15), the subsequent processing of lipids is regulated by fluctuations in pH (14). The hydrolases essential for extracellular processing of SC lipid precursors become inactive when SC is exposed to a neutral pH (14), consistent with their acidic pH optimum (6,16,17). pH is thought to play a similar role in other epidermal processes such as desquamation (5) and antimicrobial defense (18,19), although due to the complex interplay of the many enzymes and targets involved, the chain of events is not as clear.

While pH as a physical dimension is a measure of H^{+} ion concentration in aqueous media (20,21), the nature of pH in the dense, lipid- and protein-rich compartment of the SC, which is largely devoid of water, is a matter of debate. Yet, the more-than-a-century-long history of measurements has firmly established a characteristic range of pH values in healthy skin as a physiologic parameter, which is now routinely assessed.

Furthermore, since the first descriptions of pH in SC, theories about possible sources of acidity abound as much as roles proposed (22,23, and references therein). The rather recent observation of a pH gradient across the SC (24,25) even suggests a signaling role for pH. Nevertheless, this observation carries its own discussion about technical approach and the conclusions possible (26–28). Unfortunately, even some of the most long-standing and widely accepted theories surrounding these questions have not been rigidly tested, again, oftentimes, due to the complexity of processes involved and the general difficulty of studying epidermis in its interplay with SC. Lately, this debate has been renewed by a larger discussion about the nature of the epidermal barrier (29–31), where a significant barrier function of tight junctions in the stratum granulosum (SG) layer was found. Furthermore, there is a variety of theories surrounding more intricate questions of

lipid, protein, and solute arrangements in SC itself (32–34). In this setting, ever more importance must be placed on physically correct measurements in the established routine. Nevertheless, novel insights and progress in solving the larger questions should be expected with technological advances.

This review will try to give a brief overview of methods employed to measure and depict epidermal pH, with a discussion of advantages and disadvantages of established and experimental methods available. The ongoing discussion about the origin of SC acidity as well as the above-mentioned extensive discussion about the nature of the epidermal barrier are both beyond the scope of this review, although brief references must occasionally be made in order to place a given method in the context of ongoing research.

ESTABLISHED TECHNIQUE

Traditionally, pH in SC has been assessed using a planar glass electrode, where active and reference electrodes are combined in such a way that surfaces can be measured through the current between the two (35). Electrodes used for aqueous measurements differ from planar ones only in that active and reference electrodes are not arranged side-by-side, as solutes are accessible as a volume. The planar, “flat” arrangement, although necessary and convenient for surfaces, at the same time defines the limitation of its spatial resolution; a distance of approximately 4 to 5 mm is required for the electrodes arrangement, and any measured value must therefore represent an average across that distance. Distinction between intracellular and extracellular pH can therefore not be made, and x , y , or z directions are accessible on a macroscopic scale only. As SC surface generally is dry, a pH electrode requires a minimal volume of water at its tip, and in order to limit solute extraction from deeper layers, limitation of the reading period is recommended. This is crucial for observations of the SC pH gradient, where progressively lower layers of the SC are accessed by sequential removal of SC layers with tape stripping. In some commercially available devices specifically designed for skin-surface measurements, limitation of the reading period is internally implemented (36). A thorough review of the method and the necessary precautions to assure reliable and reproducible measurements has been published recently (37). For the initial display of measured values, a conventional pH-meter is employed, with analog or digital readout. Data display finally makes use of graphical methods; no images are obtained.

The very first report on the skin's acidity used a colorimetric method (1), which was refined over time (38). With advancing technology, electrometric methods were introduced, the “Glockenelektrode” (2) and microquinhydrone electrode (39). Eventually, systematic study of skin surface pH, using the flat electrode, was introduced in 1939 (35). These experiments already confirmed numerous earlier studies and added findings about variations in surface pH; newer techniques therefore are expected to offer further aspects and detail in order to improve the understanding of the biology of epidermal pH.

ALTERNATIVE APPROACHES

Microelectrodes have been used to measure skin pH, if only to assess dermal values (40). More refined devices discerned intra- and extracellular pH values of normal and diseased tissues successfully in the study of various tumors, including

squamous cell carcinoma (41,42). Motor-driven devices have been designed, which can control the position of the electrode tip deep in tissue by micrometer increments, and were used to map extracellular pH in isolated brain preparations (43,44) and gastric mucosa (45). Overall, this approach does not appear to offer a considerable gain for skin measurements. The lack of visual control and specifically the invasive character of such devices do not justify extensive use of this method in skin.

In neurological research, slices of whole brain were blotted onto a membrane, a method termed "in situ blotting" (46). A variation of this approach has been used, applying a range of dyes to blotting membranes, to depict the distribution of pH and other ions (47). Evidently, this method requires sectioned tissue, where the stability of ion distribution over any length of time is at question. Yet, the results obtained with this method confirm accepted knowledge about the SC pH gradient. Resolution is necessarily poor, and only qualitative, not quantitative results are obtained, limiting the usefulness of this method.

IMAGING APPROACHES

Functional Magnetic Resonance Imaging [also termed "magnetic resonance spectroscopy (MRS)] is widely used in neurology to map brain metabolism. [^1H]MRS (48) requires specific buffers to map pH, whereas [^{31}P]MRS visualizes pH via shifts in phosphorous protonation (49,50); both approaches therefore measure pH indirectly only. Nevertheless, molecular imaging should be possible with improved contrast reagents in the future (51). Whether the spatial resolution required to distinguish between individual epidermal, and, more importantly, SC layers, may be achieved with this method remains to be tested. To date, the high cost and the psychological stress placed on study subjects in such measurements limit its use when more readily applicable methods are available in dermatology.

A technique mostly used in materials analysis, secondary ion mass spectrometry (SIMS; nano-SIMS and other acronyms for technical variations and improvements), uses low-energy ions to irradiate a sample and measures the reflected secondary ions via their nuclear mass. While this method provides high resolution and selectivity, measuring a range of ions, it requires elaborate sample preparation and fixation (52), does not address the biologic state of the structures analyzed, and is therefore not suited for pH measurements in skin.

A so far untested approach is offered through RAMAN spectroscopy. In general, this method allows to selectively identify chemical structures (53). Protonated versus deprotonated compounds in SC can thus be identified. Unfortunately, a device to identify and simultaneously localize proton-harboring structures is not available commercially, but reportedly has been tested in a developmental setting (54). Yet, the "real" protonated compound or structure, which would be at the core of this approach, remains a matter of debate.

THE MICROSCOPIC APPROACH

The established method, flat electrode, does not render images; the alternative approaches discussed do not seem to offer a considerable gain of information, and imaging devices have not been widely used in addressing the question of pH in epidermis. The natural choice, therefore, microscopy, will be the focus of the following paragraphs.

The challenges for a method in microscopy applied to the question of epidermal pH distribution are numerous: First and foremost, the least disturbing approach should be chosen—in other terms—the closer to an unaltered *in vivo* situation tissue can be observed, the better. Optical sectioning, therefore, seems to be greatly preferable over actual tissue sectioning, or tape stripping for questions regarding the layered structure of SC, while *in vivo* measurements would be the ultimate goal. Second, to visualize protons, a pH-sensitive probe needs to be applied without altering the native pH state, i.e., buffering through the probe itself. The effects of route of application, such as solvents or other means, need to be assessed separately from the probe itself, for which the sensitivity must match the expected pH range. Because of the very barrier properties of skin, staining with selective dyes is usually performed on biopsies, where the nature of ionic distributions or even gradients is a very feeble one, making the results obtained from processed tissues appear quite artifact laden. Also, traditionally any quantitation in microscopy is based on light intensities, where penetration across the barrier introduces a concentration gradient for the dye, which would need to be quantified before the parameter of interest can be calculated, rendering conventional measurements close to impossible (25,55–57). Most of the concerns listed above are based on the method successfully used on cells, specifically keratinocytes *in vitro*, ratiometric pH measurements using pH sensitive fluorescent dyes (58), and the problems that would arise applying such methods to full-thickness skin (59). There are additional technical difficulties inherent to fluorescence-based methods such as photobleaching and phototoxic effects apart from the loss of intensity or resolution due to light-scattering or -penetration effects (also see next section) (60).

FLUORESCENCE LIFETIME IMAGING MICROSCOPY

Confocal microscopy allows to selectively access deeper epidermal layers by optical sectioning. To perform this light-sparingly multiphoton excitation can be employed, which effectively limits fluorescence to the focal volume, eliminating high intensity light from out-of-focus areas and thus enables selective observation of regions of interest in three dimensions. Lastly, a light intensity-independent measurement of fluorescence is required, to eliminate the barrier/penetration conundrum for the pH-sensitive probe. The ideally suited dimension of fluorescence is therefore not its intensity and/or wavelength, but its lifetime. Fluorescence lifetime τ is the decay rate of fluorescence, which comprises two components: The electrons of an individual dye molecule revert from an excited state to a nonexcited state by the emission of fluorescent light. Interactions with the environment modulate this decay by nonradiative energy transfer. As τ is dependent only on these two processes, lifetime emerges as a molecular constant effectively eliminating the “how much” of dye concentration and fluorescence intensity.

In general, lifetime measurement techniques are either time resolved or frequency resolved. Time domain measurements require a pulsed light source, because this approach measures the fluorescence decay over time following the excitation event. This involves collection of as many photons as possible along the decay curve, explaining the term “time-correlated single photon counting.” Lifetime values depend on the dye, and generally vary in the pico- or nanosecond range; hence very sensitive equipment is necessary. Mostly highly light-sensitive photomultipliers are used, and lately advances in camera design made their use

feasible also. Additionally, in gated measurements that limit data acquisition to a section (the time gate) of the decay curve, larger image areas and/or higher frame rates are possible. Frequency domain measurements require continuous excitation, sinusoidally modulated at a frequency. The emitted fluorescence results in the same frequency at lesser modulation depth shifted in phase, as it is delayed by the lifetime τ . This delay is the angle between the two sinusoidal curves, measured in degrees, or simply the delay between excitation and emission. Figure 1 gives a simplified view of the various aspects of lifetime. In panel A, the excitation event (Ex) results in a number of emitted photons, initial growth followed by slow decay of fluorescence intensity (E), shown as the decay curve (Em) accumulated over time (t). A section of this decay curve, usually following the growth phase is recorded in gated measurements. In the frequency domain as idealized in panel B, a modulated excitation (Ex) results in emission (Em) of lesser modulation or intensity (E), at the same frequency although shifted in phase, as the delay between blue and red peaks symbolizes (61–63).

There are a number of systems commercially available measuring the various modalities of lifetime, in a wide range of technical setups. From a practical

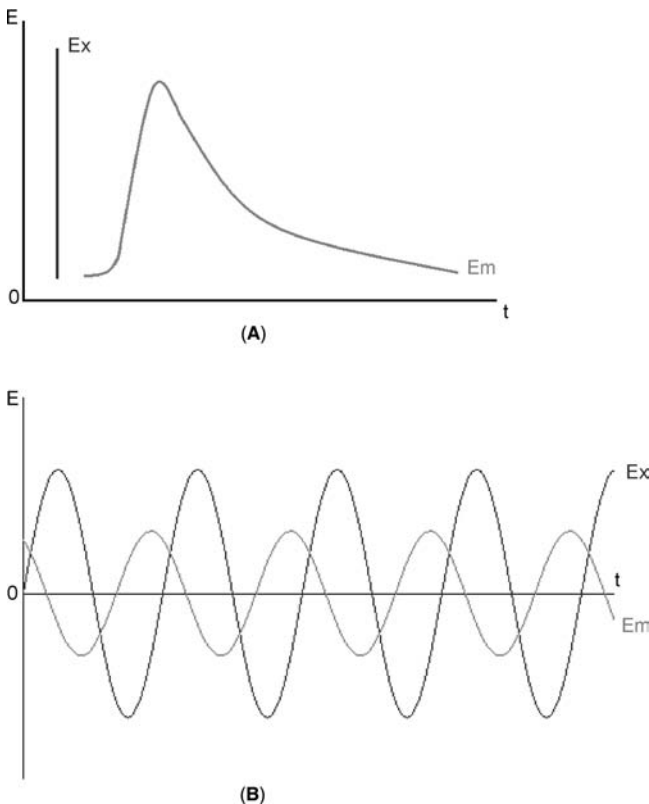


FIGURE 1 Schematic view of fluorescence. (A) Energy distribution over t of photons Em following a single Ex event. (B) Light as a sine wave, Ex light and resultant Em fluorescence. Abbreviations: t , time; Em , emission; Ex , excitation.

perspective, the choice of an optical system with all its components is determined by the eventual use. It would therefore be quite beyond the scope of this review to present the various and constantly improving designs. Instead, a list of websites with pertinent information may help to orient the reader (see Appendix).

Essentially, fluorescence lifetime imaging microscopy (FLIM) is an area of active technical development, where improvements from a number of areas converge. Microscope optics and design, lasers and other excitation light sources, and photomultipliers and cameras with high sensitivity and speed needed to acquire data, computer hardware to record and process the large amounts of data, the software used to evaluate raw lifetime data, and finally software to present complex imaging data, all have undergone rapid change and improvements over the last years. The need for such ongoing development may be further illustrated by the fact that lifetime as a theory was confirmed only a little over 50 years ago (64), and confocal microscopy itself, which stands at the center from which advanced microscopic methods such as FLIM developed, was invented and patented in the late 1950s (65), to reach a practical and commercial stage not before the early 1980s when microscopes, computers, and lasers were finally brought together.

Finally, only a specific probe makes selective observation of a signal, in this case pH dependent, possible. The photophysical behavior of such a dye needs to be characterized carefully in order to validate pH dependence of lifetime changes, and their independence from other variables in the tissue (66–68). Ideally, a dye should exhibit monoexponential lifetime decay. Nevertheless, with increasing computing power and with gated measurements, occurrence of higher-order decay and/or multiple fluorescent species no longer pose absolute impediments to data analysis (62). Still, a thorough assessment of the decay characteristics is necessary to establish the usefulness of a specific dye. In our experiments (69–71), we used 2',7'-bis-(2-carboxyethyl)-5-(and-6)-carboxyfluorescein (BCECF) as the pH-sensitive probe. A number of papers suggested this and similar dyes (58,66,25,72).

To illustrate the power of this approach, here one example (Fig. 2) demonstrating the dimension FLIM adds to conventional microscopy, and to the analysis of questions regarding epidermal pH distribution. For details of the method, please refer to the publications listed above and references therein (60,61,69–71,73).

The panels show first an intensity image (A, B), generated through fluorescence from BCECF topically applied to mouse skin. A number of details are visible; the unevenness of the skin surface (A) from partially adherent corneocytes and, optically focused down to the SC/SG interface (B), a much more regular tissue structure becomes apparent. A hair follicle is evident here (arrowhead), while at the surface not quite recognizable. Next, lifetime images are given (C, D), corresponding to the intensity images—in fact the same images, only showing fluorescence lifetime instead of intensity. These images are calibrated to the color/pH scale below (G), which together with the intensity images make a correlation of structure and pH possible. The lifetime-color-to-pH calibration uses setup-specific constants and a calibration curve, which are computed via the Henderson–Hasselbalch equation (70). Surface and intercellular areas appear green (approximately pH 6), whereas intracellular/intracorneocyte areas appear orange (approximately neutral). This is confirmed in the histograms (E, F), giving the frequency at which a certain pH occurs within the lifetime image. The histograms allow to assess the overall change in pH distribution; using the histogram, it becomes evident that SC comprises two predominant domains, approximately pH 6 and pH 7, and by matching these domains via their color (green for acidic

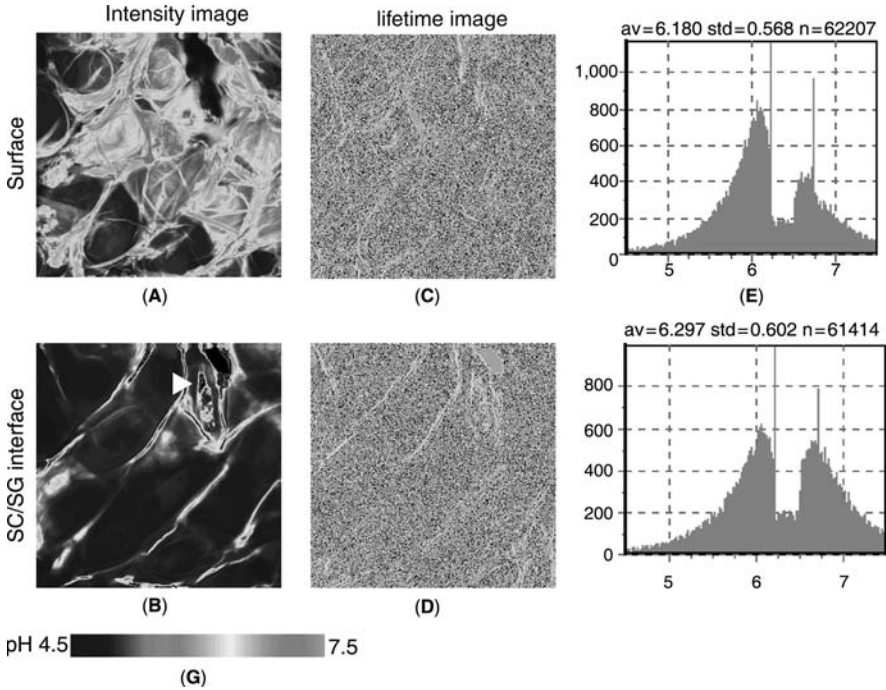


FIGURE 2 (See color insert) Example of FLIM analysis. Image stack from skin surface to dermis: represented by panels for epidermal surface (**A**, **C**, **E**), and SC/SG interface (**B**, **D**, **F**). Analysis consists of fluorescence intensity images (**A**, **B**), fluorescence lifetime images (**C**, **D**) with a color/value scale (**G**), and lifetime histograms (**E**, **F**).

and orange for neutral) to the tissue structure in panels A and B, the increase of acidity toward the surface becomes quantifiable. In the histograms, this is visible as the proportion of neutral:acidic peaks; in the lifetime panels, it is the relation of orange:green areas, and back to tissue structure acidic can be localized to extracellular, neutral to intracorneocyte, and SG-intracellular areas. Finally, the average pH given at the top of histogram E, the surface, matches the surface pH measured for this animal via flat electrode. Here, the detail of information gained via FLIM is most obvious, i.e., the only information available by flat electrode is the average pH. Necessarily, the average pH in histogram F, at the SC/SG interface, is different from what pH measurements via flat electrode have revealed for this area, i.e., close to neutral, as such values, obtained through a different method (i.e., tape stripping), with a different and more disruptive character introduce artifact. In fact, tape-stripping would produce also a quite different image, which at a microscopic scale most likely would not be representative for the SC/SG junction, but for a mixture of SC depths, as shown repeatedly (27,28). The images obtained through FLIM, therefore, not only demonstrate tissue structure in three dimensions (the image-stack from surface to deeper layers), but also adds the fourth dimension of pH.

FLIM pH measurements, which show acidic microdomains at the SC/SG interface (69,71), now explain how pH-dependent lipid processing can occur in this domain (6). Further, as the extracellular domain may be viewed as a rather

homogeneous and contiguous compartment (34, and references therein), the pH measurements with FLIM demonstrate this compartment to be of equal pH independent of SC depth, rather than to display a gradient. In conclusion, FLIM for measurement and localization of epidermal pH allows spatial correlation of pH and structure, and thereby correlation to specific functions and biochemical processes. Such correlations are the added dimension from FLIM, leading to larger conclusions and insight into biological processes not possible via other, long-established methods.

Caveats of this method are first to be seen in the limitations of the multiphoton system. The physical dimensions of the two-photon focus or the point-spread function of the microscopic system limit resolution (60,74–76). Also, the object itself may interfere with signals in the sense of second harmonics generation (77–79) and autofluorescence (73,80–84). Wavelength- and intensity dependently the light used to induce specific fluorescence will also generate these sources of artifact, and careful adjustment of excitation wavelengths and intensities are therefore essential; filters to separate the specific signal from other emissions may also become necessary. Further, with increasing tissue depth, loss of intensity and resolution due to light-scattering or -penetration effects will occur (85,60). The above-mentioned optical sectioning also has limitations that are based on the characteristics of the object (86). More specific caveats stem from already mentioned multiple factors in calibration and choice of probe. Overall, despite such caveats, and as other methods did not advance understanding of the nature of epidermal pH over a rather long time, FLIM to date is the most appealing approach to elucidate ion-dependent processes in epidermis.

APPENDIX: WEB RESOURCES TO ORIENT THE READER

Microscopes supporting FLIM

<http://www.zeiss.com/>
<http://www.lavision.de/>
<http://www.olympusmicro.com/>
<http://www.leica-microsystems.com/>
<http://www.microscopyu.com/>

Specific photon counting equipment

<http://www.becker-hickl.de/>
<http://www.picoquant.com/>
<http://www.hamamatsu.com/>
<http://www.lambert-instruments.com/>
<http://www.andor.com/>
<http://www.roperscientific.com/>

Lasers

<http://www.spectraphysics.com/>
<http://www.coherentinc.com/>

Websites with general information

<http://listserv.acsu.buffalo.edu/archives/confocal.html>
<http://www.cyto.purdue.edu/>
<http://www.photonics.com/dictionary/>
<http://www.opticsinfobase.org/>
<http://probes.invitrogen.com/>

REFERENCES

1. Heuss E. Die Reaktion des Schweißes beim gesunden Menschen. *Monatsschr Prakt Dermatol* 1892; 14:343, 400, 501.
2. Schade H, Marchionini A. Der Säuremantel der Haut (nach Gaskettenmessungen). *Klin Wochenschr* 1928; 7:12–14.
3. Anderson DS. The acid-base balance of the skin. *Br J Dermatol* 1951; 63(8–9):283–296.
4. Jolly HW Jr., Hailey CW, Netick J, et al. pH determinations of the skin. Readings under normal and abnormal conditions. *J Invest Dermatol* 1961; 36:305–308.
5. Ohman H, Vahlquist A. The pH gradient over the stratum corneum differs in X-linked recessive and autosomal dominant ichthyosis: a clue to the molecular origin of the “acid skin mantle”? *J Invest Dermatol* 1998; 111(4):674–677.
6. Takagi Y, Kriehuber E, et al. Beta-glucocerebrosidase activity in mammalian stratum corneum. *J Lipid Res* 1999; 40(5):861–869.
7. Zlotogorski A. Distribution of skin surface pH on the forehead and cheek of adults. *Arch Dermatol Res* 1987; 279(6):398–401.
8. Berardesca E, Pirot F, et al. Differences in stratum corneum pH gradient when comparing white Caucasian and black African-American skin. *Br J Dermatol* 1998; 139(5): 855–857.
9. Korting HC, Kober M, et al. Influence of repeated washings with soap and synthetic detergents on pH and resident flora of the skin of forehead and forearm. Results of a cross-over trial in health probationers. *Acta Derm Venereol* 1987; 67(1):41–47.
10. Draize JH. The determination of the pH of the skin of man and common laboratory animals. *J Invest Dermatol* 1942; 5:77–85.
11. Meyer W, Neurand K. Comparison of skin pH in domesticated and laboratory mammals. *Arch Dermatol Res* 1991; 283(1):16–18.
12. Thune P, Nilsen T, et al. The water barrier function of the skin in relation to the water content of stratum corneum, pH and skin lipids. The effect of alkaline soap and syndet on dry skin in elderly, non-atopic patients. *Acta Derm Venereol* 1988; 68(4):277–283.
13. Berg RW, Milligan MC, et al. Association of skin wetness and pH with diaper dermatitis. *Pediatr Dermatol* 1994; 11(1):18–20.
14. Mauro T, Holleran WM, et al. Barrier recovery is impeded at neutral pH, independent of ionic effects: implications for extracellular lipid processing. *Arch Dermatol Res* 1998; 290(4):215–222.
15. Lee SH, Elias PM, et al. A role for ions in barrier recovery after acute perturbation. *J Invest Dermatol* 1994; 102(6):976–979.
16. Jensen JM, Schutze S, et al. Roles for tumor necrosis factor receptor p55 and sphingomyelinase in repairing the cutaneous permeability barrier. *J Clin Invest* 1999; 104(12):1761–1770.
17. Schmuth M, Man MQ, et al. Permeability barrier disorder in Niemann-Pick disease: sphingomyelin-ceramide processing required for normal barrier homeostasis. *J Invest Dermatol* 2000; 115(3):459–466.
18. Aly R, Shirley C, et al. Effect of prolonged occlusion on the microbial flora, pH, carbon dioxide and transepidermal water loss on human skin. *J Invest Dermatol* 1978; 71(6):378–381.
19. Korting HC, Hubner K, et al. Differences in the skin surface pH and bacterial microflora due to the long-term application of synthetic detergent preparations of pH 5.5 and pH 7.0. Results of a crossover trial in healthy volunteers. *Acta Derm Venereol* 1990; 70(5):429–431.
20. Buck RP, Rondinini S, et al. Measurement of pH. Definition, standards, and procedures. (IUPAC Recommendations 2002). *Pure Appl Chem* 2002; 74(11):2169–2200.
21. Rondinini S. pH measurements in non-aqueous and aqueous-organic solvents—definition of standard procedures. *Anal Bioanal Chem* 2002; 374(5):813–816.
22. Fluhr JW, Elias PM. Stratum corneum pH: formation and function of the “Acid mantle.” *Exog Dermatol* 2002; 1:163–175.
23. Rippke F, Schreiner V, et al. The acidic milieu of the horny layer: new findings on the physiology and pathophysiology of skin pH. *Am J Clin Dermatol* 2002; 3(4):261–272.

24. Ohman H, Vahlquist A. In vivo studies concerning a pH gradient in human stratum corneum and upper epidermis. *Acta Derm Venereol* 1994; 74(5):375–379.
25. Turner NG, Cullander C, et al. Determination of the pH gradient across the stratum corneum. *J Invest Dermatol Symp Proc* 1998; 3(2):110–113.
26. Pierard GE. EEMCO guidance for the assessment of dry skin (xerosis) and ichthyosis: evaluation by stratum corneum strippings. *Skin Res Technol* 1996; 2:3–11.
27. van der Molen RG, Spies F, et al. Tape stripping of human stratum corneum yields cell layers that originate from various depths because of furrows in the skin. *Arch Dermatol Res* 1997; 289(9):514–518.
28. Bashir SJ, Chew AL, et al. Physical and physiological effects of stratum corneum tape stripping. *Skin Res Technol* 2001; 7(1):40–48.
29. Brandner JM, Kief S, et al. Organization and formation of the tight junction system in human epidermis and cultured keratinocytes. *Eur J Cell Biol* 2002; 81(5):253–263.
30. Furuse M, Hata M, et al. Claudin-based tight junctions are crucial for the mammalian epidermal barrier: a lesson from claudin-1-deficient mice. *J Cell Biol* 2002; 156(6):1099–1111.
31. Tunggal JA, Helfrich I, et al. E-cadherin is essential for in vivo epidermal barrier function by regulating tight junctions. *Embo J* 2005; 24(6):1146–1156.
32. Bouwstra JA, de Graaff A, et al. Water distribution and related morphology in human stratum corneum at different hydration levels. *J Invest Dermatol* 2003; 120(5):750–758.
33. Bouwstra JA, Honeywell-Nguyen PL, et al. Structure of the skin barrier and its modulation by vesicular formulations. *Prog Lipid Res* 2003; 42(1):1–36.
34. Norlen L. Molecular skin barrier models and some central problems for the understanding of skin barrier structure and function. *Skin Pharmacol Appl Skin Physiol* 2003; 16(4):203–211.
35. Blank IH. Measurement of pH of the skin surface. II. pH of the exposed surfaces of adults with no apparent skin lesions. *J Invest Dermatol* 1939; 2:75–79.
36. Ehlers C, Ivens UI, et al. Comparison of two pH meters used for skin surface pH measurement: the pH meter 'pH900' from Courage & Khazaka versus the pH meter "1140" from Mettler Toledo. *Skin Res Technol* 2001; 7(2):84–89.
37. Parra JL, Paye M. EEMCO guidance for the in vivo assessment of skin surface pH. *Skin Pharmacol Appl Skin Physiol* 2003; 16(3):188–202.
38. Sharlit H, Scheer M. The hydrogen-ion concentration of the surface of healthy intact skin. *Arch Derm Syph* 1923; 154:592–598.
39. Levin O, Silvers S. The reaction of the skin and its secretions in eczema. *Arch Derm Syph* 1932; 25:825–834.
40. Harrison DK, Walker WF. Micro-electrode measurement of skin pH in humans during ischaemia, hypoxia and local hypothermia. *J Physiol* 1979; 291:339–350.
41. Gerweck LE, Seetharaman K. Cellular pH gradient in tumor versus normal tissue: potential exploitation for the treatment of cancer. *Cancer Res* 1996; 56(6):1194–1198.
42. Gerweck LE. Tumor pH: implications for treatment and novel drug design. *Semin Radiat Oncol* 1998; 8(3):176–182.
43. Okada Y, Muckenhoff K, et al. Depth profiles of pH and PO₂ in the isolated brain stem-spinal cord of the neonatal rat. *Respir Physiol* 1993; 93(3):315–326.
44. Muckenhoff K, Schreiber S, et al. Ion-sensitive microelectrode system with short response time. *J Neurosci Methods* 1994; 51(2):147–153.
45. Schreiber S, Nguyen TH, et al. Demonstration of a pH gradient in the gastric gland of the acid-secreting guinea pig mucosa. *Am J Physiol Gastrointest Liver Physiol* 2000; 279(3):G597–G604.
46. Okabe M, Nyakas C, et al. In situ blotting: a novel method for direct transfer of native proteins from sectioned tissue to blotting membrane: procedure and some applications. *J Histochem Cytochem* 1993; 41(6):927–934.
47. Denda M, Hosoi J, et al. Visual imaging of ion distribution in human epidermis. *Biochem Biophys Res Commun* 2000; 272(1):134–137.
48. Garcia-Martin ML, Herigault G, et al. Mapping extracellular pH in rat brain gliomas in vivo by ¹H magnetic resonance spectroscopic imaging: comparison with maps of metabolites. *Cancer Res* 2001; 61(17):6524–6531.

49. Petroff OA, Prichard JW, et al. Cerebral intracellular pH by ^{31}P nuclear magnetic resonance spectroscopy. *Neurology* 1985; 35(6):781–788.
50. Laxer KD, Hubesch B, et al. Increased pH and inorganic phosphate in temporal seizure foci demonstrated by ^{31}P MRS. *Epilepsia* 1992; 33(4):618–623.
51. Delikatny EJ, Poptani H. MR techniques for in vivo molecular and cellular imaging. *Radiol Clin North Am* 2005; 43(1):205–220.
52. Chandra S, Smith DR, et al. Subcellular imaging by dynamic SIMS ion microscopy. *Anal Chem* 2000; 72(3):104A–114A.
53. Caspers PJ, Lucassen GW, et al. In vivo confocal Raman microspectroscopy of the skin: noninvasive determination of molecular concentration profiles. *J Invest Dermatol* 2001; 116(3):434–442.
54. Caspers PJ, Lucassen GW, et al. Combined in vivo confocal Raman spectroscopy and confocal microscopy of human skin. *Biophys J* 2003; 85(1):572–580.
55. Siddiqui O. Physicochemical, physiological, and mathematical considerations in optimizing percutaneous absorption of drugs. *Crit Rev Ther Drug Carrier Syst* 1989; 6(1):1–38.
56. Wiechers JW. The barrier function of the skin in relation to percutaneous absorption of drugs. *Pharm Weekbl Sci* 1989; 11(6):185–198.
57. Marjukka Suhonen T, Bouwstra JA, et al. Chemical enhancement of percutaneous absorption in relation to stratum corneum structural alterations. *J Control Release* 1999; 59(2):149–161.
58. van Erp PE, Jansen MJ, et al. Ratiometric measurement of intracellular pH in cultured human keratinocytes using carboxy-SNARF-1 and flow cytometry. *Cytometry* 1991; 12(2):127–132.
59. Opas M. Measurement of intracellular pH and pCa with a confocal microscope. *Trends Cell Biol* 1997; 7:75–80.
60. Rubart M. Two-photon microscopy of cells and tissue. *Circ Res* 2004; 95(12):1154–1166.
61. Schneider PC, Clegg RM. Rapid acquisition, analysis, and display of fluorescence lifetime-resolved images for real-time applications. *Rev Sci Instrum* 1997; 68(11):4107–4119.
62. Bastiaens PI, Squire A. Fluorescence lifetime imaging microscopy: spatial resolution of biochemical processes in the cell. *Trends Cell Biol* 1999; 9(2):48–52.
63. Tadrous PJ. Methods for imaging the structure and function of living tissues and cells. 2. Fluorescence lifetime imaging. *J Pathol* 2000; 191(3):229–234.
64. Pringsheim P. Fluorescence and Phosphorescence. New York: Interscience, 1949.
65. Minsky M. Memoir on inventing the confocal scanning microscope. *Scanning* 1988; 10:128–138.
66. Szmacinski H, Lakowicz JR. Optical measurements of pH using fluorescence lifetimes and phase-modulation fluorometry. *Anal Chem* 1993; 65(13):1668–1674.
67. Tatikolov AS, Costa SM. Photophysics and photochemistry of hydrophilic cyanine dyes in normal and reverse micelles. *Photochem Photobiol Sci* 2002; 1(3):211–218.
68. Eggeling C, Volkmer A, et al. Molecular photobleaching kinetics of rhodamine 6G by one- and two-photon induced confocal fluorescence microscopy. *Chemphyschem* 2005; 6(5):791–804.
69. Behne MJ, Meyer JW, et al. NHE1 regulates the stratum corneum permeability barrier homeostasis. Microenvironment acidification assessed with fluorescence lifetime imaging. *J Biol Chem* 2002; 277(49):47399–47406.
70. Hanson KM, Behne MJ, et al. Two-photon fluorescence lifetime imaging of the skin stratum corneum pH gradient. *Biophys J* 2002; 83(3):1682–1690.
71. Behne MJ, Barry NP, et al. Neonatal development of the stratum corneum pH gradient: localization and mechanisms leading to emergence of optimal barrier function. *J Invest Dermatol* 2003; 120(6):998–1006.
72. Lin HJ, Szmacinski H, et al. Lifetime-based pH sensors: indicators for acidic environments. *Anal Biochem* 1999; 269(1):162–167.
73. Masters BR, So PT, et al. Multiphoton excitation microscopy of in vivo human skin. Functional and morphological optical biopsy based on three-dimensional imaging, lifetime measurements and fluorescence spectroscopy. *Ann NY Acad Sci* 1998; 838:58–67.

74. Diaspro A, Robello M. Two-photon excitation of fluorescence in three-dimensional microscopy. *Eur J Histochem* 1999; 43(3):169–178.
75. Diaspro A, Robello M. Two-photon excitation of fluorescence for three-dimensional optical imaging of biological structures. *J Photochem Photobiol B* 2000; 55(1):1–8.
76. Diaspro A, Federici F, et al. Influence of refractive-index mismatch in high-resolution three-dimensional confocal microscopy. *Appl Opt* 2002; 41(4):685–690.
77. Kim BM, Eichler J, et al. Collagen structure and nonlinear susceptibility: effects of heat, glycation, and enzymatic cleavage on second harmonic signal intensity. *Lasers Surg Med* 2000; 27(4):329–335.
78. Konig K, Riemann I. High-resolution multiphoton tomography of human skin with subcellular spatial resolution and picosecond time resolution. *J Biomed Opt* 2003; 8(3):432–439.
79. Lin SJ, Wu R Jr, et al. Evaluating cutaneous photoaging by use of multiphoton fluorescence and second-harmonic generation microscopy. *Opt Lett* 2005; 30(17):2275–2277.
80. Masters BR, So PT, et al. Multiphoton excitation fluorescence microscopy and spectroscopy of in vivo human skin. *Biophys J* 1997; 72(6):2405–2412.
81. Masters BR, So PT, et al. Multiphoton excitation microscopy, confocal microscopy, and spectroscopy of living cells and tissues; functional metabolic imaging of human skin in vivo. *Methods Enzymol* 1999; 307:513–536.
82. Na R, Stender IM, et al. Autofluorescence spectrum of skin: component bands and body site variations. *Skin Res Technol* 2000; 6(3):112–117.
83. Hoffmann K, Stucker M, et al. Selective femtosecond pulse-excitation of melanin fluorescence in tissue. *J Invest Dermatol* 2001; 116(4):629–630.
84. Na R, Stender IM, et al. Autofluorescence of human skin is age-related after correction for skin pigmentation and redness. *J Invest Dermatol* 2001; 116(4):536–540.
85. Schilders SP, Gu M. Limiting factors on image quality in imaging through turbid media under single-photon and two-photon excitation. *Microsc Microanal* 2000; 6(2):156–160.
86. Pawley JB. Limitations on optical sectioning in live-cell confocal microscopy. *Scanning* 2002; 24(5):241–246.

Markus Stücker

Department of Dermatology, Ruhr-University Bochum, St. Josef Hospital, Bochum, Germany

Paul Hartmann

Roche Diagnostics GmbH, Graz, Austria

Dietrich W. Lübbers

Max Planck Institut für Molekulare Physiologie, Dortmund, Germany

David Harrison

Regional Medical Physics Department, Durham Unit, University Hospital of North Durham, U.K.

Peter Altmeyer

Department of Dermatology, Ruhr-University, and Dermatological Clinic of the Ruhr-University, St. Josef Hospital, Bochum, Germany

HETEROGENEITY OF SKIN OXYGENATION

The oxygen supply of the skin can be evaluated by quantifying the transcutaneous oxygen pressure (tcpO_2) with Clark electrodes (1). However, this measuring technique has a poor reproducibility when measuring tcpO_2 at single points of the skin because of heterogeneity of skin and cutaneous oxygen supply. This corresponds to the heterogeneity of the arterioles, capillaries, and venules in the upper corium. The blood flow of these vessels can be visualized by using the laser Doppler perfusion imaging technique (2,3), but the laser Doppler signal allows only a restricted assertion about oxygen supply. In some diseases, for example chronic venous insufficiency, the laser Doppler signal may be increased and at the same time the tcpO_2 may be decreased (4).

OXYGEN UPTAKE FROM THE ATMOSPHERE

Since 1851, it is known that the oxygen supply to the upper layers of the skin is provided not only by cutaneous blood flow, but also by diffusion from the surrounding air (5). Using needle electrodes, it could be demonstrated that the pO_2 decreases continuously from a maximum at the surface of the skin until a minimum in the papillary dermis before increasing again under the influence of the vascular supply of oxygen in the corium (6). During these experiments, an hyperemia was induced by the needle puncture and the skin was covered by a film of water. This resulted in a lowering of the surface pO_2 from atmospheric values (~ 150 Torr) to a mean of 78 Torr. Under these conditions, the minimum pO_2 was observed at a depth of about $100\ \mu\text{m}$. As the oxygen transport within the tissue occurs along the pO_2 -gradient from higher to lower pO_2 -values, there is an O_2 flux from the higher pO_2 of the atmosphere through the epidermis and the whole

volume above this minimum is supplied by external oxygen. Therefore, it is desirable to measure not only the oxygen transport of the blood, but also the cutaneous oxygen uptake from the atmosphere.

MEASURING TRANSCUTANEOUS OXYGEN FLUX

In 1994, a fluorescence-based O_2 -fluxoptode for measuring oxygen flux was developed for measuring the cutaneous O_2 -uptake from the atmosphere noninvasively (7,8). Using simultaneous measurement of transcutaneous oxygen flux ($tcJO_2$, $tcpO_2$), and laser Doppler fluxmetry, it could be demonstrated that the epidermal oxygen uptake from the atmosphere is in balance with the blood-borne oxygen supply (9,10). Corresponding to a decrease of $tcJO_2$ in hyperemized skin, a stop of skin perfusion by suprasystolic occlusion resulted in an increased $tcJO_2$, but the later change was moderate. Although in hyperemic skin the transcutaneous O_2 -flux decreased on average by about 29%, a increase of only 9% was observed during a suprasystolic occlusion.

Even if one assumes that the skin surface pO_2 is not yet in equilibrium with the changes in deeper skin layers after a five minutes suprasystolic occlusion, comparison with the time course of the skin surface pO_2 after inducing a hyperemia proves that a stop of skin perfusion has a minor effect on the $tcJO_2$. These findings indicate that in normal, nonhyperemized skin, the transcutaneous oxygen uptake from the atmosphere represents the main contribution to the oxygen supply of the upper layers whereas the capillary transport plays a minor role. The balance between the hematogenic O_2 -transport and the $tcJO_2$ varies. In hyperemic skin, it is shifted toward the capillary oxygen supply (9).

In normal forearm skin, the total $tcJO_2$ was quantified as $0.5 \text{ mL m}^{-2} \text{ min}^{-1}$ (11).

IMAGING OF $tcpO_2$ and $tcJO_2$

On the basis of a sensing layer containing the oxygen indicator tris(1,10'-phenanthroline) ruthenium(II) chloride, two different types of sensors were prepared, both consisting of three layers. $tcpO_2$ membranes consist of a opaque silicone layer, the oxygen-sensitive layer ($50 \mu\text{m}$ thickness), and a relatively

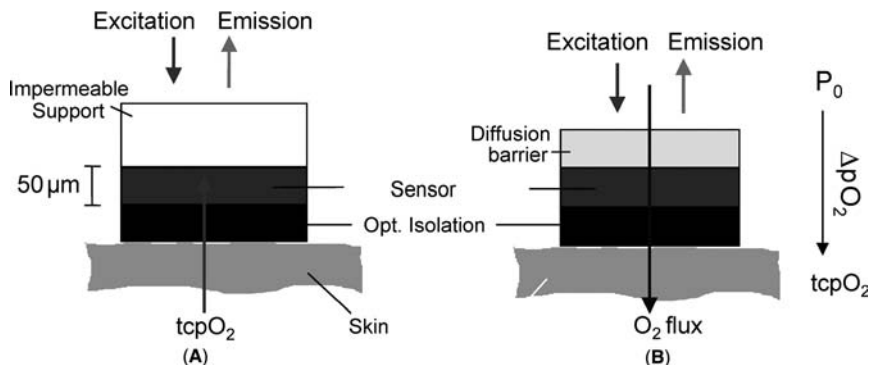


FIGURE 1 Schematic diagram of (A) the pO_2 sensor and (B) the transcutaneous oxygen flux sensor. Abbreviation: $tcpO_2$, transcutaneous oxygen pressure. Source: From Ref. 12.

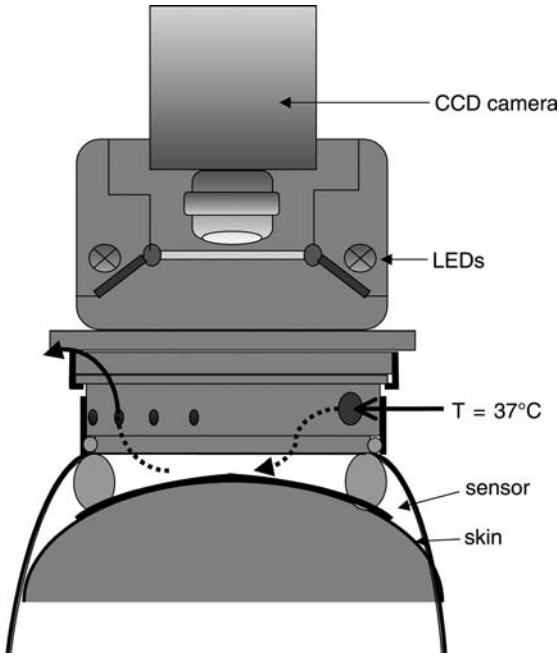


FIGURE 2 Schematic diagram of the practical setup for imaging transcutaneous oxygen flux. *Abbreviations:* CCD, charge-coupled device; LED, light emitting diode. *Source:* From Ref. 16.

impermeable transparent carrier foil, which terminates the oxygen diffusion through the sensor.

Oxygen flux ($tcJO_2$) membranes consisted of a similar three-layer arrangement, but the previous impermeable carrier membrane of the oxygen optode was replaced by an oxygen permeable polymer (Fig. 1). Details concerning the manufacturing methods of the sensor membranes are given in Ref. 12. For a given oxygen permeability of the diffusion barrier, the pressure difference ΔpO_2 between skin surface pO_2 and atmospheric pO_2 is proportional to the oxygen flux $tcJO_2$ [$tcJO_2 = (P/d) \times \Delta pO_2$, where P is the permeability of the diffusion barrier and d its thickness].

Charge-coupled device (CCD) camera, the central detection part of the device, is used for imaging, which allows demodulation of the detected sensor emission and is modulated sinusoidally at a high frequency (13–15). The obtained images are pixel-by-pixel related to the lifetime of the sensor luminescence, which can be calibrated to pO_2 values at both 33°C and 37°C. Technical details to the optical imaging of $tcpO_2$ and oxygen flux (Fig. 2) (14,15). In contrast to phosphorescence lifetime imaging of intravenous (IV) markers, in fluorescence lifetime imaging of noninvasive oxygen sensors no oxyphore solution has to be administered IV, which typically results in a transient increase in blood pressure for a few minutes (17).

MEASURING PROCEDURE

The subjects, lying in a comfortable position with slightly raised upper body, were acclimatized for 20 to 25 minutes at a room temperature of 22°C to 23°C. Prior to application of the probe, the skin to be examined was shaved, if necessary, and cleaned. The superficial horny scales were eliminated by stripping with an

adhesive tape. After humidifying the skin of the measuring area by water, the measuring sensors were stuck on. The temperature of the skin surface was adjusted to 33°C or 37°C.

EXAMPLES FOR VISUALIZATION OF SKIN OXYGENATION

Hyperemia After Intracutaneous Injection of Histamine

Intracutaneous histamine injection induced a small centrally located swelling in an hyperemic area (erythema). Histamine (0.05 mL) was injected intracutaneously into the forearms. Images with the tcpO₂ sensor were recorded 20 to 35 minutes after injection at a temperature of 37°C. It could be visualized and quantified that the tcpO₂ increased in comparison to the adjoining normal skin (Fig. 3).

Localized Inflammation

Localized inflammation was induced by intracutaneous application of tetanus antigen. The inflammatory reaction induced during the tetanus recall antigen test is very similar to the type IV reaction induced by the tuberculin test. The blood flow and oxygen supply to skin during these reactions has been well studied (18–20). Two different responses could be detected by measuring the tcJO₂ (Fig. 4). Some of the subjects developed only smaller reactions, for example, with an induration 5 mm in diameter that was surrounded by an erythema with axes 17 × 13 mm. A significant hyperemia could be visualized by laser Doppler perfusion imaging. In this hyperemic field, the oxygen flux image displayed a decrease in tcJO₂. Ultrasonography indicated only minor thickening of the corium from 790 to 1120 μm.

The majority of subjects developed stronger reaction, for example, with an 8 mm diameter region of induration surrounded by an erythema with axes 25 × 20 mm. The increase of blood flow in laser Doppler perfusion was similar to that of the first mentioned subject. However, in this case, an increase in tcJO₂ compared with the neighboring, normal skin could be visualized. The increase of corium thickness was much higher (1140–2840 μm), caused by a major inflammatory infiltrate. The increased O₂ uptake from the atmosphere can be explained by the higher oxygen consumption in high number of infiltrating cells. In cases

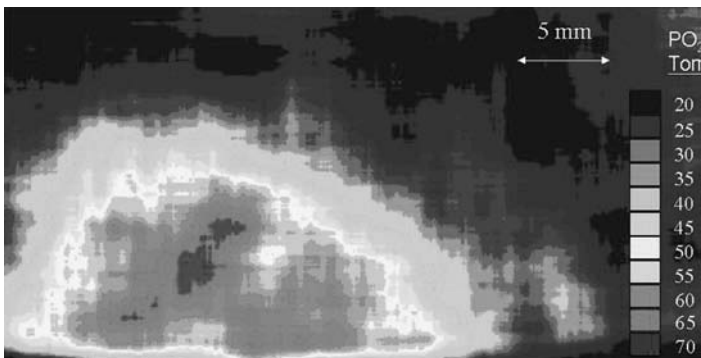


FIGURE 3 (See color insert) Transcutaneous oxygen pressure image (3 × 6 cm²). The image was recorded 33 minutes after intracutaneous injection of 0.05 mL histamine (trunk, measurement temperature: 37°C). An increase of the transcutaneous partial pressure of oxygen within the histamine reaction can be observed. Source: From Ref. 15.

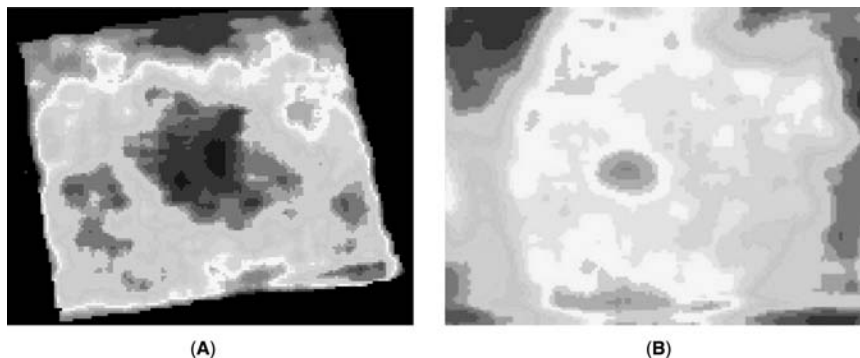


FIGURE 4 (See color insert) Transcutaneous oxygen flux (tcJO₂) imaging. Oxygen flux in two individuals 48 hours after intracutaneous application of tetanus antigen. (A) tcJO₂ is decreased in a hyperemic area of a reaction with a weak inflammatory cell infiltrate. (B) tcJO₂ compared with the neighboring, normal skin is increased in a strong reaction with strong infiltration by inflammatory cells with a higher oxygen consumption. Abbreviation: tcJO₂, transcutaneous oxygen flux. Source: From Ref. 10.

displaying a decrease in tcJO₂, the increase in blood-borne oxygen supply may exceed the metabolic demands of the infiltrating cells and the tcJO₂ will be reduced as in other types of hyperemia (10,11).

Near-Infrared Spectroscopic Imaging

Because of the different spectra of oxyhemoglobin and deoxyhemoglobin, near-infrared spectroscopic imaging could be an alternative of the described techniques. Images are measured in the near-infrared wavelength region between 650 and 1050 nm (21). They can visualize the changes of total hemoglobin volume and of ratios of oxyhemoglobin to total hemoglobin and of desoxy hemoglobin to total hemoglobin. The calculation of absolute values is still a point of discussion. Thus, the main disadvantages of this technique are that the measuring depth is not known exactly and that mainly ratios are given but no absolute values. On the other hand, in contrast to the fluorescence lifetime imaging, information on oxygen supply of the skin is obtainable without skin contact (21).

CONCLUSION

Many diseases which are accompanied by disturbances of blood supply, are characterized by a heterogeneity of the perfusion pattern. Therefore, results of the well-established one-dimensional measurements of the tcpO₂ depend strongly on the electrode position. Instead of measurements by Clark electrodes at multiple positions, two-dimensional fluorescence lifetime imaging can be used for measuring skin oxygenation.

ACKNOWLEDGMENTS

The work was supported by grants from the Deutsche Forschungsgemeinschaft (A13389-1 and 389-2). We are grateful to Roche Diagnostics (Graz, Austria) for the prototype of the camera system for oxygen imaging and for producing the sensor foils.

REFERENCES

1. Huch R, Huch A, Lübbers DW. Transcutaneous PO₂. Stuttgart-New York: Thieme-Stratton Inc., 1981.
2. Stücker M, Auer T, Hoffmann K, Altmeyer P. Two-dimensional blood flow determinations in allergic reactions using laser Doppler scanning. *Contact Dermatitis* 1995; 33:299–303.
3. Stücker M, Heese A, Hoffmann K, el Gammal C, Altmeyer P. Quantification of vascular dysregulation in atopic dermatitis using laser Doppler perfusion imaging. *Skin Res Technol* 1998; 4:9–13.
4. Partsch H. Hyperaemia hypoxia in venous ulceration. *Br J Dermatol* 1984; 110:249–251.
5. Gerlach A. Über das Hautathmen. *Arch Anat Physiol* 1851; 431–479.
6. Baumgärtl HA, Ehrly M, Saeger-Lorenz K, Lübbers DW. Initial results of intracutaneous measurements of PO₂ profiles. In: Ehrly AM, Hauss J, Huch R, eds. *Clinical Oxygen Pressure Measurement*. Berlin: Springer-Verlag, 1987:121–128.
7. Holst G. Entwicklung und Erprobung einer Sauerstoff-Flux-Optode mit einem Sauerstoff-Sensor nach dem Prinzip der dynamischen Fluoreszenzlöschung. Düsseldorf: VDI Verlag, 1994.
8. Holst G, Köster T, Voges E, Lübbers DW. FLOX—an oxygen-flux measuring system using a phase-modulation method to evaluate the oxygen-dependent fluorescence lifetime. *Sens Actuators B* 1995; 29:231–239.
9. Stücker M, Altmeyer P, Struk A, et al. The transepidermal oxygen flux from the environment is in balance with capillary oxygen supply. *J Invest Dermatol* 2000; 114:533–540.
10. Harrison D, Lübbers DW, Baumgärtl H, et al. Capillary blood flow and cutaneous uptake of oxygen from the atmosphere. In: Müller GJ, Kessler M, eds. *Progress in Biomedical Optics and Imaging: Functional Monitoring and Drug-Tissue Interaction*. Spie Proc Series 2002; 4623:195–205.
11. Stücker M, Struk A, Altmeyer P, Herde M, Baumgärtl H, Lübbers DW. The cutaneous uptake of atmospheric oxygen contributes significantly to the oxygen supply of human dermis und epidermis. *J Physiol* 2002; 538.3:985–994.
12. Hartmann P, Ziegler W, Lübbers DW. Fluorescence lifetime imaging of the skin PO₂ supply. Instrumentation and results. *Adv Exp Med Biol* 1997; 428:605–611.
13. Mariott G, Clegg RM, Arndt-Jovin DJ, Jovin TM. Time resolved imaging microscopy. *Biophys J* 1991; 60:1374–1387.
14. Hartmann P, Ziegler W, Holst G, Lübbers DW. Oxygen flux fluorescence lifetime imaging. *Sens Actuators B* 1997; 38–39:110–115.
15. Stücker M, Schulze L, Pott G, et al. FLIM of luminescent oxygen sensors: clinical applications and results. *Sens Actuators B*, 1998; 51:171–175.
16. Hartmann P, Ziegler W. System for quantitative determination of the local distribution of a quantity to be measured. European Patent EP 1040788 B1, and US-Patent US 6,345,191 B1. 2002, priority date 29.3.1999.
17. Erickson K, Braun RD, Yu D, et al. Effect of longitudinal oxygen gradients on effectiveness of manipulation of tumor oxygenation. *Cancer Res* 2003; 1(63):4705–4712.
18. Harrison DK, Abbot NC, Swanson Beck J, McCollum PT. Preliminary assessment of laser Doppler imaging for measurement of skin perfusion using the tuberculin reaction in human skin as a model. *Phys Meas* 1993; 14:241–252.
19. Newton DJ, Harrison DK, McCollum PT. Oxygen extraction rates in inflamed human skin using the tuberculin reaction as a model. *Int J Microcirc Clin Exp* 1996; 16:118–123.
20. Newton DJ, Harrison DK, Delaney CJ, Swanson Beck J, McCollum PT. Comparison of macro- and micro-lightguide spectrophotometric measurements of microvascular haemoglobin oxygenation in the tuberculin reaction in normal human skin. *Phys Meas* 1994; 15:115–128.
21. Attas M, Hewko M, Payette J, Posthumus T, Sowa M, Mantsch H. Visualization of cutaneous hemoglobin oxygenation and skin hydration using near-infrared spectroscopic imaging. *Skin Res Technol* 2001; 7:238–245.

Jean-Luc Lévêque

L'Oréal Recherche, Centre Charles Zviak, Clichy, France

INTRODUCTION

Means for representing the skin surface according to its optical and thermal properties exist for years, even if great improvements have appeared recently. The same is true for the 3-D representation of the skin micro relief by the relatively recent so-called “fringe projection method.”

The last innovation in skin imaging is probably “capacitance imaging.” It is a new technology allowing the skin surface to be imaged according to its capacitance measured every $50\ \mu\text{m}$. It is based on the use of pixel-sensing technology developed by some big electronic companies for an automatic detection and characterization (for security reasons) of the fingerprints. The present chapter deals with the presentation of the technical aspects of this method with examples of its utilization in skin research.

TECHNICAL ASPECTS OF THE METHOD

SkinChip[®] Sensor

The acquisition device called SkinChip is based on the sensor developed by ST Microelectronics (Geneva, Switzerland) for sensing the fingerprints of people. It is composed of an array of 92,160 microsensors distributed over an $18 \times 12.8\ \text{mm}^2$ surface window (one microsensor every $50\ \mu\text{m}$). These sensors, protected by a thin silicon oxide layer, are driven by a feedback capacitance circuit that is modified by the application of the skin on the surface window. The conditioning electronic, allowing gain and offset to be adjusted, is integrated on the same board. The sensor is directly plugged to the universal serial bus (USB) port of any computer. Applying the sensor window onto any skin site produces immediately an image, each pixel of it corresponding to the local capacitance. Measurement is digitized in 255 gray levels: the higher the capacitance, the grayer the pixel. Images supplied by the SkinChip technology are capacitance or hydration map of the skin surface.

Dedicated Software

The following skin parameters can presently be extracted from the images: mean gray level (MGL) of the histogram, which has been thresholded in order to only consider the 20% darker pixels mean thresholded histogram 20% (MTH20), the density of corner density (CD) corresponding to the number of crossings between the primary lines by square centimeter, and the main orientations of the primary lines. For obtaining these parameters on a given region of interest, software was developed under the “Imaq Vision” platform [National Instrument (Austin Texas)].

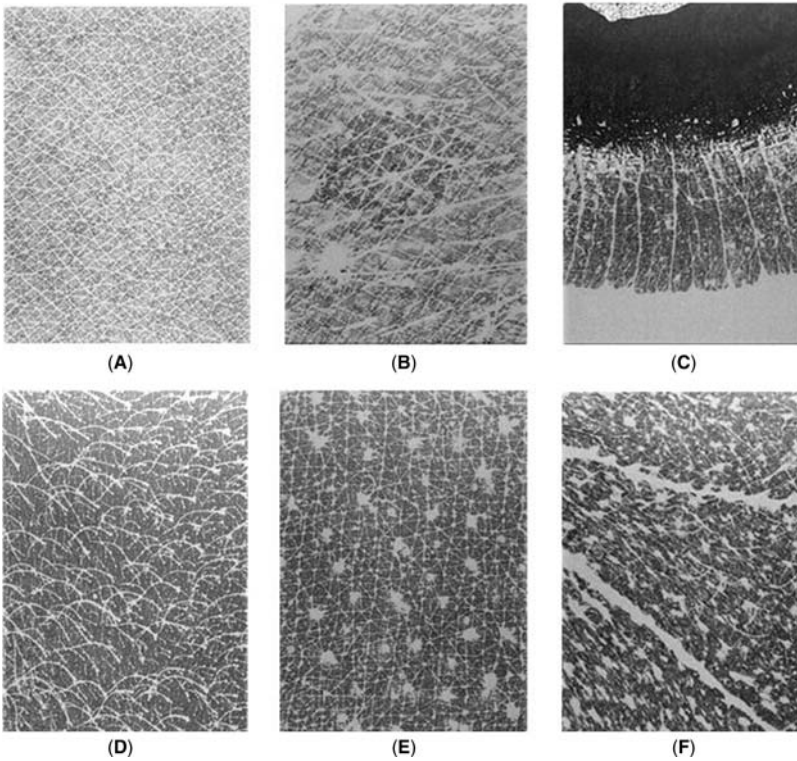


FIGURE 1 Capacitance images of the skin surface. (A) Ventral side of forearm (of a young woman); (B) dorsal side of forearm (of an aged person with a sebheoric keratose); (C) lower lip; (D) cheek (of a young woman); (E) temple (see the pore openings); and (F) wrinkles of the crow pad (of an aged man).

SKIN IMAGES

Images of different skin sites are presented in Figure 1. At a glance, we can recognize the skin micro relief texture and the openings of the sebaceous follicles. These features appear in clear gray because they are not in a close contact with the sensor window, in contrast to the skin plateau which appears darker according the skin surface hydration. Figure 2B represents the capacitance image of forearm skin treated by a moisturizer on the left-hand side (grayer zone). Histograms of the two parts of the image are also represented. In Figure 2C, we can remark that the histogram is bimodal, the second maximum corresponding to the lighter pixels that represent the skin zones (lines, pores), which are not in contact with the SkinChip window. On the contrary, the first maximum corresponds to the skin plateau, in contact with the window. When skin is hydrated, pixels of the treated zone become darker (higher capacitance). As a consequence, the histogram of the image is shifted to the left (Fig. 2A). Skin hydration can be characterized by recording the MGL of the image or, with a better sensitivity, the MGL of the left-hand side of the histogram, which takes into account only the skin plateau capacitance (MTH20).

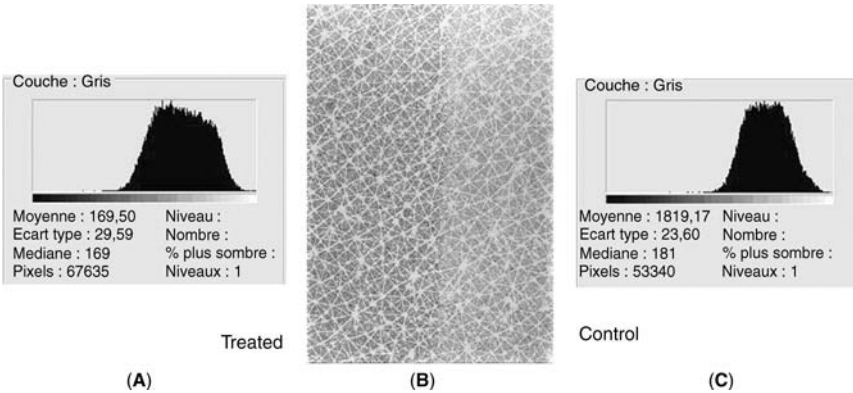


FIGURE 2 Influence of moisturization of skin on the gray level histograms of the capacitance images. (A) Histogram of the treated part of skin and (B) capacitance image of the skin. Only the left-hand part was treated by a moisturizer. (C) Histogram of the nontreated part of the skin.

RELATIONSHIP BETWEEN SKINCHIP AND CORNEOMETER PARAMETERS

A capacitance image represents exactly what the electrode of a Corneometer “sees” when it is applied on the skin. A corneometer displays the average value of the capacitance of the skin surface located under the electrode. There is then no surprise that a very good correlation exists between MGL and the Corneometer displayed value for a given skin site (1). In a recent study, based on 224 measurements, such a correlation was recently confirmed. In this study (2) both MGL and MTH20 were recorded and plotted versus the Corneometer values. The correlation is again very good but the relative variations between normal and treated zones are more marked for MTH20 than for MGL, confirming that, MTH20, the parameter related to the left-hand part of the histogram, is more sensitive than MGL for assessing skin hydration. In Figure 3 are plotted results obtained after the application of a cosmetic product on the both sides of forearms of volunteers for three weeks. One forearm, not treated, is the control. Variations in the Corneometer and in MGL of the SkinChip images are quite similar for both mean and standard deviation.

SKIN SURFACE HYDRATION MAPPING

As mentioned above, capacitance imaging allows measurement of skin hydration just as a Corneometer does, but in addition, it supplies images containing important supplementary information. For example, capacitance images obtained on photo exposed zones (outer forearm, top of hand, V of neck) display very inhomogeneous zones in terms of gray levels, corresponding to very different hydration levels of the skin surface (2). Examples appear in Figure 4. According to different studies in homogeneity of skin, hydration would be linked to severity of the skin photoaging (2). The origin of these hydration variations in exposed aged skin would come from two main origins: pigmentation disorders and altered desquamation. Concerning pigmentation, it is well documented that unevenness of pigmentation is a characteristic of exposed aged skin. In our studies of pigmented

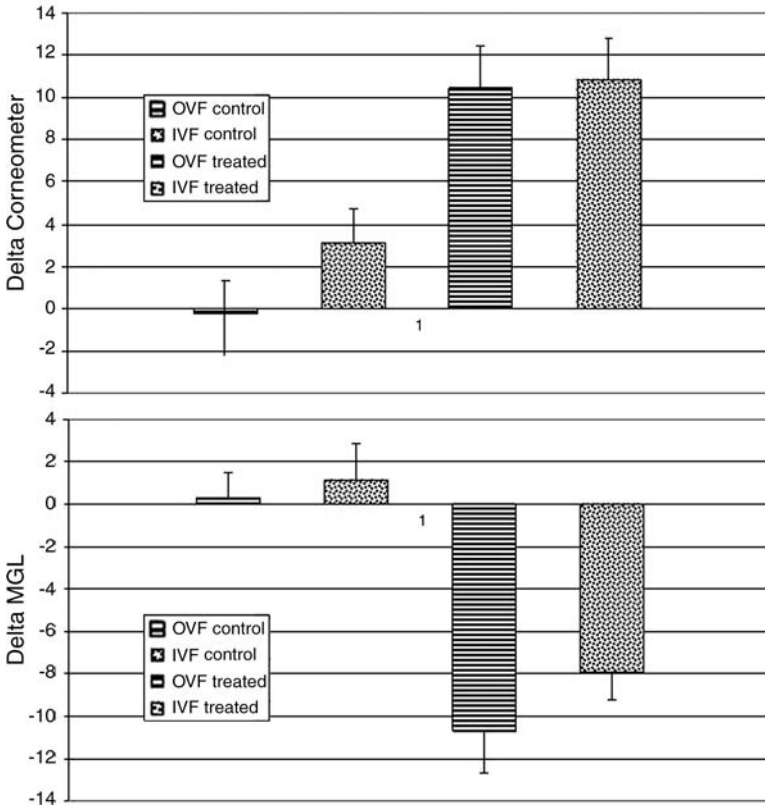


FIGURE 3 Comparative results of skin hydration obtained by means of a Corneometer and by capacitance imaging after a one month treatment on one forearm, the other serving as the control zone. Only variations between T0 and T4 weeks for the MGL and Corneometer values are displayed (mean and S.E.). *Abbreviations:* IVF, inner volar forearm; OVF, outer volar forearm; MGL, mean gray level.

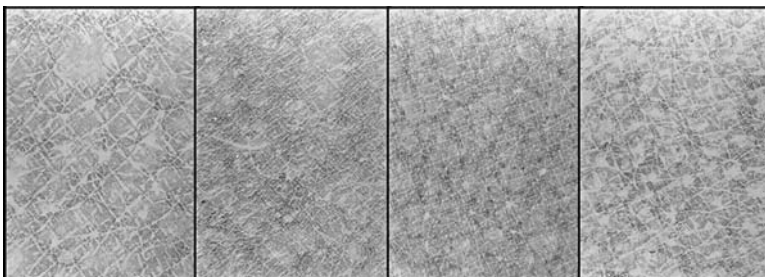


FIGURE 4 Different aspects of the inhomogeneity of hydration in case of photoaged skin. Some of the white zones correspond to pigmented areas.

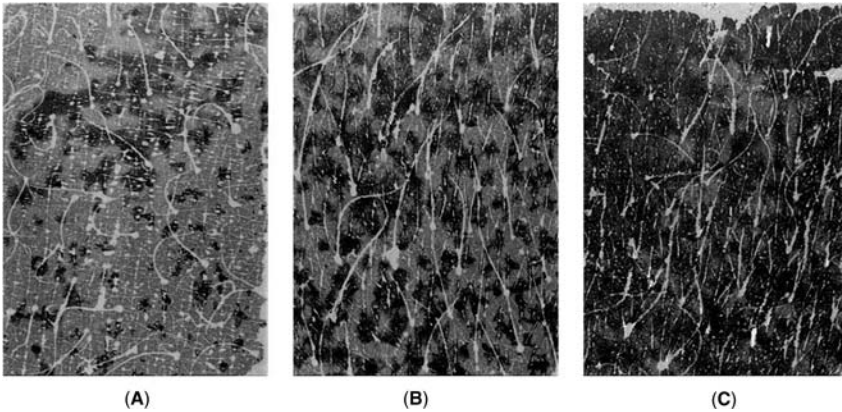


FIGURE 5 Capacitance imaging of a sweating zone (chest). (A) Onset of the phenomenon, (B) five minutes later, and (C) one hour later.

spots, their capacitance images are sometimes clearer or sometimes darker than the surrounding skin according to their nature. For example, hand lentigenes appear in general clearer and nevus darker than surrounding skin. It appears also that altered desquamation in photoaged skin occurs in discontinuous spots.

Treating dry skin with an efficient moisturizer modifies its capacitance image. Image becomes darker (more hydrated) with, in some cases, a more regular pattern of the primary lines of the micro relief (3). The exact meaning of such a phenomenon is presently under investigation.

Sweating is also an interesting phenomenon to be observed: At the onset of the phenomenon, only black dots appear, marking the sweating glands apertures. Progressively, these black dots become larger and larger till they merge in a continuous black area (Fig. 5). By measuring MGL of each image versus time, the kinetic of the phenomenon as well as the possible effect of a treatment can be studied.

SKIN MICRORELIEF

Skin surface pattern can easily be viewed and studied by using SkinChip. Measurement of CD is quite immediate and gives objective information about the "skin texture." In a recent study carried out on the forearm, it was shown that this parameter decreases versus age, passing from about 380 to 200/cm² with great variations from one person to another (Fig. 6). Such a decrease was established first on Caucasian volunteers and then confirmed in populations of other ethnical origins (S. Diridollou, to be published). These results are in line with those obtained through the study of skin replicas by Corcuff et al., in 1986 (4).

As mentioned above, software allowing the determination and display of the main orientations of the micro relief primary lines can be used. On adults, two main orientations exist at about 90°. According to the work by Corcuff et al., these two main orientations would come closer versus age and finally merge in a unique orientation, along the forearm axis, for aged persons. This result has not yet been confirmed in the studies carried out with SkinChip. In fact, for studying the skin micro relief, the precise position of arm and forearm is critical. It has been

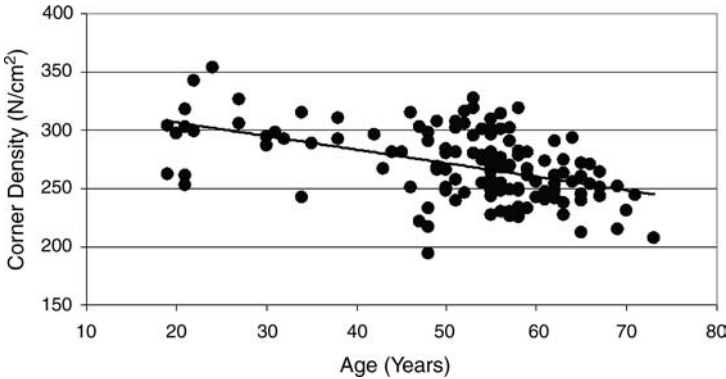


FIGURE 6 Variation of the corner density versus age. The linear inverse correlation is significant at the $p < 0.01$ level ($N = 134$).

shown that the aperture of the arm produces some changes in the lines orientation and density (5).

Follicular openings (pores) appear as white areas of different density and size according to the anatomical sites (6). This contrast is due to the fact that pores are filled with nonconductive material (sebum) and also because they are not totally in contact with the measurement window. An example of pore image is represented in Figure 1E.

Some skin pathologies (psoriasis, acne, etc.) were also imaged by using this technology (7,8). Some cases of pityriasis versicolor lesions are striking: quite invisible to naked eyes; some of them appear very clearly on the SkinChip images, probably because skin surface is covered by nonconductive materials (germs, fungi filaments) (9). According to the authors of these works, capacitance imaging could be of great interest for characterizing and differentiating pathological lesions [Uhoda E, Pierard GE. Contrasted skin capacitance imaging of seborrheic keratoses and melancytic nevi (to be published)].

SkinChip was also used for studying micro relief lines of women's lips versus age and assessing the beneficial effect of a special lipstick designed for treating dry lips (10). This technique allowed an easy way to record and to classify in three categories the different lip patterns. Comparing the gray levels of the images of lips (treated vs. nontreated) allowed demonstrating the hydrating effect of a tested lipstick.

CONCLUSION

This technique is based on very clear physical principles. Another great advantage of this technique comes from its simplicity of use: In a few seconds, images can be recorded and stored, some parameters relative to skin surface hydration and skin micro relief being routinely obtained. Today, most of the applications of this technique concern the cosmetic area (moisturizers and lipsticks) and the description of the skin surface characteristics versus age, ethnic origins, environment etc. Skin reactivity toward irritants and/or allergic material, skin diseases are also domains, where such a technique could be of great usefulness.

REFERENCES

1. Lévêque JL, Querleux B. SkinChip. A new tool for investigating the skin surface in vivo. *Skin Res Technol* 2003; 9:343–347
2. Batisse D, Giron F, Lévêque JL. Capacitance imaging of the skin surface. *Skin Res Technol* 2006; 12:1–6.
3. Beradesca E, Primavera G, Zahouani H, Lévêque JL. Capacitance imaging: new parameters for characterizing the skin surface texture, effect of hydration. World Congress on Non Invasive Studies of the Skin. Philadelphia, Sept 28–Oct 1, 2005.
4. Corcuff P, de Rigal J, Makki S, Agache P, Lévêque JL. Skin relief and ageing. *J Soc Cosmet Chem* 1983; 34:177–183.
5. Corcuff P, de Lacharrière, Lévêque JL. Extension-induced changes in the micro-relief of human volar forearm: variations with age. *J Gerontol* 1991; 46:223–227.
6. Uhoda E, Pierard-Franchimont C, Petit L, Pierard GE. The conundrum of skin pores in dermocosmetology. *Dermatology* 2005; 210:3–7.
7. Uhoda E, Pierard GE. Capacitance imaging of acne lesions. *Skin Res Technol* 2006. In press.
8. Uhoda E, Pierard-Franchimont C, Pierard GE. Skin capacitance mapping of psoriasis. *J Eur Acad Dermatol Venereol* 2006. In press.
9. Uhoda E, Pierard-Franchimont E, Pierard GE. Pityriasis versicolor anhydrotique. *Dermatol Actual* 2006; 89:16–17.
10. Lévêque JL, Gubanova E. Influence of age on lips and the perioral skin. *Dermatology* 2004; 208:307–313.

Applications of Reflectance Confocal Microscopy in Clinical Dermatology

Cristiane Benvenuto-Andrade, Anna Liza C. Agero, Yogesh G. Patel, Milind Rajadhyaksha, Allan Halpern, and Salvador Gonzalez

Dermatology Service, Memorial Sloan-Kettering Cancer Center, New York, New York, U.S.A.

Susanne Astner

Department of Dermatology, Venerology and Allergology, Charité University Medicine Berlin, Charitéplatz, Berlin, Germany

IMAGING PARAMETERS FOR REFLECTANCE-MODE SCANNING LASER CONFOCAL MICROSCOPY

A confocal microscope consists of a small light source, a condenser, objective lenses, and a detector (Fig. 1). The light source illuminates a small three-dimensional spot within an object such as skin. This illuminated spot is then imaged onto the detector through a small aperture. The small aperture allows only light that originates from the focused illumination spot to be detected, while the light that originates away from the spot is rejected (1). The light source, illuminated spot, and detection aperture are in optically conjugate focal locations and thus this arrangement is called "confocal." To create a two-dimensional image, the illumination spot is raster-scanned over the area of interest within the object and the image is produced point-by-point (i.e., pixel-by-pixel). Due to the confocal arrangement, the detected image is of a thin two-dimensional plane. This process is known as "optical sectioning:"

Optimum parameters for confocal optical sectioning to be comparable to the 5 μm -sectioning of routine histology have been determined under experimental conditions (1). These parameters are presented in Table 1.

CONFOCAL MICROSCOPY OF NORMAL SKIN

Images obtained by reflectance-mode confocal microscopy (RCM) are "en face" images as compared to vertical sections obtained by routine histology. While in routine histology tissue staining with exogenous dyes is required for an evaluation, confocal images are resolved in gray scale. Confocal imaging is based on the principles of light reflection, absorption, and scattering (1), and images are obtained due to the presence of endogenous contrast, which is provided by microstructures such as melanin, hemoglobin, or cellular organelles (2). Structures, therefore, are visualized based on optical properties such as the refraction index and the reflectivity of the tissue under investigation (3,4).

Using reflectance confocal microscopy, the top layer is the stratum corneum, which has a very high refraction index. Thus by reflecting the illuminating wavelengths the stratum corneum can be made to appear intensely bright upon confocal

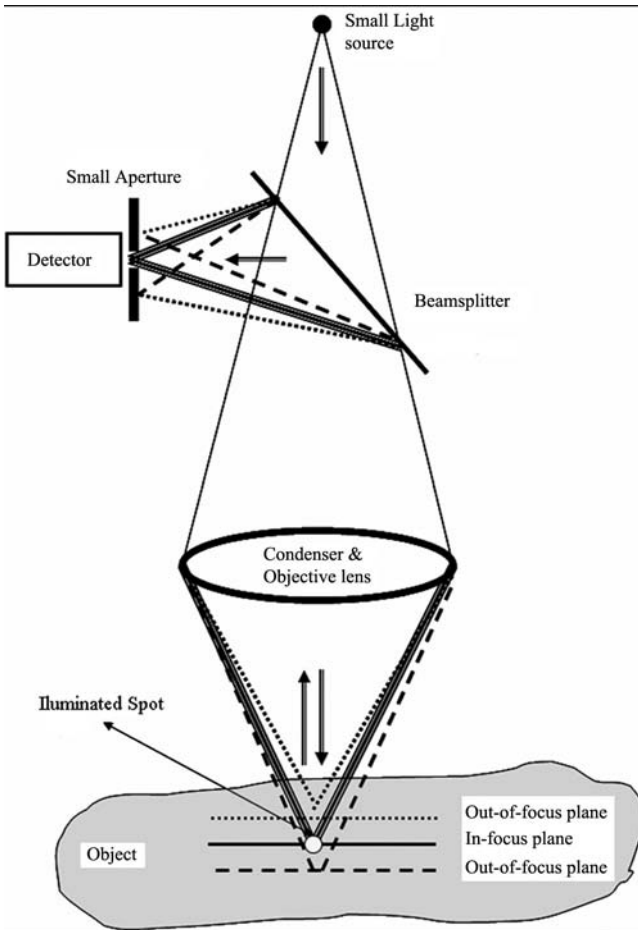


FIGURE 1 Confocal microscope is an arrangement showing a small detection aperture that is optically conjugate to the small illuminated spot within an object. In reflectance contrast, back-scattered light that is in focus (i.e., solid lines that are exactly from the illuminated spot in the in-focus plane) passes through the small aperture and is detected. Back-scattered light that is not in focus (dashed and dotted lines originating in the out-of-focus planes) is not detected.

evaluation. Gross epidermal microanatomy can easily be visualized, islands of corneocytes can be shown within individual skin folds, and hair follicles and sweat ducts can be identified (5,6). Individual corneocytes appear as large, anucleated, bright polygonal cells sized about 25 to 35 μm .

The next layer is the stratum granulosum, consisting of large polygonal cells with a large, centrally placed nucleus surrounded by a characteristic cytoplasm with a somewhat grainy appearance. Cells are between 25 and 30 μm in diameter, and are arranged in a homogenous pattern. Deeper into the epidermis, the cells of the spinous layer are smaller than the granular keratinocytes, measuring about 15 μm in diameter. The nucleus is dark, centrally placed and the cells are arranged in a characteristic honeycomb pattern. Directly below the spinous layer,

TABLE 1 Optimum Range Parameters for Confocal Imaging of Human and Animal Skin

Wavelength of light source for	
1–3 μm sectioning in the epidermis	Visible 488–514 nm
3–5 μm in the deeper dermis	Near-infrared 800–1064 nm
Objective lens magnification	30–100x
Field-of-view	0.5–0.15 mm
Objective lens numerical aperture	0.7–1.2, water immersion
Lateral resolution	0.5–1.0 μm
Axial resolution (optical section thickness)	2–5 μm
Detector aperture diameter	1–5x lateral resolution
Illumination power	up to 40 mW
Imaging rate	8–30 frames/sec

the basal keratinocytes can be seen as bright, highly refractile cells located on the tip of a dermal papilla. The high refractivity stems from the presence of melanin and melanosomes, with endogenous variation among skin phototypes and the anatomic location. On “en face” confocal images, basal keratinocytes are located surrounding each dermal papilla. The melanin in basal keratinocytes is typically arranged in a supranuclear position, often referred to as “melanin caps” or “umbrellas” implying their protective function. A reticular collagen network and small capillaries can be seen in the center of dermal papillae.

REFLECTANCE CONFOCAL MICROSCOPY FINDINGS OF INFLAMMATORY SKIN CONDITIONS

RCM has previously been used to describe inflammatory skin conditions noninvasively and in vivo. Psoriasis (7), Contact dermatitis (CD) (8–11), and bacterial (12) and fungal infections (13) have been evaluated to define their characteristic confocal features. The advantage of RCM in the diagnosis of cutaneous pathologies is that a majority of benign inflammatory skin conditions are limited to epidermal and upper dermal processes, a level where RCM has a resolution that is comparable to routine histology.

Contact Dermatitis

CD is the most common form of occupational skin disease in dermatology and affects approximately 20% of the population in the United States (14). The differentiation of allergic and irritant CD (ACD and ICD respectively) can pose a significant challenge to the dermatologist, as the clinical presentation, immunologic profile, and histopathologic features in ACD and ICD are remarkably similar (1,15–21). Patch testing remains the gold standard for diagnosis of CD, yet often the interpretation of patch tests results for mild cases of ICD and ACD is not too reliable, and inconclusive results are common (16). Our group has performed an extensive amount of work in the field of CD. By correlating RCM with conventional histopathology, distinctive characteristics for ACD and ICD have been identified (Fig. 2) (8,9,11). While ACD predominantly demonstrated vesicle formation, inflammatory infiltrate, and spongiosis (8,11), ICD was typically associated with pronounced superficial changes involving the stratum corneum, intraepidermal necrosis, and a prominent epidermal hyperproliferation with visible nucleoli (8,10). In these studies, both ACD and ICD reactions have demonstrated

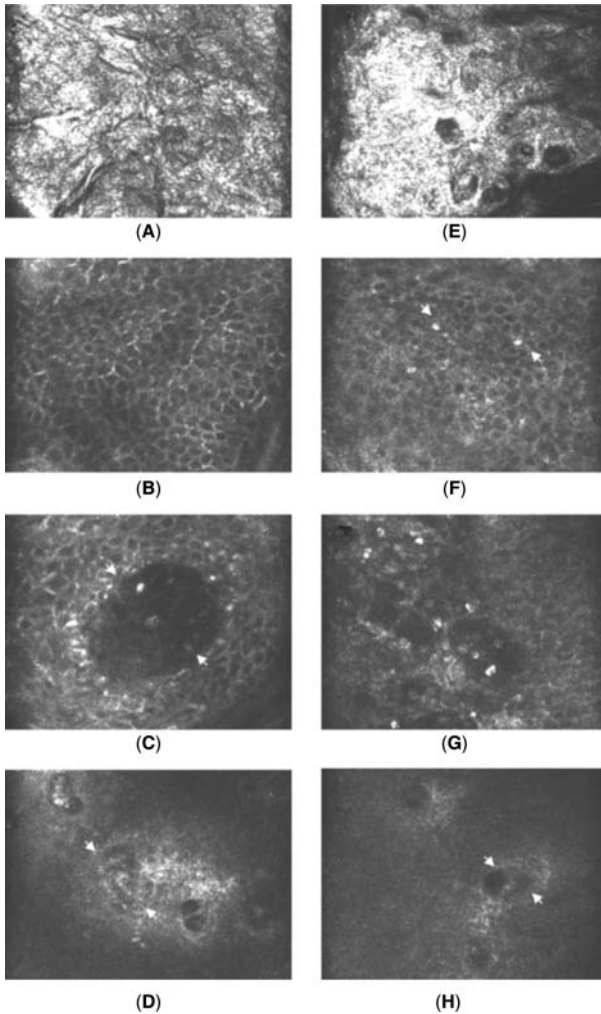


FIGURE 2 Selected features of ACD (*left*) and ICD (*right*). Left panel (**A–D**) with (**A**) intact stratum corneum (**B**) marked spongiosis of the granular layer (**C**) vesicle formation of the granular layer (*arrowheads*) and (**D**) dilated capillaries in the upper papillary dermis. Right panel (**E–H**) with features of ICD; (**E**) with parakeratosis (*arrowheads*) (**F**) spongiosis and inflammatory infiltrate (*arrowheads*) of the granular layer (**G**) with intraepidermal necrosis and (**H**) with dilated capillaries in the upper papillary dermis. *Abbreviations:* ACD, allergic contact dermatitis; ICD, irritant contact dermatitis.

similar degrees of spongiosis, and this feature does not facilitate the differentiation between these two reactions.

When looking at the kinetic evolution over time, characteristic patterns of ACD and ICD can be identified using RCM. First, the onset of disruptive changes is generally much faster for ICD when compared to ACD. The characteristic superficial changes in the stratum corneum are visible within few hours following the application of the contact irritants while stratum corneum alterations are generally

less prominent in acute ACD. Secondly, ACD characteristically presents with microvesicle formation while ICD also demonstrates features of intraepidermal necrosis (8,11). Finally, the epidermal hyperproliferation associated with ICD reactions can easily be followed using RCM, and seems to be a sensitive parameter for the activity of ICD reactions. Overall, ICD has a faster onset and a shorter duration than the cutaneous changes in ACD. Preliminary data on the sensitivity and specificity of RCM in the diagnosis of ACD indicated that selected RCM parameters such as spongiosis and exocytosis of the spinous layer have a high sensitivity and specificity in reference to patch testing. These results indicate that RCM may allow the interpretation of patch tests on a cellular level, in addition to clinical evaluation thus potentially enhancing ACD diagnosis.

Recently, investigations have also been aimed at the evaluation of ethnic variability in skin response to experimental contact irritants such as sodium lauryl sulfate (SLS) and common household detergents such as Ivory dishwashing liquid. In preliminary studies performed with Caucasians and African-Americans, participants exhibited different degrees of stratum corneum disruption and intraepidermal changes that may indicate differences as a function of skin color (10). Furthermore, RCM was able to visualize subclinical degrees of cutaneous irritation, demonstrating the ability of this technique to detect irritation at subthreshold irritant concentrations. Future studies are needed to confirm these findings and determine their applicability to other irritants and detergents.

Overall, RCM is a promising tool for the noninvasive evaluation of CD. Future work will be aimed at the investigation of individual allergens, different allergen concentrations, and the testing of additional contact irritants and cosmetics.

Psoriasis Vulgaris

Psoriasis is a common benign, proliferative skin disorder with histopathological features that can be visualized using RCM. In this regard, acanthosis, papillomatosis, parakeratosis, Munro's microabscesses, thinning of the granular layer, and increased tortuosity of the dermal vasculature may be easily elucidated by RCM (22). Lesional skin and adjacent uninvolved (normal) skin in a psoriatic lesion can be further delineated, allowing the demarcation of lateral margins to the surrounding normal skin (23). These findings suggest the potential use of RCM for precise, real-time detection of lesion margins *in vivo*.

Rosacea

Acne rosacea is a benign, inflammatory skin disorder of unknown etiology with a female preponderance. The disease typically presents on the face with dilated vasculature and acneiform inflammatory papules and pustules. RCM histopathology reveals increased diameters of the pilosebaceous ducts, tortuous capillaries, and a characteristic perifollicular and perivascular inflammatory infiltrate (12).

Pyogenic Granuloma

Pyogenic granuloma or so-called capillary hemangioma is an entity that arises within skin sites of minor trauma, such as insect bites or scratches, and is most commonly seen in infants and small children. The lesions are benign, yet the increased vascularization can be problematic and frequently leads to episodes of bleeding. Histopathologically, these lesions consist of proliferative, dilated

capillaries, and leucocyte infiltration. Upon RCM imaging, these lesions show an increased number of dilatated and tortuous blood vessels, pronounced spongiosis and exocytosis, which allows the differentiation from other hypervascular lesions, where inflammation is generally absent.

REFLECTANCE CONFOCAL MICROSCOPY FINDINGS OF NONMELANOCYTIC SKIN LESIONS

Actinic Keratoses

Biopsies for the definitive diagnosis of actinic keratoses (AK) are needed for some lesions that may be difficult to be clinically differentiated from other tumors (24,25). The utility of RCM has been applied to the study of these precancerous skin lesions with the intention of enabling *in vivo* diagnosis without a biopsy. Significant features of these lesions that have been described are presented in Table 2. However, full visualization of the epidermis (including the dermoepidermal junction) in hypertrophic and hyperkeratotic lesions is currently prevented by the limited imaging depth of RCM (26), leading to difficulty in diagnosis using RCM in these lesions.

Squamous Cell Carcinoma

In the same way, it is difficult to identify squamous cell carcinoma (SCC) by *in vivo* RCM. Due to its present inability to adequately assess the dermoepidermal junction in hyperkeratotic lesions, it is not possible to assess invasion into the superficial dermis in these lesions. Therefore, to date, it is not yet feasible to distinguish between superficially invasive SCC and SCC *in situ* with RCM. Nonetheless, RCM features suggestive of SCC have been described (26) and are presented in Table 2. Other pathologic features suggestive of SCC, such as vascular patterns and keratin pearls, need further investigation.

Basal Cell Carcinoma

Among the nonmelanocytic neoplasms, basal cell carcinoma (BCC) has been the most studied, and several well-defined confocal imaging features have been

TABLE 2 RCM Features of Nonmelanocytic Skin Tumors

Skin Lesion	Features
Actinic keratosis	Irregular hyperkeratosis Epidermal nuclear enlargement and pleomorphism Architectural disarray limited to lower portion of epidermis
Squamous cell carcinoma	Nuclear enlargement with pleomorphism Full thickness architectural disarray of epidermis
Basal cell carcinoma	Islands of tumor cells with monomorphic elongated basaloid nuclei Polarization of tumor cell nuclei along the same spatial axis throughout epidermis Prominent inflammatory infiltrate admixed or closely apposed with tumor cells Increased dermal vasculature with tortuous dilated blood vessels and leukocyte accumulation and rolling along endothelial lining Pleomorphism and architectural disorder of overlying epidermis

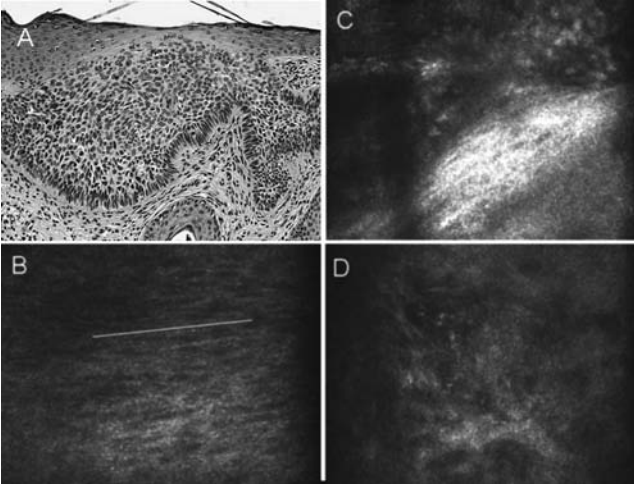


FIGURE 3 (A) Histology section showing proliferation of basaloid cells in a superficial pattern immediately below the epidermis. (B) Confocal image showing a population of cells with elongated nuclei, polarized along one axis. (C) Prominent inflammatory infiltrate near tumor cells. (D) Dilated blood vessels with leukocyte trafficking. Scale bar: 25 μm .

reported (27–29). The histologically correlated RCM features of BCC, regardless of subtype, are presented in Table 2. Figures 3, 4 present some of these features. A large retrospective, multicenter study has evaluated the sensitivity and specificity of RCM in diagnosing BCC *in vivo* by utilizing these features, with the finding that RCM is both sensitive and specific; the presence of two or more features had 100% sensitivity, while presence of four or more features had a specificity of 95.7% and 82.9% sensitivity. The diagnosis of BCC was significantly improved when confocal

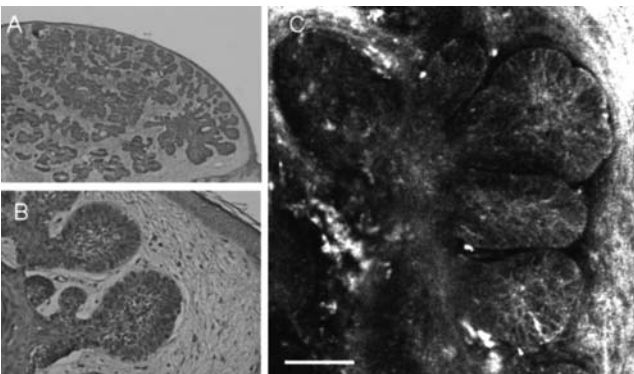


FIGURE 4 (A) Histology section showing proliferation of basaloid cells in a multinodular pattern. (B) Higher powered view of the same lesion. (C) Nesting and nodularity of tumor cells abutting the dermis. Scale bar: 100 μm .

images were examined together with clinical photographs. Little variability was seen across BCC subtypes in this study (30).

Specific BCC subtypes have also been described, with the following additional preliminary findings: (i) pigmented BCCs exhibit melanophages within the papillary dermis and between the islands or nests of tumor cells; melanophages appear as bright oval to stellate structures with indistinct borders (31,32); (ii) solid nodular BCCs show nesting and nodularity of epithelial cells at the level of papillary dermis (27) together with clefting and palisading of tumor cells (Figure 4) and (iii) fibrosing/infiltrating type of BCCs have curled bundles of collagen with large cells, representing the tumor stroma (28). Impetiginized BCC has also been imaged by RCM, with findings of parakeratosis (presence of nucleated keratinocytes in the horny layer) and subcorneal pustule (presence of polymorphonuclear leukocytes) (27).

REFLECTANCE CONFOCAL MICROSCOPY OF MELANOCYTIC SKIN LESIONS

Melanocytic Nevi

Differential RCM diagnosis of melanocytic lesions requires the analysis of architectural and cellular aspects of the skin, including melanocyte and keratinocyte shape and distribution (33,34). Melanin and melanosomes are strong sources of contrast in RCM (1,2). Thus, the large amount of melanin present in melanocytic lesions makes RCM imaging helpful in the differential diagnosis of benign and malignant pigmented skin lesions in the clinical research setting (2,35).

Different types of melanocytic nevi may be recognized by the distribution of melanocytes on the skin. Nevertheless, all types share characteristics described as very suggestive of a benign process under RCM (Table 3) (34,36,37). Figures 5,6 present some of these characteristics.

TABLE 3 Reflectance-Mode Confocal Microscopy Features of Melanocytic Skin Tumors

Skin Lesion	Features
Melanocytic nevi	<p>Preserved honeycomb appearance of keratinocytes in the epidermis</p> <p>Populations of monomorphous round to oval bright refractile cells with centrally positioned nuclei in the basal layer (pigmented keratinocytes and melanocytes)</p> <p>Regular and uniform dermal papillae</p> <p>Clusters of bright round cells in the dermis of compound nevi (nests)</p>
Cutaneous melanoma	<p>Disarray of keratinocytes (loss of the honeycomb appearance of the epidermis)</p> <p>Pleomorphic bright cells within the epidermis, with eccentrically placed large nuclei</p> <p>Coarse branching dendritic structures in the epidermis</p> <p>Small and irregular dermal papillae</p> <p>Bright grainy particles in the epidermis</p> <p>Dermal cell clusters (nests) may have multilobate, cerebriform, aspect when present</p> <p>Enlarged round or dendritic highly refractive cells ascending in the epidermis (pagetoid spread)</p>

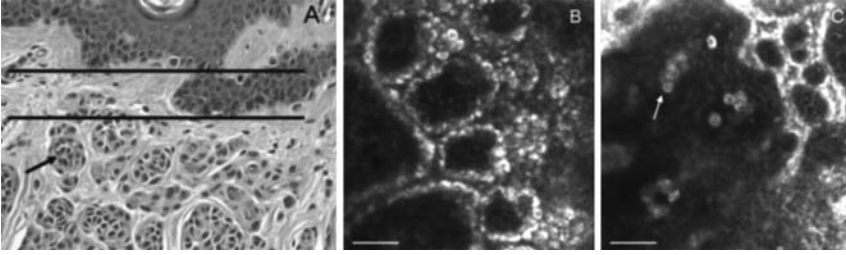


FIGURE 5 (A) Histology section of a lentiginous compound melanocytic nevus. The bars in image A show the level in which confocal images B (upper bar) and C (lower bar) were taken. Image (B) shows a rim of monomorphous refractive cells around dermal papillae, corresponding to small melanocytes and melanin-rich keratinocytes in the basal layer. Homogeneous refractive cells grouped in clusters (*nests*) can be seen in image (C) (*arrow*). These clusters of cells correspond to nests of melanocytes present in the dermis (A), (*arrow*). Scale bar: 100 μm

Atypical nevi present intermediate characteristics under RCM when compared to nevi and melanoma, and may be difficult to diagnose. They show focal loss of keratinocyte demarcation within the epidermis overlying the lesion and bright granules within the epidermis, probably representing melanin bodies. Dysplastic lesions may show a great variety in melanocyte size and shape, though cells still tend to be rounded or oval rather than dendritic (Fig. 7).

Cutaneous Melanoma

RCM images of melanomas are filled with pleomorphic bright cells within the epidermis and, sometimes, in the dermis (27). These cells may be oval, stellate, or fusiform in shape; possess coarse branching dendritic processes; and present eccentrically placed large nuclei (Fig. 8) (36,38,39). Table 3 summarizes RCM features of melanomas.

Gerger et al. assessed morphological features of 117 melanocytic skin tumors (90 benign nevi and 27 melanomas) under RCM and found sensitivity and specificity for melanoma of 88.15% and 97.60%, respectively (40). The morphological

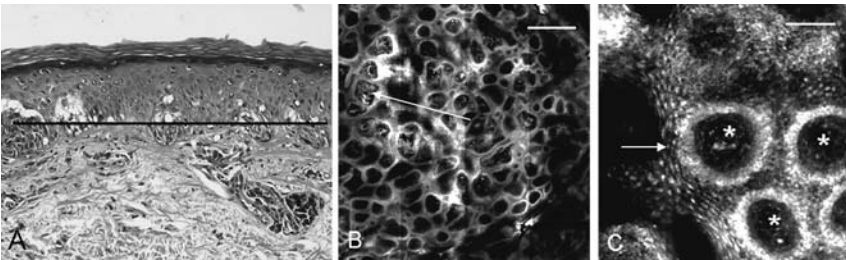


FIGURE 6 (A) Histology section of a compound melanocytic nevus. Note the regular shape of dermal papillae (*) and the rim of refractive cells corresponding to melanocytes and pigmented keratinocytes (*arrow*) in confocal image C. A bright dermal component can be seen within dermal papillae of confocal image B, corresponding to nests of melanocytes and melanophages (*arrow*). Scale bar: (B) 500 μm ; (C) 100 μm .

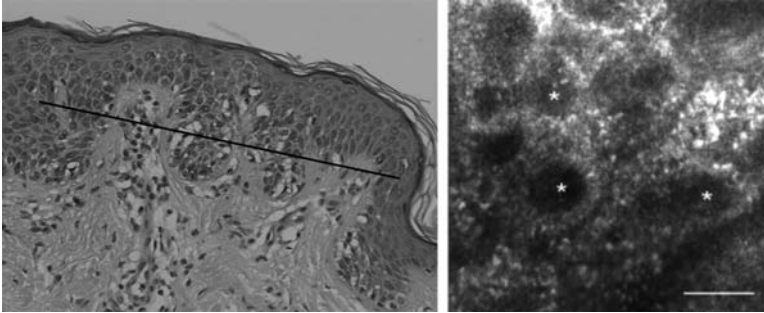


FIGURE 7 Histology sections of a dysplastic nevus (*left*) and confocal image of the same lesion (*right*) showing heterogenous brightness of the epidermis and irregular dermal papillae (*). Scale bar: 100 μm .

features used in this study were those previously described by Langley et al. (36) and Busam et al. (37), comprising: (i) melanocytic morphology and architecture; (ii) keratinocyte borders; (iii) presence or absence, as well as branching pattern, of dendrite-like structures; and (iv) homogeneity of melanocytic cell brightness (40).

A very important and useful characteristic of RCM is the ability to identify the abnormal intraepidermal melanocytic proliferation, as well as granules and dendritic structures, in clinically amelanotic melanomas (41,42). Presumably, it is possible due to the presence of melanosomes in the cytoplasm, an endogenous source of contrast due to their size (0.6–1.2 μm) and refractive index (1.70), and/or the presence of some melanin in premelanosomes (1,38). Confocal has been successfully used to map and evaluate response to treatment in these lesions (41–43). A limitation for the use of RCM in melanoma diagnosis is imaging depth. Lesion depth has been shown to be a very important prognostic factor for patients diagnosed with melanoma. However, available instruments can image down to 200 to 350 μm , and the presence of refractive structures in the dermis, such as inflammatory cells and collagen bundles, may decrease contrast and difficult melanocyte visualization (41). Thus, although RCM has been shown useful for the differential diagnosis of intraepidermal processes, little or no information about dermal cells and structures can be obtained, limiting the use of this technique for deeper lesions.

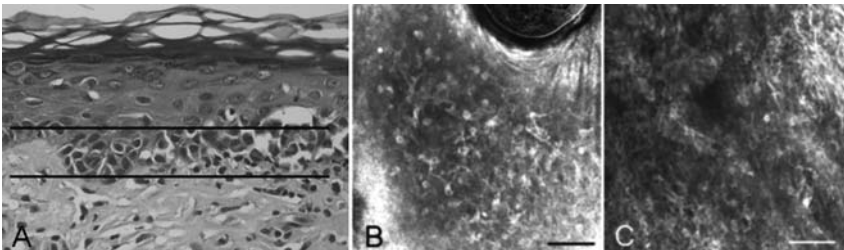


FIGURE 8 (A) Histology section of a melanoma. The bars in image A show the level in which confocal images B (*upper bar*) and C (*lower bar*) were taken. Figures (B and C) show the presence of enlarged (atypical) melanocytes ascending in the epidermis (pagetoid spread), within a background of marked loss of keratinocyte demarcation. Scale bar: 100 μm .

REFLECTANCE CONFOCAL MICROSCOPY AS AN ADJUVANT FOR MOHS MICROGRAPHIC SURGERY

Mohs micrographic surgery is a multistep-staged procedure for removing cutaneous malignancies and is routinely performed for the excision of BCCs and SCCs (44). Serial excisions are performed with each excision being guided by the examination of frozen histology specimens. This approach makes Mohs surgery a tedious and time-consuming procedure. The use of real-time confocal reflectance microscopy may make Mohs surgery more efficient by enabling rapid detection of BCCs and SCCs directly in fresh, unprocessed excisions, and thus possibly minimizing the need for frozen histology and reducing overall patient treatment time.

For RCM imaging of BCCs, an acetowhitening technique is implemented to enhance the contrast and detectability of the tumor relative to the surrounding dermis (45). The acetowhitening of excised slices brightens the nuclei by compacting chromatin and enhancing nuclear light backscattering. Early laboratory experiments demonstrated the detectability of large, macronodular BCCs with good correlation to routine histology using 5% acetic acid for three minutes (46). Recent and ongoing preclinical experiments show that the optimum combination for imaging various histologic subtypes of BCCs, such as macronodular, micronodular, superficial, and infiltrative BCCs, would be an acetic acid concentration of 2% and washing time of two minutes.

To observe large areas of an excision, a two-dimensional sequence of images is captured and stitched in software to display a mosaic with larger field-of-view. At present, 30×30 images may be stitched together to display a field-of-view of $12 \text{ mm} \times 12 \text{ mm}$ (Fig. 9).

FURTHER DEVELOPMENTS AND APPLICATIONS OF RCM

RCM has the potential to eliminate invasive biopsies by facilitating *in vivo* diagnosis of both benign and malignant pigmented and nonpigmented lesions. Unfortunately, a major limitation to this technology is the limited imaging depth, especially in hyperkeratotic lesions, largely due to intensity attenuation secondary to light absorption and scattering (47). Further improvements regarding increasing the RCM power and depth of optical penetration, and using optimal immersion media with good diffusion properties may help address this issue (26).

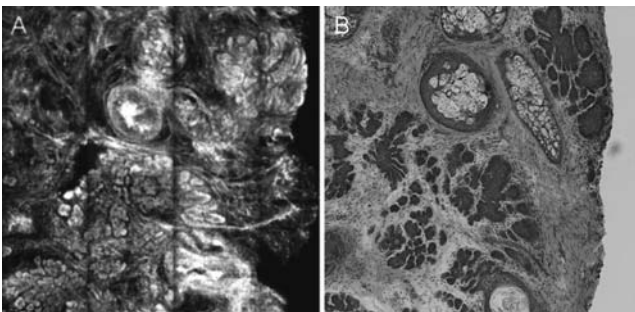


FIGURE 9 Mohs micrographic surgery. (A) Confocal 4×4 submosaic, 6x magnification displaying field of view of 3 mm, 2% acetic acid, two minutes washing time. (B) Frozen histopathology, 10x objective magnification, H and E staining.

RCM presents the opportunity for noninvasive evaluation of skin lesions at histological detail. It may be employed as a guide for performing biopsies, by helping determine which areas have features suspicious for malignancy and reducing sampling error (42), or as an adjunct to Mohs surgery and therapy (45,48) by mapping out the margins or extent of involvement prior to excision or other therapies (38,49). RCM can be repeated indefinitely, and therefore can be used to monitor progression or resolution of lesions through time. In this regard, RCM may be valuable in examining histopathological response of tumors to therapy. Progressive normalization of architecture in lesions of AK treated with photodynamic therapy has been observed under RCM monitoring (50). RCM is also being used to monitor response of AK to topical imiquimod in an ongoing study (51), and has been employed to confirm complete clearance of BCC and resulting inflammatory response from a lesion treated with topical imiquimod (52).

REFERENCES

1. Rajadhyaksha M, González S, Zavislan JM. Detectability of contrast agents for confocal reflectance imaging of skin and microcirculation. *J Biomed Opt* 2004; 9(2):323–331.
2. Rajadhyaksha M, Grossman M, Esterowitz D, et al. In vivo confocal scanning laser microscopy of human skin: melanin provides strong contrast. *J Invest Dermatol* 1995; 104(6):946–952.
3. Carlsson K. The influence of specimen refractive index, detector signal integration, and non-uniform scan speed on the imaging properties in confocal microscopy. *J Microsc* 1991; 163:167–178.
4. Hell S, Reiner G, Cremer C, Stelzer EHK. Aberrations in confocal fluorescence microscopy induced by mismatches in refractive index. *J Microsc* 1993; 169:391–405.
5. Rajadhyaksha M, Anderson RR, Webb RH. Video-rate confocal scanning laser microscope for imaging human tissues in vivo. *Appl Opt* 1999; 38(10):1–12.
6. Rajadhyaksha M, González S, Zavislan JM, Anderson RR, Webb RH. In vivo confocal scanning laser microscopy of human skin II: Advances in instrumentation and comparison with histology. *J Invest Dermatol* 1999; 13:293–303.
7. González S, Rajadhyaksha M, Rubinstein G, Anderson RR. Characterization of psoriasis in vivo by reflectance confocal microscopy. *J Med* 1999; 30(5–6):337–356.
8. Astner S, Gonzalez E, Cheung AC, et al. Non-invasive evaluation of the kinetics of allergic and irritant contact dermatitis. *J Invest Dermatol* 2005; 124(2):351–359.
9. González S, Gonzalez E, White MW, et al. Allergic contact dermatitis: correlation of in vivo confocal imaging to routine histology. *J Am Acad Dermatol* 1999; 40:708–713.
10. Hicks S, Swindolls KJ, Middelkamp-Hup MA, et al. Confocal histopathology of irritant contact dermatitis in vivo and the impact of skin color (black vs white). *J Am Acad Dermatol* 2003; 48(5):727–734.
11. Swindells K, Burnett N, Rius-Diaz F, Gonzalez E, Mihm MC, Gonzalez S. Reflectance confocal microscopy may differentiate acute allergic and irritant contact dermatitis in vivo. *J Am Acad Dermatol* 2004; 50(2):220–228.
12. González S, Rajadhyaksha M, Gonzalez-Serva A, et al. Confocal reflectance imaging of folliculitis in vivo: correlation with routine histology. *J Cutan Pathol* 1999; 26(4):201–205.
13. Hongcharu W, Dwyer P, González S, et al. Confirmation of onychomycosis by in vivo confocal microscopy. *J Am Acad Dermatol* 2000; 42:214–216.
14. Mathias CG. The cost of occupational skin disease. *Arch Dermatol* 1985; 89:332–334.
15. Brasch J, Burgard J, Sterry W. Common pathogenetic pathways in allergic and irritant contact dermatitis. *J Invest Dermatol* 1992; 98:166–170.
16. Rietschel RL, Fowler JF, Fisher AA. *Fisher's Contact Dermatitis*. 5th ed. Lippincott Williams & Wilkins, 2001.
17. Willis CM, Young E, Brandon DR, Wilkinson JD. Immunopathological and ultrastructural findings in human allergic and irritant contact dermatitis. *J Dermatol* 1986; 115:305–316.

18. Scheynius A, Fischer T, Forsum U, Klareskog L. Phenotypic characterization in situ of inflammatory cells in allergic and irritant contact dermatitis in man. *Clin Exp Immunol* 1984; 55:81–90.
19. Scheynius A, Fischer T. Phenotypic difference between allergic and irritant patch test reactions in man. *Contact Dermatitis* 1986; 14:297–302.
20. Flier J, Boorsma DM, Bruynzeel DP, et al. The CXCR activating chemokines IP-10, Mig, and IP-9 are expressed in allergic but not in irritant patch test reactions. *J Invest Dermatol* 1999; 113:574–578.
21. Ulfgren AK, Klareskog L, Lindberg M. An immunohistochemical analysis of cytokine expression in allergic and irritant contact dermatitis. *Acta Derm Venereol* 2000; 80:167–170.
22. González S, White WM, Rajadhyaksha M, et al. Confocal imaging of sebaceous gland hyperplasia in vivo to assess efficacy and mechanism of pulsed dye laser treatment. *Lasers Surg Med* 1999; 25:8–12.
23. González S, Rajadhyaksha M, Anderson RR. Non-invasive (real-time) imaging of histologic margin of a proliferative skin lesion in vivo. *J Invest Dermatol* 1998; 3:538–539.
24. Whited JD, Horner RD, Hall RP, et al. The influence of history on interobserver agreement for diagnosing actinic keratoses and malignant skin lesions. *J Am Acad Dermatol* 1995; 33:603–607.
25. Whited JD, Hall RP, Simel DL, et al. Primary care clinicians' performance for detecting actinic keratoses and skin cancer. *Arch Intern Med* 1997; 157:985–990.
26. Aghassi D, Anderson RR, González S. Confocal laser microscopic imaging of actinic keratoses in vivo: a preliminary report. *J Am Acad Dermatol* 2000; 43:42–48.
27. González S, Tannous Z. Real-time, in vivo confocal reflectance microscopy of basal cell carcinoma. *J Am Acad Dermatol* 2002; 47:869–874.
28. Sauermann K, Gambichler T, Wilmert M, et al. Investigation of basal cell carcinoma [correction of carcinoma] by confocal laser scanning microscopy in vivo. *Skin Res Technol* 2002; 8:141–147.
29. González S, Gilaberte-Calzada Y, Gonzalez-Rodriguez A, et al. In vivo reflectance-mode confocal scanning laser microscopy in dermatology. *Adv Dermatol* 2004; 20:371–387.
30. Nori S, Rius-Diaz F, Cuevas J, et al. Sensitivity and specificity of reflectance-mode confocal microscopy for in vivo diagnosis of basal cell carcinoma: a multicenter study. *J Am Acad Dermatol* 2004; 51:923–930.
31. Ruocco E, Argenziano G, Pellacani G, et al. Noninvasive imaging of skin tumors. *Dermatol Surg* 2004; 30:301–310.
32. Charles CA, Marghoob AA, Busam KJ, et al. Melanoma or pigmented basal cell carcinoma: a clinical-pathologic correlation with dermoscopy, in vivo confocal scanning laser microscopy, and routine histology. *Skin Res Technol* 2002; 8:282–287.
33. Pellacani G, Cesinaro AM, Seidenari S. In vivo assessment of melanocytic nests in nevi and melanomas by reflectance confocal microscopy. *Mod Pathol* 2005; 18:469–474.
34. Pellacani G, Cesinaro AM, Longo C, et al. Microscopic in vivo description of cellular architecture of dermoscopic pigment network in nevi and melanomas. *Arch Dermatol* 2005; 141:147–154.
35. Yamashita T, Kuwahara T, Gonzalez S, et al. Non-invasive visualization of melanin and melanocytes by reflectance-mode confocal microscopy. *J Invest Dermatol* 2005; 124: 235–240.
36. Langley RG, Rajadhyaksha M, Dwyer PJ, et al. Confocal scanning laser microscopy of benign and malignant melanocytic skin lesions in vivo. *J Am Acad Dermatol* 2001; 45:365–376.
37. Busam KJ, Charles C, Lee G, et al. Morphologic features of melanocytes, pigmented keratinocytes, and melanophages by in vivo confocal scanning laser microscopy. *Mod Pathol* 2001; 14:862–868.
38. Busam KJ, Hoster K, Charles C, et al. Detection of clinically amelanotic malignant melanoma and assessment of its margins by in vivo confocal scanning laser microscopy. *Arch Dermatol* 2001; 137:923–929.
39. Tannous ZS, Mihm MC, Flotte TJ, et al. In vivo examination of lentigo maligna and malignant melanoma in situ, lentigo maligna type by near-infrared reflectance confocal

- microscopy: comparison of in vivo confocal images with histologic sections. *J Am Acad Dermatol* 2002; 46:260–263.
40. Gerger A, Koller S, Kern T, et al. Diagnostic applicability of in vivo confocal laser scanning microscopy in melanocytic skin tumors. *J Invest Dermatol* 2005; 124:493–498.
 41. Curiel-Lewandrowski C, Williams CM, Swindells KJ, et al. Use of in vivo confocal microscopy in malignant melanoma: an aid in diagnosis and assessment of surgical and nonsurgical therapeutic approaches. *Arch Dermatol* 2004; 140:1127–1132.
 42. Busam KJ, Charles C, Lohmann CM, et al. Detection of intraepidermal malignant melanoma in vivo by confocal scanning laser microscopy. *Melanoma Res* 2002; 12:349–355.
 43. Chen CS, Elias M, Busam K, et al. Multi-modal in vivo optical imaging, including confocal microscopy, facilitate pre-surgical margin mapping for clinically complex lentigo maligna melanoma. *Br J Dermatol* 2005; 153:1031–1036.
 44. Mohs F. Chemosurgery—a microscopically controlled method of cancer excision. *Arch Surg* 1941; 42:278–295.
 45. Rajadhyaksha M, Menaker G, Flotte T, et al. Confocal examination of nonmelanoma cancers in thick skin excisions to potentially guide mohs micrographic surgery without frozen histopathology. *J Invest Dermatol* 2001; 117:1137–1143.
 46. Chung VQ, Dwyer PJ, Nehal KS, et al. Use of ex vivo confocal scanning laser microscopy during mohs surgery for nonmelanoma skin cancers. *Dermatol Surg* 2004; 30:1470–1478.
 47. Sun Y, Rajwa B, Robinson JP. Adaptive image-processing technique and effective visualization of confocal microscopy images. *Microsc Res Tech* 2004; 64:156–163.
 48. Tannous Z, Torres A, González S. In vivo real-time confocal reflectance microscopy: a noninvasive guide for Mohs micrographic surgery facilitated by aluminum chloride, an excellent contrast enhancer. *Dermatol Surg* 2003; 29:839–846.
 49. Torres A, Niemeyer A, Berkes B, et al. 5% imiquimod cream and reflectance-mode confocal microscopy as adjunct modalities to mohs micrographic surgery for treatment of Basal cell carcinoma. *Dermatol Surg* 2004; 30:1462–1469.
 50. Trehan M, Taylor C, Racette A. Confocal microscopic imaging of actinic keratoses post photodynamic therapy with 5-ALA [Abstr]. In 20th World Congress of Dermatology, Paris, 2002.
 51. González S, Swindells K, Rajadhyaksha M, et al. Changing paradigms in dermatology: confocal microscopy in clinical and surgical dermatology. *Clin Dermatol* 2003; 21:359–369.
 52. Goldgeier M, Fox CA, Zavislan JM, et al. Noninvasive imaging, treatment, and microscopic confirmation of clearance of basal cell carcinoma. *Dermatol Surg* 2003; 29:205–210.

Stephan El Gammal

Dermatological Clinic, Hospital Bethesda, Freudenberg, Germany

Claudia El Gammal

Department of Dermatology, Medical Care Center, Jung-Stilling Hospital, Siegen, Germany

Peter Altmeyer

Department of Dermatology, Ruhr-University, and Dermatological Clinic of the Ruhr-University, St. Josef Hospital, Bochum, Germany

Michael Vogt and Helmut Ermert

Institute of High Frequency Engineering, Ruhr-University Bochum, Bochum, Germany

INTRODUCTION

It is a characteristic feature of the dermatological specialty that the whole spectrum of diseases, from slight irritations to malignant transformations, lies directly before one's eyes. Clinical examination by inspection and palpation thus plays a crucial role in dermatological diagnosis.

When examining tumorous or inflammatory diseases, in depth expansion of the process is a further important clinical parameter. Sonography is an interesting candidate.

In the past sonography has already conquered many specialities in medicine. Ultrasound imaging systems, which are currently used to study inner organs, are—due to their poor resolution—of minor interest for those studying the skin. Until 1975, ultrasound transducers with a center frequency and band width of maximal 7.5 MHz were available. In dermatology, this equipment is used to evaluate the peripheral lymph nodes of patients with skin tumors (1,2) or the testes (3–5). Attempts to evaluate inflammatory and tumorous processes in the skin using 1.5–5 MHz transducers delivered very unsatisfactory results (6).

In 1980's 15 to 20 MHz ultrasound imaging systems were developed. During the last decade new noninvasive skin imaging techniques that have been developed, have enabled us to improve the evaluation of skin diseases prior to biopsy.

Figure 1 shows medline publications on noninvasive skin imaging methods in the past 25 years. Ultrasound is the oldest noninvasive technique that enables us to look at skin layers "beneath" the skin surface.

During the past 15 years, 25 MHz sonography of the skin has gained increasing importance as a noninvasive imaging method in dermatology. Clinical applications are the preoperative determination of the extension of skin tumors (7–13), the monitoring of inflammatory lesions (14–18) and sclerotic processes (19–25), and the objective judgement of skin tests such as patch test reactions (26–28) and tuberculin test reaction (29), to name but a few. Today, 25 MHz ultrasound equipment has become widely available at reasonable cost.

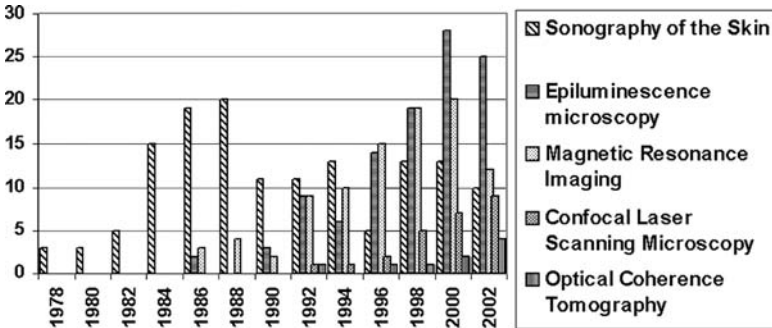


FIGURE 1 Medline-Publications on noninvasive skin imaging methods. Sonography was the oldest method introduced in clinical dermatology. In the past decades, epiluminescence microscopy has gained great interest in the scientific community because of its usefulness in differential diagnosis in pigmented skin tumors.

Sonograms of normal skin show at their upper border, a thin, very echogenic line, the so-called “skin entry echo.” Beneath this, a broad, echogenic band with scattered reflexes is seen, which corresponds to the dermis (Fig. 2). The subcutaneous fatty tissue is echolucent with obliquely oriented echogenic connective tissue septae.

The epidermis cannot be visualized, and certainly structures within the epidermis cannot be differentiated (8,11), due to the lack of resolution using commercially available transducers with center frequencies below 20 MHz.

The axial resolution is mainly influenced by the bandwidth (Fig. 3A). The lateral resolution is proportional to the center frequency and indirectly proportional

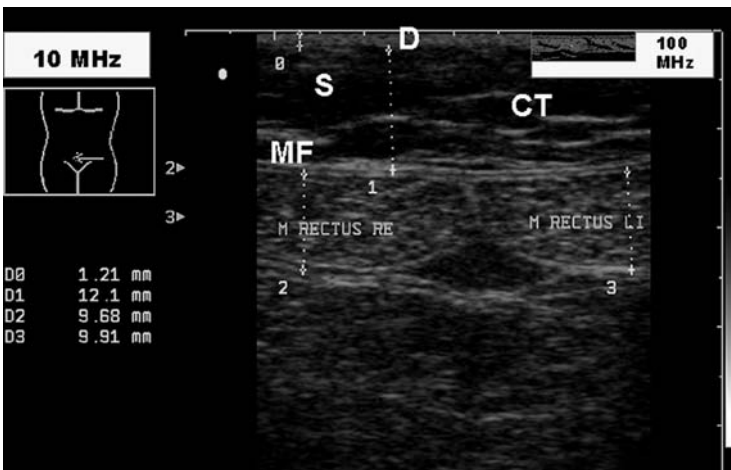
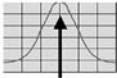


FIGURE 2 Comparison of 10 and 100 MHz sonography (inset). At 10 MHz the dermis is a ill-defined line at the upper part of sonogram due to insufficient resolution, at 100 MHz structures within the dermis are visualised (e.g., obliquely oriented hair follicles). D, S, MF, CT septae in the subcutaneous fatty tissue. The distance between two neighboring lines (right border of 10 MHz picture) is 5 mm. *Abbreviations:* D, dermis; S, subcutis; MF, muscle fascia; CT, connective tissue.

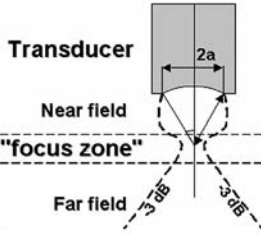
$$\text{Axial Resolution} = \frac{2 \times \ln(2) \times c \text{ [m/s]}}{\pi \times \Delta f \text{ [MHz]}}$$

$\Delta f = \text{bandwidth}$

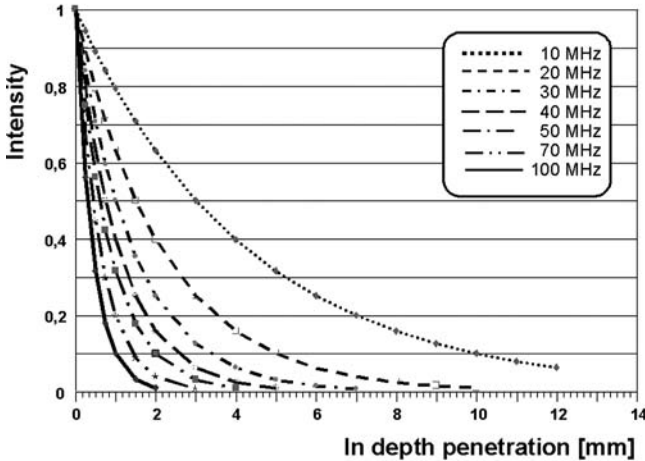


Mean Frequency

Lateral Resolution



(A)



(B)

FIGURE 3 (A) Physical parameters influencing the axial and lateral resolution. The axial resolution is mainly influenced by the bandwidth of the transducer, the lateral resolution by the geometry of the transducer in the focus zone. The near and far field of the transducer bear multiple artifacts. $c = 1580$ m/sec in soft tissue. (B) Effect of the center frequency on in-depth penetration of the ultrasound beam. When the center frequency is raised (and thereby the axial resolution is improved), the in-depth penetration of the ultrasound beam decreases significantly.

to the focal length (30–32). To investigate the epidermis, both the axial and lateral resolution must be improved. By raising the center frequency and bandwidth of the ultrasound transducer, resolution is increased, but the signal penetration depth into the skin is reduced (Fig. 3B).

We modified the 100 MHz transducer technology in such a way that skin structures up to 2 mm depth can be visualized (32,33) at very high resolution.

Considering that dermatology includes all structures from the skin surface to the muscle fascia, lower frequencies are necessary to study deep skin structures (Fig. 4).

Range	Examined Structure	Range	In-depth penetration	Resolution (axial)
5-15 MHz	Subcutaneous lymphnodes large arteries and veins subcutis and fatty tissue, muscles	5 MHz	> 3 cm	0,4 mm
15-25 MHz	Dermis (overview and sonometry) subcutis (detailed architecture) arterioles and venoses	20 MHz	8 mm	80 μ m
25-50 MHz	Epidermis (palms and soles) Skin appendages dermis (detailed architecture)	50 MHz	4 mm	40 μ m
50-150 MHz	epidermis (detailed architecture) mucosa upper dermis	100 MHz	2 mm	11 μ m

FIGURE 4 Sonography in dermatology. Lower frequencies are needed when studying structures which lie deep beneath the skin surface, for example lymph nodes.

METHODS AND PATIENTS

Sonographic Equipment

To study the subcutis we used an Esaote AU5 ultrasound unit equipped with a 7.5/10 MHz linear array applicator. Ultrasound gel was used as coupling medium.

Examination of the dermis, epidermis and stratum corneum was done using high resolution sonography. An experimental ultrasound imaging unit was developed which can be operated with different transducers in a frequency range of 20–250 MHz. Technical details have been published elsewhere (31–33). To study the epidermis, we used a 100 MHz ceramic transducer. The characteristics of this transducer are summarized in Table 1.

To obtain an excellent lateral resolution we used a highly focused transducer (with a short length of the focus zone of only 400 μ m). In order to obtain a sharp

TABLE 1 Characteristics of the 100 MHz Transducer

Manufacturer	Ultran Laboratories Inc., Boalsburg, PA, U.S.	
Construction	Ceramic transducer with a quartz coupling layer	
Piezoelectric properties	Center frequency (influenced by the water coupling medium)	$f_m = 86$ MHz
	Center frequency (after compensation for the water coupling medium)	$f_m = 95$ MHz
Geometry	Band width	$\Delta f = 107$ MHz
	Radius of curvature (focus length)	$d = 4.3$ mm
	Diameter of the acoustic surface	$D = 3.2$ mm
	Angle of aperture	$\theta_{\max} = 20^\circ$
	Relative focus length	$F = 1.34$
Resolution	Length of the focus zone	$d_f = 400$ μ m
	Axial (theoretical)	6.6 μ m
	Axial (in practice ^a)	8.7 μ m
	Axial (in biological tissue)	11 μ m
	Lateral (in the focus zone)	30 μ m

Note: The axial resolution was calculated using the width of the ± 6 dB level of the received echo signal and assuming a mean sound speed of 1580 m/sec in soft tissue.

^aMeasured on a glass plate.

image not only from a stripe of 400 μm . In order to obtain a sharp image not only from a strip of 400 μm , but from a wider part of the skin, we developed a mechanical focusing procedure, which we call Brightness/depth-scan (B/D-scan). The principle of this method is to compose the sonogram of several 400 μm wide image stripes, which are recorded one after the other, each in the focus zone of the transducer (31,33). After the uppermost stripe is recorded by lateral movement of the transducer over the selected area, the transducer is moved vertically 400 μm towards the skin surface, before the next image stripe is recorded. To eliminate movement artifacts between adjacent stripes, the overlapping parts (nearfield and farfield) are used for adjustment by the computer program, which puts together the final image.

Image processing involved two steps for every picture. First, the internal echoes of the 100 MHz transducer were eliminated. The oscillation curves of all neighboring A-scans of the image were averaged and the mean oscillation curve was then subtracted from every single A-scan. Secondly, the A-scans were demodulated. The envelope curve was determined by two complex fast fourier transformations for every A-scan. This procedure provides optimal results, but does not allow to promptly view the recorded data. For this purpose, we additionally implemented a fast method of demodulation consisting of a digital rectification of the high-frequency A-scan combined with a nonrecursive digital filter of the order of 10. This linear phase filter has a passband cutoff-frequency of 150 MHz.

Patients and Volunteers

All volunteers and patients gave informed consent for all examinations.

Subcutis: Over a time period of eight years, sonograms of different pathological conditions were collected in a huge data bank (over 5000 patients). More than 800 patients with malignant melanoma were followed up on a regular basis using lymph node sonography (inguinal, axilla, neck region). We studied lymph nodes in 300 patients documenting palpation and visualisation of lymph nodes (benign and malignant lymphadenopathy) using sonography.

Normal Palmar Skin: 10 right-handed volunteers with healthy skin (five men and five women, age 29 to 76, mean 56.4) were investigated. The index finger tip of the left hand was occluded for 30 minutes with an emulsion using a finn chamber.

Normal Glabrous Skin: Sonograms were taken from volunteers with healthy skin (age 20–32, mean 24.1) on abdomen about 3 cm lateral the umbilicus ($n=8$), the upper back over the scapula ($n=11$), the dorsal forearm ($n=9$) and the calf ($n=14$). In several persons, we took sonograms on the volar wrist at the transition from palmar to glabrous skin.

Psoriasis Vulgaris and Lichen Planus: Thirty-five untreated, infiltrated and slightly scaly psoriatic lesions on the extremities of 18 patients with chronic plaque-type psoriasis vulgaris and 10 lichen planus papules of six patients were investigated. Sonograms were taken in the center and the margin of the lesions and in the surrounding normal skin.

Skin Tumors: Sonograms were taken from skin tumors (basal cell carcinoma, malignant melanoma, seborrheic keratosis, nevocellular nevi) and normal adjacent or contralateral skin. Then the tumors were excised for histology (see below). Only skin tumors with a poor subluminal infiltrate in histology were included in our study: a total of 27 superficial basal cell carcinoma, 13 malignant melanoma, 16 nevocellular nevi and 11 seborrheic keratoses were evaluated using statistical methods.

Image Processing and Statistical Evaluation

For image analysis, we used the program AnalySIS[®] (Soft Imaging Software GmbH, Münster, Germany). The structure of interest within the sonographic image [e.g., entry echo or echopoor band (EPB)] was manually delimited by a polygon, using a position cursor. Its mean diameter in *y*-axis was calculated as the average length of all A-scans in the polygon. The mean gray level of the polygon area was also determined; its value ranges from 0 (black) to 255 (white).

In every sonogram, structures of interest (thickness of the skin entry echo, echodensity of the skin entry echo, echodensity of the echopoor tumor area, echodensity of the subtumoral region) were measured in the skin tumor region and in the adjacent or contralateral normal skin. Values were calculated as an index (% of the normal skin) to correct for differences between different anatomical locations.

Finally, the U-test (Mann-Whitney-Wilcoxon) for unpaired observations was used to compare the parameters mentioned above. Values of $p < 0.05$ were considered significant.

Correlation with Histology

In 79 patients (psoriasis plaques: $n = 11$, lichen planus papules: $n = 6$, basal cell carcinoma: $n = 27$, malignant melanoma: $n = 13$, nevocellular nevi: $n = 16$, seborrheic keratoses: $n = 6$), a biopsy was taken after sonography. In order to obtain exactly correlating sonographic and histologic images, a 10 mm long line was drawn on the skin in the plane of the B-scan. After local anaesthesia of the area, the skin was cut along this line down to the subcutis. Then a spindle-shaped excision was performed with this cut in the center. The two halves of the tissue spindle were separated and their central cutting planes placed on cardbord. This prevents warping of the tissue during formalin fixation. In the histological sections, the thickness of the epidermis (from the stratum granulosum to the lowest points of the rete pegs), the thickness of the inflammatory infiltrate (from the uppermost parts of the dermal papillae downwards) and the thickness of both the epidermis plus the infiltrated dermis were measured.

By means of the linear regression analysis, we checked whether there is a significant correlation between the thickness measurements in sonographic images and the corresponding histologic sections.

RESULTS

Subcutis

Sonography of the range 7.5–15 MHz is very suitable to study structures in the deep fatty tissue. Such structures are large arteries and veins, connective tissue routes, muscle fascia and lymph nodes (Fig. 4). Soft tissue tumors, such as lipoma are easily identified. They are seen as ovaloid structures with a homogeneous echo texture (Fig. 5) within the rather echopoor fatty tissue.

Connective tissue diseases such as scleroderma, dermatoliposclerosis in venous leg disease, varicose veins or inflammatory diseases such as acute cellulite can be easily quantified, to name just a few.

Acute cellulite is accompanied by a localized swelling and inflammation of the skin. Sonography exhibits multiple "lymphfissures" (Fig. 6) in the upper subcutis. Typically these "lymph fissures" disappear when a gentle pressure is

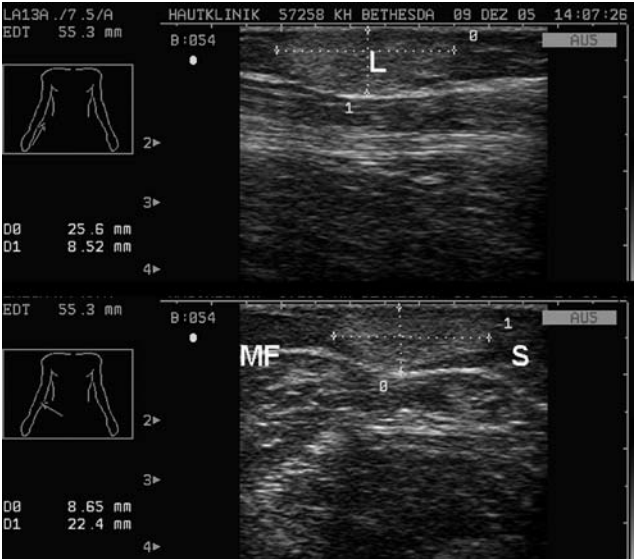


FIGURE 5 Lipoma on the lower arm of a 67-year-old woman. The two sonograms were registered perpendicularly. *Abbreviations:* L, lipoma; S, subcutis; MF, muscle fascia.

applied on the tissue, because the liquid is moved laterally. In chronic lymphoedema, multiple lymphfissures are observed at all levels of the subcutaneous fatty tissue (Fig. 7). In acute thrombophlebitis, lymphfissures surround the involved vein and the vein is no longer compressible.

Lymph node sonography has become a routine method in dermatology used for skin tumor staging and skin tumor follow-up programs. In most body regions, normal lymphnodes are too small to be visualised using 7.5 or 10 MHz sonography.

Activation or malignant proliferation brings about an enlargement of the lymph node. We examined lymph nodes in more than 300 patients (axilla and

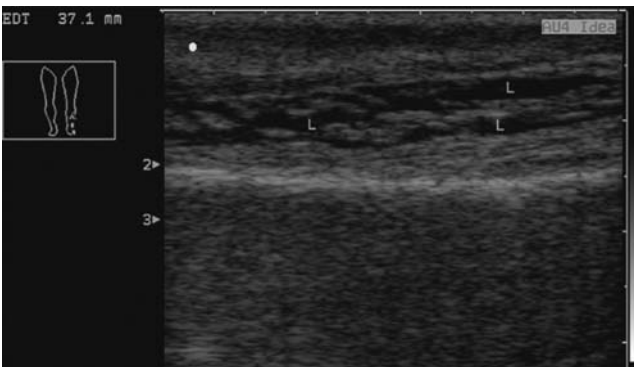


FIGURE 6 Acute cellulite: lymph fissures are visualised in the subcutis. They disappear when applying local pressure. Distance between two distance lines at the upper and right border: 5 mm. *Abbreviation:* L, lymph fissures.

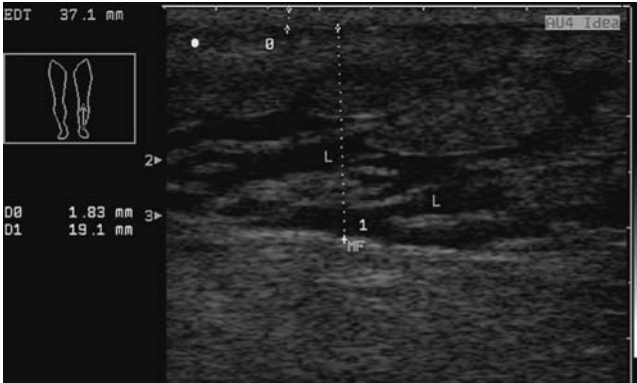


FIGURE 7 Chronic lymphoedema. Lymph fissures are seen at all levels of the subcutaneous fatty tissue. Distance between two distance lines at the upper and right border: 5 mm. *Abbreviations:* L, lymph fissures; MF, muscle fascia.

inguinal region) and found that, in particular concerning small lymph nodes, sonography is by far superior to palpation (Fig. 8). This finding has also been confirmed by other authors. Loose et al. (34) reported concerning detection of regional metastatic lymphnodes in patients with malignant melanoma, that in the groin 61% and in the neck 67% of the sonographically enlarged lymph nodes were also palpable, while in the axilla only 45% were palpable.

After the inflammatory process has ended, most lymph nodes become smaller again, normally over six to twelve weeks. Sometimes, however, postinfectious lymph nodes remain enlarged. It has been speculated, that new lymph follicles develop in the medulla region, due to a persisting stimulus. These lymphnodes often exhibit an echorich medulla region and are often referred to as “reactive lymph

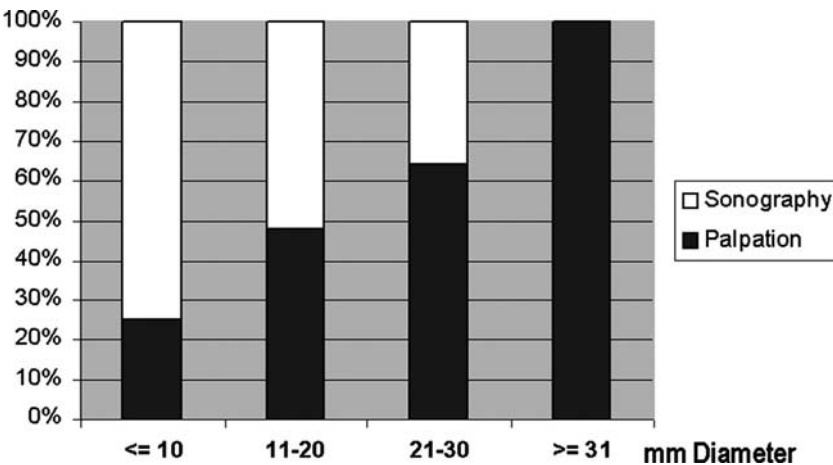


FIGURE 8 Large lymph nodes are easily palpated and visualised by sonography ($n = 300$). Small lymph nodes may be missed by palpation. Only 25% of the lymph nodes smaller than 10 mm of diameter which were seen sonographically were also detected by palpation.

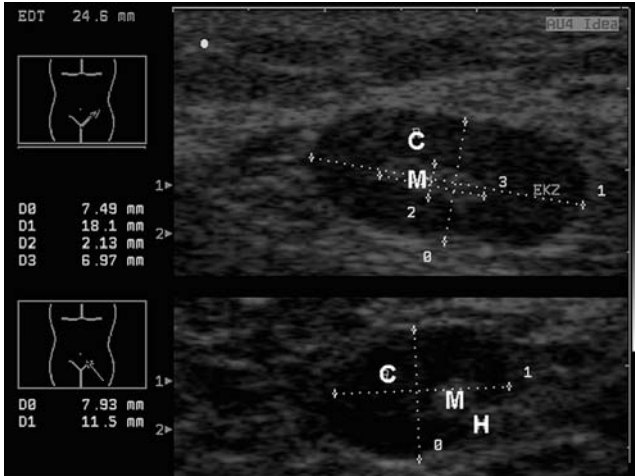


FIGURE 9 Benign lymphadenopathy. Sonograms in two perpendicular axes, left groin. Solbiati-index = 2.3. Abbreviations: C, cortex; M, medulla region; H, hilus region.

nodes." Figure 9 shows an enlarged lymph node from the groin region with an tiny medulla and an enlarged cortex region. Changes of the size of the lymph node by keeping the shape constant are typical for benign lymphadenopathies (Fig. 12).

A simple way to evaluate changes of the shape of a lymph node is calculation of the Solbiati-Index (35). The suspect lymph node is visualised in two perpendicular axes, the maximal longitudinal diameter (L) and the minimal width (W) of the lymph node are measured and the L/W quotient is calculated. An L/W -quotient < 2 means that the lymphnode is more ball-shaped ($L/W = 1$).

Lymph nodes can also be the battle field of primary and secondary malignancies. Vassallo et al. (36) studied benign and malignant lymphadenopathies sonographically, excised them and classified them after histopathological examination. They could show, that 85% of all examined benign lymphadenopathies had an $L/W > 2$. In 86% of all primary malignant lymphadenopathies (e.g., lymphoma) and 85% of all secondary malignant lymphadenopathies (lymph node metastases) the L/W was < 2 . Obviously, tumor masses destruct the inner architecture, such as trabecula of the lymph node. Therefore the shape of the lymph node changes in malignant lymphadenopathies.

Figure 10 exhibits an metastatic lymph node in two axes perpendicular to each other. The Solbiati-index is nearly one. Note that the medulla and hilus region are no longer visible.

Figure 11 exhibits primary malignant lymphadenopathy. Note that the medulla region is tent-shaped and the cortex region excentrically enlarged. The lymph node has changed its shape considerably. Figure 12 shows that in benign lymphadenopathy, the enlarged lymph nodes keep their shape while the relation between the medulla and cortex region may vary. In malignant lymphadenopathy the shape is altered, because the lymph node becomes more ball-shaped and/or because there is an excentric lymph node enlargement. However, because there is an overlap of 15% between both groups of enlarged lymph nodes, it is wise to repeat sonography after six weeks. Malignant lymph nodes will continue to

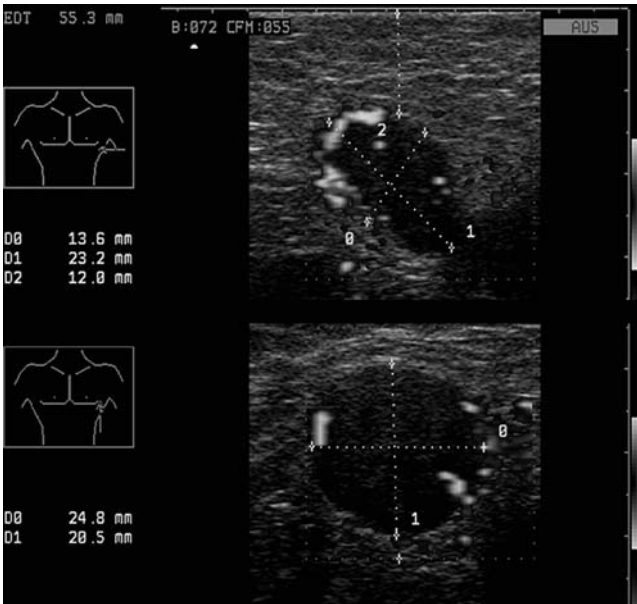


FIGURE 10 Metastatic lymphnode. The lymphnode has become ball-shaped. In Power-Doppler-Modus it can be shown, that the blood vessels are mainly located in periphery of the cortex region of the lymph node.

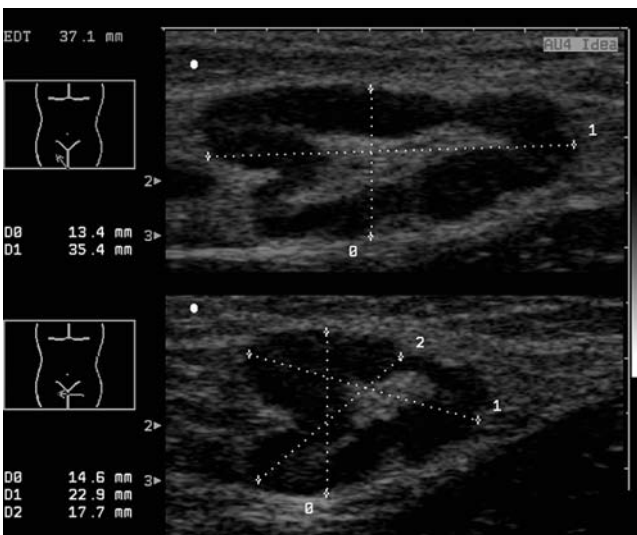


FIGURE 11 Lymphoma in the right groin of a 60-year-old woman. The medulla region has become tent-shaped and the cortex region is excentrically enlarged. The shape of the lymph node has changed considerably.

enlarge, while benign lymphadenopathies tend to become smaller after inflammation. In case of uncertainty, lymph node biopsy should be taken into consideration.

Sonography of the Dermis and Epidermis

Normal Glabrous Skin

Sonograms of normal skin show at their upper border a thin, very echogenic line, the so-called skin entry echo. The skin entry echo is due to an impedance jump at the intersection between the water (water is used as coupling medium) and the waterproof stratum corneum. The thin stratum corneum of glabrous skin obviously cannot be differentiated in 100 MHz sonograms. There is a tiny echopoor band (EPB) between the entry echo and the dermal reflexes. Below, a broad, echogenic band with scattered reflexes is seen, which corresponds to the dermis (Fig. 13A and B). The subcutaneous fatty tissue is echolucent with obliquely oriented echogenic connective tissue septae.

The reticular dermis is visible as an echogenic zone with densely scattered, confluent echo reflexes. It is sharply demarcated from the very echopoor subcutaneous fat. Within the dermis, hair follicle complexes are visible as homogeneous echopoor structures. When they are cut longitudinally (Fig. 13A), anagen from telogen follicles can be differentiated.

Normal Palmar Skin

In 100 MHz sonograms of palmar skin, an echogenic entry echo is seen at the upper border (Figs. 14 and 15). Where the dermatoglyphics are crossly cut (which is mostly the case), the entry echo is wavy; in parts with longitudinally cut dermatoglyphics, it is a straight line. Below the entry echo, there is an echopoor band, which we will call EPB1. It is followed by an echogenic line, which runs parallel to the entry echo but is less intense, (4 and 5). Gammal et al. (32) could show by

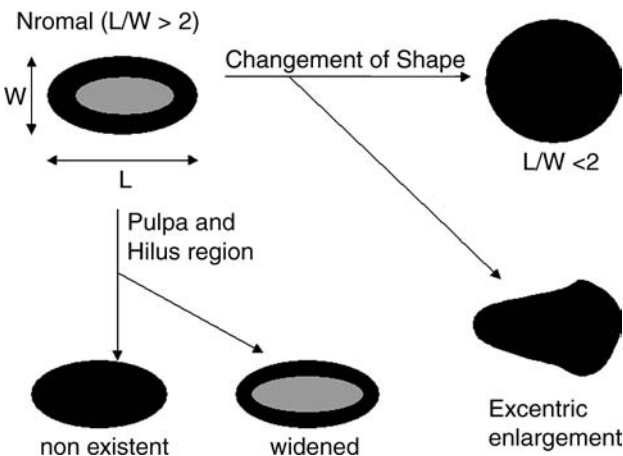


FIGURE 12 Changes in size and shape of lymph nodes. L largest longitudinal diameter, W width of the lymph node. The L/W quotient (Solbiati-index) >2 is often found in benign lymphadenopathies, an index <2 in malignant lymphadenopathies (the lymph node becomes ball-shaped).

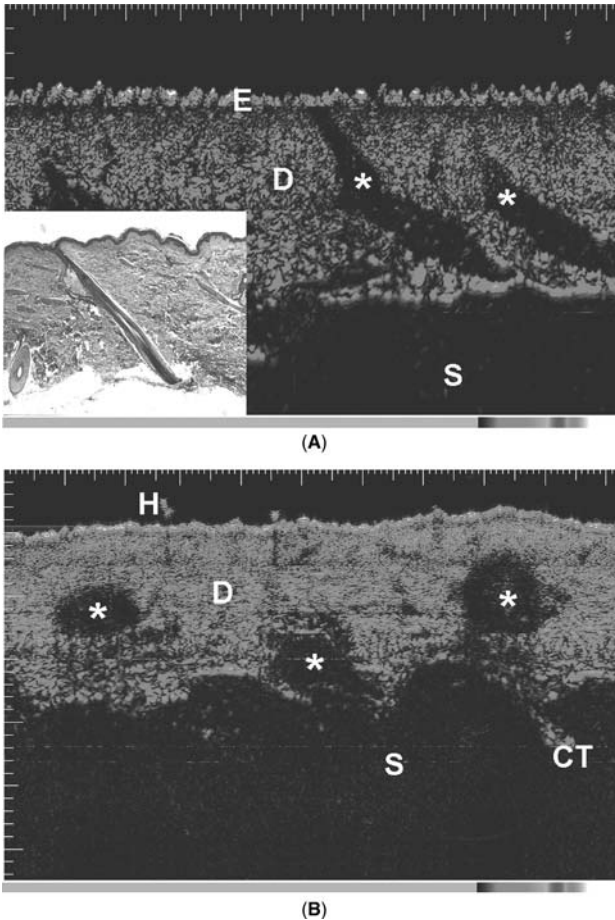


FIGURE 13 (See color insert) Hair follicles are represented as echopoor structures in the echorich dermis. **(A)** Thigh; * longitudinal section of hair follicles; *Inset*: correlating histology. **(B)** Thigh; * cross sections of hair follicles. *Abbreviations*: E, skin entry echo; D, dermis; S, subcutaneous fatty tissue; CT connective tissue septae in the subcutis; H, hair (cross-sectioned). Distance between two graduation marks = 100 µm. The pseudo color spectrum we used for the grey-levels is visible at the lower border of the images.

removal (tape stripping) and swelling (occlusion with petrolatum) of the horny layer, that the EPB1 truly represents the stratum corneum.

Below the EPB1, a second echopoor band is seen, which we will call EPB2. Neither removal nor swelling of the horny layer changes its thickness significantly (32). The EPB2 is separated from the EPB1 by an echorich line. Obviously this line represents the interface between the waterpoor stratum corneum and the moist, living part of the epidermis. The lower border of the EPB2 is defined by the scattered reflexes of the dermis (4,5). This border is too straight to correspond to the undulating dermo-epidermal junction (5), it rather represents the interface between the papillary and reticular dermis.

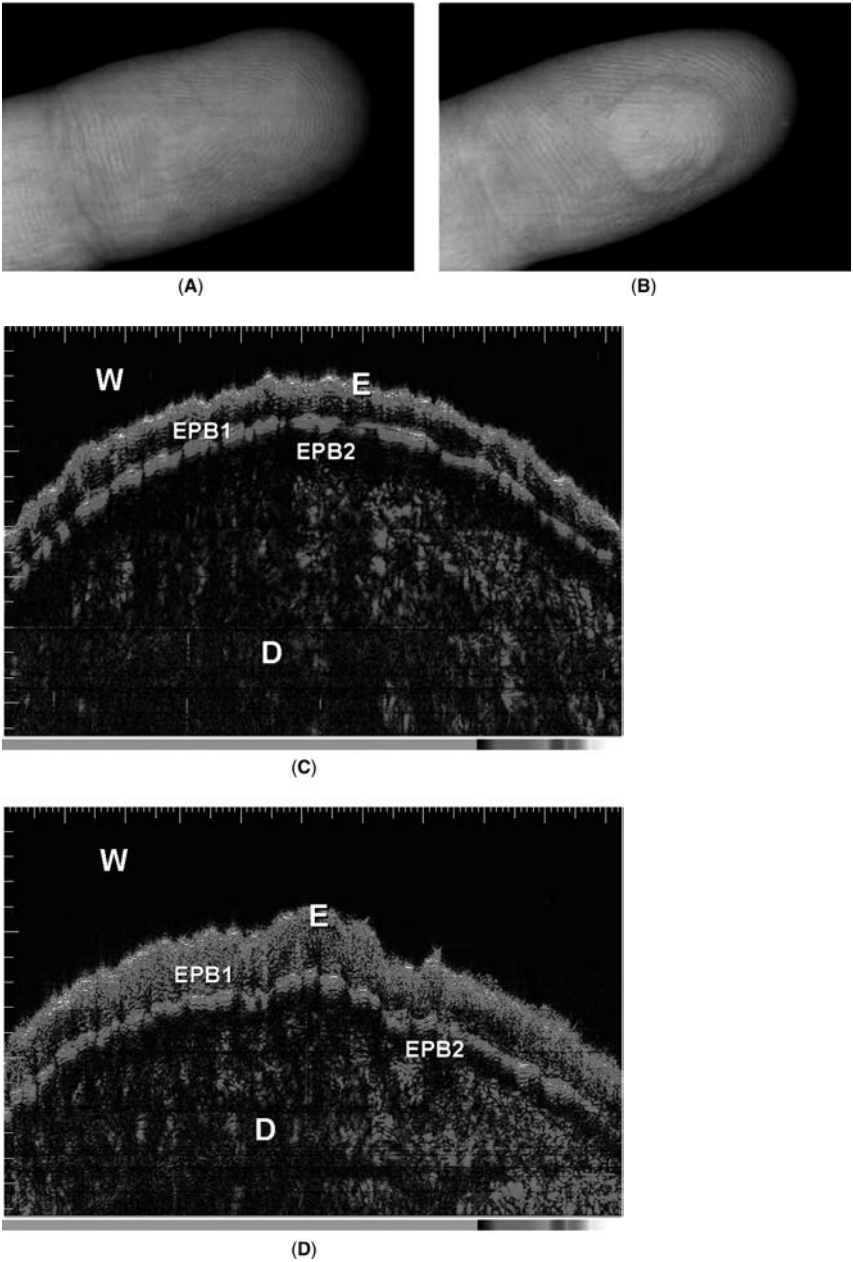


FIGURE 14 (See color insert for **C** and **D**) Palmar side of left index finger of a 30-year-old woman (distal phalanx). Photo **(A)** before and **(B)** after 30 minutes occlusion of an emulsion. Sonograms before **(C)** and after **(D)** 30 minutes occlusion of an emulsion. *Abbreviations:* W, water (coupling medium); E, entry echo; EPB1, echopoor band 1; EPB2, echopoor band 2; D, dermis.

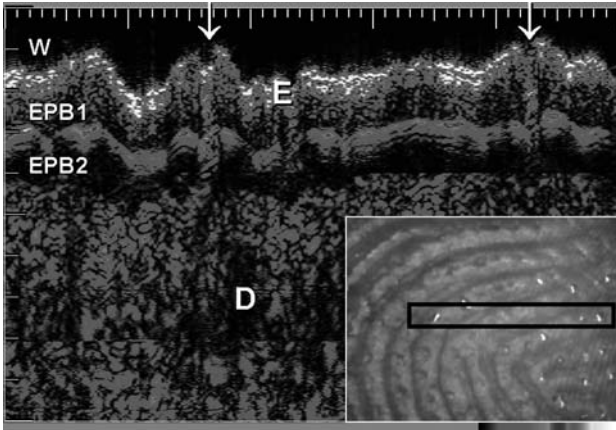


FIGURE 15 (See color insert) Palmar side of the right index finger of a 39-year-old man at high magnification. (Arrows) Sweat gland duct orifices. Distance between two gradation marks = $100\ \mu\text{m}$. (Inset): Epiluminescence microscopic picture of the left index finger. On the crests of the dermatoglyphics, white points in a row are seen, which represent sweat gland ducts. (Rectangle) Orientation of the sonogram. Abbreviations: W, water (coupling medium); E, entry echo; D, dermis; EPB1, echo poor band 1; EPB2, echo poor band 2.

In the EPB1, twisted, echogenic, about $100\ \mu\text{m}$ wide structures are seen, which cross the EPB1 vertically. The distance between two of them is $800\text{--}950\ \mu\text{m}$ or a multiple. Each of them ends in a small dip on top of a dermatoglyphic crest (5). These structures represent eccrine sweat gland ducts. In the EPB 2 they are rarely visible, in the echogenic dermis, they cannot be detected either.

Figure 16 shows the transition from palmar to glabrous skin on the wrist. The upper and lower border of the EPB1 (skin entry echo and echogenic line below)

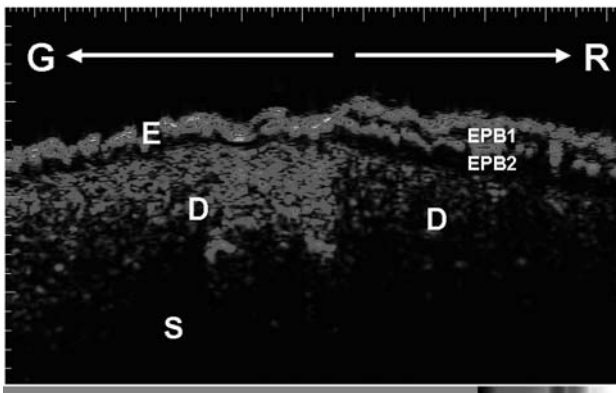


FIGURE 16 (See color insert) At the transition from glabrous to the palmar skin, a second echogenic line separates the EPB1 (upper EPB) from the EPB2 (lower EPB). Wrist of a 33-year-old woman. E skin entry echo, G glabrous skin, R ridged (palmar) skin, D dermis, S subcutis. Distance between two gradation marks = $100\ \mu\text{m}$. Abbreviations: E, entry echo; D, dermis; G, glabrous skin; R, ridged (palmar) skin; S, subcutis; EPB1, echo poor band 1; EPB2, echo poor band 2.

merge into one echorich line in glabrous skin, so that the EPB1 disappears. The thin stratum corneum of glabrous skin obviously cannot be differentiated in 100 MHz sonograms. The EPB2 remains as the only EPB between the entry echo and the dermal reflexes. While the thickness of the entry echo is about the same as in palmar skin (32), the EPB of glabrous skin is markedly thinner than on the palms. On the lower extremities it is thicker than on the trunk (32).

Concurrent with the sudden appearance of EPB1, when moving from glabrous to ridged skin (palmar and plantar), the echogenicity of the dermis is reduced compared to the glabrous skin. This is due to the strong absorption of the ultrasound energy in the upper layers of the stratum corneum.

Inflammatory Skin Diseases

Psoriasis Vulgaris: Compared to normal skin, lesions of psoriasis vulgaris exhibit distinct alterations of the upper dermis.

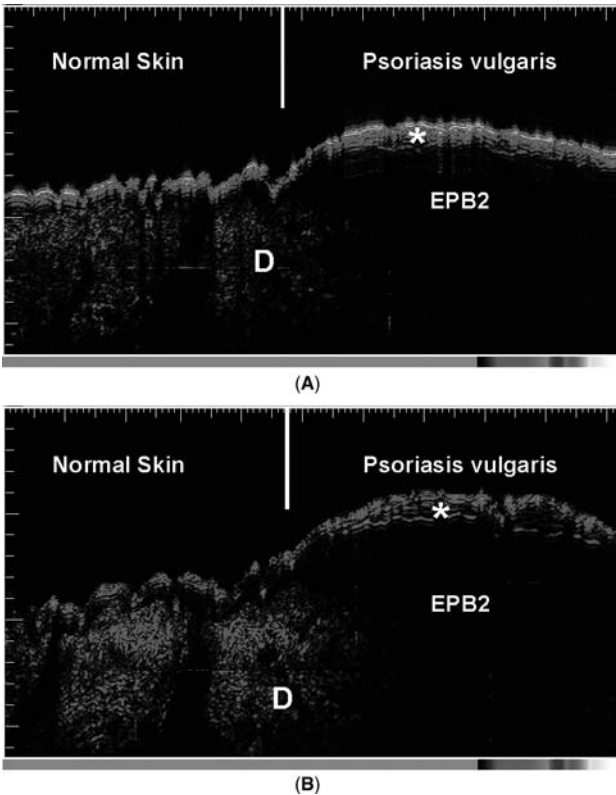


FIGURE 17 (See color insert) Border of a psoriatic plaque on the thigh of a 65-year-old woman. **(A)** Before treatment. In the psoriatic plaque, the entry echo and the echorich lines underneath form a homogeneous echorich band (*), corresponding to the horny layer. Below, the EPB2 cannot be separated from the dermis D because of a strong dorsal signal attenuation. **(B)** After occlusion with petrolatum for 60 minutes, the above mentioned band (*) is increased in thickness and decreased in echodensity. It is now demarcated by the entry echo and an echorich line at the bottom. Distance between two graduation marks = 100 μm . *Abbreviations:* EPB2, echopoor band 2; D, dermis.

At the border of a psoriatic lesion, the EPB of normal skin widens into a broad EPB. The thickness of this band correlates very well with the thickness of the acanthotic epidermis plus the dermis with the inflammatory infiltrate in the corresponding histology ($r=0.94$). No significant correlation was observed between the thickness of the EPB and the epidermis respectively the infiltrated dermis alone (32). The lower, quite straight border of EPB2 is defined by the scattered reflexes of the dermis.

Furthermore, distinct alterations of the entry echo are observed in psoriasis lesions as compared to normal skin. In untreated scaly plaques, directly below the entry echo, several parallel, echogenic lines are seen (Fig. 17A). They melt with the entry echo into an echogenic band, which is significantly thicker than the entry echo in normal skin ($111 \pm 16 \mu\text{m}$, $n = 35$, $p < 0,001$) and has a much more irregular surface (Fig. 17A).

The following observations show that the described band with varying echodensity represents the hyperkeratotic horny layer: After application of petrolatum under occlusion for 60 minutes on a hyperkeratotic psoriatic plaque, the thickness of the band increases, and its echodensity markedly decreases. In its whole length, it can now be distinguished as an EPB with the entry echo as upper and a thin echogenic line as lower border (Fig. 17B). Repeated tape stripping of the scaly surface results in a gradual decrease in the thickness of the echogenic band. When the scales are removed entirely, only a single echogenic line remains.

In conclusion, the horny layer is echogenic in untreated scaly psoriatic plaques; after treatment with Petrolatum its echodensity decreases. Furthermore the acanthotic epidermis and the dermis with the inflammatory infiltrate are represented as one EPB.

Lichen planus: In lichen planus papules, the EPB of normal glabrous skin focally widens into a spindle-shaped echopoor area. The maximal thickness of this band correlates well with the maximal thickness of the acanthotic epidermis plus the dermis with inflammatory infiltrate in the corresponding histology ($r = 0.86$).

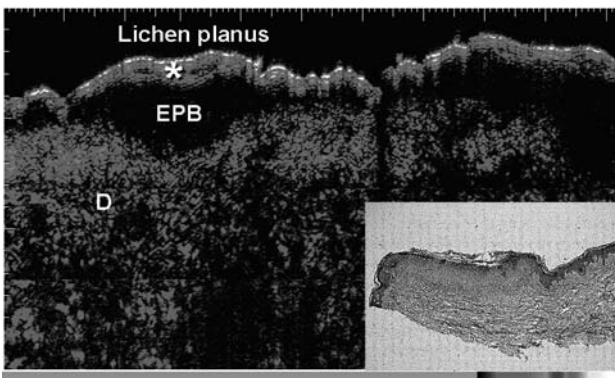


FIGURE 18 (See color insert) Lichen planus papule on the thigh of a 65-year-old woman. In the middle of papule an echopoor line (*) is seen between the skin entry echo and the echogenic line beneath. Corresponding histology (inset) exhibits that this region has a significant hyperkeratosis. The histology exhibits furthermore, that the EPB2 corresponds to the stratum Malpighii and the inflammatory infiltrate in the upper dermis. Distance between two graduation marks = $100 \mu\text{m}$. Abbreviations: EPB2, echopoor band 2; D, dermis.

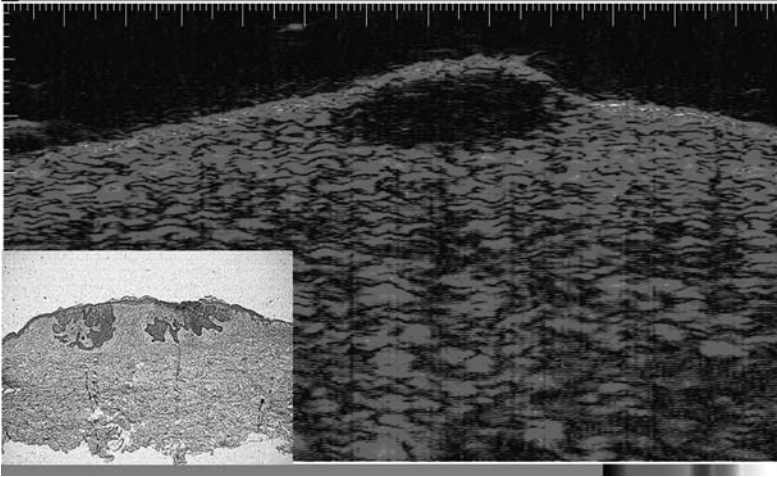


FIGURE 19 (See color insert) Basal cell carcinoma on the back of a 78-year-old woman. Corresponding histology (inset) reveals that tumor parenchyma and stroma (together 912 μm thick) are summed up to a spindle shaped echopoor area (maximal thickness 770 μm) in the upper dermis of the sonogram. Distance between two graduation marks = 100 μm.

Thick lichen planus papules (Fig. 18) often exhibit an echopoor line (EPB1) beneath the skin entry echo (32).

Skin Tumors

To study whether the improved resolution at 100 MHz has an impact on visualization of skin tumor details, we examined thin basal cell carcinoma using image analysis. Correlation of sonograms and histology reveals, that the tumor parenchyma and stroma seen histologically as separate structures (inset, Fig. 19) are summed up to an uniform spindle-shaped echopoor area in the upper dermis in sonograms (19). Tumor parenchyma and stroma are represented as one echopoor area.

TABLE 2 Statistical Analysis of Different Regions of Interest in Pigmented Skin Tumors

		NCN	MM	SebK	Bas
Skin entry echo	Thickness	N.S.	N.S.	$p=0.02$	N.S.
	Mean echo intensity of the neighbouring normal epidermis (%)	N.S.	N.S.	N.S.	N.S.
Echopoor tumor area	Mean echo intensity of the neighbouring normal dermis (%)	33% ± 9%	16% ± 6%	13% ± 6%	25% ± 9%
	Subtumoral region	71% ± 23%	50% ± 15%	25% ± 3%	86% ± 24%

Abbreviations: N.S., non significant; NCN, nevocellular nevus; MM, malignant melanoma; SebK, seborrheic keratosis; Bas, basal cell carcinoma.

To evaluate the potential of 100 MHz sonography we studied thin pigmented skin tumors (basal cell carcinoma, malignant melanoma, seborrheic keratosis, nevocellular nevi) using sonography and histology. Sonograms were evaluated by comparing the skin tumor region with the adjacent or contralateral normal skin (% change of the normal skin). Most parameters were not significant (Table 2). In seborrheic keratosis, the thickness of the skin entry echo was significantly increased. Furthermore in seborrheic keratosis, the mean echointensity of the sub-tumoral region correlated with the thickness of the skin entry echo ($r = 0.92$).

In all tumors, the echopoor tumor region (Fig. 20A) was not statistically significant from each other, save seborrheic keratosis versus nevocellular nevus ($p = 0.05$). The subtumoral area was significantly ($p < 0.01$) different for all tumors (Fig. 20B), save for malignant melanoma versus nevocellular nevus ($p < 0.05$).

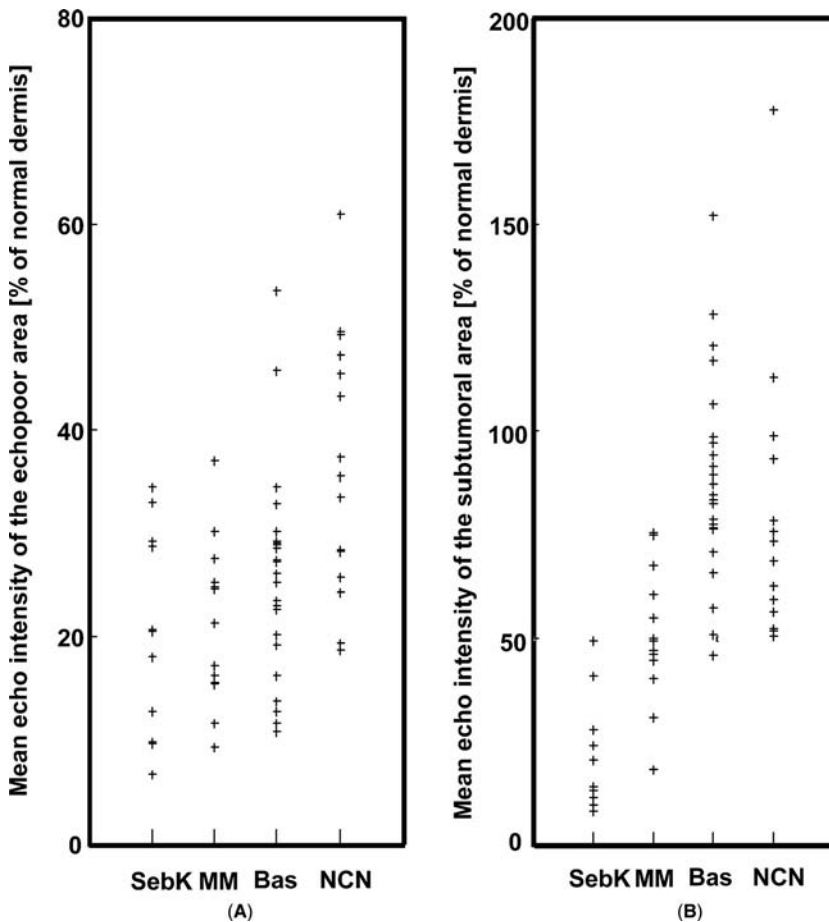


FIGURE 20 Evaluation of skin tumors, focusing on (A) the tumoral echopoor region is not statistically significant from each other, save SebK versus NCN ($p = 0.05$). (B) The subtumoral area is significantly ($p < 0.01$) different for all tumors, save for MM versus NCN ($p < 0.05$). Abbreviations: SebK, seborrheic keratosis; MM, malignant melanoma; Bas, basal cell carcinoma; NCN, nevocellular nevus.

We can conclude that differentiation between skin tumors is not possible by studying the echodensity of the echopoor tumor region. On the other hand, the echodensity of the subtumoral (normal) dermis gives an indirect hint about the absorption characteristics of the tumor region: Our findings suggest that the absorption of echo reflexes is significantly different for all examined pigmented skin tumors, save malignant melanoma versus nevocellular nevus.

DISCUSSION

Dermatology deals with all skin structures from the skin surface to the muscle fascia. We therefore need methods to look beneath the skin. Sonography is an particularly interesting candidate, because it is a noninvasive method, is harmless and can be repeated if necessary.

7.5–15 MHz sonography has become a great tool to study the subcutis and subcutaneous pathologies. Typical examples are connective tissue diseases, cellulite, blood vessel diseases, soft tissue tumors and lymph node pathology. In the past decades, dermatooncologists have introduced sentinel lymph node biopsy (e.g. for tumor staging in malignant melanoma). Furthermore sonography of peripheral lymph nodes has been introduced in many national health follow-up programs (50,51)

20 MHz sonography is also very useful to study the dermis. Different pathological processes (virtually all skin tumors, inflammatory infiltrates, edema, scar tissue, elastosis) as well as skin appendages and large blood vessels are represented as echopoor areas (8,11,39) within the echorich dermis.

Our 100 MHz experimental sonography unit allows a far more detailed visualization of the upper skin layers as compared to 20 MHz sonography. Especially with regard to the *in vivo*-assessment of the horny layer, 100 MHz sonography is a valuable tool. Whereas, in normal glabrous skin, the stratum corneum is too thin [(40): about 12–15 μm ; (41): mean thickness of 15 μm for dry stratum corneum and 48 μm after hydration]; (52): stratum corneum thickness (cell layers) varies at different body locations] to be separated from the entry echo, in palmar skin and hyperkeratotic states it is represented as a distinct band and its thickness can be easily determined. Our results suggest that the echodensity of the horny layer depends on its water content: psoriatic scales, appearing silvery because of the included air, are for example much more echorich than the moist stratum corneum of the palms. The significant impedance gap between the stratum corneum and the Malpighian layer—visible as an echorich line—can be explained by the different hydration states of these layers. As demonstrated by various methods, e.g., magnetic resonance imaging (43,44) or measurement of the transepidermal water loss (45), there is a sudden increase in water content at the border between the horny layer and the viable epidermis.

Today most authors agree that the skin entry echo is an artefact caused by the change in impedance between the coupling water and the horny layer (28,46,47). This hypothesis is confirmed by our results: The thickness and echodensity of the entry echo remains constant, no matter whether the horny layer is stripped, occluded with topical agents or entirely removed (32). In most 20 MHz studies, the echo signal was strongly amplified to reach a high signal depth penetration. This however leads to a significant blurring of the entry echo. This effect as well as the low lateral resolution of only 200 μm entails that the entry echo is represented as a 100–250 μm thick, relatively homogeneous band (47). During image acquisition of the 100 MHz sonograms, we applied the B/D-scan technology, which

allows to select a specific amplification for each of the four to eight horizontal stripes, which compose the sonographic image. An overamplification of the entry echo is thus avoided. Its thickness is about 80 μm and due to the high lateral resolution of 27 μm it, reflects even fine irregularities of the skin surface like the dermatoglyphics or the rough surface of psoriatic lesions.

In 20 MHz sonograms of normal glabrous skin, the dermal reflexes are directly adjacent to the entry echo; the viable epidermis, which is about 80 μm thick, cannot be visualized. At 100 MHz, the resolution is sufficient to show in normal skin a thin EPB above the dermal reflexes. Its thickness and its straight lower border suggest that it represents the viable epidermis together with the papillary dermis. At the transition from normal skin to a psoriatic plaque this band widens into a 400–500 μm thick echolucent band. An echolucent band of comparable thickness can be observed also in 20 MHz sonograms of psoriatic lesions (8,14–17,28). Conflicting theories have been proposed regarding its nature. While some authors equate it with the sum of acanthosis and the upper dermis with the inflammatory infiltrate (8,17,48), others interpret it as correlate of the papillary dermis (14–16). Our results favor the first hypothesis: Comparison with the corresponding histology revealed an excellent correlation between the thickness of this band and the histometric thickness of the Malpighian layer plus the inflammatory infiltrate. Moreover, in 100 MHz sonograms, this EPB always has a fairly straight upper and lower border. If it represented the viable epidermis only, we would expect an undulating lower border; if it was the correlate of the papillary dermis, the upper border would be wavy, especially in psoriatic lesions where there are prominent rete pegs. The lateral resolution of the 100 MHz transducer is high enough to depict structures of this dimension, as the cross-sections of the dermatoglyphics in palmar skin demonstrate. We can conclude that both the viable epidermis and the infiltrated dermis are echopoor and cannot be differentiated from each other.

These reflections illustrate that it is not only a question of resolution, whether a structure is visualized sonographically. As we could show, the resolution of 100 MHz sonography allows to detect structures as small as a sweat gland duct in the horny layer. On the other hand, the viable epidermis cannot be distinguished from the papillary dermis, and, as we learned from the study of skin tumors, the stroma of basal cell carcinoma cannot be distinguished from the tumor cell nests (Fig. 19).

How can this be explained? According to Fields and Dunn (49), echoes are only reflected from the border between two tissues, when they have a different acoustic impedance at the applied frequency. Obviously, there is no difference in impedance between the viable epidermis, compact tumor masses, dense lymphocytic infiltrate and fine fibrillary connective tissue at 100 MHz but only between these structures and the reticular dermis. These acoustic tissue properties are the reason why Gupta et al. (13) and Semple et al. (12) using 40–60 MHz transducers could not improve imaging of skin tumors as compared with 20 MHz.

An entirely exact correlation of histometry and sonometry cannot be expected as various artifacts influence the measurements in both methods. Histological processing leads to tissue shrinkage; the stratum corneum shows the characteristic basket-weave structure which does not correspond to the in-vivo anatomy. Sonographic examination requires water as coupling medium which itself may lead to swelling of the horny layer. Sonometry is also influenced by the sound speed which is taken as basis for distance calculations. In dermatological sonography, distance calculations from the echo signal time-lapse are usually

based on the sound speed of the dermis (1580 m/sec) (29,50). In the nail plate however, Finlay et al. (51) found a sound speed of 2140 m/sec comparing 20 MHz sonography and thickness measurements by a micrometer-screw. Jemec and Serup (52) divided the nail into two compartments with different speeds, an upper dry one (3103 m/sec) and a lower humid one (2125 m/sec). Obviously, a similar situation must be postulated for the stratum corneum which consists of keratin and has a low content of water thereby having similar properties than the upper nail compartment.

We can conclude that high-resolution sonography enables in-vivo examination of fine structural details of the epidermis. In order to obtain images with significant information, understanding of the basic physics of ultrasound principles is indispensable. Only optimal pre-amplification, implementation of a B/D-scan to increase in-depth penetration at 100 MHz and knowledge about the influence of resolution on the echo-character enable correct interpretation of the sonograms.

REFERENCES

1. Beyer D, Peters PE, Friedmann G. Leistungsbreite der real-time-sonographie bei lymphknotenerkrankungen. *Röntgenpraxis* 1982; 35:393-402.
2. Brockmann WP, Maas R, Voigt H, Thoma G, Schweer S. Veränderungen peripherer lymphknoten im ultraschall. *Ultraschall* 1985; 6:164-169.
3. Haller J, Gritzmann N, Czembirek H, et al. Der okkulte und der klinisch verdächtige hodentumor. Abklärung mittels realtime-sonographie. *Radiologie* 1987; 27:113-117.
4. Leopold GR, Woo VL, Scheible W, Nachtsheim D, Gosink B. High-resolution ultrasonography of scrotal pathology. *Radiology* 1979; 131:719-722.
5. Schwerek WB, Schwerek WN. Sonographie des skrotalinhaltendes (III-1.9.4.). In: Braun B, Günther R, Schwerek B, eds. *Ultraschalldiagnostik. Lehrbuch und Atlas*. München: Ecomed, 1989:1-70.
6. Rukinava B, Mohar N. An approach of ultrasound diagnostic techniques of the skin and subcutaneous tissue. *Dermatologica* 1979; 158:81-92.
7. Hoffmann K, el-Gammal S, Winkler K, Jung J, Pistorius K, Altmeyer P. Skin tumours in high-frequency ultrasound. In: Altmeyer P, el-Gammal S, Hoffmann K, eds. *Ultrasound in Dermatology*. Heidelberg, New York: Springer Verlag, 1992:181.
8. Fornage BD, McGavran MH, Duvic M, Waldron CA. Imaging of the skin with 20 MHz US. *Radiology* 1993; 189:69-76.
9. Gropper CA, Stiller MJ, Shupack JL, Driller J, Rorke M, Lizzi F. Diagnostic high-resolution ultrasound in dermatology. *Int J Dermatol* 1993; 32:243-250.
10. Harland CC, Bamber JC, Gusterson BA, Mortimer PS. High frequency, high resolution B-scan ultrasound in the assessment of skin tumours. *Br J Dermatol* 1993; 128:525-532.
11. El Gammal S, Auer T, Hoffmann K, Altmeyer P, Paßmann C, Ermert H. Grundlagen, anwendungsgebiete und grenzen des hochfrequenten (20-50 MHz) ultraschalls in der dermatologie. *Zbl Haut* 1993; 162:817-838.
12. Semple JL, Gupta AK, From L, et al. Does high-frequency (40-60 MHz) ultrasound imaging play a role in the clinical management of cutaneous melanoma. *Ann Plast Surg* 1995; 34:599-605.
13. Gupta AK, Turnbull DH, Foster FS, et al. High-frequency 40 MHz ultrasound. A possible noninvasive method for the assessment of boundary of basal cell carcinoma. *Dermatol Surg* 1996; 22:131-136.
14. Di Nardo A, Seidenari S, Giannetti A. B-scanning evaluation with image analysis of psoriatic skin. *Exp Dermatol* 1992; 1:121-125.
15. Stiller MJ, Gropper CA, Shupack JL, Lizzi F, Driller J, Rorke M. Diagnostic ultrasound in dermatology: current uses and future potential. *Cutis* 1994; 53:44-48.
16. Vaillant L, Berson M, Machel L, Callens A, Pourcelot L, Lorette G. Ultrasound imaging of psoriatic skin: a non-invasive technique to evaluate treatment of psoriasis. *Int J Dermatol* 1994; 33:786-790.

17. Hoffmann K, Dirschka T, Schwarze H, et al. 20 MHz sonography, colorimetry and image analysis in the evaluation of psoriasis vulgaris. *J Dermatol Sci* 1995; 9:103–110.
18. Gupta AK, Turnbull DH, Harasiewicz KA, et al. The use of high-frequency ultrasound as a method of assessing the severity of a plaque of psoriasis. *Arch Dermatol* 1996b; 132:658–662.
19. Cole CW, Handler SJ, Burnett K. The ultrasonic evaluation of skin thickness in scleroderma. *J clin Ultrasound (N.Y.)* 1981; 9:501–503.
20. Serup J. Decreased skin thickness of pigmented spots appearing in localized scleroderma (morphoea)—measurement of skin thickness by 15 MHz pulsed ultrasound. *Arch dermatol Res* 1984; 276:135–137.
21. Myers SL, Cohen JS, Sheets PW, Bies JR. B-mode ultrasound evaluation of skin thickness in progressive systemic sclerosis. *J Rheumatol* 1986; 13:577–580.
22. Akesson A, Forsberg L, Hederström E, Wollheim E. Ultrasound examination of skin thickness in patients with progressive systemic sclerosis (scleroderma). *Acta Radiol Diagn* 1986; 27:91–94.
23. Hoffmann K, el-Gammal S, Gerbaulet U, Schatz H, Altmeyer P. Altmeyer P: Examination of circumscribed scleroderma using 20 MHz B-scan ultrasound. In: Altmeyer P, el-Gammal S, Hoffmann K, eds. *Ultrasound in Dermatology*. Heidelberg, New York: Springer Verlag, 1992:231.
24. Lévy J, Gasmüller J, Audring H, Brenke A, Albrecht-Nebe H. Darstellung der subkutanen atrophie bei der zirkumskripten sklerodermie im 20 MHz-B-scan ultraschall. *Hautarzt* 1993; 44:446–451.
25. Ihn H, Shimozuma M, Fujimoto M, et al. Ultrasound measurement of skin thickness in systemic sclerosis. *Br J Rheumatol* 1995; 24:535–538.
26. Serup J, Staberg B. Ultrasound for assessment of allergic and irritant patch test reactions. *Contact Dermatitis* 1987; 17:80–84.
27. Seidenari S, Di Nardo A. B scanning evaluation of irritant reactions with binary transformation and image analysis. *Acta Derm Venereol Suppl (Stockh)* 1992; 175:9–13.
28. Seidenari S. High-frequency sonography combined with image analysis: a non-invasive objective method for skin evaluation and description. *Clin Dermatol* 1995; 13:349–359.
29. Beck JS, Speace VA, Lowe JG, Gibbs JH. Measurement of skin swelling in the tuberculin test by ultrasonography. *J Immunol Methods* 1986; 86:125.
30. El Gammal S, Auer T, Hoffmann K, et al. High-frequency ultrasound: a non-invasive method for use in Dermatology. In: Frosch P, Kligman AM, eds. *Non-invasive methods in dermatology*. Heidelberg, New York: Springer Verlag, 1993:104.
31. El Gammal S, Auer T, Hoffmann K, Paßmann C, Ermert H. High resolution ultrasound of the human epidermis. In: Serup J, Jemec GBE, eds. *In Vivo Examination of the Skin: A Handbook of Non-Invasive Methods*. Ann Arbor, London, Tokyo: CRC Press, 1995:125.
32. El Gammal S, El Gammal C, Kaspar K, et al. Sonography of the skin at 100 MHz enables in-vivo-visualization of stratum corneum and viable epidermis in palmar skin and psoriatic plaques. *J Invest Dermatol* 1999; 113:821–829.
33. Paßmann C, Ermert H, Auer T, Kaspar K, el-Gammal S, Altmeyer P. In vivo ultrasound biomicroscopy. *IEEE Ultrason Symp Proc* 1993; 1015.
34. Loose R, Weiss J, Kühn W, Simon R, Teubner J, Georgi M. Comparison of ultrasound with clinical findings in the early detection of regional metastatic lymph nodes in patients with malignant melanoma. In: Altmeyer P, El Gammal S, Hoffmann K, eds. *Ultrasound in Dermatology*. Heidelberg, NY: Springer Verlag, 1992:93–99.
35. Solbiati L, Rizzato G, Bellotti E et al. High resolution sonography of cervical lymph nodes in head and neck cancer: criteria for differentiation of reactive versus malignant nodes. *Radiology* 1988; 169:113.
36. Vassallo P, Edel G, Roos N et al. In-vitro high resolution ultrasonography of benign and malignant lymphnodes. A sonographic-pathologic correlation. *Invest Radiol* 1993; 28: 698–705.
37. Blum A, Dill-Müller D. Sonographie der Lymphknoten und der Subkutis in der Dermatologie; Teil 1. *Hautarzt* 1998; 49:942–949.

38. Blum A, Dill-Müller D. Sonographie der Lymphknoten und der Subkutis in der Dermatologie; Teil 2. *Hautarzt* 1999; 50:62–73.
39. Altmeyer P, Hoffmann K, Stücker M, Goertz S, el-Gammal S. General phenomena of ultrasound in dermatology. In: Altmeyer P, el-Gammal S, Hoffmann K, eds. *Ultrasound in Dermatology*. Berlin, Heidelberg, New York: Springer-Verlag, 1992:55.
40. Kligman AM. The biology of the stratum corneum. In: Montagna W, Lobitz WC, eds. *The epidermis*. New York: Academic Press, 1964:387.
41. Idson B. Hydration and percutaneous absorption. *Curr Probl Dermatol* 1978; 7:132–134.
42. Holbrook KA, Odland GF. Regional differences in the thickness (cell layers) of the human stratum corneum: an ultrastructural analysis. *J Invest Dermatol* 1974; 62:415–422.
43. Ablett S, Burdett NG, Carpenter TA, Hall LD, Salter DC. Short echo time MRI enables visualisation of the natural state of human stratum corneum water in vivo. *Magn Reson Imaging* 1996; 13:357–360.
44. Querleux B, Richard S, Bittoun J, et al. In vivo hydration profile in skin layers by high-resolution magnetic resonance imaging. *Skin Pharmacol* 1994; 7:210–216.
45. Kalia YN, Pirot F, Guy RH. Homogeneous transport in a heterogeneous membrane: water diffusion across human stratum corneum in vivo. *Biophys J* 1996; 71:2692–2700.
46. Gniadecka M, Gniadecki R, Serup J, Søndergaard J. Ultrasound structure and digital image analysis of the subepidermal low echogenic band in aged human skin: diurnal changes and interindividual variability. *J Invest Dermatol* 1994; 102:362–365.
47. Hoffmann K, Stücker M, Dirschka T, et al. Twenty MHz B-scan sonography for visualization and skin thickness measurement of human skin. *J Eur Acad Dermatol* 1994; 3:302–313.
48. Murakami S, Miki Y. Human skin histology using high-resolution echography. *J Clin Ultrasound* 1989; 17:77–82.
49. Fields S, Dunn F. Correlation of echographic visualizability of tissue with biological composition and physiological state. *J Acoust Soc Amer* 1973; 54:809–812.
50. Alexander H, Miller DL. Determining skin thickness with pulsed ultrasound. *J Invest Dermatol* 1979; 72:17–19.
51. Finlay AY, Moseley H, Duggan TC. Ultrasound transmission time: an in vivo guide to nail thickness. *Brit J Dermatol* 1987; 117:765–770.
52. Jemec GB, Serup J. Ultrasound structure of the human nail plate. *Arch Dermatol* 1989; 125:643–646.

Noninvasive Imaging in the Evaluation of Cellulite

Theresa Callaghan

*proDERM Institute for Applied Dermatological Research, Kiebitzweg,
Hamburg, Germany*

Klaus-P. Wilhelm

*University of Lübeck, Lübeck, and proDERM Institute for Applied Dermatological
Research, Schenefeld/Hamburg, Germany*

INTRODUCTION

There is little coherency or consistency within the scientific literature as to the manifestation of so-called cellulite which is neither a skin disorder, disease, nor a tissue dystrophy (1–11). It is an inevitable reality of the genetic makeup of the female human species interlinked with steroid hormones and external influences. Cellulite (Fig. 1) is a condition that needs to be managed since it cannot be cured inside the strict confines of cosmetic definition. There are a number of clinical methods available to evaluate cellulite, though the limitations of each method alone are such that more than one method is required in order to correlate clinical findings with any laboratory findings. From a scientific viewpoint, a clearer understanding of the influences on adipose tissue metabolism, and connective tissue structure, is required for the development of new test methods in order to advance a more rational approach to understanding cellulite. Furthermore the development of clinical methods, which can correlate *in vitro* studies, will finally bring logic and understanding to the scientific literature, the condition, and ultimately manage the continued expectations and unmet needs of the consumer.

Cellulite affects almost all women, and up to 30% of their subcutaneous fat can physically appear as visible cellulite. Supermodels, anorexics and Olympic athletes all have this condition. As a group of individuals they could not be more different, yet they all have one thing in common apart from their gender and connective tissue organization—stress. Stress in the skin manifests itself in a number of ways—the most widely acknowledged being “aging” of connective tissues (12–14) leading to wrinkling and skin laxity etc. Stress in subcutaneous tissues *i.e.*, in adipose tissues, is less understood (15–17), and the biochemistry of stress in this area of dermato-cosmetics has not been given much consideration. The role of hormones, lymph flux, vascularity, inflammation, adipose biochemistry, and stress-related aging effects on connective and adipose tissue, in the occurrence of cellulite, have been described elsewhere (18,19).

Based on the limited knowledge of cellulite, the closest work to date as to a reasoned understanding of the condition is that of Pièrard *et al.* (20). In these studies, histopathology identifies superficial fat lobules protruding the dermis—papillae adiposae, and an unevenness and lack of integrity of collagen and elastin fibers. These papillae adiposae are normal in all women and are gender specific. Gender differences in adipose tissue have been described (21–44). Pinching of

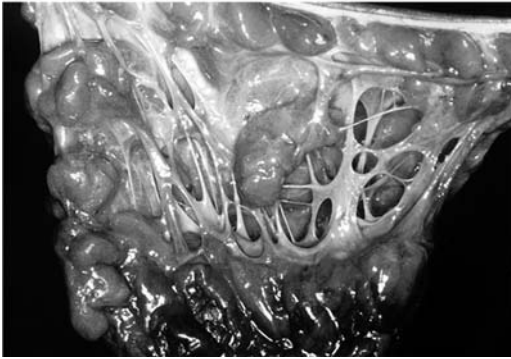
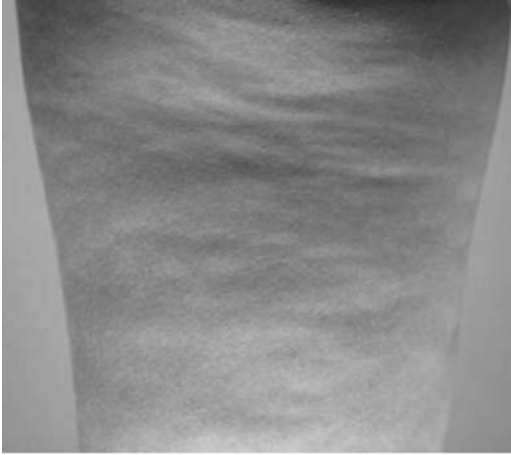


FIGURE 1 Clinical aspects of cellulite—dimpling of the skin on the female thighs is a visible characteristic of cellulite. Note also the torsion of the skin diagonally across the skin. The full thickness biopsy shows the fibrosclerotic nature of the connective tissue with corresponding bulging of the surrounding adipose. *Source:* Courtesy of G.Pièrard.

the skin in females without visible cellulite reveals a “peau d’orange” skin, yet the papillae adiposae are contained and hence no dimpling is observed externally when the pinch is released. In observed “unpinched” cellulite, at the site of dimpling, fibrous strands are enlarged reminiscent of striae distensae, and the papillae adiposae protrude upwards contributing to dimple formation. There is however no tissue dystrophy or lipoatrophy and the bumpy appearance is due to a network of connective tissue strands which are nonuniform, thickened, and fibrosclerotic.

Although histopathology is excellent for visualizing cellular, pathological and biochemical changes in the cellulite condition, the limitation of this method is that it is a highly invasive *ex vivo* technique, and therefore limited to small scientific studies. It can be used however to support image analyses from any of the techniques described herein.

This chapter deals with currently available imagining methods and their opportunities and limitations in the understanding and evaluation of cellulite.

EVALUATING THE CONDITION—CLINICAL CONSIDERATIONS

Without a coherent understanding of the appearance of cellulite, much of the clinical aspects regarding evaluation have relied on subjective methods which do not

provide information indicating whether treatments have improved the condition. They only indicate a change in adipose thickness, since there is no categorical demonstration of changes in the fibrosclerotic tissue that would lead to a physical change in preventing the protrusion and/or development of papillae adipose. Although histopathology studies have provided a clear insight into the physical manifestation of cellulite, a real need remains for useful and reproducible methods in order to visualize cellulite at cellular and structural levels. This is necessary to verify the true effectiveness of so-called anticellulite products/ingredients, and to provide coherency to literature findings and current methods. There are a number of clinical methods available to evaluate the cellulite condition though the limitations of each alone are such that more than one is required in order to correlate clinical findings with any laboratory findings.

Ultrasound

Many clinical studies for evaluating cellulite have relied on either echography or ultrasound. This method measures the acoustic signal recorded from a digital ultrasound wave. Currently, high-resolution ultrasound is a common technique for clinical cellulite imaging. With ultrasound techniques, the skin receives pulses of waves sent through a skin probe.

The technique will only provide information on tissue irregularity rather than ultrastructural resolution (Fig. 2). What is observed is that the dermis is rich in ultrasound reflections (echo dense) whereas the interphase to the subcutaneous fat which is echo poor is well defined. However the benefit of this technique is that it can measure the ratio of the subcutis to the surface of the skin because of the protrusion of fat into the dermis. In cellulite, the length of the dermal ridge is increased and comparing this length which is extended in cellulite to the surface of the epidermis gives an indication of the severity of adipose protrusion into the dermis.

The limitation of the method is that the ultrastructural resolution is poor and it only indicates a change in adipose thickness and protrusion. The suitability of the technique is in studies focusing on subcutaneous protrusion into the dermis.

Magnetic Resonance Imaging (MRI)

This method has been published in three cellulite studies by Querleux et al. (2), Mirrashed et al. (1), and more recently Smalls et al. (45). High-resolution



FIGURE 2 Full skin thickness scan (20 MHz) using ultrasound (Cortex Technology ApS, Denmark) and the different skin regions are well defined.

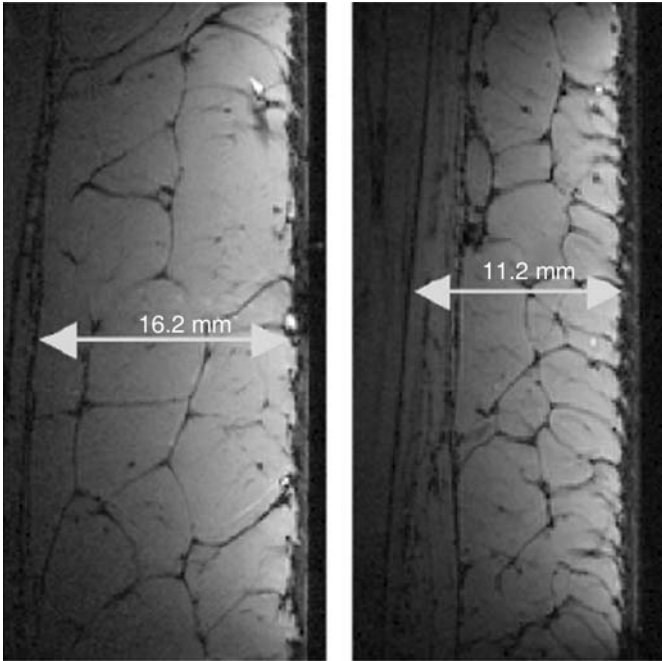


FIGURE 3 Magnetic resonance imaging scan of full thickness skin. Adipose tissue unlike the dermis is clearly defined. *Source:* From Ref. 1.

microimaging MRI visualizes the architecture of the skin layers at the hypodermal level. It clearly shows the thickness and structural alterations of the connective tissue in both the dermis and subcutaneous adipose tissue (Fig. 3). For studies focusing on anatomical changes in adipose thickness and gross changes in connective tissue organization, it has good resolution. Although a very useful method, unfortunately clinical high field MRI systems capable of high-resolution imaging are not yet readily available, and these are needed to focus at the level of the dermis.

Despite these limitations, the method at its current resolution of imaging would demonstrate a reduction in adipose thickness, if, an appropriate formulation could be developed to deliver actives to the desired site of action. However, since cellulite is clearly about defects in connective tissue structure, MRI would need to be combined with other techniques such as confocal microscopy (CFM) and histopathology. The suitability of the technique is for studies focusing on anatomical changes adipose thickness and gross connective tissue organization.

Optical Coherence Tomography

Optical coherence tomography (OCT) utilizes advanced photonics and fiber optics to obtain images and tissue characterization in human skin. Fully exploited, the technology has the potential to change the way researchers and scientists see and understand the skin. The technology combines the principles of ultrasound with the imaging performance of a microscope. Whereas ultrasound produces images from backscattered sound “echoes,” OCT uses infrared light waves that

reflect off the internal microstructure within the biological tissues. The frequencies and bandwidths of infrared light are orders of magnitude higher than medical ultrasound signals—resulting in greatly increased image resolution—8 to 25 times greater than any existing modality.

Although the resolution of OCT is good, it only extends approximately 500 μm into the skin, and although the epidermis and papillary dermis can be visualized, the subcutis remains obscure. As with ultrasound, the resolution needs to be improved if the technology is to be used to visualize subcutaneous adipose tissue at the ultrastructural level and to demonstrate changes in connective tissue structure and organization. The suitability of the technique is for studies focusing on effects of cellulite on the papillary dermis and consequences in the epidermis.

Lymphography

The role for insufficient lymphatic transport and lymphedema in cellulite is argumentative and controversial with a clear deficiency in studies attempting to prove this (7–9). However where there is insufficient lymphatic transport an accumulation of macromolecular proteins and hyaluronan is evident within the extracellular space. Lymphedema is accompanied by an accumulation of lymphocytes (macrophages), and an increased fibroblast, keratinocyte and adipocyte content of the affected tissue. Overgrowth of connective and adipose tissue will occur and is accompanied by an increase in collagen deposition. Where there is an excess of adipose tissue (e.g., cellulite), a deficiency in vascularity occurs in the peripheral regions characterized by mild inflammation releasing cytokines, chemokines and angiogenic factors (46). There is also inflammation which is an adaptive response to hypoxia in clusters of enlarged adipocytes within an expanding adipose mass. Since adipose is an active endocrine and paracrine organ that releases cytokines which influence body weight homeostasis, inflammation, fibrolysis and insulin resistance, increased levels of saturated fatty acid drive oxidative stress which in turn increases the level of cytokines/adipokines (47–49). With poor vascularity there is an increase in the likelihood of edema and venous insufficiency leading to the phenomenon of “heavy legs” often felt by many women with cellulite.

This procedure of (microfluorescence) lymphography (Fig. 4) serves to visualize lymph vessels via radiographic examination of the lymphatic system using an injection of contrast medium. If only lymph vessels are to be visualized, water soluble contrast media are used; however, to show the storage pattern of lymph nodes, oily contrast material is required. Radiological demonstration of lymph vessels and nodes is achieved by direct injection of contrast medium into a peripheral lymph vessel. Several types of needles and/or cannulae are available for cannulation of the lymph vessels, and automatic injectors are used for slow continuous injection of the viscous oily contrast medium. Water-soluble contrast medium is injected by hand.

To date this technique has not been used in the clinical evaluation of the involvement of lymphatics in the cellulite condition, and *before* this approach can be considered, clear factual knowledge as to whether cellulite affects lymph draining or causes fibrosclerosis of the lymph vessels is required. This knowledge requirement could be developed using histopathological techniques. With investigation, the suitability of the technique is for studies elucidating a role of cellulite in the abnormalities of the lymphatic system leading to heavy legs and poor vascularity associated in women with cellulite.

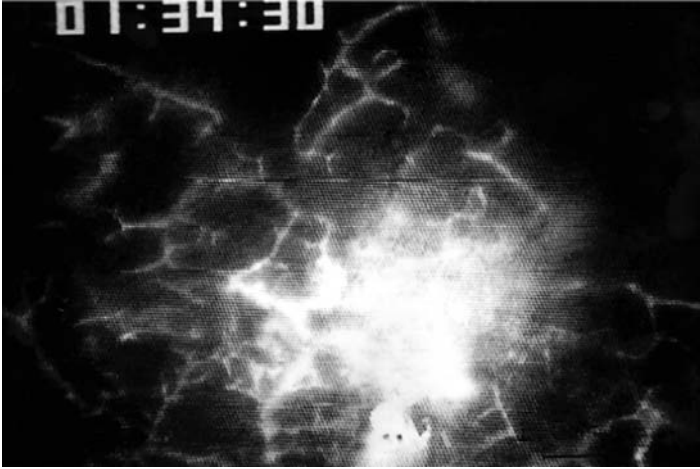


FIGURE 4 Fluorescence microlymphography. *Source:* From Ref. 50.

Dielectric Devices

Easily applicable and inexpensive water-specific techniques to evaluate local edema, swollen tissue problems and fluid retention in humans are not available. Edema is an excess of interstitial fluid volume which manifests itself as peau d'orange due to the expansion of the interfollicular dermis whereas subcutaneous edema gives rise to pitting. Edema develops when there is an imbalance between capillary filtration rate that exceeds lymphatic drainage. Lymphedema on the other hand, is a swelling of soft tissues resulting from an accumulation of protein-rich interstitial fluid caused by a low output failure of lymph.

A recently constructed noninvasive device for a local measurement of changes in tissue water in human skin and subcutaneous fat has been developed (50). The instrument transmits an ultra high-frequency electromagnetic (EM) wave of 300 MHz into a coaxial line and further into an open-ended coaxial probe that is in contact with the skin. Due to the dimensions of the applied probe, the penetration of the EM field extends to subcutaneous fat. A major part of the EM energy is absorbed by tissue water while the rest is reflected back into a coaxial line. From the information of the reflected wave, an electrical parameter, directly proportional to tissue water content, called a dielectric constant of subcutaneous fat, is calculated. The value increases with increasing water content. The measurement range from normal skin and subcutaneous tissue is from about 15 to 40. The dielectric constant of water is 79 and of adipose tissue about 10 to 20. The measuring depth can be adjusted by changing the dimensions of the probe.

The measured dielectric constant is saved as a single value or a mean of three or five samples. This new device enables an easy and noninvasive measurement technique to assess changes of tissue water in subcutaneous fat.

In terms of suitability of the technique, although the method has yet to be seriously considered and evaluated fully for cellulite studies, it offers excellent potential for demonstrating whether or not water retention and ultimately water structure plays a role in the manifestation of the cellulite condition.

PRIMOS (Fringe Projection)

PRIMOS is a well known application for measuring changes in skin surface texture and wrinkles. The optical device can also complete 3D measurement of parts of human body. In instances of measuring an area of 300×200 mm, the measurement of the 3D profile is performed with an accuracy of $50 \mu\text{m}$. This high accuracy enables application in the cosmetic and medical fields, including dermatology. Furthermore, the technique offers rapid measurements, micron resolution in all axes to ensure precise determination of all measured parameters, highly precise matching of skin areas measured before and after a treatment, determination of those characteristics essential for the investigation, and description of body parts with only one instrument. PRIMOS should also detect alterations to the subcutis/cutis structure if this affects the surface topography i.e., PRIMOS measures the surface irrespective of the causes for changes in skin surface topography.

In terms of suitability of the technique, PRIMOS could easily lend application for topical cellulite products developed for visualizing cosmetic surface changes of female thigh skin rather than those products attempting to address the fibrosclerosis or adipose defects.

In Vivo (Video) Confocal Microscopy

In vivo confocal microscopy (CFM) is a noninvasive microscopic technique capable of visualizing at the cellular level structural components of the skin with resolution to the level of the papillary dermis. This technique was employed in a recent study (18) in an attempt to identify specific characteristics of subcutaneous cellulite based on published histopathological findings. The main objective was to determine the impact of cellulite adipose protrusion at the papillary dermis, using in vivo CFM in the subcutaneous adipose in healthy nondiabetic, females was compared to that of healthy nondiabetic, males. Eleven subjects five males and six females were recruited onto the study. Height, weight and body mass index (BMI) were recorded. All females had visual cellulite on the thighs. In vivo confocal imaging was captured on the front, side and back aspects of the thighs—15 image captures per site.

Initial results found that “striae” were seen penetrating into papillary dermis, which were not seen in male skin. Surrounding these “epidermal” striae—which were located and observed within the epidermis at the basal-spinous cell layers—were strands of sclerotic collagen fibers (Fig. 5). In contrast, collagen observed in males at the same thigh point was normal—sparse and fine, with minimal obvious density (Fig. 6).

In males, imaging before loss of microscope resolution extended to $170 \mu\text{m}$, whereas in females this was extended to $200 \mu\text{m}$. The average epidermal thickness in males was $55 \mu\text{m}$ compared to $51 \mu\text{m}$ in females. Larger differences were seen in full thickness measurements (stratum corneum to subpapillary layer of papillary dermis). However, this may be attributed to loss of resolution in male subjects. Clear differences were observed between females with average BMI and females with greater than average BMI. Females with greater-than-average BMI had thinner full thickness measurements ($156 \mu\text{m}$) than average BMI females ($178 \mu\text{m}$). Epidermal thickness in females with greater-than-average BMI was less ($45.5 \mu\text{m}$) than in females with average BMI ($62 \mu\text{m}$).

Collagen as a finely woven meshwork of collagen fibers is found at the papillary layer of the dermis which includes not only the subepidermal papillae

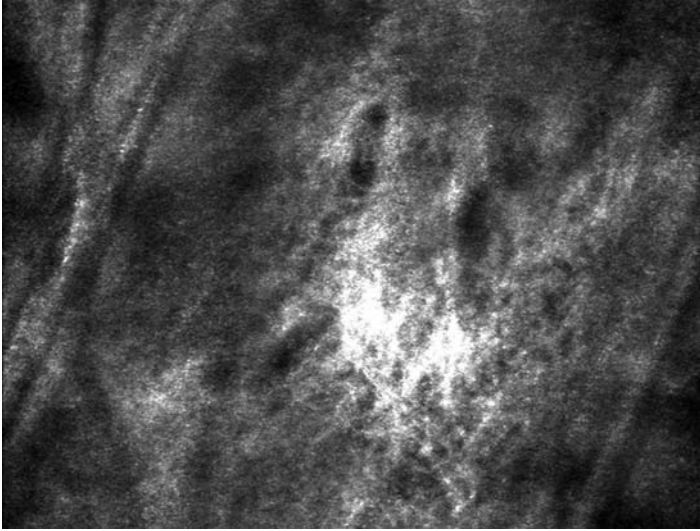


FIGURE 5 Striae observed at the basal-spinous cell layer in female thigh skin. The arrows indicate stretched collagen appearing tightly compact and taut.

situated between the rete ridges but also the subpapillary layer forming a narrow ribbon between the rete ridges and the subpapillary blood vessels—papillary dermis. The collagen at this site is composed mainly of type I collagen (ranging from 2–15 μm). At the reticular dermis, although not resolved using the CFM the reticular collagen here is very thin (0.2–1 μm) and composed mainly of type III collagen and at the basement membrane zone collagen is present as thin

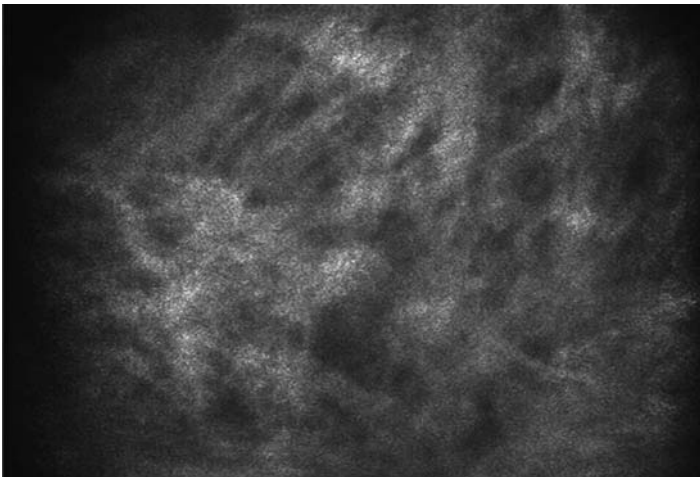


FIGURE 6 Image taken of male thigh skin at same resolution to Figure 5. The collagen appears light and very fine ("fluffy") and sparse.

reticular fibers that are not converted to thicker fibers. With regard to the observed collagen patterns, in all males, these were random and sparse at all sites. In females with average BMI, collagen patterns on the front thigh were also random and sparse, however at the side and back of the thigh, the collagen was stretched (resembling striae).

Furthermore, at the back of the thigh in females, dark fluid filled spaces were observed. Resolution in average BMI women was still permissible with resolution of blood flow and individual collagen fibers. In females with greater-than-average BMI at all sites, collagen was stretched (resembling striae) and many dark fluid filled spaces were observed at all sites compared to females with average BMI. Resolution in greater-than-average BMI women was not permissible with loss of resolution of blood flow and individual collagen fibers. The observed dark fluid filled spaces index matched to water. Another observation particular to female skin, was the presence of so-called "puncture" zones surrounded by blood flow (Fig. 7). The collagen appeared very dense and "stretched" in one direction and the epidermis very thin with little resolution of the basal cell layer. Although the observations appeared as actual "holes," they are not considered to be actual adipose tissue puncturing the dermis, but the indentations as seen by Querleux et al. (2) and subsequently considered as tightly packed dermal papillae. However since the dark fluid-filled spaces index match to water, neither is it ruled out that these observed dark spaces in the image could be where adipose had protruded through, such as the observed fat "herniation" by Piérard et al. (20). Furthermore, electron microscopy studies of increased pressure to the skin as in the case of stages leading to pressure-sores have clearly demonstrated disintegration of the upper portions of dermal papillae leaving "holes" (51). In cellulite, the skin is clearly under pressure from subcutaneous fat protrusions and from the stretch forces of dermal collagen at the papillary dermis and below.

There are reports of increased glycosaminoglycans (GAGs) in the cellulite condition (3), which are a component of the ground substance that fills the spaces between collagen fibers and collagen bundles. GAGs trap bulk (tetrahedron) water that is unable to bind to proteins resulting in rigidity and instability of the collagen

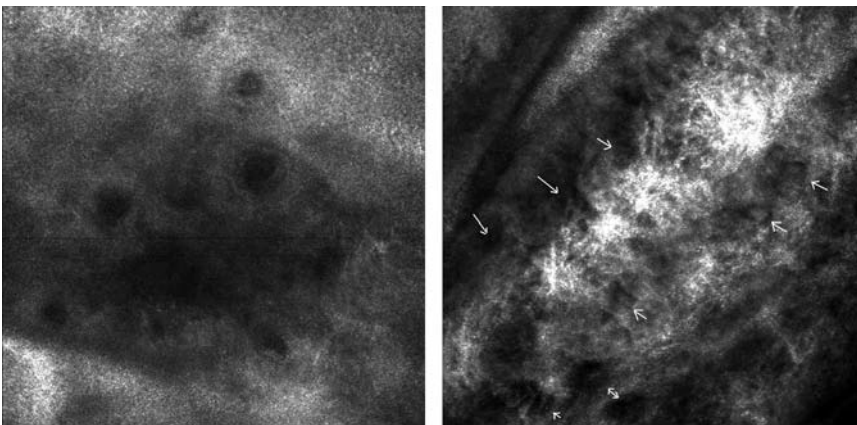


FIGURE 7 Indentations into the dermal-epidermal layers (*left*). The arrows (*right*) indicate actual blood flow within the capillaries.

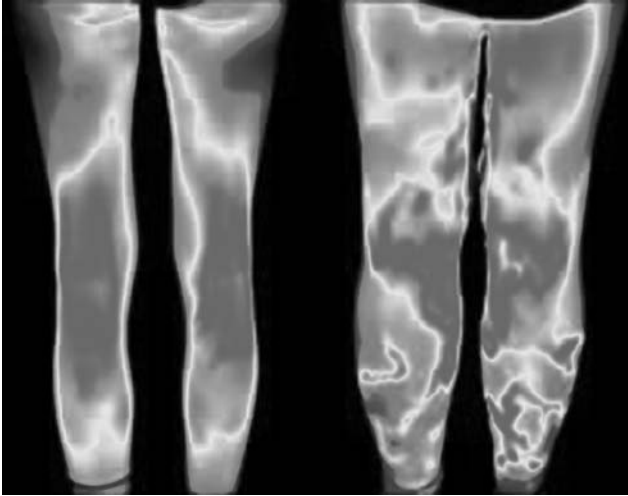


FIGURE 8 (See color insert) Thermography of normal (*left*) and abnormal (*right*) female legs (Infra Tec GmbH, Germany).

fibers—also seen in striae distensae. If the collagen as observed in cellulite is stretched more spaces appear giving rise to an increase in the potential for more bulk water that could be observed as dark spaces which are not blood vessels. If there are abnormally increased amounts of reticular collagen (thinner) then they are suspect to rupture. Moreover, increased amounts of reticular collagen could be examined to see if in cellulite prone females there is an abnormality in active fibroblasts, since active growth fibroblasts also cause an increase in GAGs.

Although the limitations of this technique as with other image analysis systems are obtaining clear resolution beyond the upper portion of the dermal papillae, *in vivo* CFM is suitable for identifying changes in collagen organization, dimpling of the skin at the epidermal-dermal junctions, distortions and pressure effects on the dermal papillae at the cellular level.

Thermal Imaging

Thermal imaging can measure alterations or variations in skin temperature and thus any skin disorder affecting directly or indirectly the microcirculation of the skin becomes a candidate for thermal evaluation (Fig. 8). Consideration of the application of thermal imaging to cellulite should be given. In compressed subcutaneous adipose tissue as seen in cellulite and visualized by several of the image techniques described in this paper, the microvasculature is pressed considerably against the papillary dermis. The amount of heat generated could be compared to that observed in noncellulite skin.

CONCLUSIONS

Dimpling of the skin of the peripheral regions of the female body commonly called cellulite is wrongly presumed to be an abnormality of adipose tissues rather than

normal reality. Cellulite is a condition reflected in differences in adipose biochemistry and connective tissue structure in the female gluteal-femoral adipose. At this stage of current understanding of the condition, it is concluded that the main cause of "visual cellulite" is a consequence of the inability of collagen at the papillary dermis to contain adipose protrusion (papillae adiposae) through a "thin" dermis that is not observed in males. Papillae adiposae represent a gender-linked characteristic rather than a typical aspect of cellulite.

Image analysis surmises that pressure participates in dimpling of the skin as a consequence of enlarged fat lobules. External compression and tension forces bulging and the fibrosclerosis of thin loose connective tissue strands combined with excessive tension and stress result in striae. Adipocyte volume enhances these effects. There is no lipatrophy since there is no tissue dystrophy.

Due to the limitations of each technique available, there is no one method at present that can be used to evaluate cellulite. Furthermore current formulations do not penetrate sufficiently into the adipose tissue to cause an effect.

Although cellulite appears incurable, the subject itself needs a clearer understanding, a consistent approach, coherency to prevent misinterpretation and misunderstanding in both the scientific and popular literature, formulations that "deliver," correlation of data, good clinical development of methods, the management and understanding of the psychological and social aspects of the condition. Only then can the unmet need of managing the expectations of the consumer, regulatory and advertising authorities be achieved.

REFERENCES

1. Mirrashed F, Sharp J, Krause V, et al. Pilot study of dermal and subcutaneous fat structures by MRI in individuals who differ in gender, BMI and cellulite grading. *Skin Res Technol* 2004; 10:161-168.
2. Querleux B, Cornillon C, Jolivet O, et al. Anatomy and physiology of subcutaneous adipose tissue by in vivo magnetic resonance imaging and spectroscopy: relationship with sex and presence of cellulite. *J Skin Res Technol* 2002; 8:118-124.
3. Lotti T, Ghersetich I, Grappone C, Dini G. Proteoglycans in so-called cellulite. *Intl J Dermatol* 1990; 29:272-274.
4. Bertin C, Zunino H, Pittet JC, et al. A double-blind evaluation of the activity of an anti-cellulite product containing retinol, caffeine and ruscogenine by a combination of several non-invasive methods. *J Cosmet Sci* 2001; 52:99-210.
5. Pièrard-Franchimont C, Pièrard GE, Henry F, Vroome V, Cauwenbergh G. A randomized placebo-controlled trial of topical retinol in the treatment of cellulite. *Am J Dermatol* 2000; 1:369-374.
6. Nurnberger F, Muller GJ. So-called cellulite: an invented disease. *Dermatol Surg Oncol* 1978; 4:221-229.
7. Curri SB. Cellulite and fatty tissue microcirculation. *Cosmet Toilet* 1993; 108:51-58.
8. Curri SB, Bombardelli E. Local lipodystrophy and districtual microcirculation. *Cosmet Toilet* 1994; 109:51-65.
9. Draelos ZD, Marenus KD. Cellulite etiology and purported treatment. *Dermatol Surg* 1997; 23:1177-1181.
10. Rosenbaum M, Prieto V, Hellmer J, et al. An exploratory investigation of the morphology and biochemistry of cellulite. *Plast Reconstr Surg* 1998; 101:1934-1939.
11. Kligman AM. Cellulite: facts and fiction. *J Geriatr Dermatol* 1999; 5:136-139.
12. Wulf FC, Sandby-Moller J, Kobayasi T, Gnaidecki R. Skin ageing and natural photoprotection. *Micron* 2004; 55:185-191.
13. Tzaphlidou M. The role of collagen and elastin in aged skin: an image processing approach. *Micron* 2004; 35:173-177.

14. Labat-Robert J. Age dependant remodeling of connective tissues: role of fibronectin and laminin. *Pathol Biol (Paris)* 2003; 51:563–568.
15. Djurhuus C, Gravholt C, Nielsen S, et al. Additive effects of cortisol and growth hormone on regional and systemic lipolysis in humans. *Am J Physiol Endocrin Metab* 2004; 286:488–494.
16. Peter A, Schweiger U, Pellerin L, et al. The selfish brain: competition for energy resources. *Neurosci Biobehav Rev* 2004; 28:143–180.
17. Frey F, Odermatt A, Frey B. Glucocorticoid-mediated mineralocorticoid receptor activation and hypertension. *Curr Opin Nephrol Hypertens* 2004; 13:451–458.
18. Callaghan T. Evaluating cellulite: reality redirecting the dream to dispel the myth. Proceedings of the 23rd IFSCC Congress, Orlando, Florida, October 2004.
19. Callaghan T. Is cellulite an aging phenomenon. Abstracts and Presentations of the 3rd ProDERM Scientific Seminar, Monaco, October 21, 2005.
20. Pièrard GE, Nizet JL, Pièrard-Franchimont C. Cellulite: from standing fat herniation to hypodermal stretch marks. *Am J Dermatopathol* 2000; 22:34–37.
21. Bjorntorp P, Karlsson M, Pettersson P. Expansion of adipose storage capacity at different ages in rats. *Metabolism* 1982; 31:366–373.
22. Rebuffe-Scrive M, Bronnegard M, Nilsson A, et al. Steroid hormone receptors in human adipose tissue. *J Clin Endocrinol Metab* 1990; 71:1215–1219.
23. Bjorntorp P. Adipose tissue distribution and function. *Int J Obesity* 1991; 15:67–81 (and references cited therein).
24. McTernan P, Andersen L, Anwar A, et al. Glucocorticoid regulation of P450 aromastase activity in human adipose tissue: gender and site differences. *J Clin Endocrinol Metab* 2002; 87:1327–1336.
25. Boullu-Ciocca S, Paulmyer-Lacroix O, Fina F, et al. Expression of the mRNA's codifying for the glucocorticoid receptor isoforms in obesity. *Obes Res* 2003; 11:925–929.
26. Gravholt C, Dall R, Christiansen J, et al. Preferential stimulation of abdominal subcutaneous lipolysis after prednelisone exposure in humans. *Obes Res* 2002; 10:774–811.
27. Katz J, Mohamed-Ali V, Wood P, et al. An in vitro study of the cortisol-cortisone shuttle in subcutaneous abdominal tissue. *Clin Endocrinol* 1999; 50:63–68.
28. Petersen S, Kristensen K, Richelson B. Anti-glucocorticoid effects of progesterone in vivo on rat adipose tissue metabolism. *Steroids* 2003; 68:543–550.
29. Rebuffe-Scrive M, Eldh J, Hafstrom L, et al. Metabolism of mammary, abdominal and femoral adipocytes in women before and after menopause. *Metabolism* 1986; 35:792–797.
30. Pedersen SB, Kristensen K, Hermann PA, et al. Estrogen controls lipolysis by up-regulating alpha-2A-adrenergic receptors directly in human adipose tissue through the estrogen receptor alpha. Implications for female fat distribution. *J Clin Endocrinol Metab* 2004; 89:1869–1878.
31. Xu X, DePergola G, Bjorntorp P. Testosterone increases lipolysis and the number of beta-adrenergic receptors in male rat adipocytes. *Endocrinology* 1991; 128:379–383.
32. Quinkler M, Oelkers W, Diederich S. Clinical implications of glucocorticoid metabolism by 11-beta-hydroxysteroid dehydrogenases in target tissues. *Eur J Endocrinol* 2001; 144:87–97.
33. Engeli S, Bohnke J, Feldpausch M, et al. Regulation of 11-beta-hydroxysterid dehydrogeanse genes in human adipose tissue: influence of central obesity and weight loss. *Obes Res* 2004; 12:9–17.
34. Masuzaki H, Flier J. Tissue-specific glucocorticoid reactivating enzyme 11-beta-hydroxysteroid dehydrogenase type-1 (11betaHSD-1)—a promising drug target for the treatment of metabolic syndrome. *Curr Drug Targ Imm Endocrin Metab Disord* 2003; 3:255–262.
35. Morton N, Ramage L, Seckl J. Down-regulation of adipose 11-beta-hydroxysteroid dehydrogenase type-1 by high fat feeding in mice: a potent adaptive mechanism counteracting metabolic disease. *Endocrinology* 2004; 145:2707–2712.
36. Banks W. The many lives of Leptin. *Peptides* 2004; 25:331–338.
37. Alvarez G, Ballard T, Beske S, et al. Subcutaneous obesity is not associated with sympathetic neural activation. *Am J Physiol Heart Circ Physiol* 2004; 287:414–418.

38. Putignano P, Brunani A, Dubini A, et al. Effect of small doses of dexamethasone on plasma Leptin levels in normal and obese subjects: a dose response study. *J Endocrinol Invest* 2003; 26:111–116.
39. Pananetti P, Garrapa G, Mantero F, et al. Adipose tissue as an endocrine organ? A review of recent data related to cardiovascular complications of endocrine dysfunctions. *Clin Exp Hypertens* 2004; 26:387–398.
40. Nagy T, Gower B, Trowbridge C, et al. Effects of gender ethnicity body composition and fat distribution on serum Leptin concentrations in children. *J Clin Endocrinol Metab* 1997; 82:2148–2152.
41. Potter J, Rennie-Tankersley L, Mezey E. Leptin deficiency prevents the activation of the murine alpha 2(I) collagen promoter by acetaldehyde. *Arch Biochem Biophys* 2004; 426:73–77.
42. Tang M, Potter J, Mezey E. Activation of the human alpha1 (I) collagen promoter by Leptin is not mediated by transforming growth factor beta responsive elements. *Biochem Biophys Res Commun* 2003; 312:629–633.
43. Matsubara M, Maruoka S, Katayose S. Inverse relationship between plasma adiponectin and Leptin concentrations in normal-weight and obese women. *Eur J Endocrinol* 2002; 147:173–180.
44. Spiegelman B. PPAR- γ : adipogenic regulator and thiazolidinedione receptor. *Diabetes* 1998; 47:507–514.
45. Smalls L, Lee CY, Whitestone J, Kitzmiller WJ, Wickett RR, Visscher MO. Quantitative model of cellulite: three-dimensional skin surface topography, biophysical characterization, and relationship to human perception. *J Cosmet Sci* 2004; 56(2):105–120.
46. Fantuzzi G. Adipose tissue, adipokines, and inflammation. *J Allergy Clin Immunol* 2005; 115:911–919.
47. Martin L, Woo J, Daniels S, Goodman E, Dolan L. The relationship of adiponectin with insulin and lipids are strengthened with increasing adiposity. *J Clin Endocrinol Metab* 2005; 90.
48. Kadowaki T, Yamanuchi T. Adiponectin and adiponectin receptors. *Endocr Rev* 2005; 26:439–451.
49. Fernandez-Real J, Pugeat M, Lopez-Bermejo A, Bornet H, Ricart W. Corticosteroid-binding globulin affects the relationship between circulating adiponectin and cortisol in men and women. *Metabolism* 2005; 54:584–589.
50. Husmann M, Roedel C, Leu A, et al. Lymphoedema, lymphatic microangiopathy and increased lymphatic and interstitial pressure in a patient with Parkinson's disease. *Schweiz Med Wochenschr* 1999; 129:410–412.
51. Nuutinen J, Ikaheimo R, Lahtinen T. Validation of a new dielectric device to assess changes of tissue water in skin and subcutaneous fat. *Physiol Meas* 2004; 25:447–454.
52. Arao H, Obata M, Shimada T, Hagiwara S. Morphological characteristics of the dermal papillae in the development of pressure sores. *J Tiss Viab* 1998; 8:17–23.

Minehiro Okuda

Kao Corporation, Safety and Microbial Control Research Center, Tochigi, Japan

Keiichi Kawai

Kawai Medical Laboratory for Cutaneous Health, Shimogyo-ku, Kyoto, Japan

WHAT IS DETERGENT?

Soap obtained by neutralizing fatty acids was the only surfactant that we could use until the late 19th century. The manufacturing method of synthetic soap substitutes was then developed when there were not enough oils and fats due to World War I. As the variety of synthetic soaps rapidly expanded, their applications and the quantity consumed remarkably increased (1).

The term “detergent” is generally used in two meanings; one refers to a commercial product which removes dirt and grease from clothing as in laundry detergent and the other refers to a chemical compound itself, i.e., surfactant. In our everyday life, we use the term detergent mostly to describe commercial products containing surfactants.

Detergent as a commercial product usually includes personal care products such as shampoo and household products that remove dirt from clothing, dishes, and living spaces. In order to improve its performance, additives suitable for each use are added to a surfactant of which soap is a typical example (2).

To laundry detergent, enzymes and builders are added. Due to the alkaline property of the builders, free fatty acids in dirt turn into soap and enhance detergency naturally. To shampoo, silicon and some other ingredients are added to generate much foam and to prevent hair from being entangled when washing. Perfumes are also added to give fragrance.

Thus, when we study the effects of detergents on the skin, not only surfactants but also the activities of various ingredients need to be taken into consideration. When the detergent that includes these constituents is used directly on the body or comes in contact with the skin in washing, in addition to the targeted dirt, skin surface lipids, intercellular lipids, and natural moisturizing factors (NMF) are sometimes forced to be removed from the skin as well as the targeted dirt (3).

Another major property of surfactants is emulsification. It has been applied to produce cosmetic cream, shaving cream and so forth. Emulsifying agents are employed to stabilize lipid-soluble substances and to improve the effects of topical products by intensifying skin penetration. We can find numerous examples of applications of surfactants or substances with surfactancy in most cosmetics and household products around us (2).

Type of Surfactants

A surfactant is defined as a compound which characteristically gathers around the interface between two different materials and alters the properties of the interface

remarkably and so is termed "surface-active agent." It basically consists of two different groups of structure, namely, a hydrophilic group that is easily soluble in water and a hydrophobic (lipophilic) group easily soluble in oil. This dual nature, being intimate with both oil and water, is termed amphipathy and is characteristic of surfactants. Detergents are classified into four types according to their structures and characteristics (Fig. 1). They are anionic, cationic, nonionic, and amphoteric types. Anionic surfactants are used as a main ingredient of washing agents of which fatty acid soap is a typical example. Cationic surfactants are used for fabric softener and hair conditioner. Nonionic surfactants do not ionize when dissolved in water. They are mostly used as foam stabilizers and foam boosters in washing and emulsifying agents. Amphoteric surfactants consist of an anionic component and a cationic component. Their activity depends on the pH of the solution. Thus, the functions and the applications of surfactants are generally classified by the type of hydrophilic group.

In addition, even in the same class of surfactant, surfactancy differs greatly according to the structure and the chain length of the molecules of the hydrophilic group and the hydrophobic group. Accordingly, the effects of surfactants on the skin largely differ. These effects depend on the balance between the hydrophilic group and the hydrophobic group, not simply on the chain length of the hydrophobic group. For instance, of anionic surfactants which have the same hydrophilic group (the group of sodium alkyl sulfate), the surfactant with the middle-length chain shows maximum skin irritancy (4,5).

Surface Activating Effect and Micelle Formation

In aqueous solutions, surfactants gather around the interface between water and air with hydrophilic groups being oriented to water and hydrophobic groups to air, because the hydrophobic groups repel water. This is termed adsorption. As the concentration of the surfactants increases to a certain level, the surfactant molecules begin to form aggregates in which the hydrophilic groups are oriented outside (to water) and the hydrophobic groups are oriented inside to avoid water. These aggregates are called micelle. The number of micelles increases, as the concentration of the surfactants increases. The minimum concentration at which

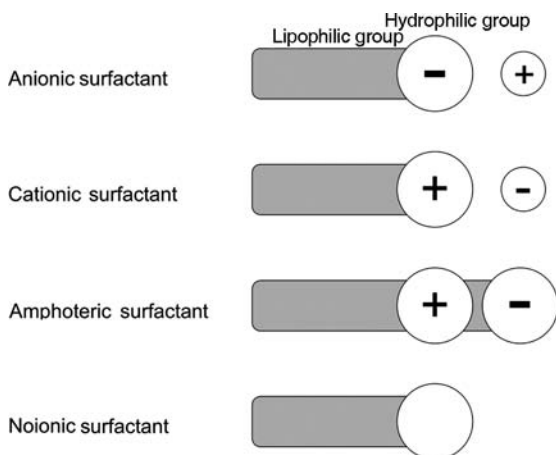


FIGURE 1 Types of surfactants. Surfactants consist of two different groups of atoms, namely a hydrophilic group, which is easily soluble in water, and a hydrophobic (lipophilic) group easily soluble in oily materials. Surfactants are classified into anionic, cationic, nonionic, and amphoteric types by conditions of an electric charge when dissolved in water.

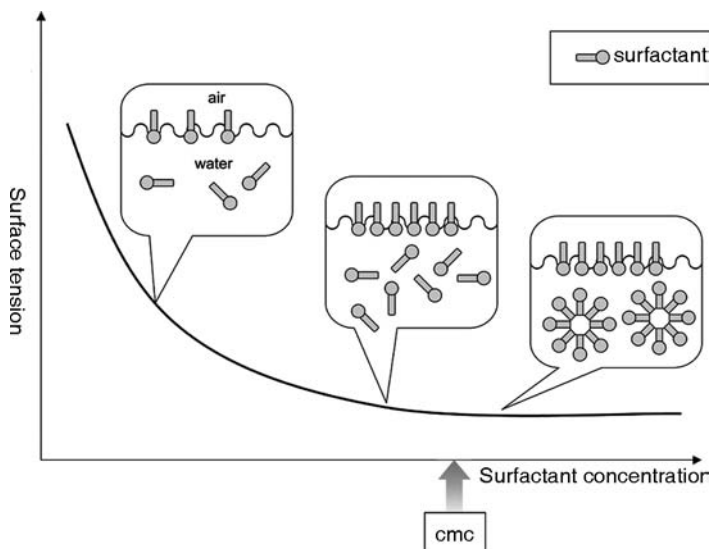


FIGURE 2 Critical micelle concentration (CMC). Surface tension of water is depressing with surfactant concentration. As the concentration of the surfactants increases to a certain level (*arrow*: the CMC), the surfactant molecules begin to form aggregates in which the hydrophilic groups are oriented outside (to water) and the hydrophobic groups are oriented inside to avoid water. These aggregates are called micelle.

surfactant molecules begin to form micelles is termed critical micelle concentration, abbreviated as CMC. The lower the CMC value, the higher is the surface activity (Fig. 2). In a mixed solution such as a cleaner, the CMC value is affected by other substances in the solution.

Emulsion and Suspension

Surfactants have a function which adsorbs to the surface of the particles of a liquid and a solid, and disperse them uniformly in the liquid. It is called emulsion when fine particles of a liquid are dispersed and suspension when fine particles of a solid are dispersed. It is called the oil-in-water (O/W) type when the dispersed particles by surfactants in the liquid consist of oil. Conversely, it is called the water-in-oil (W/O) type when the dispersed particles in oil consist of water. This feature is utilized for topical products such as a cream in order to enhance skin penetration by dispersing oil-soluble substances uniformly (Fig. 3).

Mechanism of Washing

When oily dirt adhered to the surface of the human skin or fabric is soaked in a solution of surfactants, the surfactants adsorb to the surface of the dirt. The dirt is then removed from the target by the dispersing/emulsifying effect of the surfactants.

This is the basic mechanism of washing. In some commercial products, alkaline agents and chelating agents are added for the purpose of intensifying detergency. Soil redeposition agents are also added to inhibit the dirt from redeposition.

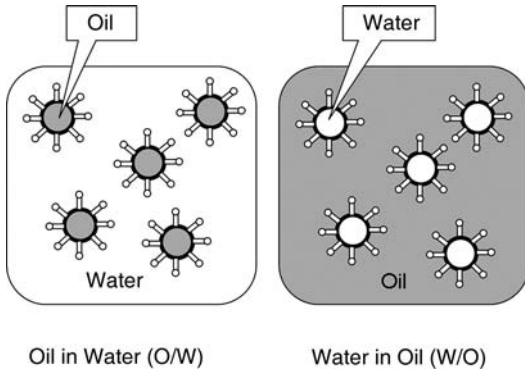


FIGURE 3 Type of emulsion. It is called emulsion when fine particles of a liquid are dispersed and suspension when fine particles of a solid are dispersed. It is called the oil-in-water (O/W) type when the dispersed particles by surfactants in the liquid consist of oil. Conversely, it is called the water-in-oil (W/O) type when the dispersed particles in oil consist of water.

This mechanism is the same whether the target is human skin or the surface of materials (Fig. 4).

EFFECTS OF DETERGENTS ON THE SKIN

Positive Effects of Detergent on the Skin

Detergent, especially a body cleanser and shampoo, is applied to a human body primarily to remove the secretions of the organism, such as grime and sebum,

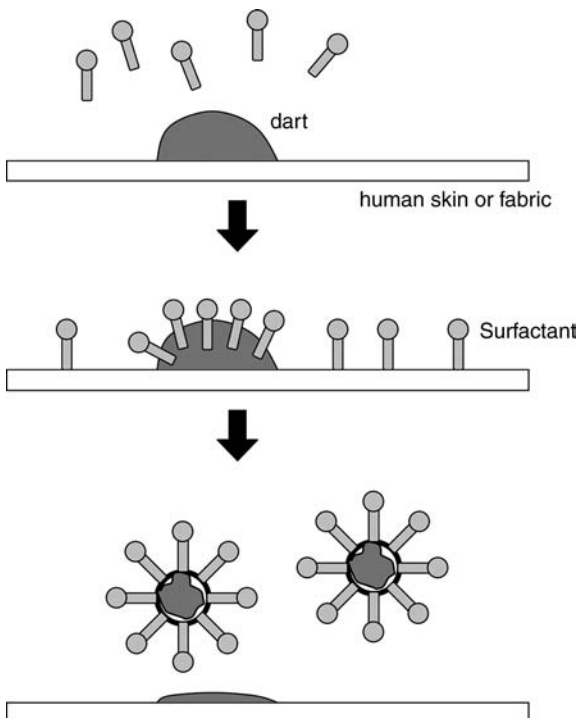


FIGURE 4 Emulsion and suspension of dirt. When oily dirt adhered to the surface of the human skin or fabric is soaked in a solution of surfactants, the surfactants adsorb to the surface of the dirt. The dirt is then removed from the target by the dispersing/emulsifying effect of the surfactants.

along with the dirt adhered to the skin. Some constituents of dirt contain substances that can cause skin irritancy when they reside on the skin. Moreover, they can induce acne and miliaria by obstructing the opening of hair follicles and sweat glands. In case of dirt such as mite antigen, because of its protease activity, the dirt can cause impairment of the barrier functions of the skin when adhered to and left on the skin (6). Therefore, it is very important to keep the skin clean by washing with cleanser when we consider skin hygiene.

Direct Effects of Detergents on the Skin

Even if detergents such as laundry detergent and dishwasher detergent come in contact with the skin at high concentration, skin irritation is not observed if rinsed immediately after their contact. But if they remain on the skin, primary skin irritation can be observed because the surfactants contained in the detergents can elicit irritant skin reactions (7). In the 24 hours of closed patch test with sodium lauryl sulfate (SLS) (5%), obvious erythema and bullae occur, but if rinsed quickly only temporary dryness occurs by the loss of epidermal lipids and it will be repaired in a short time. As contact time gets longer, however, the number and the thickness of the horny layer decreases with SLS even at 1% (8).

The guidelines on the applications of surfactants have been thus proposed (9–12) based on the extensive studies of the effects of surfactants on the skin by utilizing SLS as a positive control.

A simple buffer solution without surfactant causes similar effects when dissolved in an alkaline solution. For example, when a peeled human stratum corneum sheet is soaked into a buffer solution (with no surfactant) at pH 3 to 11, for 24 hours, dissolution of intercellular lipids and impairment of the horny layer are observed in an alkaline range by an electron microscope (Fig. 5) (13). Moreover, when the skin is washed by a surfactant solution dissolved in a buffer solution at the same pH range, the dissolution of intercellular lipids and amino acids occurs more frequently in the alkaline range than in the acidulous range.

When surfactancy is decreased by adding a large quantity of oily substances to the detergent, washing performance declines and the detergent causes less skin irritancy.

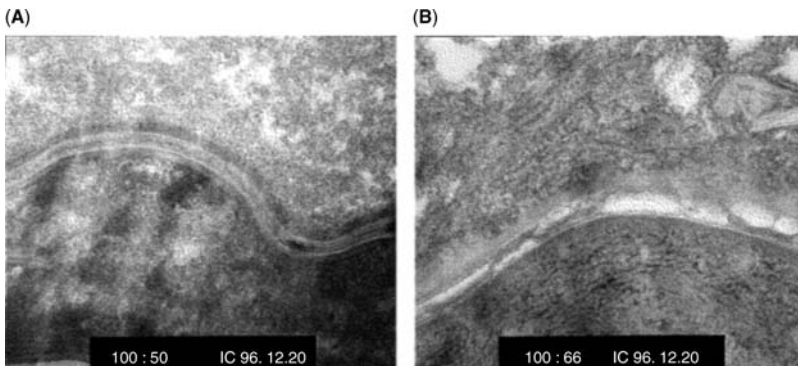


FIGURE 5 Disruption of Intercellular lipid layer with alkali treatment. Removed stratum corneum sheet are immersed to the surfactant solution (A) pH 7.0 or (B) pH 9.0. Intercellular layer is maintained its structure at pH 7.0, in contrast braked or gapped layers are observed at pH 9.0.

Therefore, when we evaluate a skin irritancy of the detergents and the surfactants, we need to understand that both their potential as a chemical substance and the effects by the property of the solution should be taken into consideration. In the surfactants that have a similar basic structure, skin irritancy differs according to the chain length of each surfactant. On the other hand, when the same surfactant is dissolved into a buffer solution, skin irritancy differs according to the pH.

Indirect Effects of Detergents on the Skin

When a detergent, such as skin cleanser comes in contact with the skin, not only dirt but epidermal lipids also are forced to be washed away. The lost epidermal lipids are repaired in a short time. However, when hands are washed frequently and excessively before the epidermal lipids are completely repaired as usually occurred to medical practitioners, NMF such as amino acids and ceramides in the stratum corneum and intercellular region are removed. The lost ceramides and amino acids are gradually repaired, but the moisturizing factors and the barrier functions are reduced during the recovering period (14). When washing is repeated further, a large quantity of water permeates through the horny layer during washing and rinsing due to the impairment of the barrier function. As a result, swelling is caused (15). Moreover, when a large quantity of intercellular lipids is

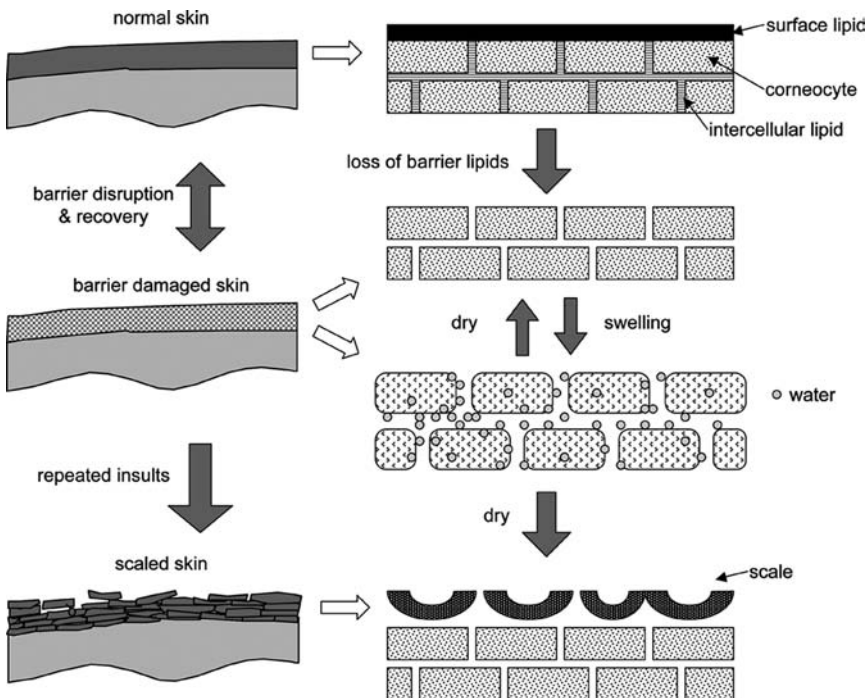


FIGURE 6 Morphological changes of the skin surface. After wash-off treatment, normal stratum corneum is swelling with water and then smoothly recovering its shape. But when barrier deficient stratum corneum is excessively swelling with water, surface layers of stratum corneum are morphologically changed to the scaly skin.

removed, it causes scaling, increase in transepidermal water loss (TEWL), and decrease in skin conductance (15,16). Because of impairment of the barrier function, various substances that come in contact with the skin in our everyday life can easily permeate through the skin as well as a detergent. This also leads to skin tightness and the forming of scaling and crack (Fig. 6) (17). The scaled skin sometimes provides skin resident flora and transit flora with a place to increase.

Consequently, contact dermatitis, infectious diseases, and atopic dermatitis can also be initiated or worsened. These effects are brought about not only by a surfactant contained in a detergent but also by the methods of washing (7,13), the pH of a detergent solution, and the care taken after the contact with the detergent, as proved in the following experiment.

A glass cup is applied on the forearm of a subject and the skin is washed with detergent solutions adjusted at several different concentrations. When we measured a skin conductance of the treated site, it showed an increase immediately after the washing, because the stratum corneum contained a large quantity of water during the washing. After that, water evaporated from the skin surface gradually, so the quantity of water in the stratum corneum rapidly decreased. It became even less than that present before the test depending on the washing condition, causing hyper dryness (Fig. 7) (18).

Due to the hyper dryness, the stratum corneum rapidly constricts and deforms. This is perceived as constriction after washing. When it is excessive, and the hyper dryness and its repair repeatedly occur, the stratum corneum of the skin surface desquamates, causing scaling and crack (Figs. 6 and 8) (17,19).

These irritant skin responses differ largely according to the surfactant contained in the detergent. In general, fatty acid soaps cause strong skin irritancy and a morphological change of the skin is large because of the alkaline property

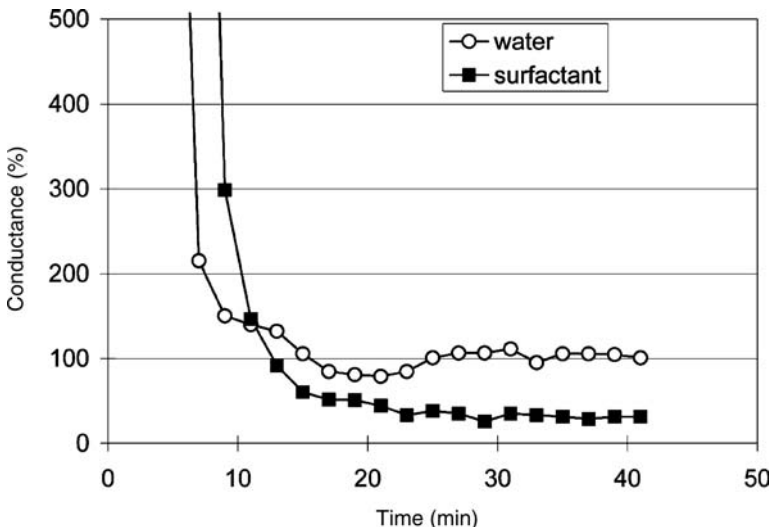


FIGURE 7 Hyper-dryness. Circle indicates control (water treated) and square indicates the treatment of surfactant solution. After wash-off treatment, skin surface is dried up but its range is excess. Hyper-dryness is caused by this surfactant treatment.



FIGURE 8 Skin surface changes. Skin surface is changed to scaly and dry conditions after hand immersion test.

of the solution. Also, fatty acid soap generates fatty acid calcium combining with calcium ions in tap water during the process of rinsing and it resides on the skin as scum (Fig. 9). The skin touch changes according to the structure and the quantity of the residual scum, largely affecting physical conditions of the skin surface. On the other hand, in a surfactant, such as amino acid type surfactant and monoalkylphosphate, a morphological change of the skin surface is small. When a skin cleanser contains polyols and an oily substance such as ceramides, an acute hyper dryness is prevented (Fig. 10) and the morphological change of the skin surface is small as a result (18).



FIGURE 9 Skin surface scum. White plate-like shape is scum of soap.

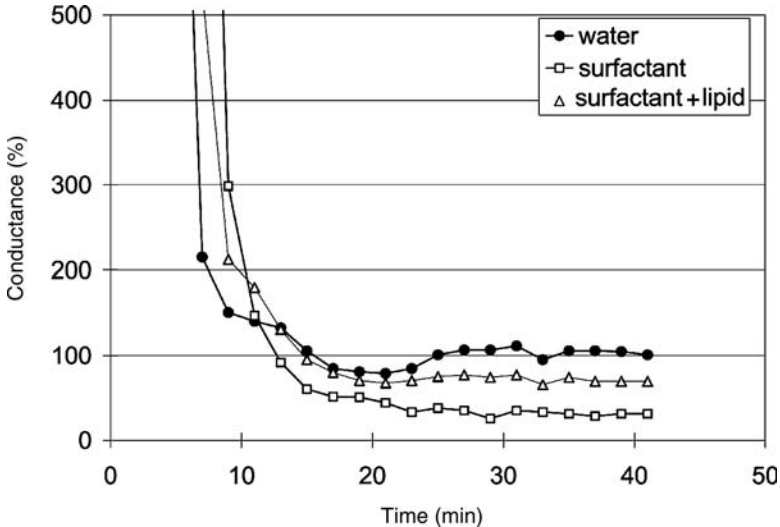


FIGURE 10 Effect of additive. Circle indicates control (water treated), square indicates positive control (treated with surfactant solution) and triangle indicates lipid-additive effect in solution of surfactant. Hyper-dryness is repressed with added lipids.

As mentioned previously, when the skin is washed by a detergent solution at several different pHs, intercellular lipids and amino acids dissolve much more in an alkaline range than in acidic range, even when the same surfactant is used. Furthermore, impairment of the barrier function (increase of TEWL and penetration through the skin surface) is observed and hyper dryness is induced. It is considered that the washing in the acidic range is less skin irritant by the observation of lamellae in the stratum corneum cells and of scaling of the skin surface.

These indirect effects are caused not only by a surfactant and a detergent as a chemical stimulus but also by cumulative effects and dryness due to the removal of lipids and NMFs. Thus, a single patch test is not satisfactory. Cumulative and repeated washing tests should be conducted to observe overall effects to the skin.

Methods of Evaluating Effects of Detergents on the Skin

A patch test is one of the most frequently used methods in evaluating acute skin irritancy (direct effects on the skin) caused by detergents and surfactants. In a patch test, test substance is applied on the skin and its effects are evaluated. The 24 hours of closed patch tests are widely performed and open patch tests are sometimes performed depending on the test substance. Basketter et al. have recently proposed the evaluation method of four hours of patch tests and reported the results obtained by this method (20–22).

The evaluation of patch test results is usually conducted by visual observation of the skin responses and judgment is made by previously designed criteria. In visual observations, the data are subjective and the observers sometimes report different results. Being different from the evaluation of allergies and dermal corrosivity, the evaluation of irritancy caused by detergents is especially difficult, because slight inflammatory reactions should be evaluated in most cases. The

results can thus easily differ depending on the observers. In order to enhance accuracy and reproducibility of the evaluation, skill development programs for the observers and an approach to subdivide the evaluation of weak inflammation have been proposed (22,23).

In order to observe the microscopic slight changes of the skin surface, Kawai's method (Replica method) is used. By this method, it is possible to predict subtle changes due to weak inflammation before visible erythema occurs on the skin (24–26).

A number of bioengineering techniques have been developed recently to measure different skin functions with a device. For instance, skin damage caused by the test substance can be quantitated by measuring water in the horny layer [skin conductance (27,28)] and by measuring impairment of the barrier function TEWL by an evaporimeter. Erythema can be also quantitated by a colorimeter. It is possible to obtain more accurate and objective data by these methods using a device (29).

Other evaluation methods *in vitro* (30) include corneosurfametry, the evaluation by swelling of desquamated stratum corneum, and the evaluation by cell damage using with a single-layer cultured human skin and a three-dimensional cultured human skin. These methods are effective in evaluating several different substances under the same condition (30). The evaluation of skin corrosivity *in vitro* is regulated by the OECD guidelines 431.

The judgment of these various evaluation methods should be conducted comprehensively, taking an advantage of each method (12,27,28,31).

Cumulative irritancy is thought to be caused by a different mechanism from that of acute irritancy and the evaluation methods are different accordingly. It is believed to be caused by repeated exposure to detergents and water by excessive rinsing and dryness thereafter. Thus, a single patch test is not satisfactory. The effects of repeated washing need to be observed for a certain period of time (16).

Monitored usage tests are more realistic than *in vitro* tests as they reflect the conditions of washing in everyday life, but the effects of environmental conditions of the subjects cannot be excluded. Alternatively, when washing tests are performed under a fixed condition in a laboratory, it is easier to control such environmental conditions; in order to facilitate tests by increasing the number of times of washing. The examples of these tests are the cup shake method (32), the perfusion method, the washing tests of cubital fossa using with fingers and wash cloth, the soaking method, and the interdigital falling-drop method.

Similar to the evaluations of acute skin irritancy, the evaluations of visual observations of erythema are sometimes conducted to assess the treated site. However, the evaluations of morphological changes and skin functions are more frequently conducted because cumulative irritancy is closely related to morphological changes and functional disorders of stratum corneum in most cases, rather than inflammatory changes. To evaluate morphological changes of the stratum corneum, the skin replica method is used. To evaluate the functions of the stratum corneum, the method of measuring skin conductance and TEWL with a device is used. Other methods are the tape stripping method in which removed stratum corneum is collected and turnover velocity is measured by its dimension and nucleated ratio, and the method of measuring disappearing time of fluorescent substances penetrated through the treated site by turnover of the stratum corneum. Moreover, the method of measuring elasticity of the stratum corneum and the method of measuring denaturation of the stratum corneum by dynamic viscoelasticity of

the desquamated horny layer are also used. In order to assess the degree of impairment of the barrier function, permeating quantity of riboflavin is measured in addition to TEWL as mentioned previously (13).

These methods have been developed to detect cumulative effects of washing by meeting specific requirements each time. Each method possesses its own advantage and thus several different methods should be combined to measure more precise cutaneous changes.

REFERENCES

1. Sitting M. Detergent Manufacture. New Jersey: Noyes Data Corporation, 1976:1-6.
2. Flick EW. Cosmetic and Toiletry Formulations. 2d ed. New Jersey: Noyes Publications, 1989:1-864.
3. Imokawa G. Comparative study on the mechanism of irritation by sulfate and phosphate type of anionic surfactant. *J Soc Cosmet Chem* 1980; 31:45-66.
4. Emery BE, Edwards LD. The pharmacology of soaps. III. The irritant action of sodium alkyl sulfates on human skin. *J Amer Pharm Assoc* 1962; 29:254-260.
5. Kligman AM, Wooding WM. A method for the measurement and evaluation of irritants on human skin. *J Inv Derm* 1967; 49:78-94.
6. Takai T, Kato T, Sakata Y, et al. Recombinant Der p 1 and Der f 1 exhibit cysteine protease activity but no serine protease activity. *Biochem Biophys Res Commun* 2005; 328:944-952.
7. Imokawa G, Sumura M, Katsumi A. Correlation between adsorption of surfactant onto callus and skin roughness caused by the surfactant. *J Jpn Oil Chem Soc* 1974; 23:17-23.
8. Chilcott RP, Patel A, Ashkey Z, et al. *The Essential Stratum Corneum*. Oxford: Martin Dunitz, 2002 (chap. 45).
9. Effendy I, Maibach HI. Detergent and skin irritation. *Clin Dermatol* 1996; 14:15-21.
10. Tupker RA, Willis C, Berardesca E, et al. Guidelines on sodium lauryl sulfate (SLS) exposure tests, a report from the standardization group of the European Society of Contact Dermatitis. *Contact Dermatitis* 1973; 37:53-69.
11. Lee Ch, Maibach HI. The sodium lauryl sulfate model: an overview. *Contact Dermatitis* 1995; 33:1-7.
12. Di Nardo A, Sugino K, Wertz K, et al. Sodium lauryl sulfate (SLS) induced irritant contact dermatitis: a correlation study between ceramides and in vivo parameters of irritation. *Contact Dermatitis* 1996; 35:86-91.
13. Okuda M, Yoshiike T. Correlation between epidermal barrier function and skin cleansing methods. *Jpn J Dermatol* 2000; 110:2115-2122.
14. Okuda M, Yoshiike T, Ogawa H. Evaluation method of stratum corneum barrier function utilizing riboflavin. *Jpn J Dermatol* 1999; 109:2103-2109.
15. Putterman GJ, Wolejsza NF, Wilfram MA, et al. The effect of detergents on swelling of stratum corneum. *JSCC* 1977; 28:521-532.
16. Wilhelm K-P, Freitag G, Wolff HH. Surfactant-induced skin irritation and skin repair, evaluation of a cumulative human irritation model by noninvasive techniques. *J Am Acad Dermatol* 1994; 31:981-987.
17. Denda M, Koyama R, Namba R, et al. Stratum corneum lipid morphology and transepidermal water loss in normal skin and surfactant-induced scaly skin. *Arch Dermatol Res* 1994; 286:41-46.
18. Kondo T, Okuda M, Imokawa G. The inhibitory effect of monoglyceride on skin roughness induced by dish-washing surfactants. *Jpn J Dermatol* 1995; 105:1217-1225.
19. Misra M, Ananthapadmanabhan KP, Hoyberg K, et al. Correlation between surfactant-induced ultrastructural change in epidermis and transepidermal water loss. *J Soc Cosmet Chem* 1997; 48:219-234.
20. Basketter D, Chamberlain M, Griffiths HA, et al. The classification of skin irritants by human patch test. *Food Chem Toxicol* 1997; 35:845-852.
21. York M, Basketter DA, Cuthbert JA, et al. Skin irritation testing in man for hazard assessment—evaluation of four patch systems. *Human Exp Toxicol* 1995; 14:729-734.

22. Basketter D, Reynolds F, Rowson M, et al. Visual assessment of human skin irritation: a sensitive and reproducible tool. *Contact Dermatitis* 1997; 37:218–220.
23. Kawai K, Yoshimura I, Sonoda I, et al. Study on the reliability and reproducibility of visual assessment for human skin irritation test. *Environ Dermatol* 2003; 10:145–155.
24. Kawai K. Study of determination methods of patch test based on microscopical observation. *Acta Derm (Kyoto)* 1971; 66:161–182.
25. Kawai K, Nakagawa M, Kawai J, et al. Evaluation of skin irritancy of sodium lauryl sulfate: a comparative study between the replica methods and visual evaluation. *Contact Dermatitis* 1992; 27:174–181.
26. Kawai J. Follow-up study about Kawai's method. *J Jpn Soc Cutan Health* 1991; 27: 156–166.
27. Ollnar S, Nyren M, Nicander I, et al. Electrical impedance compared with other non-invasive bioengineering techniques and visual scoring for detection of irritation in human skin. *Br J Dermatol* 1994; 130:29–36.
28. Nicander I, Ollnar S, EEK A, et al. Correlation of impedance response patterns to histological findings in irritant skin reactions induced by various surfactants. *Br J Dermatol* 1996; 134:221–228.
29. Agner T, Serup J. Sodium lauryl sulphate for irritant patch testing- a dose-response study using bioengineering methods for determination of skin irritation. *J Invest Dermatol* 1990; 95:543–547.
30. Goffin V, Paye M, Pierard GE. Comparison of in vitro predictive tests for irritation induced by anionic surfactant. *Contact Dermatitis* 1995; 33:38–41.
31. Shukuwa T, Kligman AM, Stoudemayer TJ. A new model for assessing the damaging effect of soaps and surfactants on human stratum corneum. *Acta Derm Venereol (Stockh)* 1997; 77:29–34.
32. Paye M, Morrison BM Jr, Wihelm K-P. Skin irritancy classification of body cleansing products, Comparison of two test methodologies. *Skin Res Technol* 1995; 1:30–35.

Monitoring Skin Hydration by Near-Infrared Spectroscopy and Multispectral Imaging

Shuliang L. Zhang

*Unilever Research and Development, Trumbull Measurement Science,
Trumbull, Connecticut, U.S.A.*

INTRODUCTION

Optimal hydration is one of the key factors for effective functioning of the stratum corneum (SC) to maintain flexibility and to facilitate the enzymatic reactions that drive SC maturation (1). Decreased water content impairs the natural desquamation process and leads to the formation of dry scaly skin (2). Moisturizing products are typically used to relieve the symptoms of dry skin and the efficacy of these products is determined in part by evaluating their ability to improve skin hydration. The state of skin hydration has been often assessed through instrumental methods that depend on the correlation of skin hydration with the electrical conductance and capacitance responses of the skin (3–5). These electrical methods have been used previously in differentiating products with large differences in hydration benefits, for example, between harsh soap and syndet cleansing bars and between moisturizers and moisturizing cleansing liquids. While it is widely accepted that these electrical measures correlate with skin hydration, they are both indirect, contact methods and the relationship between the electrical response and the skin hydration level is not straightforward. Their reliability may be an issue, as well, particularly if ingredients deposited on the skin from skin care products have a significant contribution (positive or negative) to the electrical property measured (6). Additionally, it is evident that substances or treatments that interact with the keratin-water network of the SC can change the electrical properties of skin without actually altering water content (5).

Near-infrared (NIR) spectroscopy, on the other hand, directly measures water content of living tissue from tissue reflectance in the NIR region of the spectrum. NIR has been previously used to assess tissue water content and to study nature of water in the tissue (7–10). A number of intense absorption bands exist in the NIR spectral region of the skin spectrum, as shown in Figure 1. The major bands that appear at approximately 960, 1200, 1450, and 1950 nm are due predominantly to absorption by water. A combination vibration of the fundamental symmetric and asymmetric OH stretching modes with an HOH bending mode gives rise to the intense band centered at 1950 nm. This band consists of multiple unresolved transitions and its complex band shape is highly influenced by water environment (11). The first overtone vibration of the symmetric and asymmetric OH stretches as well as the combination vibration of these fundamental stretches provides transition intensity in the 1450 nm region. The combination of the first overtone of the symmetric or asymmetric OH-stretching mode with an HOH-bending mode gives rise to the intensity in the 1200 nm region. However, the second CH and NH stretching overtones also contribute to transition intensity in this region of the spectrum.

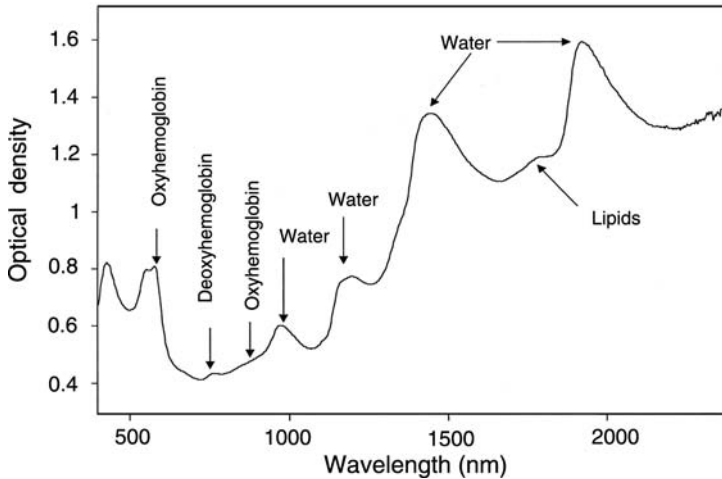


FIGURE 1 Reflectance spectrum of in vivo human skin.

At 960 nm, the second symmetric and asymmetric OH-stretching overtones as well as OH stretch-stretch combinations provide transition intensity. Higher OH-stretching overtones and combinations of these progressions provide weaker transitions around 840 and 740 nm.

Despite the complexity of the band shapes of the water spectrum, the integrated OH stretching overtone/combination band intensity can be used to measure the water content of water-rich tissue. The method assumes that water is the dominant source of OH stretching overtone/combination intensity in the sample. It also assumes that the overtone/combination band area is conserved in the face of shifting band maxima and changing band shape as a result of environmental and compositional changes in the spectroscopically sampled tissue. Previous studies have shown a linear correlation between the NIR absorption intensity and the concentration of water in skin over a wide dynamic range of water concentration (7–9). NIR methods are also less susceptible to interfering factors such as the deposition of the electrical conducting materials from moisturizing and cleansing products.

A quantitative measurement of skin hydration can also be achieved by imaging spectroscopy, providing a visualization tool that can aid in assessing consumer perception and preference with respect to skin moisturization technologies. Various microscopic skin imaging techniques, including confocal microscopy, fluorescence imaging and polarized microscopy have been used to visualize changes in skin hydration following various skin treatments. NIR reflectance-based imaging using a digital camera and tunable filter provides the most direct measure of the skin moisture content on the length scale relevant to consumers' perception of the skin condition. It has recently been shown in a clinical study that it is possible to distinguish between different levels of skin hydration under treatments with a skin moisturizer and artificial dehydration using a solvent (12–16).

In a further study testing marketed skin products (17), it was demonstrated that the NIR imaging technique had the ability to discriminate between cleansers and moisturizers, showed good correlation of measured skin hydration to visual

dryness, and separated a moisturizing effect from a drying effect. In another study (18), the NIR imaging technique was used to measure the changes in skin hydration following treatment with a series of mild cleansers. The imaging method was also compared with the standard instrumental methods under these conditions where the product-induced hydration changes were expected to be smaller than those tested previously.

The infrared imaging technique, measuring only the overall skin hydration, does not provide depth-resolved information on skin hydration. It is well known that NIR light penetrates into the skin well beyond the SC, although the depth of penetration is greatly reduced at the water absorption bands. Confocal Raman spectroscopy has been recently shown to be a useful tool for measuring the water content of skin as a function of depth (19).

In this chapter, we review the NIR imaging technique and summarize its applications as it is applied for testing the performance of different types of skin cleansing and care products. We compare the imaging technique with the visual assessment of dryness—which is a gross but consumer-relevant evaluation of skin moisturization.

INSTRUMENTATION

The NIR imaging system is schematically shown in Figure 2 and briefly described below. The infrared digital camera, manufactured by Sensors Unlimited, Inc. (Princeton, New Jersey, U.S.A.), contains a 320×240 -pixel indium-gallium arsenide (InGaAs) array sensitive to light with wavelengths from 960 to 1700 nm. The camera operates at room temperature and incorporates an electronic shutter with no moving parts. The signal from the camera sensor is digitized to 12 bits of intensity resolution within the camera and sent via parallel cable to a frame grabber card (National Instruments, Austin, Texas, U.S.A.) installed in the data-acquisition computer (Dell, Austin, Texas, U.S.A.). Custom software based on the LabView graphical programming language (National Instruments, Austin, Texas, U.S.A.) was written to control the camera. It also controls the liquid crystal

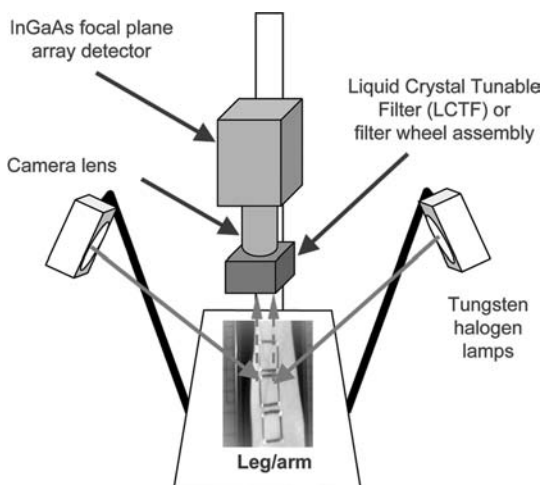


FIGURE 2 Schematic of the near-infrared imaging system. The setup was tilted back so that the camera points to the imaging subject horizontally when a leg is imaged.

tunable filter (LCTF) through a serial connection and synchronizes the camera exposure with the tuning of the LCTF. The tunable filter, manufactured by Cambridge Research & Instrumentation (Woburn, Massachusetts, U.S.A.), is a custom unit with band pass of approximately 6 nm tunable from 900 to 1700 nm. It was affixed to the front of the objective lens. Through the software, the user can request that a dark frame (background) be subtracted from each image, and can choose both the integration time and the set of wavelengths for the spectroscopic image set. A set of 75 images, spanning the wavelength range from 960 to 1700 nm in 10 nm increments, could be collected in approximately 90 seconds. This time included the collection and transfer of 10 individual 16.67 msec exposures at each wavelength, which were summed on the fly by the control software.

In the feasibility study reported previously (13,14,16), each image set contained 75 images spanning the wavelength range from 960 to 1700 nm in 10 nm increments. Acquisition time for the entire data set took approximately 90 seconds. In addition, the 1450 nm band was shown to be the only band that could be used to detect a change in hydration in the superficial layer of the skin, while the other two bands at 960 and 1200 nm accessible by the imaging system provided information on the deeper tissue (14). Therefore, the NIR images collected in our later studies were only taken across the most intense water band at seven preselected wavelengths (Rockland, Massachusetts, U.S.A.) The filters (Omega optical, Inc., Brattleboro Vermont, U.S.A.) had slightly wider width with a 10 nm FWHM (full width at half maximum). The preselected wavelengths were 1280, 1390, 1410, 1430, 1450, 1470, and 1620 nm. With these fixed wavelengths, another imaging system with a set of narrow band-pass filters was set up. It used an eight-position filter wheel assembly (Prior Scientific, Rockland, Massachusetts, U.S.A.) fitted with seven filters with the band centers at the above wavelengths. The filters (Omega Optical, Inc., Brattleboro, Vermont, U.S.A.) had slightly wider width with a 10 nm FWHM (full width at half maximum) and the blocking range of 925–1800 nm. The control software was modified to run the filter wheel and camera system. Both systems took approximately 12 seconds to collect the entire set of seven images using 10 or 15 individual 16.67 msec exposures summed for each of the seven wavelength images. A reference image set of a Kodak white or gray card was also taken using the same measurement parameters.

CLINICAL DESIGN AND EVALUATION METHODS

For all clinical studies, an informed consent was obtained from each subject and the study procedures were approved by Institutional Review Board prior to the start of the studies. Two different types of tests were conducted of the product effect on skin hydration, a forearm controlled application technique (FCAT) (20) and a six-hour time moisturization test (21). The FCAT procedure has been described elsewhere (20) and the results from our studies using FCAT are presented in this Chapter only to illustrate that the NIR imaging technique is a great tool to visualize the skin hydration and its change induced by skin products. Quantitative analysis of the study result will be presented elsewhere.

A six-hour time moisturization test of a single wash application was performed on the outer lower legs of female subjects. Before the start of the product application, all subjects entered a five-day in-home conditioning phase. They were asked to use a mild cleansing bar for all general cleansing. Subjects were also asked to refrain from using any other skin products (creams, lotions, moisturizers,

sunscreens, etc.) and washing appliances (sponge, wash cloth, loofah, etc.) on or near their lower legs. Upon completion of the conditioning phase, subjects continuing to meet the inclusion/exclusion criteria and having dryness scores of 1.0 to 2.0 and erythema scores of no greater than 2.0 (on the scale of 0 to 4) on their lower legs entered the six-hour time moisturization test.

Subjects had each of their outer lower leg divided and marked with a skin marker pen into three-test sites of approximately 6×7 cm (height \times width) each, as depicted in Figure 3. Six sites (upper, middle, and lower on both left and right legs) from each subject were randomized with four product treatments with an untreated control site on each leg. Study clinicians then performed a single application of 0.20 mL of a liquid cleanser to each test site for a 30 seconds wash, 15 seconds rinse, and pat-dry wash regime. For moisturizer, 0.20 mL was glove-rubbed into the test site until completely absorbed. A similar procedure was followed for the water application.

Visual and instrument evaluations were made a total of four times in the time moisturization studies, just prior to (baseline), and one, two and six hours postproduct treatments. Visual assessment of dryness and erythema was conducted by a trained expert grader. The test sites were each graded on the scale of 0 to 4 in 0.5 increments (9-point grading scale). The erythema grades were used for safety check only and no further analysis of the grades was made. Table 1 shows the grading scale for visual dryness. A reduction in dryness score means improved skin condition. After the visual grading, the subjects were climatized in a temperature ($21 \pm 1^\circ\text{C}$) and humidity ($38 \pm 5\%$ RH) controlled room for 20 minutes prior to the instrumental measurements.



FIGURE 3 The marking of the test sites. The leg was placed behind a window for near-infrared imaging; the white labels were placed in the gaps separating test sites prior to collecting images.

TABLE 1 Clinical Grading of Skin Dryness

Grade	Observations
0	No flakes
1	Slightly flaking/uplifting of flakes (patchy) and/or powdered appearance)
2	Moderate flaking/uplifting flakes (uniform) and/or slight scaling
3	Severe flaking/uplifting, uplifting of scales and/or slight fissuring
4	Severe scaling/uplifting scales with severe fissuring/cracking

Following the visual assessment, the images were taken of each leg with the leg placed behind a window, as depicted in Figure 3. There were four imaging sessions with two sets of images in each session—one from the left leg and one from the right leg. Conductance and capacitance measurements were also performed, but the data will not be used in this discussion.

HYDRATION IMAGES AND DATA ANALYSIS

The NIR image data were processed using in-house routines written in Matlab (The MathWorks, Natick, Massachusetts, U.S.A.). The first step in the processing sequence was to convert the raw reflection intensity data to optical density format. Further processes were all performed on the optical density data. The integrated O-H absorption intensity was calculated between the spectral points at 1280 and 1620 nm as the sum of the intensity values at the other five wavelengths near the band center around 1450 nm after removal of the spectral baseline. This was done for each pixel and as a result, an image of the O-H intensity was generated as a false color image, which is simply referred to as the hydration image. To visualize the change of the posttreatment hydration image from its baseline, a difference image was also generated for each subject at each posttreatment time point, following a procedure similar to that reported previously (12–14).

A rectangle area in the center of the test site was used to obtain the average pixel intensity, which is reported as the NIR score for the test site. The change-from-baseline (CFB) scores were obtained by subtracting the baseline NIR score from the scores of the postproduct application. A positive change means an increased water absorption and hence more hydrated skin, and vice versa.

Within-product and between-products comparisons were performed based on the changes (CFBs) in the visual dryness and NIR scores of the postproduct applications from their corresponding baseline values. Comparisons were made independently at each time point and no temporal correlation was taken into account. The Wilcoxon Signed Rank test (22) with the Pratt–Lehman adjustment (23) for ties was used for the nonparametric variables of the visual grades and *t*-test for the parametric variables of the instrumental measurements. Based on the study design, a level of 0.10 was chosen for the analysis of statistical significance. Statistical analysis was performed using JMP (version 5, SAS) and Clinskin, an SAS-based in-house data analysis package.

RESULTS AND DISCUSSION

Application I: Soap vs. Syndet Bars in a Forearm Controlled Application Technique Study

A sample forearm image is shown in Figure 4 from an FCAT study displaying the changes in skin hydration on day 5 from its baseline. Three test sites are marked in

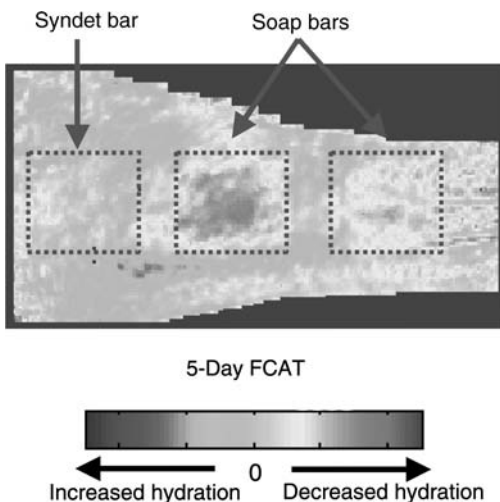


FIGURE 4 (See color insert) A forearm image from an FCAT study. The false color image represents the difference in water absorption intensity between post-application (after multiple applications) and its baseline. The squares, each approximately 4×4 cm, mark the test sites that were washed by cleansing bars as indicated. *Abbreviation:* FCAT, forearm controlled application technique.

square boxes, each approximately 4×4 cm². The test site closest to elbow (left site) was washed with a syndet bar. Its color scale indicates nearly unchanged skin hydration. The other two sites washed with two different soap-based bars showed a significant decrease in skin hydration at the endpoint of the study. This indicates that the syndet bar did not dry the skin as the soap-based bars did and the NIR image may provide a communication tool for consumer understanding of the mildness of a syndet bar.

Application II: Cleansers vs. Moisturizers in a Time Moisturization Study

Materials

Four products were used in this study: leave-on moisturizing cream, water (control), and two liquid cleansers (17). The liquid cleansers consisted of two main types of marketed liquid body washes, a traditional body wash (TBW)(low to no emollients), and a premium moisturizing body wash (MBW)(high level of emollients). Examples of the main ingredients from each liquid cleanser type are listed below.

Traditional Body Wash

- Water
- Sodium Laureth Sulfate
- Cocamidopropyl Betaine
- Sodium Lauryl Sulfate
- Fragrance
- Thickener salts
- Preservatives
- Color

Moisturizing Body Wash

- Water
- Sunflower Oil (emollient)
- Sodium Laureth Sulfate

- Cocamidopropyl Betaine
- Glycerin
- Petrolatum
- Foam Booster
- Fragrance
- Thickeners salts
- Preservatives

Visualizing Changes in Skin Hydration

Fourteen subjects completed the six-hour time-moisturization study. Sample hydration images are shown in Figure 5 for subject 6, left leg and 8, right leg. These false color images represent the changes in skin hydration on the same leg from their baseline to one-hour (top panels) and six-hour (bottom panels) postproduct applications, respectively.

For subject 6 (left leg on the left panels), both TBW and MBW treated sites exhibited a slightly increased hydration level compared to the untreated (middle site) at one-hour postapplication. At six-hour postapplication, the TBW site became clearly drier than the control site, while the MBW site maintained the level of hydration similar to that of the control site. For subject 8 (right leg on the right panels), the one-hour posttreatment image clearly indicates increased water content in both moisturizing cream treated site (left site) and MBW treated site (right site), compared to the control site in the middle. However, the increased water content at the MBW site disappeared mostly by six hours after treatment, while the cream site still maintained a significant level of increased water content, although reduced from the one-hour level. This is expected because the moisturizing cream is a leave-on product that usually provides a longer-lasting benefit than a wash-off product (MBW, a cleanser).

Differentiating Product Performance

The average responses over all subjects ($N = 14$) from visual evaluation and NIR imaging are compared in Figure 6. The error bar indicates the standard error of the mean (SEM). The mean differences of the dryness scores in Figure 6A are provided for descriptive purposes.

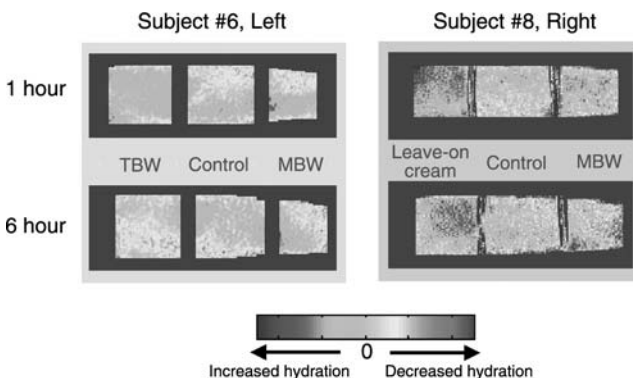
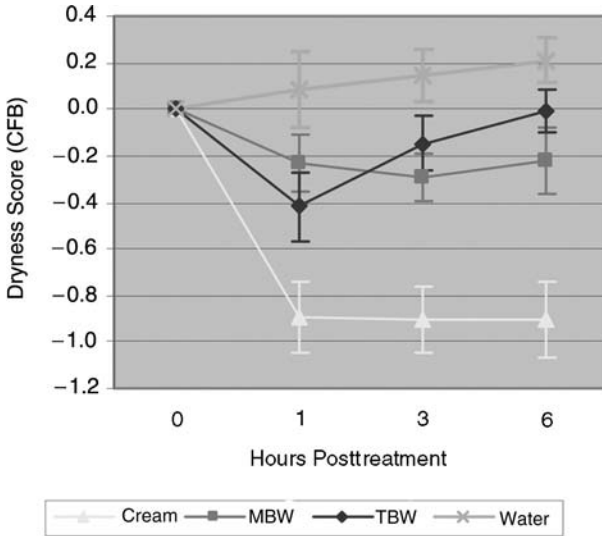
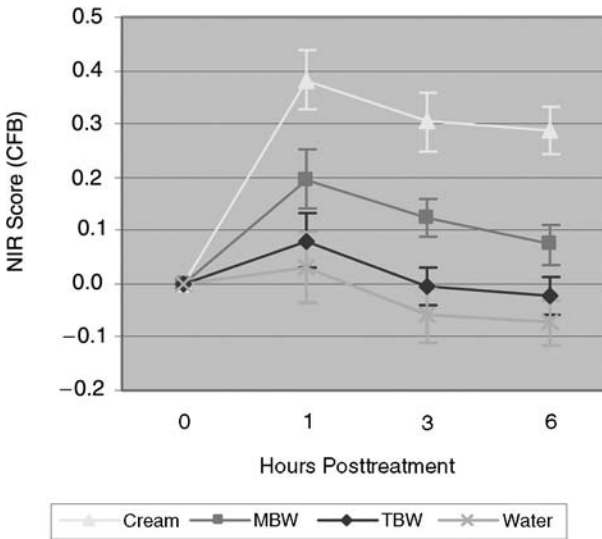


FIGURE 5 (See color insert) Leg images from a time moisturization study. The knee is on the left end and ankle on the right end of the image. The false color image represents the difference in water absorption intensity between postapplication and its baseline for the time points as indicated. *Abbreviations:* TBW, traditional body wash; MBW, moisturizing body wash.



(A)



(B)

FIGURE 6 Time responses of the skin condition as measured by (A) visual evaluation of dryness and (B) near-infrared imaging of water absorption. The error bars indicate \pm SEM. Four products (see text for details) were tested in this study—cream, a moisturizer; MBW, a cleanser; TBW, also a cleanser; and water. *Abbreviations:* SEM, standard error of the mean; MBW, moisturizing body wash; TBW, traditional body wash; NIR, near-infrared; CFB, change-from-baseline.

Both evaluation methods detected changes in skin hydration upon product application and indicated a significantly positive hydration benefit provided by the moisturizing cream. For MBW the visual evaluation (Fig. 6A) showed reduced skin dryness, i.e., improved skin hydration. For TBW, reduced dryness was

detected at one-hour and the effect diminished to the baseline at six-hour. The result obtained by the NIR imaging (Fig. 6B) is very similar. A positive benefit was detected for MBW. For TBW and water, the NIR method indicated little change from the baseline, although there seemed to be a reduced skin hydration as time progressed. This is consistent with the visual grades of skin dryness.

For between-product comparison, both evaluation methods separated the moisturizing cream into its own class with statistical significance. The expert evaluation of dryness also separated water from the cleansers, but only showed an insignificant difference between MBW and TBW. The NIR method placed TBW and water in the same category and separated MBW by itself at the three and six-hour time-points all with statistical significance. The combined measures indicate a moisturizing effect from MBW that may last for hours, albeit it was not as great as the moisturizer. TBW did not dry the skin and in fact, may provide a short-term (approximately one hour) positive benefit. Water seemed to slightly dry the skin, which might be due to water leaching away some of skin's natural moisturizers.

In summary, the NIR imaging technique was able to separate the effect of a moisturizer from that of cleansers. Its evaluation of product performance is consistent with expert grading of skin dryness. It also provides a tool to visualize skin hydration and its changes induced by product use that can aid in assessing consumer perception and preference for the development of new moisturization technologies.

Application III: Various Liquid Cleansers in a Time Moisturization Study

Materials

The four products included in the study (18) fall into the following categories of marketed liquid cleansers. A is a low foaming emollient body wash containing water, cetyl alcohol, propylene glycol, sodium lauryl sulfate, stearyl alcohol, and preservatives. B is a facial cleansing liquid containing water, polyethylene glycol (PEG)-200 hydrogenated glyceryl palmate and PEG-7 glyceryl cocoate, sodium laureth sarcosinate, glycerin, sodium laureth sulfate and preservatives. C is a foaming facial cleanser containing water, glycerin, sodium myristyl sarcosinate, PEG-120 methyl glucose dioleate, sodium lauroamphoacetate, tocopheryl acetate, PEG-150 pentaerythrityl tetrastearate, polyquaternium-10, glycol distearate, sodium laureth sulfate, cocamide mea, laureth-10, disodium lauroamphodiacetate, sodium trideceth sulfate and preservatives. D is a nonfoaming facial cleanser lotion containing water, petrolatum, stearic acid, mineral oil, glycol stearate, fragrance, thickener salts, and preservatives.

Differentiating Product Performance

Twelve subjects completed this six-hour time moisturization study. Among the four liquid products, B and D were shown to be statistically different by both visual dryness and the NIR imaging. The other two products (A and C) are ranked in between B and D and their differences from B and D are statistically insignificant. Figure 7 summarizes the average responses of the products over all test subjects from the visual evaluation and NIR imaging. For clarity, products A

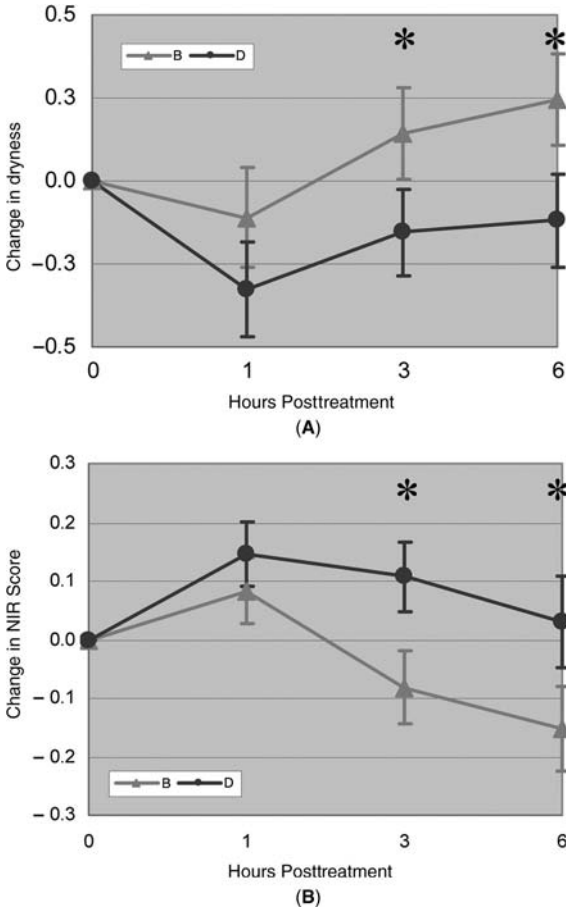


FIGURE 7 Time responses of the skin condition as measured by (A) visual evaluation of dryness and (B) NIR imaging of water absorption. The error bars indicate \pm SEM. Four products were tested in this study. Products A and C are between B and D on the graphs and for clarity, not plotted. An asterisk indicates a statistical significance between the products at the given time-point. *Abbreviations:* SEM, standard error of the mean; NIR, near-infrared.

and C are omitted from the figure. It is clear that similar trends are observed between the visual dryness and the NIR method. Both products B and D showed a moisturizing effect within one hour of product application and such a positive effect is significant for product D by either visual dryness (A) or NIR (B). At the later hours, the skin treated with product D continued to show the moisturizing effect, although the effect is statistically significant only at hour three as measured by NIR. At the same time, the skin treated with product B showed an increased dryness (Fig. 7A) and reduced NIR absorption (Fig. 7B) and these changes became significant at hour 6 as measured by either of these two techniques.

A further comparison of the NIR imaging and the visual grading results can be made through their correlation. As stated earlier, the nonparametric treatment was usually applied to the visual grades, while the parametric treatment was applied to the instrumental data. However, it is also within common practice to use parametric methods for the grading data with 9-point ordinal scales. Therefore, the mean values from the visual grades are used for a correlation analysis with the instrumental data.

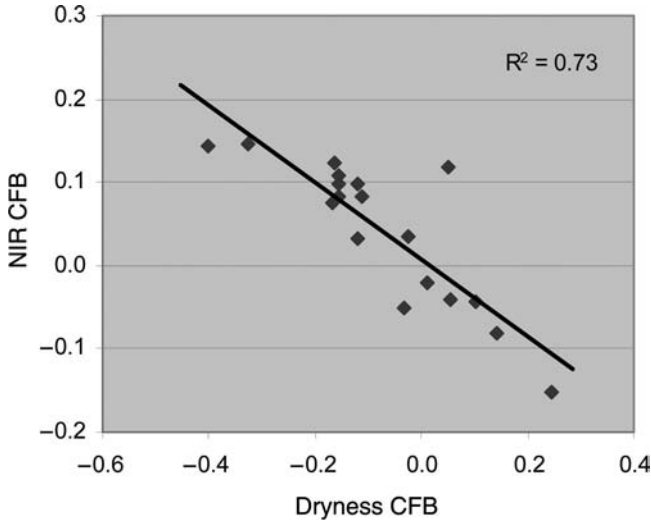


FIGURE 8 The correlation between the NIR imaging of water absorption and visual assessment of skin dryness. Plotted values are the mean responses for all six sites and at three time-points postproduct application. The solid straight-line was fitted with all the data. *Abbreviations:* NIR, near-infrared; CFB, change-from-baseline.

Figure 8 shows the correlation of the CFBs between the visual dryness and the NIR scores. A total of 18 mean values are plotted representing six treatments (four products and two untreated sites) at three time-points postproduct application. A linear fit performed on the data gave $R^2 = 0.73$ across both positive and negative changes around the baseline. This indicates a strong correlation between these two evaluation methods. It should be pointed out that the correlation presented here is not intended as predictive of one measure from the other. It does, however, show the visual grading and NIR imaging measure hydration related properties of the skin in a similar way, which may not be true between other measures of skin hydration such as the electrical properties and visual dryness of the skin (17,18).

In summary, the NIR technique was able to discriminate changes in skin hydration induced by different moisturizing cleansers in a way similar to the visual assessment of skin dryness, indicating a high relevance of the imaging tool to the visual appearance of the skin.

CONCLUSION

The novel NIR imaging method has been recently developed for measuring skin hydration through direct imaging of water in skin. It is rapid, noncontact and non-invasive. The utility for measuring skin hydration levels and differentiating product performance has been demonstrated with several types of skin cleansing and care products. A large positive hydration change upon treatment by a moisturizing cream can be easily detected by the imaging technique. It can also differentiate products whose effects on skin hydration are not as great as that from a moisturizing cream, which is typically observed for moisturizing cleansers.

A comparison of the NIR imaging technique with the visual assessment of skin dryness reveals that they measure the skin hydration-related property in a similar way and their results are strongly correlated. In addition, the imaging technique is a great tool to visualize the hydration difference contrasted between the neighboring test sites induced by different products or between time responses.

ACKNOWLEDGMENT

The author would like to acknowledge the following current and former Unilever colleagues for conducting the clinical studies used in this Chapter and their support in the development of the imaging technique: Ms. B. Eursken, Mr. T. Hancewicz, Dr. S. Hawkins, Dr. P. Kaplan, Dr. F. Meyer, Ms. C.L. Meyers, Mr. D. Palatini, Dr. K. Subramanyan and Dr. R. Velthuisen.

REFERENCES

1. Rawlings AV, Harding CR. Moisturization and skin barrier function. *Dermatol Ther* 2004; 17:43–48.
2. Rawlings AV, Harding CR, Watkinson A, Scott I. In: Leyden JJ, Rawlings AV, eds. *Skin Moisturization*. New York: Marcel Dekker Inc., 2002:19–143.
3. Tagami H. In: Serup J, Jemec GBE, eds. *Handbook of Non-Invasive Methods and the Skin*. Boca Raton: CRC Press Inc., 1995:159–164.
4. Barel AO, Clarys P, Serup J, Jemec GBE, eds. *Handbook of Non-Invasive Methods and the Skin*. Boca Raton: CRC Press Inc., 1995:165–170.
5. Berardesca E. EEMCO guidance for the assessment of stratum corneum hydration: electrical methods. *Skin Res Technol* 1997; 3:126–132.
6. Li F, Conroy E, Visscher M, Wickett RR. The ability of electrical measurements to predict skin moisturization. I. Effects of NaCl and glycerin on short-term measurements. *J Cosmet Sci* 2001; 52(1):13–22.
7. Walling PL, Dabney JM. Moisture in skin by near-infrared reflectance spectroscopy. *J Soc Cosmet Chem* 1989; 40:151–171.
8. Martin K. Direct measurement of moisture in skin by NIR spectroscopy. *J Soc Cosmet Chem* 1993; 44:249–261.
9. de Rigo J, Losch MJ, Bazin C, et al. Near-infrared spectroscopy: a new approach to the characterization of dry skin. *J Soc Cosmet Chem* 1993; 44:197–209.
10. Wiechers JW, Snieder M, Dekker NAG, Hansen WG. Factors influencing skin moisturization signal using near infrared spectroscopy. *Proceedings of 22nd IFSCC Congress*, 2002.
11. Martin K. In vivo measurements of water in skin by near-infrared reflectance. *Appl Spectrosc* 1998; 52:1001–1007.
12. Attas M, Posthumus T, Schattka B, Sowa M, Mantsch H, Zhang SL. Skin hydration imaging using a long-wavelength near infrared digital camera. In: Bearman GH, Bornhop DJ, Levenson RM, eds. *Proceedings of SPIE* 2001; 425:75–84.
13. Attas EM, Sowa MG, Posthumus TB, Schattka BJ, Mantsch HH, Zhang SL. Skin hydration by spectroscopic imaging using multiple near-infrared bands. In: Mahadevan-Jansen A, Mantsch HH, Puppels GJ, eds. *Proceedings of SPIE* 2002; 4614:79–88.
14. Attas EM, Sowa MG, Posthumus TB, Schattka BJ, Mantsch HH, Zhang SL. Near-IR spectroscopic imaging for skin hydration: the long and the short of it. *Biopolymers (Biospectroscopy)* 2002; 67:96–106.
15. Attas EM, Sowa MG, Posthumus TB, Schattka BJ, Mantsch HH, Zhang SL. Skin hydration images from near-infrared reflectance spectra. *Am Clin Lab J Mol Diagn* 2002; 21(8):32–36.
16. Attas M, Posthumus T, Schattka B, Sowa M, Mantsch H, Zhang SL. Long-wavelength near-infrared spectroscopic imaging for in-vivo skin hydration measurements. *Vibrational Spectrosc* 2002; 28:37–43.

17. Zhang SL, Meyers CL, Subramanyan K, Hancewicz TM. Near infrared imaging for measuring and visualizing skin hydration. A comparison with visual assessment and electrical methods. *J Biomed Opt* 2005; 10(3):31–107.
18. Zhang SL, Meyers CL, Subramanyan K. Near-Infrared Imaging. A better approach to measure and visualize skin hydration and to assess the mildness of skin cleansers. Proceedings of IFSCC (International Federation of Society of Cosmetic Chemistry) Congress 2004, Orlando, Florida, USA, 209.
19. Caspers PJ, Lucassen GW, Carter EA, Bruining HA, Puppels GJ. In vivo confocal Raman microspectroscopy of the skin: noninvasive determination of molecular concentration profiles. *J Invest Dermatol* 2001; 116:434–442.
20. Ertel KD, Keswick BH, Bryant PB. A forearm controlled application technique for estimating the relative mildness of personal cleansing products. *J Soc Cosmet Chem* 1995; 46:67–76.
21. Patrick E, Tallman DM. Studies Exploring Moisturization Potential of Personal Wash Products. American Academy of Dermatology, Academy Meeting, Chicago, IL, Jul 31–Aug 4, 1998.
22. Lehmann EL. *Nonparametrics: Statistical Methods Based on Ranks* (Holden-Day, 1975).
23. Pratt JW. Remarks on zeros and ties in the Wilcoxon signed-rank procedures. *J Am Stat Assoc* 1959; 544:655.

Claudia Rona*Department of Dermatology, University of Pavia, Pavia, Italy***Enzo Berardesca***San Gallicano Dermatological Institute, Rome, Italy***INTRODUCTION**

Cellulite (local lipodystrophy) represents a very common skin condition among women; the main clinical feature of this process being the appearance of “orange peel” skin in the affected areas (1–3).

The target of cellulite is firstly a subcutaneous compartment, which develops an altered blood and lymphatic microcirculation. As secondary events, accumulation of fat material and fibrotic changes occur.

Cellulite represents the most common lipodystrophic disease, which differs from diffuse adiposity, because it develops just in limited areas such as abdomen, buttocks, trochanteric and perimalleolar area, anterior, posterior, medial, and lateral thigh and knee (2).

Clinically it can be graded as follows (1,4):

- 0 = no cellulite
- 1 = slight dimpling of skin surface
- 2 = dimpling and skin depressions
- 3 = dimpling and depressed striation
- 4 = palpable nodules and depressed striations

CELLULITIC SKIN FEATURES

There are some features, partly subjective, partly objective, which are very often reported, and so are quite peculiar. In particular, we can list both subjective symptoms (reported by patients), and objective features (reported by investigators) as follows:

1. Symptoms more frequently reported by patients:
 - Heaviness and tension at lower limbs
 - Cold feet
 - Nightly cramps
 - Paresthesias
 - Pain, rarely spontaneous, generally induced by trauma, even slight
2. Objective features more frequently reported by investigators:
 - Diffuse (orange peel) and local (mattress peel) unevenness
 - Stretched marks
 - Cutaneous color changes (dischromic or hyperpigmented skin)

Clinical examination often reveals venous stasis and insufficiency at lower limbs on the basis of perimalleolar edema, telangiectasia and/or microvaricosity, varices, and cutaneous trophic alterations.

Other peculiarities can be appreciated, such as:

- Lack of elasticity
- Increase of skin pliability
- Fine texture
- Micronodules and, easier to remark, macronodules, often painful at palpation

CELLULITE STAGES

Cellulite develops through progressive stages (4):

Precellulite conditions: Skin appears smooth and firm; ultrasounds show a thick dermis, with minimal fluids retention; there is neither accumulation of linked collagen fibres nor elastin nodules. Adipocytes have regular diameter, and are not yet engorged with lipids. No fatty deposits seem to protrude into the dermis. A thick blood and lymphatic vessels network supplies subcutaneous tissue of nourishment and oxygen, removing toxins and discarding elements.

Stage I: Occurs at a deep cellular layer without cosmetic implications. Vessels walls become so permeable that they induce loss of fluids into the spaces between adipocytes (edema), making the fatty layer to swell. Adipocytes become engorged with lipids, they are bigger and clump together. Furthermore, deranged lymphatic circulation makes it difficult to remove fluids that accumulate and promote edema. At this stage, probably hormones play an important role. Many hypotheses have been proposed as regards to the causes of this metabolic alteration (involving changes of the levels of cyclic adenosine monophosphate (cAMP) and Protein kinase C), but not satisfactory explanation has been provided (5,6).

Stage II: Dermal and subdermal involvement is much more marked. Adipocytes clumping together and collagen fibres linkage hamper blood circulation and cause homeostasis: all these events happen heterogeneously, so areas with a good microcirculation are near to severely damaged ones. Accumulation of fluids increases the heterogeneity of the subdermal region, and the orange peel appearance becomes evident, because of the thinning of epidermis and dermis.

Stage III: The vascular impairment has more marked effects on dermis giving rise to its metabolic alteration and thinning, due to the reduction in protein synthesis and the recovering processes. Adipocytes, cut off from supply and toxin removing events, clump together, constituting micronodules surrounded by a thick and hard collagen layer and fatty masses. Skin palpation shows clearly orange peel phenomenon.

Stage IV: Micronodules clump together to form hard macronodules in dermal layer, whose dimensions range from 2 to 20 mm. Subjects often feel pain or trouble at this stage, because nerves can be compressed by nodules in involved areas (2).

Later stages are irreversible and refractory to any cosmetic treatment.

PATHOGENESIS

The pathogenesis of cellulite onset is still unknown. It results from blood and lymphatic microcirculation damage, which gives rise to structural changes in fatty layer and surrounding collagen matrix. In particular, superficial microcirculation

appears to be less efficient, and this results in subcutaneous edema due to altered permeability of blood vessels; this condition can induce sclerosis, and a reduced replacement of collagen fibres. An impaired trophic reaction of adipocytes to endocrine and/or neuroendocrine stimuli, associated with edema, vascular, and fibrotic damage can also be present (7).

An increased accumulation of some unmetabolized compounds such as sugars, lipids, and proteins can lead to the synthesis and accumulation of triglycerides in adipocytes. Therefore, there clearly seems to be a deranged lipolytic process in the onset of cellulite. Lipolysis is partially controlled by nerves: the beta-adrenergic receptors activation or the alpha2-adrenergic receptors blockage promote lipolysis; in particular, beta-adrenergic stimulation leads to an increase of AMPc intracellular levels due to an antiphosphodiesterase action; AMPc promotes the hydrolytic degradation of lipids, whereas alpha2-adrenergic receptors stimulation results in a reduction of AMPc intracellular levels, with consequent inhibition of lipids release and therefore degradation (3). Cellulite is more marked in specific anatomical sites (thighs and buttocks in women) because of the presence of adrenergic receptors in these sites. Clinically, cellulite is more evident in women, because of the particular structure of the subcutaneous tissue (so-called "mattress-like") at the interface between dermis and hypodermis, with small parallel collagen bands, which link the dermis to the hypodermis giving rise to the "orange peel" appearance when deformed by lipid accumulation.

NONINVASIVE TECHNIQUES TO EVALUATE CELLULITE

The variety of anticellulite products and professional (surgical or not) approaches to treat cellulite is quite huge: ranging from topical products to oral regimens, from manual or mechanical massages to garments, among which the most recent is made up by copper and zinc fibres (Rona C, Mosca M. Medical-scientific aspects of methallotherapy, 2003, Unpublished data), which exerts a mild, continuous, and quite effective electromagnetic current; we can find out many strategies to afford such a condition, a borderline one with pathology.

However, all of those systems are aimed to stimulate the impaired blood and lymphatic circulation. In general, the efficacy of cellulite treatments is often debated and objective studies are needed for claim support. Furthermore, cellulite is very difficult to investigate by bioengineering methods. The main noninvasive techniques helpful in monitoring some physical parameters related to the cellulite condition are discussed in the following sections.

Tight Circumference Measurements

The easiest among the others, this traditional measure indicates the reduction of thigh circumference, due to both the reduction of edema, and the effect on the fatty layer.

It is recorded on hips, ankles, and thighs as follows:

1. Hip: The tape-measure is positioned around the hips, putting it finally on the super-anterior iliac crest.
2. Thigh: The tape-measure is placed around the thigh, marking the site of interest.
3. Ankle: The tape-measure is placed around the ankle, exactly above the malleolar bone (4).

Ultrasonography

Ultrasound is used to study the thickness and the quality of the connective tissue, and the edematous component of cellulite. When an ultrasound beam goes through differently structured portions of a tissue, it generates an echo according to the acoustic properties of the regions under examination; the echoes produce an electrical signal in the transducer, which is shown as an amplitude on an oscilloscope (A-mode). In B-mode scanning, the transducer is automatically moved tangentially over the skin surface and a number of A-scans are depicted and processed electronically, resulting in a cross-sectional image of the skin in two dimensions. Frequencies between 10 and 15 MHz should be chosen for skin examination. With higher frequencies, it becomes more difficult to view in depth. To calculate the total skin thickness, the time elapsed between the first echo (the interface between the sensor and the skin surface) and the second high amplitude echo (interface between dermis and hypodermis) is measured. Thickness of measured tissue equals transit time of the ultrasound through the skin by normal speed of ultrasound in the skin (1540 m/sec) (8).

Laser Doppler Flussimetry

Laser doppler flussimetry is an optical technique used to evaluate skin microcirculation, which provides information on blood flow and erythema. The method consists of a Ne-He laser source of 632 nm wavelength applied to the skin via a small probe. The incident radiation enters the skin and is scattered and reflected by nonmoving tissue components and by mobile red blood cells encountered as the radiation penetrates to a depth of 1 to 1.5 mm. A portion of the scattered and reflected incident radiation exits the skin and is collected by a second optical fibre that carries the light back to a photodetector where it is converted to an electrical signal. Stationary skin tissue reflects and backscatters light at the same frequency as the incident source, while moving erythrocytes reflect the frequency-shifted radiation. The shift increases with increasing erythrocytes speed. The Laser Doppler Flowmetry (LDF) extracts the frequency-shifted signal and derives an output proportional to the flux of erythrocytes of the blood flow. LDF is a reliable method to estimate cutaneous microcirculation (9).

Thermography

Anticellulite products are meant to increase local skin blood flow. By increasing the blood flow, they increase the local skin temperature. Thermography is an electro-optical method for the imaging of temperature. The current technology used is based on the detection of the infrared radiation emitted by the skin. A conventional color thermogram uses a spectral color range, where blue is cold, and red–white is hot. Intermediary temperatures are shown as shades of green, yellow, orange, etc . . . (10).

Mechanical Properties

Bioengineering devices for the assessment of the mechanical skin parameters differ greatly with regard to the physical principle behind the measurement. Devices based on tension, suction, torsion, and vibration have been developed and used. Each particular approach has its own advantages and disadvantages. Anyhow, determination of skin distensibility, elasticity, and hysteresis, has been quite standardized (at least in suction and torsion devices), and is currently used in quantification of cosmetic efficacy (11).

Plicometry

The technique implies the use of the Plicometer, a device which allows to evaluate the thickness of cutaneous plicae or folds, from which it is possible to calculate the fat percentage in human body. The measurement is usually performed on the thigh, on a defined point, which can be determined by measuring the half distance between the iliac crest and the center of the knee as reference points. During measurements, the leg is relaxed. All measurements are performed in standard conditions, which guarantee reliability and suitability of collected data. In particular:

- measurements are performed on dry skin;
- the subject has to maintain the leg as relaxed as possible;
- measurements are performed always on the same site, and each measurement is repeated twice for each data point;
- the exact measuring point (*reper point*) is set by using a tape measure;
- plicae are obtained by catching tissues between thumb and forefinger, and gently pulling a little outside; and
- the Plicometer has to be put on the precise point to be measured perpendicularly to the skin and 1 cm away from the fingers keeping the plica.

Magnetic Resonance Microimaging

Amongst *in vivo* skin imaging methods, magnetic resonance (MR) imaging (12) is the most recent approach, being of high interest not only for its ability to distinguish structures at a submillimeter scale, but also for its ability to describe the physiology of the different skin layers through the measurement of their intrinsic MR parameters. High spatial resolution MR imaging allows to differentiate the different skin departments: epidermis, dermis, and hypodermis, giving new and interesting opportunities for the evaluation of anticellulite treatments. Actually, some authors (13) found that changes in skin architecture with cellulite can be well visualized by that method, pointing out clearly in the images the skin fat layers beneath the dermis and down to the level of muscles. Also, the diffuse pattern of extrusion of underlying adipose tissue into dermis is clearly imaged, and was found to correlate with cellulite grading.

In turn, other researchers (14) applying such a technique characterized the topography of the dermo-hypodermal junction, and the three-dimensional (3D) architecture of the subcutaneous fibrous septae, giving as more clear frame of skin condition in areas affected by cellulite. In association with MR microimaging, the same team measured water and lipid fractions within a fat lobule, and T1 and T2 values of the detected compounds. All these data were analyzed according to sex and presence of cellulite by using proton spectroscopy. Authors showed that MR imaging allows to quantify deeper indentations of adipose tissue into the dermis, and evidenced a great increase in the thickness of the inner fat layer in women with cellulite. Moreover, 3D reconstruction of the fibrous septae network showed a higher percentage of septae in a direction perpendicular to the skin surface in women with cellulite; but their study also draw the tortuous aspect of this network. This trial gives evidence about the possibility to show by MR imaging that the 3D architecture of fibrous septae allowing, moreover, to confutate the hypothesis of increased water content in the adipose tissue of women affected by cellulite, as suggested by others, but if such water would be located in the connective septae.

CONCLUSIONS

In conclusion, the study shows that effective treatment of cellulite can be achieved and assessed. Ultrasound is the most reliable technique to assess skin thickness as to subcutaneous department, and the amount of fat deposits at the interface between dermis and hypodermis. Laser Doppler velocimetry can give a good estimate of the improvement in skin microcirculation. The improvement in skin condition of the placebo-treated sites is mainly due to massage subsequential to product application. It is known that massage can play an important role in modifying some physical properties of the skin, resulting in a lower degree of cellulite (Rona C, Mosca M. Medical-scientific aspects of methallotherapy, 2003, Unpublished data). Changes in other biophysical parameters, such as mechanical properties, have a minor importance in this condition and are less recommended. Furthermore, the study shows that the improvement of skin microcirculation with topically applied diosmin in lesional skin associated with other compounds are capable to reduce fluid retention, and can be helpful in controlling cellulite.

REFERENCES

1. Curri SB, Ryan TJ. Panniculopathy and fibrosclerosis of the female breast and thigh. In: Ryan TJ, Curri SB, eds. *Cutaneous Adipose Tissue*. Philadelphia: Lippincott, 1989:107–119.
2. Curri SB, Bombardelli E. Local lipodistrophy and districtal microcirculation. *Cosmet Toilet* 1994; 109:51–65.
3. Di Salvo RM. Controlling the appearance of cellulite. *Cosmet Toilet* 1995; 110:50–59.
4. Smith PW. Cellulite treatments: snake oils or skin science. *Cosmet Toilet* 1995; 110:61–70.
5. Gasparro V, Vettorello GF. Treating cellulite. *Cosmet Toilet* 1992; 107:64–66.
6. Vague J, Fenasse R. Comparative anatomy of adipose tissue. In: *Handbook of Physiology*, Washington DC, American Physiology Society, 1965:25–35.
7. Curri SB. Inquadramento nosografico e classificazione delle pannicolopatie da stasi. *Flebologia* 1990; 1:15–19.
8. Serup J. Skin imaging techniques. In: *Bioengineering and the Skin: Methods and Instrumentation*. Boca Raton: CRC Press, 1995:65–79.
9. Bernardi L, Berardesca E. Measurements of skin blood flow by laser doppler flowmetry. In: *Bioengineering and the Skin: Methods and Instrumentation*. Boca Raton: CRC Press, 1995:13–28.
10. Sherman RA, Woerman AL, Arstetter KW. Comparative effectiveness of videothermography, contact thermography, and infrared beam thermography for scanning relative skin temperature. *J Rehabil Res Dev* 1996; 33:377–386.
11. Elsner P. Skin elasticity. In: *Bioengineering and the Skin: Methods and Instrumentation*. Boca Raton: CRC Press, 1995:53–64.
12. Querleux B. Magnetic resonance imaging and spectroscopy of skin and subcutis. *J Cosmet Dermat* 2004; 3(3):156.
13. Mirrashed F, Sharp JC, Krause V, Morgan J, et al. Pilot study of dermal and subcutaneous fat structures by MRI in individuals who differ in gender, BMI and cellulite grading. *Skin Res Technol* 2004; 10(3):161–168.
14. Querleux B, Cornillon C, Jolivet O, et al. Anatomy and physiology of subcutaneous adipose tissue by in vivo magnetic resonance imaging and spectroscopy: relationships with sex and presence of cellulite. *Skin Res Technol* 2002; 8(2):118–124.

Digital Imaging as an Effective Means of Recording and Measuring the Visual Signs of Skin Aging

Paul J. Matts

Procter & Gamble, Rusham Park Technical Centre, Egham, Surrey, U.K.

Kukizo Miyamoto

Department of Dermatology, School of Medicine, The University of Tokushima, Kuramoto-cho, Tokushima, and Research and Development, Personal Beauty Care, Tokushima, and Procter & Gamble Company, Higashinada-Ku, Kobe, Japan, and Procter & Gamble Company, Cincinnati, Ohio, U.S.A.

Greg G. Hillebrand

Procter & Gamble Company, Higashinada-Ku, Kobe, Japan, and Procter & Gamble Company, Cincinnati, Ohio, U.S.A.

INTRODUCTION

When Fox Talbot acquired the very first permanent photographic images of living objects in 1835 using a camera obscura and simple silver chemistry, a new era was ushered in, allowing the first faithful capture of permanent records of appearance. Up to this point in time, human skin appearance had been recorded by the artist and lithographer, subjectively interpreting and translating into solid media their perception of the subject on hand. The “photograph” (literally “a written record of light,” from the Greek “φωτος” meaning “light” and the Greek suffix “graph” denoting a transcribed record), however, was revolutionary—suddenly, life-like images reminiscent of human vision itself were being captured and printed within a few hours. This seeming miraculous advance was possible, of course, because a device was now being used that was derived from the optical principles of human vision itself—a lens apparatus to focus incident radiation and a photo-reactive array (i.e., the light-sensitive cells of the human retina), with a response spanning the 400 to 700 nm bandwidth. The advent of this new technology not only revolutionized the world of art, but also provided the clinician with the first truly objective means of recording the appearance of human biology. Within 40 years of the first Talbot photographs, the camera was being used to faithfully record the anatomy of normal and diseased skin and, in 1883, the definitive anatomy text, “Gray’s Anatomy,” contained clinical photographs for the first time.

By the 1960s, although huge advances had been made in film emulsion sensitivity and resolution, the original chemistry first used by Talbot had, in fact, hardly changed. In 1969, however, there was a renaissance in photography when George Smith and Willard Boyle at Bell Laboratories invented the charge-coupled device (CCD), as a new means of storing large amounts of computer data. It soon became apparent, that the CCD could be used for imaging. The device they invented stored data, represented by discrete packets of electrical charge, in arrays of closely spaced semiconductor capacitors. This array of capacitors could be formed into a regular

arrangement of picture elements (or “pixels”) such that incident radiation with wavelengths complementary to their response function would form a two-dimensional record of the objects from which the radiation was reflected/remitted. By 1970, the Bell Laboratories’ researchers had built the CCD into the world’s first solid-state video camera and, as the technology became more refined, it became rapidly apparent that this new imaging method offered considerable potential advantages over traditional film photography. These included the following:

1. Excellent quantum efficiency, giving superb sensitivity to low-intensity light without loss of resolution
2. Instant access to the image, allowing real-time quality control
3. Potential black/white and color calibration, allowing full confidence in image stability, even in studies spanning months or years
4. A truly stable permanent record (in contrast with the inevitable degradation of celluloid film stock and prints over time)
5. The effective elimination of unavoidable variation in the development process and celluloid film specification

This chapter concentrates on the use of standardized digital imaging in faithfully recording the appearance of skin as it changes in response to the intrinsic/extrinsic aging processes and treatment effects.

FIRST PRINCIPLES: UNDERSTANDING THE INTERACTION OF LIGHT WITH AGING SKIN

If the human eye and the modern digital camera both respond in a similar fashion to a narrow bandwidth of the electromagnetic spectrum (so-called “visible light,” a nominal 400–700 nm), the interaction of these wavelengths with skin, therefore, is of utmost importance in (i) our understanding of the way we perceive others and are ourselves perceived and (ii) designing the best imaging systems for this substrate.

A modern understanding of cutaneous optics is based largely on the development of increasingly sophisticated mathematical models to explain the interaction of light with skin. Such models, dating back as far as 1931 [for the multilayered models derived by Kubelka and Munk (1–3)], indicate a mechanism of light transport within the skin that may be summarized very briefly as follows (4–12).

Incident light at normal to the surface of healthy skin will always have a regular reflectance of between 4% and 8% (subject to the Fresnel equations). In other words, 92% to 96% of normally incident visible light will enter the surface of the stratum corneum where it is both diffused and subject to strong forward scatter with virtually no spectral modification (although this percentage transmission will reduce considerably when the stratum corneum is dehydrated). The ultrastructure of the viable epidermis also promotes forward scatter, with some specific absorption of short-wave ultraviolet (UV) and visible light by eumelanin/pheomelanin chromophores within keratinocyte-bound melanosomes and melanin “dust.” The modified light enters the papillary dermis, where it experiences intense back scattering (i.e., it is directed strongly back toward the skin surface) due to interaction with the very fine fibrillar structure of collagen in this layer (diameter of an order of magnitude less than incident visible light) and this protein’s well-known birefringent optical properties. Light back scattered from within this structure is also highly spectrally modified due to absorption by oxygenated and reduced hemoglobin (and some small contribution from other blood-borne chromophores

such as bilirubin and β -carotene) within the dermal vasculature. Due to the considerably larger fibrillar nature of collagen in the underlying reticular dermis, the small amount of light reaching this structure is forward scattered to be lost within the body, and does not contribute to the spectrum remitted from the skin. Light ejected from the papillary dermis, therefore, experiences a second forward scatter (toward the surface) and absorption in the viable epidermis and stratum corneum and is finally remitted from the skin surface. The integration of reflection and backward scatter from all cutaneous layers reaches our trichromatic retinae combining the red, green, and blue (RGB) registrations in an ordered array, to form a perceived red-yellow hue within our visual cortex, which we interpret as "flesh" tone with associated textural detail.

While it is noted above that β -carotene and bilirubin have quite distinctive absorption spectra in the visible waveband, the blood molar concentrations of these chromophores in normal, healthy subjects are so low that they provide negligible contribution to skin color. If this is so, therefore, it can be seen from the model presented above that human skin coloration is driven overwhelmingly by only three components, that is, absorption (and associated spectral modification) by the melanin and hemoglobin chromophores, and subsurface scattering by collagen. It follows, therefore, that the incredible kaleidoscope of both inter- and intraindividual skin coloration is derived solely from unique blends of these three optical components. The final optical component of the skin system is stratum corneum surface topography. Understanding how the expression and presentation of this topography and these molecules change with age, therefore, is critical in truly understanding the changing appearance of skin across a human lifetime.

CHANGES IN THE EXPRESSION AND PRESENTATION OF MELANIN, HEMOGLOBIN, COLLAGEN, AND IN SURFACE TOPOGRAPHY WITH AGE

Melanin

The melanin chromophore is expressed in discreet organelles, "melanosomes." These 1 μ m membrane-bound bodies are assembled within the epidermal melanocytes. When mature, they are transported along melanocyte dendritic processes via intracellular cytoplasmic filaments. The tip of the melanocyte dendrite becomes embedded within the cytoplasm of a neighboring keratinocyte and the end is pinched off. A package of melanosomes is, thus, donated to the keratinocyte (that acts, in fact, as a phagocyte).

This process is responsible for two types of melanin-based pigmentation in humans. The first is "constitutive" skin color, that is, skin color determined genetically in the absence of sun exposure and other extrinsic factors. The other type is "facultative" skin color, that is, an inducible, temporary "tan" resulting from exposure to UV radiation (UVR) in ordinary sunlight.

In young, healthy skin (in the absence of endocrine effects or pathologies such as Addison's disease), both constitutive and facultative melanin expression are uniform and synchronous, resulting in an extremely homogeneous distribution of the melanin chromophore in both basal skin tone and sun-exposed sites. Distribution is so homogenous that skin coloration is essentially featureless, lacking contrast. This situation changes considerably, however, under the influence of so-called "photoaging." Photoaging is the term given to the superimposition

of chronic sun damage upon the intrinsic (chronological) aging process. In contrast with the apparent age-related loss of melanogenic activity in non-sun-exposed skin (13), it is now well established that cumulative lifetime exposure to solar UVR results in a progressive accumulation of "mottled hyperpigmentation" (14,15), including "diffuse hyperpigmentation" [the "wispy" dyspigmentation commonly present on sun-exposed skin, not related to systemic disease (12,16) and solar lentigines (known also as lentigo senilis, "age spots," or "liver spots" (12,16–20)]. All of these features are characterized by local communities of "cloned" melanocytes, all exhibiting abnormal, increased rates of melanogenesis. At present, the mechanisms underlying the solar UVR-induced hyperpigmentation in these lesions are still not clear, although it has been proposed that an accentuated expression of the endothelin-1/endothelin B receptor cascade and also of epidermal stem cell factor may play an important role in the induction and propagation of these permanent, expanding communities of abnormal melanocytes in lesional skin (21–23).

Other common melanotic skin features include ephelides (otherwise known as "freckles," small, uniformly pigmented, sharply defined macules, 1–5 mm in diameter) and, while these often appear within sun-exposed areas, they can also be inherited as an autosomal dominant trait and have recently been shown to be more associated with constitutional host factors such as fair skin and/or red hair (24–26). Seborrheic keratoses are also common melanotic lesions found to an increasing extent in normal aging skin, presenting as sharply defined, light brown lesions, often slightly raised with a finely verrucous surface (27–29); there is thought to be some relationship between sunlight and observed frequency of these lesions, although the association is not as strong as that established for solar lentigos (30).

In addition to increasing inhomogeneity caused by hypermelanized features, photoaging also induces a known increased incidence of idiopathic guttate hypomelanosis, the 2 to 5 mm white spots commonly found on sun-exposed areas of skin (31,32). These lesions are characterized by a permanent, localized cessation of melanogenesis. It is quite common to find both hyper- and hypomelanotic lesions within the same area of sun-damaged skin.

Net, the process of aging and, in particular, photoaging produces localized concentration and an increasingly heterogeneous distribution of melanin in human skin. The visual impact of this effect will be discussed separately.

Hemoglobin

In human skin, hemoglobin is confined to membrane-bound red blood corpuscles, which are in turn confined to blood contained within the rich network of blood vessels supplying this organ. The arteries entering the skin form a "deep plexus," the "fascial network." Vessels rise from the fascial network to the border between the subcutaneous adipose tissue and the corium, and together, these vessels form the "cutaneous network." This network provides ascending arterioles to supply the "subpapillary plexus," which in turn forms capillary loops within the "rete ridges" that characterize the dermal-epidermal junction. Visually, therefore, this pigment is expressed in young, healthy skin as a pink-colored, highly diffused "bloom" representing the "umbrella" structures of the deeper plexus, superimposed with discreet, regularly spaced punctate dots approximately 10 to 12 μm in diameter, that represent papillary loops (both arterial and venous).

Whereas it is generally accepted that intrinsic aging produces a reduction in the superficial horizontal capillary plexus (16,33–35), once again, the vasculature of

sun-exposed skin is markedly different. Photoaging results in capillaries that are tortuous and dilated, producing a spectrum of severity of telangiectasia (16,36,37). Within areas of chronic sun exposure, the vessel wall appears to thicken as a result of the peripheral addition of a layer of basement membrane-like material (38–40). A combination of this increased vascular rigidity and a reduction in density of the supportive, perivascular connective tissue produces fragile vessel walls that are less able to support the internal turgor of blood volume and external mechanical stress. As a result of this mechanical failure, chronic dilation, the formation of sinuses, galleries and, to a limited extent, low-grade purpura drive the progressive and classic appearance of telangiectasia and “blotchiness” associated with aging skin and, in particular, sun-exposed areas.

Importantly, once again, aging produces a steady accumulation of local concentrations of this chromophore in human skin and an associated increase in heterogeneity of hemoglobin-based features, particularly in sun-exposed areas.

Collagen

In young, healthy skin, the fibrillar protein collagen represents some 75% of the dry weight and 18% to 30% of the volume of the dermis. It has a primary fiber of 15 μm diameter, which itself is made of a bundle of parallel unbranching fibrils approximately 100 nm in diameter, with characteristic striations of periodicity 60 to 70 nm. The most common form of collagen, Type I collagen, is found in the reticular dermis, whereas Type III collagen is localized in the papillary dermis.

For some 40 years now, it has been known that, from early adulthood onward, there is a progressive decrease in absolute quantity of collagen per unit area of skin, occurring more rapidly in women than in men (37,41–44). This is linked directly to significant changes in collagen ultrastructure with age, appearing as progressive fragmentation of collagen fibrils with accompanying clumping together of these fragments; this process appears to be associated with an increased expression of matrix metalloproteinases (MMP) released from keratinocytes and dermal fibroblasts and a sustained reduction in fibroblast activity and procollagen synthesis (44,45). This degeneration is both exaggerated and accelerated in sun-exposed skin and, once again, this is strongly associated with a significant increase in expression of MMP (43–51).

The relationship between this prolonged degradation and compromised skin mechanical properties is now well understood (44). It is not widely appreciated, however, that there is also an impact on skin optics. As collagen is the primary optical scattering component within human skin, this progressive reduction in collagen density drives an accompanying reduction in skin intracutaneous bulk light transport and, therefore, “glow” or “brightness.”

The intrinsic and extrinsic age-related changes in the main optical components of human skin described above can, therefore, be summarized as follows:

- A progressive increase in heterogeneity of distribution of the two chromophores responsible for skin color, melanin, and hemoglobin, characterized by an accumulation of features containing localized concentrations of these two molecules.
- A progressive decrease in the quality and density of dermal collagen and an increase in heterogeneity of distribution, with accompanying mechanical and optical changes.

Skin Surface Topography

Skin surface topography is inherently programmed from within the dermis itself and changes throughout a human lifetime are due, therefore, largely to dermal events. As discussed above, young, healthy skin contains an abundance of good-quality, high-density connective tissue, resulting in bulk-tissue mechanical properties characterized by both high elastic and tensile strength. These enviable biomechanics bestow resilience on young skin, resulting in topography that is almost entirely composed of so-called "microrelief."

Microrelief is composed of an intricate isotropic arrangement of discrete primary and secondary lines of 20 to 200 μm in depth, intersecting at regular intervals to form polygonal plateaus (52). As the result of both intrinsic aging and, particularly, cumulative lifetime solar UVR dose, however, this delicate structure changes progressively such that much of the finer secondary structure is lost and anisotropy increases because the primary lines become the dominant feature (53–55). Superimposed upon these changes is the progressive development of deeper invaginations of the skin surface, forming the structures commonly known as "lines and wrinkles." These features are in the order of multiples of 100 μm in depth and develop particularly in areas of both chronic sun exposure and repeated flex (the periorbital and nasolabial areas of the aging face being classically associated with these features). There is varying opinion over the classification of wrinkles, although the four classes proposed and reviewed by Pierard and Uroda (55) (Type I, atrophic; Type II, elastotic; Type III, expressional; and Type IV, gravitational) all have their ultimate root in the compromised mechanics of atrophied dermal tissue, driven primarily by chronic photodamage.

THE EFFECT OF CHROMOPHORE AND TOPOGRAPHY CHANGES IN AGING SKIN UPON PERCEPTION OF AGE, HEALTH, AND BEAUTY

We view the world through sensitive visible-light meters and, therefore, the phenomenon of "contrast sensitivity" is of critical importance when considering the perception of chromophore changes in human skin. "Contrast" can be defined simply as a ratio of adjacent luminance values, and "contrast sensitivity" is a measure of how faded or washed-out an image can become before it is indistinguishable from a uniform field. It has been determined experimentally that the minimum discernible difference in gray-scale level that the human eye can detect is about 2% of full brightness (56,57). This outstanding contrast sensitivity allows us to perceive the world around us in great detail; indeed, without contrast (and a means for achieving this via a variable-focus mechanism), we would effectively be rendered blind. The human eye, therefore, is drawn automatically to areas with high ratios of adjacent luminance—in simple terms, we view the world through "edges" created by "contrast."

Contrast sensitivity is a function of the size or spatial frequency of the features in the image. However, this is not a direct relationship because larger objects are not always easier to see than smaller objects, due to reduced contrast. Contrast is highest, therefore, when both adjacent luminance ratios are high and when features that contain these values are large.

In young skin, reflection from the skin surface is largely diffuse, due to the very large number of reflecting polygonal plateaus that make up "microrelief," and this has been found to be predictive for perception of soft, firm skin (58). Because microrelief is lost with increasing age and cumulative photodamage,

so too is this natural “soft-focus” effect, driving low-contrast optics. In aging human skin, contrast is certainly increased by high ratios of adjacent luminance values due to shadowing formed by high amplitude/low frequency surface topography—and especially so in the case of linear features such as “lines,” “furrows,” and “wrinkles.”

Color, however, also plays an important role in the perception of age, health, and beauty. It has already been established that the process of intrinsic and extrinsic aging drives a steady accumulation of enlarging, localized concentrations of the two colored chromophores, melanin and hemoglobin. In other words, therefore, independent of contrast formed by shape and/or topography, localized concentration of chromophores in aging skin causes a significant increase in contrast, particularly in sun-exposed areas such as the face, neck, and décolletage.

A recent study (59) has shown that, independent of facial shape, form, or skin topography, contrast attributable solely to chromophore distribution is significantly positively correlated to perception of age and significantly negatively correlated to perception of health and beauty. Moreover, skin color distribution alone was found to account for approximately 20 years of age perception, independent of facial shape, form, or skin surface topography. This provides empirical evidence that facial skin, which is free of lesions, moles, lentigines, freckles, and other inhomogeneities, is probably among the most universally desired human features (60).

In summary, therefore, understanding cutaneous optics provides the simple blueprint for effective imaging of aging skin. One should be able to:

- Manipulate illumination to maximize and tune contrast caused by shadowing, if surface topography is the target end point.
- Disentangle effectively competing surface and subsurface optics if accurate color information is the target end point.

Finally, if a rigorous approach is adopted, mapping the concentration and distribution of the melanin and hemoglobin chromophores responsible for skin coloration will provide an explanation, and not only a description, of aging skin appearance. This very process is described later in this chapter.

THE CORE PRINCIPLE OF EFFECTIVE DIGITAL IMAGING—REPRODUCIBILITY

Over the past 10 years, there has been a dramatic increase in the resolution and sensitivity of consumer-level digital camera systems, but an equally dramatic decrease in relative cost. For example, the Kodak DCS-100 single-lens reflex (SLR) digital camera that used a 1.3 megapixel (1024 × 1280) CCD and a Nikon F3 body was marketed in 1991 at a price of \$30,000. Today, a camera such as the Fuji S3 Pro that uses a Nikon F80 body and contains a six-megapixel CCD with dual photodiodes at each pixel location retails for just \$1700. Theoretical technical digital image quality driven by either modern camera optics or CCD resolution is no guarantee, however, of faithfully capturing either (i) a true record of skin condition or (ii) a treatment or time-related change in skin condition. Too many supposedly standardized clinical imaging pairs, that are meant to show a treatment or a time-related difference are fundamentally flawed by combinations of poor lighting control, variable subject position, magnification changes, differing backgrounds, or distractions within the image including clothing and jewelry.

If only one rule is adopted for effective digital imaging of aging skin, it should be this—*reproducibility*. Put differently, when using digital imaging as a serious documentation and/or measurement tool, the *only* variable one actually *desires* is the passing of time or the effect of a treatment. This section, therefore, briefly reviews the various essential aspects of the digital imaging process that should be standardized and tightly controlled to achieve reproducibility.

Incident Angle of Illumination

Reproducibility of incident angle of illumination is absolutely critical to faithful capture of apparent skin topographical and color information. Fresnel's law can be used to predict light interaction with the skin surface, determining the amount that is both regularly reflected from and forward scattered into the stratum corneum. In practice, even small changes in the position of either the light source or the subject will drive these physical laws. Figure 1 demonstrates this effect and shows how a deviation of just 10° causes visible changes in both apparent surface texture and skin color, which will only be magnified as the images are processed, analyzed, and quantified.

It is essential, therefore, that the light source(s) is very securely and permanently fixed to a solid support, preferably within a rig that also incorporates the subject positioning and camera systems, to ensure maintenance of optical geometry. Likewise, a robust means of maintaining subject position needs to be incorporated into the imaging rig. Taking the example of facial imaging, at least one point of solid contact needs to be made with the subject's face and this is most easily achieved by a chin rest. In this author's experience, however, this still leaves several axes of possible movement to the often untrained, naïve subject [e.g., even though the chin is fixed, the subject can (and will) tilt the top of their head left, right, backwards, or forwards or swivel the whole of their head using the chin rest

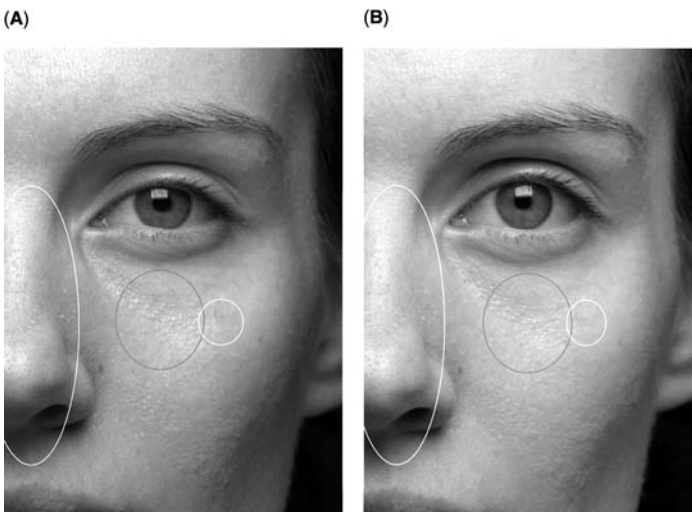


FIGURE 1 (See color insert) (A) Same subject imaged under D65 continuous lighting, perpendicular to subject's face and (B) 10° offset from perpendicular (to subject's left side). Note differences in apparent texture (*thick gray line*) and color (*light gray line*).



FIGURE 2 Example of subject positioning using a chin rest and bite stick. Note the use of a color calibration chart also.

as a pivot]. As a strong recommendation, therefore, at least one more solid point of contact is needed to help ensure reproducibility of incident illumination angle. This may take the form of a so-called “bite stick” (Fig. 2) or even a “pincer” device that inserts (safely and hygienically!) into the subject’s ears.

We have devised our own highly effective means of subject repositioning. In short, a second, low-resolution image is grabbed of a subject at their initial or study baseline visit by an off-center video camera. This image is then stored and displayed as a “ghost” on a separate monitor at subsequent visits. The operator helps the subjects to position their head such that the live image superimposes upon the baseline “ghost” image precisely. When perfect repositioning has been achieved, a new high-resolution image is captured. This process can be seen simulated in Figure 3.

Lighting Stability

There are two aspects to ensuring reproducibility of incident lighting, namely (i) stabilizing source flux and (ii) stabilizing the spectral power distribution of the source. With continuous sources, therefore, stabilizing the power supply by means of a voltage regulator is essential. Because many sources display spectral aberration with varying power, this will tend to help reduce both flux and spectral variation. Many sources also display characteristic spectral deterioration with age and this process is often recognized and described by the manufacturer in data



FIGURE 3 (See color insert) (A) Repositioning achieved by recalling a “ghost” image taken at the first visit, (B) live orientation of the subject’s head, and (C) perfect realignment at a subsequent visit.

sheets for the respective source. It is essential, therefore, that the source characteristics are studied closely, in collaboration with the manufacturer if necessary, that a log of usage hours is kept to ensure that deterioration of the spectral quality of the output is kept to a minimum and that a standard operating procedure is in place to ensure that the source is replaced and/or serviced on a regular basis.

Black/White and Color Calibration

All modern, quality digital cameras now allow black and white balancing and this should be performed before every imaging session. As described above, however, perfect stability of lighting conditions can be approached by proper controls, but never fully achieved. It is, therefore, highly desirable to also color calibrate digital

imaging systems using known color standards (e.g., Munsell standard color charts, Macbeth Division of the Kollmorgen Corporation, Baltimore, Maryland, U.S.A.). If these are incorporated into the image field in some form, the image may, theoretically, be corrected so that the imaged standard color matches that of the actual standard. This may be done before an imaging session (by setting rig position/lighting conditions for the session), “on-the-fly,” or as a postprocess.

Reproducibility in Elimination of Distractions

Once standardized digital images have been taken, they may be used for a very wide variety of different analyses. If these include subjective analyses of any form, it is essential that reproducibility is also extended to the elimination of any visual distractions within the image. These include the following:

1. providing a constant background—we have found that black fabric, well behind the subject and focal plane of the camera and filling the field of view, provides an excellent standard backdrop to standardized digital images,
2. concealing hair and clothing—a simple headband/hairnet (preferably black) should be used to both keep hair off the face of the subject and cover the subject’s hair. Likewise, a simple black cape can be used to good effect to cover the subject’s own clothing, and
3. removal of jewelry—all items of jewelry, including earrings, facial piercings, etc., should be removed before every imaging session.

The use of black backgrounds, hairbands, and capes also helps minimize stray light reflection.

THE PRACTICAL USE OF IMAGING OF AGING SKIN

Once sound procedures are in place to ensure reproducibility, standardized digital imaging becomes an extremely powerful tool that may be used to not only capture appearance, but also measure it. To illustrate this, a study is summarized here, where we set out to establish and model visible end points of aging skin across different ethnic populations, using standardized digital imaging and image analysis (61). Whereas skin color is the most obvious visible skin feature that distinguishes one race from another [related to the number, size, type and distribution of cytoplasmic melanosomes (62)], racial differences in constitutive pigmentation (63) are also related to corresponding differences in the incidence of pigmentation disorders (64) and the visible signs of skin aging such as skin wrinkling (65). It has been proposed that darker skin types are less prone to acute and chronic UVR photodamage (65,66). As regards acute protection, Kollias et al. (67) measured the minimum erythema dose (MED) in both heavily pigmented subjects (Fitzpatrick skin Type V) and fair-skinned Caucasians (Fitzpatrick skin Types I and II). The MED of skin Type V subjects was about twice that of skin Types I and II, in close agreement with the ratio of pigment in the two groups. As regards chronic UVR photodamage and photoprotection, the association between skin type and the visible signs of skin aging, e.g., wrinkling and hyperpigmentation, is less well quantified. Standardized digital imaging provided the perfect tool to study this area and the study design, method, and results are summarized briefly below.

A standardized digital imaging rig was used to capture the visible facial skin condition of females from various racial/ethnic groups living in specific

TABLE 1 Race, Geography, and Subject Numbers Used in the Ethnic Aging Study

Race	City	<i>n</i>
Caucasian	Los Angeles	439
Caucasian	London	469
Caucasian	Rome	445
Asian-Indian	London	474
African-American	Los Angeles	435
Latino/Hispanic	Los Angeles	310
East Asian ^a	Los Angeles	207
Japanese	Akita	381

^aChinese, Japanese, and Korean.

geographies around the world. The study data were collected during the autumn and winter months (October–March), starting in February 1999 to March 2000. A total of 3160 females were recruited from different racial groups and details are shown in Table 1.

Facial images were collected using a 1.3 megapixel CCD camera (Fuji DS330) equipped with a close-up lens mounted into a standardized illumination rig (6500°K high frequency fluorescent white light sources) fitted with head positioning aids. The camera system was calibrated daily. Images of the left side of subjects' faces were captured and saved for subsequent analysis (an example image is shown in Fig. 4). The region of interest (ROI) on each image was defined for all images using predefined anatomical landmarks on the face (e.g., left and right corners of eye, bridge of nose, and corner of mouth). The ROI for each image was analyzed using customized image analysis algorithms that automatically identified and quantified end points including (i) wrinkles and fine lines, (ii) rough texture, (iii) pores, and (iv) hyperpigmented spots (both red and brown pigmented spots). Figure 5 shows a subject with an image analysis overlay within the ROI for wrinkles, hyperpigmented spots, and visible pores. The calculated absolute amount of each skin feature (e.g., total number of pores, total number of spots, total area of wrinkles,

**FIGURE 4** Example of a digital image taken during the ethnic aging study.

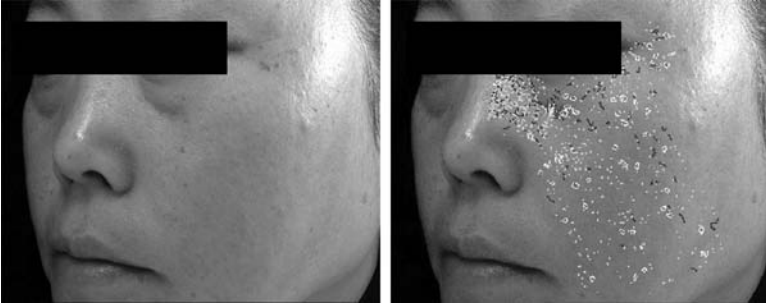


FIGURE 5 (See color insert) Example of a digital image taken during the ethnic aging study with pigmented spots (*yellow*), lines (*dark blue*), and visible pores (*light blue*) identified by image analysis within the region of interest (*right*).

or total area of texture) was indexed (normalized) versus the size of the ROI, enabling the expression of specific end points to be compared between subjects.

Figure 6 shows the mean wrinkle area fraction by race and age group for (A) subjects living in Los Angeles and (B) all subjects in all geographies in this study. In Los Angeles subjects (Fig. 6A), expression of facial wrinkling increased commensurate with age in all racial groups. There were, however, differences in relative expression between racial groups, with wrinkling increasing in the order East Asians < Latinos = African-Americans < Caucasians. Considering all racial groups in all geographies (Fig. 6B), there was no significant difference in skin wrinkling between East Asians living in Los Angeles and Japanese living in Akita (although both oriental groups showed significantly less wrinkling than all other groups). In a similar trend, there was also no significant difference in wrinkling between Caucasians living in London and Caucasians living in Los Angeles (although both groups showed significantly more skin wrinkling compared to all other groups in all geographies).

As regards hyperpigmentation, Figure 7 shows facial hyperpigmented spot count fraction by race and age group for (A) subjects living in Los Angeles and (B) all subjects in this study. In Los Angeles subjects (Fig. 7A), facial hyperpigmentation increased commensurate within all groups. As with wrinkling, there were differences between racial groups, in the order East Asian = Latino < Caucasian < African-American. Comparing all racial groups from all geographies (Fig. 7B), the Japanese and East Asians showed the least expression of facial hyperpigmentation while African-Americans and Caucasians from Los Angeles and Caucasians from London showed the most.

This remarkable study, quantifying for the first time the expression and time-tabling of visible end points of the intrinsic and extrinsic aging process, was possible only because fully standardized and reproducible digital imaging techniques were used.

STATE-OF-THE-ART COLOR ANALYSIS OF AGING SKIN— THE EMERGING SCIENCE OF CHROMOPHORE MAPPING

The section within this chapter discussing the interaction of light with skin was included not without good reason. It follows that a method to map the concentration

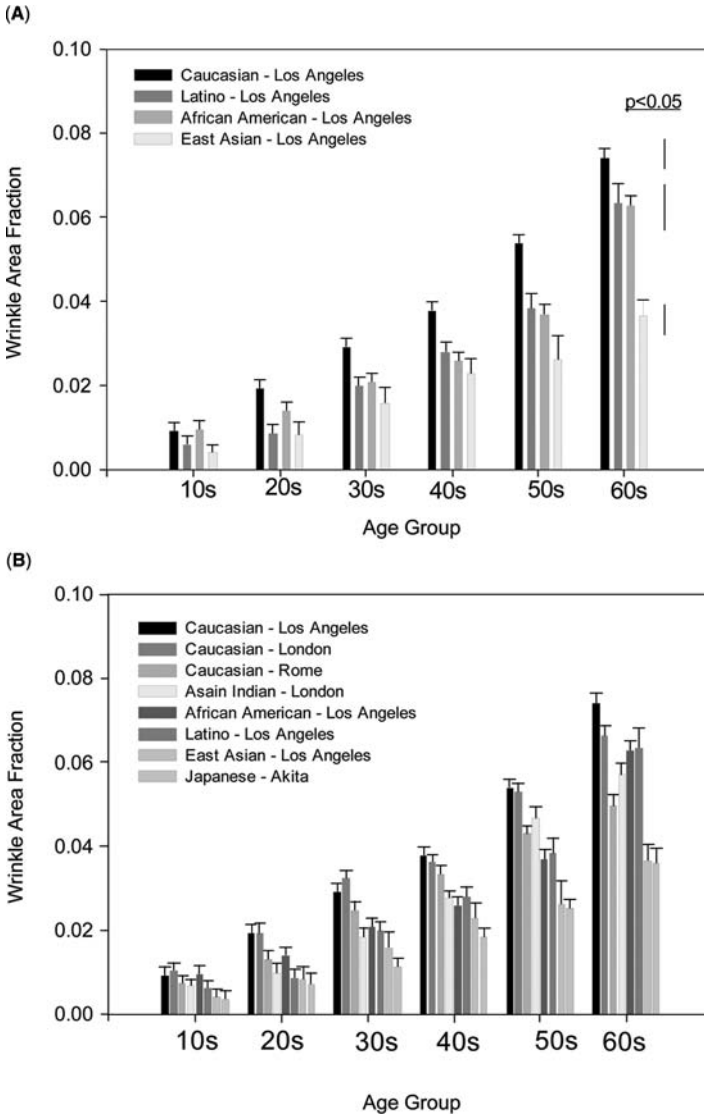


FIGURE 6 (A) Facial wrinkling by race and age group—Los Angeles subjects only. (B) Facial wrinkling by race and age group—all racial groups in all geographies.

and spatial distribution of melanin, hemoglobin, and collagen (“chromophore mapping”) would provide a means by which to map the very components responsible for driving a major part of human perception of age, health, and beauty.

Whereas there are a plethora of methods to characterize and quantify skin surface topography, “chromophore mapping,” as it relates to human skin appearance, remains a remarkably unresearched area. This represents a significant gap in our

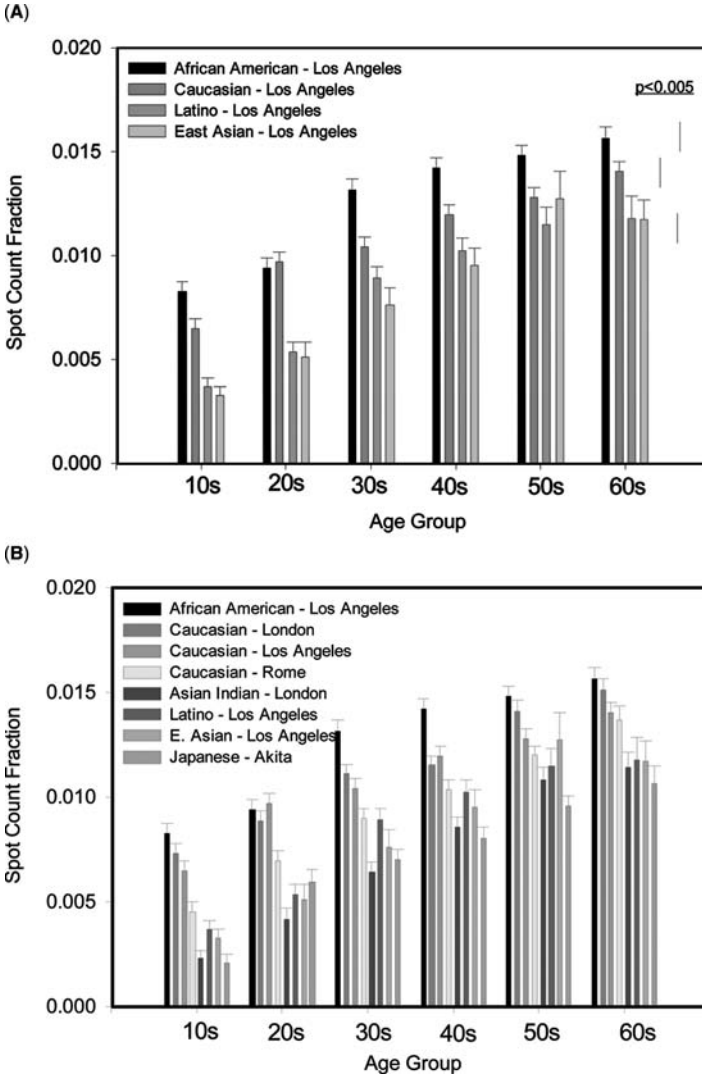


FIGURE 7 (A) Hyperpigmented spots by race and age group—Los Angeles subjects only. (B) Hyperpigmented spots by race and age group—all racial groups in all geographies.

understanding as in short, whereas digital imaging “describes” human skin coloration, chromophore mapping will yield a data-set that effectively “explains” it.

In this respect, those methods that could potentially be used provide only incomplete information (e.g., colorimetry, reflectance spectrophotometry, and commercialized devices such as the Mexameter™). Some or all of the following limit these techniques: availability, expense, inability to measure multiple chromophores sequentially or simultaneously, questionable specificity and lack of useful diagnostic detail. Setting these aside, the ideal clinical tool developed to map human

intracutaneous chromophores would be in vivo, rapid, accurate, and noninvasive and have the ability to map multiple chromophores simultaneously.

“Contact” SIAscopy™

A new technique, SIAscopy™ (Astron Clinica Ltd., Cambridge, U.K.; Spectrophotometric Intracutaneous Analysis), conforms to all the requirements set out above. The SIAscopy™ is now a commercially-available product and, while it has been shown to have excellent sensitivity and specificity in the early identification of malignant melanoma, the principle of chromophore mapping that it employs can be readily applied to normal, healthy skin (68–72). The technique is based upon a unique combination of dermatoscopy, contact remittance spectrophotometry, and hyperspectral imaging. In short, the SIAscope is able to obtain a high-resolution white-light image of the skin over a 12×12 mm area, and four additional chromophore maps that display the concentration of epidermal melanin, hemoglobin, collagen, and melanin in the papillary dermis, pixel by pixel. The dermal melanin end point is the key diagnostic criterion used in melanoma diagnosis and is not of concern to us with regard to normal skin.

How is the SIAscope able to achieve this? The instrument uses a suite of new, custom algorithms that are derived from a two-flux model based on Kubelka–Munk theory. This model computes the remitted and transmitted light separately for each layer of the substrate. The model requires that the incident light is diffuse. This condition is fulfilled because, as can be recalled from the earlier description of intracutaneous light transport, light is diffused as it passes through the stratum corneum. This model has been used by other researchers with good results. An alternative approach to modelling of the remitted light is a stochastic Monte-Carlo method. A comparison of the spectra generated by the Kubelka–Munk method with those from the Monte-Carlo method found that the results from both methods were in a good agreement.

The three principle layers of optical consequence, namely the epidermis, papillary dermis, and reticular dermis are defined in the model:

- Epidermis: characterized by the wavelength-dependent set of absorption coefficients for melanin and melanin concentration
- Papillary dermis: characterized by the wavelength-dependent set of absorption coefficients for hemoglobin, hemoglobin concentration, the scattering coefficient for collagen, and the thickness of the collagen layer
- Reticular dermis: characterized by its scattering coefficient and layer thickness

By supplying these parameters and the spectral composition of the incident light to a model of light transport, the spectral composition of the light remitted from the skin can be computed. In the final step, a color vector $[r \ g \ b \ nir]$ is derived from the remitted spectrum by convolving it with suitable spectral response functions for the red, green, blue, and near-infrared primaries. This last step completes the process of computing the color of light remitted from the skin surface for a given set of input parameters.

Parameters in the model of light transport above can be subdivided into those, which characterize the entire tissue type and those, which characterize a specific instance of the tissue. The absorption and scattering coefficients belong to the first group and their specific values are based on well-attested, published data. The thickness of the reticular dermis can be assumed constant as, due to

its strong forward-scattering properties, even a thin layer will prevent any remission of light. Melanin and hemoglobin concentrations and thickness of the papillary dermis vary both between individuals and for different anatomies. The model captures this variability by computing a set of color vectors for parameters spanning the entire range of histologically valid concentrations and thicknesses. In this way, a cross-reference between histology and color is formed.

This forward process explicitly computes tissue color, given a set of histological parameters. As the mapping between the parameters and the primaries is unique for the skin, *inverse mapping is possible: that is, from the tissue color to its histological parameters. The derived quantities for melanin, hemoglobin, and collagen are then used to construct parametric concentration maps. This is the critical step in the measurement approach of this new technique.*

In terms of the hardware design and its relationship to these computations, the SIAscope uses high-intensity light emitting diodes (LEDs) to emit four discreet wavebands between $\lambda = 400$ nm and 1200 nm to sequentially illuminate the skin sample, spanning the entire visible spectrum and a small range of NIR. The wavelengths used for computations are taken at equal intervals of 30 nm, giving 30 discrete points for each spectrum. The incident light is "white," i.e., it has equal contributions from each discrete wavelength. The $[r\ g\ b\ nir]$ vectors are derived from the computed spectra using a set of response functions equivalent to physical filters used by a specific camera. These relationships constitute the model of skin coloration. Because there is a one-to-one mapping between the colors and the chromophore parameters, the individual chromophore parameter values can be retrieved from the model, given the color vector obtained from each point in a color image of the skin. The magnitude of each chromophore parameter is then displayed at each pixel location in a separate image, giving three parametric maps: epidermal melanin, dermal hemoglobin, and collagen.

These images now represent eight-bit 1024×1024 gray-scale maps of chromophore concentration in portable network graphics (PNG) image file format and, as such, are readily amenable to sophisticated image analysis techniques for calculation of a variety of relevant end points. The image corresponds to a 12 mm diameter circular field of view. Sample chromophore concentration maps are shown in Figure 8.

In practice, the contact SIAscope comprises a hand-held scanner with a flat glass-fronted probe. The scanner is placed in contact with the skin using light, but firm, pressure (to avoid blanching). The best results are obtained if a drop of water/ethanol is used as a matching fluid (in exactly the same way as immersion oil is used in light microscopy to remove the refractive index of air and maximize resolving power of the system). The measurement itself takes less than five seconds, during which time the scanner is held as still as possible. The calculations described above are performed in less than 30 seconds, and the resulting white-light image and melanin, hemoglobin and collagen maps displayed, allowing the operator to perform live quality control and either accept or reject the measurement.

Results of study performed on 400 female Caucasian subjects aged 10 to 70, recruited in equal five-year cohorts (73,74) demonstrated remarkable relationships for the melanin, hemoglobin, and collagen end points with age, consistent with ongoing hypotheses relating to the extent and timetabling of expression for each of these optical skin components. Moreover, sufficient dynamic range was present within the data to allow the use of this technique to track changes in these chromophores due to treatment.

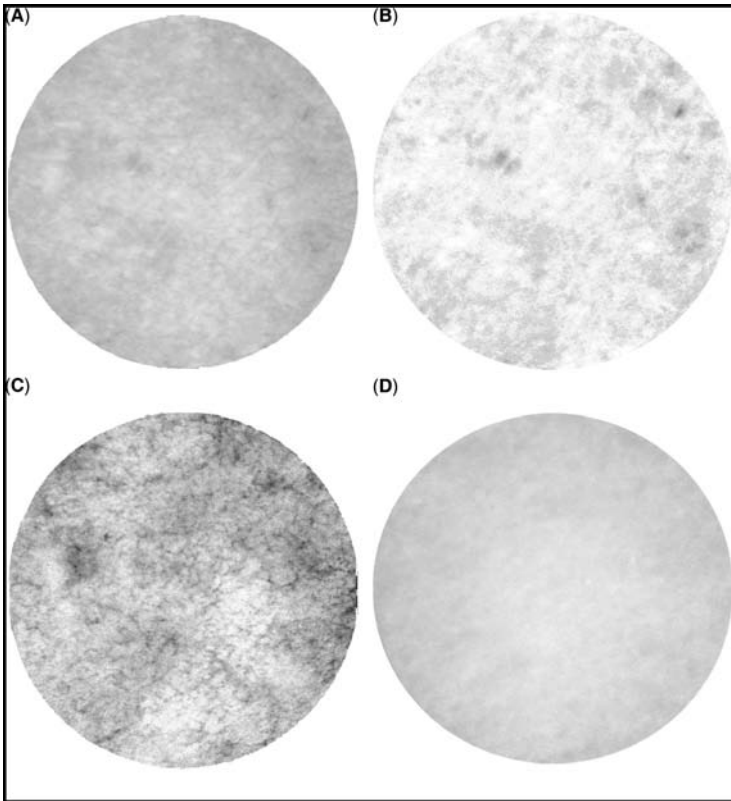


FIGURE 8 (See color insert) Example of contact SIAscope image and chromophore maps—(A) white-light image (12 mm diameter), (B) corresponding melanin map, (C) corresponding hemoglobin map, and (D) corresponding collagen map.

“Noncontact” SIAscopy™

While the contact SIAscopy method has proven to provide sensitive, high-resolution exclusive chromophore mapping over small areas (up to 12 mm), it is also of interest to apply this same technique to larger areas, for example, a human face. In order for this to be possible, the technique would need to be modified such that it were insensitive to scene geometry and illumination intensity—in other words, the unavoidable artifacts of measuring three-dimensional objects, rather than flat surfaces.

“Noncontact” SIAscopy has been successfully implemented (75,76) such that an essentially conventional (although finely calibrated) camera and lighting system may be used to acquire large-field melanin and hemoglobin chromophore maps. For the purposes of this chapter, the technique can go by the code “NCS” (Noncontact SIAscopy). With the NCS technique, the camera is treated not so much as an imaging device, but more as a simple three-waveband spectrometer, making use of the RGB Bayer filter over the CCD. The spectral power distribution of the light source and the raw response of the CCD are determined accurately over the visible range (400–700 nm) and are used as calibration data for the NCS algorithm, based

on the SIA mathematical model of light transport within skin. In short, for every pixel of the original raw image, NCS calculations are performed to yield exclusive concentrations of melanin and hemoglobin. When recombined as an array, a parametric concentration map is produced, directly analogous to those calculated using the contact technique. It should be noted that a fully cross-polarized lighting system is needed to eliminate specular reflection (containing no subsurface information). Sample NCS chromophore concentration maps are shown in Figure 9.

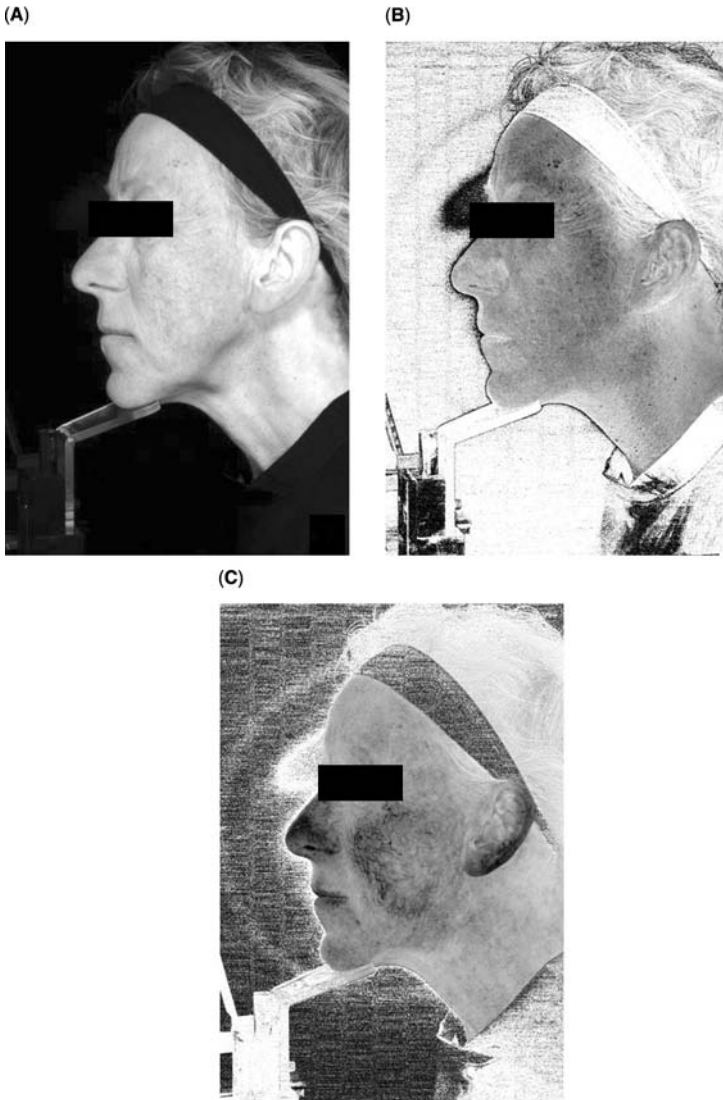


FIGURE 9 (See color insert) Example of noncontact SIAscope image and chromophore maps. (A) Original cross-polarized white-light image, (B) corresponding melanin map, and (C) corresponding hemoglobin map.

How does the technique deal with the issues of varying scene geometry and illumination intensity? An elegant, yet simple, solution has been developed by Astron Clinica Ltd (Cambridge, UK) to solve this problem. In short, by ratioing both the blue and the green channels relative to the red channel, intra-image light levels are normalized, effectively eliminating shadowing caused by form and curvature. It can also be seen how this approach would also eliminate inter-image (e.g., images from repeated clinical visits for the same subject) variation in lighting levels. It could be predicted, therefore, that the ratioing method employed by NCS would result in greater stability and robustness versus current color imaging/analysis techniques. This is indeed the case (75,76).

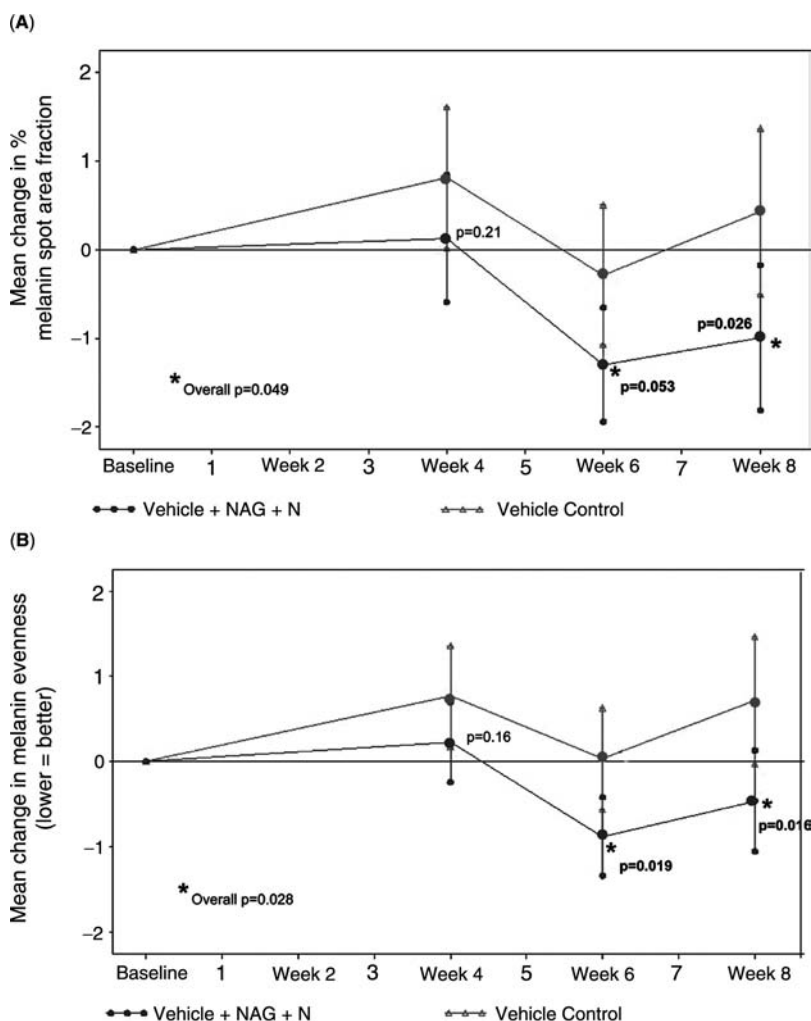


FIGURE 10 (A) Mean change in percentage of melanin spot area fraction. (B) Mean change in melanin evenness. Abbreviations: NAG, *N*-acetyl glucosamine; N, niacinamide.

The NCS technique now allows routine acquisition of full-face melanin and hemoglobin chromophore maps, and the method has proven an ideal clinical partner. In a recent double-blinded study, NCS was used to provide a quantitative means of measuring the effect of a vehicle containing 2% *N*-acetyl glucosamine (NAG) and 4% niacinamide (N) versus a vehicle control, applied topically, full face, twice daily for eight weeks, to two groups of 100 females aged 40 to 60, respectively, on melanized hyperpigmented spots (77). Analysis of the NCS melanin maps demonstrated clear treatment effects for the NAG + N combination versus vehicle control, resulting in a significant ($p < 0.05$) reduction in melanin spot area fraction and a significant ($p < 0.05$) increase in melanin evenness (Fig. 10). A separate study by this author (paper in preparation) has shown an excellent correlation between NCS-derived melanin concentrations and eumelanin concentrations in human skin biopsies, spanning Fitzpatrick skin Types I to VI. It must be concluded, therefore, that large-field chromophore mapping by NCS brings a new level of sensitivity and specificity to measurement of human skin color and constitutes a breakthrough in imaging of aging human skin.

CONCLUSION

The modern advent of digital imaging now provides the researcher and clinician alike with a powerful new tool to both record and measure the visible signs of skin aging in humans. As we have seen, however, access to state-of-the-art imaging tools is no guarantee of quality and, therefore, reproducibility and standardization in this relatively new area are essential prerequisites to success. Based on the relentless pace of development and innovation within the last 30 years of digital imaging, the next 30 years should prove extremely interesting.

REFERENCES

1. Kubelka P, Munk F. Ein Beitrag zur Optik Der Farbanstriche. *Zeitschrift technisc Phys* 1931; 12:593–601.
2. Kubelka P. New contributions to the optics of intensely light-scattering material, Part I. *J Opt Soc Am* 1948; 38:448–457.
3. Kubelka P. New contributions to the optics of intensely light-scattering materials, Part II. *J Opt Soc Am* 1954; 44:330–335.
4. Anderson RR, Parrish JA. The optics of human skin. *J Invest Dermatol* 1981; 77(1):13–19.
5. Wan S, Anderson RR, Parrish JA. Analytical modeling for the optical properties of the skin with in vitro and in vivo applications. *Photochem Photobiol* 1981; 34(4):493–499.
6. Jacques SL. Origins of tissue optical properties in the UVA, visible and NIR regions. *OSA TOPS on advances in optical imaging and photon migration* 1996; 2:364–71.
7. Cheong WF, Prahl SA, Welch AJ. A review of the optical properties of biological tissues. *IEEE J Quantum Electron* 1990; 26:2166–2185.
8. Bashkatov AA, Genina EA, Kochubey VI, Tuchin VV. Optical properties of human skin, subcutaneous and mucous tissues in the wavelength range from 400 to 2000 nm. *J Phys D: Appl Phys* 2005; 38:2543–2555.
9. Dawson JB, Barker DJ, Ellis DJ, et al. A theoretical and experimental study of light absorption and scattering by in vivo skin. *Phys Med Biol* 1980; 25: 695–709.
10. Zonios G, Bykowski J, Kollias N. Skin melanin, hemoglobin, and light scattering properties can be quantitatively assessed in vivo using diffuse reflectance spectroscopy. *J Invest Dermatol* 2001; 117(6):1452–1457.
11. Flock ST, Patterson MS, Wilson BC, Wyman DR. Monte carlo modeling of light propagation in highly scattering tissues. *IEEE TransBiomed Eng* 1989; 36(12):1162–1168.

12. Matts PJ. Understanding and measuring the optics that drive visual perception of skin appearance. In: Marks, Leveque, Voegeli, eds. *The Essential Stratum Corneum*. London: Martin Dunitz, 2002:213–222.
13. Gilchrist BA, Blog FB, Szabo G. Effects of aging and chronic sun exposure on melanocytes in human skin. *J Invest Dermatol* 1979; 73(2):141–143.
14. American Academy of Dermatology Consensus Conference. Photoaging/Photodamage as a Public Health Concern, March 3–4, 1988.
15. Sunlight, Ultraviolet Radiation, and the Skin. National Institutes of Health Consensus Development Conference Statement. Vol. 7(8), May 8–10, 1989.
16. Griffiths CEM. The clinical identification and quantification of photodamage. *Br J Dermatol* 1992; 127(suppl 41):37–42.
17. Bastiaens M, Hoefnagel J, Westendorp R, Vermeer BJ, Bouwes Bavinck JN. Solar lentigines are strongly related to sun exposure in contrast to ephelides. *Pigment Cell Res* 2004; 17(3):225–229.
18. Green AC. Premature ageing of the skin in a Queensland population. *Med J Aust* 1991; 155(7):473–474, 477–478.
19. Andersen WK, Labadie RR, Bhawan J. Histopathology of solar lentigines of the face: a quantitative study. *J Am Acad Dermatol* 1997; 36(3 Pt 1):444–447.
20. Montagna W, Hu F, Carlisle K. A reinvestigation of solar lentigines. *Arch Dermatol* 1980; 116(10):1151–1154.
21. Kadono S, Manaka I, Kawashima M, Kobayashi T, Imokawa G. The role of the epidermal endothelin cascade in the hyperpigmentation mechanism of lentigo senilis. *J Invest Dermatol* 2001; 116(4):571–577.
22. Hattori H, Kawashima M, Ichikawa Y, Imokawa G. The epidermal stem cell factor is over-expressed in lentigo senilis: implication for the mechanism of hyperpigmentation. *J Invest Dermatol* 2004; 122(5):1256–1265.
23. Imokawa G, Kobayashi T, Miyagishi M, Higashi K, Yada Y. The role of endothelin-1 in epidermal hyperpigmentation and signaling mechanisms of mitogenesis and melanogenesis. *Pigment Cell Res* 1997; 10(4):218–228.
24. Rhodes AR, Albert LS, Barnhill RL, Weinstock MA. Sun-induced freckles in children and young adults. A correlation of clinical and histopathologic features. *Cancer* 1991; 67(7):1990–2001.
25. Nicholls EM. Genetic susceptibility and somatic mutation in the production of freckles, birthmarks, and moles. *Lancet* 1968; 1(7533):71–73.
26. McLean DI, Gallagher RP. “Sunburn” freckles, cafe-au-lait macules, and other pigmented lesions of schoolchildren: the Vancouver mole study. *J Am Acad Dermatol* 1995; 32(4):565–570.
27. Reches A. Seborrheic keratoses: are they delayed hereditary nevi? *Arch Dermatol Syphilol* 1952; 65:596.
28. Eads TJ, Hood AF, Chuang TY. The diagnostic yield of histologic examination of seborrheic keratoses. *Arch Dermatol* 1997; 133(11):1417–1420.
29. Yeatman JM, Kilkenny M, Marks R. The prevalence of seborrheic keratoses in an Australian population: does exposure to sunlight play a part in their frequency? *Br J Dermatol* 1997; 137(3):411–414.
30. Elgart GW. Seborrheic keratoses, solar lentigines, and lichenoid keratoses. Dermatoscopic features and correlation to histology and clinical signs. *Dermatol Clin* 2001; 19(2):347–357.
31. Pagnoni A, Kligman AM, Sadiq I, Stoudemayer T. Hypopigmented macules of photo-damaged skin and their treatment with topical tretinoin. *Acta Derm Venereol* 1999; 79(4):305–310.
32. Wallace ML, Grichnik JM, Prieto VG, Shea CR. Numbers and differentiation status of melanocytes in idiopathic guttate hypomelanosis. *J Cutan Pathol* 1998; 25(7):375–379.
33. Ryan T. The ageing of the blood supply and the lymphatic drainage of the skin. *Micron* 2004; 35(3):161–171.
34. Montagna W, Carlisle K. Structural changes in ageing skin. *Br J Dermatol* 1990; 122(suppl 35):61–70.

35. Braverman IM. Elastic fiber and microvascular abnormalities in aging skin. *Dermatol Clin* 1986; 4(3):391–405.
36. Kennedy C, Bastiaens MT, Bajdik CD, Willemze R, Westendorp RG, Bouwes Bavinck JN. Effect of smoking and sun on the aging skin. *J Invest Dermatol* 2003; 120(4):548–554.
37. Leyden JJ. Clinical features of ageing skin. *Br J Dermatol* 1990; 122(suppl 35):1–3.
38. Braverman IM, Fonferko E. Studies in cutaneous aging: II. The microvasculature. *J Invest Dermatol* 1982; 78(5):444–448.
39. Toyoda M, Nakamura M, Luo Y, Morohashi M. Ultrastructural characterization of microvasculature in photoaging. *J Dermatol Sci* 2001; 27(suppl 1):S32–S41.
40. Braverman IM. Ultrastructure and organization of the cutaneous microvasculature in normal and pathologic states. *J Invest Dermatol* 1989; 93(suppl 2):2S–9S.
41. Shuster S, Bottoms E. Senile degeneration of skin collagen. *Clin Sci* 1963; 25:487–491.
42. Hall G, Phillips TJ. Estrogen and skin: the effects of estrogen, menopause, and hormone replacement therapy on the skin. *J Am Acad Dermatol* 2005; 53(4):555–568.
43. Smith JG, Davidson EA, Sams WM, Clark RD. Alterations in human dermal connective tissue with age and chronic sun damage. *J Invest Dermatol* 1962; 39:347–350.
44. Varani J, Warner RL, Gharraee-Kermani M, et al. Vitamin A antagonizes decreased cell growth and elevated collagen-degrading matrix metalloproteinases and stimulates collagen accumulation in naturally aged human skin. *J Invest Dermatol* 2000; 114(3):480–486.
45. Fligel SE, Varani J, Datta SC, Kang S, Fisher GJ, Voorhees JJ. Collagen degradation in aged/photodamaged skin in vivo and after exposure to matrix metalloproteinase-1 in vitro. *J Invest Dermatol* 2003; 120(5):842–848.
46. Schwartz E, Cruickshank FA, Perlish JS, Fleischmajer R. Alterations in dermal collagen in ultraviolet irradiated hairless mice. *J Invest Dermatol* 1989; 93(1):142–146.
47. Schwartz E, Cruickshank FA, Christensen CC, Perlish JS, Lebowitz M. Collagen alterations in chronically sun-damaged human skin. *Photochem Photobiol* 1993; 58(6):841–844.
48. Moloney SJ, Edmonds SH, Giddens LD, Learn DB. The hairless mouse model of photoaging: evaluation of the relationship between dermal elastin, collagen, skin thickness and wrinkles. *Photochem Photobiol* 1992; 56(4):505–511.
49. Bailey AJ. Molecular mechanisms of ageing in connective tissues. *Mech Ageing Dev* 2001; 122(7):735–755.
50. Fisher GJ, Datta SC, Talwar HS, et al. Molecular basis of sun-induced premature skin ageing and retinoid antagonism. *Nature* 1996; 379(6563):335–339.
51. Fisher GJ, Wang ZQ, Datta SC, Varani J, Kang S, Voorhees JJ. Pathophysiology of premature skin aging induced by ultraviolet light. *N Engl J Med* 1997; 337(20):1419–1428.
52. Pierard GE, Hermanns JF, Lapiere CH. Stereologie de l'interface dermo-epidermique. *Dermatologica* 1974; 149:266–273.
53. Corcuff P, Francois AM, Leveque JL, Porte G. Microrelief changes in chronically sun-exposed skin. *Photodermatol* 1988; 5:92–95.
54. Leveque JL. EEMCO guidance for the assessment of skin topography. *J Eur Acad Dermatol Venereol* 1999; 12:103–114.
55. Pierard GE, Uhoda I, Pierard-Franchimont C. From skin microrelief to wrinkles. An area ripe for investigation. *J Cosmet Dermatol* 2004; 2:21–28.
56. Blackwell HR. Contrast thresholds of the human eye. *J Opt Soc Am* 1946; 36:42–643.
57. Campbell FW, Robson JG. Application of Fourier analysis to the visibility of gratings. *Physiol* 1968; 197(3):551–566.
58. Matts PJ, Solechnick ND. Predicting visual perception of human skin surface texture using multiple-angle reflectance spectrophotometry. *American Academy of Dermatology 58th Annual Conference*, 2000.
59. Fink B, Grammer K, Matts PJ. Visible skin colour distribution plays a role in the perception of age, attractiveness, and health in female subjects. 18th Annual meeting of the human behaviour and evolution society, 2006.
60. Morris D. *The Naked Ape: A Zoologist's Study of the Human Animal*. New York: McGraw-Hill, 1967.

61. Hillebrand GG, Levine MJ, Miyamoto K. The age-dependent changes in skin conditions in African Americans, Asian Indians, Caucasians, East Asians and Latinos. *IFSCC Magazine* 2001; 4:259–66.
62. Kollias N. The physical basis of skin colour and its evaluation. *Clin Dermatol* 1995; 13:361–367.
63. Roh K, Kim D, Ha S, Ro Y, Kim J, Lee H. Pigmentation in Koreans: study of the differences from Caucasians in age, gender and seasonal variations. *Br J Dermatol* 2001; 144:94–99.
64. Jimbow M, Jimbow K. Pigmentary disorders in oriental skin. *Clin Dermatol* 1989; 7: 11–27.
65. Goh SH. The treatment of visible signs of senescence: the Asian experience. *Br J Dermatol* 1990; 122(S35):105–109.
66. Marks R. Ageing and photodamage. In: Marks R, ed. *Sun Damaged Skin*. London: Martin Dunitz, 1992:5–7.
67. Kollias N, Malallah YH, Al-Ajmi H, Baqer A, Johnson BE, Gonzales S. Erythema and melanogenesis action spectra in heavily-pigmented individuals as compared to fair-skinned Caucasians. *Photodermatol Photoimmunol Photomed* 1996; 12:183–188.
68. Cotton SD, Claridge E. Developing a predictive model of human skin colouring. *Proc SPIE Med Imaging* 1996; 2708:814–825.
69. Cotton SD, Claridge E, Hall PN. Noninvasive skin imaging. In: Duncan J, Gindi G, eds. *Information Processing in Medical Imaging IPMI'97*. Springer, 1997:501–506.
70. Moncrieff M, Cotton S, Claridge E, Hall P. Spectrophotometric intracutaneous analysis—a new technique for imaging pigmented skin lesions. *Br J Dermatol* 2002; 146(3):448–457.
71. Cotton SD, Hall PN, Rashbass J, Claridge E. Assisting diagnosis of melanoma through the “noninvasive biopsy” of skin lesions. *Proceedings of Medical Image Understanding and Analysis'97*, Oxford, Jul 7–8, 1997:177–180.
72. Cotton SD. A non-invasive imaging system for assisting in the diagnosis of malignant melanoma. PhD thesis. Birmingham University, 1998.
73. Matts PJ, Carey J, Cotton SD. Chromophore mapping: a new technique to characterize ageing human skin, *in vivo*. American Academy of Dermatology 63rd Annual Conference, 2005.
74. Matts PJ, Cotton SD. Chromophore mapping: a new technique to characterise and measure ageing human skin, *in vivo*. European Academy of Dermatology 14th Congress, 2005.
75. Preece S, Cotton SD, Claridge E. Imaging the pigments of skin with a technique which is invariant to changes in surface geometry and intensity of illuminating light. In: Barber D, ed. *Medical Image Understanding and Analysis*. 2003:145–148.
76. Cotton SD, Preece S, Morse R, Matts PJ. Wide field, geometry invariant, chromophore imaging of human skin. *World Congress on Non-Invasive Studies of the Skin*, Philadelphia, 2005.
77. Matts PJ, Miyamoto K, Bissett DL, Cotton SD. The use of chromophore mapping to measure the effects of a topical *N*-acetyl glucosamine/niacinamide complex on pigmentation in human skin. American Academy of Dermatology 64th Annual Conference, 2006.

Evaluation of Comedogenic Activity by Skin Fluorescence Imaging Analysis (Skin Analyzing Fluorescence Imaging Recorder)

Andreas Herpens, Silke Schagen, Stefan Scheede, and
Boris Kristof

Department of Bioengineering, Beiersdorf AG Research, Hamburg, Germany

INTRODUCTION

The history of an inflamed acne lesion normally starts with a comedone colonized by entrapped bacteria of the genus *Propionibacterium*. Comedones occur as a result of hyperkeratinization of the cells lining the orifice of sebaceous follicles, and they form when an increased rate of sebum production accompanies a simultaneous blockage of the sebaceous gland openings. A comedone can be manifested as a microcomedone, which is not visible to the naked eye, a black- or whitehead, or a macrocomedone. There is a significant correlation between the severity of acne and the number and size of microcomedones. It is therefore pivotal for the manufacturers of topical agents to know if their products increase the number and size of comedones, and thus have a comedogenic effect. Conversely, in case of all products designed for the treatment or prevention of acne, their potency with regard to the reduction of microcomedones, thus their comedolytic activity, has to be known. In principle, three assays are available to assess the comedogenic or comedolytic activity of compounds and final formulations of topical products.

The first one is the rabbit ear comedogenicity assay as introduced in 1968 by Kligman (1) and in a modified form in 1979 by Kligman and Kwong (2). The rabbit ear assay is the best animal model presently available. It is highly sensitive, and an ingredient found negative in the rabbit ear assay can normally be regarded safe on acne-prone skin. However, the assay has some intrinsic disadvantages. The rabbit ear assay can only detect a comedogenic activity, but not a comedolytic activity of a test item. Furthermore, the pilosebaceous units of rabbit and man differ anatomically, and comedones are more readily produced in response to topically applied substances in rabbit ear skin, which limits the predictivity of the assay for the human situation. Most of all, the rabbit ear assay is an *in vivo* animal assay, and animal experiments are banned for the testing of cosmetic products. As a consequence, the rabbit ear comedogenicity assay may remain a valuable tool in the hand of the toxicologist, but it is of little relevance for the manufacturer of cosmetic products, especially as it is generally agreed that human-based tests on cosmetics are more informative in all respects.

The second method to assess the comedogenic/comedolytic activity is the skin surface biopsy procedure using cyanoacrylates (3). In this procedure, microcomedones are sampled by applying a cyanoacrylate gel to the skin surface. A glass microscopic slide is then placed on top of the gel and pressed firmly onto the skin for a short period of time. Cyanoacrylates, also known as CA superglue, are

sufficiently safe for short exposure to the skin. They rapidly polymerize in the presence of trace amounts of water to a hard plastic with optical properties comparable to glass, which adheres tightly to the keratin of the stratum corneum. After careful removal of the glass slide the upper part of the stratum corneum and microcomedones are taken with it, which can subsequently be analyzed by microscopy or any other appropriate method. The skin surface biopsy technique is a simple noninvasive method for examining pathological changes in the stratum corneum, or the contents of the pilosebaceous follicles. It is well suited for studies in human volunteers. However, using this technique, the size of the funnel-shaped openings and the size and composition of comedones can only be examined in comparison with normal or untreated skin. Due to the abrasion of corneocyte layers and mechanical modification of comedones, the method is not suitable to compare identical skin areas before and after treatment. Furthermore, the method becomes less reliable with increasing oiliness of the skin, which may interfere with the polymerization process. Necessary cleansing of the skin before applying the CA gel may itself cause alterations to the comedones to be analyzed.

This report is dedicated to another non-invasive method to assess the comedogenic/comedolytic potential of topical formulations using UV-induced fluorescence of comedones and the "Skin Analyzing Fluorescence Imaging Recorder" (SAFIR). This method allows a precise *in vivo* characterization of follicular changes after topical product application on the same test site, and even down to a single individual comedone.

ORIGINS OF FLUORESCENCE SIGNALS FROM SEBACEOUS FOLLICLES

Sebaceous follicles emit light in the visible spectrum when excited by UV light (Fig. 1). This phenomenon of "orange-red lightning of pores" was first described by the German dermatologist Bommer in 1927 (4). The main fluorescent chromophore responsible for red fluorescence of sebaceous follicles could already be identified as bacterial protoporphyrin by Cornelius and Ludwig in 1967 (5). In 1989 Sauermaun et al. showed by fluorescence spectroscopy that the follicular fluorescence is indeed mainly caused and dominated by porphyrins, but also other fluorophores emitting light in the green-yellow range are involved (6). Red and green fluorescence in this case can often be located in different layers of the pilosebaceous follicle (Fig. 2). In 1989, Kligman and Pagnoni were able to demonstrate a strong decrease of red bacterial porphyrin fluorescence during treatment with the anti-bacterial compound benzoyl peroxide (BPO) (7), whereas a greenish fluorescence of the follicles remained unaltered (Fig. 3).

Given the above results, we assumed that the fluorescence signal of the comedone is composed of two components: a red component stemming from bacterial porphyrins, and a green one stemming from endogenous fluorochromes which are not sensitive to antibacterial treatment. This implies that an *in vivo* follicular spectroscopy with the capability differentiate and quantitate both green and red fluorescence in parallel would give additional valuable information about comedones. The green fluorescence, which we attribute to endogenous fluorochromes, would indicate sebaceous gland activity, whereas the red fluorescence, whose source is bacterial porphyrins, would indicate the microbiological status of the sebaceous duct. Thus, in an attempt to identify fluorophores in human comedonal sebum, we extracted a large number of follicles from about 30 volunteers

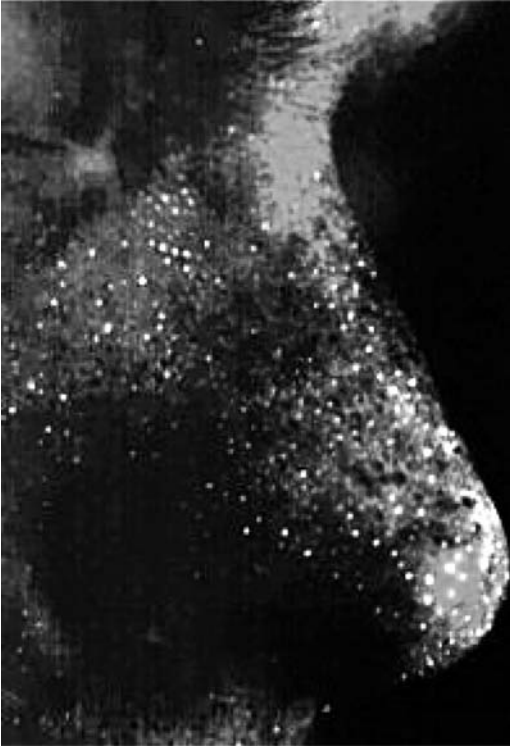


FIGURE 1 (See color insert) Wood's Light image of subject's nose with UV sensitive film. Source: Photograph from Sauermaann et al. 1990.

using the two-finger-squeeze-method. Under the fluorescence microscope, most of them showed both the green and the red color, sometimes with a spatial distribution as seen in Figure 2.

The collected follicles were transferred into tetrahydrofurane with three drops of sodium hydroxide as a base and treated with ultrasound for five minutes

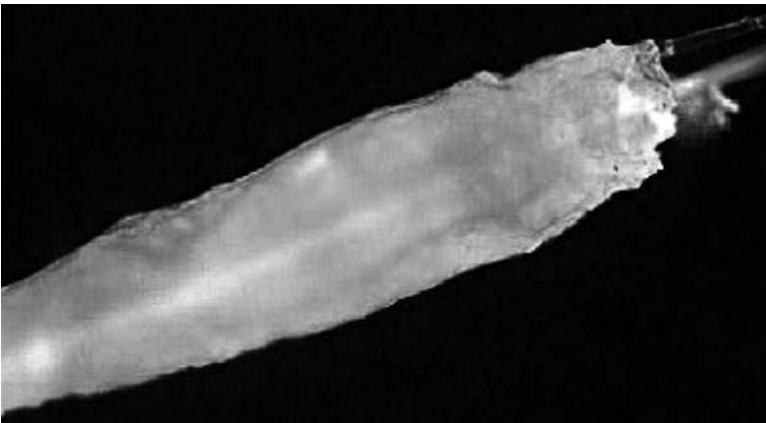


FIGURE 2 (See color insert) Sebaceous follicle under fluorescence microscope.

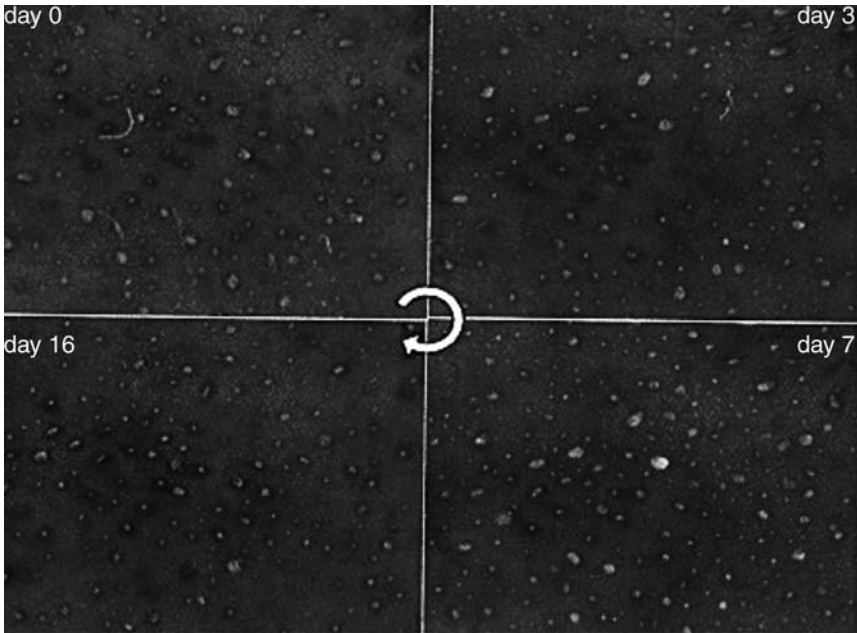


FIGURE 3 (See color insert) Digital fluorescence photography of the effect of benzoyl peroxide for seven days and recovery of protoporphyrin fluorescence after 16 days. Source: From Ref. 7.

to dissolve all the fluorophores from the sebum. The resulting solution was filtered through a $0.2\ \mu\text{m}$ filter to eliminate insoluble compounds, mostly lipids, and analyzed by high performance liquid chromatography (HPLC) with a connected fluorescence detector. The collected comedonal material of $0.32\ \text{mg/mL}$ from about 30 subjects contained about $1\ \text{ng/mL}$ (corresponding to 3.1 ppm) bacterial protoporphyrin IX (PPIX), and about $10\ \text{ng/mL}$ (corresponding to 31.3 ppm) of flavins (e.g., riboflavin). The fluorescence emission spectra of both components are depicted in Figure 4. Riboflavin and other flavins are essential components of the mitochondrial respiratory chain. Since the sebum lipids are released into the lumen of the sebaceous gland by a holocrine process, mitochondrial components may survive the process and accumulate in the sebaceous gland. Bilirubin, another potential endogenous fluorochrome with an emission spectrum in the green range, was neither detected by HPLC nor by the more sensitive liquid chromatography with mass selective detector. Since bilirubin is easily oxidized by light or other oxidants, it has yet to be clarified whether its apparent absence in comedonal sebum might be due its decomposition during isolation and/or analysis.

THE SKIN ANALYZING FLUORESCENCE IMAGING RECORDER AND FLUORESCENCE IMAGING SYSTEM

In 1993 Sauermaann et al. managed to assess comedogenic as well as comedolytic effects of topical treatments by measuring the changes of the protoporphyrin fluorescence of comedones. This was achieved by employing a sensitive black-and-white

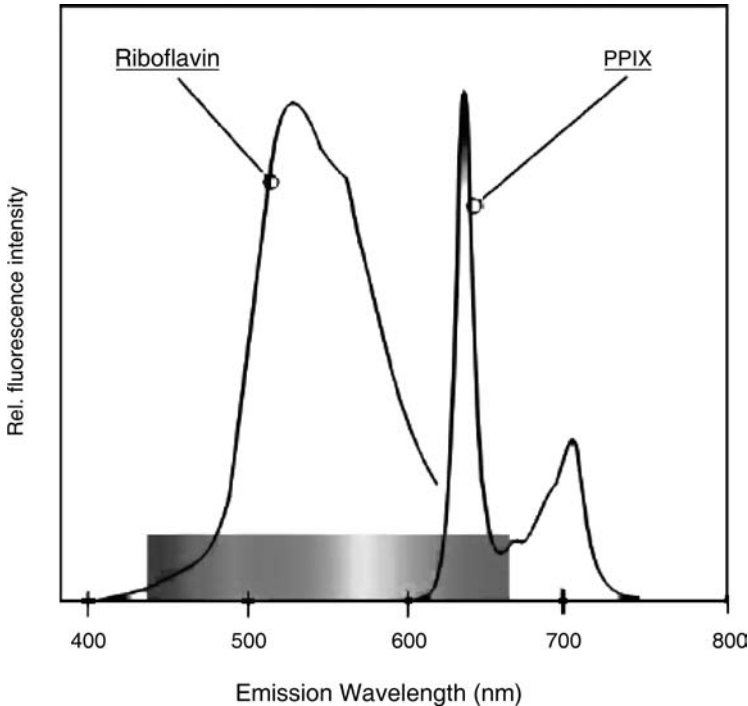


FIGURE 4 Fluorescence emission spectra of riboflavin and protoporphyrin IX.

Hamamatsu camera system with an intensive UVA-excitation source, special filter equipment and computer assisted image analysis (8). The camera and filter system was designed to detect the red-orange porphyrin fluorescence of comedones without getting into contact with the skin. However, unlike follicular biopsies where all follicles could be measured, only one third of the follicles actually displayed red fluorescence *in vivo* and could be utilized for further analysis.

Two inherent problems of the original system motivated us to improve the system for the detection of follicles and/or comedones in human skin. On the one hand, the original device as described in 1999 by Sauer mann (9) could only detect the red fluorescence of PPIX, and thus disregarded a substantial body of potential information contained in the green fluorescence. On the other hand, movements of the volunteers during the measurement often caused blurred images.

The new system denoted SAFIR, as depicted in Figure 5 (for technical specifications Table 1), is based on the combination of a high resolution digital camera and a UV-flashlight system. Both are connected by a special filter system that enables the combination of the optical pathways of excitation and emission to avoid spectral distortions. The lens focus adapter can be pressed directly on the skin surface of e.g., forehead or back to obtain sharp and bright fluorescence images of sebaceous follicles. The images are stored on a PC hard disc for further image analysis. Image analysis using the SAFIR system is a two-step process encompassing the exact spatial matching of consecutive images taken from an individual test site, and the data extraction from the respective site. When taking

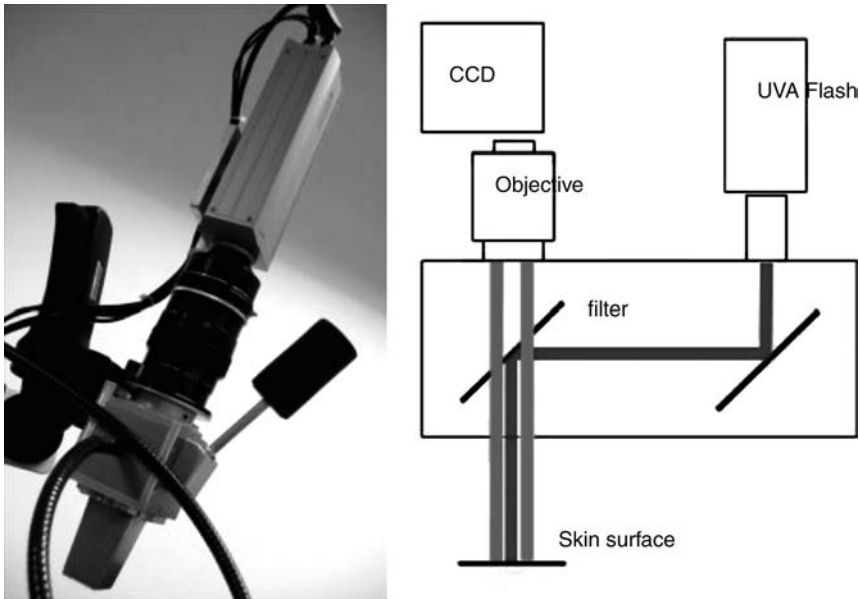


FIGURE 5 Scheme and image of the new skin analyzing fluorescence imaging recorder system.

consecutive fluorescence images during a six week administration period, we experienced rotational and planar shifts within the images due to imprecise positioning of the camera system on the 20×30 mm skin area, as well as small movements of the volunteers and camera system. To overcome this problem we designed a program to match the time linked images based on neural algorithms, employing a multiple step nearest neighborhood algorithm.

The precision and reliability of the new matching program was tested by comparing a series of images taken twice daily from the same test site over a period of seven days. Figure 6 depicts how planar and rotational shifts of 15 consecutive images of the same skin site are aligned by the software, which then determines the corresponding matching areas. The matching area present in all images of this example covers 78% of the original site and includes 130 follicles, which can be analyzed for intensity and number of spots with red porphyrin and green riboflavin fluorescence respectively. Data extraction from the matched

TABLE 1 Technical Specifications of the Skin Analyzing Fluorescence Imaging Recorder Fluorescence Evaluation System

Color digital camera	Kappa (1200×1600 px), 8 msec illumination time
UVA flashlight	Rapp Optoelectronic flash UVA <1 mW/cm ²
Fluorescence emission	450–750 nm
Fluorescence excitation	385 ± 11 nm
Image analysis	ZEISS KS400 and neural image matching software; Green and red segmentation for mean size and total count of fluorescent follicles
Skin area size	20×30 mm

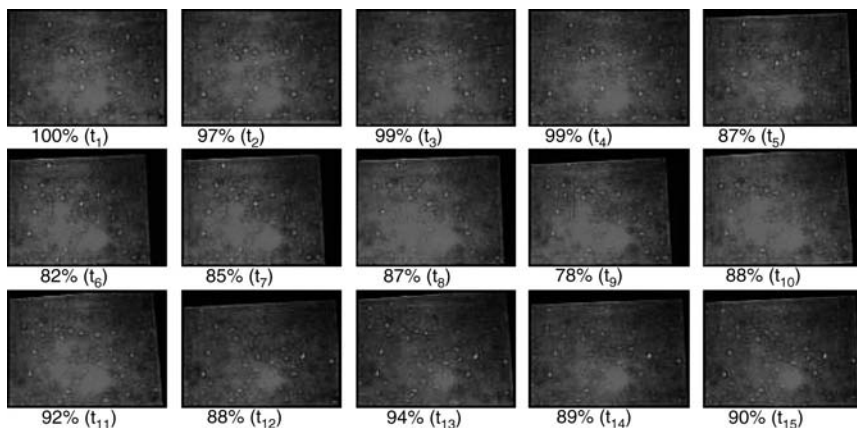


FIGURE 6 (See color insert) Time based shift of 15 consecutive measurements and correction by the neural software.

area is done by a program based on ZEISS KS400 software. The original image is transformed in gray, and shading is corrected before the final dynamic segmentation is done either for yellow-green or for orange-red fluorescence according to Figure 7. The resulting data are subject to further descriptive or statistical evaluation according to Table 2. Data relating to the reproducibility of 15 successive replicate measurements on the same matching skin area of a study subject are depicted in Figure 8. With the exception of red fluorescence data for fluorescence area (Area_red) and the number of red fluorescent follicles (Count_red), coefficients of variation are in the range of 10% to 15%, which makes SAFIR a very precise method for the assessment of biological parameters in vivo.

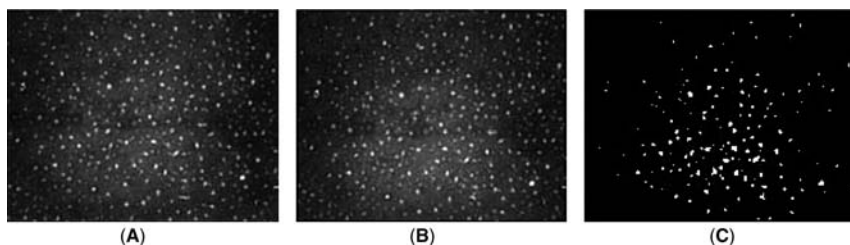


FIGURE 7 (See color insert) Image segmentation: (A) original, (B) grey transformed, and (C) segmented.

TABLE 2 Parameters for Statistical Analysis

Area_red	Mean area of the orange-red porphyrin follicles
Count_red	Number of orange-red porphyrin follicles
Area_green	Mean area of the yellow-green riboflavin follicles
Count_green	Number of yellow-green riboflavin follicles
Area_all	Mean area of all fluorescent follicles
Count_all	Number of all fluorescent follicles

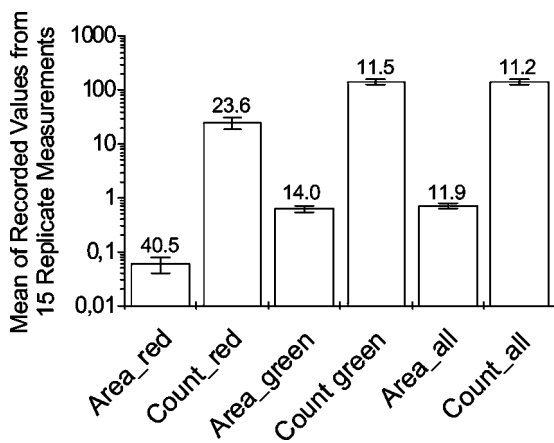


FIGURE 8 Means of recorded values (according to Table 2) using skin analyzing fluorescence imaging recorder from 15 successive replicate measurements on the same matched skin area of a study subject. Data represent mean \pm SD. Numeric values are the calculated coefficients of variation (CV%).

BIOLOGICAL QUALIFICATION OF THE SAFIR FLUORESCENCE IMAGING SYSTEM

BPO has a strong antibacterial and disinfectant activity. It furthermore destroys bacterial PPIX by oxidation. Changes to individual comedones during repeated topical administration of a cream base containing 5% BPO are depicted in Figure 9. The photographs taken in three weeks intervals demonstrate an almost complete disappearance of the red fluorescence during the first three weeks, leaving only green follicles, followed by a reduction in follicle size during the second three weeks of treatment. Thus, both the antibacterial and the comedolytic activities of BPO can be clearly visualized using the SAFIR method.

In a broader study design using several known comedogenic and comedolytic agents, the suitability of the SAFIR method for dermatological studies was assessed. BPO, salicylic acid, lactic acid, acetylated lanoline, and isopropyl palmitate (IPP) are compounds with known effects on human sebaceous follicles. In order to qualify the SAFIR system for the assessment of comedogenic/comedolytic activities of topical formulations, the above compounds were administered to the skin of the upper back of test subjects twice daily over a period of four weeks, followed by a regular recording of comedone size and fluorescence. The results are depicted in Figure 10 and summarized in Table 3 (see also Fig. 3).

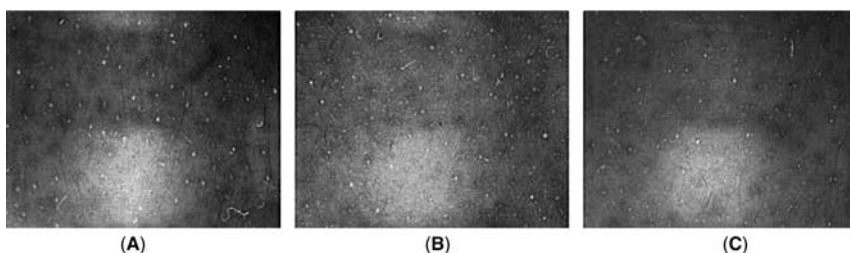


FIGURE 9 (See color insert) Effects of benzoyl peroxide (A) at the beginning (t_0 ; red/green = 60/20), (B) three weeks (red/green = 0/96), and (C) six weeks (red/green = 0/30).

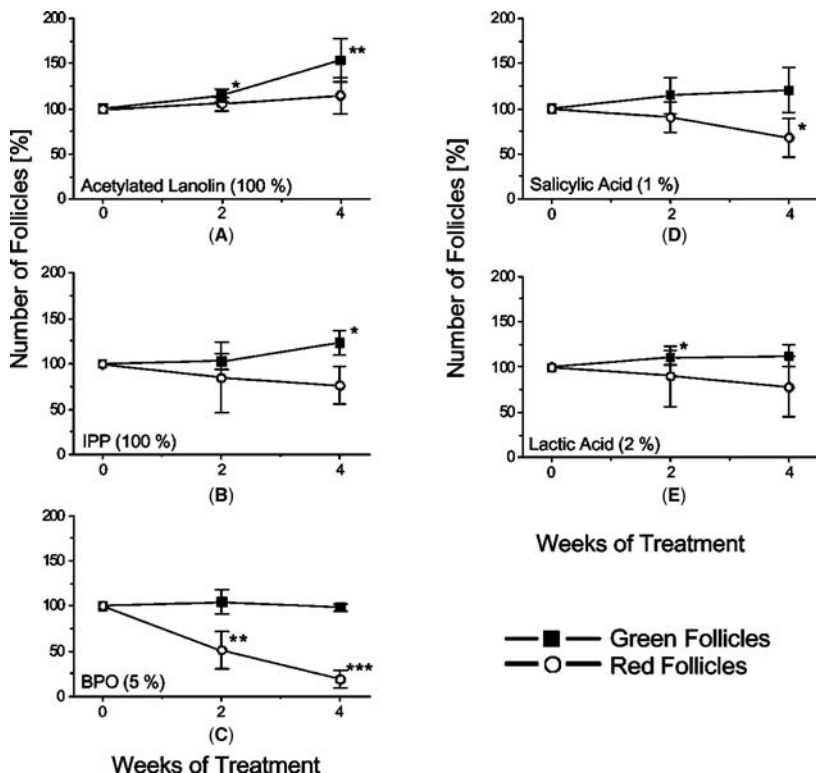


FIGURE 10 Effects of different topical compounds on the number of green and red follicles, as assessed by skin analyzing fluorescence imaging recorder, during four weeks daily topical application. Data represent mean percentages of initial follicle numbers. Mean \pm SD of five volunteers per group. Closed squares: green follicles; open circles: red follicles. * $p < 0.05$; ** $p < 0.01$; *** $p < 0.001$; week X versus week 0.

Our results at least in part disprove previously published data about comedogenicity. As expected, BPO strongly reduced the number of red follicles, but left the number of green follicles unaffected. Conversely, IPP and acetylated lanolin showed a comedogenic effect, as measured by an increase of the green sebum fluorescence. These latter compounds either left the number of red fluorescent follicles unaffected, or caused a slight reduction. Salicylic and lactic acid moderately

TABLE 3 Four Weeks In Vivo Study; Tested Ingredients and Effect on Follicle Fluorescence

Ingredient	% (w/w) in product	Green fluorescence (counts)	Red fluorescence (counts)
Acetylated lanolin	100	Strong increase	Moderate increase
Isopropyl palmitate	100	Moderate increase	Moderate decrease
Benzoyl peroxide	5	No change/effect	Strong decrease
Salicylic acid	1	Moderate increase	Moderate decrease
Lactic acid	2	Minor increase	Minor decrease

reduced the red fluorescence of bacterial origin, but on the other hand slightly increased the green follicle fluorescence. In many cases, green and red fluorescence change in different direction during treatment. Therefore, only the assessment of both kinds of fluorescence will give a comprehensive answer about comedolytic, antibacterial or comedogenic effects on the skin.

Since the SAFIR method allows an assessment of both, the bacterial action as well as the sebaceous activity and size of the pores by different fluorescence qualities, the method was further used to evaluate special cleansing effects claimed as

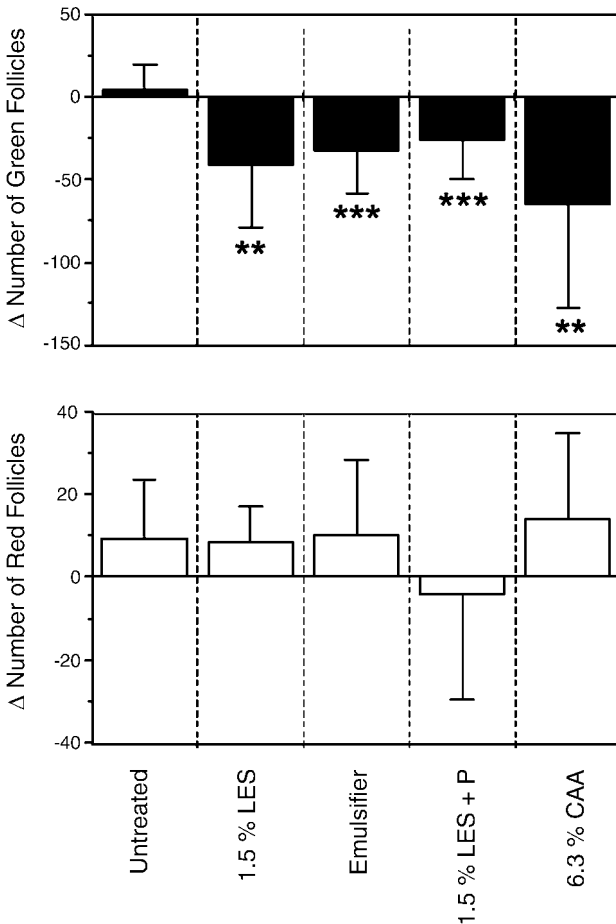


FIGURE 11 Deep pore cleansing effects of different cosmetic detergent formulations, as assessed by skin analyzing fluorescence imaging recorder (SAFIR). Areas of the forehead were washed for 30 seconds with detergent formulations containing either 1.5% of lauryl ether sulphate, with or without peeling particles (P), or 6.3% of cocoamphoacetate, or the corresponding emulsifier mix. Follicle counts were recorded immediately before (t_0) and after the treatment (t_1) using the SAFIR system. Data represent differences of pre- and post-treatment counts for green (closed bars) and red (open bars) follicles, and are compared to the respective counts on a non-treated skin area. Mean \pm SD of 13 test subjects. ** $p < 0.01$; *** $p < 0.001$; treated versus nontreated.

“deep pore cleansing” and “pore refining.” Knowing that detergents are able to solubilize most of skin lipids and lipophilic dirt particles, we followed the hypothesis that the effects of single washing procedures should have an impact on the pore content. A study on 13 test subjects was therefore designed, and three different cosmetic detergent formulations, as well as a corresponding emulsifier mix, were tested in comparison to an untreated site in a special crossover design. The aim of the study was to find out whether the products had a significant cleansing effect and could be differentiated by their different contents of detergents or their formulation. As shown in Figure 11, all the products had a significant cleansing effect after single washing for 30 seconds, as measured by the strong reduction of the green flavin fluorescence. All products, even the emulsifier mix, reduced the fluorescence significantly compared to the untreated control. Due to the testing protocol the influence of pH-shifts and increased moisturization have to be controlled and avoided for best results. In contradiction to the original view, our data indicate that “deep pore cleansing” means that only the outer part of green fluorescent sebum is removed, causing a remarkable increase of the red bacteria fluorescence. This increase is due to a better quantum yield resulting from a lower re-absorption by the upper sebum layers.

CONCLUSION

In our hands, fluorescence imaging of sebaceous follicles using the SAFIR system has become a valuable tool for the assessment of follicular changes due to topical treatment. Effects of new acne medications as well as the safety of new cosmetic products and ingredients can be investigated at an early stage with high accuracy and good predictivity. The use of a sensitive digital camera system with a high optical resolution gives a precise view on the fluorescence properties of individual sebaceous follicles. The use of a neural software for image matching furthermore allows a follow-up of individual follicles over extended periods of time. The fact that both qualities of the fluorescence signal, the yellow-green and the red component, become simultaneously accessible, allows a discrimination of effects relating to the sebum production itself from effects related to the microbial status of follicles. The only limitation of this method lies in the fact, that the fluorescence signals can be modified by variable physical conditions of the skin like the degree of melanization, pH, or dryness of the skin. These variable factors, which may change between individual measurements, have to be taken into account during measurement and data analysis.

Taken together, the new SAFIR system is able to collect a high density of information on the size and composition of human sebaceous follicles, and to assign them to a time axis. The system enables the researcher to perform kinetic studies on individual follicles and microcomedones and can thus be regarded as an important step ahead in the safety and efficacy assessment of cosmetic products.

ACKNOWLEDGMENT

We would like to thank Prof. Kruse and his coworkers from the University of Magdeburg for the neural image tool.

REFERENCES

1. Kligman AM, Katz AG. Pathogenesis of acne vulgaris. I. Comedogenic properties of human sebum in external ear canal of the rabbit. *Arch Dermatol* 1968; 98:53–57.
2. Kligman AM, Kwong T. An improved rabbit ear model for assessing comedogenic substances. *Br J Dermatol* 1979; 100:699–702.
3. Mills OH Jr., Kligman AM. The follicular biopsy. *Dermatologica* 1983; 167:57–63.
4. Bommer S. Hautuntersuchungen im gefilterten Quarzlicht. *Klin Wochenschrift* 1927; 6:1142–1144.
5. Cornelius CE III, Ludwig GD. Red fluorescence of comedones: production of porphyrins by *Corynebacterium acnes*. *J Invest Dermatol* 1967;49:368–370.
6. Sauermann G, Ebens B, Hoppe U. Analysis of facial comedones by porphyrin fluorescence and image analysis. *J Toxicol – Cutan Ocular Toxicol* 1989; 9:369–385.
7. Pagnoni A, Kligman AM, Kollias N, Goldberg S, Stoudemayer T. Digital fluorescence photography can assess the suppressive effect of benzoyl peroxide on *Propionibacterium acnes*. *J Am Acad Dermatol* 1999; 41:710–716.
8. Sauermann G, Herpens A, Hoppe U. The quantification of comedogenesis and comedolysis by image analysis of fluorescent bacterial porphyrins. Oral Presentation at Regional Meeting of the International Society for Bioengineering and the Skin (ISBS). Lübeck, Germany, 1993; 4:23–25.
9. Sauermann G, Herpens A, Hoppe U, Kligman AM. A novel fluorometric method to investigate sebaceous glands in humans. In: Frosch PJ, Kligman AM, eds. *Noninvasive Methods for the Quantification of Skin Functions*. Springer Verlag, 1999:252–271.

Quantifying Skin Ashing Using Cross-Polarized Imaging

Robert Velthuisen, Helene Santanastasio, and Srinivasan Krishnan

Unilever Research and Development, Trumbull, Connecticut, U.S.A.

INTRODUCTION

“Ashiness” is a term frequently cited by darker-skin consumers when describing skin surface conditions associated with dryness and a concomitant loss of natural skin shine. Ashen or ashing skin is often used in reference to body sites such as the elbows and knees. On these sites, the discoloration or whitening observed at the grooved surface is a predominant visual feature.

Dry skin is associated with a low water content of the outer layers of the stratum corneum, causing a reduction of skin flexibility and dysfunctional desquamation due to loss of enzymatic activity that requires sufficient water (1). Poor desquamation exhibits itself as a disorganization of the outer layers and the appearance of flakes of compacted corneocytes. As a consequence, light reaching the surface of the skin is scattered at multiple disorganized air–tissue interfaces. The visual symptom of dry skin is diffuse surface reflection of uncolored (white) light. Because of its contrast, this is particularly visible on dark skin.

Certain dermatopathological conditions may also give rise to ashen skin. In particular, erythema dyschromic perstans is also described as ashy dermatosis (2). While the methods described here may be applicable to quantifying ashiness in those conditions, we have not evaluated such use.

Novel methods were required to evaluate and develop products targeted to the needs of the dark-skin consumer. A clinical grading scale for general use and building on cross-polarized imaging was first presented by Santanastasio et al., which will be further addressed in this chapter (3). Since then, Uhoda et al. developed a scale, particularly directed at Black Africans, using a method called “ultraviolet-enhanced visualization” (ULEV). The computer methods described below can in principle be adapted for the ULEV images (4). In the following, we will present an algorithm and the training of its parameters to be used with microscope images as an alternative to visual grading, building on the scale developed with cross-polarized imaging.

VISUAL GRADING SCALE

A visual ash scale describing the intensity, pattern, and degree of whitening of a skin surface without flaking was developed and tested by Santanastasio et al. during studies in Brazil and in the United States (3). Female subjects between 18 and 60 years of age and with a skin phototype II to VI were enrolled. The skin phototype was determined on the basis of CIELab readings obtained using a spectrophotometer (CM-2002, Konica Minolta, Ramsey, New Jersey, U.S.A.), and

TABLE 1 Skin Phototype and Corresponding ITA° value

Skin phototype	Sunburn and tanning history	ITA°
I	Always burns easily; never tans	>55
II	Always burns easily; tans minimally	41–55
III	Burns moderately, tans gradually and uniformly (light brown)	28–41
IV	Burns minimally; always tans well (moderate brown)	10–28
V	Rarely burns; tans profusely	–30 to 10
VI	Never burns, deeply pigmented (black)	<–30

Note: Individual typology angle (ITA°) = arc tangent $[(L^* - 50)/b^*] \times 180 \times \pi$.

using Table 1 (5,6). Prior to assessment, subjects acclimated in a temperature-controlled area (70°F, 40–50% relative humidity). Assessments included visual examination and grading as well as imaging with a video microscope (Charm View, Moritex Corp, Tokyo, Japan).

The visual grading scale is tabulated in Table 2 (3). A set of color benchmark photographs for this scale was created to aid the training of observers and to illustrate the scale. For reproduction here, the images are presented in gray

TABLE 2 Visual Ash Grading Scale

Ash grade	Overall visual impression of test area	Description with cross-polarization and magnification
0	No ash or whiteness	No visible whiteness. Skin may appear hydrated, healthy, or plump
10	Traces of white	Traces of white residue of low intensity are scattered within the test site. The skin does not look healthy and may appear dull or hazy
20	Light whiteness, low intensity	Skin lines filled slightly with white residue, creating perceptible white web and/or outlined patches of white, scattered throughout the test site
30	Light-to-moderate whiteness, low intensity	The amount of white residue in the skin lines is increasing. The perception of white web and/or outlined patches/pattern is stronger
40	Moderate whiteness, moderate intensity	All skin lines are visible with moderate intensity of white residue and/or greater areas/patches of white are scattered across the test site. Skin pattern may include deep grooves
60	High whiteness, moderate to high intensity	Significant amount of white residue fills all visible skin lines and/or whiteness starts to branch off the main lines with moderate-to-high intensity throughout the test site
80	High-to-very high whiteness, high intensity	Skin lines heavily filled with white residue and the whiteness spreads beyond lines with high intensity. Outlines of corneocytes may be observed. Skin structure appears damaged.
100	Total ashiness/dryness	All visible lines and areas between them are heavily filled with white residue, the intensity is very high. Physiological changes in the skin are apparent (corneocytes begin lifting).

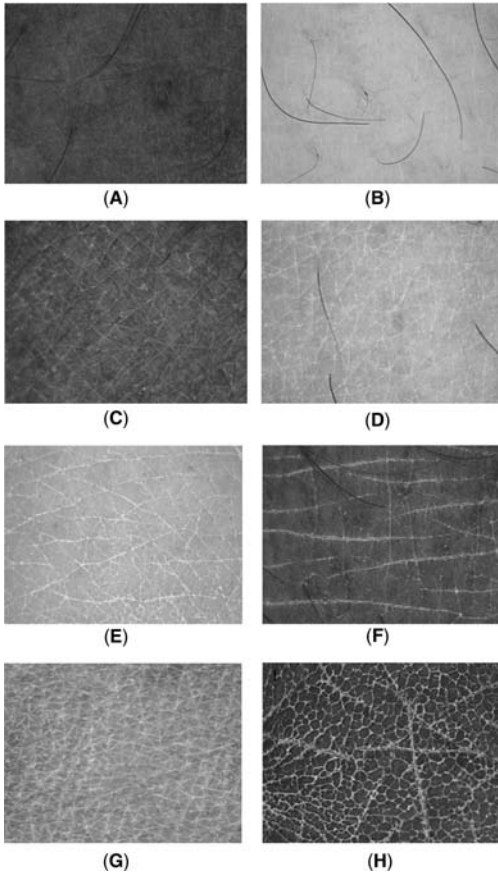


FIGURE 1 Benchmark images of the ash scale descriptors, presented here, in gray scale. **(A)** Ash grade 0. **(B)** Ash grade 10. **(C)** Ash grade 20. **(D)** Ash grade 30. **(E)** Ash grade 40. **(F)** Ash grade 60. **(G)** Ash grade 80. **(H)** Ash grade 100.

scale in Figure 1. In the clinical setting, the skin may be visually graded “live,” with the aid of magnification or cross-polarization. Alternatively, the images of the skin captured using the video microscope can be graded. Expert visual grading is independent of skin color.

DIGITAL IMAGE ANALYSIS

While visual grading is a satisfactory and reliable method, it requires a trained expert to carefully evaluate skin or images of the skin. Additionally, in multicenter clinical trials, the total number of images requiring assessment may be prohibitively high for evaluation with the same grader or set of graders. It is therefore useful to develop a method to score ashing automatically from the images. In the following, we will describe the algorithm, the training of its parameters, and evaluation of such method.

In the cross-polarized video microscope images, ashiness is represented by white lines or, in the more severe cases, by white areas. In the digital image, this corresponds to elevated pixel values potentially reaching the 8-bit maximum of

255 in all three-color channels. In addition, the spatial distribution of the white areas reflects increased levels of ashiness (Table 2). The automatic scoring method is based on these observations.

Training and Test Sets

For the development and evaluation of the digital image analysis, a set of 348 images of subjects with phototypes IV to VI was used. Subjects had no more than a low level of visual dryness, but were not limited in degree of ashing. The images were assessed independently by two experts ash graders. The set was split in the first 240 images as training set and the remaining 108 images the test set. The images were obtained during a test of a liquid shower/bathing product. No subjects in the training set were present in the test set, i.e., the sets were independent.

Background Removal

Ashiness is represented by elevated pixel intensity levels in all three-color channels. However, the background on which the ashiness is visible varies over the image due to lighting nonuniformity (video microscopes tend to have some circular symmetric lighting), and spatially slow changes in skin color. The first step is then to correct for the background variation. We found that a second degree two-dimensional polynomial fit captures much of the variation and can simply be subtracted from each of the R, G, and B color channels (Fig. 2A–C).

Thresholding

Using the training set of images with previously determined ashiness grades, optimal thresholds for each of the three-color channels can be learned with some multidimensional minimization procedure such as downhill simplex method of Nelder and Mead (7). Thresholding converts the color image to a binary image (Fig. 2D). The number of pixels in the binary image is used as a first parameter in the ashiness calculation.

Lines and Flakes

As can be seen in Table 2, ashiness grading involves assessing the amount of white as well as the distribution of white in the image: scattered white dots to light and then heavy lines to, at the edge of visual dryness, flakes. The following method is applied to the binary image obtained in the previous section. A connected component analysis allows the calculation of the size of each of the white areas. While discarding the very small regions, the mean and standard deviation of the log of the white area sizes are taken as measures of line heaviness. The log of the size is used to prevent a single or few heavy lines to affect the estimate disproportionately.

Regression Analysis

Using the number of pixels in the thresholded image, and the mean and standard deviations of the log of the white area sizes as independent variables, a linear fit to the image-ashing grades yields the coefficients that allow the calculation of the ashiness grade on a new image without the intervention of a trained grader.

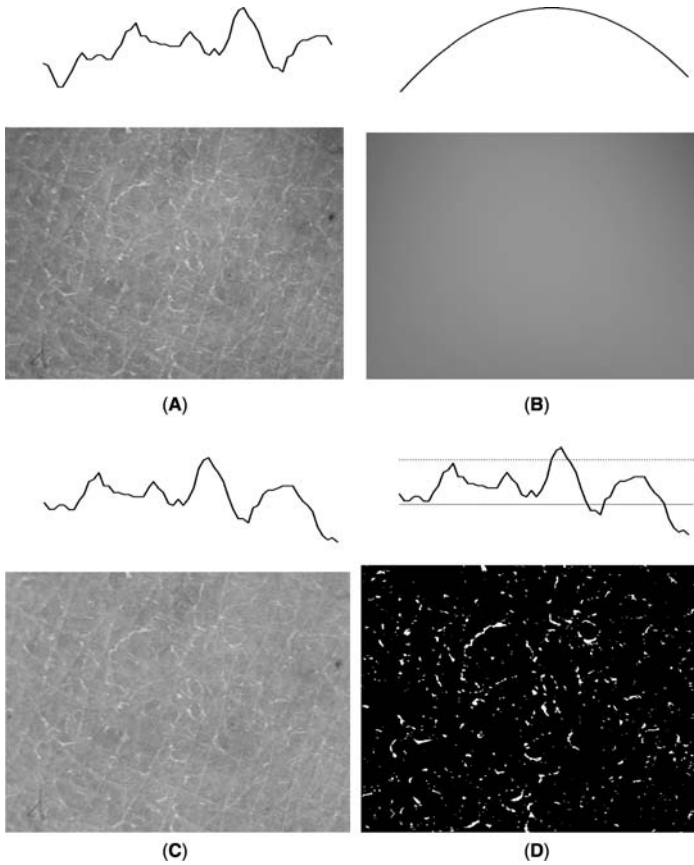


FIGURE 2 Illustration of the thresholding procedure. The two horizontal lines in Figure 2D represent the zero-level (*solid*) and the threshold value (*dotted*). (A) Source image. (B) Background. (C) Image after background removal. (D) Binary image after three-channel thresholding.

The final ashiness calculation program was coded in interactive data language (Research Systems, Boulder, Colorado, U.S.A.).

RESULTS

The ashing program was tested both on the training set ("apparent error") and on the training set of 108 images. The ash grades corresponding to each of the images were used to calculate accuracy. In addition, measures of product effect were compared between the grades and the computer scores. Interobserver variability was calculated as the standard deviation of the differences between the grades of the two graders. The accuracy of the computer program was calculated, using the differences with the average of the two graders. Comparisons were made to the interobserver variability. In the following, the accuracy of the method is expressed in two ways: the linear relationship between visual and computed grade (Pearson correlation R) and the histogram of errors, together with the mean and standard deviation of differences.

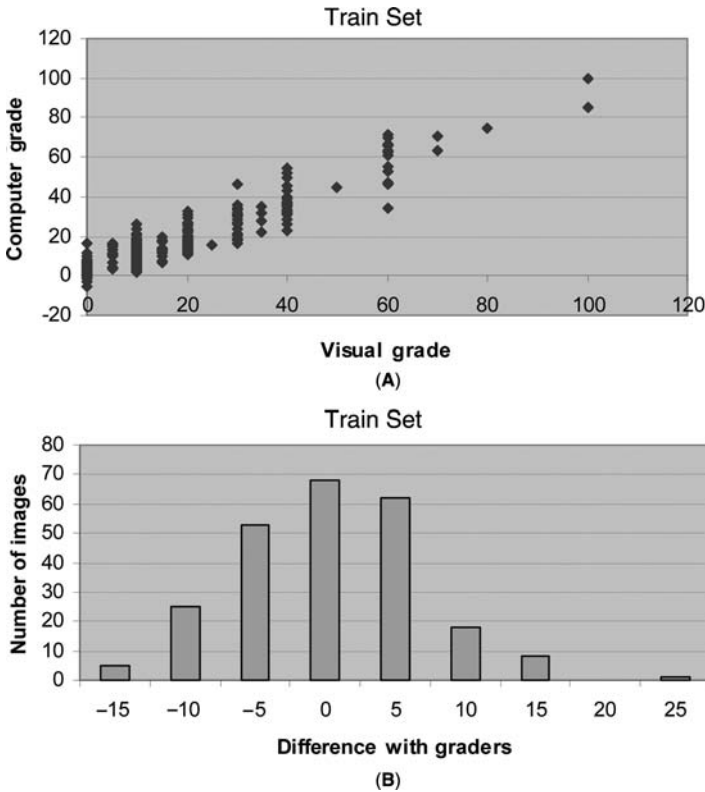


FIGURE 3 Comparison of calculated ashiness grades with expert visual grades using the train set ("apparent error"). (A) Linear relationship ($R=0.93$); (B) histogram of errors (mean 0.002, standard deviation of errors 6.6).

Apparent Error: Error on the Training Set

Figure 3 shows the accuracy of the computer program on the training set of 240 images. The computer scores are compared to the averages of the two expert graders. The relationship is clearly linear with a correlation coefficient of $R=0.93$. The histogram of errors in Figure 3B shows that the computer algorithm is usually very close to the graders. Because the parameters of the algorithm were learned on this training set, the average error is almost 0. The standard deviation of the differences in Figure 3B is 6.6.

The same comparisons can be made between the two graders. Table 3 summarizes the results on the computer versus average comparisons, and grader one versus grader two. On the training set, the two graders are somewhat different (average grade difference is 1.2), and their differences have a standard deviation of 4.2. The standard deviation of differences with the computer grading is therefore almost as good as individual graders.

Performance on the Test Set

Figure 4 and Table 3 list the results on the test set of 108 images, more. While the two expert graders agree strongly with each other on this set than on the training

TABLE 3 Results of Comparisons Between Graders and Computer with Graders

Data	N	Variability	Pearson's <i>R</i>	Mean of differences	Standard deviation of differences
Training set	240	Intergrader	0.97	1.208	4.2
		Grader computer	0.93	0.002	6.6
Test set	108	Inter-grader	0.99	0.648	2.5
		Grader computer	0.89	8.077	7.6
Product effect 2 hr	96	Intergrader	0.95	-1.354	5.7
		Grader computer	0.88	-2.301	8.4

set, there is an offset in the computer assessment. The standard deviation of the difference is comparable to that in the training set.

Product Effect: Two Hours After Wash

Product effect is the change in ash grade between baseline and at two hours after wash. Usually the wash reduces the ash level due to a combination of exfoliation of

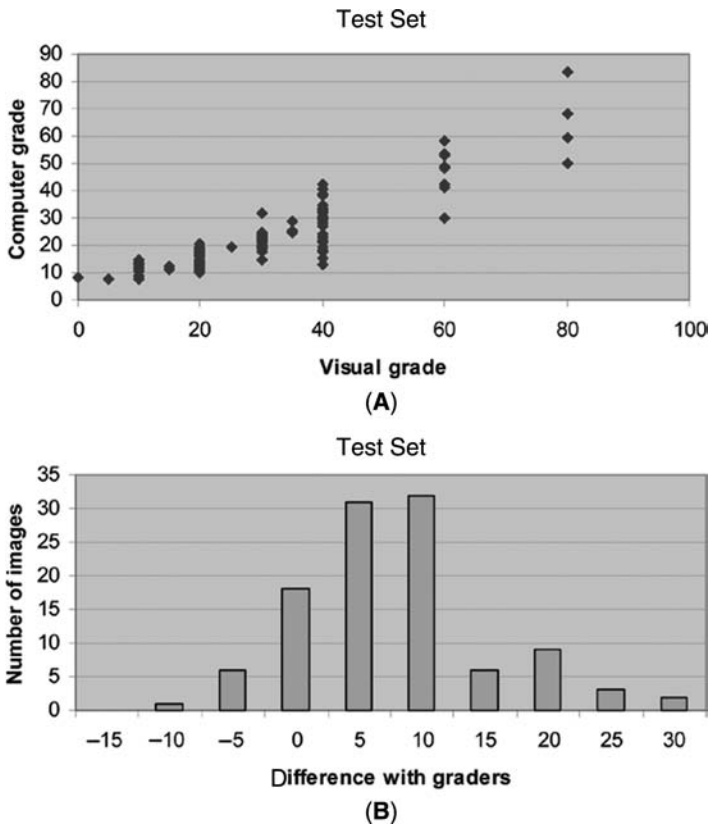


FIGURE 4 Comparison of calculated ashiness grades with expert visual grades using the independent test set of 108 images. (A) Linear relationship ($R=0.89$); (B) histogram of errors (mean 8.1, standard deviation of errors 7.6).

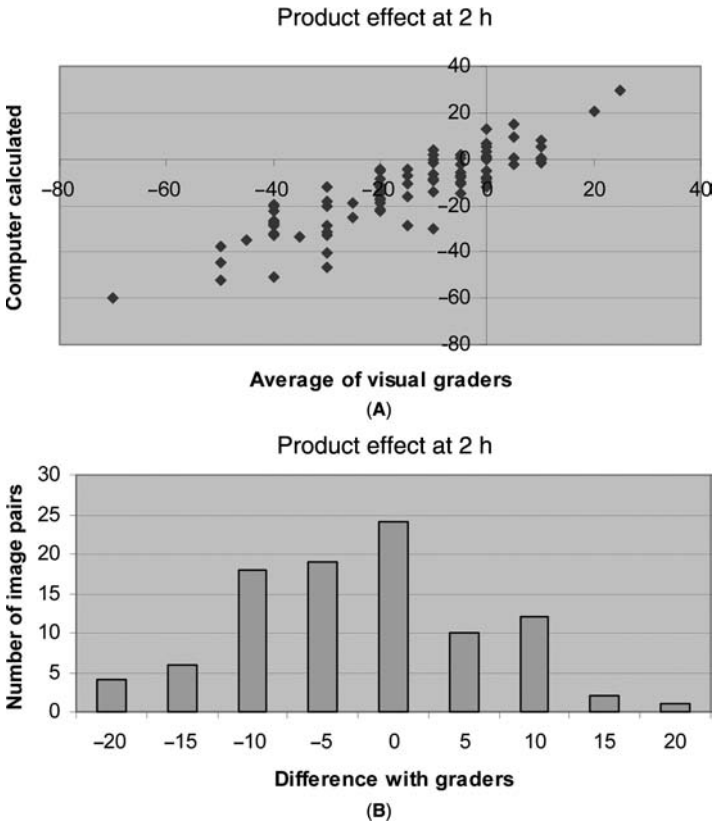


FIGURE 5 Comparison of product effect from computer ashiness grades versus expert visual grades using 96 image pairs. **(A)** Linear relationship ($R=0.88$); **(B)** histogram of errors (mean -2.3, standard deviation of errors 8.4).

loose corneocytes and flakes and hydration of the skin surface. The effect is strongest for very ashen skin. In the total set of 348 images, 96 pairs of baseline and two-hour postwash images are available. As shown in Table 3 and Figure 5, the accuracy of the computer algorithm to assess product effect is presented analogously to the previous sections. As expected, the standard deviations of the differences have both increased because the assessment of product effect requires two ash grade assessments. The computer error is again comparable to the disagreement between the two expert graders.

DISCUSSION AND CONCLUSIONS

A computer algorithm was developed to automatically assess the ash grade of a subject in the absence of a trained visual grader. The computer program calculates the grade from a captured video microscope image. The parameters for the algorithm were learned from a training set. The results show that the algorithm works well to assess ashiness as well as product effect.

Video Capture

The accuracy on the test set was less than on the training set. While such decrease is to be expected, a careful analysis of the images hints at the possibility that some drift may have occurred in the image capture. The images captured by the charm view (or other video microscopes) can be transferred to the computer by a video capture device, e.g., Belkin F5U208 USB Video Capture Device (Belkin Corporation, Compton, California, U.S.A.). Such devices capture the images through the TWAIN interface (8), which is an image capture API for Microsoft Windows and Apple Macintosh operating systems. An image capture software program (e.g., AcdSee, ACD Systems, Victoria, British Columbia, Canada) communicates through the TWAIN interface. Generally such software packages provide controls that allow adjustments to get satisfactory images. In particular, these controls allow gain settings to get acceptable intensity images (not too dark and not saturated). These settings will affect the optimum thresholds for the purpose of ashiness calculations. It is therefore necessary to fix the settings on any video capture system to learn the parameters for application of this method. The images in the training and test sets were all acquired with the same settings of the acquisition software, but some drift may still have occurred as indicated by a slowly increasing image intensity. When using this method for clinical purposes, it is recommended to use a standard reference material [e.g., a Gretag-Macbeth color checker chart (Gretag-Macbeth, Regensdorf, Switzerland)] to check for unintended changes in image acquisition. Ideally, a standard would be visible in each image, although practical implementation may not be straightforward.

Phototype

Ashing is a condition that is most prevalent in the darker consumer. The training and test images were therefore acquired on subjects with phototype IV to VI. The method has also been applied to lighter-skinned subjects. From those tests, it is apparent that while ash grading by experts can reliably be done, the image analysis would need to be adjusted for subjects with lighter skin. This is partly due to a very limited dynamic range of the captured images, but also because the ashiness has less contrast with the light skin.

The results show that the computer algorithm performs quite well, comparable to highly trained and validated visual graders. The capture of the images and the assessment of the ash grade are easy and fast, and can be used without taking time from clinical graders. This algorithm may be useful in settings where capture and assessment may be integrated, for example, at a cosmetics counter, or when screening subjects for clinical studies. In addition, the method can be applied in clinical studies to assess the efficacy of products designed to reduce skin ashing.

ACKNOWLEDGMENTS

This work has been completed with help from Junqing Chen, Unilever R&D Trumbull.

REFERENCES

1. Rawlings AV, Matts PJ. Stratum corneum moisturization at the molecular level: an update in relation to the dry skin cycle. *J Invest Dermatol* 2005; 124(6):1099-1110.
2. Schwartz RA. Erythema dyschromicum perstans: the continuing enigma of Cinderella or ashy dermatosis. *Int J Dermatol* 2004; 43(3):230-232.

3. Santanastasio H, Zhang SL, Velthuisen RP, Krishnan SS, Shah P. Establishment of Clinical Methodology to Quantify Skin Ashing. 9th ed. Denmark: Blackwell Munksgaard. 2003; 194.
4. Uhoda E, Pièrard-Franchimont C, Petit L, Pièrard G. Skin weathering and ashiness in black Africans. *Eur J Dermatol* 2003; 13(6):574–578.
5. Pièrard GE. EEMCO guidance for the assessment of skin colour. *J Eur Acad Dermatol Venereol* 1998; 10(1):1–11.
6. Pathak MA, Fanselow DL. Photobiology of melanin pigmentation-dose-response of skin to sunlight and its contents. *J Am Acad Dermatol* 1983; 9(5):724–733.
7. Nelder JA, Mead R. A simplex method for function minimization. *Comp J* 1965; 7(4): 308–313.
8. <http://www.twain.org>

Imaging of Pore Size and Sebum Secretion by Sebumtape During Treatment for Skin Oiliness

Enzo Berardesca

San Gallicano Dermatological Institute, Rome, Italy

Claudia Rona

Department of Dermatology, University of Pavia, Pavia, Italy

M. B. Finkey and Yohin Appa

Neutrogena Corporation, Los Angeles, California, U.S.A.

INTRODUCTION

Pores, the openings on the skin surface of sweat glands, sebaceous glands, and hair follicles give the skin its texture. Pores are most obvious on the nose, nasolabial area, and chin where the oil glands are concentrated. There are about 400 to 900 pores/cm² of skin on the face (1). Not surprisingly, individuals with enlarged pores have an intense interest in altering the condition, which is regarded as unappealing. Because of genetic predisposition of physiology, it has been the understanding in the dermatological community that pore size cannot be altered (2). While this is true, surface impression of pores can be minimized by effective exfoliating treatments. We have presented findings from an evaluation of a facial treatment containing retinol and glycolic acid indicating alteration of perception of pores both by a dermatologist and the subjects themselves (3). The objective of this study was to critically examine the ability of the retinol-glycolic acid facial treatment to effect pore-size impression and sebum secretion.

MATERIALS AND METHODS

Thirty-eight women, aged 18 to 35, completed this eight-week, full-face, double-blind study. Inclusion criteria specified: Fitzpatrick skin Type I-III, in good general health, oily/rough skin with visible pores, discontinuance of products in the categories of hydroxy acids and retinoids prior to study initiation. The retinol-glycolic acid facial treatment was applied twice daily.

An ultraviolet (UV) camera (Visioscan, Courage & Khazaka, Kohln, Germany) was utilized to capture pore-size impression at baseline and following eight weeks of treatment. Measurements of changes in light transmission, induced by sebum during a 30-second period on a small plastic template (Sebuffix, Courage & Khazaka, Kohln, Germany) applied between the skin and camera probe, were taken. Sebum output was captured as distinct droplets with the size of the droplets reflecting amount of sebum and the number of droplets depicting the number of active pores. These were visualized in digital images that were then quantitated by image analysis software (National Institute of Health Image for Macintosh).

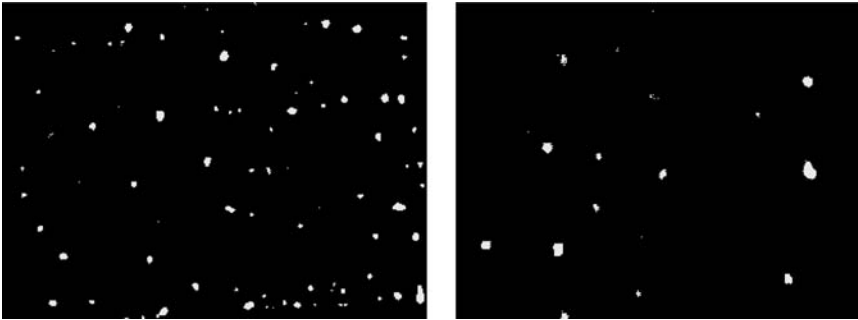


FIGURE 1 Ultraviolet camera photos visualize distribution of pores and related sebum output before and following eight weeks of treatment—Subject “29.”

Silicon replica impressions of pores were taken at baseline and at week 8 to capture pore refinement. Following swabbing the skin with alcohol, replicas were made using a silicone material (Silflo, U.K.) adjacent to the right nasolabial fold and then examined at 20X magnification.

Hydration, distensibility, and elasticity were instrumentally measured at all time points following a 30-minute acclimation period in a controlled environment with the relative humidity maintained at less than 50% and temperature maintained at $68^{\circ} \pm 2^{\circ}\text{F}$. Hydration was measured by corneometry (Corneometer 820–825, Courage & Khazaka, Kohn, Germany) on the fleshy part of the left cheek; distensibility and elasticity were measured by cutometer (Cutometer SEM 575, Courage & Khazaka, Kohn, Germany) on the left temple, approximately midway between the corner of the eye and the hairline.

At baseline, weeks 2, 4, and 8, a dermatologist visually evaluated pore size, fine lines, sallowness, roughness, clarity, and tone (10-point linear scale: 0 = absence, 9 = high degree). Subjects were monitored for erythema, edema, scaling, tightness, itching, and burning.

Finally, subjects provided self-assessment of pores and other efficacy attributes at weeks 2, 4, and 8 of the study.

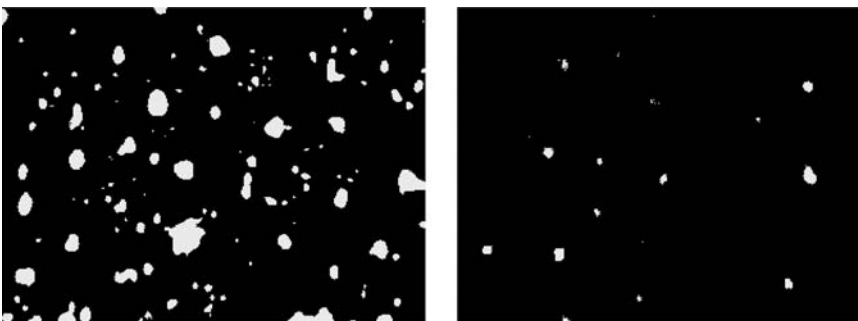


FIGURE 2 Ultraviolet camera photos visualize distribution of pores and related sebum output before and following eight weeks of treatment—Subject “49.”

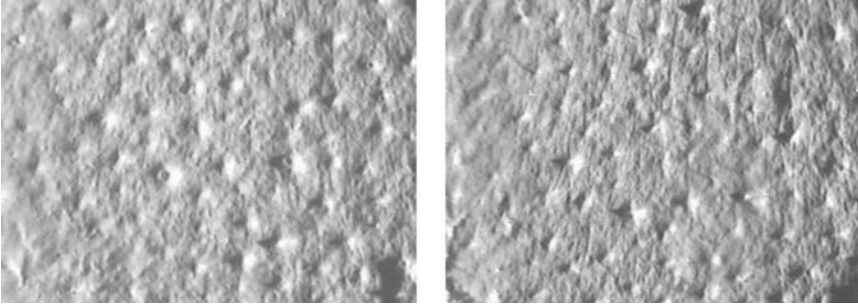


FIGURE 3 (See color insert) Silicone replicas capture pore refinement at baseline and eight weeks—Subject “29.”

RESULTS

Instrumental Evaluation

Reduction in sebum secretion activity is readily demonstrable by the images (Figs. 1 and 2). Statistical analysis (*t*-test) indicates a significant difference between the baseline and week 8 ($p < 0.007$) in the sebum output and distribution/size by quantitation of the sebum droplets using image analysis. The replicas depicting the microrelief and microtexture of the skin surface illustrate the refinement of the pores (Figs. 3 and 4). The figures shown here from two subjects are illustrative of the type of changes noted in the study. Significant improvements were determined as soon as week 2 for the measurements of hydration and distensibility. At the week 8 time point, elasticity and roughness were significantly improved (Unpublished data).

Dermatologist Assessment

Dermatological evaluation indicated a steady decrease in overall pore size throughout the study with a statistically significant difference (*) after eight weeks of use (Fig. 5). Significant improvements were noted from baseline for the attributes of fine lines and sallowness. Mean scores for clarity, tone, and roughness decreased after eight weeks of use (Table 1). The test material was well tolerated in terms of irritation.

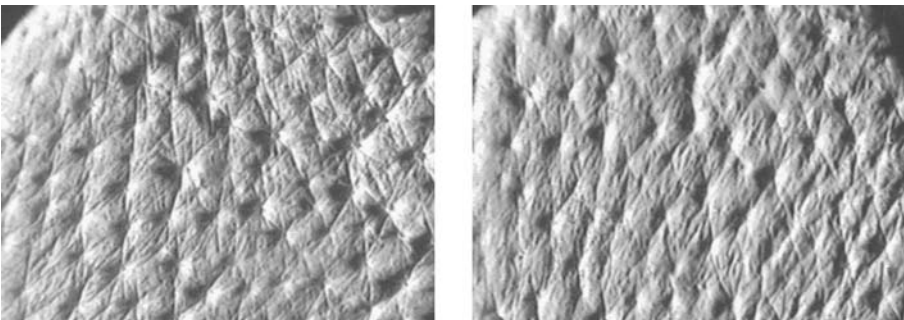


FIGURE 4 (See color insert) Silicone replicas capture pore refinement at baseline and eight weeks—Subject “49.”

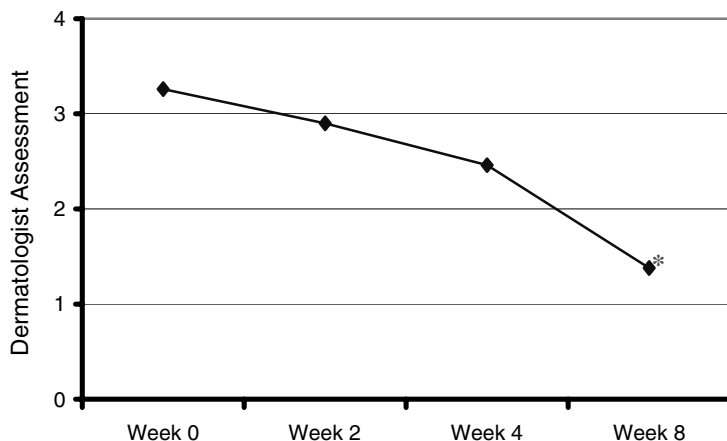


FIGURE 5 Pore impression.

Subject Self-Perception

Subjects perceived a reduction in pores size impression following eight weeks of product use, which supports the objective instrumental findings and the dermatological evaluations (Fig. 6). The test material was very well received for other efficacy attributes such as texture, clarity, and gentleness (Unpublished data).

DISCUSSION

This study focuses on the effects on skin texture and sebum secretion induced by an eight-week application of a product containing retinol and glycolic acid, an alpha hydroxy acid (AHA). Retinoids, and, in particular, retinol and retinoic acid, have been used for some time in the treatment of acne. Their application reduces desquamation as well as reduction in sebum secretion and comedone size (4,5). AHAs act on keratinocytes terminal differentiation and desquamation. They correct keratinization abnormalities (stimulate cell turn over or normalize it when excessive), and change skin appearance by diminishing aging signs (wrinkles, spots, texture, and pores). When applied to the skin, AHAs reduce calcium ion concentration in the epidermis and remove calcium ions from cell adhesion by chelation. This produces a loss of calcium ions from the cadherins of desmosomes and adherens junction, thereby disrupting cell adhesion itself and promoting

TABLE 1 Mean Scores Clinical Assessment

Attribute	Baseline	2 weeks	4 weeks	8 weeks
Appearance of pores	3.26	2.90	2.45	1.38 ^a
Fine lines	2.42	2.26	1.63	0.76 ^a
Swallowness	1.93	1.34	1.01	0.37 ^a
Clarity	6.03	6.40	6.79	7.49
Tone	6.72	6.86	6.93	7.29
Roughness	0.53	1.17	0.87	0.32

^aSignificant decrease ($p \leq 0.05$) compared to baseline.

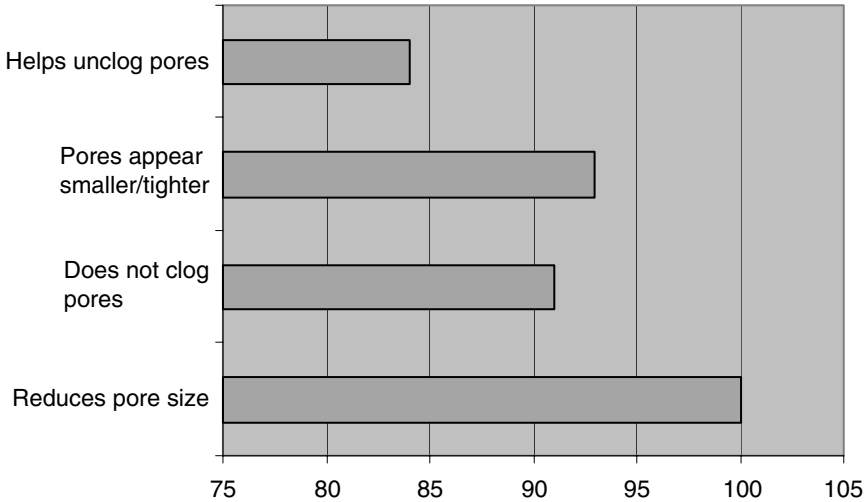


FIGURE 6 Subject self-perception percentage agreement.

desquamation and skin renewal giving rise to a young-looking skin (6). Thus, both retinol and AHA's play a role in revitalizing the skin surface.

A UV photography technique was used to capture the changes in pores. This technique is a modification of the Sebutape[®] method, introduced in 1984, which provides a reliable means of monitoring sebum excretion rate and output of individual pores. Disadvantages of the Sebutape method are the temperature storage requirements of the tape itself and ability to light specimens homogeneously for capturing images (7). The UV photography technique provides a refinement of the Sebutape method having the advantages of faster quantification and generation of digital images easily interfaced with other software.

The data show a significant reduction of pores size ($p < 0.007$) that was corroborated by the dermatologist and subjects. In addition, significant improvements in skin hydration, distensibility, elasticity, roughness, fine lines, and sallowness were noted.

CONCLUSIONS

The UV camera sebum output technique and silicone replicas together provide an objective means of quantifying and capturing pore-size refinements. The retinol/glycolic acid facial treatment refines pore size and reduces skin surface sebum output. The facial treatment provided additional significant benefits to revitalize photodamaged skin.

REFERENCES

1. Montagna W. The sebaceous glands in man. In: Montagna, Ellis, Silver, eds. *Advances in Biology of the Skin*. Vol. 4. Oxford: Pergamon Press, 1963:19-30.
2. Berger P. *Save Your Skin*. Melbourne, Australia: MacMillian Publishing, 1981:15-16.

3. Leyden JJ, Grove G, Finkey MB, Barokovic S, Asuncion AG, Appa Y. Clinical evaluation of a stabilized retinol and glycolic acid treatment for improving skin condition. 55th Annual Meeting of the American Academy of Dermatology, March 2000.
4. Orfanos CE, Ehlert R, Gollnick H. The retinoids: a review of their clinical pharmacology and therapeutic use. *Drugs* 1987; 34:459–503.
5. Morel P, Vienne MP, Beylot C, et al. Clinical efficacy and safety of a topical combination of retinaldehyde 0.1% with erythromycin 4% in acne vulgaris. *Clin Exp Dermatol* 1999; 24(5):354–357.
6. Wang X. A theory for the mechanism of action of the α -hydroxy acids applied to the skin. *Med Hypoth* 1999; 53(6):380–382.
7. El-Gammel C, el-Gammel S, Pagnoni A, Kligman AM. Sebum absorbent tape and image analysis. In: Serup J, Jemec GBE, eds. *Handbook of Non-invasive Methods and the Skin*. Boca Raton: CRC Press, 1995:518–520.

Utilization of a High-Resolution Digital Imaging System for the Objective and Quantitative Assessment of Hyperpigmented Spots on the Face

Kukizo Miyamoto

Department of Dermatology, School of Medicine, The University of Tokushima, Kuramoto-cho, Tokushima, and Research and Development, Personal Beauty Care, Tokushima, and Procter & Gamble Company, Higashinada-Ku, Kobe, Japan, and Procter & Gamble Company, Cincinnati, Ohio, U.S.A.

Hirotsugu Takiwaki

Department of Dermatology, School of Medicine, The University of Tokushima, Kuramoto-cho, Tokushima, Japan

Greg G. Hillebrand

Procter & Gamble Company, Higashinada-Ku, Kobe, Japan, and Procter & Gamble Company, Cincinnati, Ohio, U.S.A.

Seiji Arase

Department of Dermatology, School of Medicine, The University of Tokushima, Kuramoto-cho, Tokushima, Japan

INTRODUCTION

Hyperpigmentation is one of the key phenomena observed on photo-damaged skin that has been exposed to sunlight for long term (1). Of particular concern, from a cosmetic point of view, are the common benign brownish hyperpigmented spots of the middle-aged and elderly, namely solar lentigo (2), as they can detract from overall skin appearance (3). Although not related to sun-damaged skin, ephelides (freckles) and postinflammatory hyperpigmentation (frequently caused by acne) are also scattered, brownish hyperpigmented spots of concern, especially to young adults. These hyperpigmented spots are common skin lesions for all peoples of the world, but are of particular concern for those of the Asian descent (4–8). As expected, therefore, cosmetic formulations claiming efficacy in skin lightening and reduction of hyperpigmented spots are popular products in Asia. Frequently, however, clinical trials to evaluate the effects of these skin-lightening ingredients have been evaluated by inspection, as we do not have reliable systems for measuring the degree of hyperpigmented spots of the face in an objective and quantitative manner. We developed here a highly reliable image analysis system to measure the total area of hyperpigmented spots and skin color tone in a wide area of the face. To quantify overall improvement of the hyperpigmented spots by application of a skin-lightening product, we conducted split-face clinical studies using this system.

MATERIALS AND METHODS

Participants

A total of 120 healthy Japanese females aged 25 to 60 (mean age: 41.7 years), who had more than 10 small-to medium-sized hyperpigmented spots (epheledes, solar lentigines, or postinflammatory hyperpigmentation) were enrolled in the study, after being screened by a dermatologist. They were accompanied with no inflammatory acne, and no history of being treated with medical or over-the-counter preparations for skin lightening or acne at least for six months before that time. They were asked to refrain from using any skin care products other than the assigned test materials, and to avoid sun exposure as much as possible. They were informed and consented in writing regarding the study procedures.

Test Products and Design of Treatment

The test products used in this study were (i) skin-lightening moisturizer (SLM) containing 3% magnesium ascorbyl phosphate, and (ii) its vehicle. Both test products were packaged into identical 30-mL metered dose pumps labeled with the subject number and side of the face to be applied (right or left), which was determined randomly. A subject, therefore, applied SLM to one side of the face, and the vehicle to the other side. Treatments (approximately 0.3 mL dose per side of face) were continued twice a day (morning and evening) for six months. This clinical study was carried out from February to August 1997. All subjects were then rechecked at six months after discontinuing the treatment, to examine if the efficacy of the treatment still remained. Also, to examine the seasonal variation of the clinical results, three other follow-up studies of up to one month each were repeated with the same protocol and base size of subjects. These three studies were carried out in October 1997, May 1998, and September 1999.

Methods for Evaluation

Digital Imaging System

The facial imaging system used in the present study is described elsewhere. In short, this imaging system is composed of a source of illumination, whose light intensity is controlled with the dimmer, a charge-coupled device (3-CCD) video camera connected to a computer, and a positioning device to accurately align the subject's face. The captured images can be displayed side by side or superimposed upon the other images in order to compare a pair of images. Using a specific algorithm for the image analysis, this system enables us to measure both the total area of hyperpigmented spots (mm^2) and the skin color tone (quasi $L^*a^*b^*$ values) excluding the area of hyperpigmented spots in the region of interest (ROI). The quasi $L^*a^*b^*$ is a color coordinate system that is converted from RGB brightness intensities of picture elements. These values indicate brightness (L^*) and chromaticity (a^* and b^*) that correlate linearly with Communication Internationale de l'Eclairage (CIE)- $L^*a^*b^*$ values.

Image Collection Procedure

Thirty minutes prior to capturing the facial images, subjects cleansed their faces to remove all makeup and sebum and then waited for 30 minutes before image capture in a temperature and humidity-controlled environment (23–25°C, 50–60% relative humidity). Then, subjects placed their faces on the positioning device, and their facial images were taken. A baseline image was taken at the first visit, which was

used for subsequent images to accurately reposition the subject's head. Subjects were evaluated at approximately the same time of the day during the course of the study to prevent any influence of diurnal variation affecting the skin color.

Image Analysis

Before treatment, ROI was manually defined in both left and right sides of baseline facial image of each subject so as to demarcate lateral periorbital region and the cheek. This ROI was copied to all posttreatment images to enable evaluation to be done on the same region of the face. Therefore, differences between images taken before, during, and after treatment were entirely due to changes in skin color or total area of hyperpigmented spots within the ROI. We measured and monitored the change in total area of hyperpigmented spots (mm^2) and that in skin color of the face (quasi $L^*a^*b^*$) excluding the region of hyperpigmented spots. The algorithm and other details of the image analysis procedure is also described elsewhere.

Evaluation by Visual Grading

To compare the results from the image analysis with those from inspection, a visual grading of the severity of hyperpigmented spots was conducted by evaluating the displaying image pairs (before/after treatment) side by side on the computer screen that had a calibration system for color uniformity (BARCO Calibrator[®] Monitor Type 121). Eight judges including a well-trained dermatologist viewed pretreatment (baseline) and posttreatment (one, three, or six months) images of each subject, which were randomly displayed side by side on the calibrated video monitor. Based only on differences in the appearance of hyperpigmented spots in the cheek and lateral periorbital areas, the judges were asked to indicate which of the two images had less noticeable hyperpigmented spots and then to grade the difference between the images on a scale of 1 to 4 as follows:

1. I think there is a small difference.
2. I know there is a small difference.
3. I know there is a moderate difference.
4. I know there is a big difference.

This grading scale was developed based on the result of our preliminary study that the judges tended to give up comparing two images carefully and easily choose the grade for "no difference" when the difference of the two was small. To have more sensitive judgment, we did not include "no difference" statement in this scale. The graded score was assigned a positive (+) if the SLM-treated side was judged to have less noticeable spots, and assigned a negative (-) if not. After all visual inspections were completed, the average of the scores of all judges was then calculated.

Statistical Analysis

As for quasi $L^*a^*b^*$ values and total hyperpigmented spot area, the differences between the SLM and vehicle treatments were statistically compared using student's paired *t*-test, and $p < 0.05$ was considered significant. A nonparametric test (Wilcoxon) was carried out for the analysis of visual grading results.

RESULTS

Subject Accountability

Of the 120 subjects enrolled, 104 completed the full six months of the study (118 completed through three months). Measurements of 101 subjects out of 104 were

rechecked at 12 months. For three follow-up clinical studies, 107 subjects completed the study conducted in October 1997 and 112 and 117 subjects completed the studies conducted in May 1998 and September 1999, respectively. No adverse events occurred in these studies.

Image Analysis Results

Facial Skin Color Excluding Hyperpigmented Spots

There were no significant differences between the mean values of background skin color on SLM- and vehicle-treated sides during the course of the study. Also, there were no significant differences between the mean values of background skin color measured at any two different checkpoints irrespective of treatments, although the L^* values of both sides showed a decreasing trend at one month, and an increasing trend at three months (Table 1).

Area of Hyperpigmented Spots

The mean hyperpigmented spot area was significantly reduced on SLM-treated sides when compared to vehicle-treated sides at any of the one, three, and six months checkpoints. Rates of reduction in the mean hyperpigmented spot area were 6.9%, 14.2%, and 25.9% at one, three, and six months after treatment, respectively, on the SLM-treated side (Fig. 1). There was also significant reduction in the mean hyperpigmented spots area on vehicle-treated side at the six months checkpoint when compared with that of before treatment. A series of actual images from baseline to six months are shown in Figure 2, in which the improvement of hyperpigmented spots can be seen. However, at six months after discontinuing treatment, the mean hyperpigmented spot area returned to nearly the same level as that of before treatment (Fig. 1)

Evaluation by Visual Grading

The mean visual grading scores on SLM-treated side were significantly higher than the scores on vehicle-treated side at all of the one, three, and six months checkpoints (Fig. 3). These results were similar with those from the image analysis. However, there was a small discrepancy between the results obtained by the two methods. Although the difference in the degree of hyperpigmented spots between SLM- and vehicle-treated sides was judged stable after one month by visual grading, the difference became larger at six and three months checkpoints by image analysis. The scores of visual grading by the dermatologist were similar to the averaged scores recorded by other judges without dermatological knowledge.

TABLE 1 Change from Baseline Quasi $L^*a^*b^*$ Values (Mean \pm S.D.) on Skin-Lightening Moisturizer- and the Vehicle-Treated Sides Before and During the Treatment Period

Materials	Change from the			
	baseline	1 mo	3 mo	6 mo
Skin-lightening moisturizer	Quasi L^*	-0.27 ± 0.44	0.78 ± 0.69	-0.04 ± 0.55
	Quasi a^*	-0.03 ± 0.37	-0.15 ± 0.73	-0.02 ± 0.41
	Quasi b^*	-0.11 ± 0.31	-0.02 ± 0.52	0.05 ± 0.47
Vehicle	Quasi L^*	-0.26 ± 0.72	0.96 ± 1.25	-0.20 ± 0.46
	Quasi a^*	0.10 ± 0.37	-0.18 ± 0.45	0.15 ± 0.31
	Quasi b^*	0.03 ± 0.70	0.01 ± 0.53	-0.03 ± 0.45

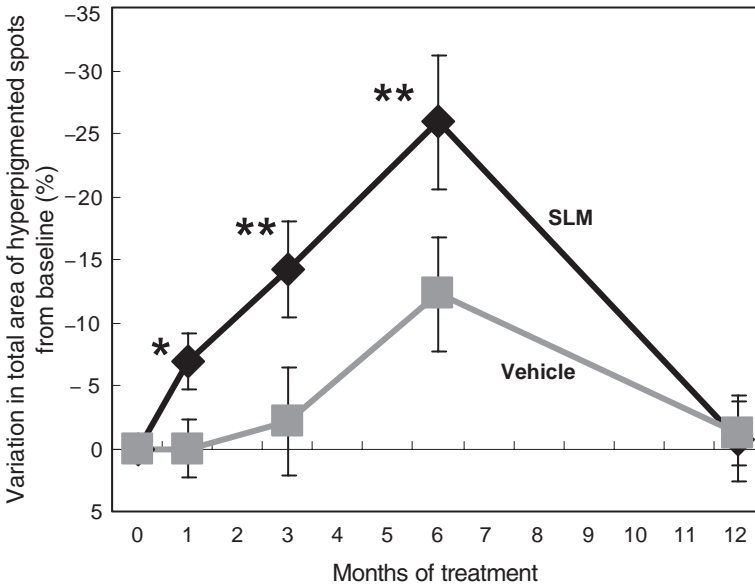


FIGURE 1 Total area of hyperpigmented spots on SLM- and the vehicle-treated sides measured with image analysis before, during, and after treatment (* $p < 0.05$, ** $p < 0.01$: SLM vs. the vehicle). Abbreviation: SLM, skin-lightening moisturizer.

Reproducibility and Seasonal Variation of Test Results

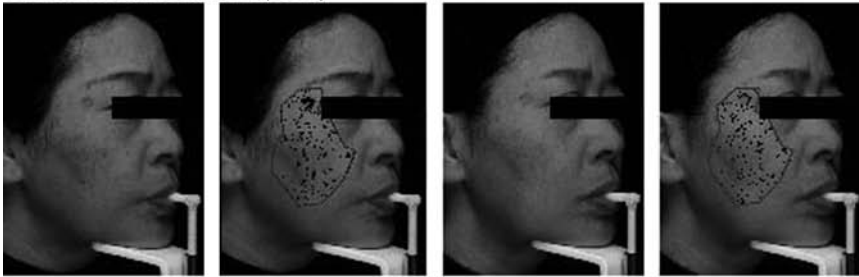
All four clinical studies showed similar results to those of the first study that significant reduction in hyperpigmentation was noted only on the SLM-treated side one month after the treatment, regardless of the seasons when these studies were performed (Fig. 4).

DISCUSSION AND CONCLUSIONS

Most clinical trials of some topical agents, such as tretinoin, for pigmentary disorders of the face in the past have been evaluated by visual assessment (10,11). In general, however, it is difficult to discriminate the small differences in the degrees of hyperpigmented spots on the face in quantitative manner, especially if small spots are scattered in a wide area. The efficacy of ordinary cosmetic formulations claiming skin lightening is usually mild, and, therefore, it may be difficult to determine if these formulations are really effective for pigmented skin lesions. Therefore, objective, sensitive, and reliable methods for quantitative measurement have been required. We developed such a method for evaluation of hyperpigmented spots on the face by using an image analysis system. We also employed a split-face treatment design in the present study to fairly compare test materials and statistically analyze the acquired results.

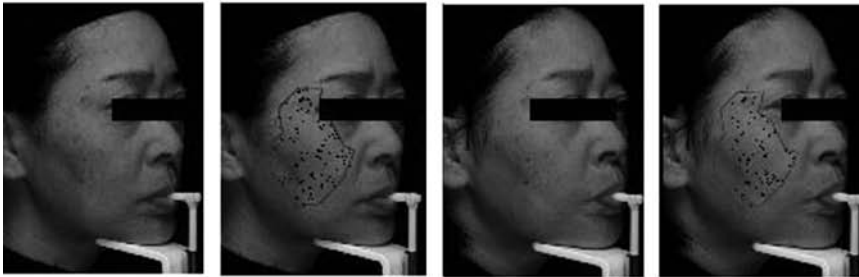
As a result of this study, it was demonstrated that SLM significantly reduced hyperpigmented spots on the face after one month of application, and this efficacy was increased through six months of treatment period. Although we observed a reduction in the total area of hyperpigmented spots, there was no significant change in skin color excluding the hyperpigmented spots during the course of

Test Material Treatment (SLM)



Baseline

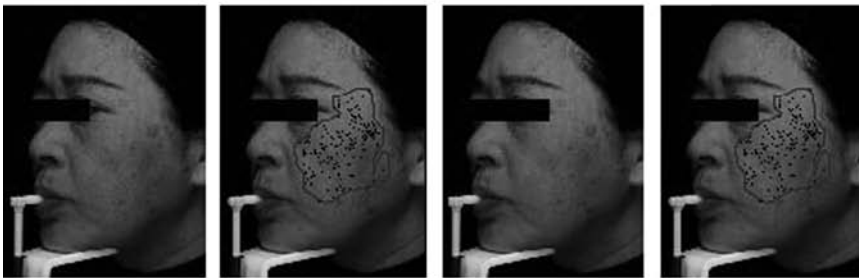
1 month



3 months

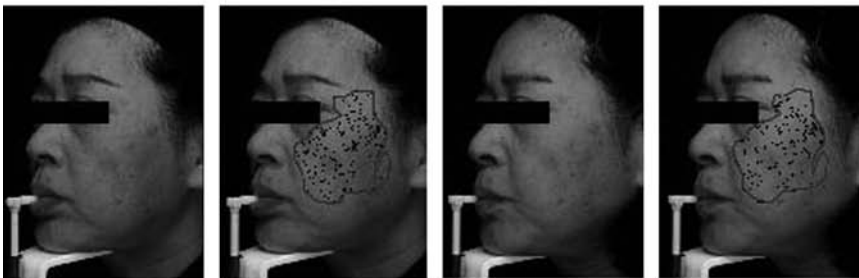
6 months

Respective Control (Vehicle)



Baseline

1 month



3 months

6 months

FIGURE 2 Course of facial images of a subject with overlaid hyperpigmented lesions detected automatically using image analysis.

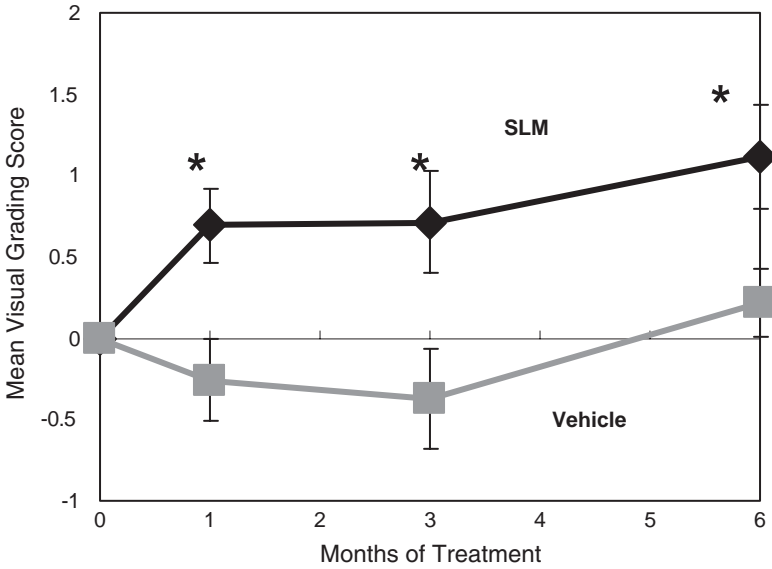


FIGURE 3 Results of visual grading by eight judges (* $p < 0.05$: SLM vs. the vehicle). *Abbreviation:* SLM, skin-lightening moisturizer.

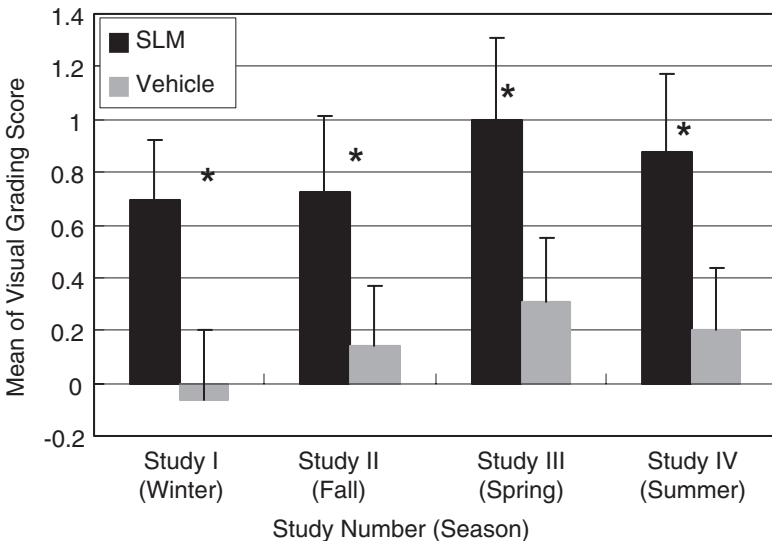


FIGURE 4 Total area of hyperpigmented spots on SLM- and the vehicle-treated sides, measured at before and one month after starting treatment in a series of four subsequent clinical studies (* $p < 0.05$: SLM vs. the vehicle). *Abbreviation:* SLM, skin-lightening moisturizer.

the study. Therefore, it is most likely that the SLM acted in fading out the hyperpigmented spots rather than lightening the overall facial skin color. We obtained similar results over four subsequent clinical studies in four different seasons and subjects, which confirmed the results of the initial study. However, in spite of a significant reduction of hyperpigmented spots during the six months of the treatment, the improvement in hyperpigmented lesions disappeared six months after discontinuing the treatment. Therefore, SLM is probably effective for reducing melanogenesis only during the period of treatment.

In conclusion, we confirmed that our method was sensitive and reliable enough to show the overall improvement of hyperpigmented spots, mainly composed of solar lentigines, by SLM treatment. In spite of small discrepancies between the results by inspection, it is of note that the obtained results were really quantitative and reproducible. As there are already many studies on observing detailed appearances of hyperpigmentation with the video microscope (12–14), the combined use of our facial imaging system as “macro” analysis and a video microscope as “micro” analysis could be the best evaluation method to provide more detailed information on the morphological changes of pigmented spots during a course of treatment.

REFERENCES

1. Breathnach AS, Nazzaro-Porro M, Passi S, Picardo M. Ultrastructure of melanocytes in chronically sun-exposed skin of elderly subjects. *Pigment Cell Res* 1991; 4:71–79.
2. Mehregan AH. Lentigo senilis and its evolutions. *J Invest Derm* 1975; 65:429–433.
3. Castanet J, Ortonne JP. Pigmentary changes in aged and photoaged skin. *Arch Dermatol* 1997; 133:1296–1299.
4. Kligman AM, Willis I. A new formula for depigmenting human skin. *Arch Dermatol* 1975; 111:40–48.
5. Masuda M, Tejima T, Suzuki T, Imokawa G. Skin lighteners. *Cosmet Toilet* 1996; 111:65–77.
6. Kameyama K, Sakai C, Kondoh S, et al. Inhibitory effect of magnesium L-ascorbyl-2-phosphate (VC-PMG) on melanogenesis in vitro and in vivo. *J Am Acad Dermatol* 1996; 34:29–33.
7. Gao X, Chen H, Kligman A. Topical tretinoin for photoaging. The China experience. *J Appl Cosmetol* 1997; 15:77–83.
8. Kligman AM, Grove GL, Hirose R, Leyden JJ. Topical tretinoin for photoaged skin. *J Am Acad Dermatol* 1986; 15:836–859.
9. Miyamoto K, Takiwaki H, Hillebrand GG, Arase S. Development of a digital imaging system for the objective measurement of hyperpigmented spots on the face. *Skin Research and Technology* 2002; 8:227–235.
10. Kimbrough-Green CK, Griffiths CE, Finkel LJ, et al. Topical retinoic acid (tretinoin) for melasma in black patients. A vehicle-controlled clinical trial. *Arch Dermatol* 1994; 130(6):727–733.
11. Fleischer AB, Schwartzel EH, Colby SI, Altman DJ. The combination of 2% 4-hydroxynanisole (Mequinol) and 0.01% tretinoin is effective in improving the appearance of solar lentigines and related hyperpigmented spots in two double-blind multicenter clinical studies. *J Am Acad Dermatol* 2000; 42(3):459–467.
12. Schindewolf T, Schiffner R, Stolz W, Albert R, Abmayr W, Harms H. Evaluation of different image acquisition techniques for a computer vision system in the diagnosis of malignant melanoma. *J Am Acad Dermatol* 1994; 31(1):33–41.
13. Green A, Martin N, Pfitzner J, O'Rourke M, Knight N. Computer image analysis in the diagnosis of melanoma. *J Am Acad Dermatol* 1994; 31(6):958–964.
14. McGregor B, Pfitzner J, Zhu G, et al. Genetic and environmental contributions to size, color, shape, and other characteristics of melanocytic naevi in a sample of adolescent twins. *Genet Epidemiol* 1999; 16(1):40–53.

Index

- 2',7'-bis-(2-carboxyethyl)-5-(and-6)-
carboxyfluorescein (BCECF), 318
- 1,10'-Phenanthroline ruthenium(II)
chloride, 326
- 3D skin surface contour
measurement by
stereoimage optical topometer
(SOT), 191
parameters for, 195–197
- ABCD rule for dermoscopy, 307
- “A” asymmetry assessment, 307–308
color, 308
dark areas evaluation, 308
pigmentation, 307
shape, 307
tuebingen method, 307
- “B” border
- “C” colors, 309
RGB color, 308
- “D” differential structures, 309–310
pattern analysis and identification
of, 309–310
evaluation, 308–309
- Acanthosis, 131
- Acne rosacea, 343
- Acridine orange, 159, 161
- Actinic keratoses (AK), diagnosis of, 344
- Active image triangulation, principle
of, 137–140
- Acute skin irritancy, evaluations of,
400, 401
- Adhesive tapes, 74, 77
- Adipocytes, 418
- Adipose tissue
deficiency, 377
subcutaneous, 380, 381, 382
- Allergic contact dermatitis (ACD), 342
- Alopecia, 281
- Alpha2-adrenergic receptors, 419
- Alpha hydroxy acid
(AHA), 472
- Aluminum-morin fluorescence, 158
- Amino acids as NMF, 396
- Anagen follicles, 276
- AnalySIS (Soft Imaging Software GmbH,
Munster, Germany), 358
- Androgenetic alopecia (AGA) in man,
stages of, 281
- Anisotropy, 267
- Anti-Stokes Raman scattering, 248
- Anticellulite products/ingredients, 379
- Antihistamines, efficacy of, 262
- Antiperspirants, 158, 159
- Apparent diffusion coefficients (APC)
measured, in skin layers, 104
- Argon ion lasers, 153
- Argon–Krypton lasers, 153
- Artificial neural networks (ANNs)
models, 300
motivating factor, 300
nonlinear nature and higher flexibility
of, 301
paradigm in medical applications,
301
- Atopic dermatitis (AD), 291
clinical assessment, 199
dry skin of, 200
measurement by
bioengineering methods, 198,
200, 208
by Corneometer[®], 198, 199, 200
SCORAD index, 198, 200
stereoimage optical topometer,
191, 193
severity, 197–201
- Atopic eczema, resolution of, 291

- Autofluorescence, detection of, 112, 113, 114
- Axillary skin, 160
- Balcar Duolite tungsten light source, 209
- Balcar Fluxlite[®] tungsten light source, 209
- BARCO Calibrator[®], 477
- Basal cell carcinoma, 130, 268, 344
diagnosis, 346
RCM features, 344
- Basal keratinocytes, 341
- Basalioma, image fusion, 23, 27
- Benign lymphadenopathies, 361
- Benign nevi, 131
- Benzoyl peroxide (BPO), effects, 448
- Biopsies, follicular
distribution on face, 73
map of skin, 72–73
orifices, groups, 72
sebum output, 74, 75
- Blistering diseases, 129
- Body mass index (BMI), 383
- Catmull-Rom spline curves, 309
- Cell adhesion
by chelation, 472
loss, 36
- Cell biological applications, 149
- Cellulite, 377, 417
acute, 358
characteristics of subcutaneous, 383
clinical methods, 377
contact thermography, 386
dielectric devices, 382–383
in vivo (video) confocal microscopy, 383–386
lymphography, 381
magnetic resonance imaging (MRI), 379–380
optical coherence tomography, 380–381
PRIMOS (fringe projection), 383
ultrasound, 379
noninvasive techniques, 419–421
laser doppler flussimetry, 420
- [Cellulite]
magnetic resonance microimaging, 421
mechanical properties, 420
plicometry, 421
thermography method, 420
tight circumference measurements, 419
ultrasonography, 420
- pathogenesis, 418–419
precellulite conditions, 418
skin
features, 417–418
peculiarities, 418
symptoms, 417
stage (I–IV), 418
target, 417
- Ceramides as NMF, 396
- Charge-coupled device (CCD), 423
advantages, 424
camera, 112, 137, 327
detectors, 251
- Chinese hamster ovary cells, 123
- Cholesterol sulfate cycle,
epidermal, 47
- Choma Meter CR-200[®], 292
- Chromophore mapping, 435–438, 441
limiting factors in, 425–426
- Coenzymes, NAD(P)H, 112
- Comedogenesis, 73–74, 295
- Comedogenic activity, 446
rabbit ear assay, 447
skin analyzing fluorescence imaging recorder (SAFIR), 448
skin surface biopsy procedure, 447
- Comedolysis, 73–74, 295
- Comedone
components of, 448, 449
red-orange porphyrin fluorescence of, 451
- Communication Internationale de l'Éclairage (CIE) $L^*a^*b^*$ values, 210
correlation between Quasi and, 217
- Confocal fluorescence microscopy, limitations of, 112
- Confocal laser scanning microscopy (CLSM), 53, 112, 187, 250

- [Confocal laser scanning microscopy (CLSM)]
 - epidermal cell nuclei visualization by, 183
 - fluorescence, 149
 - images of stratum corneum layer, 182, 186
 - mean cell size determination by, 188
 - reflectance, 149, 155
 - in skin, 177
 - experiment analysis, 178
 - penetration depth, 178
 - pinhole detection, 178
 - reflectance images, 180, 185, 189
 - TPFM and, 179–180
- Confocal microscopy, 149, 151, 153
 - advantages, 151
 - applications of, 154
 - fluorescence mode of, 151
 - lateral resolution for, 151
 - operating modes, 149
 - reflectance mode of, 149, 151
 - single beam, 153
 - target-specific fluorescence signals by, 158
 - technical realization, 153
 - types of, 153
- Confocal pinhole, 250
- Confocal systems
 - axial resolution in, 151, 155
 - image acquisition in, 153
- Confocal three-dimensional image stacks, 154
- Contact dermatitis, 341–343
- Conventional optical profilometer (COP), 191, 197
 - to measure moon craters, 191
 - and stereoisage optical topometer (SOT), 197, 205
- Corneocytes, 2–4
- Corneocyte-cell-extensions, 59
- Corneodesmosomes, 60, 65
- Corneometer[®], 198–200
- Corticosteroid treatment, of epidermis, 132, 169, 173
- Critical micelle concentration (CMC), 393–394
- Cryofixation, 53, 55
- Cryogenic detector, 99, 105
- Cryogenic skin probes, 108
- Cryoimmobilization techniques, 52, 67
- Cryoprocessing techniques, 52
- Cutaneous melanoma
 - RCM features, 406
- Cuticle cells, 156, 157
- Cyanoacrylate follicular biopsies (CFBs), 71
 - advantages of, 71
 - image analysis of, 72
 - applications of, 72–74
 - types of errors in, 72
 - sample collection of, 71–72
 - as skin surface biopsy, 71
 - uses, 74
- Cyanoacrylate glue, 71
- Cyclobutane pyridine dimers, formation, 123
- Cytoplasmic lamellar bodies, 35, 36

- D-Squame[®], 8, 71, 76, 225
 - advantages of, 81
 - applications, 75–76
 - moisturization efficacy, 78
 - skin irritation, 79
 - collection, 71–72
 - image analysis, 72
 - tape method, 200
- Darier's disease, 4
- Darsa Pro 3000 System
 - Spectrophotometer, 198
- Deoxyhemoglobin, 329
- Derma-Spectrometer[®], 292
- Dermainspect, multiphoton imaging system, 116, 117, 124
- Dermal matrix, deterioration of, 7
- Dermal melanin, in melanoma diagnosis, 438
- Dermal papillae, 171, 341
 - density, 168, 174
- Dermal-epidermal junction, 426
- Dermatoscopy, 17, 18
 - ABCD rule in, 298, 307
 - diagnostic performance, 298
 - melanoma diagnosis, 298
 - telemedical applications, 300
- Dermis and epidermis, sonography of, 189, 363
- Desmosomes, 35, 45

- Desquamation index (DI), 77
- Detectors, in MRI
 - cryogenic, 105
 - highly sensitive superconducting, 105–106
 - pinhole-free, 114
- Detergent, effects on skin, 391
 - direct and indirect, 395–399
 - evaluation methods, 399–401
 - types of, 392
- Diffuse hyperpigmentation, 426
- Digital image analysis, 461, 476–477
 - cross-polarized video microscope images, 461
 - evaluation, 461
 - multicenter clinical trials, 461
- Digital micromirror device (DMDTM), 137
- DNA, damage studies, 123
- Doppler-Optical coherence tomography (OCT), 128, 135
- Downhill simplex method, of Nelder, 462
- Drug screening, in situ, 122, 284
- Dry skin in atopic patients
 - clinical presentation, 289
 - quantification of skin surface, 290
 - resolution of atopic eczema, 291
- Echo signal spectrum, 92
- Echopoor band (EPB), 358
- Echopoor tumor region, 370
- Elasticity, loss of, 7, 13
- Elastin, 188
- Emulsion
 - films, remission confocal laser scanning microscopy (CLSM) imaging of, 156
 - and suspension, 393–394
 - types of, 392, 393
- Endothelin-1/endothelin B receptor cascade, 426
- Enzymes, hydrolytic, 256
- Ephelides, 426
- Epidermal–dermal junction, visualization, 173, 182
 - Epidermal-dermal interdigitation, flattening, 169
- Epidermis, 183, 184, 188
 - barrier homeostasis, 313
 - changes of, 131
 - morphological, 127
 - visible, 129
 - cholesterol sulfate cycle, 47
 - definition by SIAscope model, 515
 - in drug related effects on epidermis, 169
 - electrical capacitance of, 198, 200, 201
 - horny cells, 31, 32
 - hyperplasia, 169
 - hyperproliferation, 343
 - interdigitation of, 174
 - minimal, 171
 - overall, 169
 - thickness, 167
 - variation with age, 169
- Epiluminescence microscopy (ELM), advantages, 17, 22, 27
- Epithelial tumors, 130
- Erythema, 400
 - dyschromic perstans, 459
 - measure of, 199
- Eumelanin/pheomelanin chromophores, 425
- Evaporimeter[®], 225
- Exocytosis, RCM parameters, 343
- Exogenous fluorescent probes, advantage, 112
- Förster resonance energy transfer (FRET), in skin research, 162
- Face, hyperpigmented spots on, 209, 435
- Facial biopsies, 73
- Facial imaging system, 435, 476
 - accuracy and reliability determination, 213
 - areas of hyperpigmented spot detection, 217
 - color calibration, 211, 213
 - components, 210
 - experimental analysis, 209
 - illumination by
 - Balcar Duolite tungsten light source, 209
 - Balcar Fluxlite[®] tungsten light source, 209

- [Facial imaging system]
 - image collection and analysis
 - procedure, 211–213
 - method validation, 213–214
 - quantification of color in, 210–213
 - skin color tone measurement
 - by, 213
 - colorimetric instruments, 217
 - stability, 213–214, 476
 - system calibration, 217
 - white balancing of camera in, 210
- Facial treatment, evaluation, 469
- Facial wrinkling, 435
- Fibroblasts, cytoplasmic structures
 - of, 161
- Fibrous histiocytoma, 130
- Filaggrin, digestion of, 35, 47
- Fluorescence
 - based O₂-fluxoptode, 326
 - detection of, 115
- Fluorescence emission spectra, of
 - riboflavin and protoporphyrin IX, 450–454
- Fluorescence imaging system, 152, 451–454
 - parameters, 453
 - skin analyzing fluorescence imaging recorder, 450–454
- Fluorescence lifetime image (FLIM), 115, 316–320
 - development, 318
 - pH measurements, 319
 - Fluorescence life-time imaging (FLIM), skin, 149
- Fluorescence recovery after photobleaching (FRAP), 162
- Fluorescent dyes, for skin, 158, 159, 161
- Fluorescent proteins, 149
- Fluorophores
 - advantages, 111
 - blue/green emitting, 114
 - endogenous, 115, 177, 121
 - exogenous, 111, 112
 - intrinsic skin, 162
 - monitoring, 115
- FOITS system, 137
- Follicle(s)
 - fluorescence, effect on, 455
 - orifices, 264
- [Follicle(s)]
 - activity of sebaceous, 73, 75
 - density, 12
- Forearm controlled application
 - technique (FCAT), 406
 - forearm image from, 408
 - of skin hydration, 406, 408
 - of soap versus syndet bars, 408
- Fourier transform (FT) Raman spectroscopy, 249
- Frame grabber card, 298
- Fringe projection method, 331
- Gallium arsenide laser diode, 178
- Galvoscaner, 114, 116
- Glabrous skin, normal, 363
- Glass–stratum corneum transition, 185
- Glomus tumors, 101
- Glycosaminoglycans (GAGs), 385
- Granular cells, upper, 35
- Granular layer, 166
 - cell size, 173
 - epidermal differentiation estimation, 173
- Granuloma, pyogenic, 343
- GretagMacbeth ColorChecker, 210, 213
- GretagMacbeth Munsell Color Sheets, 213
- Hair
 - classification, 275
 - club, 271
 - cycling process, aspects, 280
 - density, 278
 - fibers, thickness of, 281
 - follicle openings, 11, 12, 129, 469
 - miniaturization, absence of, 281
 - nonvisible, 284
 - photography and imaging, 274–277
 - analytical methods, 279–282
 - calibrated scoring systems
 - method, 279
 - categorical classification systems
 - method, 277–279
 - for computerized measurements, improving, 277–279
- Global vision and imaging
 - methods, 279

- [Hair]
 roughness measurement, 155
 scalp, 271, 279
 structure and function, 271–272
 texture, measurement of, 154–157
 thin, 284
 topography, 156, 157
- Hamamatsu H, 71–78
- Helium–Neon lasers, 154
- Hemangioma, capillary, 343
- Hematoxylin–eosin staining, 32
- Hemoglobin, 426–427
- Henderson–Hasselbalch equation, 318
- High-frequency ultrasound imaging
 scanner, 18–19, 88–89
 echo signal processing and image
 generation, 89–91
 system design, 88–89
 system performance measurement
 and analysis, 91–92
- High performance liquid
 chromatography (HPLC), 450
- High-pressure freezing (HPF), 52
- High-resolution digital imaging
 system, 477
 materials and methods, 476–477
 digital imaging system, 476
 image analysis, 476–477
 by visual grading, 477
 treatment, 477
- High-resolution magnetic resonance
 imaging (HR-MRI), 17, 20
- High-temperature superconducting
 (HTS) coil, 105
- Histamine injection, intracutaneous, 328
- Horny cells, epidermal, 31, 36, 37
 adhesion and compactness of, 48
 hexagonal-shaped, 44
 layer, thickness of, 36
 superficial, 36, 47
 thin lamellar, 45
- Horny layer (DSC)
 confocal images of, 166
 thickness, 166–167
- Hybrid imaging concept, 21
- Hydration, skin, 103, 333, 403–406, 408
- Hyperemia, 326, 328
 injection of histamine, 328–329
 visualization, 328
- Hyperkeratotic inflammation
 disorders, 2
- Hyperkeratotic lesions,
 rhagadiform, 41
- Hyperpigmentation, 475
 diffuse, 426
 reduction in, 479
 mottled, 426
 accuracy of color and area
 measurement, 214–215
 area of, 211, 214, 215
 color contrast measurement of, 211
 correlation between CEI $L^*a^*b^*$ and
 Quasi $L^*a^*b^*$ values, 214
- Hyperpigmented spots, 479
 area of, 478
 facial skin color excluding, 478–479
 improvement of, 478
 severity of, 477
 detection, 211, 242
 ephelides, 218
 pigmented nevi, 218
 simple lentigo, 218
 solar lentigo, 218
- digital imaging system equipment
 for, 209
 advantages, 209, 218
 evaluation methods
 extraction, 211
 pixels counting, 218
 image analysis for measuring, 212
 simulation by mannequin head,
 213–215, 218
 skin color tone, 213, 214
- Hyperplasia, epidermal, 169
- Hyperproliferation, epidermal, 343
- Ichtyosis vulgaris*, 292–293
- Inflammatory skin diseases, 129–131,
 369–371
 conditions, 341
 monitoring, 134
- Intercellular lipid membrane bilayers,
 causes, 1, 3, 13
- International Contact Dermatitis
 Research Group, 202
- Irritant contact dermatitis (ICD), 342
- Isopropyl palmitate (IPP), 454

- Keratin filaments, aggregation of, 35, 36, 47
 Keratin, 177, 202
 Keratinization, disorders of, 11
 Keratinocyte-bound melanosomes, 424
 Keratinocytes, 131
 basal, 341
 differentiation of, 173
 flattening of, 173
 origin, 31, 32
 Krazy Glue[®], 12, 71
 Kubelka–Munk theory, 438
- Labview[™], 178, 250
 Lamellar bodies, cytoplasmic, 32, 57–58
Lamellar ichthyosis, 292
 Laser doppler fluxmetry, 326, 420
 Laser profilometry, skin surface
 contours by, measurement of, 191
 Lentiginosus. *See* Solar lentigines
 Lichen planus, 368–369
 Lichen sclerosus, extragenital, 169
 Lipid membrane bilayers, intercellular,
 causes, 1, 3, 13
 Lipids, 57–58
 Lipodystrophic disease, 417
 Lipolysis, 419
 Liquid cleansers
 in time moisturization study, 412
 types of, 412
 Liquid crystal tunable filter (LCTF), 406
 Lymph node
 changes in size and shape of, 361
 peripheral, 353
 sonography, 359
 Lymph vessels network, 381, 418
 Lymphedema, in cellulite, 381
 Lymphocyte, estimation of, 262
 Lymphography, 381–382
- Macrophage migration area, 262
 Magnetization transfer (MT)
 technique, 103
 Malignant lymphadenopathies, 361
 Malignant melanoma, 131, 268, 297
 prognosis of, 294
 Matlab (MathWorks, Natick,
 Massachusetts, U.S.A.), 253
- Matrix metalloproteinases (MMP),
 expression of, 427
 Mean cell size (MCS)
 Fourier analysis of, 186–189
 variation across the epidermal
 layer, 188
 Mean gray level (MGL), 334
 skin hydration characterization, 332
 Melanin, 425–426
 in basal keratinocytes, 341
 chromophore, 425
 dust, 424
 evenness, 442, 443
 Melanin-based pigmentation
 types
 constitutive skin color, 425
 facultative skin color, 425
 Melanocytes, 131
 Melanocytic nevi, 131, 346–347
 RCM features of, 406
 types of, 406
 Melanocytic skin lesions, 346–348
 diagnosis of, 346
 Melanocytic skin tumors, RCM features
 of, 406
 Melanogenesis, 209
 Melanoma, 268
 clinical presentation, 293
 dark areas of, 308
 detection, 121, 122, 305
 diagnostic techniques, 297, 301–302,
 307
 dermatoscopy, 298
 epiluminescence microscopy, 298
 differentiation between malignant and
 benign lesions, 305, 310–311
 abrupt border cut-off, 307
 asymmetry, 307–310
 colors, 308–309
 differential structures, 309–310
 feature extraction, 298–300
 global descriptors, 299
 local descriptors, 299
 human–computer comparison,
 310–311
 image
 analysis methods, 299
 data acquisition and preprocessing,
 298
 multiphoton, 121

- [Melanoma]
 segmentation, 298–299
 malignant, 131, 268, 297
 quantification of the skin surface,
 291–295
- Melanosomes, 341, 425
- Melanotic skin features, 426
- Mesenchymal tumors, 130
- Mexameter™, 437
- Micelle formation, 392–393
- Michelson interferometry, 127
- Microcomedones, 294
 image analysis, 72
- MicroDERM system, 18
- Microquinhydrone electrode, 313
- Minimum erythema dose (MED),
 433–435
- Minolta CR 200 colorimeter, 12
- Minolta CR-300 Chromameter®, 210
- Mitochondrial-reduced
 coenzyme, 111
- Moisturizers, 77, 78
 efficacy of, 78–79
 example of, 78
- Moisturizing body wash (MBW)
 ingredients of, 409
 traditional body wash (TBW) and,
 comparison of, 409
- Morphometry
 area determination, 260–262
 area fraction determination, 262–265
 length determination, 266
 principles and applications in 2D,
 260–267
- Mottled hyperpigmentation, 426
- Multimodal skin imaging, 20–21, 64–65
- Multiphoton fluorophore, 113
- Multiphoton imaging system,
 DermaInspect, 117, 124
- Multiphoton laser scanning microscopy
 (MPLSM), 58, 161
- Munsell Color Chart, 213
- N*-acetyl glucosamine (NAG), 443
- NADH
 cellular, 177, 179
 coenzymes, 115, 120
- Natural moisturizing factor (NMF),
 253, 391
- [Natural moisturizing factor (NMF)]
 distribution, 253–256
- Near-infrared (NIR) region, 403–406
- Nevus sebaceous, 40–42
- Nipkow systems, multiple beam
 approach to, 153
- Noncontact SIAscopy (NCS) technique,
 440–443
 advantages, 439
 chromophore concentration maps
 hemoglobin map, 439
 melanin and eumelanin
 maps, 443
- Nonfoaming facial cleanser lotion, 412
- Nonmelanocytic skin
 lesions, 344–346
- Nonmelanocytic skin tumors, RCM
 features of, 344, 345
- Nonoptical techniques, 111
- Novel multidimensional imaging
 technology, 111
- OCT. *See* Optical coherence tomography
 spectral radar, 128
 studies in dermatology, 128–129
 healthy skin, 128–129
 treatment effects, 131–133
 technique, 127
 potential of, 133
- Oil-in-water (O/W) emulsion type, 393
- Optical coherence technique
 19–20, 67, 111–112, 114
 advantage of, 18, 20, 27
 Doppler, 128, 135
 elastography, 135
 no-motion, 128
 noninvasive imaging method, 134
 polarization-sensitive, 128
 principle of, 127
- Optical skin surface imaging, 18
- Optical topometry, 145, 146
- Orange peel skin, 417
- Orange-red lightning of pores, 448
- Ovary cells, Chinese hamster, 123
- Oxygen flux membranes, 326
- Oxyhemoglobin, 329
- Palmar skin, normal, 357, 363–367
- Palmoplantar skin, 101–102, 129

- Papillae adiposae, 387
- Papillary dermis, 129
 definition by SIAscope model, 438
- Parakeratosis, 2, 129, 132, 346
- Patch testing
 for acute skin irritancy, 399
 by visual scoring system, 202
- Pearson correlation coefficient, 166
- Phase-contrast microscopy, 2
- Photoaging, 426
- Photochemical effect, 123
- Photodetector, 112
- Photomultiplier tube (PMT)
 detector, 151
 in photon counting mode, 178
- Phototrichogram (PTG), 276, 279
 variants of, 282
- Piezo mechanical focusing drive
 (PIFOC), 178
- Pinhole, 112–113
 confocal, 250
- Pinhole-free detectors, 114
- Pityriasis versicolor lesions, 336
- Planar glass electrode, 314
- Plaques of morphea, 293
- Plexus
 deep, 428
 subpapillary, 426
- Plicometer, use of, 421
- Plumpness, parameter, 145
- Pores
 definition, 469
 refining effects, 457
 silicon replica impressions
 of, 470
 surface impression of, 469
- Pre-chirp prism assembly, 179
- Prick test reaction, 263
- PRIMOS system, 142–143
- Probes, cryogenic skin, 107, 108
- Probes, exogenous fluorescent,
 advantage of, 112
- Profilaggrin, degradation of, 36
- Proteases, activity of, 40
- Proton density, skin layers, 102
- Protoporphyrin IX (PPIX), 450, 452
- Psoriasis area and severity
 index (PASI) scores, 201
- Psoriasis, 2, 10, 132
 vulgaris, 343, 357, 367
- Psoriatic lesion severity
 determination of, 201–203
- Psoriatic plaques
 clinical presentation, 291
 quantification of the skin surface,
 291–292
- Pyogenic granuloma, 343–344
- Quasi $L^*a^*b^*$ values, 210
 correlation between CIE and, 214, 215
 RGB values transformation to, 210,
 214
- Rabbit ear comedogenicity assay
 disadvantages of, 447
 for comedogenic/comedolytic
 activity, 447
 for testing of cosmetic
 products, 447
 in vivo animal assay, 447
- Radio frequency (RF) echo signals, 89
- Raman and confocal laser scanning
 microscopy (CLSM),
 data processing, 253
 instrumentation, 250–252
 methods, 252
- Raman scattering
 anti-Stokes, 248
 Stokes, 248
- Raman spectroscopy, 247
 instrumentation, 249
- Red, green, and blue (RGB) Bayer
 filter, 440
- Red, green, and blue (RGB) near
 infrared radiation (NIR), 440
- Reflectance spectrophotometry, 292
- Reflectance-mode confocal microscopy
 (RCM), 339
 advantages, 341
 applications, 349
 findings
 inflammatory skin conditions,
 341–344
 melanocytic skin lesions, 346–348
 nonmelanocytic skin lesions,
 344–346
- Remission confocal laser scanning
 microscopy (CLSM) imaging, of
 emulsion films, 156

- Resin-embedded skin samples,
blockface imaging of, 159
- Reticular dermis, 129, 363
definition by SIAscope model, 438
- Retinol-glycolic acid facial
treatment, 473
- Rhagadiform hyperkeratotic lesions,
41, 48
- Riboflavin, 451
- Rosacea, 343
- Roughness parameters, 7, 144–145, 291
- Safranin T, 159
- Scaling index (SI), 9
calculation of, 77
- Scalp
hair, 271, 279
immersion photography, 281
skin, 277, 279
- Scalp coverage scores (SCSs), 279
- SCORAD index, 198
bioengineering methods and,
correlation coefficients of, 201
- Sebaceous follicles, 448–450
compounds with, 454
fluorescence signals origins from,
448–450
and sebum, 75–76
- Sebaceous glands, surface of, 473
- Seborrhea, 74–75
- Seborrheic keratosis, 370, 426
- Sebosuppression, 75–76
- Sebum
excretion, 264
output estimation, 74–75
production, 13
rate monitoring, 473
secretion activity, 469, 471
spots and sebaceous follicles, 75–76
- Sebutape[®], 71, 74, 264
applications, 74–75
disadvantages, 473
image analysis, 72–74
modification, 473
sample collection, 77–78
sebum spot on, 86–87
- Second harmonic generation (SHG), 115
- Secondary ion mass spectrometry
(SIMS), 315
- SIAscopy[™]
contact, 430–432
applications of, 438
high-resolution white-light image of
skin by, 438
image and chromophore maps, 438
techniques, 438
definitions for
epidermis, 438
papillary dermis, 438
reticular dermis, 438
histology and color formation
by, 439
light emitting diodes (LEDs) in, 439
noncontact, 440–442
components, 439
image and chromophore maps, 439
techniques, 439
parameters subdivisions of, 438
- Silflo[®] (Flexico Ltd., U.K.), 4
- Silica gel particles, 92
- Silicon exafin skin replicas, 197, 207
- Single photon counting, time-correlated,
316
- Single-lens reflex (SLR) digital
camera, 429
- Skin
acidity, 313
appendages, 11–12
atrophy, 132
autofluorophores, 151, 162
barrier
dynamic changes, 62
in epidermis at the live-death
transition, 63–64
essentials, 57–58
multimodal imaging of, 63–64
properties, 56–57
repair preparation, 200
biochemical characterization, 102
biopsies, 52, 55, 159
cells staining, 151, 157
cellulitic, 417–418
changes by moisturizing cream, 174
chromophores excitation, 162
CLSM of, 179–182
color, 12–13, 201, 430
tone measurement, 213
condition time responses, 412, 415
confocal images of, 166, 339–341

[Skin]

- contour
 - aging process, 206
 - morphologic studies, 225
 - validity and reliability test, 197
- corrosivity evaluation, 401
- detergent effects on, 395–399
 - direct, 395–396
 - indirect, 396–399
 - evaluation methods, 399–401
 - positive, 395
- diseases, 290–293
- dryness, 412
 - clinical grading, 408
- elasticity, 13
- electrical properties, 403
- entry echo, 363
- erythema visual assessment, 407
- ethnic aging study, 434, 435
- fold measurement, 157–158
- fluorophores, 162
- furrow stereoiimage, 202, 205
- glabrous, normal, 363
 - and hair surfaces, 154
- histometric measurements, 165
- horizontal parameters, 173
- hyperemic, 328
- images, 332
 - capacitance image of
 - forearm, 332
 - technologies, 18, 21, 112–113
- irritation, 79
- layers, 17–18, 259
 - apparent diffusion coefficients
 - measured in, 104
 - epidermis, 171
 - horny layer, 166–167
 - proton density of, 99, 102, 103
 - spatial resolution and water
 - behavior in, 103–104
 - target molecules in, 151
 - gradient, 309
 - nonmelanocytic, 344–346
 - pigmented, 301–302
 - thickness measurements,
 - 184–185
- lines and wrinkles, 428
- malignant melanoma of, 297
- mean cell size (MCS) determination
 - of, 186–188

[Skin]

- measurement conditions, 494
 - in situ blotting in, 315
 - metabolism mapping, 315
- mechanical properties, 412, 428
- micro relief, 331–332, 335–336, 428
- micro-roughness, 157
- moisture content, 404
- molecular targets in, labeling of, 158
- multiphoton sectioning of, 117–119
- noninvasive in vivo imaging of,
 - 177, 179
- object density parameters, 173–174
- orange peel, 417
- occlusion, 185–186, 205
- organization, 152
- oxygen uptake by
 - air diffusion, 325
 - cutaneous blood flow, 325
- oxygenation
 - evaluation, 325
 - heterogeneity of, 325
 - measuring procedure, 327–328
 - visualization, 325, 328–329
- in palmo-plantar regions, 101
- pathologies, 40–48
 - acne, 336
 - psoriasis, 336
 - variations, 333
- parameters
 - corner density (CD), 331
 - mean gray level (MGL) of
 - histogram, 334
 - orientations of primary
 - mines, 331
- pH
 - in enzyme activity regulation, 313
 - in epidermal processes, 313
 - measurement, 314–316
 - visualization, 313
- photoaging, 209
 - characterization, 333
- pigmentation, 1, 12–13
- probes, cryogenic, 108
- qualities of healthy, 428
- reflectance and fluorescence, 177, 182
- replicas, 197
- Res Technol 2005, 333
- role of immersion water in, 166
- samples

- [Skin]
- confocal microscopic images of, 149, 160
 - three-dimensional visualization of, 160
 - topographic measurement of, 151, 155
 - protein targets in, fluorescence-labeling of, 158–160
 - SIAscope in imaging of, 438
 - sites of minor trauma, 343
 - spectroscopic analysis, 163
 - spectrum, 403
 - structure
 - in vivo investigations of, 162, 256
 - preservation of, 159
 - staining techniques, 157
 - temperature and humidity, 157
 - surfactants effects, 392, 460
 - texture
 - measurement, 154–157
 - three-dimensional images of, 155
 - topography, 154
 - thickness measurement, 165, 202
 - topography, ex vivo measurement of, 154
 - treatment
 - with facial cleansing liquid, 412
 - with foaming emollient body wash, 412
 - with foaming facial cleanser, 412
 - TPFM of, 182–185
 - visible signs of, 433
 - visual assessment, 408, 414–415
 - water absorption in, 412
- Skin aging
- chromophore changes, 428–429
 - contrast sensitivity in, 428–429
 - digital imaging of, 429–430
 - black/white and color calibration, 432–433
 - cutaneous optics in effective, 424–425
 - elimination of distractions in, 433
 - incident angle of illumination in, 430–431
 - lighting stability, 431–433
 - practical use of, 433–435
 - principle, 424–425
 - racial groups in study of, 434
- [Skin aging]
- region of interest (ROI) on, 434
 - reproducibility, 429–430
 - state-of-the-art color analysis of, 435–438
 - success, 440–443
 - interaction of light with, 424–425
 - topography changes, 428–429
 - visual signs measurement of, 423
- Skin Analyzing Fluorescence Imaging Recorder (SAFIR), 448, 450, 453–454
- aim of study of, 457
 - deep pore cleansing effects by, 457
 - image analysis, 451
 - pore refining effects by, 457
 - technical specifications, 452
- Skin ashing
- calculation program of, 463–464
 - degree of, 459
 - descriptors images, 460
- SkinChip
- in micro relief lines of lips, 336
 - skin surface pattern study by, 336
 - technology, 331
 - and corneometer parameters relationship, 333
 - images, 334
 - window, 332
- SkinChip[®] Sensor, 331
- components, 331
 - developed by Imaq Vision platform, 331
- Skin hydration, 103, 403
- changes, 410
 - characterization, 333
 - images, 403, 408, 410
 - measurements
 - confocal Raman spectroscopy, 405
 - forearm controlled application technique (FCAT), 406
 - NIR reflectance-based imaging, 404
 - six-hour time moisturization test of, 406
 - in superficial layer, 406

- Skin surface
- aluminumchlorohydrate (ACH)
 - distribution on, 160
 - biopsy procedure, 447
 - disadvantages of, 447
 - for comedogenic/comedolytic activity, 447
 - for examining changes in stratum corneum, 448
 - using cyanoacrylates, 447
 - capacitance imaging of, 332, 333
 - advantages, 336
 - Corneometer, 333
 - modification with moisturizer, 332
 - pathological lesions, 336
 - sweating zone, 335
 - technical aspects of, 331
 - contours
 - stereoimaging principle, 191
 - by conventional optical profilometer (COP), 191, 197
 - by laser profilometry, 191
 - by stereoimage optical topometer (SOT), 191, 193, 197
 - by stylus profilometer, 191
 - emulsion systems on, 156–157
 - hydration, 201
 - in vivo imaging of, 152
 - microtexture, 471
 - morphological changes, 400
 - physiological properties, 13
 - structural changes, 154
 - texture, 1
 - topography, 289, 428
 - chromophore mapping
 - in, 435–438
 - three-dimensional measurement
 - of, 155
- Skin tumors, 18, 130–131, 370
- diagnosis, 293
 - differentiations, 297, 300–301
 - pigmented, statistical analysis, 369
 - by artificial neural networks (ANNs), 300
 - by image analysis, 297
 - by machine learning models, 300
 - neural networks, 297, 300–301
 - [Skin tumors]
 - by support vector machines (SVMs), 300
- Skin-lightening ingredients, 209
- Skin-lightening moisturizer (SLM), 478, 479
- Skull, bones of, 279
- Sodium lauryl sulfate (SLS), 395–396
 - concentration, 79
- Sodium lauryl sulfate-induced edema
 - severity, 203–206
- Solar lentigines, 426
- Solar UVR-induced hyperpigmentation, 426
- Sonogram, 370–371
 - of normal skin, 358, 372
 - of palmar skin, 363
- Sonography, 83, 84
 - in dermatology, 353
 - of dermis and epidermis, 363
 - HFUS-based, 18, 19, 21
 - potential of 100MHz, 370
- Spectrophotometer[®], 198, 199, 200
- Spongiosis, RCM parameter, 343
- Squamous cell carcinoma (SCC), 23, 95, 268
 - RCM features of, 344
- Stem cells, 40
 - factor, 426
- Stereoimage optical topometer (SOT), 191, 193
 - parameters, 195–197
 - comparison, 206
 - for skin contour measurement, 191
 - techniques, 191
 - area-based method, 192, 193
 - feature-based method, 193
- Stereology, 267–268
 - definition of, 259
- Stereopsis, nonconvergence model of, 194
- Sterile biopsy chambers (MiniCeM-biopsy, JenLab GmbH), 117
- Steroid sulfatase, deficiency, 45, 47
- Stokes Raman scattering, 248
- Stratum basale, 119, 169
- Stratum corneum (SC), 7, 53, 71–72, 173, 459
 - extracellular processing, 313

- [Stratum corneum (SC)]
 - fluorescence signal in, 183
 - hydration effects on, 61–63, 186
 - keratin-water network of, 403
 - lipid precursors, 313
 - morphology and cohesion, 58–61
 - multimodal imaging of, 63
 - occlusion effects on, 185
 - pH assessment in, 313
 - in palmo-plantar regions, 102
 - pliability, 1, 13
 - removal, 313
 - swelling, 155–156
 - thickness determination, 132, 134, 186
- Stratum granulosum (SG), 57, 118–119, 167, 313
- Stratum spinosum (SS), 119
- Stroma, 369
- Stylus profilometer, skin surface contours measurement, 191–193
- Subcutaneous adipose tissue, 380
- Subcutaneous fat (SSF), 377, 382
- Support vector machines (SVMs) models, 301
- Suprapapillary plate, 167
- Surfactants on skin
 - concentration of, 392
 - definition, 460
 - effects of, 392
 - types of, 392
- Sweating zone, capacitance imaging, 336

- Talbot photographs, 423
- Telangiectasia, 427
 - vessels, 266
- Tetanus recall antigen test, 328
- Three-color channels, intensity in, 462
- Three-dimensional (3D) high-resolution imaging, 111
- Tiffin Series 9 Polarizing Filter, 210
- Time-correlated single photon counting (TCSPC), 115
- Time-moisturization study
 - cleansers versus moisturizers, 409
 - leg images from, 410
- [Time-moisturization study]
 - liquid cleansers in, 412
 - six-hour, 410, 412
- Tissue
 - phantoms, 117
 - structure, 162
 - fluorescence staining of, 160–161
 - three-dimensional reconstruction of, 151
 - water content, 403
- Titanium sapphire laser, 179
- Toluidine blue basic fuchsin solution, 72
- Traditional body wash (TBW), ingredients, 409
- Transcutaneous oxygen pressure (tcpO₂)
 - imaging, 326–327
 - layers, 325
 - opaque silicone layer, 326
 - oxygen-sensitive layer, 326
 - transparent carrier foil, 326
 - sensors, 326–327
- Transepidermal water loss (TEWL), 198, 397
 - in atopic dermatitis patients, 208
 - measurement, 198–200
- Tretinoin, topical agents, 479
- Trichostasis, 282
- Tuberculin test, 328
- Tuebingen method, 307
- Tumor
 - diagnosis of, 134
 - echopoor region, 370
 - epithelial, 130
 - glomus, 101
 - mesenchymal, 130
 - parenchyma, 369
 - skin, 130–131
- Two-finger-squeeze-method, 448
- Two-photon femtosecond laser scanning microscope, advantages, 115
- Two-photon fluorescence microscopy (TPFM), 178–179
 - and confocal laser scanning microscopy (CLSM), 182–183
 - in skin, 178, 183
 - advantages, 188
 - experiment analysis, 178
 - images of volar forearm, 180, 185
 - penetration depth, 177, 178

- [Two-photon fluorescence microscopy (TPFM)]
 - intensity versus depth profile, 180, 184
 - stratum corneum thickness by, 180, 182, 184
- Ultrasound biomicroscopy of skin, 83–84
- Ultrasound for high-resolution imaging, high frequency and broadband, 86–87
- Ultrasound skin imaging system, 83, 85
 - high-frequency, block diagram, 88
- Ultraviolet A(UVA), 7
- Ultraviolet B(UVB), 7
- Ultraviolet-enhanced visualization, 459

- Viable epidermis (VEmin)
 - thickness calculation, 171, 196
- Video-dermatoscopy (VD), 17, 22
 - advantages, 18, 20, 27

- Visual dryness, 462
- Visual grading scale, 459–461
 - whitening degree of skin by
- VivaScope 1000 (Lucid Inc., Rochester, New York, U.S.A.), 250
- VivaScope1000™, 178
 - confocal laser scanning system, 112
- Volar forearm, 169
- Volar sites, 37–40

- Washing, mechanism, 395–396
- Water-in-oil (W/O) emulsion
 - type, 393
 - spreading, 156
- Water-rich tissue, water content of, 404
- Wispy dyspigmentation, 426
- Wrinkles, 1, 7
 - classification of, 428

- X-linked ichthyosis, 41–48
- Xerosis, 7, 9–10



Figure 3.13 Nevus sebaceous. (See p. 41)



Figure 3.17 X-linked ichthyosis. (See p. 43)

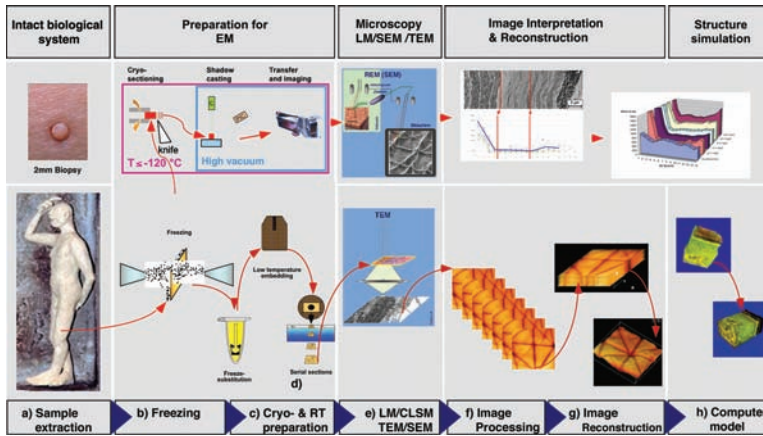


Figure 4.1 “Information-transfer-chain” for microscopical investigation of human skin biopsies. (See p. 53)

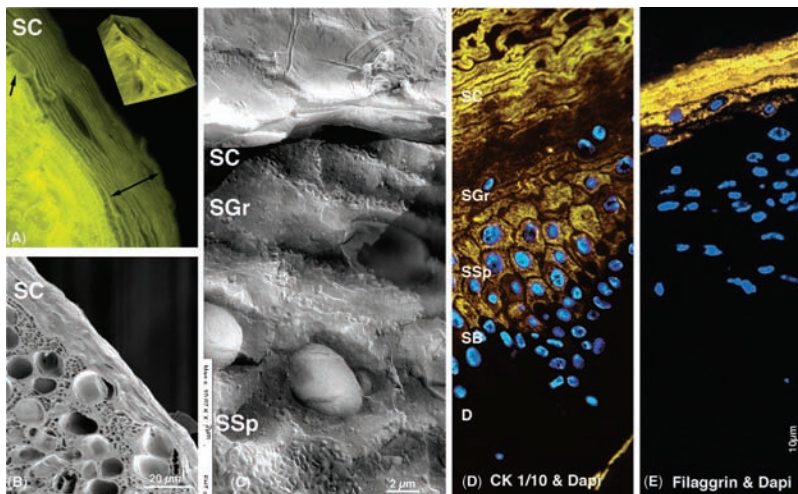


Figure 4.2 Human skin biopsies. (See p. 54)

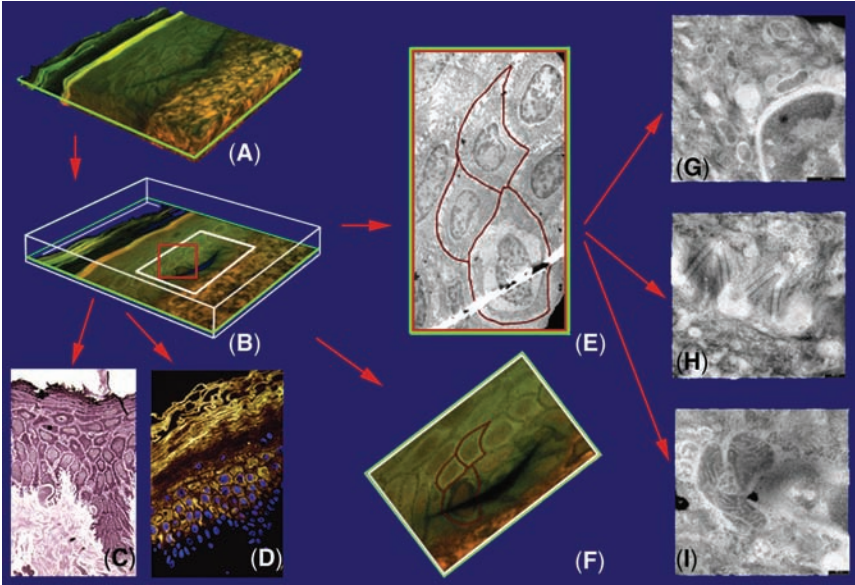


Figure 4.3 Imaging strategy of high pressure frozen, freeze-substituted and embedded skin biopsies. (See p. 55)

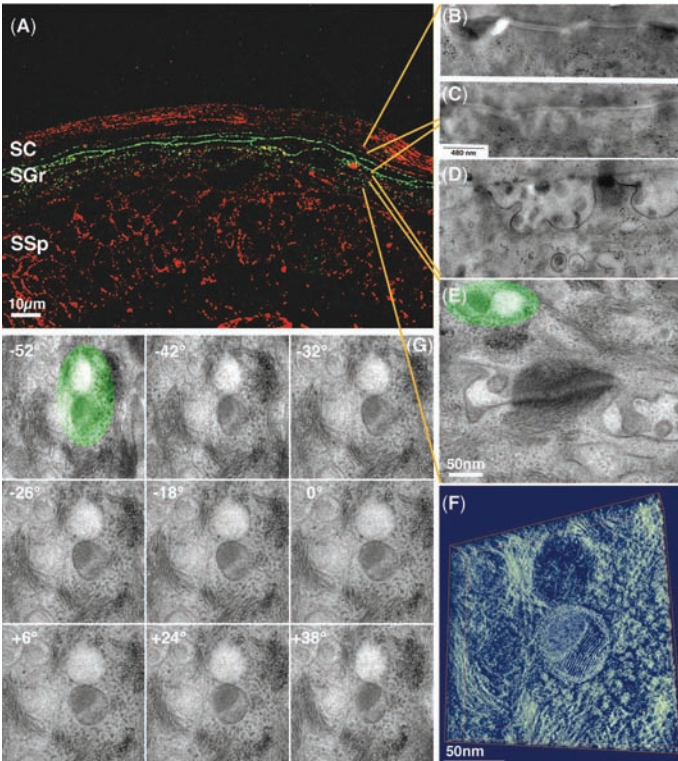


Figure 4.4 Lipids in human skin imaged after high pressure freezing and freeze-substitution. (See p. 56)

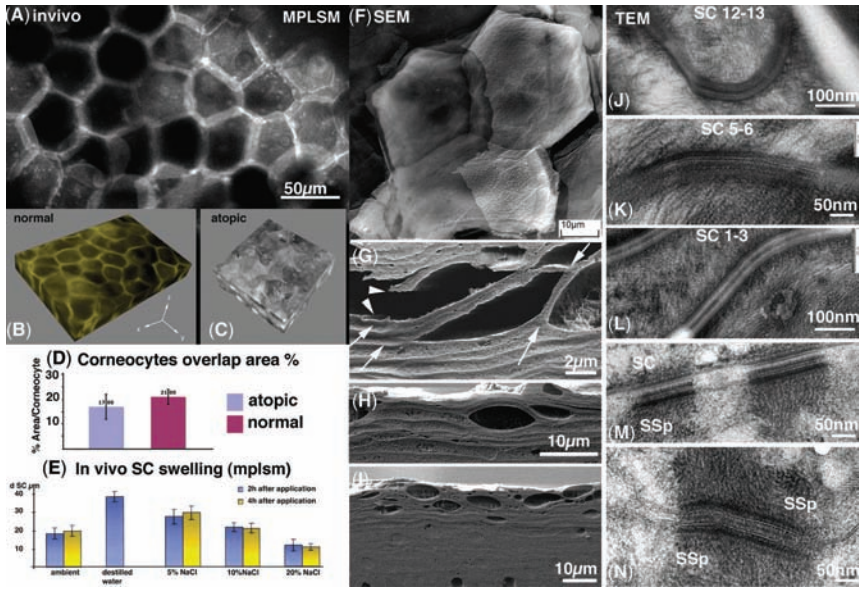


Figure 4.6 Multimodal imaging of the Stratum corneum from in vivo to frozen-hydrated or with molecular resolution. (See p. 60)

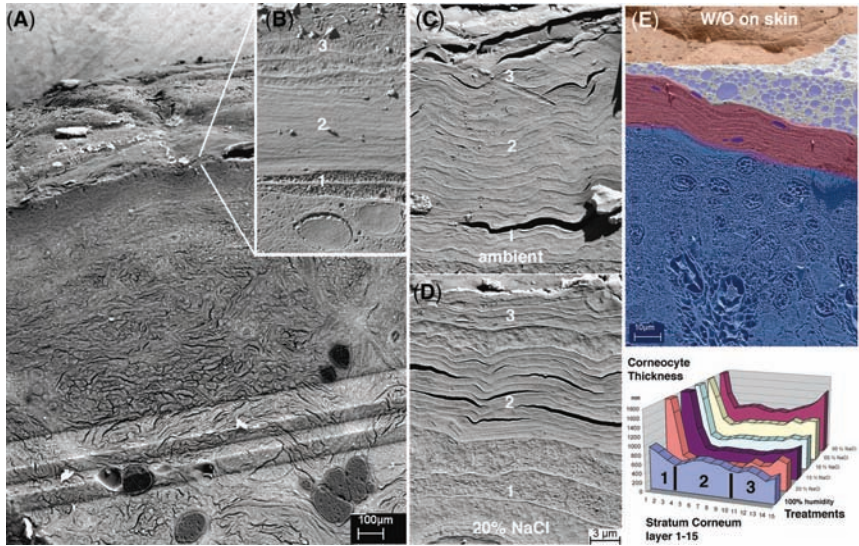


Figure 4.7 Hydration changes of the stratum corneum investigated in a cryo-SEM. (See p. 61)

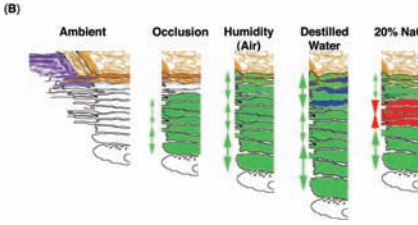
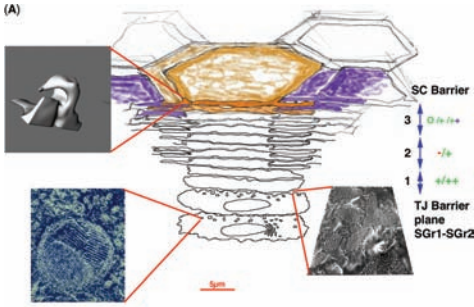


Figure 4.9 New findings by multi-modal imaging of human skin biopsies to review the organization of the stratum corneum toward a structural based holistic model. (See p. 66)

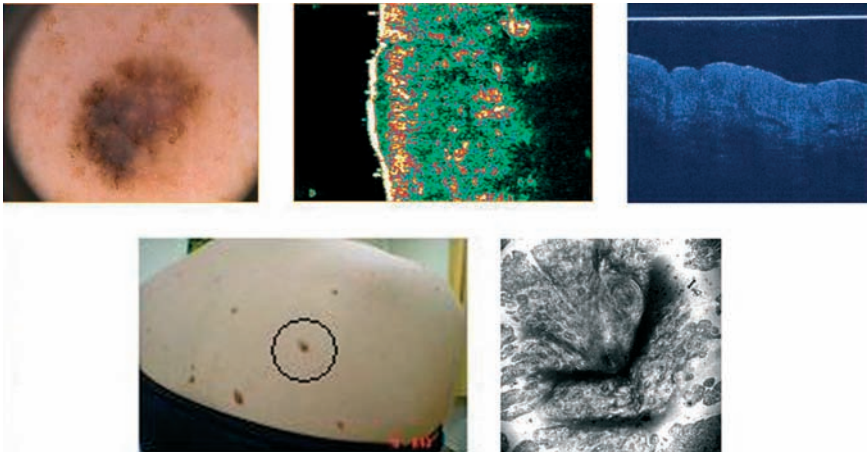


Figure 8.1 State-of-the-art images from a human nevus. (See p.113)

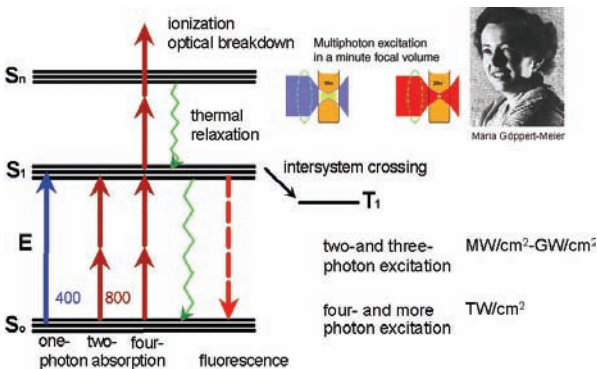


Figure 8.2 Principle of multiphoton processes. Fluorescence in the blue, green, yellow, and red spectral range can be excited via a two-photon absorption process. (See p. 114)

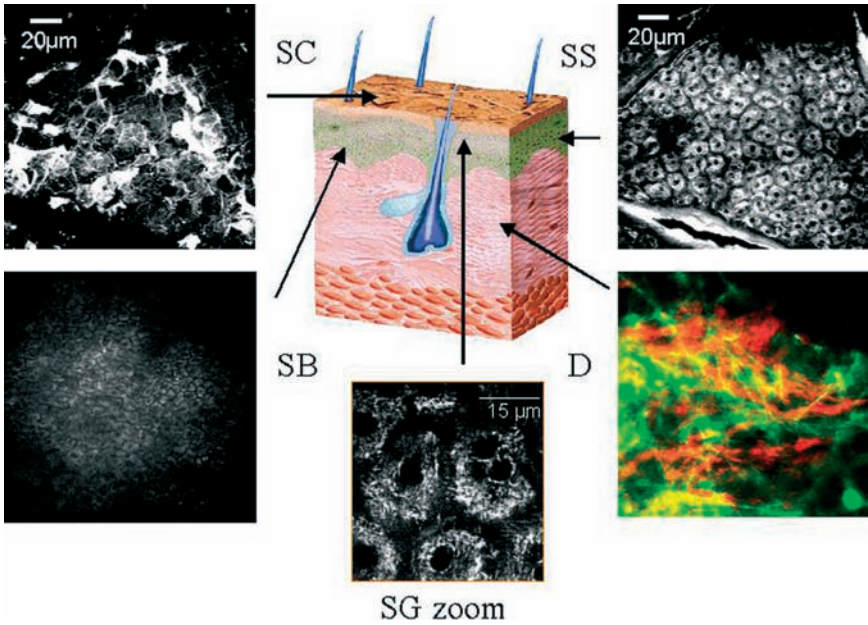


Figure 8.5 High-resolution in vivo multiphoton autofluorescence/SHG images of different skin layers. The major fluorophores are keratin in the stratum corneum, NAD(P)H in the stratum granulosum and stratum spinosum, melanin in the stratum basale, and elastin in the dermis. Collagen (red false color) can be detected by SHG. (See p. 118)

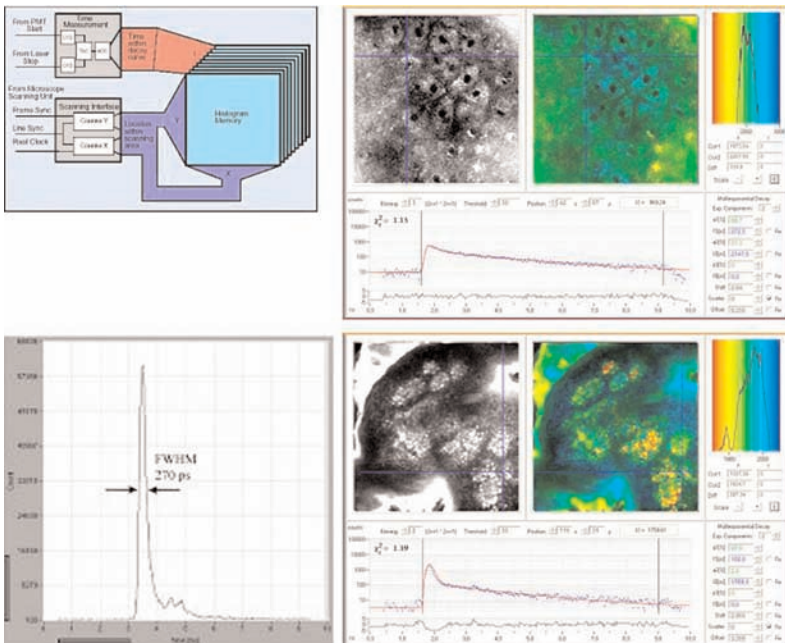


Figure 8.6 In vivo luminescence lifetime images of the stratum spinosum (right upper part) and the dermis (right lower part). (See p. 120)

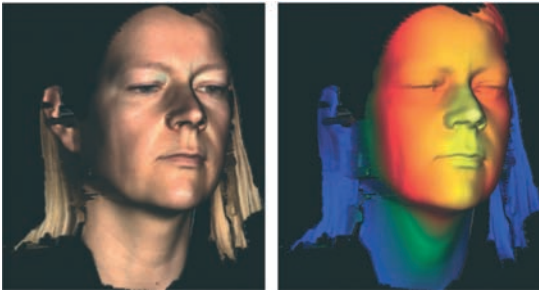


Figure 10.7 Large field measurement of the entire face. (See p. 146)

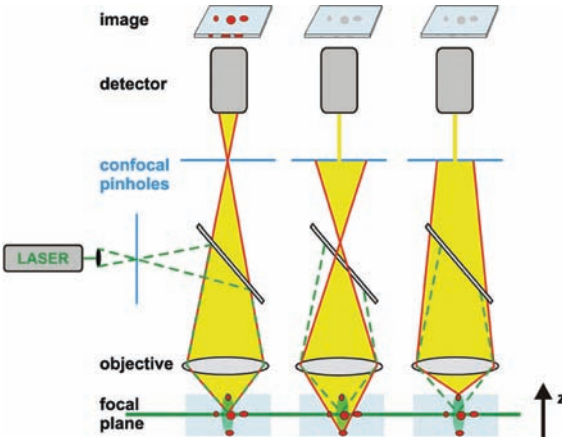


Figure 11.1 Image acquisition in confocal microscopes: The image information is derived from the focal plane, not from out-of-focus planes. This virtual cross-sectioning of the sample is reached by pinholes in the focal planes of the entrance optics and the objective lens, respectively, acting as a filter for out-of-focus-light. (See p. 153)

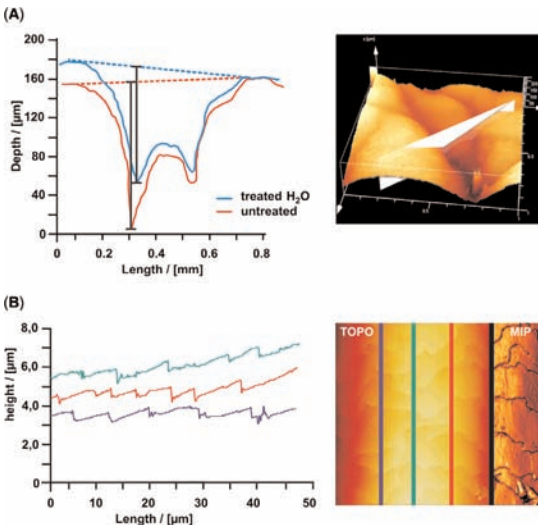


Figure 11.2 3D measurement of skin surface topography and hair roughness. The reflection mode of the confocal laser scanning microscopy is helpful to investigate skin surface topography changes after treatment. (See p. 155)

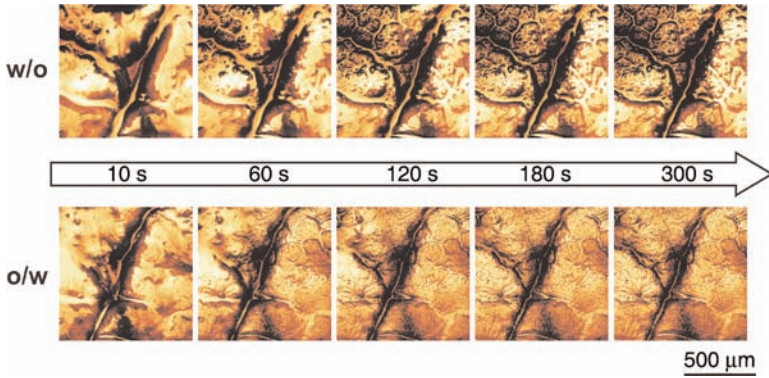


Figure 11.3 Spreading dynamics of different emulsion systems on skin surfaces. (See p. 156)

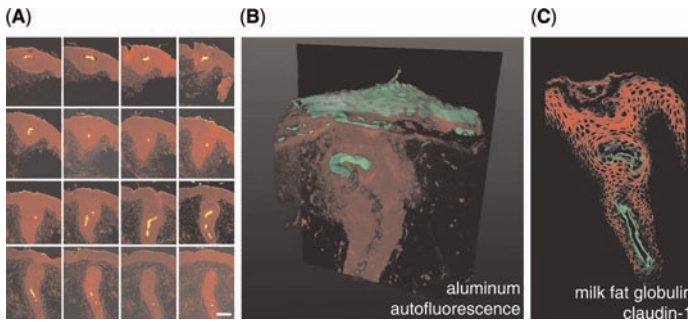


Figure 11.4 Specific labeling of molecular targets in two-dimension and three-dimension. (See p. 158)

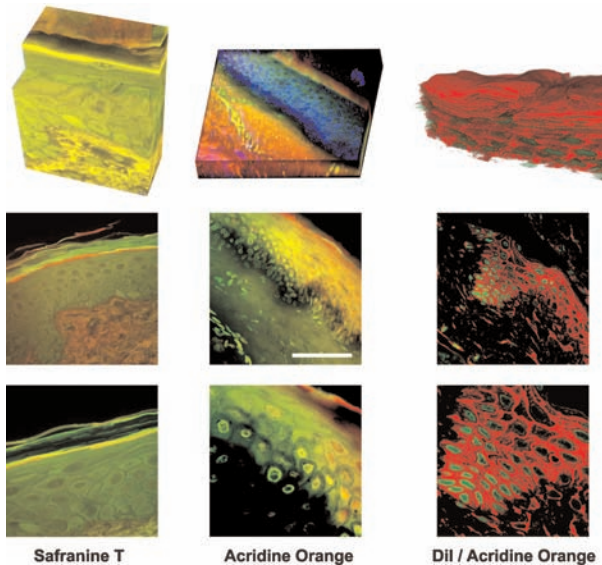


Figure 11.5 Blockface imaging of resin-embedded skin samples: optimal sample preservation for high-resolution three-dimensional light microscopy. (See p. 159)



Figure 15.3 Simulation using a mannequin head. (See p. 213)

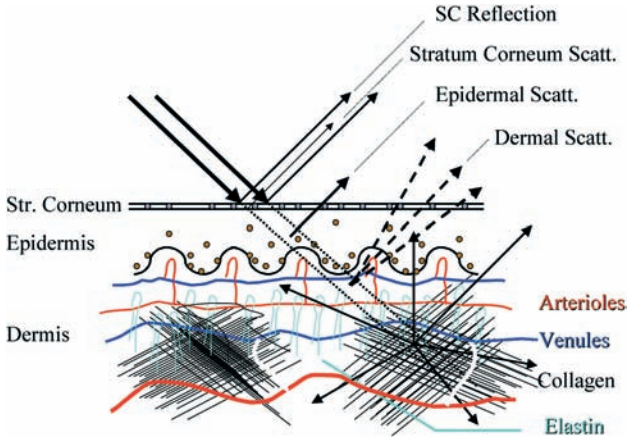


Figure 16.3 Schematic drawing of the skin and how visible light might interact. (See p. 225)

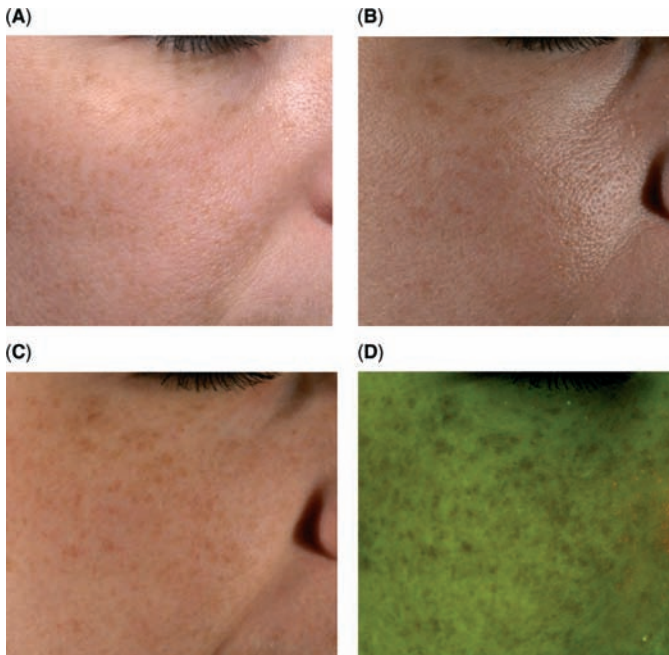


Figure 16.10 Five facial images obtained in rapid succession (in approximately five seconds). (See p. 240)

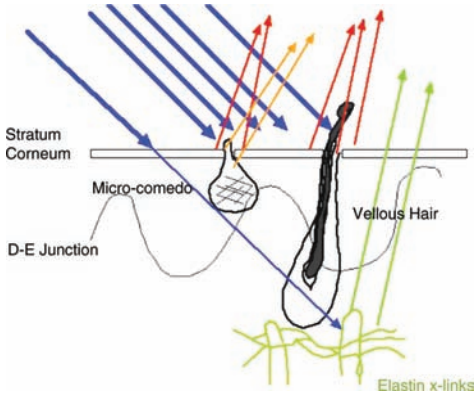


Figure 16.12 A beam of blue light (405 nm) is incident on the surface of the stratum corneum. (See p. 243)

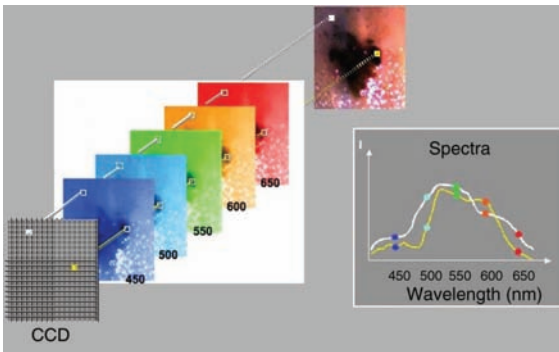


Figure 16.13 A schematic representation of spectral imaging. (See p. 245)

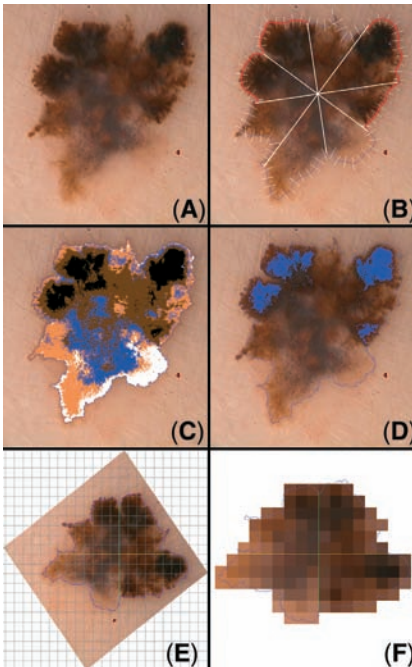


Figure 22.1 Image analysis of a thin melanoma (Breslow's thickness 0.30 mm). (See p. 306)

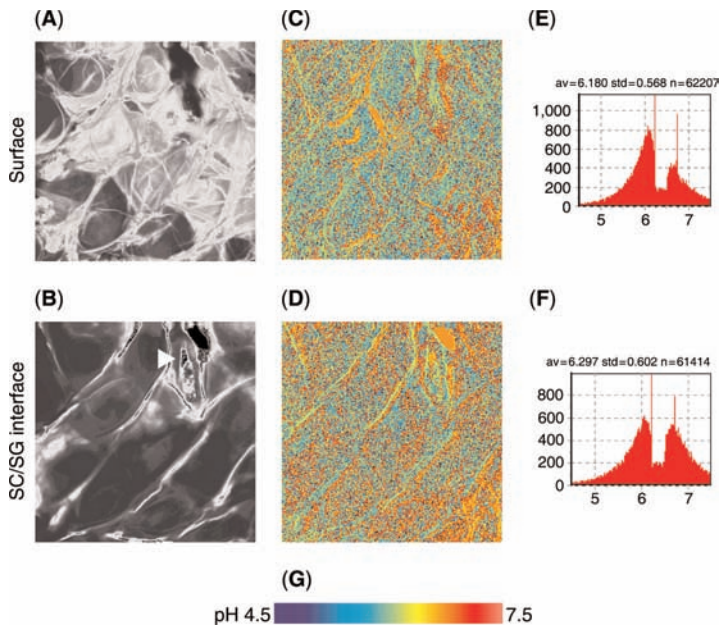


Figure 23.2 Example of FLIM analysis. Image stack from skin surface to dermis: represented by panels for epidermal surface (A, C, E), and SC/SG interface (B, D, F). Analysis consists of fluorescence intensity images (A, B), fluorescence lifetime images (C, D) with a color value scale (G), and lifetime histograms (E, F). (See p. 319)

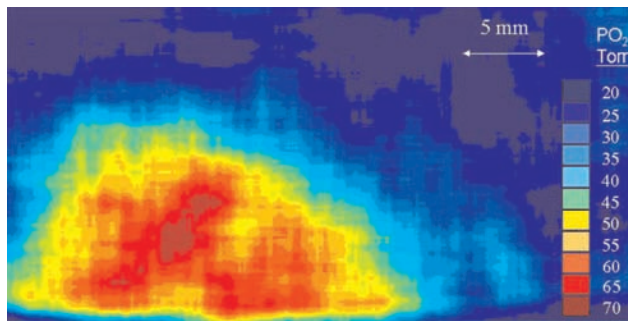


Figure 24.3 Transcutaneous oxygen pressure image recorded 33 minutes after intracutaneous injection of 0.05mL histamine. (See p. 328)

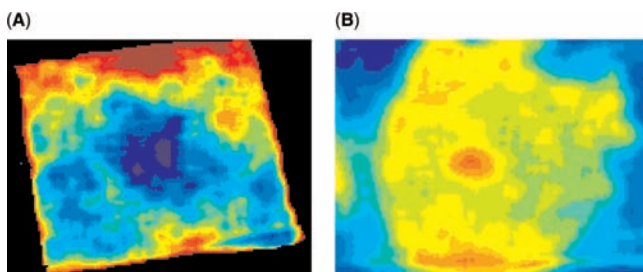


Figure 24.4 Transcutaneous oxygen flux (tcJO₂) imaging. (See p. 329)

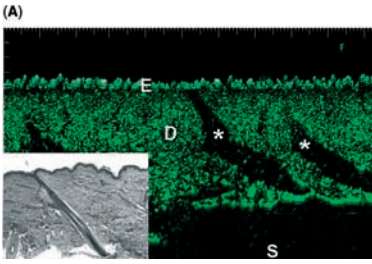


Figure 27.13 Hair follicles are echopoor structures in the echorich dermis. (See p. 364)

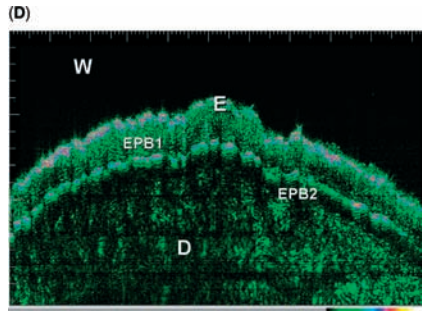
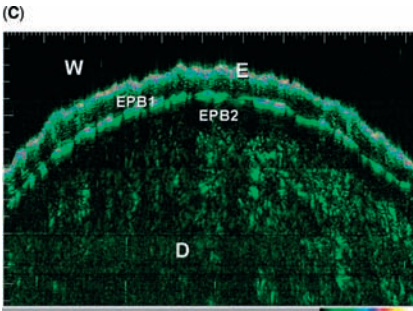


Figure 27.14 Sonograms before (C) and after (D) 30 minutes occlusion of an emulsion on index finger. (See p. 365)

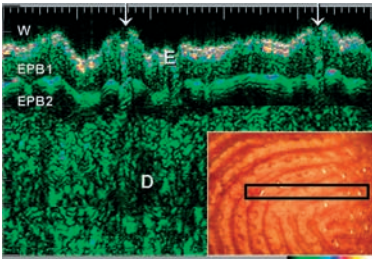


Figure 27.15 Palmar side of the right index finger. (See p. 366)

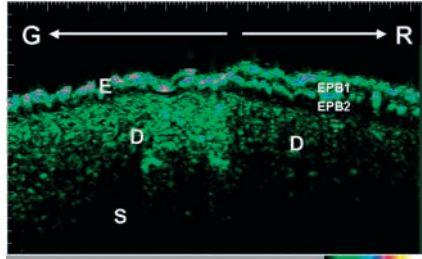


Figure 27.16 The transition from glabrous to the palmar skin shows a second echorich line separates the upper from the lower EPB. (See p. 366)

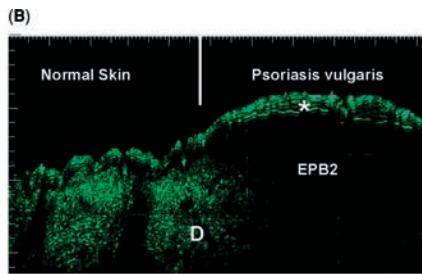
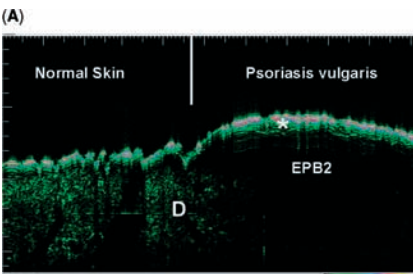


Figure 27.17 Border of a psoriatic plaque. (See p. 367)

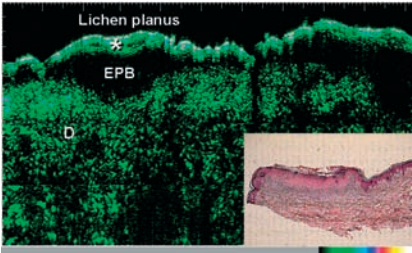


Figure 27.18 Lichen planus papule. (See p. 368)

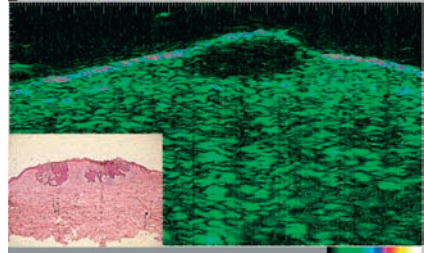


Figure 27.19 Basal cell carcinoma. (See p. 369)

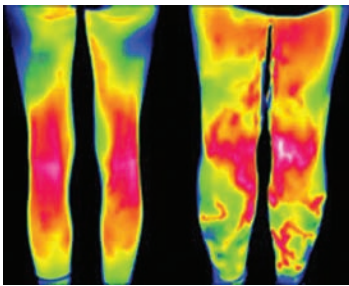


Figure 28.8 Thermography of normal (left) and abnormal (right) female legs. (See p. 386)

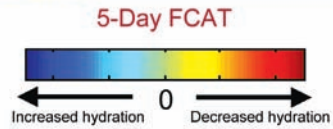
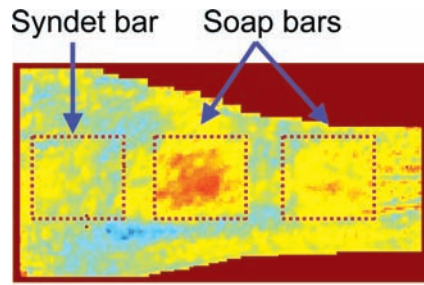


Figure 30.4 A forearm image from an FCAT study. (See p. 409)

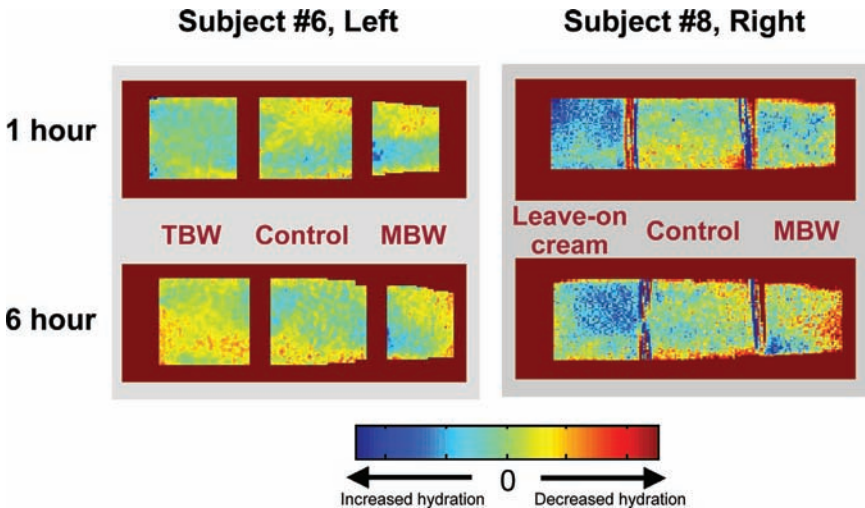


Figure 30.5 Leg images from a time moisturization study. (See p. 410)

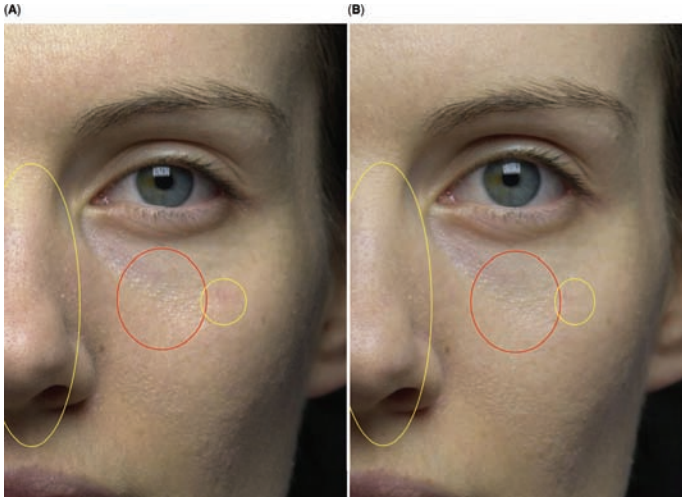


Figure 32.1 Subject imaged under D65 continuous lighting, perpendicular to subject's face (A) and 10 offset from perpendicular (to subject's left side) (B). Note differences in apparent texture (red circle line) and color (yellow circles). (See p. 430)



Figure 32.3 (A) Repositioning achieved by recalling a "ghost" image taken at the first visit, (B) live orientation of the subject's head, and (C) perfect realignment at a subsequent visit. (See p. 432)

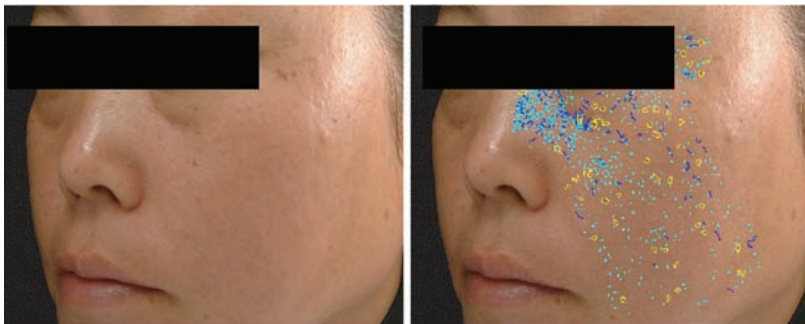


Figure 32.5 Example of a digital image taken during the ethnic aging study with pigmented spots (yellow), lines (dark blue), and visible pores (light blue) identified by image analysis within the region of interest (right). (See p. 435)

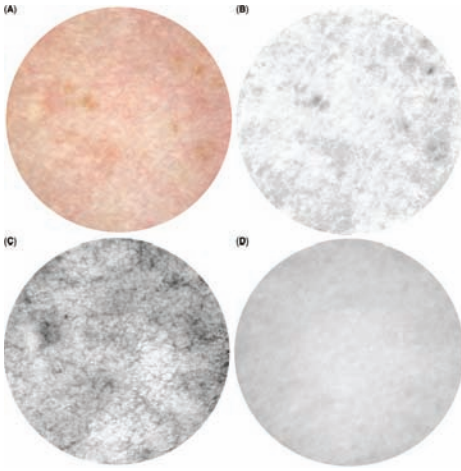


Figure 32.8 Example of contact SIAscope image and chromophore maps—(A) white-light image (12 mm diameter), (B) corresponding melanin map, (C) corresponding hemoglobin map, and (D) corresponding collagen map. (See p. 440)

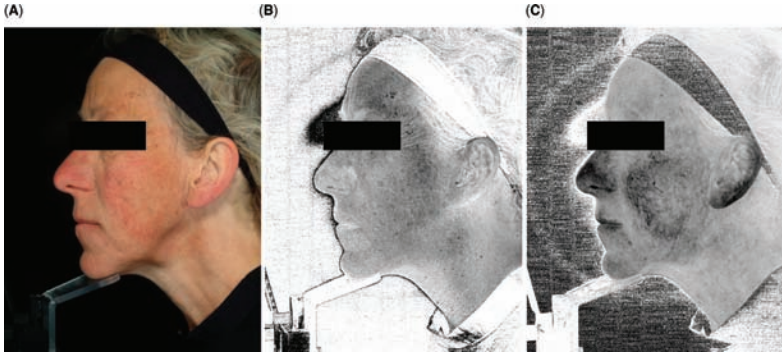


Figure 32.9 Noncontact SIAscope image and chromophore maps. (A) original cross-polarized white-light image; (B) corresponding melanin map; (C) corresponding hemoglobin map. (See p. 441)

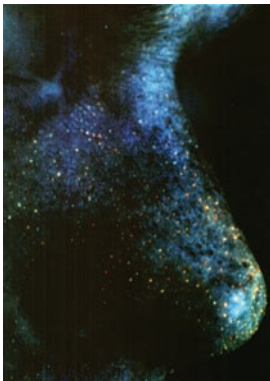


Figure 33.1 Wood's Light image of nose with UV sensitive film. Source: From Sauermaun et al. 1990. (See p. 449)

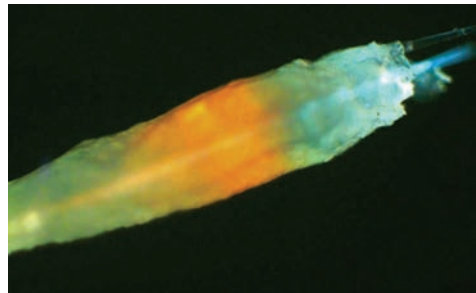


Figure 33.2 Sebaceous follicle under fluorescence microscope. (See p. 449)

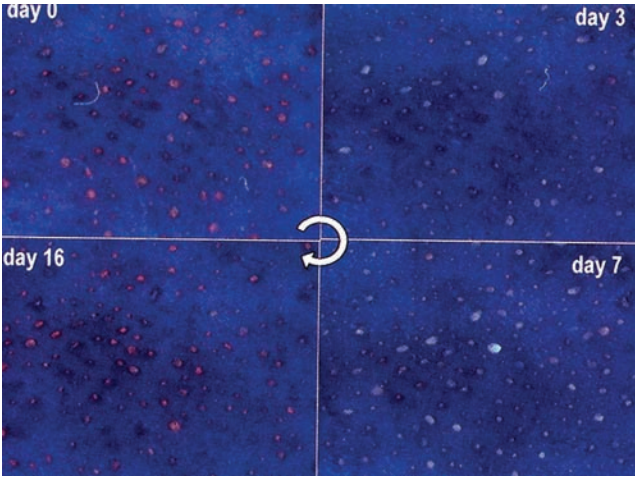


Figure 33.3 Digital fluorescence photography of the effect of benzoyl peroxide for seven days and recovery of protoporphyrin fluorescence after 16 days. (See p. 450)

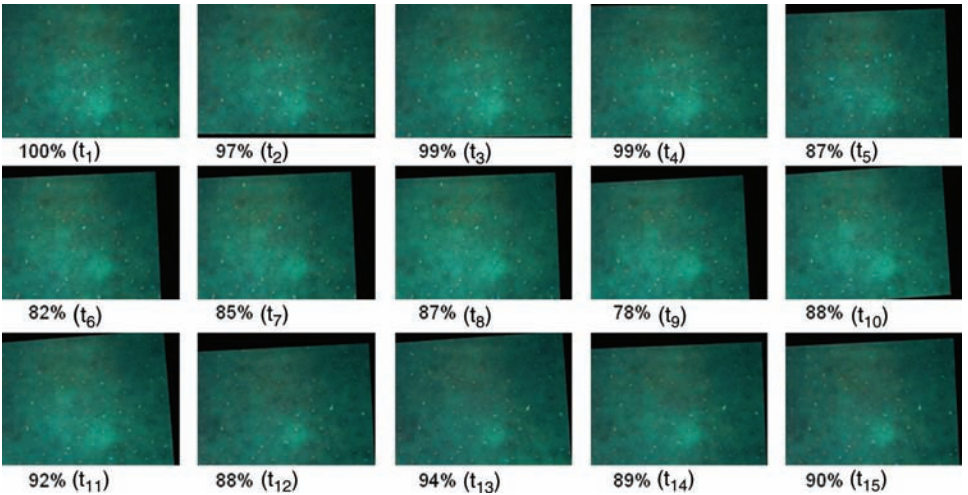


Figure 33.6 Time based shift of 15 consecutive measurements and correction by the neural software. (See p. 453)

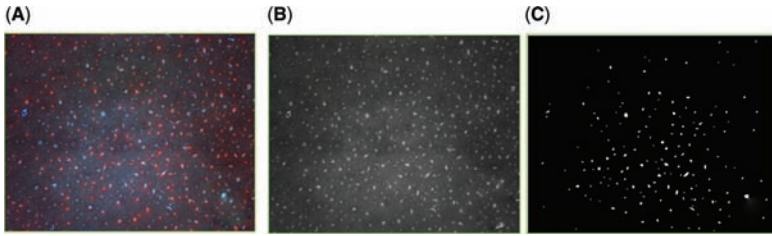


Figure 33.7 Image segmentation: (A) original, (B) grey transformed, and (C) segmented. (See p. 453)

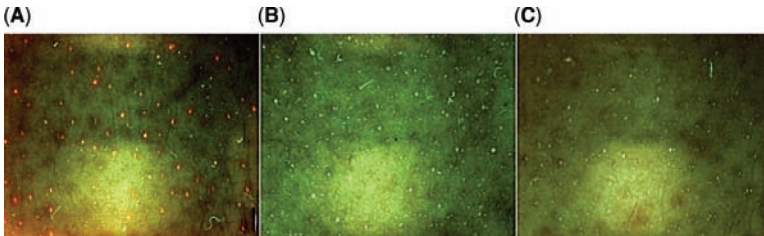


Figure 33.9 Effects of benzoyl peroxide (A) at the beginning (t_0 ; red/green 60/20), (B) 3 weeks (red/green 0/96), and (C) 6 weeks (red/green 0/30). (See p. 454)

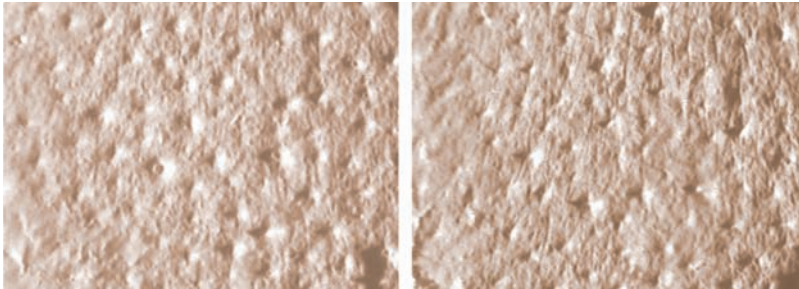


Figure 35.3 Silicone replicas capture pore refinement at baseline and eight weeks—Subject “29.” (See p. 471)

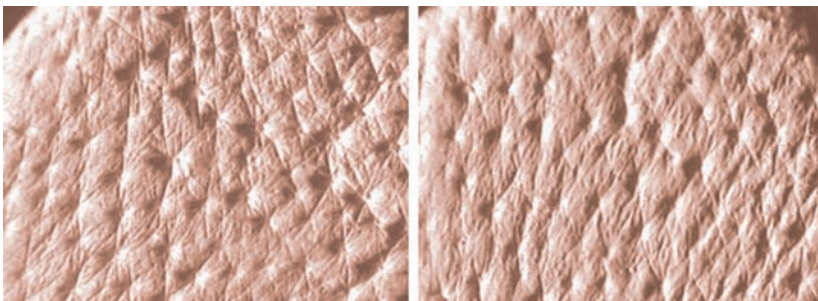


Figure 35.4 Silicone replicas capture pore refinement at baseline and eight weeks—Subject “49.” (See p. 471)

BIOENGINEERING OF THE SKIN

Skin Imaging and Analysis

Second Edition

DERMATOLOGY: CLINICAL & BASIC SCIENCE SERIES/31

Series Editor

Howard I. Maibach

about the first edition . . .

"...an indispensable manual for any cosmetic chemist and basic researcher who requires a specific technique to analyze changes in the skin surface."—*Doody's Reviews*

about the second edition . . .

Spanning the many advancements that have taken place in the field since the *First Edition* of this book was published, this *Second Edition* emphasizes the imaging of the skin in its entirety, rather than focusing solely on surface layers. The *Second Edition* includes new chapters on technologies such as in vivo confocal laser scanning microscopy, Raman spectroscopy, optical coherence tomography, nuclear magnetic imaging, high-resolution ultrasound, in vivo skin topometry, and multi-photon imaging of the skin.

Addressing engineering techniques for the visualization and analysis of skin surface images and profiles, this source offers comprehensive information on emerging instruments in the field and methods for their application in experimental studies—demonstrating why and when each technology or technique should be used in skin research and product testing...has updated and revised each chapter to remove outdated material, and include numerous photographs and illustrations...presents easily accessible information on currently available methods, covering the fundamental science, instrumentation, pitfalls, strengths, and specific applications relevant to the cosmetic industry...and includes multiple graphs, charts, comparative photographs, and analytical formulas, as well as an expansive display of current references.

about the editors . . .

KLAUS-P. WILHELM is extraordinary Professor of Dermatology at the University of Lübeck, Germany, and President and Medical Director of proDERM Institute for Applied Dermatological Research, Schenefeld/Hamburg, Germany. He is the Secretary of the International Society for Biophysics and Imaging of the Skin, and a member of several scientific associations and societies. He has published over 100 manuscripts and reviews and coauthored 2 books in the Bioengineering of the Skin series. Dr. Wilhelm received the M.D. degree from the Medical University of Lübeck, Germany.

PETER ELSNER is Professor of Dermatology and Chairman of the Department of Dermatology, University of Jena, Germany. The author of over 200 original articles and review papers and over 400 oral and poster presentations at scientific meetings worldwide, he is the author or editor of more than 20 books and special journal issues and serves as editor for the journals *Aktuelle Dermatologie* and *Exogenous Dermatology*. Dr. Elsner is past president of the International Society for Bioengineering and the Skin, board member of the German Society of Dermatology, and a member of more than 30 scientific societies and associations. He received the M.D. degree (1981) from Julius-Maximilians-University of Würzburg, Germany.

ENZO BERARDESCA is Director of Clinical Dermatology, San Gallicano Dermatological Institute, Rome, Italy. Dr. Berardesca was Chairman of the International Society for Bioengineering and the Skin (1990–1996). He is member of the editorial boards of *Skin Pharmacology*, *Skin Research and Technology*, the *American Journal of Clinical Dermatology*, and the *Journal of Cutaneous and Ocular Toxicology*. He is member of the Society for Investigative Dermatology, the European Society for Dermatological Research, and the Italian Group for Research on Contact Dermatitis, and vice-chairman of the European Group for Standardization of Efficacy Measurements of Cosmetics. Dr. Berardesca received the M.D. degree from the University of Pavia, Italy.

HOWARD I. MAIBACH is Professor of Dermatology at the University of California at San Francisco School of Medicine. The author of over 1700 papers in dermatology, toxicology, pharmacology, physiology, and related fields, he is the coeditor of several books including *Cosmeceuticals*; *Cutaneous Infection and Therapy*; *Cutaneous Infestations and Insect Bites*; *Neonatal Skin*; *Percutaneous Absorption*, *Third Edition*; and *Psoriasis*, *Third Edition* (all titles, Informa Healthcare). Dr. Maibach received the M.D. degree (1955) from Tulane University, New Orleans, Louisiana.

Printed in the United States of America

informa
healthcare
www.informahealthcare.com

270 Madison Avenue
New York, NY 10016
2 Park Square, Milton Park
Abingdon, Oxon OX14 4RN, UK

3817

ISBN 0-8493-3817-4

